

Understanding Synthetic Aperture Radar Images

**Chris Oliver
Shaun Quegan**



© 2004 by SciTech Publishing, Inc.
Raleigh, NC 27613

This is a corrected reprinting of the 1988 edition originally published by Artech House:
Boston.

All rights reserved. No part of this book may be reproduced or used in any form whatsoever
without written permission from the publisher.

Printed in the United States of America

10 9 8 7 6 5 4 3 2 1

ISBN: 1-891121-31-6

SciTech books may be purchased at quantity discounts for educational, business, or sales
promotional use. For information contact the publisher:

SciTech Publishing, Inc.
Raleigh, NC 27613
(919) 866-1501
www.scitechpub.com

Library of Congress Cataloging-in-Publication Data

Oliver, Chris

Understanding synthetic aperture radar images / Chris Oliver, Shaun Quegan.
Includes bibliographical references and index.

ISBN 1-891121-31-6

1. Synthetic aperture radar. I. Quegan, Shaun, 1949– II. Title.

TK6592.S95043 2004
621.3848—dc21

97-41709
CIP

To Betty and Sue, who understand

Foreword

Over the past few years, the development of spaceborne and airborne SAR systems for the observation of the Earth's surface has experienced a rapid growth. The ERS-1, JERS-1, ERS-2, and RADARSAT satellite systems have provided and continue to provide us with long time-series of high quality SAR data. At the same time, advanced airborne SAR systems exist in many countries of the world and provide multiple frequency and polarization observations for both civilian and military use. The SIR-C/X-SAR shuttle missions have widely demonstrated the advantages of having such multiple parameter systems in space.

Despite the enormous amount of available data, little effort has been expended in making use of the data in applications and scientific disciplines. To achieve this, both the physical content of the data and the information content of the SAR images, as well as the bridge between the two sources of information, must be understood by the users of Earth observation data.

While several early volumes in radar remote sensing covered either the physical content of SAR data, or the basics of SAR image formation and SAR image statistical properties, there is a strong need for an integrated book that brings together both the basic properties of SAR images related to image formation and those related to scene properties.

In this context, this book appears very timely to fill the above mentioned gap. It provides the readers with a synoptic understanding of SAR image fundamental properties; these are a prerequisite for the development of models and methods used in the interpretation and exploitation of SAR data for various applications.

This book deals with most aspects of SAR images on land surfaces and contains the most up-to-date coverage of the subject, including the underlying principles, recent developments, and future directions for research activities in this area. The subject is treated with the breadth and depth required for use as a reference text for graduate students, engineers, and application scientists. At the same time, the many illustrations of the underlying theoretical principles, contained in the different chapters, will certainly inspire the development of new tools and stimulate new practical applications of SAR images.

The authors have been leading authorities in the field for many years. Thus, the clear, thorough, and objective writing of the volume is a reflection of the authors' extensive experience as scientists and teachers. In addition, the authors have demonstrated that scientific texts can also be written in beautiful English language.

I am confident that this book will quickly become a well-read text for those interested in SAR images, and thus will contribute significantly to expand the effective use of SAR data in the observation and monitoring of the Earth's environment.

Thuy Le Toan
Toulouse, September 1997

Preface

The authors have been collaborating on SAR research since 1982, when Shaun Quegan joined Marconi Research Centre, Great Baddow, and Chris Oliver was at the Royal Signals and Radar Establishment, Malvern (later to become part of the Defence Research Agency (DRA), which is now the Defence Evaluation and Research Agency (DERA)). At that time the status of SAR as a means of producing images of the Earth's surface was very different from the present. Only the short-lived Seasat mission had provided spaceborne data, and few airborne systems were in operation. Images were not widely available (although the DRA X-band SAR provided us with a data source) and in most cases suffered from various types of defect. Image quality issues often overshadowed the task of information extraction so that, in common with many other researchers, we invested considerable time and effort on methods of data correction. The success of this work (such as the signal-based motion compensation schemes described in Chapter 3) in combination with significant progress in system engineering and calibration has ensured that close to ideal quality SAR data is now to be expected from modern systems. We have also seen the development of new techniques, such as polarimetric and interferometric SAR, and the advent of a diversity of SAR data providers, including spaceborne systems (ERS-1 and 2, JERS, and Radarsat) and flexible multifrequency polarimetric systems carried on aircraft or the Space Shuttle.

As the accent has changed from data correction, the information contained in SAR images has come to occupy its rightful place as the purpose of data acquisition. The investigation of methods for information extraction has formed the second and continuing strand in our long collaboration. In this we have been much helped by the complementarity of our interests. Chris Oliver

has primarily been concerned with the development of image-interpretation tools (usually for high resolution SAR in a military context), while Shaun Quegan has concentrated more on their impact on remote sensing applications. Necessarily, there has been significant overlap in our work. This combination of interests means that we can go some way towards crossing the cultural divides that hamper SAR development, in particular those that separate military from civil applications and applications from algorithm development.

Military applications are primarily concerned with detecting and recognizing targets, which usually demands imagery of the highest resolution. Civil applications, on the other hand, may require information about many diverse aspects of the environment, normally at lower resolution. The two have common ground in the need to understand the properties of distributed scatterers: in the military case because this constitutes the background clutter against which target detection takes place; in the civil case because this clutter is often the primary object of interest. More generally, both types of application have an interest in scene understanding. However, military needs, where cost may not have been a dominating issue, have given rise to sophisticated techniques that are potentially of considerable value to the civil field. These have become accessible due to the reduction in the cost of computing. Such is true of many of the developments described in this book.

The divide between remote sensing applications and algorithm development is symptomatic of the fact that SAR imaging presents many opportunities for formulating mathematical problems that can be pursued in an almost abstract way. Linking the problem and its solution to what is really needed by an application may be much harder; not enough attention has been paid to this issue. This does not mean that a rigorous approach should be avoided in the development of image-interpretation tools. On the contrary, such tools must be well grounded in the principles of optimization or conservation if they are to be of any general value. Ad hoc methods rarely prove robust. We tried to adopt such a rigorous approach throughout this book, but always with concern for validation of a technique and its relevance to applications.

In our attempt to bridge these cultural divides, the process of information extraction is viewed as a whole, from sensor parameters and their impact on image properties, through data models describing image statistics and the characteristics of the terrain, to the output information required by the application. This approach is tempered by our knowledge of the scattering process, based on physical understanding, models, and experimental findings. Such a complete view of what makes up the image is essential in identifying which properties of the scene affect the data. From this we can recognize those features (if any) that carry the information required by the application. The role of image analysis is to provide an optimum representation of these features. To achieve this, we

formulate a series of models that represent our best attempt to encapsulate the properties of the imaging process and those of the scene. Optimality can then often be defined in a framework such as that provided by a Bayesian analysis, although other criteria are possible. Always, the effectiveness of these optimal solutions must be judged by the user, whose requirements should impinge on every stage in the design of image-interpretation tools. Put briefly, we believe that these tools should be firmly based in an understanding of the nature of the SAR image; that their performance must be quantified and the best tools recognized; and that these best tools should be made available to the image interpreter, who is the final arbiter of their efficacy.

Although this sets out our philosophy, the reader may be helped by a more specific guide to the main structural components of the book. Fundamental aspects of how SAR images are formed, their basic characteristics arising from the imaging process, and their statistical properties are covered in Chapters 2, 4, and 5. These chapters underlie much of the later material. Chapter 3 is concerned with the recovery of nearly ideal images from imperfect systems; since its emphasis is on the SAR processing, it can be omitted by those readers interested only in working from the given data. Its purpose is to illustrate that current techniques should ensure that the data are of the highest quality. Image analysis tools for scene understanding in single-channel data form a central core of the book and are developed in Chapters 6 to 9. Chapter 10 deals with target detection in an overtly military context. The purpose of Chapters 11 and 12 is to cast much of the content of Chapters 5 to 9 into the forms required to handle multitemporal, multifrequency, polarimetric, and interferometric data and to explore the much enhanced range of information available when such multichannel data are available. Real examples and contact with applications are a recurrent theme throughout, but Chapter 13 becomes more closely oriented with applications because it considers image classification. This is a central concern in remote sensing. It provides a focal point where image analysis, physical understanding, scene properties, and user requirements all interact.

Finally, in Chapter 14 we present our view of the current status and prospects for further development. This ultimately depends on the extent to which the material of this book finds its way into applications. It will be obvious that currently available techniques show considerable promise and that in many cases preferred approaches can be identified. We hope that readers are persuaded to exploit the most powerful image analysis tools available, leading to more effective use of the data and thus allowing the analyst to concentrate more time on the real task of image interpretation. By the ensuing interplay of algorithms and applications, the shortcomings of our current understanding and methods will be exposed. This is the engine that will drive further development of techniques for extracting information from SAR images.

Acknowledgments

This book reflects many years of SAR research during which the authors have had the good fortune to work with, learn from, and disagree with each other and numerous associates at our own and other research establishments. It has been an exciting time. On many occasions we seem to have been forced back to re-examine our fundamental assumptions, often in heated discussion. One of the first questions we asked each other before this undertaking was, “Can you take criticism?” The give and take involved in being joint authors has only been possible because we thought (correctly) that the answer was “Yes.” This book represents the fruits of this often painful but ultimately rewarding interaction. We hope our efforts are better for it.

Chris would like to extend his grateful thanks to a large number of friends and colleagues in the DRA who have contributed to the research program. Chris Baker, Dave Belcher, Dave Blacknell, Alan Blake, Ian Finley, Andrew Horne, Richard White, and Jim Wood shared in the research into autofocus and signal-based motion compensation for SAR imaging. Dave Blacknell, Alan Blake, Eric Jakeman, Robert Tough, Keith Ward, and Richard White all contributed to the understanding of data models. Steve Luttrell provided exciting collaboration on super-resolution. Dave Blacknell, Alan Blake, and Richard White are all involved in despeckling filters and segmentation methods. Pierfrancesco Lombardo enjoyed a productive year at the DRA working on texture analysis before returning to the University of Rome, La Sapienza.

InfoSAR has been engaged in the development of real-time SAR autofocus processing and image-understanding techniques for the DRA. Chris would like to acknowledge the contributions of Mike Delves and Rod Cook, who are involved with the entire program; Keith Beckett and Gordon Pryde, who developed the real-time SAR processor and autofocus software; and Ian McConnell and Dave Stewart, who made significant progress in implementing and developing the image-understanding algorithms. Indeed, many of the algorithms described in this book, with subsequent development, are available in the InfoPACK software package from InfoSAR.¹

Chris would like to acknowledge the considerable investment made by the DRA and the Ministry of Defence, in terms of staff, equipment, and funding for the SAR research team. He is also grateful for the encouragement to undertake a review of the whole topic over the last two years that was initially reported in DRA Technical Reports Nos. DRA/LS2/TR96016 to 96021. Many illuminating discussions with Dave Blacknell and Richard White assisted in their preparation. Chapters 3 and 5 to 10 in this book are largely based on this material and are British Crown Copyright 1997/DERA (with the exception of Figures 6.12(a) and 8.1 and Table 10.2). So also are Figures 1.1, 4.1, 4.9, 12.11(d–j), and 12.12. These are published with the permission of the controller of Her British Majesty's Stationery Office.

Past and present members of Shaun Quegan's SAR Research Group within the Sheffield Centre for Earth Observation Science (SCEOS) contributed enormously to the overall research program and in putting this book together. Kevin Grover not only did most of the work on change detection in Amazonia but was willing to visit SCEOS long after his Ph.D. was completed in order to put the images in good order for Chapter 12. Jiong Jiong Yu is helping to extend the theoretical treatment of change detection and its applications. Ron Caves played a central role in developing algorithms for segmenting multidimensional SAR data and in producing quantitative measures of segmentation performance. Mike Preston moved this work forward on both fronts. Ian Rhodes, Coomaren Vencatasawmy, and Fraser Hatfield carried out much of the analysis of the MacEurope data; I am grateful to Coomaren for supplying Figure 11.6, which is taken from his M.Sc. dissertation. Mark Williams did much to improve our understanding of the relationship between backscattering models and image texture.

As far as the preparation of this book itself is concerned, we are grateful for many important contributions. From DRA, Alan Blake provided the image simulation and analysis software used throughout Chapters 5 to 9, Tony Currie

1. Many images from this book, as well as other examples, can be found at the InfoSAR website: <http://www.infosar.co.uk/>.

the interferometric image shown in Figure 4.9, and Mark Williams the simulation in Figure 5.8. Les Novak, of MIT Lincoln Laboratories, provided Table 10.2, which is taken from one of his many informative papers on target detection and recognition. A crucial input was that of Ian McConnell and Dave Stewart of N A Software who processed all the examples of reconstruction filters and segmentation algorithms illustrated in Chapters 6 to 8 as well as Figures 12.11 and 12.12. This involved a great deal of effort and was essential to the value of those chapters.

Special thanks must go to Mike Preston and Jiong Jiong Yu of SCEOS for producing many of the figures and displaying remarkable patience when Shaun realized he had asked for the wrong thing. Mike, in particular, devoted much time to solving the numerous problems that arose in getting images to Chris in the right form. Members of SCEOS were also willing to liaise with colleagues elsewhere who were kind enough to allow access to data and images. Geoff Cook-martin took care of the data provided by ESA-ESTEC that forms Figures 13.1 and 13.2. Jiong Jiong Yu did most of the hard work involved in transferring data from CESBIO and DCRS, while Mike Preston took the lead with ESA-ESRIN.

Shaun's unreserved thanks must go to Mari Bullock, who, as SCEOS secretary, not only typed his parts of the manuscript but also took care of so many of the detailed tasks involved in putting all the material together. Her initiative, care, and sheer devotion to getting the job done played a large part in making it possible. She also managed to run SCEOS very effectively while Shaun made himself incommunicado in order to write (which tells you something about how the organization really works).

A symptom of the coherence and sustained nature of the research program from which this book springs is the sharing of staff between SCEOS, DRA, and N A Software. DRA provided support for Dave Blacknell and Mark Williams while they worked in Sheffield; both are now at DRA, as is Kevin Grover. Ron Caves spent two years with N A Software before returning to Sheffield, and Ian McConnell joined N A Software from Sheffield.

The extent of the SAR research program within SCEOS would have been impossible without the continuing support of the UK Science and Engineering Research Council and later the National Environmental Research Council, when they took over responsibility for Earth Observation.

In preparing this manuscript we had tremendous help from colleagues in other research groups who have been willing to give data, advice, and time when we sought it, providing an excellent and refreshing example of the sense of community within the field.

From CESBIO, Toulouse, we must particularly thank Thuy Le Toan for advice that vastly improved Chapter 13 (though any blemishes are our responsibility) and for providing data. Florence Ribbes and Oscar Casamian did an excellent and difficult job in rendering color images into informative black-and-

white forms for our purposes. Their efforts became Figures 13.6 and 13.8. At a deeper level, Thuy's insistence on understanding what we see in SAR images was a continual spur to the spirit; she knows measurement is easier than knowing what we have measured.

The *Danish Center for Remote Sensing* (DCRS), *Department for Electromagnetic Systems* (EMI) of the *Technical University of Denmark* (DTU) provided help in two very substantial ways. First, they provided the EMISAR images; our thanks go to Soren Madsen for permission to use them and Erik Lintz for comments on the text while providing that permission. Second, much of the analysis of the EMISAR images was carried out by Jesper Schou of DCRS during a four-month individual course at Sheffield. Thanks must go to his supervisor, Henning Skriver, for instigating what turned out to be a very fruitful visit and to Jesper, for the quality of his work at Sheffield and his willingness to help in preparing material after his return to Denmark.

Colleagues from DLR who helped us include Richard Bamler and Manfred Zink. Richard supplied material on SAR processing and copies of unpublished work done with Keith Raney (now of Applied Physics Laboratory, Johns Hopkins University) on the linear system model for SAR imaging. Manfred gave advice on SAR calibration.

We have several reasons to thank the European Space Agency. First and foremost they supplied data. All the ERS images shown were provided by ESA. Those from the Tapajos site in Amazonia were given to us under the auspices of the TREES program organized by the Joint Research Centre of the European Union, Ispra, whose support we would like to acknowledge. All other ERS images were provided in the framework of the First ERS Announcement of Opportunity. In addition, ESA provided access to data from two airborne campaigns. The SAREX images used in Chapter 8 were collected in the framework of the ESA South American Radar Experiment, while the NASA/JPL AirSAR data informing Chapters 11 to 13 were acquired during the 1992 MacEurope campaign. In the latter case, ESA was a formal partner of NASA and we would like to thank both organizations. Other contributions to this book include Figures 13.1, 13.2, and 13.7, which are reproduced from ESA publications.

Individual ESA scientists also helped us greatly. Maurice Borgeaud of ESA-ESTEC made available the figures and data that form Figures 13.1 and 13.2. Henri Laur, Giorgio Emiliani, and Jose Sanchez of ESA-ESRIN provided the imagery and the calibration target analysis shown in Figure 2.9. In both cases, this was not straightforward and we gratefully acknowledge the time and effort expended on our behalf.

Most of the work we describe using data from the Tapajos site would not have been possible without the support of colleagues in the *Instituto Nacional Pesquisas Espaciais* (INPE), Sao Jose dos Campos, Brazil. Special thanks must go

to Corina Yanasse for many years of advice, discussion, and help. We are indebted to Sidnei Sant'Anna, Alejandro Frery, and Corina for permission to use Figure 13.7. This opportunity to display information on forest types using texture measured from the Radarsat satellite arose only a week before completion of the manuscript during a visit to Sheffield by Corina and Sidnei, and we were delighted by it. More generally, effective collaboration with INPE was greatly aided by discussion and material help from Luciano Dutra and Thelma Krug.

Shaun must give particular thanks to Rob Brooks, Ralph Cordey, and Paul Saich of Marconi Research Centre, Great Baddow. Rob introduced me to the fascinating field of SAR research. Ralph has been a continual source of critical appraisal, encouragement, and financial support and he and Paul have been welcome collaborators on several projects. MRC must also be thanked for seconding Dave Blacknell to Sheffield for the duration of his doctoral studies.

This book would never have been completed (almost) on schedule without the continual involvement of Susanna Taggart at Artech House in London. She managed to make her demands in such a pleasant manner that it was impossible to take offense.

When he started writing this book Chris had no conception of the demands it would make on his time and energy. He especially wishes to thank his wife Betty for her understanding and patience over the whole period, but particularly the last few hectic weeks. In contrast, Shaun knew perfectly well what was involved and went like a lamb to the slaughter. He has no words that can do justice to the forbearance of his wife Sue.

About the Authors

After earning a degree in physics from Worcester College, Oxford, **Chris Oliver** conducted his doctoral research into low-energy nuclear structure at Liverpool University. In 1967, he joined the photon statistics group at the *Royal Signals and Radar Establishment* (RSRE), Malvern [later the *Defence Research Agency* (DRA) and now the *Defence Evaluation and Research Agency* (DERA)]. He was one of the joint inventors of the technique of single-clipped photon-correlation spectroscopy exploited in the Malvern Correlator, for which he won the MacRobert Award for Engineering Achievement in 1977.

Chris Oliver led a section at the DERA (Malvern) undertaking long-term research on the extraction and processing of information from SAR images since 1981; from 1991 until 2000, he took on a consultancy role to free him from management responsibilities. He was appointed Visiting Professor of Physics at King's College London in 1987. In 1996, he was invited to become a Visiting Professor in Electronic Engineering at University College, London. He has also been a Visiting Professor at "La Sapienza," the University of Rome, in 1999 and 2001.

Chris Oliver has published in excess of 100 papers and holds 7 patents, many in both Europe and the United States in addition to the United Kingdom. His academy status was recognized within the DERA, where he was an Individual Merit Deputy Chief Scientific Officer. In 2000, he was appointed a Commander of the British Empire (CBE) in Her Britannic Majesty the Queen's Birthday Honors as recognition of his contribution to radar. Since his retirement, Chris has set up InfoSAR Ltd. (www.infosar.co.uk), which offers consultancy and training in SAR exploitation. The company has produced a SAR image interpretation software suite, InfoPACK, which exploits and extends the principles described in this book and offers significantly greater sensitivity than any others.

Shaun Quegan received his BA in mathematics in 1970 and M.Sc. in mathematical statistics in 1972, both from the University of Warwick. After teaching for several years (and running a large mathematics department) an ever-growing interest in physics led him to undertake research into large-scale modeling of the ionosphere and upper atmosphere at the University of Sheffield, leading to a Ph.D. in 1982. He then joined Marconi Research Centre as a research scientist, becoming Remote Sensing Applications Group Chief in 1984. This was a fortunate opportunity to work with an excellent team involved in SAR research, from which many fruitful long-term collaborations sprung, including that with Chris Oliver. The offer of a post at the University of Sheffield in 1986 provided an chance to build an academic SAR research group, whose activities have flourished. In 1993 he was awarded a professorship, in the same year helping to instigate the Sheffield Centre for Earth Observation Science and becoming its first director. In this role he plays a central part in coordinating and developing the wide range of remote sensing skills in the University and in bringing them to bear on environmental science and application problems.

Contents

<i>Foreword</i>	xvii
<i>Preface</i>	xix
<i>Acknowledgments</i>	xxiii
<i>About the Authors</i>	xxviii
1. Introduction	1
2. Principles of SAR Image Formation	11
2.1 Introduction	11
2.2 SAR System Parameters	12
2.3 The Range Dimension – Processing a Single Pulse	14
2.4 Linear FM (Chirp) Pulses and Pulse Compression	18
2.5 The Azimuth Dimension	25
2.6 SAR as a Linear Measurement System	29
2.7 Calibration	34
2.8 Summary	38
References	39
Appendix 2A Azimuth Processing for an Orbital SAR	40
3. Image Defects and Their Correction	43
3.1 Introduction	43
3.2 Defocus	45
3.2.1 Autofocus Methods	48

3.2.2	Limiting Accuracy of Autofocus Techniques	52
3.2.3	The Effect of Scatterer Properties on Autofocus	53
3.3	Geometric and Radiometric Distortion	55
3.3.1	Physical Cause and Associated Distortion	55
3.3.2	Signal-Based MOCO	58
3.3.3	Antenna Stabilization	59
3.4	Residual SAR Imaging Errors	60
3.4.1	Residual Geometric and Radiometric Distortion	60
3.4.2	Excess Sidelobe Levels	62
3.5	Refinements to Signal-Based MOCO	63
3.5.1	Iterated Autofocus with Phase Correction	63
3.5.2	High-Frequency Tracking with Low Distortion	64
3.5.3	Combined Signal-Based and Conventional MOCO	66
3.6	Conclusions	69
	References	72
4.	Fundamental Properties of SAR Images	75
4.1	Introduction	75
4.2	The Nature of Information in SAR Images	77
4.3	Single-Channel Image Types and Speckle	84
4.4	Estimating the RCS: Multilook Data	93
4.5	The Multiplicative Noise Model for Speckle	96
4.6	Estimating the RCS – the Effects of Imaging and Noise	99
4.7	Consequences of the Imaging Model for SAR Measurements	102

4.8	The Effects of Spatial Correlation on Multilooking	105
4.9	Compensating for System-Induced Spatial Correlation	107
4.9.1	Subsampling	107
4.9.2	Pre-Averaging	108
4.9.3	Interpolation	109
4.10	Estimating Spatial Correlation: Stationarity and Spatial Averaging	110
4.11	Limitations in the Speckle Model	113
4.12	Multidimensional SAR Images	114
4.13	Summary	118
	References	119
5.	Data Models	123
5.1	Introduction	123
5.2	Data Characterization	126
5.3	Empirical Data Distributions	128
5.4	The Product Model	130
5.4.1	The RCS Model	131
5.4.2	The Intensity PDF	133
5.5	Comparison of Distributions	135
5.6	Imaging RCS Fluctuations with Finite Resolution	138
5.7	Limitations of the Data Model	142
5.8	Simulation	145
5.9	Conclusions	151
	References	154
6.	RCS Reconstruction Filters	157
6.1	Introduction	157
6.2	The Speckle Model and Quality Measures	159
6.3	Bayesian Reconstruction	161

x Contents

6.4	Reconstruction Using the Speckle Model	162
6.4.1	Multilook Despeckling	162
6.4.2	Minimum Mean-Square Error Despeckling	164
6.5	Reconstruction Using the RCS Model	165
6.5.1	Gamma MAP Despeckling	166
6.6	Correlated Neighborhood Model	167
6.6.1	Correlated Neighborhood ML (CML) Despeckling	168
6.6.2	Correlated Neighborhood Gamma MAP (CMAP) Despeckling	169
6.7	Structural Adaptive Filtering	170
6.8	Reconstruction Using Nonlinear Iterated Processing	171
6.8.1	Iterated MMSE Despeckling	171
6.8.2	Iterated Gamma MAP Despeckling	172
6.8.3	Iterated Correlated Neighborhood ML (CML) Despeckling	173
6.8.4	Iterated Correlated Neighborhood Gamma MAP (CMAP) Despeckling	174
6.9	Reconstruction by Iterating the Structured Neighborhood Model	175
6.9.1	Simulated Annealing and the Structured Neighborhood Model	176
6.9.2	Constant RCS Model	179
6.9.3	Sloping RCS Model	180
6.9.4	Discussion of Structured Annealing Results	181
6.10	Comparison of Reconstruction Algorithms	184
6.10.1	Image Quality	184
6.10.2	Execution Times	187
6.10.3	Algorithm Selection	188

6.11	Discussion	189
References		192
7.	RCS Classification and Segmentation	195
7.1	Introduction	195
7.2	RCS Classification	195
7.3	The Cartoon Model and Segmentation	197
7.3.1	Edge Detection	199
7.3.2	Region Merging	202
7.3.3	ML Split/Merge Theory	203
7.3.4	Implementation of ML Split/Merge Theory	207
7.3.5	Region Fitting	208
7.4	Comparison of Segmentation Algorithms	212
7.4.1	Image Quality	212
7.4.2	Execution Times	217
7.4.3	Algorithm Selection	217
7.5	RCS Exploitation	218
7.5.1	Algorithm Properties	218
7.5.2	Application Example	221
References		225
8.	Texture Exploitation	229
8.1	Introduction	229
8.2	Model-Free Texture Exploitation	231
8.2.1	The Kolmogorov-Smirnov Test	231
8.2.2	Estimating Moments	232
8.2.3	Optimum Selection of Moments	234
8.2.4	Estimating the PDF	235
8.3	Model-Based Texture Parameter Estimation	235
8.3.1	Derivation of MLEs for Different PDFs	236

8.3.2	Uncertainty in Order Parameter Estimates	240
8.3.3	Texture Estimation Example	244
8.4	Texture Classification	245
8.4.1	Classification by Fitting	245
8.4.2	Direct Classification	246
8.4.3	Annealed Texture Classification	247
8.5	Texture Segmentation	249
8.5.1	Edge Detection	249
8.5.2	Model-Based Segmentation	251
8.5.3	Annealed Segmentation	251
8.6	Discussion	253
	References	255
9.	Correlated Textures	259
9.1	Introduction	259
9.2	Model-Based Parameter Estimation	261
9.3	Texture Classification	266
9.3.1	Classification by Fitting	266
9.3.2	Direct Spectrum Classification	266
9.4	ML Correlated Texture Edge Detection	271
9.4.1	ML Edge-Detection Theory	271
9.4.2	Edge-Detection Performance	272
9.5	Discussion	274
	References	275
10.	Target Information	277
10.1	Introduction	277
10.2	Introduction to Target Detection	279
10.3	Constant Target and Background RCS	282
10.3.1	Standard CFAR Target Detection	282
10.3.2	Optimized Target Detection	284

10.4	Effect of Background and Target Statistics	285
10.4.1	Standard CFAR Target Detection	287
10.4.2	Optimized Detection for the Textured Target Model	289
10.5	Further Refinements to Target Detection	294
10.6	Introduction to Target Recognition	296
10.7	Target Discrimination	299
10.8	Target Classification	305
10.9	Target Super-Resolution	308
10.9.1	Super-Resolution Theory	308
10.9.2	Super-Resolution Example	311
10.9.3	Conclusions about Super-Resolution	313
10.10	Summary	313
	References	315
11.	Information in Multichannel SAR Data	319
11.1	Introduction	319
11.2	Polarimetric Measurements	320
11.3	Polarimetric Data Distributions	322
11.3.1	Theoretical Formulation	324
11.3.2	Relation to the One-Dimensional Multiplicative Noise Model for Speckle	326
11.4	The Multidimensional Gaussian Distribution	328
11.4.1	Real and Complex Gaussian Distributions	332
11.4.2	Moments	333
11.5	Single-Look Distributions Involving Two Polarimetric Channels	333
11.6	Properties of the Distributions	336
11.6.1	The Phase Difference Distribution	336
11.6.2	The Amplitude Ratio Distribution	340

11.7	Estimation of Polarimetric Parameters	341
11.7.1	The Multilook Phase Difference Distribution	344
11.7.2	The Multilook Coherence Distribution	345
11.7.3	The Multilook Intensity Ratio	346
11.8	The Stokes Scattering Operator Formulation of Polarized Scattering	347
11.9	Texture in Polarimetric Data	350
11.9.1	Multilook Textured Data	351
11.9.2	Parameter Estimation	351
11.9.3	Texture Observations in Polarimetric Data	352
11.10	Interferometric, Multifrequency, and Multitemporal Data	355
11.11	Summary	356
References	357
Appendix 11A	Number Fluctuations and the Generalized Product Model	360
12.	Analysis Techniques for Multidimensional SAR Images	365
12.1	Introduction	365
12.2	Polarimetric Reconstruction Filters	367
12.2.1	Multilook Reconstruction	368
12.2.2	MMSE Reconstruction	368
12.2.3	Gamma MAP Estimation	373
12.3	Speckle Reduction by Polarimetric or Multichannel Filtering	375
12.3.1	Using Covariance Matrix Data	375
12.3.2	Using Intensity Data Only	380
12.3.3	Principal Components Analysis in Multichannel SAR Data	383

12.4	Measuring and Detecting Differences between Two Images	385
12.4.1	Pixel-Based Change Detection	385
12.4.2	Area-Based Difference Measures	388
12.5	Multichannel Segmentation	391
12.5.1	Multidimensional RGW Segmentation	393
12.5.2	Multidimensional Annealed Segmentation	395
12.6	Comparison of Algorithms – A Case Study	399
12.7	Concluding Remarks	409
	References	409
13.	Classification of SAR Imagery	413
13.1	Introduction	413
13.2	The Empirical Basis for Classification	416
13.2.1	Spaceborne Multitemporal Data	418
13.2.2	Polarimetric Data	421
13.2.3	Texture in Classification	425
13.3	Decision Rules for Classification	426
13.4	Data-Driven Methods of Classification	427
13.4.1	Gaussian MAP Classification	427
13.4.2	Single-Frequency Polarimetric Classification	430
13.4.3	Repeat-Pass Interferometry	430
13.4.4	Uncorrelated Channels	431
13.4.5	Applications of MAP Classification	432
13.4.6	Other Data-Driven Approaches	433
13.5	Classification Based on Scattering Mechanism	434
13.6	Knowledge-Based Classification	437
13.7	Using SAR Properties to Refine a Classification	442
13.8	Concluding Remarks	444
	References	445

14. Current Status and Future Prospects	451
14.1 Introduction	451
14.2 Are the Models Complete?	453
14.3 Are the Models Accurate?	456
14.4 Are the Models Tractable?	456
14.5 Are the Models Useful?	457
14.6 Future Developments	459
References	461
Index	465

1

Introduction

In the last few years, high quality images of the Earth produced by *synthetic aperture radar* (SAR) systems carried on a variety of airborne and spaceborne platforms have become increasingly available. Two major leaps forward were provided by the launch of the ERS-1 satellite by the European Space Agency in 1991 and the advent of very flexible airborne systems carrying multifrequency polarimetric SARs, of which the NASA/JPL AirSAR provides perhaps the single most influential example. These systems ushered in a new era of civilian radar remote sensing because of their emphasis on SAR as a measurement device, with great attention being paid to data quality and calibration. This emphasis continues to play a major part in the development, deployment, and application of current systems.

ERS-1 was the first in a series of orbital SARs planned to have long lifetimes and semioperational capabilities. The JERS-1, ERS-2, and Radarsat satellite systems are currently in orbit, with ENVISAT planned for launch in 1999. By providing a long time series of accurate measurements of the backscattering coefficient, these satellites allow dynamic processes to be observed over most of the Earth's surface, with impacts in many areas, such as vegetation mapping and monitoring, hydrology, sea-ice mapping, and geology. The unique capability of SAR to exploit signal phase in interferometry has given rise to completely new tools for glaciology and the study of tectonic activity.

Because of the constraints imposed by deploying a radar in space, these systems are simple, in the sense of using single frequencies and polarizations with modest resolution. By contrast, airborne systems have been able to demonstrate the advantages of having multiple frequencies and polarizations avail-

able. These advantages were further demonstrated, but from space, by the SIR-C/X-SAR mission of the Space Shuttle. In addition, the AirSAR system indicated that longer wavelength radars can have a special role in Earth observation due to their ability to penetrate vegetation canopies and interact with structural elements of trees and the underlying soil. Much longer wavelength systems are now in operation and promise to provide effective methods for reconnaissance and remote sensing over heavily vegetated areas.

While civilian systems have concentrated on radiometric accuracy and investigation of natural targets, the priority of military systems is the detection and recognition of man-made targets (often vehicles) against a clutter background. The need for rapid reconnaissance has placed considerable emphasis on airborne systems that can be deployed on demand. By its nature, the military recognition task usually demands resolution better than 1m and systems that can operate at long range, for survivability. These two requirements enforce long synthetic apertures that, because airborne systems are preferred, have needed the development of sophisticated *motion-compensation* (MOCO) techniques.

While an enormous amount of effort has been expended on systems to acquire SAR data, comparatively little has been expended on making the best use of those data. Two lines of attack are needed to achieve this. One is the investigation of the physical content of the data, by means of experiment, observation, and modeling. The other is to examine the actual properties of the data in light of what is known about the physics, the general properties of the world, and the applications of interest, to identify and extract optimal estimates of the information-bearing components of the data. This bridging role between what we know about the data and how we best get at the information they contain is the subject of this book.

Radar systems are capable of producing very high quality images of the Earth, as demonstrated by the high-resolution image shown in Figure 1.1. In order for this imagery to have value it must be interpreted so as to yield information about the region under study. An image analyst soon learns to recognize features such as trees, hedges, fields (with internal structure and texture), shadows, and buildings, which encompass a range of natural and man-made objects. However, it is a time-consuming task to extract the information, particularly when large areas must be examined. Furthermore, there is no guarantee of consistency between analysts or measure of the performance they achieve. These limitations motivate the search for automatic algorithms to derive the relevant information more quickly and reproducibly, or, in some circumstances, more sensitively.

The need for automatic or semiautomatic methods becomes even more pressing when polarimetric, multifrequency, and/or multitemporal images are

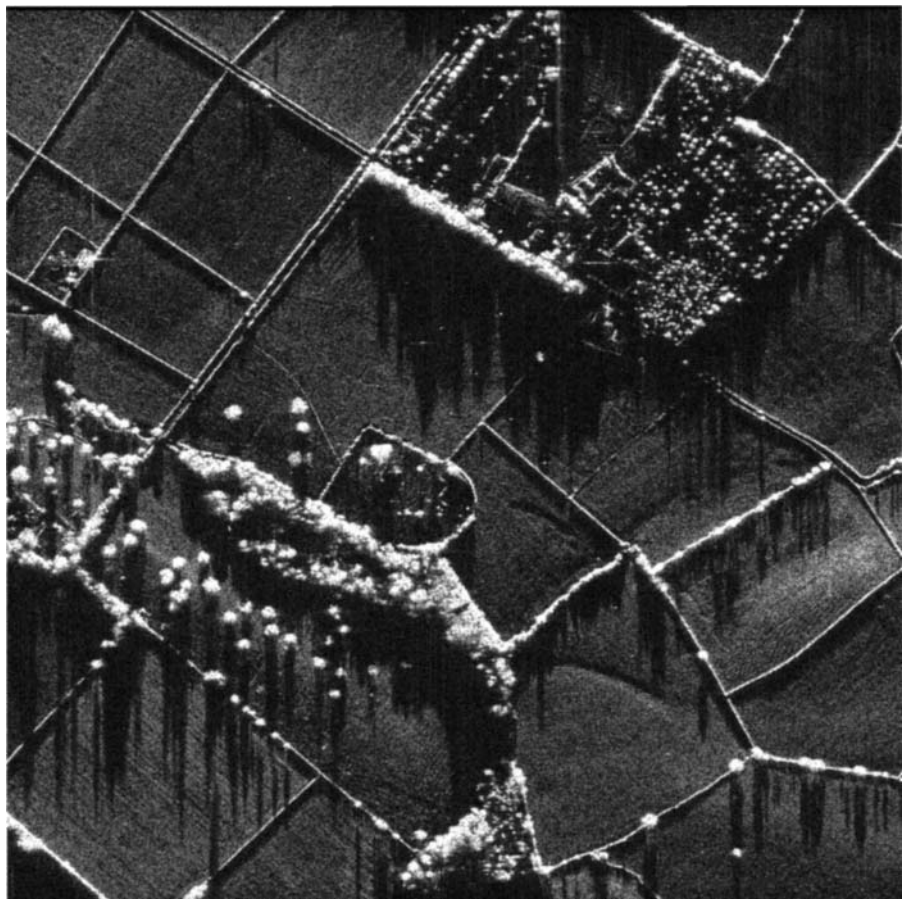


Figure 1.1 High-resolution ($< 1\text{m}$) DRA X-band SAR image of typical rural scene. (British Crown Copyright 1997/DERA.)

available. For such multidimensional data it is first necessary to define the quantities to be made available to the analyst: which parameters carry the information? When there are more independent pieces of information at each pixel than can be sensibly represented, for example, by color overlays, how should the data be organized and displayed to pick out its salient points? In such circumstances, it may be better to let some of the decisions be made automatically as long as they have a solid basis in understanding how information is embodied in the data. This is particularly true when there are time constraints and large amounts of data to analyze.

Automatic image understanding must take place on two different scales.

- Low-level analysis provides a series of tools for identifying and quantifying details of *local* image structure.
- High-level analysis then uses this detail to construct a *global* structural description of the scene, which is the information required by the image analyst.

Note that low-level algorithms are not sufficient; local details have to be incorporated into some overall form of understanding. This demands methods for overcoming defects in the detailed picture, for example, by joining edges across gaps or merging regions where appropriate. On the other hand, sophisticated high-level techniques are of no value if the underlying tools are incapable of bringing out the information with sufficient sensitivity. The aim of this book is to develop and relate the tools needed at both these levels. It is comprised of the following six principal components:

- The imaging process (Chapters 2 and 3);
- Properties of SAR images (Chapters 4 and 5);
- Single-image exploitation (Chapters 6 to 10);
- Multiple-image exploitation (Chapters 11 and 12);
- Application in image classification (Chapter 13);
- Further developments (Chapter 14).

Radar images have properties that are unfamiliar to those of us more used to optical data and photographs. Anyone intending to make effective use of SAR needs to understand and appreciate some of these basic properties. Those connected with the sensor-scene geometry and the signal processing involved in image formation are described in Chapter 2. Here the basic principles of SAR image formation are outlined and used to define two fundamental characteristics of the system and the impact they have on the images being produced. The first of these is the spatial resolution of the imagery. The azimuth resolution of the SAR is independent of range, but the range resolution varies with position if an image is displayed in a map reference frame. This has important consequences for the visibility of objects in the images and the number of pixels available to measure their properties. The second fundamental quantity is the *point spread function* (PSF), which determines the correlation and sampling properties of the imagery. It is an essential concept when describing the properties of images of both point and distributed targets. The

interplay of these two generic target types is shown to be central in calibrating the SAR. Calibration is essential if accurate measurements of the geophysical quantities known as the radar cross section and radar backscattering coefficient are to be made. Only by working in terms of such sensor-independent quantities can measurements from different sensors, images gathered at different times, or measurements from different parts of an image be sensibly compared.

The treatment in Chapter 2 assumes an ideal SAR system, but, in practice, images can suffer from a number of defects. Inadequate calibration leading to radiometric or phase distortion forms only part of the problem. Particularly for airborne systems, unknown or uncorrected perturbations of the sensor position (on the scale of fractions of a wavelength) about its expected trajectory can cause defocusing, geometric and radiometric distortion, and increased (unpredictable) sidelobe levels. In Chapter 3 we show how autofocus techniques can be combined with a simple dynamics model for the sensor platform to recover nearly ideal image quality, as epitomized by Figure 1.1. This signal-based motion-compensation scheme is equally applicable to airborne and satellite systems. Chapter 3 is atypical in that the techniques it describes use the raw (unprocessed) SAR data, whereas elsewhere we start from image data. However, it should be noted that the methods involve postprocessing algorithms that can be applied whenever full bandwidth complex data are available. For example, they are applicable in principle to the ERS-1 SLC product. Readers with no desire to become embroiled in the details of SAR processing may prefer to ignore this chapter. They should nonetheless be aware that images of the highest quality can be routinely produced, even by airborne systems operating at high resolutions and long ranges, by making use of the techniques set out here. This is particularly important where high-resolution data are essential to enable the detailed structure and position of objects within the scene to be determined.

Succeeding chapters deal with the issue of extracting information from the images themselves. Chapter 4 is concerned with the fundamental properties of SAR images and how we represent the nature of information within them. It sets up a framework within which the properties of the data are described in a series of physical and empirical models (*data models*). Prior knowledge is encapsulated in a series of *world models* that can be applied to different image-interpretation functions. Both types of model can be combined in a Bayesian approach in which the output takes the form of a *maximum likelihood* (ML) or *maximum a posteriori* (MAP) solution, given the data and the world models.

After setting up this framework, we examine the consequences of the fact that the SAR is a linear measurement system providing an estimate of the complex reflectivity at each pixel. There are then various ways of representing the SAR data, all based on the complex image. These different image types all contain different manifestations of the phenomenon known as speckle, which

results from interference between many random scatterers within a resolution cell. Speckle influences our ability to estimate image properties and thus is central to information retrieval from individual SAR images. For many purposes the phase inherent in the single-look complex imagery carries no useful information and can be discarded. The information at each pixel is then carried by the *radar cross section* (RCS) or *backscattering coefficient* σ^0 . For distributed targets, where resolution is not a critical issue, discarding the phase allows for the incoherent averaging of pixels or independent images to provide better estimates of σ^0 (a process known as multilooking). Finally, we introduce the image types that become available when multichannel data are available. In doing so, the nature of speckle as a true electromagnetic scattering phenomenon becomes manifest through its exploitation in polarimetry and interferometry.

Figure 1.1 indicates that information about the scene is contained in the variations of the RCS. These can be at large scales (e.g., the hedgerows, shadows, and bright areas of woodland present in this image) or at a smaller scale where they provide a textural effect within a single type of land cover. In Chapter 5 we discuss models that describe this latter type of image property. Most importantly, we introduce the product model that describes SAR images, particularly those arising from natural clutter, as a combination of an underlying RCS and speckle. A gamma-distributed RCS is shown to lead to a K-distributed intensity or amplitude that provides a good description of many natural clutter regions. This model provides the crucial component in our approach to extracting information from single SAR images, as described in Chapters 6 to 10.

From Figure 1.1 it is obvious that the overall structure in the scene is dominated by the deterministic manner in which the RCS varies as a function of position. Strong returns correspond to identifiable objects, such as individual trees. In Chapter 6 we introduce a series of world models (discussed in Chapter 4) and exploit them in reconstructing this deterministic RCS by separating it from the speckle. In Chapter 7 we introduce the cartoon model, which asserts that the image is made up of regions of constant RCS, leading to segmentation. The role of the exploitation tool is then to define the position and strength of the different segments within the scene. We compare both the reconstructions (from Chapter 6) and the segmentations (from Chapter 7) in terms of a quality measure based on the speckle model. This enables a quantitative assessment of the different algorithms to be made.

The underlying variation of RCS is not the only source of information within a SAR image. Many of the fields in Figure 1.1 show texture, corresponding to plowed furrows. In this context the *presence* of furrows, indicating a property of the field, is often more important than their individual *positions*. The same is true for many types of natural clutter, such as woodland. Again, we are not so much concerned with the positions of individual trees but with the

texture properties that characterize large regions of woodland. These properties, encapsulated in the single-point statistics (described in Chapter 8) and the correlation properties (discussed in Chapter 9), can then be exploited for region classification or segmentation.

In Chapter 10 we introduce a new model that is intended to describe man-made objects, such as targets in a military application. Extracting information about these can be factorized into processes of detection, discrimination, and classification. These functions operate on the detailed local level to provide a global picture of the presence of targets within the scene. Initially we introduce a Bayesian treatment of target detection and apply it to a uniform or textured RCS applied to both background and targets. We discuss suitable simple discriminants capable of rejecting false detections, leading to a formulation of classification based on a Bayesian approach. In practice, this may be too complicated and associated suboptimum classifiers may be preferable. Man-made objects generally comprise only a few individual scatterers, so the deterministic interference between these becomes crucial. This can be exploited in superresolution.

Earlier chapters deal with individual SAR images for which speckle can be treated as a noiselike phenomenon dominating information extraction. However, increasingly important are multichannel data in which images of the same scene are acquired under different operating conditions. Multidimensional data types form the subject matter of Chapter 11. We concentrate initially on the properties of polarimetric SAR, since this type of data illustrates many of the major issues involved in combining images, in particular those properties associated with interchannel coherence. As would be expected, the existence of extra channels provides an enhanced capacity for extracting information from the images. Indeed, fully polarimetric systems provide a complete description of the scattering properties of the scene for a given operating frequency. Physically, different polarization configurations interact differently with the various components of the scattering medium. Particularly when used in combination with frequency diversity, polarization provides a means of probing the physical properties of the medium. We provide strong theoretical and experimental evidence to illustrate that the one-dimensional product model for texture extends readily to polarimetric data, and this reveals that the multidimensional Gaussian model plays a central role in representing the data. All the important image types needed to capture the information in the data follow immediately from this data model. We examine the properties of these images and develop a complete theory of the distributions involved, including the estimation properties of the important parameters. These theoretical results are verified by comparison with measurements from multifrequency polarimetric systems. We also develop the theory needed to take account of fluctuations in the number of scatterers

contributing to the polarimetric signal and examine the textural information present in data as a function of frequency. Finally, the theory developed for polarimetric data is related to other multifrequency data types, in particular those encountered in interferometric, multifrequency, and multitemporal images.

Chapter 12 is concerned with using the image model derived and verified in Chapter 11 to develop techniques for extracting information from a variety of multidimensional images. We first deal with the tools needed to estimate the key parameters defined by the product model. These are very much based on methods developed for single-channel data; it is very satisfying to see how readily these extend to higher dimensional data. However, the extension is not entirely straightforward. In particular, the concept of speckle that permeated almost all the work for single-channel data has no obvious counterpart in higher dimensions, unless all the channels are uncorrelated. This changes the nature of some of the optimization problems that must be posed and solved to get at the information in the data. However, the distinction between structural and parametric information that runs as a thread through all the work on single channels is just as pertinent here. Methods are described that improve our ability to perceive structure, by forming intensity images with reduced normalized variance compared with single-channel speckle. Change detection is an important process when handling multiple images gathered at different times. This is, in principle, a higher level process since it exploits joint properties of different images. The information in this type of data can take two forms: statistical information that describes individual regions, such as the return from a distributed target, and structural information that is concerned with the boundaries between these regions. We show how the type of information required has a direct impact on the methods used to interpret the data. The ultimate test of any image-understanding technique is the extent to which it brings out the information required in a given application. A high-level approach is adopted in Section 12.6, which describes a case study comparing the ability of different algorithms to provide useful information in tropical forest monitoring.

Throughout this book our approach consists of building optimized tools for information extraction based on our best understanding of the data and world models underlying the observations. These are continually modified as we apply them to real data and assess their performance. A focal point of this effort occurs in Chapter 13, which addresses one of the central issues for many applications, namely, image classification. Here much of our work on learning image structure and making optimal estimates of the parameters describing objects in the scene comes face to face with attaching meaning to these constructs. In particular, we wish to associate parameter values at a pixel or within a region to empirically defined classes of objects in the scene, such as fields,

woods, and towns. Approaches to this problem fall into three broad categories: (1) purely data-driven, whose fundamental weakness is their unknown scope for generalizability; (2) classification purely on scattering mechanism, which in principle gives considerable insight into what the classification means but provides no discrimination when desired target classes are dominated by similar mechanisms; and (3) rule-based methods based on an understanding of the physical processes underlying observations. Many of the most promising methods fall into this latter category, which combines pragmatism with insight to provide robust, transferable classification schemes. We also show how the particular properties of SAR can allow an initial classification to be refined to retrieve more information about individual classes in the scene.

In the final chapter we review the extent to which our model-based approach provides a complete, accurate, tractable, and useful framework for information extraction from SAR images. In doing so we establish the status of our best methods and algorithms and indicate directions for progress in light of the real-world examples encountered throughout the book. In our view, the key issue is the extent to which this work becomes embodied in applications of SAR data. The tools have been brought to a high level of refinement but must be judged by their ability to help in the use of the data. The interplay of tools and the tasks to which they are applied will provide the major motivation for any further development.

2

Principles of SAR Image Formation

2.1 Introduction

When trying to extract information from SAR images, we need to distinguish two types of image property. The more important is where properties of the scene (e.g., its dielectric constant, its geometry, its motion, etc.) produce effects in the image; measurements or examination of the image then can provide information about the scene. The second is generated purely by the system and the signal processing. This is important for anyone interested in characterizing system performance, but within the context of this book, its primary significance is in how it affects our ability to recognize image properties generated by the external world. The system can modify, distort, or produce uncertainties in these properties. An important distinction is between intrinsic properties of the imaging system, which cannot be overcome, and artifacts produced by errors or inadequacies in the system behavior and the signal processing. In this chapter, our main concern will be to establish an ideal model for SAR imaging and to show that many of the intrinsic properties are determined by a small number of choices in the system design. Effects due to system failings and how to overcome them are dealt with in Chapter 3. The remainder of the book is mainly concerned with data free from such problems. The treatment of SAR processing underlying this chapter is deliberately simplified so that the key issues in how image properties are dependent on system decisions are not obscured. Readers who desire a more sophisticated

approach will find several excellent texts [1–4]; simpler treatments are given in [5,6].

2.2 SAR System Parameters

The basic geometry of a SAR is shown in Figure 2.1. A platform moving with velocity V at altitude h carries a side-looking radar antenna that illuminates the Earth's surface with pulses of electromagnetic radiation. The direction of travel of the platform is known as the *azimuth* direction; distance from the radar track is measured in the *range* direction. For simplicity, we deal only with the case where the antenna is oriented parallel to the flight line, not squinted.

Typically the antenna is rectangular with dimensions $d_a \times d_e$, where a and e denote azimuth and elevation, respectively. These dimensions are significant because they determine the area illuminated by the antenna. As a rule of thumb, the radiation from an antenna of length d spreads out over an angle

$$\psi = \lambda/d \quad [\text{radians}] \quad (2.1)$$

where λ is the radar wavelength. This relation determines both the azimuth and elevation beamwidths, Ψ_a and Ψ_e ; only the former is marked on Figure 2.1. Wavelength is related to the radar carrier frequency f_0 (in Hz) by

$$\lambda f_0 = c \quad (2.2)$$

where c is the speed of light. Although we will use (2.1) when describing basic properties of SAR images, other definitions of beamwidth are often used. More complete descriptions of the two-dimensional antenna pattern are also important because high-quality SAR imaging must account for the spatial variation of the illumination pattern [2,4]. Later sections in this chapter deal with these issues.

While the radar beam sweeps over a fixed scatterer X , the distance R between the scatterer and the platform will vary symmetrically about its minimum value R_0 . For the case of interest to us, the scatterer will be imaged at an azimuth position determined by this broadside position of closest approach and at a range determined by R_0 . The corresponding ground range R_g (see Section 2.3) is also marked on Figure 2.1.

Important parameters of the pulses that modulate the carrier signal are the *pulse length* τ_p , the *bandwidth* B , and the *pulse repetition frequency* (PRF). Values of these parameters for the ERS-1 satellite SAR and representative values for an airborne SAR are given in Table 2.1. Also recorded in the table is the polarization configuration of the systems. This design choice affects the nature of the radar

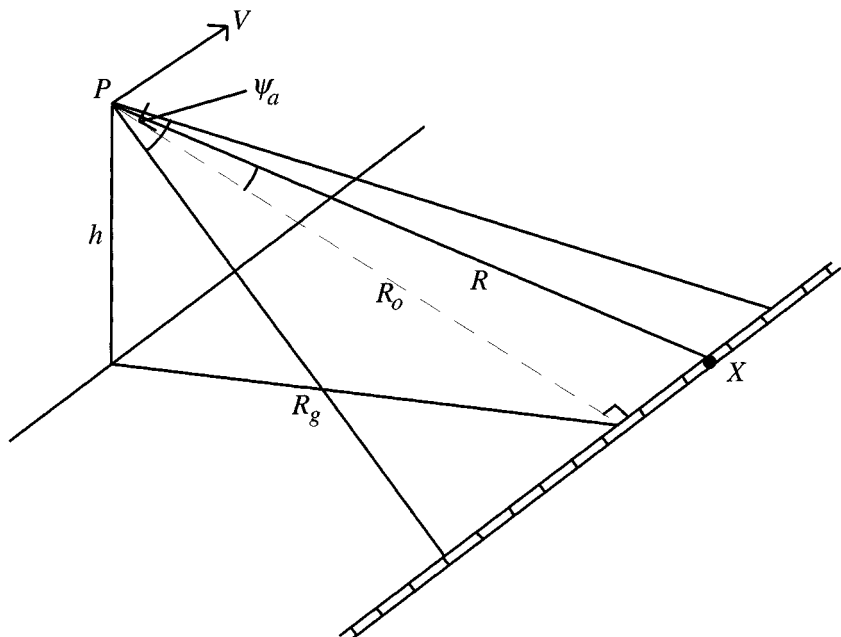


Figure 2.1 The basic flat-Earth geometry of an airborne SAR.

response but, for a single-channel system, has no significance as far as the processing goes or for the system-induced image properties discussed in this chapter. However, when multiple polarizations are simultaneously available, the range of possible image types increases, as described in Chapter 4.

Table 2.1
System Parameters for Satellite and Airborne SAR Systems

	ERS-1	DRA Airborne SAR
Wavelength (λ)	5.67 cm (C-band)	3.1 cm (X-band)
Polarization	VV	HH
Bandwidth (B)	15.5 MHz	100 MHz
Transmitted pulsedwidth (τ_p)	37.1 μ s	5 μ s
PRF	1,680 Hz	adjustable ~ 1.1 kHz
Antenna size (azimuth \times elevation)	10m \times 1m	1.8m \times 0.18m
Altitude	785 km	< 14 km

2.3 The Range Dimension—Processing a Single Pulse

A simplification implicit in Figure 2.1 is that it illustrates the airborne case, in which for most purposes the Earth can be treated as flat. This is true even for long-range airborne systems. However, many applications of SAR rely on spaceborne radar data, for which Earth curvature is important. The spherical geometry needed in this case is illustrated in Figure 2.2(a) and, for our purposes, is particularly relevant to the range dimension of the SAR image.

In this figure, as in Figure 2.1, R_0 denotes the distance of closest approach, R_g and h are as defined in the previous figure, and the other symbols are defined later. Figure 2.2(b) is an illustration of how a pulse of duration τ_p spreads out from the radar, viewed along the azimuth direction, for a spherical geometry. Also shown is the polar diagram that indicates how much power is transmitted in each direction. In this schematic there is a direction of maximum power (the beam center or boresight) in the main beam and lower power sidelobes. This angular distribution of power from the antenna means that the power per unit

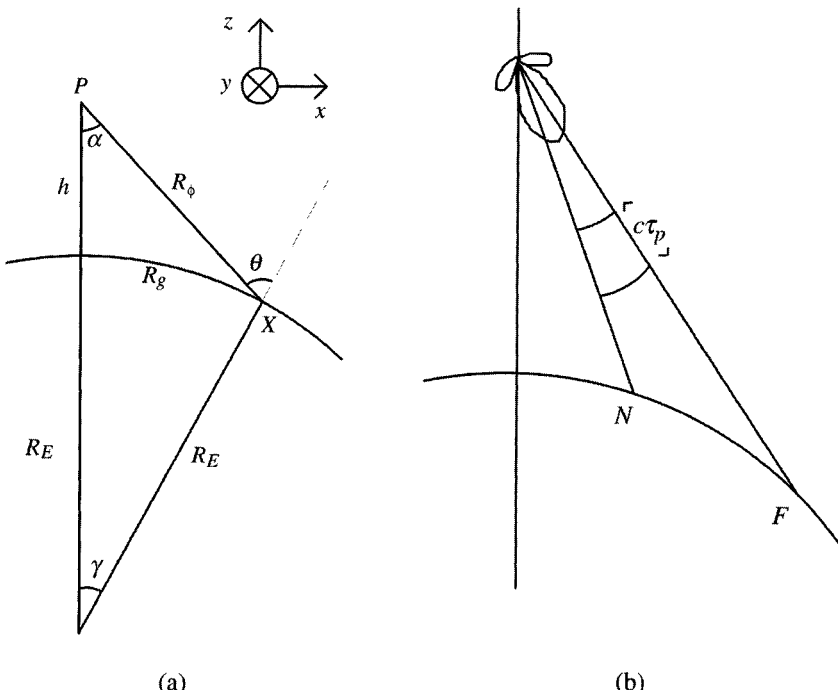


Figure 2.2 (a) The spherical geometry appropriate to spaceborne SAR and (b) illustration of a spreading pulse of duration τ_p ; also indicated is the elevation antenna pattern.

area received at a point on the ground depends on which part of the beam is illuminating that point. The square law decrease of energy with range further affects the power at the ground. Similar considerations apply to the received signal. For the monostatic geometry of most interest to us, the transmit and receive antenna patterns will normally be the same (but this may not be the case for systems using active phased array antennas).

The radiated pulse spreads out as a growing shell of thickness $c\tau_p$. A point object whose distance from the radar is R_0 will therefore return a signal of duration τ_p that will arrive back at the platform with the time delay

$$\tau_d = 2R_0 / c \quad (2.3)$$

after transmission. By time-gating the received signal, scatterers at different ranges can be separated. The minimum and maximum ranges (usually referred to as *near* and *far* range and marked as N and F in Figure 2.2(b)) are determined by the time between the pulse transmission and the start and end of the reception period. The difference between these ranges is the *swathwidth* (more correctly, the slant swathwidth). The swath is always selected to lie within the main lobe of the elevation beam. Since transmission and reception cannot overlap, the swathwidth is restricted by the PRF, and the condition

$$\text{slant swathwidth} < \frac{c}{2 \times \text{PRF}} \quad (2.4)$$

must hold. As we shall see, the PRF cannot be chosen freely but must exceed a lower limit imposed by the azimuth processing. A slight complication in the case of spaceborne radar, where ranges are very long, is that the reception period does not correspond to the previous pulse. For example, the reception period of the ERS-1 radar following the N th pulse corresponds to the $(N - 9)$ th preceding pulse [4].

For a SAR, two different range measurements are commonly used. Corresponding to the *slant range* R_0 is the distance from the subplatform track on the Earth's surface, known as the *ground range* R_g (see Figure 2.2(a)). The ground range may also be referenced to some other locus, such as that of the beam center or of the first near range pixel. Note that the ground range requires a reference surface or projection for its measurement. We treat only the simple case of a perfectly spherical Earth (of radius $R_E \approx 6,370$ km). Other important quantities marked on Figure 2.2(a) are the platform altitude h and the local incidence angle θ .

Conversion between variables is straightforward by means of the relations

$$R_0 = (R_E + h) \frac{\sin \gamma}{\sin \theta} \approx (R_E + h) \frac{\gamma}{\sin \theta} \quad (2.5a)$$

$$R_0^2 = R_E^2 + (R_E + h)^2 - 2R_E(R_E + h)\cos \gamma \quad (2.5b)$$

$$R_g = R_E \gamma \quad (2.5c)$$

$$\gamma = \theta - \alpha \quad (2.5d)$$

$$\sin \alpha = \frac{R_E}{R_E + h} \sin \theta \quad (2.5e)$$

where the approximation in (2.5a) is for γ small. The slant range R_0 is inferred directly from the time delay using (2.3), but given any one of R_0 , R_g , θ , α , or γ , the other four can be found. For airborne platforms, $h \ll R_E$, in which case (2.5a,b) reduce to the flat-Earth approximations

$$R_0 = \frac{R_g}{\sin \theta} \quad (2.6a)$$

$$R_0^2 = h^2 + R_g^2 \quad (2.6b)$$

An important concern is the resolution of the time measurement r_t since this determines the spatial resolution of the instrument in the slant range direction. A fundamental relation in radar theory is that the best attainable time resolution is inversely proportional to the bandwidth B of the transmitted signal. This is explained further in the next section where it is shown that in the ideal case the constant of proportionality can be taken to be 1, so that

$$r_t = 1/B \quad (2.7)$$

From (2.3), the slant range resolution corresponding to a time change of r_t is

$$r_s = c/2B \quad (2.8)$$

The ground range resolution r_g is the change in ground range associated with a slant range change of r_s . Using (2.5a–c) yields

$$\frac{r_g}{r_s} \approx \frac{dR_g}{dR_0} = \frac{R_0}{(R_E + h) \sin \gamma} = \frac{1}{\sin \theta} \quad (2.9)$$

so the ground range resolution varies nonlinearly across the swath. This can have important consequences for image properties, particularly for spaceborne or short-range airborne systems, as will be seen later in this chapter.

To illustrate these relations, we shall use parameters from ERS-1, as summarized in Table 2.1. The time delays for near and far range are selected so that the incidence angle θ varies from 19.3 to 26.4 degrees between near and far range. This gives a total ground swath of 99.3 km; the equivalent slant swath-width is 38.6 km. Since the transmitted signal bandwidth is 15.5 MHz, the slant range resolution is fixed at 9.68m, but the ground range resolution degrades from 21.8m at far range to 29.3m at near range.

For short-range airborne systems, the resolution change across the swath can be much greater. As an example, a system operating with incidence angles between 15 and 60 degrees would have ground range resolutions at far range that are a factor 0.3 of the near range resolution. In image terms, such changes in resolution can have serious consequences. Features that are clearly distinguishable at far range can become nearly invisible at near range. Within distributed targets, such as agricultural fields, there are fewer measurements available to estimate target properties at near range. In this airborne example, fields at near range would contain only 30% as many pixels as at far range, despite having the same size on the ground.

These effects are less significant for long-range airborne systems, such as those of most importance in military applications, which operate over a range of incidence angles much nearer grazing angle. For example, if an aircraft is flying at an altitude of 10 km the incidence angle at a slant range of 100 km is 84.3 degrees. If this is near range and the ground swath is 10 km wide, the incidence angle at far range is 84.8 degrees, corresponding to a change in ground range resolution of $\approx 0.1\%$ across the swath. The difference between slant range and ground range resolution in this case is less than 0.5%.

When displaying SAR data, there is therefore a choice between handling slant range or ground range data. In slant range, each pixel corresponds to the actual SAR measurement (subject to any calibration corrections made in the processing), but the geometry is distorted relative to a map projection. Alternatively, the data can be resampled to ground range so that the geometry is correct in the map projection. Assuming a sensible interpolation scheme (this is not

always the case [7]) the interpolated measurements will have the correct values, but considerable spatial correlation may have been introduced between pixels. This correlation will be higher at near range than at far range simply as a consequence of there being fewer actual measurements per unit length at near range.

Data from ERS-1 illustrate these effects well. These data are available both in *slant range complex* (SLC) format, with a slant range spacing of 7.9m, and in the standard *precision image* (PRI) format, which is resampled to a ground spacing of 12.5m. The geometry of these two types of data is shown in Figure 2.3, where the same region on the ground is depicted as derived from (a) SLC data, (b) SLC data in which pixels have been averaged in blocks of five along azimuth, and (c) PRI data. Azimuth here runs from the top to the bottom of the page. The SLC pixel spacing is 4m in azimuth, so the range and azimuth pixel dimensions are very different on the ground, leading to the obvious distortion. The PRI data are geometrically correct, while the azimuth averaged data are close to correct geometry. (Figure 2.3(b) is discussed further in Section 4.9.)

The spacing in the PRI data is 57.3% of the ground range solution at far range and 42.7% at near range. The higher degree of correlation at near range is not visually obvious but can be seen in the range correlation coefficients shown in Figure 2.4. The four panels in this figure show intensity correlation coefficients (see Section 4.6) calculated from slant range data at near (Figure 2.4(a)) and far (Figure 2.4(b)) range and the corresponding quantities measured from PRI data (Figure 2.4(c,d)). For slant range, the system-induced correlation is independent of location in the image, having values around 0.25 at lag one and effectively zero thereafter. For the PRI data, at near range the correlation coefficient at lag 1 exceeds 0.6 and is near 0.2 at lag 2; at far range, the corresponding value at lag 1 is ~ 0.5 and the lag-2 correlation is indistinguishable from the noise.

2.4 Linear FM (Chirp) Pulses and Pulse Compression

Before considering the azimuth direction, it is worthwhile to describe in more detail the basis for relation (2.7) that connects time resolution to bandwidth. From Table 2.1, one will note that for ERS-1, $\tau_p = 37.1 \mu\text{s}$, giving the pulse a spatial extent of $c\tau_p = 11.13 \text{ km}$, which is approximately one-third of the total slant swathwidth. For simple pulses, this would imply a slant range resolution of 5.56 km. The means by which this long pulse is compressed to yield resolutions of the order of 10m makes use of the form of the transmitted pulse.



(a)



(b)



(c)

Figure 2.3 ERS-1 images of an agricultural region derived from (a) SLC data, (b) SLC data averaged (in intensity) in blocks of 5 pixels along azimuth, and (c) PRI data. All images are shown in amplitude (see Chapter 4). (Copyright ESA, 1992.)

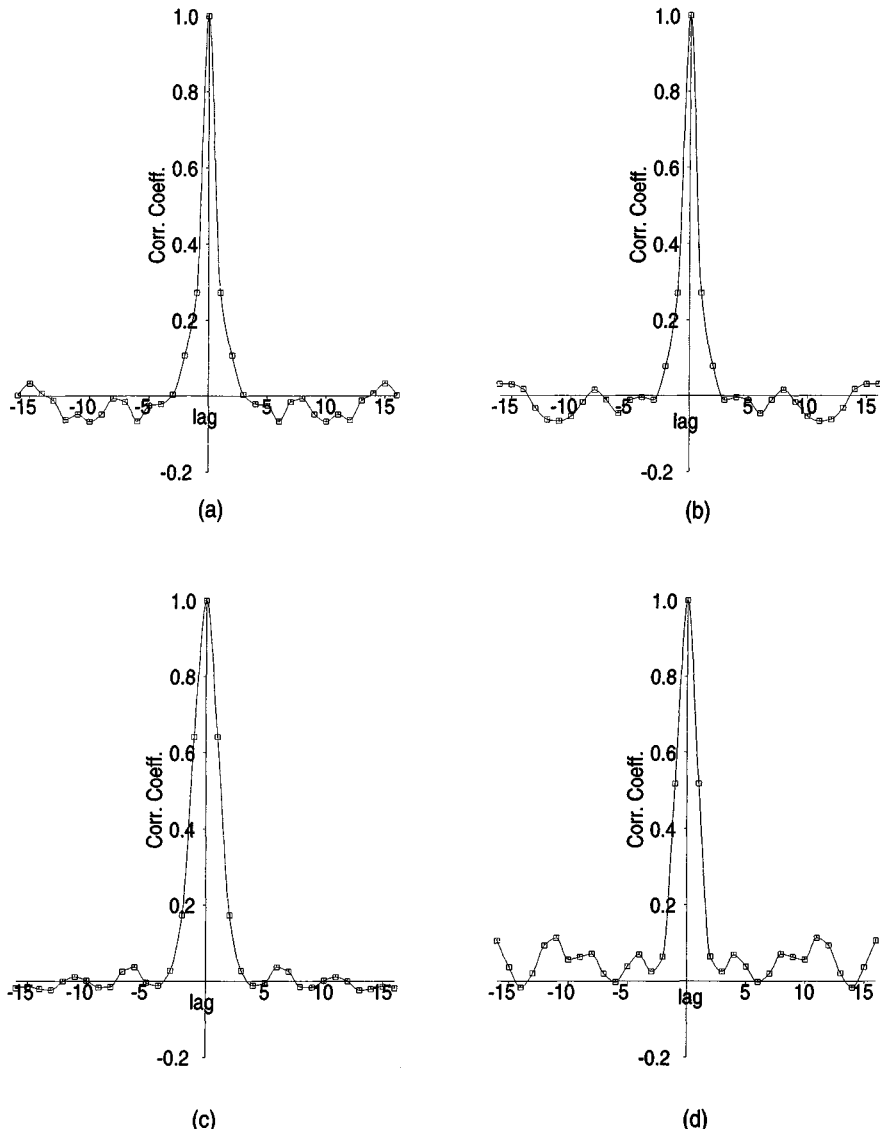


Figure 2.4 Intensity correlation coefficients calculated in the range direction for ERS-1 data from an agricultural area: (a) SLC, near range; (b) SLC, far range; (c) PRI, near range; and (d) PRI, far range.

In many SAR systems the transmitted waveform $p(t)$ is of the form

$$p(t) = \exp\{i(\omega_0 t - \beta t^2)\} \text{ for } |t| \leq \tau_p / 2 \quad (2.10)$$

where ω_0 is the carrier frequency of the radar expressed as radians/s⁻¹. The phase of the signal is therefore

$$\phi(t) = \omega_0 t - \beta t^2 \quad [\text{radians}] \quad (2.11)$$

and the instantaneous frequency (given by the time derivative of the phase) is

$$f(t) = (\omega_0 - 2\beta t)/2\pi \quad [\text{Hz}] \quad (2.12)$$

Since the frequency changes linearly with time, this sort of signal is referred to as linear *frequency modulation* (FM) or chirp, with an FM rate of β/π Hz/s⁻¹. Plots of the phase, the real part, and the instantaneous frequency of the complex envelope $\exp(-i\beta t^2)$ against distance are shown in Figure 2.5, where time has been converted to distance units using the relation $x = ct$. The total frequency sweep or bandwidth is seen to be

$$B = \beta\tau_p/\pi \quad [\text{Hz}] \quad (2.13)$$

(A more exact treatment of bandwidth is given in [8,9].) The pulse shown in Figure 2.5 has $B = 100$ MHz and $\tau_p = 10^{-6}$ sec.

Processing the returned signal involves stripping off the carrier frequency and performing a correlation with a copy of the transmitted signal (this is known as matched filtering [10]). To establish the temporal resolution associated with this operation, we need to know the response it elicits from a point scatterer (the *slant range* PSF). For the pulse given by (2.10) this is straightforward. Since the return from a point scatterer is a delayed, scaled version of the transmitted pulse, after matched filtering it produces a response whose shape is given by

$$h_r(t) = \int_{-\tau_p/2}^{\tau_p/2} \exp(i\beta s^2) \exp(-i\beta[s + t]^2) \text{rect}\left(\frac{s + t}{\tau_p}\right) ds \quad (2.14a)$$

$$= (\tau_p - |t|) \text{sinc}\left(\frac{\beta}{\pi} t [\tau_p - |t|]\right) \text{rect}\left(t / \tau_p\right) \quad (2.14b)$$

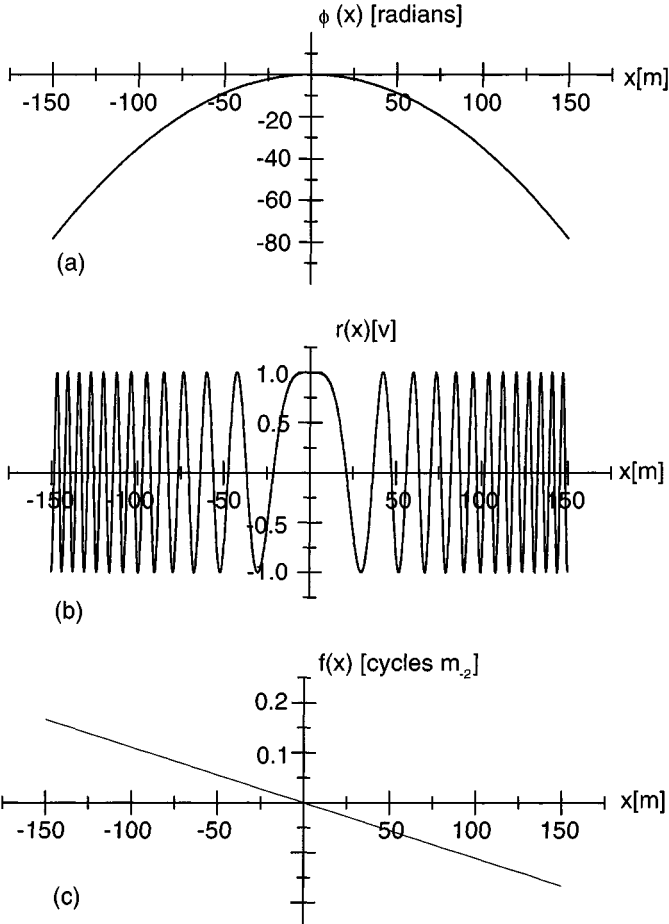


Figure 2.5 (a) Plots of phase, (b) real part of signal, and (c) frequency of signal for the complex envelope of a chirp signal with bandwidth $B = 100$ MHz and pulse length $\tau_p = 10^{-6}$ sec. Time (t) is converted to distance (x) units by the relation $x = ct$.

where

$$\text{rect}(t) = \begin{cases} 1 & |t| \leq \frac{1}{2} \\ 0 & |t| > \frac{1}{2} \end{cases} \quad \text{and} \quad \text{sinc}(t) = \frac{\sin \pi t}{\pi t}$$

Because $b_r(t)$ is formed by correlating the signal modulation $k(t) = \exp(-i\beta t^2)$ with itself, it is often referred to as the *autocorrelation function*

(ACF) of $k(t)$, which we will write as $R_k(t)$. This concept will be used further in Section 4.6.

The first positive zero of this signal (and others of related type) is often taken as a measure of the time resolution r_t . This is controlled by the sinc function and occurs when $\beta t (\tau_p - t) = \pi$, with solution

$$t = r_t = \frac{\tau_p}{2} \left(1 - \sqrt{1 - \frac{4}{B\tau_p}} \right)$$

Since imaging radars are designed so that the *time-bandwidth product* $B\tau_p$ is large, a good approximate solution is $r_t \approx 1/B$, which is the basis for (2.7).

The ratio of the resolution after processing to the original pulse length is known as the *compression ratio*. Using (2.7) we see that

$$\text{compression ratio} = \frac{\tau_p}{r_t} = B\tau_p \quad (2.15)$$

so the compression ratio is equal to the time-bandwidth product. For ERS-1, the compression ratio is 575, so the 37.1- μ s pulse has resolution equivalent to a simple pulse of duration 64.5 ns.

Note that for a large time-bandwidth product, $b_r(t)$ can be written to a good approximation as

$$b_r(t) \cong \tau_p \operatorname{sinc} \left(\beta\tau_p t / \pi \right) = \tau_p \operatorname{sinc} (Bt) \quad (2.16)$$

We will often refer to this as the *ideal* form of the SAR PSF. Plots of the pulses described by (2.14b) and the ideal pulse (2.16) are given in Figure 2.6, where, as previously, we have used the parameters $B = 100$ MHz and $\tau_p = 10^{-6}$ sec. We have also converted to distance units [m] by the replacement $x = ct$ and scaled each plot by $1/\tau_p$.

The effects of matched filtering when there is more than one target present are illustrated by Figure 2.7. The top panel shows the real part of the complex envelope of the returned signal, while the bottom panel plots the amplitude of the output signal after filtering. In this simulation, the scattering was taken to be from two point objects of amplitudes 1 and 2 at positions $x = -5$ and $x = 5$. Although they are invisible in the uncompressed envelope, they are clearly

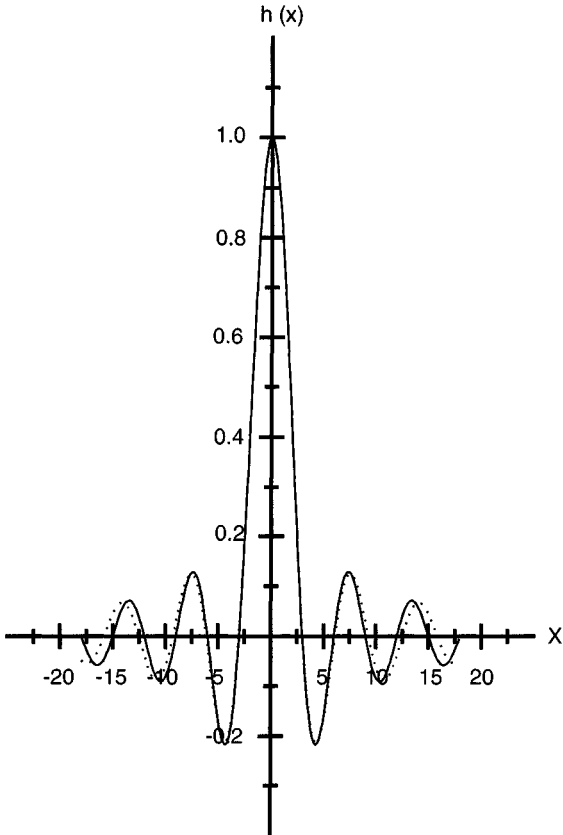


Figure 2.6 Plots of the exact (dashed curve) and ideal (solid curve) compressed chirp pulse for $B = 100$ MHz and $\tau_p = 10^{-6}$ sec, with conversion to distance units using $x = ct$.

resolved at the right positions and with approximately the right magnitudes after the processing.

This treatment has ignored two important processing aspects. First, the point target response shown in Figure 2.6 has significant sidelobes. These are often reduced by applying a weighting to the correlation operation described by (2.14a). This tends to degrade the resolution from the ideal value of $1/B$. Second, in modern digital systems the compressed signal is sampled (at the Nyquist rate or above), so each pulse yields a vector of measurements. Subsequent operations on the compressed pulse are therefore inherently digital.

Note also that it is not mandatory to use a frequency-modulated pulse to gain good range resolution. Short simple pulses can be used instead, but very

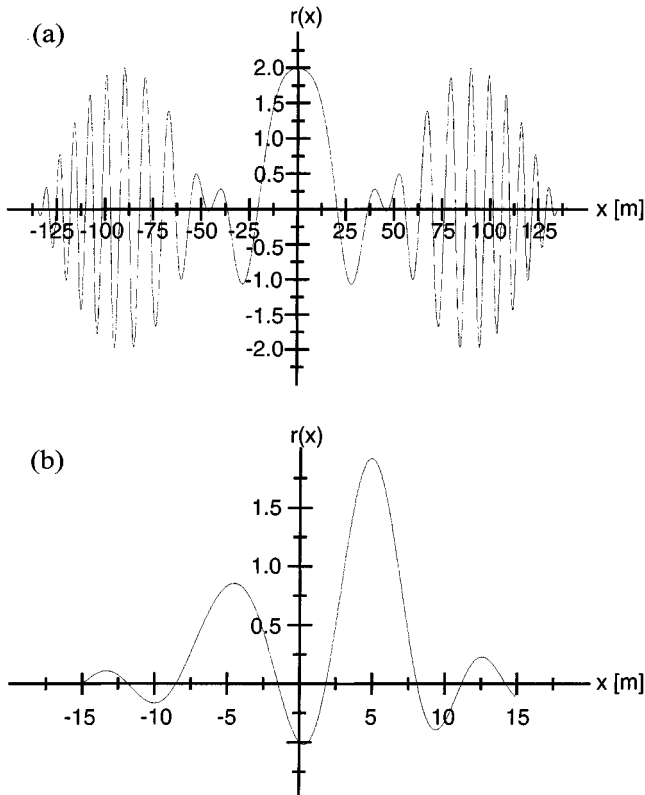


Figure 2.7 (a) The real part of the uncompressed signal envelope when there are two scatterers present and (b) the output signal after pulse compression. The scatterers are of amplitude 2 at $x = 5$ and 1 at $x = -5$.

high power transmitters are then required. The fundamental determinant of resolution is still the signal bandwidth [11].

2.5 The Azimuth Dimension

The pulse compression in the range direction is often carried out on a pulse-by-pulse basis and is a standard form of processing used in many sorts of radars. The particular technology of SAR (and the source of much of its complexity) manifests itself in the azimuth direction.

After range processing on a single pulse, the measurement in each range gate contains a contribution from each scatterer in an azimuthally extended and

curved strip whose width is controlled by the azimuth beamwidth. We ignore the range curvature and treat the strip as straight (see Figure 2.1); for a full treatment see [1, 4]. A real aperture radar simply outputs the power measured at each range to produce an image whose azimuth resolution would be $R_0\psi_a$ where R_0 is the slant range at the position of closest approach and ψ_a is the azimuth beamwidth. A single point scatterer at range R_0 would effectively be smeared across a distance $R_0\psi_a$ in the azimuth direction. Using Table 2.1, a quick calculation indicates an associated resolution of the order 5 to 6 km for ERS-1. Even for an airborne X-band (3-cm wavelength) radar using a 1-m antenna at a range of only 15 km, the azimuth resolution is 450m. These values greatly exceed the available range resolution and would significantly hamper the value of radar for reconnaissance and mapping.

The essence of the SAR processing is the exploitation of the nearly quadratic range variation of a point scatterer as the beam passes over it. This variation is easily calculated for the airborne flat-Earth geometry shown in Figure 2.1. (The corresponding treatment for an orbital SAR is given in Appendix 2A.) The slant range R_0 defines a line on the ground (see Figure 2.1). For a scatterer X on this line we use a coordinate system whose x -axis points along the direction of travel and whose origin is fixed at X . If the azimuth coordinate is x , it is easy to see that the distance R between the platform and X satisfies $R^2 = R_0^2 + x^2$. For a narrow beam, X is only illuminated when $x \ll R_0$, in which case

$$R \approx R_0 + \frac{x^2}{2R_0} \quad (2.17)$$

The corresponding two-way phase delay at the carrier frequency is

$$\phi(x) = -\frac{4\pi R_0}{\lambda} - \frac{2\pi x^2}{\lambda R_0} \quad (2.18)$$

with an associated rate of change of phase with distance given by

$$\frac{d\phi}{dx} = -\frac{4\pi x}{\lambda R_0} \quad (2.19)$$

This is equivalent to linear FM in the distance variable. In spatial coordinates, the equivalent of the pulse length is the *synthetic aperture length* D_s , which is the azimuth distance illuminated at range R_0 . From Figure 2.1 it is readily seen that

$$D_s = R_0 \psi_a \quad (2.20)$$

Applying results for the chirp pulse from Section 2.4 we therefore have a spatial bandwidth given by

$$\frac{1}{2\pi} \times \frac{4\pi}{\lambda R_0} \times D_s = \frac{2}{d_a} \quad [\text{cycles m}^{-1}]$$

where we have used the relation $\psi_a = \lambda/d_a$, and an associated spatial resolution

$$r_a = \frac{d_a}{2} \quad (2.21a)$$

The corresponding expression for an orbital SAR is [12]

$$r_a = \frac{R_E}{R_E + h} \frac{d_a}{2} \quad (2.21b)$$

where R_E is the Earth's radius, and h is the platform altitude (see Appendix 2A).

This critical result (2.21) shows that the SAR azimuth resolution is half the real antenna dimension in the azimuth direction (and better than this in the orbital case) and independent of range and wavelength. For ERS-1, we therefore expect azimuth resolutions of the order of 4.45m, while aircraft can achieve resolutions of the order 0.5m. Notice that these resolutions assume a fixed pointing direction of the antenna, broadside to the platform track, so the SAR is operating in *strip map* mode. A higher resolution is obtainable if the beam is steered (normally electronically) to keep a target in the beam for a larger time and thus to form a longer synthetic antenna. This is known as *spotlight mode* SAR and is capable of improving the azimuth resolution considerably, at the expense of spatial coverage [3].

The azimuth processing is often described by the term *SAR focusing*, and we will refer to the coefficient of the quadratic phase term β as the *focusing parameter*. SAR focusing is equivalent to synthesizing a large antenna, of length D_s , given by (2.20), from all the pulses impinging on a given scatterer as the beam passes over it. Since ψ_a is proportional to λ , this means that D_s is linearly proportional to both the slant range and the wavelength. Hence, increasing the range or wavelength gives a longer effective antenna, which is the fundamental reason why SAR produces resolution independent of either range or wavelength. There is, however, an associated cost. The data are sampled in the azimuth

direction, and the Nyquist condition means that the sample spacing must not exceed the resolution length [2,5]. This constraint imposes a lower limit on the PRF, as already noted in Section 2.3. Hence, the number of samples that must be stored and processed is directly proportional to both range and wavelength.

The above formulation of the azimuth processing in terms of distance illustrates that the motion of the platform is not fundamental, only that samples are gathered coherently along the synthetic aperture. However, for a moving platform, it is common to make use of equivalent temporal expressions, by means of the relation $x = Vt$. These are summarized in Table 2.2. Of particular note is the expression

$$f_d = \frac{1}{2\pi} \frac{d\phi}{dt} = -\frac{2V^2 t}{\lambda R_0} \quad [\text{Hz}] \quad (2.22)$$

This temporal rate of change of phase is equivalent to a Doppler shift, and azimuth processing is often described in these terms [2,12].

Quoted resolutions are usually not as good as expected from (2.21), for two reasons. The first is the result of weighting introduced in the processing to reduce sidelobes (just as in the range direction), which increases the width of the main lobe of the response. Most engineering definitions of resolution are based on this width rather than on the first zero of the PSF used in (2.7). Relating this value to that given by (2.21) therefore depends on the details of the processing and of the precise definition used for resolution. The second

Table 2.2
Azimuth Processing Parameters (Flat Earth)

	Time Coordinates	Space Coordinates
FM rate, β/π	$2V^2/\lambda R_0$ [Hz s ⁻¹]	$2/\lambda R_0$ [cycles m ⁻²]
Phase history	$\phi(t) = -\frac{2\pi V^2 t^2}{\lambda R_0}$ [rads]	$\phi(x) = -\frac{2\pi x^2}{\lambda R_0}$ [rads]
Frequency	$f_d(t) = -\frac{2V^2 t}{\lambda R_0}$ [Hz]	$f_d(x) = -\frac{2x}{\lambda R_0}$ [cycles m ⁻¹]
Synthetic aperture time (τ_p) and length (D_s)	$R_0 \psi_a / V$ [s]	$R_0 \psi_a$ [m]
Bandwidth B	$2V/d_a$ [Hz]	$2/d_a$ [cycles m ⁻¹]
Ideal compressed signal (azimuth PSF)	$h_a(t) = \frac{R_0 \psi_a}{V} \operatorname{sinc} \frac{2Vt}{d_a}$	$h_a(x) = R_0 \psi_a \operatorname{sinc} \frac{2x}{d_a}$

reason is that it may be preferable to sacrifice resolution to combat speckle using a process known as *multilooking*. In this technique, the set of samples used for the full synthetic aperture is split into several adjacent subsets. Each of these subsets can be used to form a separate image, known as a *look*, each of which views a given point from a slightly different angle (equivalently, each one occupies a different part of the Doppler spectrum). By averaging the looks in *power*, the radiometric accuracy of the measurements is improved (see Section 4.3) but at the price of resolution. Splitting the synthetic aperture into L nonoverlapping sections means that each has an effective aperture of length D_s/L , so the resolution is degraded by a factor L . The ERS-1 PRI image uses three looks, with an azimuth resolution of the order of 18m [13]. Degraded resolution compared to the ideal may also occur because the processing is not perfect. Such issues are addressed in Chapter 3.

2.6 SAR as a Linear Measurement System

The prior simplified treatment dealt with the response of an isolated point target mainly as a means of discussing system resolution. However, radiometric properties of the image are also important, and we now consider how the radar reflectivity of the scene is translated into image brightness. In doing so, we will provide a more general and flexible description of the SAR processing than that given in Section 2.5.

For a point target, the most general description of its scattering behavior at a single frequency is provided by the *complex scattering amplitude*, S_{pq} , which we will also refer to as *complex reflectivity*. This quantifies the scattering into polarization state p of an incident plane wave with polarization q through the relation [14]

$$\begin{pmatrix} E_p^s \\ E_q^s \end{pmatrix} = \frac{e^{2\pi i R/\lambda}}{R} \begin{pmatrix} S_{pp} & S_{pq} \\ S_{qp} & S_{qq} \end{pmatrix} \begin{pmatrix} E_p^i \\ E_q^i \end{pmatrix} \quad (2.23)$$

Here we assume orthogonal polarizations, p and q , and free-space propagation to the observation point at distance R in the far-field of the scatterer. The incident electric field has complex (p, q) components given by E_p^i and E_q^i ; the scattered field components E_p^s and E_q^s are defined similarly (for a full discussion, see [14]). The 2×2 matrix on the right-hand side of (2.23) is known as the *scattering matrix*. A completely general treatment would take into account a bistatic geometry, but we will only treat the monostatic backscattering case. For many purposes, the phase of a point scatterer is of less interest than its backscattered power, so a more commonly used descriptor is the RCS defined by [14]

$$\sigma_{pq} = 4\pi|S_{pq}|^2 \quad (2.24)$$

Polarimetric data are treated in Chapter 11. In the early chapters of this book, where we are mainly dealing with single-channel data, we will omit the subscripts and write the complex scattering amplitude and RCS simply as S and σ .

Consider now a point scatterer with complex reflectivity S at azimuth position x' and slant range R when the platform is at azimuth position x . If a pulse is emitted at time $t = 0$, after pulse compression the received signal is

$$E(x) = S K'(R) h_r \left(t - \frac{2R}{c} \right) a \left(\frac{x - x'}{R} \right) e^{-4i\pi R/\lambda} \quad (2.25)$$

Here $K'(R)$ accounts for the elevation antenna pattern, processing gain during the range compression, and the range spreading loss, which is proportional to R^{-2} ; while the two-way amplitude azimuth antenna pattern is $a(\phi)$. The term $h_r(t - 2R/c)$ describes the time delay in the range PSF (see (2.14)) and hence allows the target to be positioned in the range direction. The terms $K'(R)$, $h_r(t - 2R/c)$, and $a(x/R)$ vary much more slowly with range than the phase of the exponential term $4i\pi R/\lambda$. We therefore make the simplification that in these three terms, R can be replaced by R_0 , the range of closest approach.

The range R has a variation with along-track separation $x - x'$ described by (2.17) and can be written

$$R = R_0 + \frac{\lambda\beta}{4\pi} (x - x')^2$$

where β is the focusing parameter. Expressions for β in the spaceborne and airborne cases are given by (2A.1) or Table 2.2, respectively. With the further assumption of negligible range migration (or its correction in the processing) we can write the received signal appropriate to range R_0 as

$$E(x) = K(R_0) S a \left(\frac{x - x'}{R_0} \right) \exp(-i\beta[x - x']^2) \quad (2.26a)$$

where

$$K(R_0) = K'(R_0) h_r(t - 2R_0/c) \exp(-4i\pi R_0/\lambda) \quad (2.26b)$$

(More refined treatments taking account of the coupling between range and azimuth in the processing will be found in [1,3,4,15].)

By considering the azimuth strip at range R_0 to be made up of point targets (represented by delta functions) or elementary scattering areas, the expression (2.26) can be generalized to include a continuous complex reflectivity function $S(x, R)$. For the strip of interest, $R = R_0$ and we shall abbreviate this to $S(x)$. Then the received signal is a convolution:

$$\begin{aligned} E(x) &= K(R_0) \int_{-\infty}^{\infty} S(x') a\left(\frac{x - x'}{R_0}\right) \exp(-i\beta[x - x']^2) dx' \\ &= K(R_0) S(x) * k(x) \end{aligned} \quad (2.27)$$

where

$$k(x) = a\left(\frac{x}{R_0}\right) \exp(-i\beta x^2) \quad (2.28)$$

We can regard $k(x)$ as a prefilter containing two effects, the *beam weighting* given by the polar diagram $a(\phi)$ of the antenna in the azimuth direction and the *range variation* or *Doppler shift* term caused by relative motion of the platform and the scatterer [8,16,17].

In treating $S(x)$ as continuous we move from point to distributed targets. A key property of such targets is that the phase of the scattered field has a correlation length that is much shorter than the resolution of the radar measurement. At scales comparable with this correlation length the target has a well-defined RCS and we can define a *differential backscattering coefficient* σ° as

$$\sigma^\circ \Delta A = 4\pi R^2 \frac{P_s}{P_i} \quad (2.29)$$

where ΔA is the elemental area or facet over which the phase is coherent (effectively constant), P_i is the incident power per unit area, and P_s is the power per unit area scattered from the facet, observed at range R . However, since different facets contribute independent phases, the observed electric field is dominated by interference effects, giving rise to the phenomenon known as *speckle* (see Chapter 4). For distributed targets, the quantity of interest is the average value of σ° within a pixel; from (2.29), this requires normalization by

the illuminated area (see Section 4.6 for a fuller discussion). A target is described as *uniform* if σ^o is constant within it.

The range-compressed *raw data* $E(x)$ is digital, being built up sequentially at each range by gathering pulse returns and saving them in memory. As we have seen, the azimuth processing is a correlation with this stored data and, hence, can be represented as a second filtering operation, giving the output

$$\mathcal{E}(x) = E(x) * l(x) = K(R_0)S(x) * h_a(x) \quad (2.30)$$

where

$$h_a(x) = k(x) * l(x) \quad (2.31)$$

The quantity $h_a(x)$ is known as the *azimuth PSF*. Typically the SAR processing filter $l(x)$ will contain an amplitude weighting term $W(x/R_0)$, but it will *always* have as its main purpose the removal of the quadratic phase term [8]; that is, $l(x)$ will have the form

$$l(x) = W\left(\frac{x}{R_0}\right) \exp(i\beta x^2) \quad (2.32)$$

Hence,

$$h_a(x) = \exp(i\beta x^2) \int_{-\infty}^{\infty} a\left(-\frac{y}{R_0}\right) W\left(\frac{x-y}{R_0}\right) \exp(-2i\beta xy) dy \quad (2.33)$$

To relate (2.30) and (2.33) to earlier results, note that a unit strength point target can be represented as $S(x) = \delta(x)$, where $\delta(x)$ is the Dirac delta function, so

$$\mathcal{E}(x) = \delta(x) * h_a(x) = h_a(x)$$

For a beamshape that is uniform over the beamwidth ψ_a and zero elsewhere and the same processor weighting, we can set $a(\phi) = W(\phi) = \text{rect}(\phi/\psi_a)$. Then the point target response $h_a(x)$ gives the same result as (2.14) except for the range dependent term $K(R_0)$. The associated values for the FM rate and aperture length are $2/\lambda R_0$ and $R_0 \psi_a$ as given in Table 2.2.

To complete the system description, we must include system noise. The model for the azimuth processing at range R (see Figure 2.8) then becomes

$$\begin{aligned}\mathcal{E}(x) &= (C(R)S(x)*k(x) + n(x))*l(x) \\ &= C(R)S(x)*h_a(x) + n(x)*l(x)\end{aligned}\quad (2.34)$$

The range-dependent system terms found in (2.26b) are absorbed into the coefficient $C(R)$ whose magnitude is given by

$$|C(R)|^2 = \frac{P_T G_R^2 \lambda^2 G_p}{(4\pi)^3 R^4 L} \quad (2.35)$$

where P_T is the peak transmitted power, G_R is the one-way power gain of the antenna pattern at the specified range, L allows for system losses, and G_p is the processing gain due to the range compression. The system noise appearing in each range gate after the range compression is unaffected by the antenna pattern or the Doppler shifts present in signals scattered from real targets and so appears in the system diagram after the prefiltering by $k(x)$. It would be expected to be white, zero-mean, and Gaussian. However, because the noise in the image has passed through the range compression, it will usually exhibit range dependence because of corrections carried out in the processing.

Although the voltage equation (2.34) is applicable to any form of target, for single-channel observations of distributed targets it is more useful to deal with the backscattered power. As will be explained in Chapter 4, the mean power in the received signal from a uniform distributed target with backscattering coefficient σ° can then be written

$$\langle |\mathcal{E}(x)|^2 \rangle = |C(R)|^2 \sigma^\circ E_{h_a} + NE_l \quad (2.36)$$

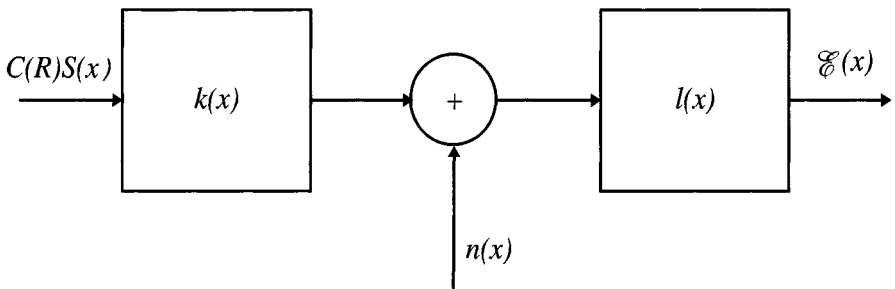


Figure 2.8 Schematic representing the azimuth processing at a fixed range.

where $E_{h_a} = \int_{-\infty}^{\infty} |h_a(x)|^2 dx$ is the *energy* in h_a (often referred to as the SAR processor gain in this context) and E_l is defined similarly. This equation connects the observed power to the geophysical quantity σ^o . Since E_{h_a} is approximately linearly proportional to R , the mean power from a uniform distributed target exhibits an R^{-3} dependence. In contrast, (2.34) and (2.35) imply that, after imaging, the returned power from a point target falls off as R^{-4} . This is dealt with in more detail in Section 4.6.

This treatment has shown that the slant range image can be approximated by the two-dimensional convolution

$$\mathcal{E}(x, R) = C(R) S(x, R) \ast\ast h(x, R) \quad (2.37)$$

where the two-dimensional SAR PSF, $h(x, R)$, can be separated into the slant range and azimuth PSFs as

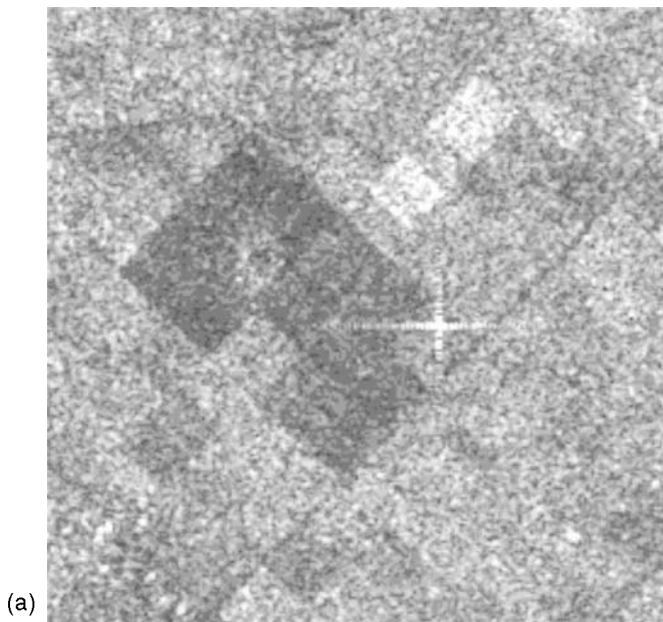
$$h(x, R) = h_a(x) h_r(R) \quad (2.38)$$

This implies that the PSF is independent of position, which is the design aim of most SARs. For a less well-designed system, the PSF may vary slowly with position, but (2.38) still provides a useful and meaningful local approximation.

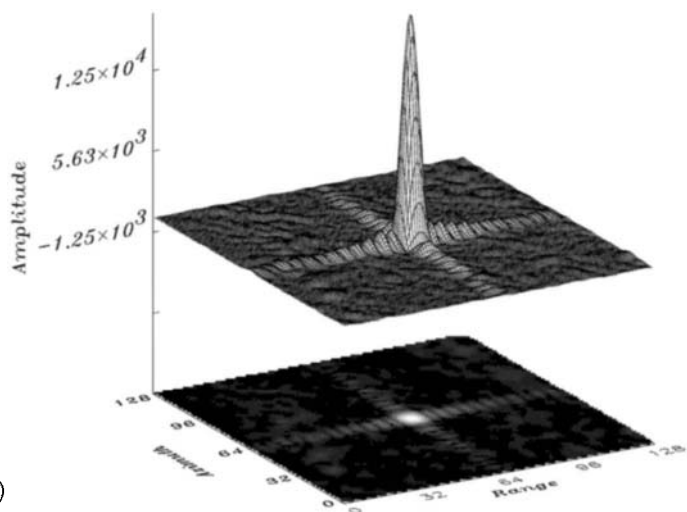
Equations (2.14) and (2.33) show that the azimuth and range PSFs can be derived theoretically for known beam patterns and processor weighting and (2.38) implies that the complete SAR PSF is known if the range and azimuth PSF are known separately. In practice, uncertainties in the real antenna pattern and effects in the processing motivate investigation of the performance of the system by *direct measurements* of the (local) PSF using pointlike calibration devices. Figure 2.9 shows an example of such a measurement together with cuts through the peak response in both range and azimuth. This figure was provided by ESA-ESRIN, Frascati, and is based on measurements by the ERS-1 satellite from a calibration target [18]. The sample spacing is 7.9m in slant range and 4m in azimuth.

2.7 Calibration

Applications of SAR data can exploit two aspects of SAR images. On the one hand, we have *image structure* making up the features we see. This is the critical issue in SAR as a mapping or target detection device. In this case, resolution and geometric accuracy are the important concerns, at least for single images;



(a)



(b)

Figure 2.9 Measured ERS-1 PSF using a calibration target shown (a) in the PRI amplitude image (Copyright ESA, 1995); (b) two-dimensional plot of the amplitude of the SLC PSF and its corresponding three-dimensional representation; (c) profiles through the peak response in the range and azimuth dimensions, interpolated by a factor of 2.

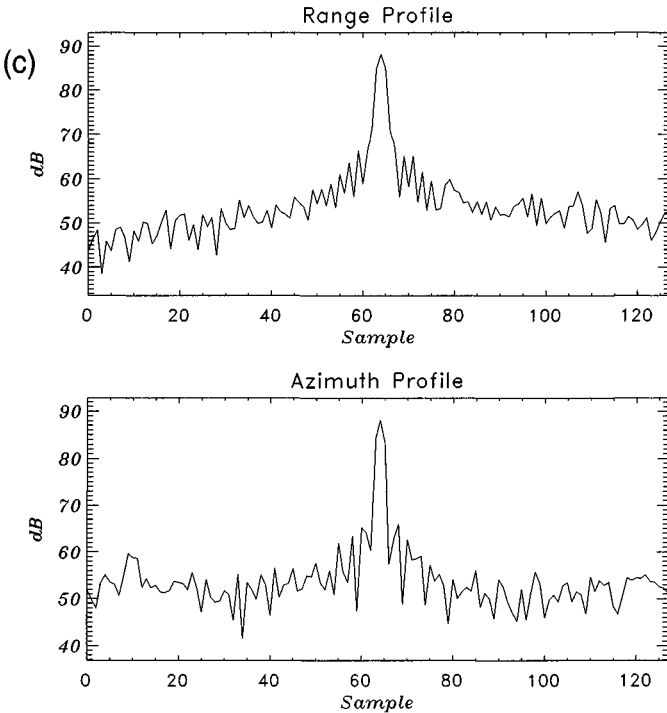


Figure 2.9 (continued).

radiometry and phase integrity only become important when feature detection relies on methods that combine information from different images. On the other hand, SAR is a measuring instrument providing estimates of the complex radar reflectivity or backscattering coefficient of the scene. Here radiometry and phase preservation are critical. Without accurate estimates, there is no basis for meaningful comparisons of target properties measured at different positions, incidence angles, polarizations, frequencies, or times.

The process of converting measured voltages in the *in-phase* (I) and *quadrature* (Q) channels of the radar into accurate estimates of complex reflectivity normally requires very careful calibration. A full treatment of this subject is beyond the scope of this book, but an excellent review article and reference list is provided in [19]. However, the essence of the problem is contained in (2.34) and (2.36), where it can be seen that the effects of noise, azimuth processing (as described by $h_a(x)$), and the gain term C (which contains range antenna pattern, propagation, and range compression terms; see (2.35)) must all be accounted for in estimating the complex reflectivity or backscattering coefficient from the measured voltages.

For single-channel data, spatially dependent image effects associated with the gain term C include:

- The range-dependent spreading loss;
- Systematic variations in image brightness in the range direction due to inadequate compensation for the range antenna pattern, possibly caused by aircraft roll;
- “Yaw bands” caused by variations in the pointing direction of the real or synthetic antenna relative to the flight track.

The first of these is easy to correct, since the range is known from the timing, and any worthwhile processor would remove this effect. The latter effects are both often obvious, particularly in airborne images. They are frequently removed by ad hoc methods assuming that σ^0 should show no systematic variation with range or azimuth throughout the image of interest [20,21]. In doing so, real physical effects are lost (such as variation of σ^0 with incidence angle or genuine variation in scene content), and such methods should only be considered as a last resort. They can provide a form of relative calibration within a single image but are of little value if quantitative values for σ^0 are desired.

A much more satisfactory approach to removing antenna pattern effects is to make use of accurate estimates of the range antenna pattern and the elevation pointing angle of the beam center, if they are available. Acquiring this information often relies on measurements using targets of known RCS spaced across the swath. The accurate deployment of such devices is a time-consuming task, but failure to provide sufficient information to allow the correction of antenna effects has been a repeated cause of problems in extracting meaningful information from SAR data [22].

Given that the system gain term C can be accurately derived at each position in the image, the effects of processing need also to be considered. In (2.36) we see that processing acts as a multiplicative term affecting the estimate of σ^0 from the measured power; this is often referred to as processor gain [17]. As noted in [19], the SAR processor may perform many functions in addition to the basic SAR correlation (e.g., slant range to ground range conversion, look extraction, and antenna pattern correction) and errors in any of these may affect the processor gain. Different processors will normally give different outputs even on the same data. Probably the most comprehensive and successful treatment of this problem has been that applied to data from the ERS-1 satellite. Relatively simple corrections taking account of the processing strategies at different processing centers are available and have been shown to produce great consistency in the measurements [23].

Detailed structure is important when imaging point objects, and this is dependent not just on the processor gain (see (2.36)) but on the PSF itself (see (2.34)). This distinction is important, since the latter is much more sensitive to errors in the processing than the former. As a result, the appropriate method by which to measure σ depends on the quality of the SAR focusing. For well-focused data, σ can be measured directly from the peak response of the point target. However, errors in the focusing (which can occur particularly as a result of unknown or uncorrected platform motions; see Chapter 3) have motivated the development of methods based on the integrated point target response. These are comparatively insensitive to the accuracy of the focusing parameter [24,25] and are therefore often preferred, particularly when dealing with airborne data. When high-performance autofocus algorithms are used (see Chapter 3), this is a less telling consideration.

In many cases, precise measurements of σ for an unknown point target are not of interest. Instead, point targets with known σ are used to infer the quantitative behavior of the system term $Ch_a(x)$ in (2.34). It can be seen, however, from (2.36) that, for measurements of σ^o , the important quantity is $|C|^2$ times the energy in the SAR PSF. Hence, where calibration is carried out for the purposes of measuring the properties of distributed targets, integrated energy methods are to be preferred.

The interplay of point and distributed targets is also important when faced with the extra problems associated with calibrating polarimetric data. This will be discussed in Chapter 11.

2.8 Summary

This chapter dealt with a number of key concepts in SAR image formation. The geometry of SAR images creates possible problems for display and for data analysis. The natural coordinate system of a strip-map SAR is in terms of time delay and the azimuth position of closest approach (zero Doppler frequency). This implies a distortion compared to a map projection that gets worse in a nonlinear fashion toward near range as incidence angles decrease. Resampling to a map projection leads to varying resolution and interpixel correlation across the swath, whose effects may be very significant.

A central concept is the SAR PSF, which describes how a point scatterer is imaged by the SAR and how energy due to the point target becomes spread into surrounding pixels. In the ideal case, its properties are simply linked to basic system parameters. The PSF provides the basis for defining SAR resolution. We have here adopted fairly simple measurements of resolution, and many others are possible, but any such measure is essentially a way of describing the width

of the PSF. Other manifestations of the PSF are sidelobes and ambiguities, which provide known and quantifiable effects on image quality. In addition, there are image defects that are hard to classify but are often visually obvious, particularly in airborne images. These include azimuth banding (which can be caused by antenna yaw or varying azimuth pixel size), interference by alien radars, and fringes caused by multipath effects, due to reflections off the platform. Such effects can often be very difficult to deal with satisfactorily and are not considered further (but see [26]).

The SAR PSF is fundamental in the linear system description of SAR imaging, which provides the basis for relating the imaging of point scatterers to that of distributed scatterers and for dealing with system noise. The PSF also plays a key role in the use of SAR as a measuring instrument attempting to provide accurate estimates of the RCS (σ) for point scatterers or the backscattering coefficient (σ^0) for distributed scatterers because accurate estimates rely on image calibration, which is often provided by point scatterers of known RCS deployed in a scene. To characterize targets comprising a few point scatterers, typical of man-made objects, the PSF is seen to be the important quantity, while for distributed targets the energy in the PSF is more useful.

References

- [1] Curlander, J. C., and R. N. McDonough, *Synthetic Aperture Radar: Systems and Signal Processing*, New York: J. Wiley & Sons, 1991.
- [2] Ulaby, F. T., R. K. Moore, and A. K. Fung, *Microwave Remote Sensing: Active and Passive*, Vols. 1–2, Reading, MA: Addison-Wesley, 1981, 1982.
- [3] Carrara W. G., R. S. Goodman, and R. M. Majewski, *Spotlight Synthetic Aperture Radar: Signal Processing Algorithms*, Norwood, MA: Artech House, 1995.
- [4] Bamler, R., and B. Schättler, “SAR Data Acquisition and Image Formation,” *SAR Geocoding: Data and Systems*, G. Schreier (ed.), Karlsruhe: Wichmann, 1993, pp. 53–102.
- [5] Kovaly, J. J., “Radar Techniques for Planetary Mapping with an Orbiting Vehicle,” *Synthetic Aperture Radar*, J. J. Kovaly (ed.), Dedham, MA: Artech House, 1976, pp. 32–54.
- [6] Elachi, C., *Spaceborne Radar Remote Sensing: Applications and Techniques*, New York: IEEE Press, 1988.
- [7] Quegan, S., “Interpolation and Sampling in SAR Images,” *IEEE Trans. on Geoscience and Remote Sensing*, Vol. 28, 1990, pp. 641–646.
- [8] Brown, W. M., and C. J. Palermo, *Random Processes, Communications and Radar*, New York: McGraw-Hill, 1969.
- [9] Rihaczek, A. W., *Principles of High Resolution Radar*, New York: McGraw-Hill, 1969.
- [10] Papoulis, A., *Signal Analysis*, New York: McGraw-Hill, 1977.

- [11] Woodward, P. M., *Probability and Information Theory, with Applications to Radar*, Oxford: Pergamon Press, 1953.
- [12] Raney, R. K., "Considerations for SAR Image Quantification Unique to Orbital Systems," *IEEE Trans. on Geoscience and Remote Sensing*, Vol. 29, 1991, pp. 754–760.
- [13] Laur, H., and G. M. Doherty, "ERS-1 SAR Calibration: History and Results," *CEOS Workshop on SAR Calibration*, 1992.
- [14] Van Zyl, J. J., and F. T. Ulaby, "Scattering Matrix Representation for Simple Targets," *Radar Polarimetry for Geoscience Applications*, F. T. Ulaby and C. Elachi (eds.), Norwood, MA: Artech House, 1990, pp. 17–52.
- [15] Jin, M. Y., and C. Wu, "A SAR Correlation Algorithm Which Accommodates Large Range Migration," *IEEE Trans. on Geoscience and Remote Sensing*, Vol. 22, pp. 592–597.
- [16] Harger, R. O., *Synthetic Aperture Radar Systems, Theory and Design*, New York: Academic Press, 1970.
- [17] Raney, R. K., and R. Bamler, "Comments on SAR Signal and Noise Equations," Proc. IGARSS 94, Pasadena, 1994, pp. 298–300.
- [18] Woode, A. D., Y.-L. Desnos, and H. Jackson, "The Development and First Results from the ESTEC ERS-1 Active Radar Calibration Unit," *IEEE Trans. on Geoscience and Remote Sensing*, Vol. 30, 1992, pp. 1122–1130.
- [19] Freeman, A., "SAR Calibration: an Overview," *IEEE Trans. on Geoscience and Remote Sensing*, Vol. 30, 1992, pp. 1107–1121.
- [20] Quegan, S., C. C. F. Yanasse, H. de Groof, P. N. Churchill, and A. J. Sieber, "The Radiometric Quality of AgriSAR Data," *Int. J. Remote Sensing*, Vol. 12, pp. 277–302.
- [21] Bégin, D., Q. H. J. Gwyn, and F. Bonn, "Radiometric Correction of SAR Images: a New Correction Algorithm," *Int. J. Remote Sensing*, Vol. 8, 1987, pp. 385–398.
- [22] Yanasse, C. C. F., S. Quegan, and R. J. Martin, "Inferences on Spatial and Temporal Variability of the Backscatter from Growing Crops Using AgriSAR Data," *Int. J. Remote Sensing*, Vol. 13, 1992, pp. 493–507.
- [23] Laur, H., P. Bally, P. Meadows, J. Sanchez, B. Schaettler, and E. Lopinto, "ERS SAR Calibration: Derivation of the Backscattering Coefficient σ^0 in ESA ERS SAR PRI Products," *ESA Document ES-TN-RS-PM-HL09*, Issue 2, Rev. 4, 1997.
- [24] Gray, A. L., P. W. Vachon, C. E. Livingstone, and T. I. Lukowski, "Synthetic Aperture Radar Calibration Using Reference Reflectors," *IEEE Trans. on Geoscience and Remote Sensing*, Vol. 28, 1991, pp. 374–383.
- [25] Ulander, L. M. H., "Accuracy of Using Point Targets for SAR Calibration," *IEEE Trans. Aerosp. Electron. Syst.*, Vol. 27, 1991, pp. 139–148.
- [26] Massonet, D., "Radar Image Quality White Paper," CEOS SAR Cal/Val Working Group, 1991.

Appendix 2A Azimuth Processing for an Orbital SAR

A treatment of the azimuth processing in terms of quadratic range variation and linear FM was carried out for a flat-Earth geometry in Section 2.5. Here we

develop the analogous expressions for an orbital SAR, with essentially similar results. The relevant geometry is shown in Figure 2.2(a), with a convenient coordinate system in which the orbital plane of the satellite lies in the yz plane.¹ A point X fixed on the Earth's surface can then be used to define the xz plane, in which it has position $X = R_E(\sin \gamma, 0, \cos \gamma)$, where R_E is the Earth's radius and γ is as shown in Figure 2.2(a). Ignoring Earth rotation, the satellite sweeps past X with angular velocity Ω rads s^{-1} . The position of the satellite at time t is therefore

$$\mathbf{P} = (R_E + h)(0, \sin \Omega t, \cos \Omega t)$$

given that X is broadside to the satellite at time 0. The distance R between the satellite and X is

$$\begin{aligned} R &= |X - \mathbf{P}| \approx R_0 + \frac{R_E(R_E + h) \cos \gamma \Omega^2 t^2}{2R_0} \\ &= R_0 + \frac{R_E \cos \gamma s^2}{2R_0(R_E + h)} \end{aligned} \quad (2A.1)$$

where R_0 is the range of closest approach of the satellite to X and $s = (R_E + h)\Omega t$ is the distance along the satellite track. This approximation assumes that the azimuth beamwidth is small, so only small values of Ωt (when X is in the radar beam) are of interest, and hence $s \ll R_0$. It can be seen that the distance between the satellite and X has a variation that is approximately quadratic in both time and along-track distance. The corresponding two-way phase delay is given by

$$\phi(t) \approx -\frac{4\pi R_0}{\lambda} - \frac{2\pi}{\lambda} \frac{R_E(R_E + h) \cos \gamma \Omega^2 t^2}{R_0} \quad (2A.2)$$

This is equivalent to linear FM, in which the frequency variation

$$f_d = \frac{1}{2\pi} \frac{d\phi}{dt} \approx -\frac{2}{\lambda} \frac{R_E(R_E + h)}{R_0} \cos \gamma \Omega^2 t \quad [\text{Hz}] \quad (2A.3)$$

can be interpreted as Doppler shift.

The time for which X is illuminated is found by noting that the beam-

1. In most other places in this book we use a coordinate system for which x is in the azimuth direction.

width on the ground is approximately $R_0\psi_a$ and that the velocity of the beam on the ground is $V = R_E \Omega \cos \gamma$. Hence the illumination time is

$$\tau_p = \frac{R_0\psi_a}{V} = \frac{R_0\psi_a}{R_E \Omega \cos \gamma} \quad (2A.4)$$

We can now apply the results for the chirp pulse from Section 2.4. The azimuth (Doppler) bandwidth is

$$B = \frac{2}{\lambda} (R_E + b) \Omega \psi_a \quad [\text{Hz}] \quad (2A.5)$$

with associated time resolution $1/B$. In this time the beam moves a ground distance V/B , so the azimuth resolution on the ground is

$$r_a = \frac{R_E}{R_E + b} \cos \gamma \frac{\lambda}{2\psi_a} \quad (2A.6)$$

Using the approximation $\psi_a = \lambda/d_a$ and noting that γ is small, we find

$$r_a = \frac{R_E}{R_E + b} \cos \gamma \frac{d_a}{2} \approx \frac{R_E}{R_E + b} \frac{d_a}{2} \quad (2A.7)$$

These results should be compared with (2.17) to (2.22) and Table 2.2.

3

Image Defects and Their Correction

3.1 Introduction

Following the SAR image formation procedures outlined in Chapter 2 should, in principle, result in focused images with a resolution independent of range or wavelength and depending only on the length of the real aperture. In practice, however, a number of factors can degrade image quality by causing either amplitude or phase modulation of the signal. The former is a consequence of a failure of antenna stabilization. Platform roll or yaw can change the pointing angle of the antenna, as mentioned in Section 2.7, resulting in varying illumination. This is more significant at the extremes in both range and azimuth. The latter is a consequence of an unpredicted change in the range between the object and antenna. This gives rise to unknown Doppler modulation of the received signal, which impinges considerably on the pulse azimuthal compression, as we shall show.

Unpredictable **amplitude modulation** is mainly evident in the image through:

- Radiometric distortion;
- Increased sidelobe levels;

whereas unwanted phase modulation leads to:

- Image defocus;
- Geometrical distortion;

- Radiometric distortion;
- Increased sidelobe levels.

Image defocus, radiometric distortion, and increased sidelobe levels restrict target detection and recognition capability, including enhanced performance using super-resolution, as discussed in Chapter 10. Geometrical distortion prevents direct pixel-to-pixel comparison of SAR images, which is required for techniques such as multichannel registration, relevant to Chapter 12, and target change detection, discussed in Chapter 10. It also prevents the direct image/map comparison or matching of SAR with other forms of imagery, such as optical data. In terms of significance to the military user, target detection and recognition performance is primarily characterized by the geometrical structure within images, that is, by image defocus, radiometric distortion, and increased sidelobe levels. Remote sensing applications, on the other hand, in many cases depend on knowledge of absolute backscattering coefficient and often need to relate the SAR data to other spatial information and so can be severely hampered by radiometric and geometric distortion.

Some forms of amplitude modulation can be corrected by signal-based methods. However, it is preferable to minimize this effect in the original radar sensor. We return to this issue in Section 3.3.3. Once the signal data have been gathered, radiometric correction requires careful and time-consuming calibration relying on external devices, as mentioned in Section 2.7.

The effects of phase modulation can be reduced considerably if unexpected motions of the sensor are measured by accurate accelerometers and Inertial Navigation Units. The received signal can then be compensated before SAR processing. However, we shall show in this chapter that, even after such motion compensation (MOCO), there are still residual unknown phase modulations that degrade images appreciably. If the user has access to complex data at the full bandwidth, it is possible to apply post-processing techniques to derive accurate motion correction. In this chapter we describe such an approach to restoring the ideal PSF and derive the consequent residual errors in image quality, expressed in terms of the aforementioned four classes of effect. Users who do not have access to the complex data are unable to make these corrections and achieve the quality of information that can be derived from the ideal SAR image. Note that these techniques are not confined to specific radars but have been applied successfully to airborne [1], spaceborne (ERS-1) [2], and Spotlight [3] SAR systems.

Users who are already satisfied with the quality of the SAR imagery that they receive may find this chapter irrelevant to their needs. Others, particularly those concerned with making high-resolution measurements at long ranges in

airborne systems, should find the material important since it demonstrates that the full theoretical image quality can be recovered through a series of post-processing operations on the original complex data without modification to the radar sensor.

From this point, we concentrate on techniques for correcting the unpredicted phase modulation that leads to fluctuation in the apparent focus parameter. Exploiting the variations in this estimated focus parameter provides a signal-based MOCO scheme to overcome image quality deficiencies. The approach we adopt can be summarized as follows [4]:

- Demonstrate the problem;
- Identify the physical cause;
- Describe and analyze the techniques for correcting the deficiency.

We will not be concerned with the effect of deterministic factors, such as range and azimuth ambiguities, or details of the predicted sidelobe structure. Nor will we be concerned with absolute radiometric accuracy, which we assume to be ensured by calibration.

In Section 3.2 we introduce the defocus problem, describe autofocus methods (Section 3.2.2), derive theoretical limits on the determination of the focus parameter (Section 3.2.3), and examine the effects of scene properties on autofocus performance (Section 3.2.4). Various types of distortion are discussed in Section 3.3, leading to a scheme for signal-based MOCO in Section 3.3.2. In Section 3.4 we consider the residual imaging errors. Some refinements to the autofocus and phase correction methods that enable them to realize their full potential are discussed in Section 3.5. In particular, we introduce a progressive coherent autofocus scheme that allows long-term geometric distortion to be minimized.

3.2 Defocus

A striking example of image defocus is shown in Figure 3.1. This image was obtained with the DRA airborne X-band SAR at a range of about 40 km using the nominal value for the focus parameter with no conventional MOCO applied. The physical reason for the defocus is the occurrence of unknown fluctuations in the microwave path length between the antenna and the scene. One possible cause is a variation of atmospheric refractive index [5,6], which can be significant for high-resolution systems with long atmospheric paths. An important feature of atmospheric effects is that it is not enough to know the

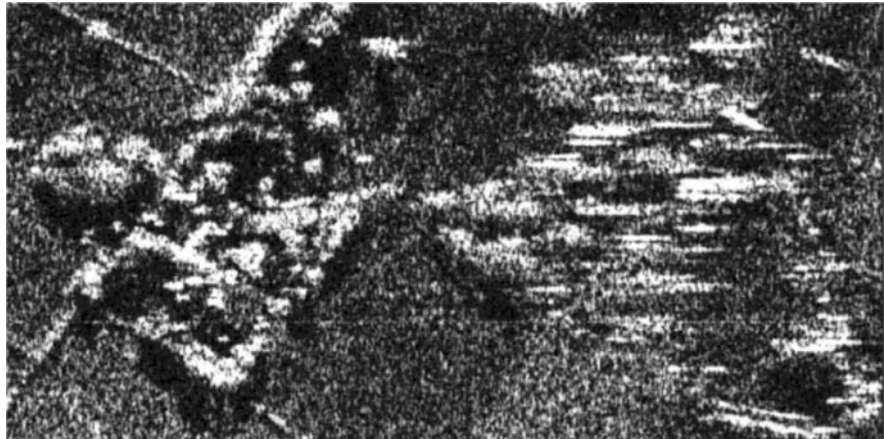


Figure 3.1 Defocused image formed by processing data with the expected focus parameter.

sensor track perfectly; only a measurement of the actual microwave path will suffice. A second cause of fluctuations in path length is the failure of the sensor to follow a defined trajectory, to within a small fraction of a wavelength, over the entire synthetic aperture. We here analyze the implications of these unknown path length fluctuations and compare means for correcting for them by autofocus processing. In practice, there is no need to distinguish the actual mechanism, since both give rise to apparent range fluctuations. However, the following discussion will be couched in terms of unknown trajectory variation since this is usually the dominant contribution.

Defocus stems from the erroneous assumption that the antenna phase center traversed a straight path at known velocity during image formation. Any departure from this defined track degrades the reconstruction. In Figure 3.2 we illustrate the impact of such an irregular track on the difference between the actual distance from a scatterer O and that if there were no unknown motions. As shown in Chapter 2, focusing the SAR involves knowing this distance accurately and correcting for the associated phase delay.

Suppose that an object, O, is imaged by a sensor traveling along the actual track AC from origin A (0, 0) at time 0 to position C (x , y) with range R' at time t and broadside range R_0 , as shown in Figure 3.2. Approximate displacements x and y , can be obtained by expansion up to the order of acceleration in each direction such that $x \approx (V + \Delta V)t + a_x t^2/2$ and $y \approx V_r t + a_r t^2/2$ where V and V_r are along-track and radial velocities, a_x and a_r the corresponding accelerations, and ΔV an along-track velocity mismatch. The expected track is AB, with the sensor ending at position B (x_0 , 0) where $x_0 = Vt$, with range R . The difference between the expected and actual ranges would be given by ΔR .

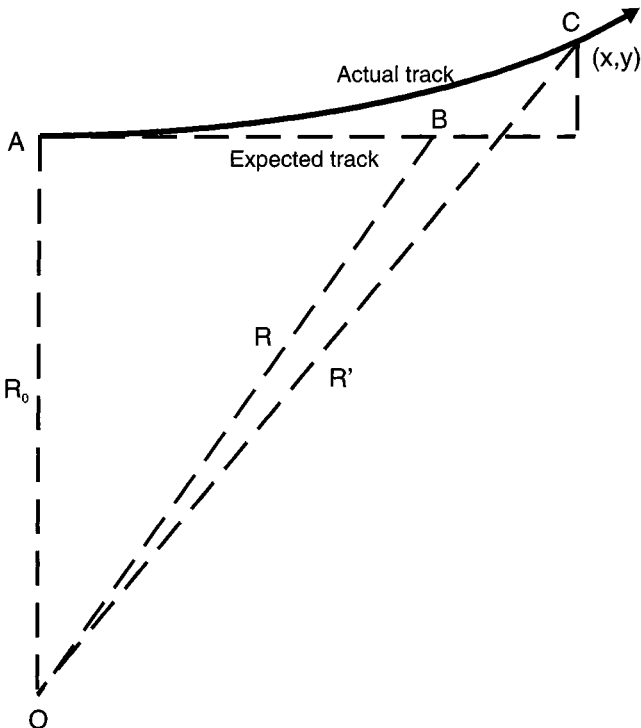


Figure 3.2 A comparison of path length for expected and actual tracks.

$\equiv R - R'$, with an associated phase difference for the two-way path of $\Delta\phi = -4\pi\Delta R/\lambda$. Provided that $Vt \ll R_0$, $V_r t \ll R_0$, and $\Delta V \ll V$, the phase difference from the distance of closest approach can be evaluated in terms of a Taylor expansion such that

$$\phi(t) = -\frac{4\pi}{\lambda} \left[V_r t + t^2 \left(\frac{V^2}{2R_0} + \frac{a_r}{2} + \frac{V^2}{R_0} \frac{\Delta V}{V} \right) + \dots \right] \equiv -\alpha t - (\beta + \Delta\beta(t))t^2 \quad (3.1)$$

to second order in t , where $\alpha (= 4\pi V_r/\lambda)$ is known as the Doppler centroid parameter and $\beta (= 2\pi V^2/R_0\lambda)$ the focus parameter, as in Table 2.2. In recognition of the fact that a_r and ΔV may vary along track, the discrepancy in the focus parameter $\Delta\beta$, is made time-dependent. The fractional discrepancy in the focus parameter is given by

$$\frac{\Delta\beta(t)}{\beta} = \frac{R_0 a_r}{V^2} + 2 \frac{\Delta V}{V} \quad (3.2)$$

From (3.1), the instantaneous frequency, or phase gradient, would be given by

$$\omega(t) = \frac{d\phi(t)}{dt} = -\alpha - 2(\beta + \Delta\beta)t \quad (3.3)$$

In sideways-looking SAR the image is formed at the position where this frequency is zero. Thus a nonzero value of the Doppler centroid term, α , shifts the image in azimuth, resulting in azimuthal distortion. If the axis of this synthetic aperture is not aligned with the real antenna there will also be a resultant modulation in the power in the SAR image. Thus, changes in α yield both geometric and radiometric distortion. However, a nonzero value of α does not degrade the focus directly. This is caused by an error in the quadratic focus term, so $\Delta\beta \neq 0$. Note that indirect degradation can be caused if the full bandwidth is not retained.

In the following sections we will consider methods for overcoming these deviations from the expected trajectory. In the first stage, autofocus processing is used to determine a correction to the quadratic focus term. In the second, this is associated with a time-dependent phase correction that resamples the phase of the received signal to match that of the reference. We will demonstrate that this approach is capable of yielding focused, geometrically undistorted imagery.

3.2.1 Autofocus Methods

In this section we shall consider a representative set of robust autofocus techniques that typifies the wide range of proposed methods in the literature (see [7–20]). A description of the implementation of most of these can be found elsewhere [7]. Our treatment concentrates on the theoretical analysis of their performance. Where strong targets exist, they can be exploited in prominent point processing (PPP) autofocus [8]. We will show that this method is potentially capable of the highest performance. However, since the method depends on the existence of dominant scatterers throughout the scene, it is somewhat less robust than techniques that merely require contrast variations. Other methods can be broadly subdivided into two categories, either coherent or incoherent. Coherent methods operate on the received signal before azimuthal compression to form the image. Phase gradient (PG) [9–11] and phase difference (PD) [12] methods fall into this category. Incoherent techniques, on the other hand, operate on the intensity of the compressed image and lose all phase information. These are typified by the Hughes Map Drift technique [13,14], which we will refer to as multilook registration (MLR), and contrast optimization (CO) [15–20]. The principle of operation of each of these autofocus methods, applied over a synthetic aperture of duration T , is summarized as follows. Note that this

analysis is based on discretely sampled data rather than the continuous form adopted in Chapter 2.

PPP provides a direct measure of the phase fluctuations that characterize the azimuthal PSF when the signal is almost noiseless. Where there is more noise, or interference from other scatterers, the received field can be fitted to the appropriate reference with an unknown focus parameter.

The PG of a complex signal can be defined in terms of the imaginary part of the product of the complex conjugate of the received signal and its derivative such that $\omega(j) \equiv \dot{\phi}(j) \equiv \text{Im}(E^*(j)\dot{E}(j))/|E(j)|^2$ [9–11], where E is the complex received signal after pulse compression. The time derivative of the signal has to be estimated from neighboring samples leading to a time dependence across the aperture illustrated in Figure 3.3. We fit this phase history to a quadratic with unknown focus parameter, leading to the best fit phase gradient line illustrated in Figure 3.3.

PD is closely related to PG. Rather than estimating the PG between neighboring samples, it constructs the PD between samples separated by half the aperture length. On taking the Fourier transform (FT) of the crosscorrelation between these samples, the k th spectral component for a scatterer in the center of the aperture is given by [12]

$$A(k) = \exp[i\pi(\alpha M\Delta T - k\Delta T + \beta M^2\Delta T^2)] \frac{\sin\left[\frac{4\pi}{M\Delta T}\left(\frac{2k}{M} - \beta M\Delta T\right)\right]}{\sin\left[\pi\left(\frac{2k}{M} - \beta M\Delta T\right)\right]} \quad (3.4)$$

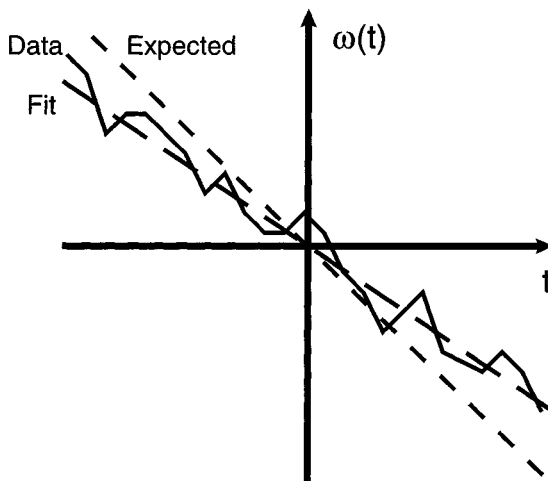


Figure 3.3 A comparison of estimated phase gradient, $\hat{\omega}(t)$, with best fit and expected reference as function of time.

where M is the number of samples of separation ΔT in the aperture T . The second part describes an envelope that has a peak when $k = \beta M^2 \Delta T / 2$, from which the focus parameter can be derived.

As already noted, PPP, PG, and PD are coherent techniques that operate directly on the complex received signal. Both MLR and CO, on the other hand, depend on the intensity of the compressed image and are therefore incoherent methods. Following Chapter 2, azimuthal compression is performed by crosscorrelating the received signal with a reference of the form $E_{\text{ref}}(j) \equiv \exp[-i(\alpha j \Delta T + \beta j^2 \Delta T^2)]$ over aperture T . This differs from the unperturbed reference in adopting unknown values of the Doppler centroid and focus parameters, α and β . The compressed image intensity is then formed by taking the square modulus of the received field. Multilook registration and contrast optimization exploit different aspects of this compressed image.

The MLR technique detects the difference between the actual and specified focus parameters in two (or more) subapertures. As shown in Figure 3.4, the gradient of the reference is determined by its specified focus parameter, β_0 . However, if the actual focus parameter is β , the compressed image will not form at the origin but will be shifted by $\Delta t/2$ in each subaperture, where $\Delta\beta \approx 2\beta\Delta t/T$. The second subaperture yields an equivalent shift for the same scatterer. The displacement between the two image positions ($= \Delta t$) is directly measurable and is caused by a change in the Doppler frequency between the subapertures, where $\Delta t = \Delta\alpha/2\beta$ from (3.3), so the mismatch in the focus parameter

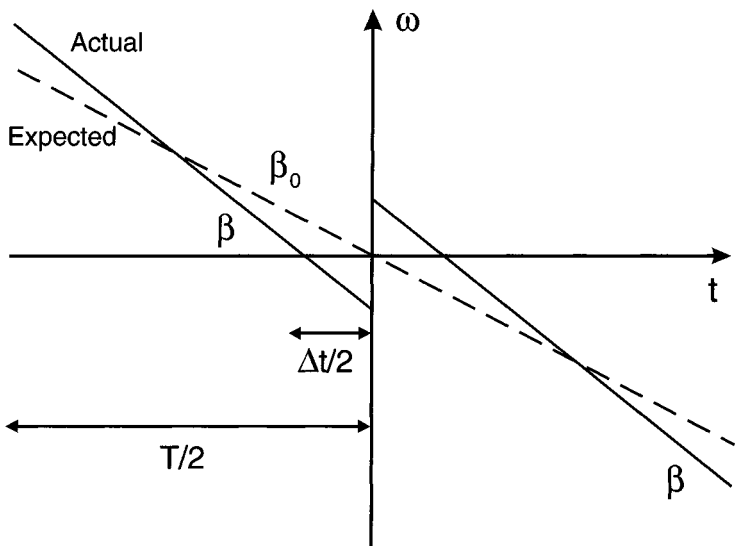


Figure 3.4 Effect of focus parameter on image formation position for two-look MLR.

is related to the change in the Doppler centroid by $\Delta\beta \approx \Delta\alpha/T$ over the aperture T .

In the CO method, the focus parameter β is varied for the complete aperture T with consequences illustrated in Figure 3.5. If the data have the same focus parameter as the reference, that is, β_0 , the compressed peak for any object in the scene has high contrast, as shown. At other values of β the image is defocused with a lower contrast peak. Thus, CO is based on the simple observation that focusing the image yields features that are both narrower and of greater intensity. The algorithm estimates the optimum value of the focus parameter by iterating over a set of reference functions with varying values of β .

PPP is restricted since it operates only on dominant scatterers. The other four autofocus processes are performed on several (e.g., 32) different range gates. This improves the accuracy of the measured focus parameter since individual estimates are independent.

Once autofocus is implemented, the blurred image in Figure 3.1 is improved as shown in Figure 3.6. In order to achieve this result, the scene was divided into eight strips along track that were focused independently (using CO) and the image displayed using the estimated β for each strip. It is apparent that defocus effects to the right of the original scene have been removed while focus on the left of the scene has been improved. Note that the horizontal line about a quarter of the way up each image is a range marker, not a feature of the

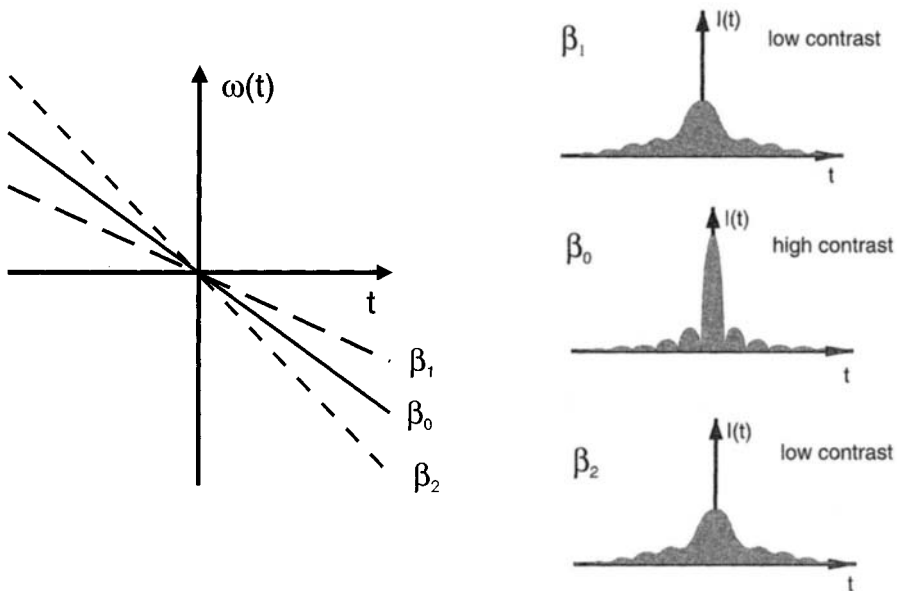


Figure 3.5 Effect of varying focus parameter on the compressed image in CO.

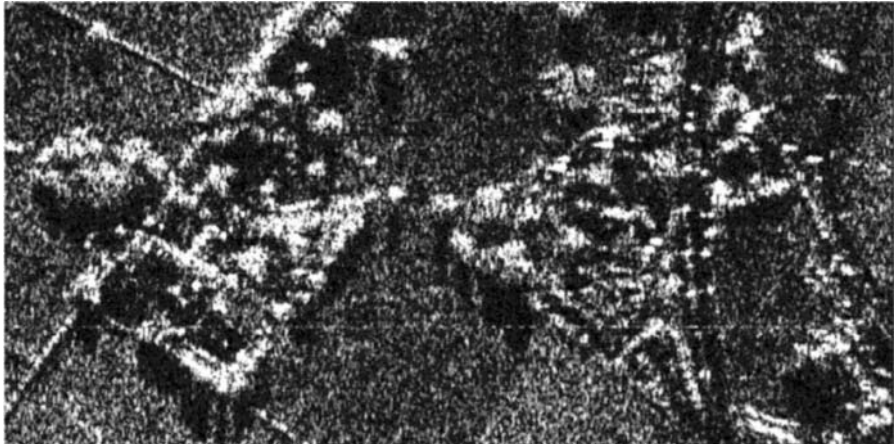


Figure 3.6 Strip autofocus version of Figure 3.1 after using the CO autofocus method.

actual image. This autofocus process is signal-based; the effect of the unknown motion on image quality is used to correct itself.

3.2.2 Limiting Accuracy of Autofocus Techniques

In comparing the sensitivity of these autofocus techniques, various **aspects of performance** need to be considered, namely:

- Fundamental limits imposed by clutter;
- Dependence on aperture length;
- Robustness to the nature of the scene.

The choice of method depends on each aspect, including an assessment of its importance [1,21–24]. The **complexity of implementation** is also an issue, but given the rapid advance of computing and signal processing, this is not the most telling consideration.

Initially we concentrate on fundamental clutter-limited sensitivity. We analyze the simple case of a single point target in a background of uniform clutter. Assuming correct focusing, we define the ratio of the peak compressed signal for the full aperture T_0 to the mean clutter background as the **signal-to-clutter ratio (SCR)**; see (4.39). Here T_0 is the transit time of an object through the illuminating beam. Changes on a faster time scale demand the use of shorter apertures of duration $T (< T_0)$ over which β remains approximately constant. An estimate of β is obtained within each aperture. Perturbation expansions of

the appropriate equations for each algorithm, in terms of the unknown parameters and the estimated quantities, then lead to a common expression for the mean-square uncertainty in the focus parameter estimate given by [21–24]

$$\langle \delta\beta^2 \rangle_T \approx \frac{c T_0}{\text{SCR} \times T^5} \quad (3.5)$$

for an aperture of duration T . Thus, all five methods have the same form for their statistical uncertainty, differing only in the value of c , which is 40 for PPP, 80 for PGA and PD, 96 for MLR, and 90 for CO.

This result applies to a single look within the aperture. However, there are T_0/T uncorrelated looks that can each be exploited for autofocusing over an aperture T . If the algorithm uses all available looks, the mean-square error in β for aperture T would be reduced by T/T_0 to [24]

$$\langle \delta\beta^2 \rangle_T \approx \frac{c}{\text{SCR} \times T^4} \quad (3.6)$$

The mean-square error in β can be further reduced by a factor N , by performing autofocus over N different range lines. It is apparent that this error is minimised by increasing the aperture duration to the maximum possible, that is, T_0 . Of course, this is only possible if β is approximately constant over this time.

3.2.3 The Effect of Scatterer Properties on Autofocus

We previously assumed a single point object in a background of weak clutter. A more realistic scenario might require autofocus on extended objects that occupy more than a single resolution cell. In addition, the spatial density of objects within the scene can affect autofocus.

3.2.3.1 Extended Objects

Many natural objects, such as bushes and trees, can be described in terms of a large number of random scatterers spread over several pixels, equivalent to a region of clutter with a higher cross section. The received signal is then derived from interference between all the scatterers that make up that object. If it occupies b pixels in the azimuth direction, its scattered field covers a frequency range $1/b\Delta T$ that reduces the maximum effective integration time from T_0 to T_0/b . The focus parameter will then be estimated with a mean-square error over the full aperture T_0 , obtained from (3.5), of

$$\langle \delta\beta^2 \rangle_{T_0} \approx \frac{cb^5}{SCR \times T_0^4} \quad (3.7)$$

where c takes the values given previously. This is a factor b^5 worse than for a point target and indicates the importance of using point targets for autofocus wherever possible. This conclusion applies equally to all autofocus techniques and so does not differentiate between them from either theoretical or practical considerations.

3.2.3.2 Object Spatial Density

Let us now consider the effect of the spatial density of objects in the along-track direction. Suppose there are N_a randomly positioned objects within the same range line over the full aperture T_0 , with an average temporal spacing of $\tau_a = T_0/N_a$. Both PPP and PG depend on extracting the phase history of a single object in each range line. Interference from another object at some unknown spacing will compromise the ability of the algorithms to follow the phase variations. It is necessary to filter out these interfering contributions [9–11] by restricting the available time to approximate the mean separation around each object so that the aperture length becomes $T \approx \tau_a$. If we utilize all the resulting N_a possible looks, the error in the focus parameter will be given by

$$\langle \delta\beta^2 \rangle_{T_0} \approx \frac{cN_a^4}{SCR \times T_0^4} \quad (3.8)$$

where $c = 40$ for PPP or $c = 80$ for PG, which represents a considerable reduction in potential focus accuracy compared with a single object, that is, $N_a = 1$.

PD has an important advantage over PPP and PG in that it can accommodate multiple scatterers [12] since each scatterer provides an independent focus estimate. Similarly, objects in MLR and CO provide independent information as long as they are resolved in the original compressed image. Thus PD, MLR, and CO lead to a mean-square error in β over the full aperture T_0 given by

$$\langle \delta\beta^2 \rangle_{T_0} \approx \frac{c}{N_a \times SCR \times T_0^4} \quad (3.9)$$

where $c = 80, 96$, and 90 , respectively.

This discussion of scatterer properties has demonstrated the importance of applying autofocus to pointlike objects wherever possible. For a sufficiently dominant scatterer PPP yields the best performance. However, the analysis has shown the superiority of the PD, MLR, and CO techniques over PPP and PG

wherever a high density of objects is encountered. This would certainly be the case within urban areas. However, the effect might not be of overriding importance in those situations since individual objects would tend to have large values of SCR leading to an error in β that might be adequate for a given application.

3.3 Geometric and Radiometric Distortion

Variations in both α and β not only affect image defocus, as discussed in the previous section, but also give rise to geometric and radiometric distortion in the SAR image. In this section we demonstrate how all three effects can be related to a mismatched focus parameter. Initially we consider azimuthal geometric distortion. To illustrate the problem, Figure 3.7 shows a strip SAR image of length 7.2 km and swathwidth 4.7 km at a range of 37 km, with antenna length $d_a = 1.8\text{m}$ and $\lambda = 0.031\text{m}$. Under these conditions the illuminated azimuth beamwidth at the center of the swath is 678m, so the strip subtends 10.6 full apertures. The image has undergone autofocusing that was applied in strips of 192m, so there are about 3.5 strips per full aperture. The local focus appears good, but overlaying the scene with map data registered at the center of the strip reveals that the image is distorted in azimuth by hundreds of meters toward the edges.

3.3.1 Physical Cause and Associated Distortion

One might expect that the same mechanism would give rise both to the defocus visible in Figure 3.1 and the geometrical azimuthal distortion in Figure 3.7. We have already demonstrated in (3.2) that the dominant causes of defocus are a mismatch between nominal and actual along-track velocities, $\Delta V/V$, or an across-track acceleration component, a_r (corresponding to variations in Doppler centroid). For the along-track velocity error the azimuthal distance traveled during time t is increased from Vt by the along-track distortion contribution

$$\Delta x_a(t) = \int_0^t \Delta V(t') dt' \quad (3.10)$$

which is independent of range. The across-track acceleration makes itself apparent through the angular displacement in the antenna beam, given by $-V_r/V$, where motion toward the sensor is positive. The along-track distortion due to radial acceleration is thus given by

$$\Delta x_r(t) = -\frac{R_0 V_r}{V} = -\frac{R_0}{V} \int_0^t a_r(t') dt' - \frac{R_0 V_r(0)}{V} \quad (3.11)$$

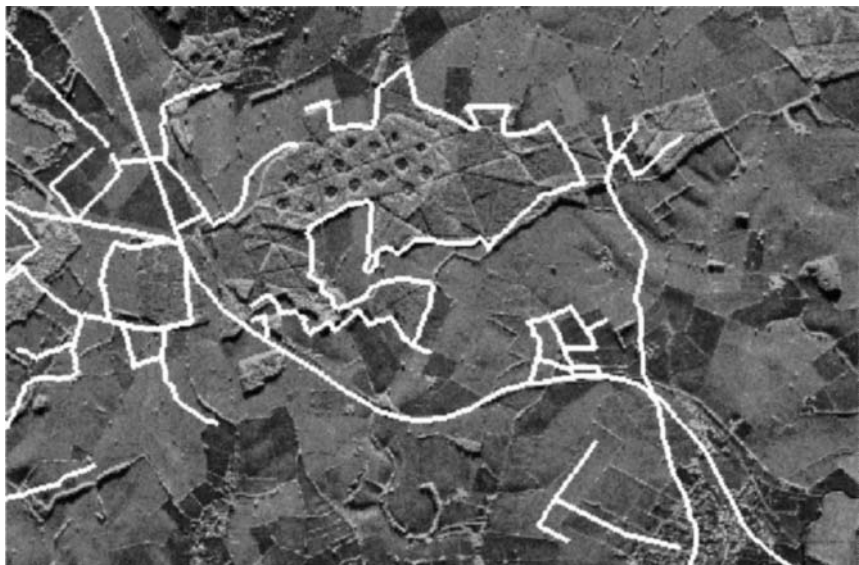


Figure 3.7 Azimuthal distortion after strip autofocus processing. The image dimension is 7.2 km by 4.7 km covering 10.6 illuminated beamwidths. The overlay is taken from map data and registered at the center.

which introduces a range-independent skew of the image without affecting the focusing capability. For convenience, $V_r(0)$ is normally selected to be the average radial velocity over the required strip length. However, this choice is somewhat arbitrary. A different value would modify image skew without degrading resolution.

Unfortunately it is not possible to combine (3.10) and (3.11) with (3.2) to express azimuthal distortion unambiguously in terms of a change in the focus parameter, $\Delta\beta$. The only way to resolve the ambiguity is to make an independent measurement of one component so that the residual can then be attributed to the other. For example, slaving the radar PRF to along-track velocity, measured by an *Inertial Navigation System* (INS) or *Global Positioning System* (GPS), greatly reduces the along-track contributions so that the defocus error is almost entirely due to radial acceleration. The final distortion then depends on the accuracy of the system used to determine this azimuthal sample spacing.

It is instructive to quantify typical defocus and distortion caused by radial and along-track uncertainties. These depend on fluctuations in the focus parameter, whose fractional variation, $\Delta\beta/\beta$, derived from the first autofocus pass, is plotted in Figure 3.8. It is apparent that changes of 10% can sometimes occur between neighboring samples, separated by 192m (or about 1 sec for $V = 200 \text{ ms}^{-1}$). Based on (3.2), the defocus visible on the right of Figure 3.1 could be caused by either a radial acceleration of 0.1 ms^{-2} or an azimuthal velocity mis-

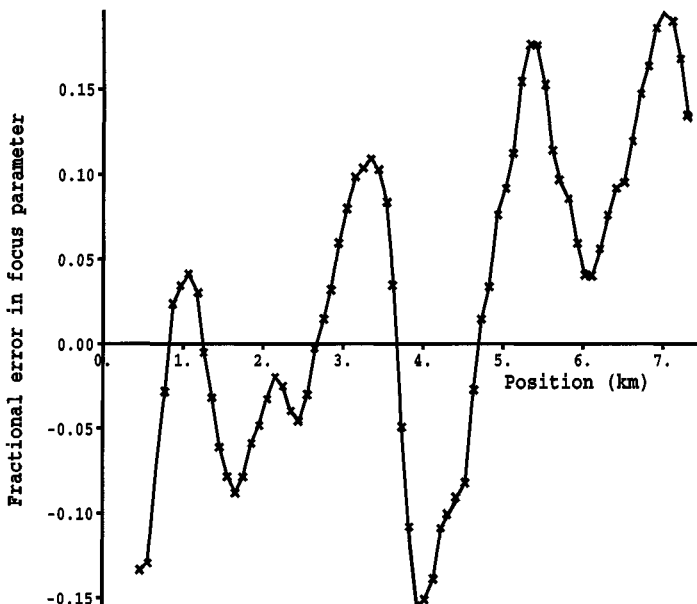


Figure 3.8 Plot of the fractional focus parameter variations derived during the first pass of strip autofocus processing.

match of 10 ms^{-1} . The change between focused imagery on the left of Figure 3.1 and the defocused output on the right could be attributed to an azimuthal acceleration of 10 ms^{-2} or a change in radial acceleration of 0.1 ms^{-2} . The former is unrealistic, so it is reasonable to interpret errors in β as predominantly due to radial acceleration in this instance. Indeed, if a SAR sensor includes conventional MOCO and INS that reduce unknown motions to effectively the same order in azimuthal and along-track directions, this result suggests that the azimuthal velocity contribution to image distortion can be ignored. Accordingly, in the following discussion we attribute all changes in focus parameter to radial motion, leading to an azimuthal distortion of [20,25–27]

$$\Delta x(t) = V \int_0^t \frac{\Delta \beta(t')}{\beta} dt' + \frac{R_0 V_r(0)}{V} \quad (3.12)$$

The across-track distortion after time t will be given by

$$\Delta y(t) = \int_0^{t'} \int_0^{t''} a_r(t'') dt'' dt' + V_r(0)t = \frac{V^2}{R_0} \int_0^{t'} \int_0^{t''} \frac{\Delta \beta(t'')}{\beta} dt'' dt' + V_r(0)t \quad (3.13)$$

with an associated phase error [18,25–27]

$$\Delta\phi(t) \equiv \frac{4\pi\Delta y(t)}{\lambda} = \frac{4\pi V^2}{\lambda R_0} \int_0^t \int_0^{t'} \frac{\Delta\beta(t'')}{\beta} dt'' dt' + \frac{4\pi V_r(0)t}{\lambda} \quad (3.14)$$

Equation (3.11) showed that azimuthal distortion was the product of the range and the pointing angle offset, $-V/\lambda$. Assuming that the real antenna was stabilized to be orthogonal to the assumed track, this would result in reduced energy in the compressed peak. The ratio of this offset angle to the real beam-width at time t is then given by

$$\epsilon(t) = \frac{Vd_a}{R_0\lambda} \int_0^t \frac{\Delta\beta(t')}{\beta} dt' + \frac{V_r(0)d_a}{V\lambda} \quad (3.15)$$

for aperture length d_a . Assuming a rectangular antenna weighting for simplicity, the power in the compressed image would then be reduced by a factor

$$P = \left(\frac{2 \sin \pi \epsilon / 2}{\pi \epsilon} \right)^2 \quad (3.16)$$

which relates radiometric distortion directly to fluctuations in the focus parameter.

3.3.2 Signal-Based MOCO

Since autofocus errors can be related to radial acceleration, they can be treated as inputs to an extended MOCO system. The phase correction derived in (3.14) can be applied to each sample to shift it to a straight line trajectory [26]. When this signal-based MOCO is applied to the data used to form the SAR image in Figure 3.7, the resulting image, in Figure 3.9, is seen to be largely free from the effects of distortion.

There may still be some distortion arising from the angular dependence in elevation of across-track acceleration, particularly for incidence angles far from grazing. Autofocusing estimates the radial acceleration component along a given line-of-sight that corresponds to a particular range in the SAR image. For given sensor acceleration components the projection at different ranges within the swath will vary in a deterministic fashion [20] allowing a range-dependent phase correction to be applied.

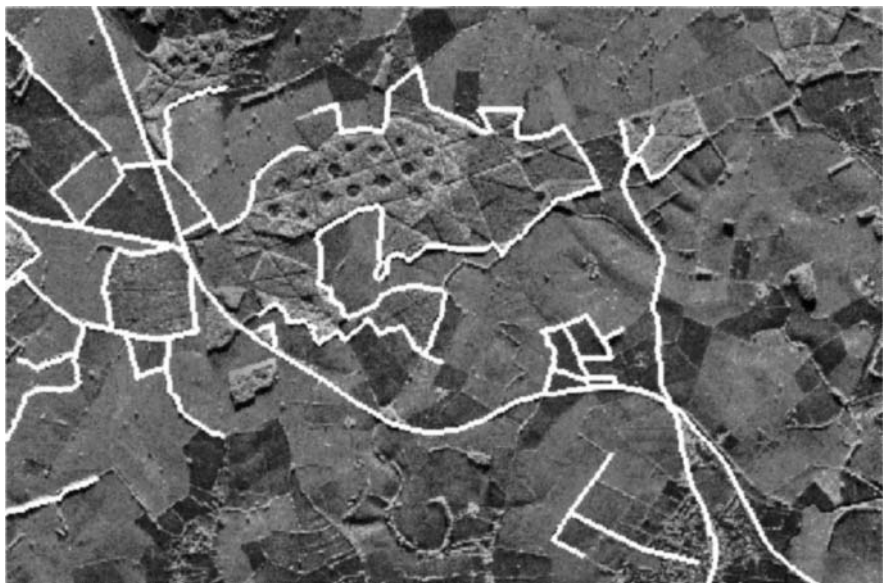


Figure 3.9 SAR image following signal-based MOCO using autofocus results for phase correction.

3.3.3 Antenna Stabilization

The described autofocus techniques provide a history of the variation in focus parameter caused by changes in the Doppler centroid. This history can be used in a variety of ways to correct different image quality deficiencies. One important aspect of the signal-based MOCO scheme in Section 3.3.2 is its impact on antenna stabilization.

Suppose the antenna orientation is locked to the axis of the sensor platform, for example, normal. If the platform then describes an arc of a circle, with its axis lying along the track, the pointing angle and associated Doppler centroid will vary and the real and synthetic apertures will have different axes leading to radiometric errors, as described in Section 3.3.1. Doppler tracking is often used to correct the data, so zero Doppler occurs at the center of the real beam. This removes radiometric variation but, unfortunately, leaves geometric distortion. If the geometric distortion corrections previously outlined are applied to the data, the trajectory of the synthetic aperture is converted to a straight line, as desired. However, the antenna retains the same orientations so that the pointing angles of the real and synthetic beams are mismatched with consequent radiometric distortion. Thus, it is incorrect to stabilize the antenna with respect to the sensor platform if geometric and radiometric corrections are both required. The pre-

ferred technique for simultaneously minimizing geometric and radiometric distortion adopts antenna stabilization to the desired average track. The relative angle of the sensor platform and antenna then vary as the platform describes a curved track. However, on resampling the track to a straight line, the real and synthetic apertures become aligned. The only discrepancy between their tracks is due to $V_r(0)$, the unknown average radial velocity contribution over the total strip duration. Provided this difference is sufficiently small, it is possible to correct the image intensity appropriately using (3.16).

3.4 Residual SAR Imaging Errors

The autofocus methods in Section 3.2 typically reduce the phase error across the aperture to about $\pi/20$ radians, corresponding to about 1% degradation in the 3-dB width of the PSF, which is comparatively insignificant. In this section we derive the effect of the residual error in the focus parameter $\delta\beta$, following signal-based MOCO, on geometric and radiometric distortion.

3.4.1 Residual Geometric and Radiometric Distortion

The residual azimuthal distortion after signal-based MOCO can be derived from (3.5) and (3.12). The distortion over the aperture T is given by $\delta x \approx VT \delta\beta/\beta$, so that the *root mean square* (rms) cumulative distortion over the full aperture, made up of T_0/T independent apertures, will be given by

$$\langle \delta x^2 \rangle_{T_0}^{1/2} \approx VT \frac{\langle \delta\beta^2 \rangle_T^{1/2}}{\beta} \sqrt{\frac{T_0}{T}} = \frac{d_a}{2\pi} \sqrt{\frac{c}{\text{SCR} \times N_r}} \frac{T_0^3}{T^3} \quad (3.17)$$

From distortion considerations, therefore, it is important to maximize the subaperture duration. Thus, autofocusing on extended clutter and using the phase gradient estimator in crowded environments is to be avoided.

This prediction is compared with measured distortions in Figure 3.10, using results obtained by performing independent autofocus and phase correction of a second SAR image of the same scene. Displacements between objects in the two scenes were then measured directly, after the scenes had been suitably registered [1]. Since the scenes suffer from independent sources of error, the rms error in a single SAR image would be reduced by a factor of $\sqrt{2}$ from about 1.5m between both images to 1.1m in a single image. The residual structure in the plot indicates that slow fluctuations are not being properly corrected, probably caused by range-dependent effects. If we ignore these, the rms distortion over the strip

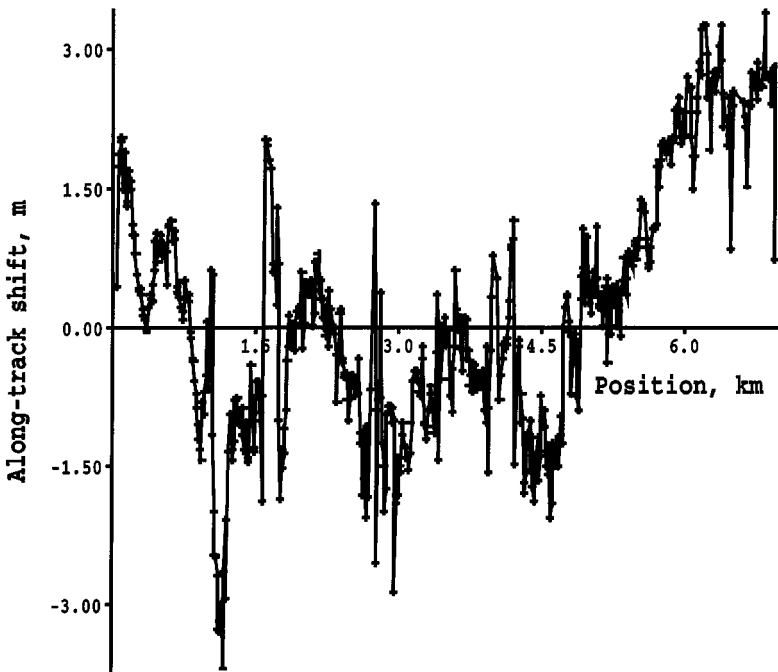


Figure 3.10 Residual azimuthal distortion after signal-based MOCO.

would be about half the total, that is, 0.55m. From (3.17), the predicted distortion for $d_a = 1.8\text{m}$, $N_r = 32$, and $c = 90$ (for contrast optimization autofocus), assuming the full aperture is used (so that $T = T_0$), would be $1.6/\sqrt{\text{SCR}}$ over the whole image strip. The observed performance indicates an SCR of about 10 dB, which is consistent with these images. A comparison with Figure 3.7 shows that phase correction has reduced distortion by about two orders of magnitude. Note that if it was not possible to use the full aperture for autofocus the residual distortion would be increased by $(T_0/T)^{3/2}$.

The corresponding result for across-track distortion is obtained from (3.5) and (3.13). The distortion over the aperture T is given by $\delta y \approx V^2 T^2 \delta \beta / 2\beta R_0$, so the rms cumulative distortion over the full aperture is given by

$$\langle \delta y^2 \rangle_{T_0}^{1/2} \approx \frac{V^2 T^2}{2R_0} \frac{\langle \delta \beta^2 \rangle_T^{1/2}}{\beta} \sqrt{\frac{T_0}{T}} = \frac{\lambda}{4\pi} \sqrt{\frac{c}{\text{SCR} \times N_r}} \frac{T_0}{T} \quad (3.18)$$

Assuming the same conditions as given previously for Figure 3.7, the predicted across-track distortion over a single aperture would be 0.0013m, leading to a

value of 0.0042m over the full strip, which is negligible compared with the range resolution.

The residual radiometric distortion depends on the ratio of the residual angular skew to the real beamwidth. It can be derived from (3.5) and (3.15). During the aperture time T the fractional pointing angle difference is given by $\delta\epsilon \approx VTd_a\delta\beta/\beta R_0\lambda$, so the rms cumulative relative skew over the full aperture is given by

$$\langle\delta\epsilon^2\rangle_{T_0}^{1/2} \approx \frac{VTd_a}{R_0\lambda} \frac{\langle\delta\beta^2\rangle_T^{1/2}}{\beta} = \frac{d_a^2}{2\pi R_0\lambda} \sqrt{\frac{c}{\text{SCR} \times N_r} \frac{T_0^3}{T^3}} \quad (3.19)$$

Under the same conditions as for Figure 3.7, the predicted skew is 0.00023 of the full beamwidth over the full aperture and 0.00071 beamwidths over the strip, which causes a negligible reduction in image intensity. The difference between the predicted track and the average over the strip is likely to be much more significant. This is determined by the stability of the sensor platform. If the trajectory could be defined by combined INS and GPS, the angular uncertainty for the average track might be about 1.5 mrad, corresponding to a fractional skew of about 0.09 for a 1.8-m antenna, which completely dominates random effects. From (3.16) we find that even this would only contribute a radiometric error of about 1%. In fact, this could be further reduced by correcting for the angular difference once the average track had been calculated during the signal-based MOCO stage.

3.4.2 Excess Sidelobe Levels

Random uncertainties in the estimated focus parameter lead to errors in the phase correction, which become evident through excess sidelobes in the PSF. Since the position and strength of these sidelobes are both random, they are best characterized by the *integrated sidelobe ratio* (ISLR), which is the ratio of the increase in sidelobe energy to the peak energy. Carrara et al. [7] show that the ISLR can be related to phase errors within the synthetic aperture such that

$$\text{ISLR} \approx \exp[\langle\delta\phi^2\rangle] - 1 \quad (3.20)$$

for small phase errors, $\delta\phi$. From (3.1), the phase error at time t within the aperture due to uncertainty in the focus parameter is given by $\delta\phi \approx \delta\beta t$. Hence, following (3.14), the mean-square residual phase error over N_r rangelines within the aperture $t = \pm T/2$ would be given by

$$\langle \delta\phi^2 \rangle_T \approx \langle \delta\beta^2 \rangle_T \frac{1}{T} \int_{-T/2}^{T/2} t^4 dt = \frac{c}{80 \times SCR \times N}, \quad (3.21)$$

with c taking the values derived in Section 3.2.3. This residual phase error is independent of aperture duration, provided that all possible looks are used in the signal-based MOCO.

For the same operating conditions as for Figure 3.7, (3.21) predicts rms residual phase errors of 0.059 rads leading to an ISLR of -24.5 dB. Typical peak sidelobe levels in a SAR system would be comparable with ISLR values about 10 dBs greater. Thus, the random integrated sidelobe power introduced by phase errors is about an order of magnitude less than the deterministic contribution. This random ISLR component could be further reduced by averaging over a larger number of rangelines, provided they contain strong scatterers.

3.5 Refinements to Signal-Based MOCO

The discussion of residual errors in the previous section has shown the importance of using the full aperture for autofocus to minimize all forms of image quality degradation. However, if the unknown motion varies on a short time scale, this will not be possible and we must use shorter apertures whose duration T represents the time over which the focus parameter is approximately constant. Even when this condition is satisfied, the response of the autofocus process will be a function of the rate of change of the focus parameter. Iterative autofocus, described in Section 3.5.1, helps to circumvent the nonuniform frequency response of a given aperture by progressively removing motion contributions until only random contributions remain. Nevertheless, the most significant limitation to autofocus processing is the requirement to use short apertures to compensate high-frequency components. As demonstrated in Section 3.4, treating each aperture independently can result in appreciable distortion and cumulative phase error for small apertures. However, in Section 3.5.2 we describe a coherent, iterative, autofocus technique that allows us to realize long-term low distortion, corresponding to the full aperture, while simultaneously correcting higher frequency components. Finally, in Section 3.5.3 we describe how a combined conventional and signal-based MOCO scheme can be implemented offering optimum performance.

3.5.1 Iterated Autofocus With Phase Correction

An effective approach to removing any motion contributions that exceed the residual uncertainty is to iterate the autofocus and phase correction process [1].

Typical results are illustrated in Figure 3.11, which shows a sequence of plots of autofocus correction as a function of iteration number for the original data of Figure 3.7, where Figure 3.11(a) is a repeat of Figure 3.8. A conventional **depth-of-focus (DOF)** criterion [20] corresponds to a phase error of $\pi/2$ at the edge of the aperture, so $\delta\beta_{\text{DOF}}/\beta = d_{\text{eff}}^2/R_0\lambda$, where d_{eff} , the effective antenna length, is twice the intended resolution. Since the latter was 1.5m in Figure 3.11, the corresponding DOF limit on $\delta\beta/\beta$ is 0.007. This is included in Figure 3.11 for comparison.

The original correction from the first iteration (a) shows fractional variations of ± 0.15 , considerably greater than the DOF limit. During the second iteration (b), fluctuations are considerably reduced by incorporating the correction from the first stage. However, there is a strong residual peak at an azimuthal position of about 4.3 km and also evidence of correlations between errors, indicating that the correction process is not complete. By the last iteration (c) the fluctuations are basically random with a fractional standard deviation of about 0.0007, an order of magnitude better than the DOF limit. Residual fluctuations for many systems are found to become negligible after three or four iterations. The residual errors in the last iteration in Figure 3.11 can be compared with predictions from (3.6). For the same operating conditions as for Figure 3.7, the predicted rms error in the focus parameter would be 0.0006, which is reasonably consistent with measurement. The corresponding rms acceleration error at this range would be $7 \times 10^{-4} \text{ ms}^{-2}$, while at twice the range it would be $1.8 \times 10^{-4} \text{ ms}^{-2}$ if the aperture duration was also doubled. The latter is about an order of magnitude smaller than can be achieved with a conventional accelerometer. This illustrates the considerable reduction in long-term distortion that can be attained using autofocus-based phase correction. This advantage increases progressively as range and integration time increase.

3.5.2 High-Frequency Tracking With Low Distortion

We have indicated the importance of adopting the maximum duration aperture to minimize the error in β . If the sensor undergoes radial motion variations on a scale shorter than the synthetic aperture, this unknown motion cannot be corrected since the autofocus response is negligible. This demands a shorter aperture to track high-frequency changes, leading to degraded image quality. However, a technique that combines both high-frequency response and low distortion [3,22,24] comprises the following stages:

1. The focus parameter is estimated over a sequence of apertures of duration T sufficiently short to correct for high-frequency motions.

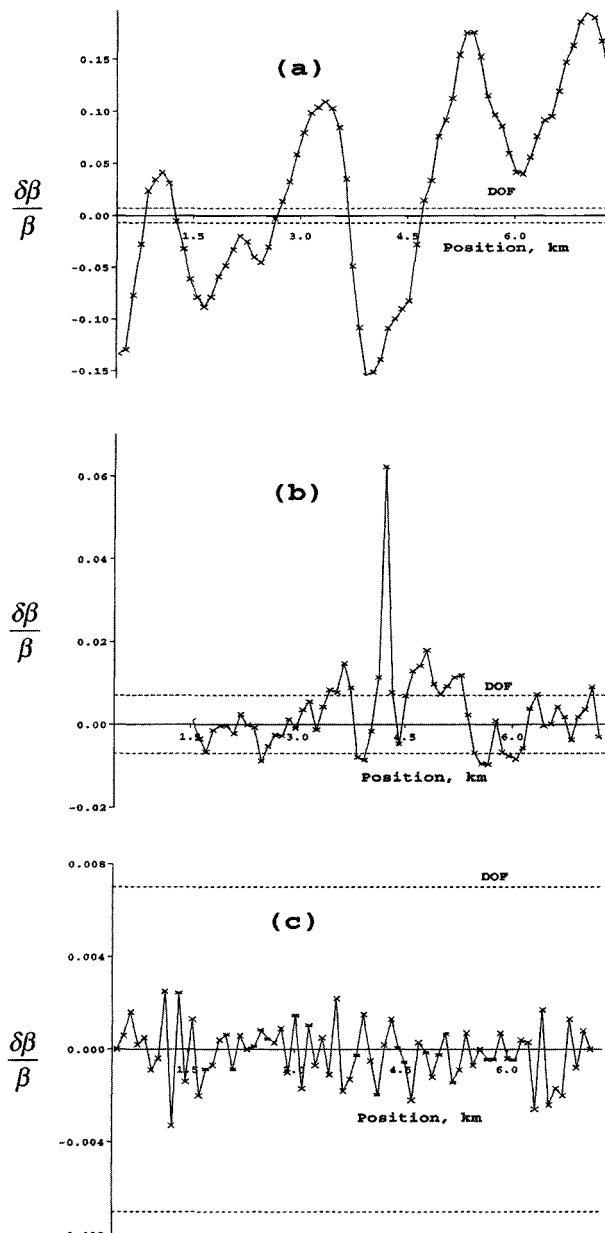


Figure 3.11 Estimated autofocus correction, $\delta\beta/\beta$, as a function of along-track position after (a) first, (b) second, and (c) tenth autofocus iteration.

The estimated correction then has the form $\Delta\beta + \eta$, where $\Delta\beta$ represents the true focus mismatch and η the estimation error.

2. The signal is phase-corrected using the focus parameters in (3.14). This has the effect of removing the true focus mismatch $\Delta\beta$ with a residual error η .
3. The aperture length is doubled and the process repeated. The residual focus errors from the previous two apertures are now averaged and contribute to the correction for the new aperture. The new residual error in β corresponds to the double-length aperture and so is a factor of 16 smaller than the previous value, from (3.6), assuming that all possible looks are used for autofocus. The cumulative along-track distortion and phase error are now determined by this larger aperture.
4. The process of doubling the aperture is repeated until it attains the full aperture length.

This technique can be applied to the PD, MLR, and CO algorithms under all circumstances and PPP and PG in a sparse scatterer environment. The final error in the focus parameter for the full aperture is then as expected from (3.6) when $T = T_0$. Thus, this approach yields the maximum sensitivity for the full aperture without compromising high-frequency tracking performance. However, the rms error in phase and azimuthal position of each sample is determined by the shortest aperture used.

3.5.3 Combined Signal-Based and Conventional MOCO

Signal-based MOCO operates most successfully when the focus parameter is changing only slowly, whereas conventional MOCO responds better to more rapid changes. There is thus an advantage in combining conventional MOCO, following well-tried methods [28,29] discussed in detail in Carrara et al. [7], with subsequent signal-based MOCO. The overlap between the ability of conventional MOCO to remove high-frequency effects and that of the autofocus-based approach to compensate for slow drifts is quantified in this section. The output of the autofocus filter for aperture T and a sensor acceleration *power spectral density* (PSD) $S(f)$, will be given by

$$A_T(f) \approx S^{1/2}(f)(1 - H_T(f)) + N_T^{1/2}(f) \quad (3.22)$$

where $N_T(f)$ is the PSD of the uncertainty introduced in the autofocus process given by $N_T(f) \approx \langle \delta a_R^2 \rangle$. The form of the response for CO, PG, and PD autofocus methods has been shown to be given by [24,30]

$$H(f) = -\frac{15}{(\pi f)^3} \left[\left(1 - \frac{3}{(\pi f)^2} \right) \sin \pi f + \frac{3}{\pi f} \cos \pi f \right] \quad (3.23)$$

while the response for MLR has a similar shape [24]. For subsequent iterations the autofocus filter operates on the output of the previous iteration, following phase correction. Hence

$$A_{T_2}(f) \approx A_{T_1}(f)(1 - H_{T_2}(f)) + N_{T_2}^{1/2}(f) \quad (3.24)$$

Repeating the process for progressively doubled apertures allows the final power spectrum of the sensor accelerations after autofocus and phase correction to be calculated for a specified sensor acceleration spectrum and autofocus filter duration. Figure 3.12 plots the predicted residual power spectrum after signal-based MOCO for the DRA Canberra system. In an earlier study [24] the approximate acceleration power spectrum for the Canberra SAR was found to be of the form

$$S(f) \approx 0.0025f^{-1.4} \quad (3.25)$$

which is shown as curve (a) in Figure 3.12. A typical X-band SAR system was assumed to have a resolution of 1m and a range of 100 km. The full aperture length would be 1.5 km, corresponding to a duration $T_0 = 7.5$ sec for $V = 200 \text{ ms}^{-1}$. The predicted performance for the combined system can be derived by supposing that the progressive autofocus and phase correction scheme described in Section 3.5.2 was implemented, commencing with the shortest aperture of 0.47 sec ($= T_0/16$, length 94m) in curve (b) and incrementing in powers of two up to the full aperture in curve (f).

Increasing aperture duration reduces low-frequency components by 12 dBs for each aperture doubling, as predicted in (3.6). A reduction of about 90 dB in the original uncompensated aircraft acceleration spectrum is expected at low frequencies. However, at high frequencies, additional spectral contributions are introduced by the estimation errors in the autofocus process. These cannot be removed by subsequent iteration since the autofocus response is near zero at these frequencies. If signal-based MOCO had commenced with a longer subaperture, however, high-frequency degradation would be significantly reduced. For example, the contributions introduced by an aperture of 0.94 sec would be a factor 12 dBs smaller. Thus, an initial stage in designing such a signal-based MOCO would begin with an aperture duration that only degraded the original high-frequency acceleration spectrum slightly.

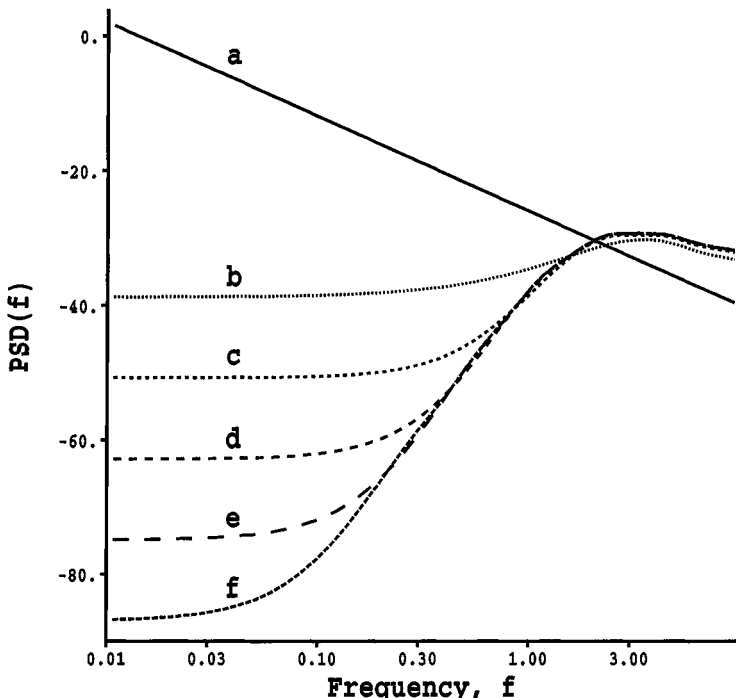


Figure 3.12 Predicted residual acceleration power spectrum after autofocusing: (a) original PSD, (b) after autofocus with $T = 0.47$ sec, (c-f) subsequent iterations with progressive doubling of aperture to $T = 7.5$ sec.

On combining signal-based and conventional MOCO we require the conventional MOCO to remove high-frequency components to the right of the response in Figure 3.12. The engineering design of such a system would investigate the compromise of introducing conventional MOCO to correct for high-frequency effects and increasing the minimum aperture to ensure that autofocus uncertainty does not degrade the result. Note that the response shown in Figure 3.12 would indicate low long-term distortion and resolution degradation, with only a slight increase in the ISLR due to phase errors.

An example of this combination of conventional and signal-based MOCO is shown in Figure 3.13. An airborne SAR was operated at long range while encountering turbulence. The original “compressed” image (a) shows little trace of a target at all. Applying conventional MOCO (b) improves the situation. However, the phase error is clearly much greater than the DOF limit. When autofocus-based MOCO (c) is included, image quality improves significantly, though it still has not achieved ideal sidelobe levels. This extreme example

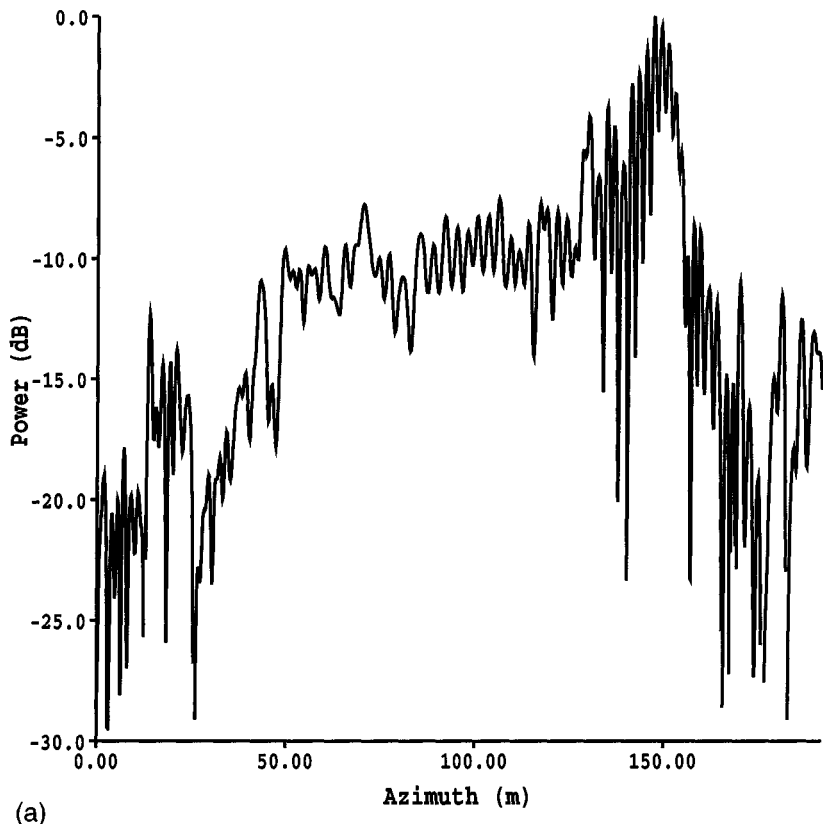


Figure 3.13 Measured azimuthal PSF at long range while encountering turbulence: (a) uncorrected response, (b) with conventional MOCO, and (c) with conventional and signal-based MOCO.

illustrates the different roles in two-component MOCO. The conventional stage removes high-frequency effects, hopefully reducing the phase error toward the DOF limit. The signal-based stage then removes most of the residual effects, allowing high-quality imagery to be achieved.

3.6 Conclusions

In this chapter the basic physical principles governing SAR image formation using signal-based MOCO techniques have been discussed. A series of algorithms has been developed to rectify SAR image defects caused by variations in

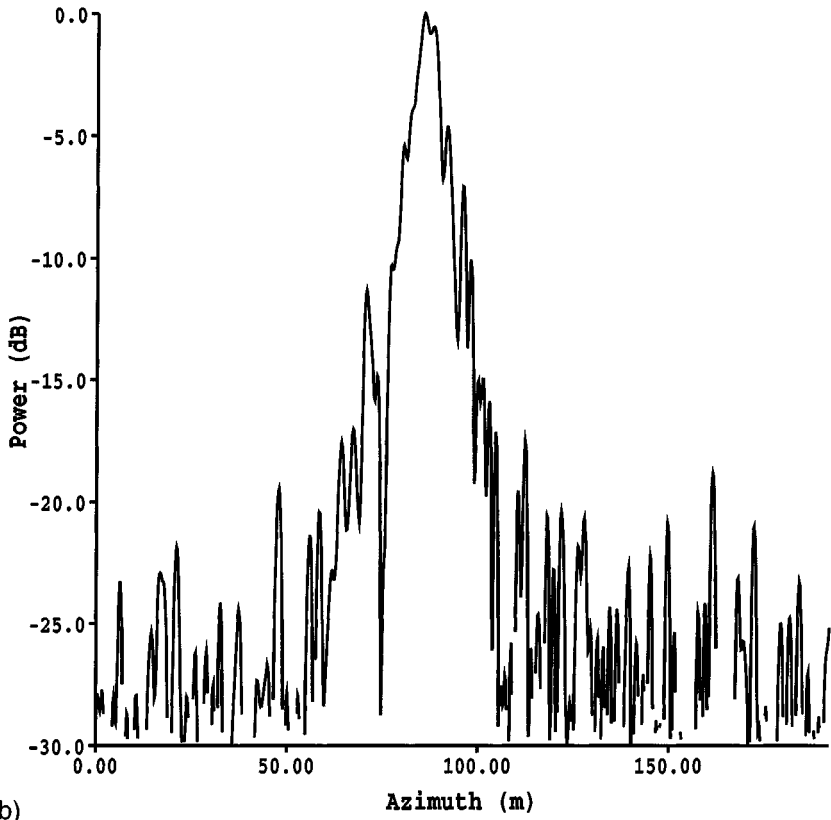


Figure 3.13 (continued).

range due to unknown sensor motion. In each case, analysis establishes the performance limits imposed by the algorithm and the radar data themselves.

Initially image defocus was corrected using autofocus methods. These yield a time-dependent focus parameter error that was shown to be the source of:

- Azimuthal and radial geometric distortion;
- Radiometric distortion;
- Excess PSF sidelobe levels.

By employing this focus-parameter error in a phase-correction MOCO process, we can simultaneously correct all these effects, leaving only very small residual data-dependent errors.

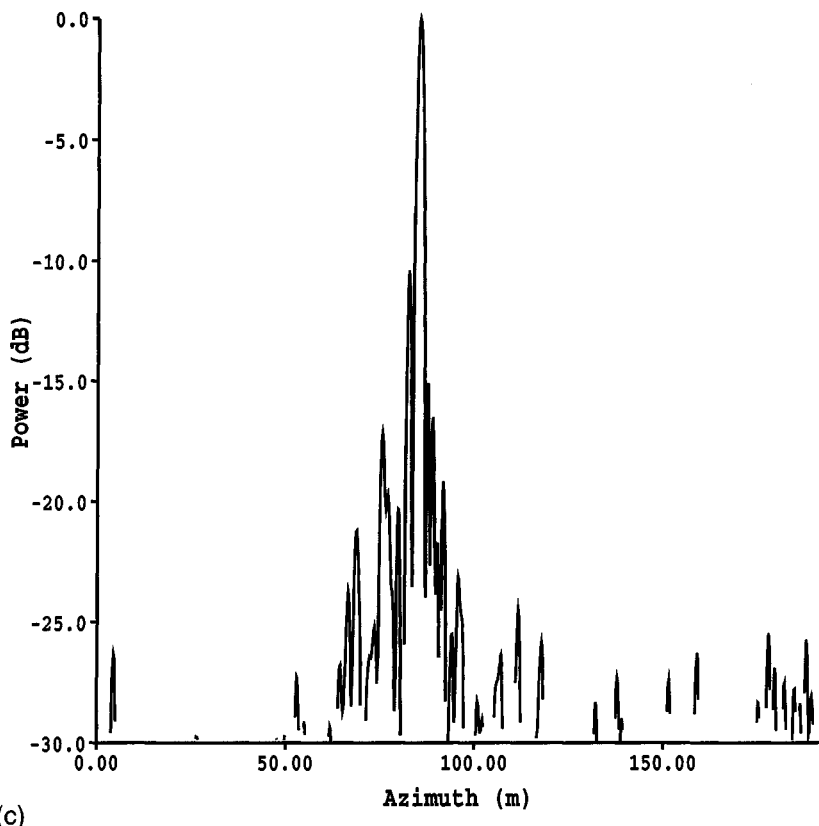


Figure 3.13 (continued).

Signal-based MOCO cannot derive information about amplitude modulation caused by antenna directional instability. It is therefore important that the antenna should be accurately stabilized to remove pointing angle errors. Signal-based MOCO can be combined with conventional MOCO for greatest effect in correcting phase modulation due to unknown sensor motion. Conventional accelerometers provide high sensitivity for rapid changes in phase, whereas signal-based MOCO is better for slow drifts. Thus, a combined system can be designed, as described, which incorporates the best of each method.

Signal-based MOCO is a post-processing stage that can be applied to raw complex SAR; it is not restricted to airborne systems and has been used with ERS-1, for example. Indeed, in this case it permits image quality similar to that attained using the high-definition orbit parameters to be achieved by correcting imagery derived using the initial low-definition orbit parameters [2]. In principle, the same process could be applied to azimuthally compressed complex data,

such as the ERS-1 SLC product. Signal-based MOCO can be applied without any modification to the original radar system and offers significant image quality improvements. Subsequent information extraction processes can thus be applied to high quality imagery, characterized almost entirely by the *theoretical* properties of the SAR system, rather than being corrupted by unknown errors in the PSF.

References

- [1] Belcher, D. P., R. G. White, C. J. Baker, and C. J. Oliver, "The Residual Distortion of Phase-Corrected Autofocused SAR images," *Int. J. Remote Sensing*, Vol. 14, 1993, pp. 769–781.
- [2] Muff, D., A. M. Horne, and C. J. Baker, "Spaceborne SAR Autofocus," *SPIE Conf. on SAR image analysis, simulation and modeling*, Paris, 1995, pp. 7–17.
- [3] Belcher, D. P., A. M. Horne, and C. J. Baker, "Spotlight Mode SAR Autofocus," *IEEE Conf. SAR 93*, Paris, 1993.
- [4] Oliver, C. J., "Problems in SAR Image Formation," DRA Tech. Report DRA/LS2/TR96016, 1997.
- [5] Porcello, L. J., "Turbulence Induced Phase Errors in Synthetic Aperture Radar," *IEEE Trans. Aerospace Electron. Systems*, Vol. AES-6, 1970, pp. 636–644.
- [6] Rondinelli, L. A., and G. W. Zeoli, "Evaluation of the Effect of Random Tropospheric Propagation Phase Errors on Synthetic Array Performance," *Eighth Annual Radar Symp. Record*, University of Michigan, 1962, pp. 235–256.
- [7] Carrara, W. G., R. S. Goodman, and R. M. Majewski, *Spotlight Synthetic Aperture Radar: Signal Processing Algorithms*, Norwood, MA: Artech House, 1995.
- [8] Werness, S. A., W. G. Carrara, L. S. Joyce, and D. B. Franczak, "Moving Target Imaging Algorithm for SAR Data," *IEEE Trans. Aerospace Electron. Systems*, Vol. 26, 1990, pp. 57–67.
- [9] Eichel, P. H., D. C. Ghiglia, and C. V. Jakowatz, "Speckle Processing Method for Synthetic-Aperture-Radar Phase Correction," *Optics Lett.*, Vol. 14, 1989, pp. 1–3.
- [10] Eichel, P. H., and C. V. Jakowatz, "Phase-Gradient Algorithm as an Optimal Estimator of the Phase Derivative," *Optics Lett.*, Vol. 14, 1989, pp. 1101–1109.
- [11] Wahl, D. E., P. H. Eichel, D. C. Ghiglia, and C. V. Jakowatz, "Phase Gradient Auto-focus—a Robust Tool for High Resolution SAR Phase Correction," *IEEE Trans. Aerospace Electron. Systems*, Vol. 30, 1994, pp. 827–834.
- [12] Yoji, G. N., "Phase Difference Auto Focusing for Synthetic Aperture Radar Imaging," United States Patent No. 4999635, 1991.
- [13] Swiger, J. M., "A Digital Autofocus Method for Synthetic Array Spotlight Radar Using Map Drift," *Hughes Aircraft Invention Disclosure*, 1976.
- [14] Mancill, C. E., and J. M. Swiger, "A Map Drift Autofocus Technique for Correcting Higher Order SAR Phase Errors," *27th Annual Tri-Service Radar Symp. Record*, Monterey, CA, 1981, pp. 391–400.

- [15] Vant, M. R., "A Spatially-Variant Autofocus Technique for Synthetic Aperture Radar," *Radar '82*, London: IEE, 1982, pp. 159–163.
- [16] Bendor, G. A., and T. W. Gedra, "Single-Pass Fine-Resolution SAR Autofocus," *Proc. IEEE National Aerospace and Electronics Conf. NAECON*, Dayton, OH, New York: IEEE, 1983, pp. 482–488.
- [17] Finley, I. P., and J. W. Wood, "An Investigation of Synthetic Aperture Radar Autofocus," DRA Memorandum No. 3790, 1985.
- [18] Wood, J. W., "The Production of Distortion-Free SAR Imagery," *Radar '87*, IEE Conf. Publ. No. 281, London: IEE, 1987, pp. 471–473.
- [19] Wood, J. W., "The Removal of Azimuthal Distortion in SAR Images," *Int. J. Remote Sensing*, Vol. 9, 1988, pp. 1097–1107.
- [20] Oliver, C. J., "Review Article—Synthetic-Aperture Radar Imaging," *J. Phys. D: Appl. Phys.*, Vol. 22, 1989, pp. 871–890.
- [21] Green, J. F., and C. J. Oliver, "The Limits on Autofocus in SAR," *Int. J. Remote Sensing*, Vol. 13, 1992, pp. 2623–2641.
- [22] Oliver, C. J., "High-Frequency Limits on SAR Autofocus and Phase Correction," *Int. J. Remote Sensing*, Vol. 14, 1993, pp. 495–519.
- [23] Blacknell, D., A. P. Blake, C. J. Oliver, and R. G. White, "A Comparison of SAR Multilook Registration and Contrast Optimisation Algorithms Applied to Real SAR Data," *Radar '92*, IEE Conf. Publ. No. 365, London: IEE, 1992, pp. 363–366.
- [24] Oliver, C. J., D. Belcher, A. P. Blake, and R. G. White, "Algorithms for Focused Linear Synthetic Aperture Radar Imaging," *SPIE Conf. on Algorithms for SAR Imagery*, Orlando, FL, *SPIE Proc.*, Vol. 2230, 1994, pp. 60–71.
- [25] Blacknell, D., I. P. Finley, A. Freeman, C. J. Oliver, S. Quegan, I. A. Ward, R. G. White, and J. W. Wood, "Geometrical Accuracy in Airborne SAR Images," *IEEE Trans. Aerospace Electron. Systems*, Vol. AES-25, 1989, pp. 241–256.
- [26] Finley, I. P., C. J. Oliver, R. G. White, and J. W. Wood, "Synthetic Aperture Radar—Automatic Change Detection," UK Patent No GB 2,234,130B, 1988, and US Patent No. 4,963,877, 1990.
- [27] Wood, J. W., R. G. White, and C. J. Oliver, "Distortion-Free SAR Imagery and Change Detection," *Proc. U.S. National Radar Conf.*, Ann Arbor, MI, 1988, pp. 95–99.
- [28] Mims, J. H., and J. L. Farrell, "Synthetic Aperture Imaging with Manoeuvres," *IEEE Trans. Aerospace Electron. Systems*, Vol. AES-8, 1972, pp. 410–418.
- [29] Kirk, J. C., "Motion Compensation for Synthetic Aperture Radar," *IEEE Trans. Aerospace Electron. Systems*, Vol. AES-11, 1975, pp. 338–348.
- [30] Blacknell, D., "SAR Motion Compensation Using Autofocus with Implications for Super-Resolution," Ph.D. Thesis, University of Sheffield, UK, 1990.

4

Fundamental Properties of SAR Images

4.1 Introduction

Chapters 2 and 3 have shown that a SAR is essentially a complicated device whose purpose is simply to measure the local interaction between the Earth's surface and an incident wave and that very high quality SAR images of this interaction can be produced by modern systems. Turning this two-dimensional set of measurements into information about the scene is what concerns us in the rest of the book, and the purpose of this chapter is to clarify the framework within which information is to be discussed.

In a certain sense, information can only be defined in the context of an application: does an image tell the user something of interest to them? In another sense, since the image is simply a representation of the local scattering properties of the Earth, all the information is carried by our knowledge of electromagnetic theory. Between the excessive particularity of the first and the over-generality of the second lies a wide range of theory and technical development whose purpose is to provide a general approach to image analysis and understanding. It is rooted principally in the fact that human beings bring a large amount of world knowledge and experience into their interpretation of images. Methods to extract information from SAR data must take account of or emulate this high-level knowledge of how the world is. Fundamental to this approach is the establishment of viable data models, in which information can be related to measurable parameters and their spatial disposition. The rationale for adopting this approach to information is developed further in Section 4.2.

A primary difficulty in exploiting this or any other approach to information in SAR imagery is that all measurements or inferences from the data must take account of **coherent speckle**. Sections 4.3 to 4.5 are concerned with the basic properties of speckle and how it manifests itself in the different image types that can be formed when complex SAR data are available. The well-developed theory for single-channel speckle is presented and confirmed by observations in Section 4.3. This leads to a data model in which the information is carried by the average intensity or RCS at each speckled pixel. However, the information content per pixel is very low within a distributed target, since in this case very large numbers of pixels can be characterized by a small number of parameters. Increasing numbers of pixels serve only to improve the accuracy of the parameter estimates. **When the useful scale of variation of RCS is larger than the resolution, it can therefore be advantageous to preaverage the supplied data.** This process, known as **multilooking**, is dealt with in Section 4.4. It reduces spatial resolution in order to improve the accuracy of the RCS estimate at each individual pixel. Section 4.5 closes this basic discussion of speckle by introducing the multiplicative noise model in which *single-channel* SAR data is treated as the product of an underlying RCS and a stationary noiselike process, corresponding to speckle. This is a very useful representation that will be much exploited in succeeding chapters.

The treatment in the earlier sections of this chapter ignores the imaging process, but this impacts significantly on the procedures needed to recover the information in the data. Section 4.6 extends the linear imaging equations developed in Chapter 2 to deal with distributed targets. This lays bare the imaging effects, which include scaling of the desired geophysical quantity, σ^0 , an additive bias in the measurement, and induced spatial correlation. Sections 4.7 and 4.8 examine the consequences for SAR measurements, developing the clutter-to-noise, signal-to-clutter, and signal-to-noise ratios, and examining the effects of correlation on multilook estimates of RCS. Because of its adverse effect on parameter estimation and image analysis techniques, methods to remove system-induced spatial correlation are discussed in Section 4.9. Practical considerations in estimating the complex correlation function from image data are dealt with in Section 4.10. We close the discussion of single-channel SAR by pointing out limitations in its formulation in Section 4.11.

The treatment of **speckle as a multiplicative noise** is of most use in the **context of single-channel data**, but **interference phenomena are still a dominant influence on the measurements made by multichannel radars**. This is illustrated in Section 4.12 in the context of the much extended range of images available from interferometric or polarimetric radars. The number of parameters needed to describe the behavior of a pixel or a region is now greatly increased. Hence, unlike single-channel data, the use of different image types is not simply to

improve visual image quality but is an essential part of conveying the information available in the data.

4.2 The Nature of Information in SAR Images

The basic quantity measured by a single-frequency single-polarization SAR at each pixel is a pair of voltages in the in-phase and quadrature channels. As discussed in Chapter 2, these measured values represent the effects of the scene on the transmitted wave, but not in a direct way. First, the finite bandwidth of the system in both range and azimuth implies that measured values are weighted averages from a region determined by the point spread function of the SAR. Second, numerous weightings need to be applied in the processing to convert the measured voltages to “geophysical” units corresponding to the complex reflectivity, RCS, or backscattering coefficient of the scene. With these provisos, the measurements made by the SAR are fundamentally determined by electromagnetic scattering processes.

As such, the most basic description of information in SAR images may be considered to be in terms of solutions of Maxwell’s equations for the propagation geometry and the scattering scene. However, both on theoretical and practical grounds, this viewpoint provides only a partial contribution to our understanding of the information available.

From the point of view of electromagnetic theory, two approaches are relevant. The first of these is the *Forward Problem*, in which the properties of the scattering medium and the incoming wave are specified and used to predict the scattered field. Solutions to this problem are currently available only by imposing considerable restrictions on the scattering medium, for example, by assuming that all length scales in the medium are large (or small) relative to the wavelength, or that only surface (not volume) scattering is occurring (or vice versa), or that occultation (shadowing) effects can be ignored. Even with such restrictions, full wave solutions are in most cases unavailable, and a more phenomenological approach based on energy flows (radiative transfer) provides the only way of making progress. Numerous books and papers are devoted to this Forward Problem [1–5], with increasingly sophisticated solution techniques and descriptions of the scattering medium.

Nonetheless, there is still a huge gap between the scattering medium as it is described in most models and the actuality of what is contained in the scattering cell because some quantities needed for the scattering models may be very difficult to measure reliably, such as the leaf angle distribution in a plant canopy or the detailed dielectric properties of the medium. Other quantities, such as the correlation length of natural surfaces, may exhibit rapid spatial

variation, so it may be hard to define a meaningful representative value for insertion into a scattering model. Other **weaknesses** of most modeling approaches include:

- **The assumption of infinite plane waves and infinite media**, instead of the imaging situation where we have a structured scene;
- **Their ability to produce only low-order moments of the scattered field** (often only the mean backscattering coefficient), whereas later chapters make clear the importance of higher moments as sources of information, especially the fourth-order field moments needed to describe intensity variance and correlation, which are critical in texture analysis.

The descriptions provided by current models are therefore incomplete. Nonetheless, progress in solving the Forward Problem has led to scattering models becoming increasingly important in SAR image interpretation. This is because, for all their shortcomings, they contain our best currently available descriptions of the physical processes occurring as the radar wave interacts with the medium. Their chief role is in most cases as semiquantitative explanatory tools, identifying the dominant scattering mechanisms and highlighting failures in our representation of the medium or in the solution procedure. Without such models, we only have phenomenology, and our ability to understand or generalize observations is severely weakened.

However, they provide only one part of the corpus of knowledge needed to discuss information in SAR images and can often be nearly irrelevant (e.g., when the scene or structures within it are very heterogeneous). Even within the context of electromagnetic theory, the Forward Problem is not the real issue when dealing with information in SAR images. Far more important is the *Inverse Problem*: what properties of an unknown scene can be inferred from the observed backscattered signal? A weaker version of the Inverse Problem may also include prior knowledge of various forms; for example, we may wish to know what can be inferred about forest properties from the backscatter, given that we know we are looking at forest.

Methods to solve the Inverse Problem mathematically are, naturally, couched in terms of the same models as the Forward Problem, with all the same limitations, and are normally difficult. However, the real source of the difficulty in the Inverse Problem is not the mathematics but that there is rarely enough information to provide a unique solution. In other words, the number of parameters needed to characterize the target in the scattering model exceeds the number of independent measurements available at the sensor. In this case, the dimensionality of the parameter space may be reduced by assuming some

parameters are known or the solution is insensitive to them (these parameters then remain unmeasurable from the observations, but access to the other parameters becomes possible) [6]. Even when a proper inversion is possible [7], measurements have often failed to confirm the theory, reflecting in some way the failure of the theory to capture the relevant physics of the scattering process.

It is also the case that direct mathematical inversion is often not the preferred route to solving the Inverse Problem because of its difficulty. Instead, repeated solution of the Forward Problem for different values of the input parameters can be used to achieve consistency with observations. Such methods only become of intrinsic merit when the dimensionality of the observations (e.g., their diversity in polarization, frequency, and/or incidence angle) is sufficient to provide tight constraints on the solution space.

These approaches to describing information in SAR images through electromagnetic theory have the apparent advantage that they map the observed signal onto physical properties of the scene, such as dielectric constant, geometrical factors (e.g., size, height, and roughness), and polarizability. In doing so, they provide a link between observations and measurable quantities on the ground. (This is often very difficult to turn into practice because of the problem of providing measurements that are truly representative of the scattering medium.) However, implicit in their use is another layer of information, which is that of image structure. Typically, both the Forward and Inverse Problems require some *a priori* knowledge before they can be invoked. The prime requirement is that the region to which they are being applied is homogeneous in some sense—it is a single target type. In all practical applications at present much stronger knowledge is needed, such as knowledge that the region is woodland or ocean or ice.

A central theme of this book is that this type of *a priori* knowledge can in many cases be inferred from the image itself. This then provides the framework within which physical understanding can be brought into full play. Far more than this, however, image structure provides our first, immediate response when confronted with an image, and we can infer many aspects of the scene without any recourse to physics. Few of us would have problems recognizing Figure 4.1 as a rural scene containing fields and field boundaries, roads, and woodland. In some sense we have a high-level understanding of the scene due solely to visual impressions and prior experience of related map representations and aerial photography. Mapping, change detection, target detection, and object recognition are essentially concerned with image understanding (although physical understanding clearly has something to say about the conditions under which these operations may be carried out successfully). Object classification provides scope for stronger interplay of physics with image properties, both in terms of how to classify and the generalizability of any adopted methods. Ultimately,



Figure 4.1 High-resolution airborne DRA X-band image of a rural area. (British Crown Copyright, 1997/DERA.)

image understanding is rooted in experience and empiricism, both as regards our broad understanding of how the world is and in experimental findings that guide our perceptions of what aspects of the image should be examined. As an illustration, most people not used to radar images would not immediately recognize the region at the lower left of the image in Figure 4.1 as an urban area, but this sort of skill is quickly learned.

At this highest level of image information, our understanding of processes is rudimentary. What we do know is that the brain attaches high information content to vertices, linear structures, and edges [8] and “fills in” areas to characterize the image by regions (segments). The eye/brain system is very sensitive to texture and can segment images by texture alone [9,10]. It is also very flexible in its choice of scale, characterizing whole regions as a single type (e.g., woodland), while capable of seeking structure within a type. In this it is greatly aided by context; human beings often know what to expect and can use this information to recognize and classify features (e.g., towns have roads associated with them). Current attempts to encapsulate the processing power of the human visual system have been successful only in fairly constrained circumstances and are out of the scope of this book.

Between the electromagnetic scattering view of the world and the high-level perceptions of human cognition lies the substance of this book. The links to the former are inescapable: the image is formed by a coherent electromagnetic scattering process, of which at least one manifestation, whatever the model, is interference between scatterers. Interference and its image manifestation as speckle constitutes a central issue in SAR image understanding and analysis. The links to the latter are equally inescapable. In many instances a prime consideration in assessing the performance of a technique is whether it fails to recognize or preserve an image property obvious to the eye. (Do small targets disappear? Has a thin line been lost? Is a segment fragmented into many pieces?)

However, these links are not boundary conditions. Visual methods rapidly run into trouble when multidimensional data are available; indeed, the whole question of how to visualize the data then becomes a key issue. For small target detection, machine methods are often superior to those of a human observer. Assessment of whether a technique preserves image radiometry requires careful measurement, which is often more sensitive than the capabilities of the eye. Equally, establishing a proper theoretical bridge between imaging, texture, and scattering theory is a matter of concern to us, since this provides the fundamental understanding about the scene property or properties about which we are gaining information when we measure image texture.

A primary concern in succeeding chapters is measurement, approached through a series of data models that are essentially statistical in nature. This

reinforces the central place of our subject matter. Physical theory without an associated theory of measurement is not physical at all [11]; capturing visual perception in measurements, if possible, opens the way to quantitative image understanding. The data models are in most cases dependent on a small number of parameters, which provides several major advantages, as long as they are consistent with the data:

- All the available information is represented by those few parameters.
- It is possible to develop soundly based estimation procedures and quantify the accuracy with which the parameters can be extracted.
- There is a rigorous basis on which to develop image analysis techniques, such as filtering, classification, and target detection.

A fourth advantage to this approach is that it strengthens and expands the links to physical models. If the data are described by a few parameters, that circumscribes what needs to be explained physically; it is the task of physics to provide a meaning for the parameters. As we shall see, this task is currently incomplete.

Our approach to data models is systematic and progressive (Figure 4.2). Starting from image properties we derive physically based and/or phenomenological descriptions of the data that provide our data model. We examine the types of image feature to which this model is applicable; this normally varies

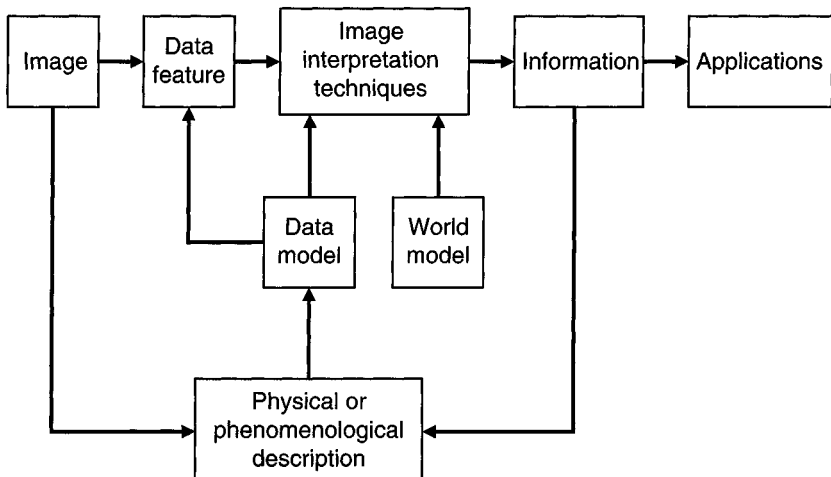


Figure 4.2 Flow chart showing the interrelation of measurements, data models, and information.

with sensor characteristics, resolution being particularly important. In combination with a “world model” embodying general types of knowledge about the scene (e.g., that an agricultural area is likely to contain fields of a single crop), the data model is exploited to formulate image interpretation techniques that are optimal in some sense. These provide a modified image in which the “information” is more clearly portrayed than in the original image. An important issue here is one of scale. When the interpretation techniques are local, we are concerned with the reconstruction of some underlying image property (parameter); this is essentially image filtering of some form. When the data model imposes a large-scale description, we are more concerned with image structuring. These two scales are not clearly distinct and there is continual interplay between local and global scales in several of the algorithms. However, whichever scale is chosen, the final determinant of information is in the context of an application: what properties of the world become detectable or measurable as a result of the interpretation technique?

While exploiting each model to its limit, we identify where those limits are and develop the models to encompass progressively more demanding data properties. Each such development is then again worked through to its limit. Initially we focus our attention on single-frequency, single-polarization systems for the sake of simplicity and to bring out some of the main issues as clearly as possible. Later chapters are more concerned with methods applicable to multichannel systems. Large amounts of the single-channel theory and approach can be successfully cast into a multidimensional framework, but new insights and problems arise, many of which still await a complete solution.

Although we described measurement as a central issue, this needs some interpretation, dependent on our application. For small target *detection* in single-channel data, image calibration is often unnecessary because we are not concerned with precise measurements of RCS or backscattering coefficient, only the contrast between the target and its background. Even slow drifts in radiometry within the image are often of no importance in this context. Similar considerations apply if our concern is structural mapping. For small target *recognition*, especially if multiple channels are to be combined, calibration becomes a far more pressing concern, although relative calibration may be more important than absolute calibration. When our application deals with distributed targets, accurate radiometry is nearly always an issue, with ensuing demands on system accuracy and post-processing. A major exception, whose importance becomes clear in Chapter 8, is when the predominant information is carried not by the single-channel mean backscattering coefficient but by image texture. This image property is independent of the mean and hence of radiometric calibration, unless the radiometric distortions occur on scales comparable with the scale lengths of textured regions.

The notion of information and its relation to measurement also needs some qualification. Particularly at large scales, we begin to encounter difficulties in consistency between an exploitable data model and human world knowledge. From Figure 4.1, it is clear that an observer will automatically classify whole regions as single entities, labeled perhaps as fields or woodland, without being concerned about local drifts in radiometry or features within a region (see, for example, the large area of woodland above the center of the image). Other world knowledge is also automatic to the observer, such as expecting field boundaries to be approximately straight over reasonable distances. This large-scale view can easily come into conflict with results generated by algorithms whose perspective is much more local. As we will see, algorithms can provide image structure (segmentation) that a human being may instantly perceive as too detailed (or omitting important features). However, within the algorithm it will be guaranteed that the inferred structure is supported by measurement. The observer can override measurement when it conflicts with the description thought to be appropriate. The distinction between information described by measurement and that derived from knowledge and application needs then becomes acute. Much of the work described throughout this book attempts to identify this distinction and lessen it where possible.

4.3 Single-Channel Image Types and Speckle

Figure 4.1, seen purely as an image, conveys information primarily through structure. We immediately recognize shapes, objects, lines, and regions, some of which are distinguished by their brightness, others by their textural qualities. If we now transfer our attention to one of the larger regions (e.g., one of the several fields in the image), we observe that individual pixels show considerable variability. Therefore, it is pertinent to ask what the source of this variability is and whether an individual pixel in a distributed target can be said to carry information.

Before answering these questions, however, we need to recognize that the image in Figure 4.1 involves a choice of how the measurements made by the SAR should be displayed. We have already seen in Chapter 2 that the primary geophysical quantity determining the SAR data is the complex radar reflectivity of the scene and that the SAR provides a measurement of this reflectivity. The complex reflectivity has been defined for a point target in (2.23) and the notion extended to distributed targets in Section 2.6. Qualitatively, this concept expresses the fact that when an electromagnetic wave scatters from position (x, y) on the Earth's surface, the physical properties of the terrain cause changes in both the phase, $\phi(x, y)$, and amplitude, $A(x, y)$, of the wave. The SAR, in fact,

measures the number pair ($A \cos\phi$, $A \sin\phi$) in the in-phase and quadrature channels of the receiver, weighted by the SAR PSF. This estimate of the local reflectivity at each pixel can also be represented by the complex number $Ae^{i\phi}$; in this form, the SAR data are known as the *complex image*.

From the complex image a variety of other products can be formed—for example, images of the real part $A \cos \phi$ (the in-phase component), the imaginary part $A \sin \phi$ (the quadrature component), the amplitude A , the phase ϕ , the intensity $I = A^2$, or the log intensity $\log I$. The use of the word “intensity” is by analogy with measurements at optical wavelengths and is synonymous with power or energy. The log image is also sometimes referred to as the “dB” image, since for calibrated data each pixel corresponds to a linearly scaled estimate of the backscattering coefficient σ^o , in dBs. The scaling will be unity only when the log image is formed by taking $10 \log_{10}$ of each pixel in the calibrated intensity image.

For a properly calibrated system, these are all true measurements of the scattering properties of the Earth’s surface (except for those effects caused by system noise), but visually they produce quite different representations, as illustrated in Figure 4.3. Typically, the real and imaginary images show some structure but appear extremely noisy, the phase image is noiselike and shows no structure, while the amplitude, intensity, and log images, though noisy, are clearly easier to interpret. Of these latter three image types, the amplitude and log images are often preferred since the large dynamic range of the intensity image can reduce the perception of detail.

The noiselike quality characteristic of these types of images (and of those produced by other coherent imaging systems using lasers, sonar, or ultrasound) is known as *speckle*. (It must be stressed that *speckle* is *noiselike*, but it is *not* noise; it is a real electromagnetic measurement, which is exploited, for example, in SAR interferometry.) Given that the SAR is making true measurements of the Earth’s scattering properties, why do such effects arise? A simple model of how the world might appear to the radar suggests an answer. In distributed targets we can think of each resolution cell as containing a number of discrete scatterers (Figure 4.4). As the wave interacts with the target, each scatterer contributes a backscattered wave with a phase and amplitude change, so the total returned modulation of the incident wave is

$$Ae^{i\phi} = \sum_{k=1}^N A_k e^{i\phi_k} \quad (4.1)$$

This summation is over the number of scatterers illuminated by the beam; it includes the weighting imposed by the SAR PSF and any attenuation effects caused by the scattering and propagation processes. The individual scattering

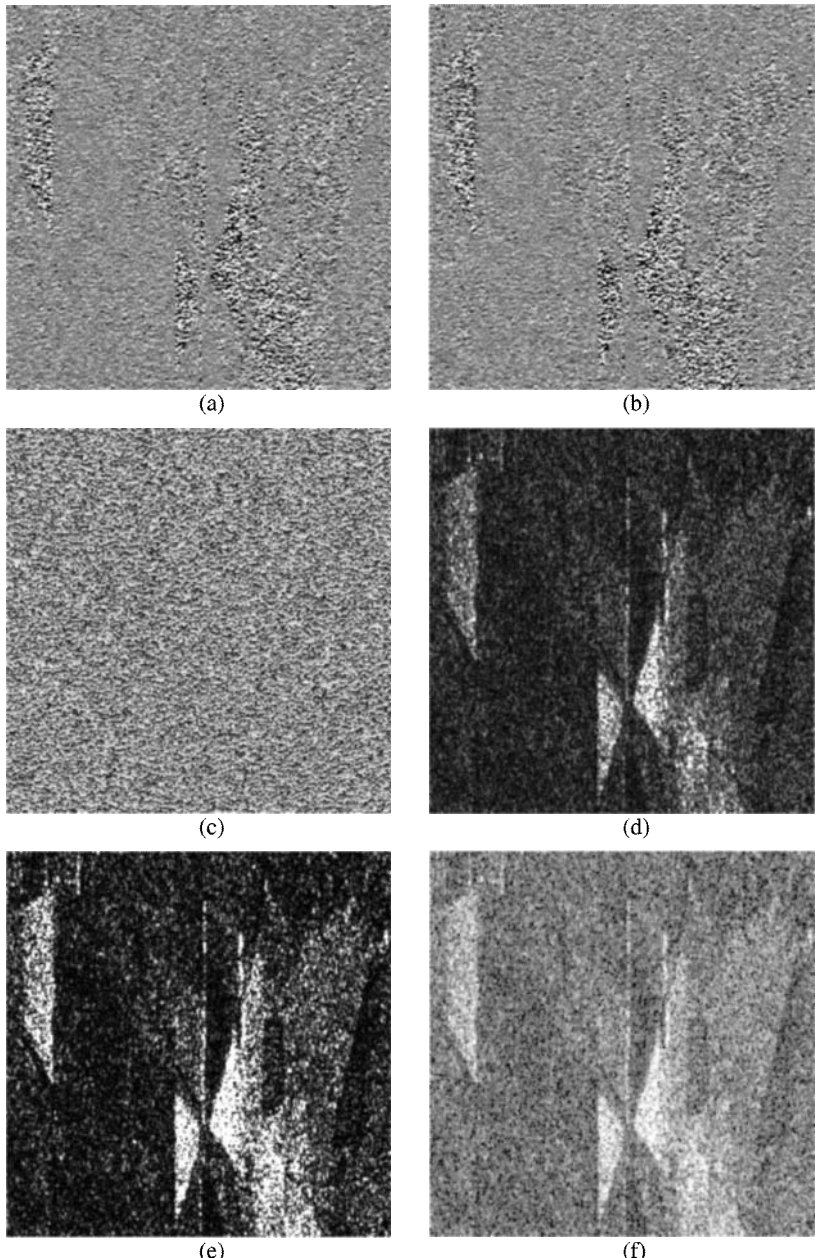


Figure 4.3 Different representations of the complex SAR image of a rural scene using ERS-1 SLC imagery (Copyright ESA, 1992): (a) in-phase (real) component, (b) quadrature (imaginary) component, (c) phase, (d) amplitude, (e) intensity, and (f) log intensity. Note the geometric distortion as in Figure 2.3(a).

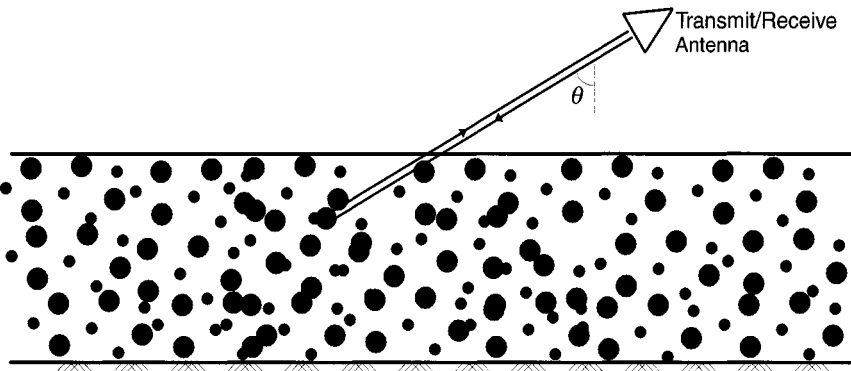


Figure 4.4 Schematic representation of a distributed scatterer as a layer of discrete point scatterers.

amplitudes A_k and phases ϕ_k are unobservable because the individual scatterers are on much smaller scales than the resolution of the SAR, and there are normally many such scatterers per resolution cell. This model has already been introduced in terms of small scattering facets in Section 2.6 and can also be considered in terms of elementary scattering volumes [12].

This simple discrete scatterer model is capable of much elaboration, forming the basis of the Neumann series expansion and approaches springing from it, such as the Born and distorted Born approximations [13–15]. These provide a means of relating the observations to the physical properties of the scattering layer, such as the dielectric constant, shape, and orientation of the scatterers. We do not exploit these possibilities here but simply note that they can all be embodied in the formulation given as (4.1).

An immediate conclusion from (4.1) is that the observed signal will be affected by interference effects as a consequence of the phase differences between scatterers. In fact, speckle can be understood as an interference phenomenon in which the principal source of the noiselike quality of the observed data is the distribution of the phase terms ϕ_k . To infer this distribution, note that the slant range resolution is typically many wavelengths across. Hence scatterers at different parts of the resolution cell will contribute very different phases to the return (4.1) even if their scattering behavior is identical. As a result, we can in practice think of the phase ϕ_k as being uniformly distributed in $[-\pi, \pi]$ and independent of the amplitude A_k . The sum (4.1) then looks like a random walk in the complex plane, where each step of length A_k is in a completely random direction. This problem has been thoroughly treated in [16] (see also Appendix 11A). For large numbers of statistically identical scatterers, the analysis reveals that:

- The observed in-phase and quadrature components, $z_1 = A \cos \phi$ and $z_2 = A \sin \phi$, will be independent identically distributed Gaussian random variables with mean zero and whose variance $\sigma^2/2$ is determined by the scattering amplitudes A_ϕ , that is, they will have a joint probability density function (PDF) given by

$$P_{z_1, z_2}(z_1, z_2) = \frac{1}{\pi\sigma} \exp\left(-\frac{z_1^2 + z_2^2}{\sigma^2}\right) \quad (4.2)$$

- The observed phase ϕ will be uniformly distributed over $[-\pi, \pi]$.
- The amplitude A will have a Rayleigh distribution

$$P_A(A) = \frac{2A}{\sigma} \exp\left(-\frac{A^2}{\sigma^2}\right) \quad A \geq 0 \quad (4.3)$$

with mean value $\frac{\sqrt{\pi}\sigma}{2}$ and standard deviation $\sqrt{\left(1 - \frac{\pi}{4}\right)\sigma^2}$. Another commonly used statistic is the coefficient of variation (CV) defined as the standard deviation divided by the mean. Hence, for amplitude data this takes the value $\sqrt{4/\pi - 1}$.

- The observed intensity or power $I = A^2$ will have a negative exponential distribution

$$P_I(I) = \frac{1}{\sigma} \exp\left(-\frac{I}{\sigma}\right) \quad I \geq 0 \quad (4.4)$$

with mean value and standard deviation both equal to σ , so that in this case CV = 1.

- The log intensity $D = \ln I$ has a Fischer-Tippett distribution [17]

$$P_D(D) = \frac{e^D}{\sigma} \exp\left(-\frac{e^D}{\sigma}\right) \quad (4.5)$$

whose mean value and variance are $\ln \sigma - \gamma_E$ and $\pi^2/6$, respectively. The symbol γ_E denotes Euler's constant whose approximate value is 0.57722 [18]. This distribution is easily converted to that for a properly normalized dB image, since we can set $D_n = 10 \log_{10} I = (10 \log_{10} e)D$ and

hence $P_{D_n}(D_n) = \frac{1}{K} P_D(D_n/K)$ where $K = 10 \log_{10} e$. Notice that for the log intensity data, the variance is *independent* of the mean value, unlike the distributions (4.2) to (4.4). Hence, log data is often preferred as a means of standardizing or stabilizing the variance, which is a common first step in statistical analysis [19].

The distributions 1 to 5 are of fundamental importance in handling SAR data. Notice that, with the exception of the phase distribution, they are completely characterized by a single parameter σ , which carries all the available information about the target. From (4.4) we can see that σ corresponds to the *average intensity*.

These distributions apply to each speckled pixel in the scene. Hence, a comparison of theory with observations would require many realizations of the scene, each with an independent speckle pattern. Since these are rarely available, and often we have just single images, we are instead obliged to test the theory by examining distributed targets assumed to have constant backscattering coefficient. Only very seldom do we have enough a priori knowledge to assert with confidence the uniformity of a target. Nonetheless, many studies support the consistency of this speckle model with observed data [20,21]. To illustrate this, Figure 4.5 shows histograms of the observed values from an agricultural field, corresponding to the distributions described in 1 to 5. These measurements are derived from ERS-1 SLC imagery. The theoretical curve is shown as the solid line in each case, and the fit with theory is obviously very good.

It is now clear why the different representations of the data shown in Figure 4.3 convey different amounts of information about distributed targets in the scene. Phase supplies nothing because its distribution is target independent. The real and imaginary channels supply information but require the eye to estimate the local standard deviation to detect differences between regions. Twice as many samples are needed to estimate the standard deviation with the same standard error as the mean (in a normal distribution) [22]; the eye may also be better at seeing mean differences rather than changes in standard deviation. The amplitude data carries the information in its mean value, though noisily because the Rayleigh distribution is quite wide. The intensity data has a wider dynamic range than the amplitude data and appears noisier than amplitude because the coefficient of variation is higher for the exponential distribution than for the Rayleigh distribution; for amplitude data it is 0.52, while for intensity data it is 1. The log data also has a reduced dynamic range compared with the intensity. In this image the eye is clearly reacting to mean value differences because the log operation standardizes the variance.

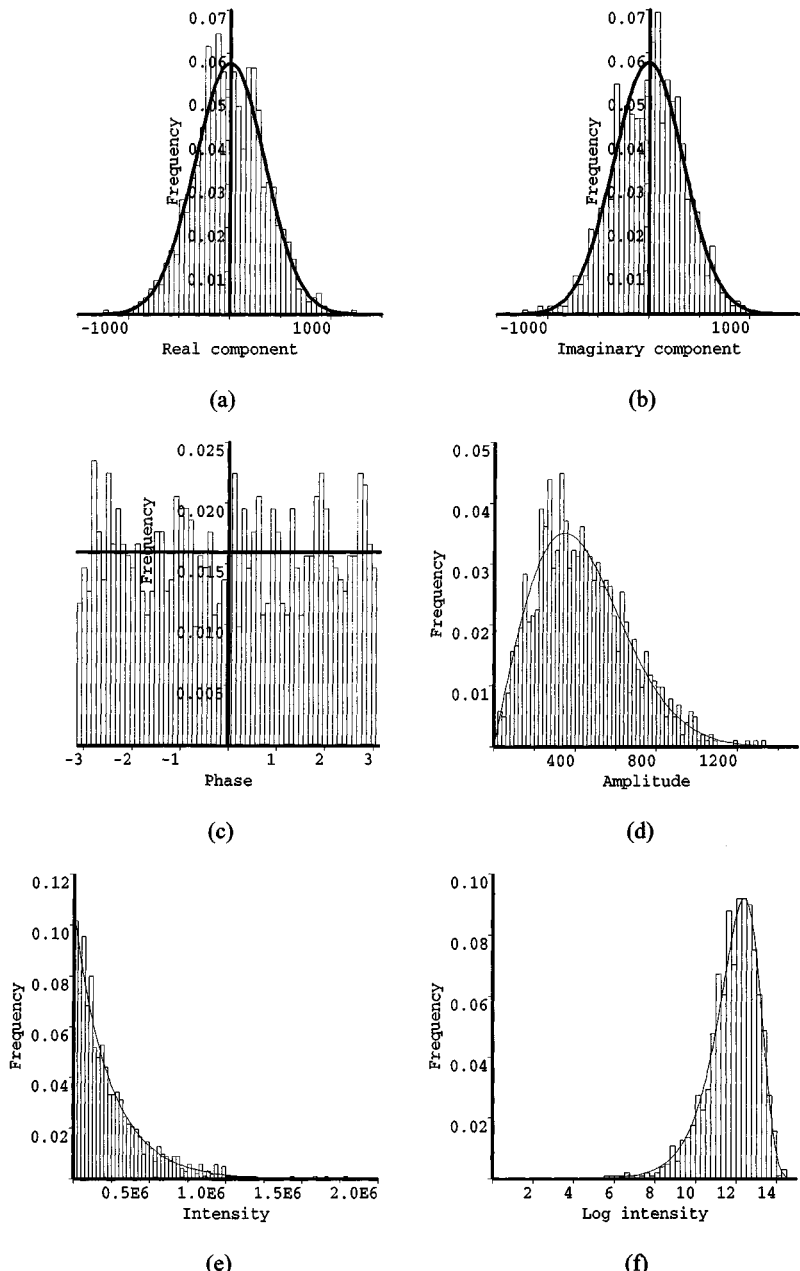


Figure 4.5 Comparison of theoretical distributions (solid curves) with observations (histograms) for a visually homogeneous area from ERS-1 SLC imagery: (a) in-phase component, (b) quadrature component, (c) phase, (d) amplitude, (e) intensity, and (f) natural log.

The implications of this speckle model are important. If our interest is in *single* images of *distributed* targets and, hence, phase provides no information, we can get rid of it and use only amplitude, log, or intensity data. Hence the initial chapters in this book are concerned almost exclusively with image data for which phase has been discarded. Phase becomes important when we turn to polarimetric and interferometric data in Chapter 11. For such data, pairs of phase images, each having a uniform distribution, can nonetheless carry information in their phase difference (see also Section 4.12 and Figures 4.9 and 4.10). In Chapter 10 we also demonstrate that phase information is critical when we wish to carry out high-performance imaging of deterministic (man-made) targets.

The observation that many distributed targets obey the simple speckle model allows us to provide a partial answer to our question about whether an image pixel carries information. Considered in isolation, each pixel supplies a real measurement of backscattered power or amplitude. When the pixel is made up of many elementary scatterers, the observed power is an estimate of an underlying RCS whose true value is being masked by interference effects. If the pixel is part of a uniform distributed target, the information per pixel is low since the collection of pixels in the target can supply only one useful number, σ . All that greater numbers of pixels do is to reduce the estimation error in σ when averaging pixels. For nonuniform but textured targets, this conclusion needs only slight modification; more parameters than the mean may be needed to characterize the region, but typically their number will be few (see Chapter 5). The information content of a pixel only becomes high when a pixel is not speckled (e.g., a single bright point scatterer) or the distributed target is made up of objects of large enough size and sufficient contrast to be resolved. A noteworthy example of the latter is when high-resolution images of urban areas are acquired.

The interpretation of the parameter σ in (4.2) to (4.5) needs a number of comments. First of all, we saw in Chapter 2 that the geophysical quantity corresponding to an intensity measurement by the SAR is an RCS (σ) for point targets or average backscattering coefficient (σ^0) for distributed targets. Working in terms of σ or σ^0 in standardized units means that measurements from different sensors (which may have different resolutions, transmitted powers, and processing gains, for example) can be directly compared. Since we are here dealing with distributed targets, σ^0 is the relevant quantity. As discussed in Section 2.7, converting measured powers to σ^0 values requires careful calibration and characterization of the system, and the supplied data may need some form of preprocessing to derive σ^0 . However, for the purposes of mapping, target detection, and texture measurement (see Chapter 8), calibration may not be necessary as long as radiometric distortions are changing

slowly relative to the features of interest in the scene. There are numerous examples, particularly of airborne missions, where the calibration has been dubious, but meaningful information has been extracted from the data [23,24]. The intensity value at each pixel of a distributed target should therefore be regarded as a scaled estimate of σ^o or, if the area correction has not been made, to the mean RCS of each pixel. With this proviso and to avoid convoluted descriptions, we will often use the terms “RCS” or “cross section” to refer to the mean intensity even when the data have not been properly calibrated. This viewpoint is adequate for most of the early chapters in this book, but a more careful approach relating observed intensity to underlying σ^o is given in Section 4.5.

A second important point is that we need to distinguish the measured value at a pixel and the parameter value σ . Figure 4.4 and (4.1) both indicate that the observed value at each pixel is the resultant of interfering Huygens wavelets unless a single scatterer completely dominates the return. Hence the value of σ is specific to each pixel; the measured value is just a sample from the distribution parameterized by σ . To make this clearer, note that the mean intensity at a pixel is given from (4.1) by

$$\langle I \rangle = \langle A^2 \rangle = \sum_{j=1}^N \sum_{k=1}^N \langle A_j A_k e^{i(\phi_j - \phi_k)} \rangle$$

Assuming that the amplitude and phase of each scatterer are independent of each other and that the phases of different scatterers are independent and uniformly distributed we have

$$\langle I \rangle = \sum_{k=1}^N \langle A_k^2 \rangle \quad (4.6)$$

Hence, the mean intensity is determined by the incoherent sum of the mean intensity of all the scatterers and is independent of their geometrical configuration (assuming their orientations are unchanged). However, changes in the positions of the scatterers will change all the phase relationships, in the process altering the observed intensity, but without altering the parameter σ . In this sense, the observed intensity at a pixel is deterministic and repeatable but for the purpose of measurement is best considered as random and as an estimate of σ . This is a crucial distinction underlying most of the later parts of this book and all work on SAR filtering and reconstruction.

4.4 Estimating the RCS: Multilook Data

Since σ is the information-bearing parameter, it is pertinent to ask how best to estimate it for a given pixel. An elementary calculation using (4.2) shows that, given the in-phase and quadrature components (z_1, z_2), the maximum likelihood estimate (MLE) of σ is given by

$$\hat{\sigma} = \sqrt{z_1^2 + z_2^2} = I \quad (4.7)$$

that is, the observed intensity. Since the distributions (4.3) to (4.5) are all transformations of the number pair (z_1, z_2), they will all lead to the same estimate [25]. Hence, in the absence of any further knowledge or assumptions, the best estimate of σ at every pixel is to form the intensity image.

Improved estimates of σ at a pixel can be gained by combining measurements at that position. Since σ is the mean power, this suggests that the correct approach, given L independent measurements, is to average the measurements in intensity (often called *incoherent* averaging because all phase information is discarded). From (4.4), this will preserve the mean value σ while reducing the variance of the measurements by a factor L to become σ/L . Indeed, it is easy to show that this provides the maximum likelihood estimator of σ given L independent exponentially distributed measurements each with the same mean value σ (see Chapter 6). Other methods (e.g., averaging in amplitude or in log intensity) provide inferior estimates of σ . Note also that averaging the complex data is of no value, since averaging L independent complex samples, each of which is zero-mean Gaussian with variance $\sigma/2$ in the I and Q channels, leads to a zero-mean Gaussian variable with variance $\sigma/(2L)$ in each channel. Thus there is no speckle reduction and the information-bearing parameter has been scaled by the factor $1/L$.

Independent measurements can be provided by splitting the synthetic aperture Doppler bandwidth, as described in Section 2.5. The separate images are referred to as looks, so that this process of averaging in intensity is known as multilooking, and the resultant image is known as L -look. The underlying premise of multilooking is that each look should be estimating the same RCS, so it is important that the looks should be at the same position, nearly simultaneous, and without relative radiometric distortion. They also need to be at the same frequency and polarization configuration. Nonetheless, marked differences between looks can occur because of the slightly different viewing angle used by each look. For example, the mean RCS over extended regions defined by field boundaries showed differences exceeding 20 dB between looks in P-band (68 cm) data produced by the NASA/JPL AirSAR system [26]. In this

case, the angular separation between looks was about 1 degree. Smaller differences occurred at L-band (24 cm), and differences were not significant at C-band [26].

A second approach to improving estimates of σ at a given position relies on making assumptions about the spatial properties of σ . Perhaps the simplest such assumption is that the RCS is constant over some neighborhood surrounding the pixel of interest. In this case, given L independent pixel values, the situation is statistically identical to that previously described, where independent looks at the same point are formed in the processor. Hence, again the measurements should be combined by averaging in intensity. Both cases are therefore referred to as multilooking, but they suppress different types of information in order to improve radiometric accuracy. In the first case, angular variation in RCS is neglected; while in the second, spatial variation is lost. Both provide equally accurate estimates of σ over a uniform target, but in heterogeneous regions the two methods may provide different estimates of the mean RCS at a given position due to the differing widths of the PSF. The use of pixel averaging clearly requires larger data volumes to be supplied but has the advantage that the averaging window can be adapted to adjust to heterogeneity in the scene. This is exploited in the filtering and segmentation procedures discussed in Chapters 6 and 7.

Note that in both cases the resolution will have been degraded. In the first case this is because each look uses only a fraction $1/L$ of the available bandwidth, so the resolution degrades by a factor L (see Section 2.5). The second case is more complicated, since the averaging acts as a low-pass filter; the value assigned to the resolution after the filtering depends on the precise definition of the resolution being used. Both cases become complicated when the looks are not independent, such as will occur if the looks are formed with overlapping Doppler bandwidths in the frequency domain or if pixels are correlated in the spatial domain [27]. This is far more likely in spatial averaging, since here sampling conditions or interpolation will often ensure that significant interpixel correlation occurs. We ignore this complication for the moment, but see Section 4.4.

A fortunate circumstance is that not only is averaging in intensity the correct way to carry out multilooking for preservation of the information-bearing parameter, but the resulting measurement has a well-known analytic PDF (unlike averaging in amplitude or dB, for example). The L -look average intensity

$$I = \frac{1}{L} \sum_{k=1}^L I_k \quad (4.8)$$

where the I_k are independent variables each exponentially distributed with mean σ is known to obey a gamma distribution with order parameter L [16]

$$P_I(I) = \frac{1}{\Gamma(L)} \left(\frac{L}{\sigma} \right)^L I^{L-1} e^{-LI/\sigma} \quad I \geq 0 \quad (4.9)$$

(Note that we often denote the average given in (4.8) by \bar{I} ; the overbar is omitted here for notational simplicity.) The average intensity has moments

$$\langle I^m \rangle = \frac{\Gamma(m+L)}{\Gamma(L)} \left(\frac{\sigma}{L} \right)^m \quad (4.10)$$

with special cases $\langle I \rangle = \sigma$ and $\text{var}(I) = \sigma^2/L$. The latter relation motivates the definition of the *equivalent number of looks* (ENL) as

$$\text{ENL} = \frac{(\text{mean})^2}{\text{variance}} \quad (4.11)$$

where the averages are carried out in intensity over a uniformly distributed target. The ENL is equivalent to the number of independent intensity values averaged per pixel. It is often applied not just to describe the original data but also to characterize the smoothing effects of post-processing operations such as image filtering. Even for the original data it may be noninteger if the looks being averaged are correlated.

When resolution is not considered critical, data are often supplied in multilook form because of the ensuing reduction in data volume. For display purposes, it may also be preferable to use the square root of multilook intensity, $A = \sqrt{I}$, since this has reduced dynamic range. The data then have what is known as a square root gamma distribution, which is readily derived from (4.9) using the change of variable relation

$$P_A(A) = 2AP_I(A^2)$$

This yields

$$P_A(A) = \frac{2}{\Gamma(L)} \left(\frac{L}{\sigma} \right)^L A^{2L-1} e^{-LA^2/\sigma} \quad A \geq 0 \quad (4.12)$$

For example, the ERS PRI data are supplied in this form, with $L = 3$. This distribution has moments

$$\langle A^m \rangle = \frac{\Gamma(L + m/2)}{\Gamma(L)} \left(\frac{\sigma}{L} \right)^{m/2} \quad (4.13)$$

Note that putting $m = 2k$ in (4.13) yields the k th moment of intensity (4.10) and that putting $L = 1$ in (4.9) and (4.12) produces the exponential and Rayleigh distributions with the appropriate moments as derived for (4.3) and (4.4). Comparisons of the distributions (4.9) and (4.12) with ERS PRI data are given in Figure 4.6, where the original amplitude image is shown as (b) while its square is shown as (a). Theoretical curves of the three-look gamma and square root gamma distributions are displayed in (c) and (d), respectively, as solid curves superimposed on histograms of measured values. There is obviously a good fit of data to theory.

4.5 The Multiplicative Noise Model for Speckle

The discrete scatterer model for distributed targets implies that all the information at each pixel in single-channel data is carried by the mean incoherent power, σ , appropriate to its particular set of scatterers. The observed intensity at each pixel then has the conditional probability

$$P_I(I|\sigma) = \frac{1}{\sigma} e^{-I/\sigma} \quad I \geq 0 \quad (4.14)$$

Making the change of variable

$$I = \sigma n \quad (4.15)$$

leads to the PDF

$$P_n(n) = e^{-n} \quad n \geq 0 \quad (4.16)$$

Hence, the observed intensity at each point can be regarded as a deterministic RCS value multiplied by unit mean exponentially distributed speckle. (The choice of the symbol n for speckle in this section is for consistency with the notation used in much of the literature and to reflect its noiselike properties, as discussed below. It must not be confused with true system noise, for which we

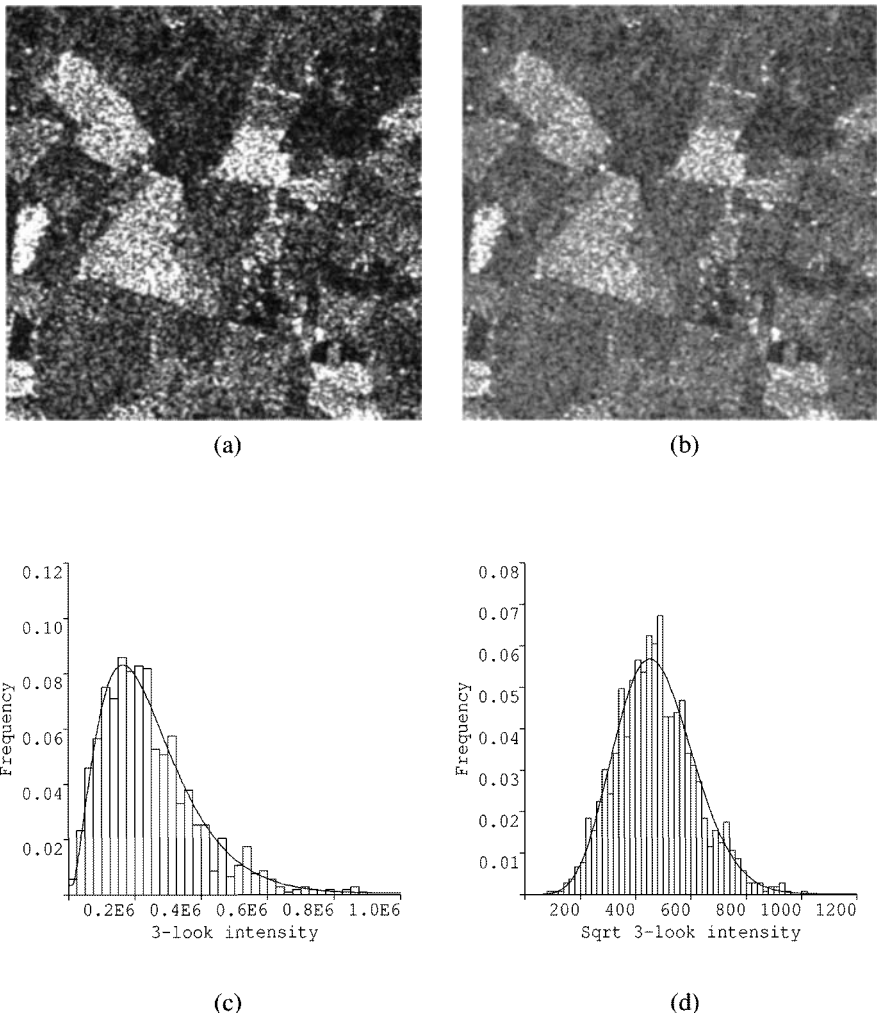


Figure 4.6 ERS PRI image displayed in (a) intensity and (b) amplitude. (Copyright ESA, 1992.)
(c) Comparison of three-look gamma distribution with histogram of squared PRI data from an agricultural field. (d) Corresponding comparison of original PRI data with square root gamma distribution with $L = 3$.

also use the symbol n in Chapter 2 and Section 4.6.) Equivalently, the complex reflectivity at each pixel can be written as

$$S = S_1 + iS_2 = \sqrt{\sigma} (m_1 + im_2) \quad (4.17)$$

where the (voltage) speckle contribution $m = m_1 + im_2$ has PDF

$$P_{m_1, m_2}(m_1, m_2) = \frac{1}{\pi} \exp(-m_1^2 - m_2^2) \quad (4.18)$$

that is, the in-phase and quadrature speckle components are independent zero-mean Gaussian random variables each with variance 1/2. Notice that we have not included a deterministic phase term in the formulation of the complex reflectivity because it would be completely randomized by the uniform phase of the speckle term. (For coherent image pairs, where phase differences are information bearing, this model is inadequate; see Chapter 11.) Again, we see that the observed signal can be regarded as the product of an underlying RCS term and a speckle term. Similarly, for L -look data, the decomposition (4.15) is possible, where n is now a unit mean gamma distributed variable with order parameter L .

This formulation of the SAR image as a deterministic RCS modulating a random stationary speckle process has led to the description of speckle as multiplicative noise, even though it is a repeatable interference phenomenon. We will see in Chapter 11 that, when dealing with multidimensional SAR data, the meaning of speckle becomes much less obvious, and its treatment as stationary signal-independent noise does not seem viable. In this sense, we regard speckle as a term most useful in the context of single-channel SAR data.

Although the RCS underlying the observed values is essentially deterministic, its magnitude is unknown and normally is most usefully described by a probabilistic model. Given a set of N pixels, we therefore need to consider the joint distribution of the RCS $\sigma = (\sigma_1, \dots, \sigma_N)$ and the speckle values $\mathbf{n} = (n_1, \dots, n_N)$. If we assume the speckle values are independent of each other and of RCS, we can write

$$P_{\sigma, \mathbf{n}}(\sigma, \mathbf{n}) = P_\sigma(\sigma) \prod_{k=1}^N P_n(n_k) \quad (4.19)$$

The corresponding intensity values $\mathbf{I} = (I_1, \dots, I_N)$ are given by $I_k = \sigma_k n_k$. A change of variables yields the joint distribution of intensity and speckle as

$$P_{I, \mathbf{n}}(I, \mathbf{n}) = P_\sigma(I_1/n_1, \dots, I_N/n_N) \prod_{k=1}^N \frac{P_n(n_k)}{n_k}$$

Integrating out the speckle terms yields the joint PDF of intensity as

$$P_I(I) = \int P_\sigma(I_1/n_1, \dots, I_N/n_N) \prod_{k=1}^N \frac{P_n(n_k)}{n_k} d\mathbf{n} \quad (4.20)$$

Hence, we can, in principle, find the joint distribution of intensity corresponding to any joint distribution of RCS; examples of bivariate distributions are given in Chapter 5.

It is clear from (4.19) that, in general, the intensity values are not independent, but clearly will be so if the σ_i are. A special case of this occurs when the σ_i are all constant, with the same value σ , so that

$$P_{\sigma}(\sigma) = \prod_{k=1}^N \delta(\sigma - \sigma_k)$$

Then

$$P_I(I) = \prod_{k=1}^N \frac{1}{\sigma} e^{-I_k/\sigma} \quad (4.21)$$

This speckle model for uniform targets underlies much of the existing work on SAR image analysis and is used extensively in later parts of this book (e.g., in the “cartoon” model for SAR segmentation in Chapter 7).

4.6 Estimating the RCS—The Effects of Imaging and Noise

The analysis in Sections 4.3 to 4.5 was in terms of the given data and ignored how the imaging process affects the information carried by the data. Essentially there are three imaging effects that must be taken into account when trying to recover the backscattering coefficient σ^0 , namely: (1) a scaling of σ^0 due to propagation, antenna pattern, and processing effects; (2) a bias in σ^0 due to system noise; and (3) spatial correlation induced by the processing. To see this, we start from the linear imaging equation (2.34) that relates the observed voltage, $\mathcal{E}(x)$, to the complex reflectivity, $S(x)$, by

$$\begin{aligned} \mathcal{E}(x) &= (C(R_0)S(x)*k(x) + n(x))*l(x) \\ &= C(R_0)S(x)*h_a(x) + n(x)*l(x) \end{aligned} \quad (4.22)$$

where the terms in the equation are as defined in Chapter 2. (Particular note must be taken, however, of the symbol R_0 for range, in order to avoid confusion with the ACF notation used below.)

For distributed targets, the rapid spatial variation of phase in $S(x)$ causes the complex reflectivity to have the same characteristics as white zero-mean

Hence, we can, in principle, find the joint distribution of intensity corresponding to any joint distribution of RCS; examples of bivariate distributions are given in Chapter 5.

It is clear from (4.19) that, in general, the intensity values are not independent, but clearly will be so if the σ_i are. A special case of this occurs when the σ_i are all constant, with the same value σ , so that

$$P_{\sigma}(\sigma) = \prod_{k=1}^N \delta(\sigma - \sigma_k)$$

Then

$$P_I(I) = \prod_{k=1}^N \frac{1}{\sigma} e^{-I_k/\sigma} \quad (4.21)$$

This speckle model for uniform targets underlies much of the existing work on SAR image analysis and is used extensively in later parts of this book (e.g., in the “cartoon” model for SAR segmentation in Chapter 7).

4.6 Estimating the RCS—The Effects of Imaging and Noise

The analysis in Sections 4.3 to 4.5 was in terms of the given data and ignored how the imaging process affects the information carried by the data. Essentially there are three imaging effects that must be taken into account when trying to recover the backscattering coefficient σ^o , namely: (1) a scaling of σ^o due to propagation, antenna pattern, and processing effects; (2) a bias in σ^o due to system noise; and (3) spatial correlation induced by the processing. To see this, we start from the linear imaging equation (2.34) that relates the observed voltage, $\mathcal{E}(x)$, to the complex reflectivity, $S(x)$, by

$$\begin{aligned} \mathcal{E}(x) &= (C(R_0)S(x)*k(x) + n(x))*l(x) \\ &= C(R_0)S(x)*h_a(x) + n(x)*l(x) \end{aligned} \quad (4.22)$$

where the terms in the equation are as defined in Chapter 2. (Particular note must be taken, however, of the symbol R_0 for range, in order to avoid confusion with the ACF notation used below.)

For distributed targets, the rapid spatial variation of phase in $S(x)$ causes the complex reflectivity to have the same characteristics as white zero-mean

Gaussian noise. Hence, $\mathcal{E}(x)$ is also zero-mean and Gaussian. In this case, the most useful statistical descriptor of $\mathcal{E}(x)$ is its spatial ACF. Assuming $S(x)$ and $n(x)$ are wide-sense stationary, so also will be $\mathcal{E}(x)$; its ACF is then defined as

$$R_{\mathcal{E}}(x) = \langle \mathcal{E}(x + y)\mathcal{E}^*(y) \rangle \quad (4.23)$$

with $\langle \cdot \rangle$ denoting an expectation over the joint distribution of $\mathcal{E}(x + y)$ and $\mathcal{E}(y)$. Since $\mathcal{E}(x)$ has mean zero, its variance or mean power is given by $R_{\mathcal{E}}(0)$.

Similar definitions apply to $S(x)$ and $n(x)$. Well-known results from linear system theory [28–30] applied to (4.22) allow us to write

$$R_{\mathcal{E}}(x) = (|C|^2 R_S(x)^* R_k(x) + R_n(x)^* R_l(x)) \quad (4.24)$$

where we have assumed that noise and signal are independent. The range dependence of C is not explicitly shown to avoid any confusion with the ACF notation. The deterministic ACF of $k(x)$ is denoted $R_k(x)$ and is defined by

$$R_k(x) = \int_{-\infty}^{\infty} k(x + y)k^*(y) dy \quad (4.25)$$

with a similar definition for $R_l(x)$. $R_k(0) = \int_{-\infty}^{\infty} |k(y)|^2 dy$ is known as the energy in $k(x)$.

Since $S(x)$ and $n(x)$ are both white, we can write

$$R_S(x) = \sigma^2 \delta(x) \quad (4.26)$$

and

$$R_n(x) = N \delta(x) \quad (4.27)$$

where N is the mean noise power. Hence,

$$R_{\mathcal{E}}(x) = |C|^2 \sigma^2 R_k(x)^* R_l(x) + N R_l(x) = |C|^2 \sigma^2 R_{k_a}(x) + N R_l(x) \quad (4.28)$$

This is the fundamental equation describing the imaging of uniformly distributed targets. A number of important consequences follow from it:

1. The mean power in the processed signal has the value

$$R_{\mathcal{E}}(0) = |C|^2 \sigma^{\circ} R_{h_a}(0) + NR_l(0) \quad (4.29)$$

Hence to estimate σ° from the observed power requires knowledge of the energies in the various filters, the mean noise power, and the range dependent term C .

2. When the noise is negligible, the correlation properties of $\mathcal{E}(x)$ are determined completely by the SAR PSF.
3. Equation (4.28) takes on a particularly simple form in the ideal case, for which $R_l(x) \propto k^*(-x)$ and

$$R_k(x) = R_0 \psi_a \operatorname{sinc}\left(\frac{2x}{d_a}\right)$$

(See discussion following (2.14); also (2.16) and Table 2.2.) Under these conditions $R_l(x) = A \operatorname{sinc}(2x/d_a)$, where A is a constant, and

$$R_{h_a}(x) = R_k(x) * R_l(x) = A \frac{R_0 \lambda}{2} \operatorname{sinc}\left(\frac{2x}{d_a}\right) \quad (4.30)$$

where the substitution $\psi_a = \lambda/d_a$ was used. Hence, the ACF of the returned signal is

$$R_{\mathcal{E}}(x) = \left(|C|^2 \sigma^{\circ} \frac{\lambda R_0}{2} + N \right) R_l(x) \quad (4.31)$$

and the signal and noise components in the complex image have identical statistical properties; the only difference is the power in the two contributions. Signal and noise are therefore inseparable at the pixel level.

4. Since the data are in fact sampled, of most interest are the correlations at multiples of the pixel spacing, x_0 . The *complex (field) correlation coefficient* at lag k in the azimuth direction is defined by

$$\rho_a[k] = \frac{\langle \mathcal{E}(x + kx_0) \mathcal{E}^*(x) \rangle}{\langle |\mathcal{E}(x)|^2 \rangle} \quad (4.32)$$

where we used the fact that $\mathcal{E}(x)$ is mean-zero and assumed stationarity.

In the ideal case, with sample spacing $d_a/2$ (Nyquist sampling), the correlation coefficient would be given by (see (4.30))

$$\rho_a[k] = \text{sinc}(k) = \frac{\sin \pi k}{\pi k} = \begin{cases} 1 & k = 0 \\ 0 & k \neq 0 \end{cases} \quad (4.33)$$

so no correlation would be observed between pixels in a uniformly distributed scatterer. In more realistic cases, the data will be oversampled and pixels will be correlated. Measured values of the ERS-1 azimuth correlation coefficients are shown in Figure 4.7. These plots should be compared with the corresponding range correlation coefficients shown as Figure 2.4. Note that values are only available at the pixel lags (indicated by the squares) and the full curves are based on interpolation. Note also that the correlation coefficients shown are for the intensity data, defined by $I = |\mathcal{E}|^2$. The correlation coefficients of complex and intensity data are related by the Siegert relationship [31]

$$\rho_{I,a}[k] = \frac{\langle I(x + kx_0)I(x) \rangle}{\text{var}(I)} - 1 = |\rho_a[k]|^2 \quad (4.34)$$

where $\text{var}(I) \equiv \langle I^2 \rangle - \langle I \rangle^2$.

It needs to be stressed that throughout this section we have been dealing with *uniformly* distributed targets. The effects of fluctuations in the underlying RCS will be considered in Chapter 5.

4.7 Consequences of the Imaging Model for SAR Measurements

Expressions (4.22) and (4.29) are fundamental in quantifying the ability to detect small targets against a distributed background and system noise and in assessing the effects of system noise on measurements of σ° . We can see from (4.29) that in the latter case, noise introduces a bias into the measurement. The level of this bias is often parameterized by the clutter-to-noise ratio (CNR), given by the ratio of the distributed target and noise terms in (4.29):

$$\text{CNR} = \frac{|C|^2 \sigma^\circ R_{h_a}(0)}{N R_I(0)} \quad (4.35)$$

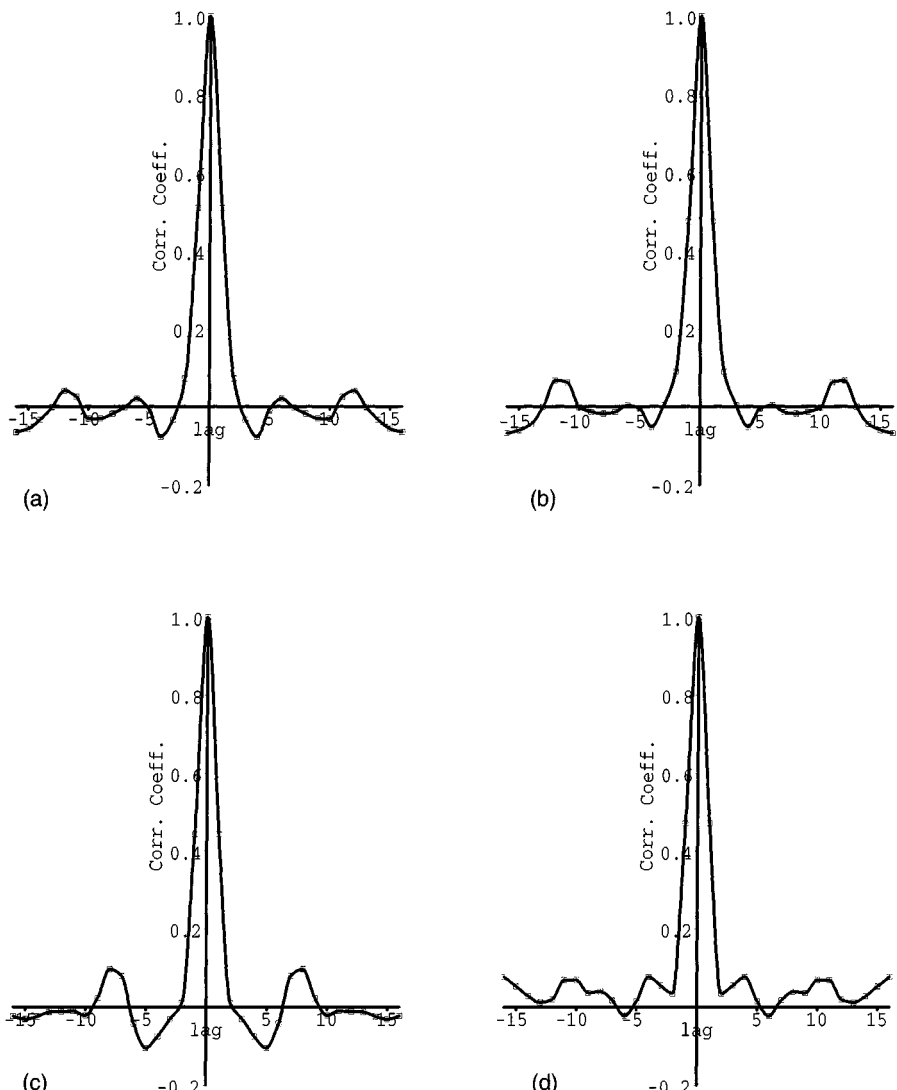


Figure 4.7 Intensity correlation coefficients calculated in the azimuth direction for ERS-1 data from an agricultural area: (a) SLC, near range; (b) SLC, far range; and (c) PRI, near range; and (d) PRI, far range.

In the ideal case (see 4.31)

$$\text{CNR} = \frac{|C|^2 \sigma^0 \lambda R_0}{2N} \quad (4.36)$$

The CNR varies widely in many SAR scenes because of variations in range and in σ^o . Since $|C|$ is proportional to R_0^{-2} (see (2.35)), the CNR can be significantly worse at far range, particularly for airborne systems. Systems are normally designed with sufficient transmitted power to prevent this from being a major problem for most targets. However, regions of low σ^o , such as water bodies under windless conditions, can often give noise-dominated responses especially when they occur at far range.

The use of the word *clutter* to describe the power from a distributed target is an indication that small target detection is hampered by this component of the returned signal as well as by the system noise. The extent of this problem is often described in terms of the square of the peak response from a point target of RCS σ compared to the powers from the clutter and noise background in which it is embedded. In (4.22), a point target of RCS σ and associated phase ϕ is represented by $S(x) = \sqrt{\sigma} e^{j\phi} \delta(x)$, giving the response $C\sqrt{\sigma} e^{j\phi} h_a(x)$. The corresponding *signal-to-clutter ratio* (SCR) is therefore

$$\text{SCR} = \frac{\sigma |h_a(0)|^2}{\sigma^o R_{h_a}(0)} \quad (4.37)$$

where we have assumed that the peak response occurs at $x = 0$. In the ideal case, this reduces to

$$\text{SCR} = \frac{2}{d_a} \frac{\sigma}{\sigma^o} \quad (4.38)$$

The *signal-to-noise ratio* (SNR) is given by

$$\text{SNR} = \text{SCR} \times \text{CNR} = \frac{|C|^2 \sigma |h_a(0)|^2}{N R_f(0)} \quad (4.39)$$

reducing, in the ideal case, to

$$\text{SNR} = \frac{|C|^2 \sigma \lambda R_0}{N d_a} \quad (4.40)$$

The *signal-to-clutter relations* (4.37) and (4.38) display the critical fact that detectability of targets in clutter is not affected by the distance from the radar, which is in marked contrast to the behavior of, for example, normal

surveillance radars where the SCR is inversely proportional to range. However, since C is inversely proportional to R_0^2 , the SNR falls off in proportion to R_0^3 . Nonetheless, in most cases, clutter is the dominant factor affecting target detection and more general analysis of scene structure. Even in those instances where noise dominates over clutter, the similarity of the properties of noise and clutter (see consequence 3 of Section 4.6) allows a unified treatment of both cases.

Note that these expressions for CNR, SCR, and SNR have been developed by an analogue treatment, but the data are sampled. This entails no modification to the expressions but only to how they are calculated, in two ways.

1. The values $R_{h_a}(0)$ and $R_l(0)$ correspond to the energies of $h_a(x)$ and $l(x)$. For adequately sampled data with spacing x_0 , the energy of $h_a(x)$ is given by

$$R_{h_a}(0) = x_0 \sum_{k=-\infty}^{\infty} |h_a(kx_0)|^2$$

with a similar result for $l(x)$.

2. The peak response $h_a(0)$ needed to calculate the SCR (4.37) and SNR (4.39) will normally require interpolation between samples.

A direct digital analysis is given in [32].

4.8 The Effects of Spatial Correlation on Multilooking

As indicated by (4.28), spatial correlation is an intrinsic feature of the imaging process, that must be taken into account when estimating parameters. As an illustration, consider the estimation of the mean intensity of an $M \times N$ block of data from a uniformly distributed target with true mean value σ . The normal multilook estimate of σ is the sample average \bar{I} , given by

$$\bar{I} = \frac{1}{MN} \sum_{i=1}^M \sum_{j=1}^N I_{ij} \quad (4.41)$$

where the intensity at position (i, j) is denoted I_{ij} . Hence, the expected value of \bar{I} is σ , but its variance depends on the spatial correlation of the pixels and is given by

$$\text{var}(\bar{I}) = \frac{\text{var}(I)}{MN} \sum_{|k| < M} \sum_{|l| < N} \left(1 - \frac{|k|}{M}\right) \left(1 - \frac{|l|}{N}\right) \rho_{I,a}[k] \rho_{I,r}[l] \quad (4.42)$$

where $\rho_{I,a}$ and $\rho_{I,r}$ are the azimuth and range intensity correlation coefficients. Note that the correlation coefficients may here include both system effects and correlation induced by the underlying RCS. Hence the same expression applies for textured data (see Chapter 5). If the pixels are independent, the correlation coefficients are zero at all lags except lag 0, so (4.42) reduces to the familiar result

$$\text{var}(\bar{I}) = \frac{1}{MN} \text{var}(I) \quad (4.43)$$

equivalent to MN independent looks.

If we use the values for ERS-1 PRI data indicated by Figures 2.4 and 4.7, the correlation coefficients are only significant at lag 1 in each direction, with

$$\rho_{I,a}[1] \sim \rho_{I,r}[1] \sim 0.5$$

in which case

$$\text{var}(\bar{I}) \sim \frac{\text{var}(I)}{MN} \left(4 - \frac{2}{M} - \frac{2}{N} + \frac{1}{MN}\right)$$

The effect of correlation is clearly dramatic. For $M = N = 10$, the standard error is inflated by a factor $\sqrt{3.61}$ (i.e., 1.9) compared to uncorrelated data. For M and N bigger than about 10, and in the case where only the first lag is significant in each direction, we can write

$$\text{var}(\bar{I}) \sim \frac{\text{var}(I)}{MN} (1 + 2\rho_{I,a}[1] + 2\rho_{I,r}[1] + 4\rho_{I,a}[1]\rho_{I,r}[1])$$

Hence, the equivalent number of independent samples (or looks; see (4.11)) is

$$\text{ENL} = \frac{MN}{(1 + 2\rho_{I,a}[1] + 2\rho_{I,r}[1] + 4\rho_{I,a}[1]\rho_{I,r}[1])} \frac{\langle I \rangle^2}{\text{var}(I)}$$

which takes the value $3 MN/4$ for the three-look ERS-1 data, when we use the measured correlation coefficients noted previously. (Notice that this analysis assumes a uniform target. If the RCS varies within the target, the spatial

correlation coefficients may be altered, as described in Chapter 5, with the effect of increasing $\text{var}(\bar{I})$ and reducing the ENL.)

Spatial correlation also implies that the multilook average (4.41) is no longer the MLE of the mean intensity. In fact, it can be shown that the MLE requires complex data and is given by

$$\hat{\sigma} = \frac{1}{MN} \text{tr}(R_S^{-1}SS^\dagger) = \frac{1}{MN} S^\dagger R_S^{-1}S$$

where R_S is the correlation matrix of the N complex samples $S = (S_1, \dots, S_{MN})$, \dagger denotes conjugate transpose, and tr denotes trace. (The data vector S can be used to represent a two-dimensional data block using any desired ordering of the data.) Hence, any estimate of σ using only intensity data is suboptimal except when the samples are uncorrelated, since R_S is then the identity matrix. A final problem with spatial correlation is that most SAR image analysis techniques are based on theory developed for uncorrelated data, and it would be difficult to modify them to take account of the increased complexity of the joint PDF when correlation is present. As a result, we next consider ways to deal with data known to be correlated by the system.

4.9 Compensating for System-Induced Spatial Correlation

Equations (4.32) and (4.34) have shown that both the complex and intensity data will normally be correlated due to the SAR processing. However, the bandwidth of the data is doubled by the squaring operation needed to form intensities. Hence, preserving the information requires that the spatial sampling of the intensity data be twice that of the complex data. (Since the data are now real, the memory requirement is the same.) For this reason, correctly sampled intensity data *always* exhibit significant spatial correlation. Clearly $\rho[k]$ or $\rho_r[k]$ are known if the PSF is known. (Since the same considerations apply to range and azimuth, we have omitted the corresponding subscript on the correlation coefficients.) However, uncertainties in the PSF often make it preferable to measure $\rho[k]$ from the data. Methods to do this are discussed in the next section; here we are simply concerned with removing system-induced correlation. Possible approaches are described in the following subsections.

4.9.1 Subsampling

If the system-induced correlation becomes negligible beyond a certain lag k_0 , the data can simply be subsampled at this spacing. This method clearly discards

information and degrades resolution but does not distort the single point PDF. When used as a precursor to edge or segment detection it may be acceptable since the objects of interest are large and the image structure found in this way can be reimposed on the original data. However, single pixels may contain most of the relevant information when small objects or detailed structure are of interest, and this approach is then not suitable.

4.9.2 Pre-Averaging

Averaging blocks of nonoverlapping pixels reduces correlation at the expense of resolution. For example, if the data are averaged in azimuth in blocks of N to form

$$J[i] = \frac{1}{N} \sum_{k=(i-1)N+1}^{iN} I_k$$

then the correlation coefficient of neighboring values of $J[i]$ is given by

$$\frac{\sum_{|k| < N} (1 - |k|/N) \rho_I[N - k]}{\sum_{|k| < N} (1 - |k|/N) \rho_I[k]}$$

For the ERS-1 PRI values shown in Figure 4.7, taking $N = 2$ would lead to a correlation coefficient of $1/6$, while with $N = 3$ this drops to a value of $1/10$. Figure 4.8 shows measured azimuthal intensity correlation coefficients

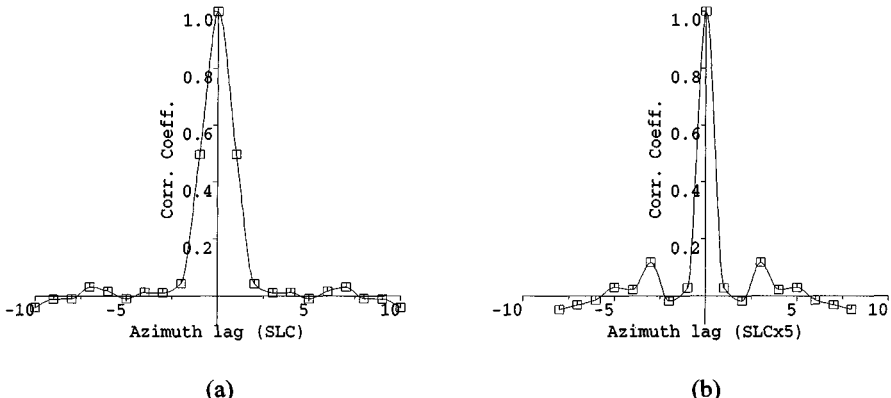


Figure 4.8 Azimuthal intensity correlation coefficients for (a) ERS SLC data and (b) SLC data that were first averaged in intensity in blocks of 5 pixels along azimuth.

based on (a) original ERS SLC data and (b) SLC data that have been averaged in intensity in blocks of 5 pixels in azimuth [33] (see Figure 2.3). The reduced correlation at lag 1 is obvious; the peak at lag 3 (corresponding to lag 15 in the original data) is not significant.

Using this method of reducing correlation will clearly change the PDF of the data. For example, the averaged data will have reduced variance (see (4.42)). Exact expressions for the PDF of averages of correlated intensity data can be derived using methods described in [16]. These require that the *complex* ACF be available; this can be inferred from the ACF of the intensity data, using the Siegert relationship (4.34), only when the complex ACF is known to be real and positive. This approach to reducing correlation therefore leads to considerably increased complication if rigorous analysis is to be applied to the averaged data.

4.9.3 Interpolation

For data sampled at or above the Nyquist rate, the original analogue signal can be reconstructed from the samples and a new set of samples taken with spacing chosen to remove correlation or reduce it to negligible levels. This is equivalent to interpolating a new set of samples whose spacing exceeds that of the original data. The classical method for carrying out this operation uses the Shannon–Whittaker sampling theorem and is based on interpolation using sinc functions. When the spacing of the new samples is related to the old spacing by an integer multiple of 2^{-n} (e.g., $3/2$, $5/4$, etc.), this operation can be carried out efficiently using the *fast Fourier transform* (FFT). In this method, the data are first interpolated onto a finer grid and then samples are discarded.

To illustrate this, assume that we wish to increase the sample spacing to $9/8$ times the original, in one dimension only. A data sample of length M (which must be a power of 2 for FFT methods) is Fourier transformed. The transformed data vector is made eight times longer by appending $7M$ zeros to it (*zero-padding*), and the inverse transform of this lengthened data set is taken. This yields data interpolated onto a grid eight times denser than the original. Finally we discard eight out of every nine samples. Extending this approach to two dimensions is straightforward, either directly by using two-dimensional FFTs or by carrying out the interpolation first in one dimension, and then the other.

A full discussion of interpolation methods would be lengthy, involved, and out of place in this text, but we note the following points:

- When the reduced sample spacing is not a multiple of 2^{-n} , other methods are required based on sinc interpolation or other forms of interpolation, such as cubic convolution [34]. This requires care if information is not to be distorted [35].

- The discussion here has made no distinction between complex and intensity data because the principles are the same in both cases. However, we have already noted that the correlation of samples is expected to be significantly greater for intensity data. Also, most of the image analysis methods discussed in this book are applied to intensity data (more generally, to second-order products of complex data in the context of polarimetric data). An important distinction between interpolation of complex and intensity data is that in the former case the single point distribution is unaltered (assuming a simple condition on the interpolation coefficients is satisfied) whereas in the latter case the distribution and moments are normally changed [35].
- Resampling the intensity data to remove correlation inevitably leads to loss of information, because this will give rise to sampling below the Nyquist limit. However, this will be less, in general, than when we simply discard samples.
- The complete removal of correlation requires an ACF with uniformly spaced zeros and sampling at this spacing. Only for the ideal case with rectangular weighted processing and a sinc PSF is this condition satisfied because then the complex correlation coefficient is given by (see (4.33))

$$\rho_a(x) = \text{sinc}\left(\frac{2x}{d_a}\right)$$

and zeros occur at spacing $d_a/2$. (For simplicity, we only describe the azimuth direction.) More usually, this condition will be only approximately satisfied. Where the ACF varies across an image (as will always occur, for example, in an image that has been resampled to ground range, such as the ERS PRI product), only approximate methods are available unless unequal spacing is adopted, with consequent adverse geometric effects.

4.10 Estimating Spatial Correlation: Stationarity and Spatial Averaging

The analysis in Section 4.6 assumed a wide-sense stationary [30] target in order to define the spatial correlation induced by the system. Here we make a more careful treatment that has considerable practical consequences for estimating

this correlation. In essence, the imaging equation (4.22) tells us that the complex image, $\mathcal{E}(x)$, is zero-mean and Gaussian [28]; hence, its statistical properties are entirely described if we know the two-point correlation function

$$R_g(x, x') = \langle \mathcal{E}(x)\mathcal{E}^*(x') \rangle = \int_{-\infty}^{\infty} \langle \sigma(u) \rangle h(x-u)h^*(x'-u) du \quad (4.44)$$

(Although written in one dimension, the discussion here is equally valid if x is regarded as a two-dimensional variable. It is based on the noise-free version of (4.22), from which we have omitted multiplicative factors since they have no impact on the argument.) If $\sigma(x)$ is stationary (which in the context of a deterministic RCS model implies that the target is uniform), then

$$R_g(x, x') = \langle \sigma \rangle R_h(x - x') \quad (4.45)$$

The assumption of stationarity allows us to separate out the RCS term $\langle \sigma \rangle$ from the speckle term and to regard the speckle as a correlated unit mean process (assuming that $h(x)$ is normalized to unit energy) multiplying the mean RCS.

A consequence of (4.45) is that the distribution of the Gaussian process $\mathcal{E}(x)$ is known, so the joint distribution of intensity and phase can be written down for an arbitrary set of pixels, using the change of variables

$$\mathcal{E}(x) = \sqrt{I(x)} e^{j\theta(x)}$$

To obtain the joint PDF of intensity alone requires the phase to be integrated out, but this rapidly becomes very complicated. Fortunately we have little need for the multipoint joint distribution of intensity, although extensive use will be made of two-point statistics. For a pair of pixels the analysis is identical to that carried out in Chapter 11 when analyzing the joint distributions of correlated polarimetric channels. Analogous treatments for the spatial and temporal domains will be found in [16,28]. A detailed analysis of the intensity correlation function and the effects of RCS variations is given in Section 5.6.

From (4.45), it can be seen that the ACF of the complex data is stationary and proportional to the deterministic ACF of the PSF as long as the mean RCS is stationary within the target. Similarly, fourth-order moments of the complex data depend on the stationarity of the second-order moments of RCS (see Chapter 5). These statements need some comment. The data model used when we discuss image filtering and segmentation in Chapters 6 and 7 is that at each pixel in the image there is a well-defined RCS that we are trying to estimate. In that sense, the RCS is deterministic and speckle due to interference effects is the

only source of fluctuation. While speckle is stationary, RCS varies from place to place, so ensemble statistics (over many speckle patterns) and spatial statistics are equivalent only in regions of constant RCS. That being the case, (4.45) would be true only over such uniform targets.

This becomes of concern when (4.45) is used to estimate $R_b(x)$. It is obvious from Figure 4.1 that most images are nonstationary at large scales. When we consider individual scene components, such as fields or woodland areas in Figure 4.1, it is no longer at all clear whether stationarity holds or not. In some cases, trends in mean brightness across a field may be visible, but tests on visually uniform targets often display statistically significant trends [36]. These tests rely on least squares fitting of a polynomial form (for example, a linear polynomial) to observations. Tests based on distributional fitting were found to be less sensitive to trends in the mean RCS [36].

This appears to call the usefulness of (4.45) into question. However, it can be shown that (4.45) is valid if $\langle \sigma \rangle$ is interpreted as the average RCS across a region as long as (1) the RCS varies slowly on a scale comparable with the length over which the PSF takes values significantly different from zero and (2) the test region is much bigger than the scale length of the PSF. Hence, an estimation of the complex ACF does not rely on knowing that the test region is stationary.

The intensity moments relevant in texture analysis (Chapter 8) are not so robust to target heterogeneity. In this case, an important consideration is the scale of variation in the target compared with the region used for estimation. If the RCS is assumed to have a correlation length that is comparable to or greater than the region used for estimation, trends will normally occur across the region and the estimate will be distorted. If the correlation length is much shorter than the estimation region, a proper sampling of the distribution of RCS is available and accurate estimates will be possible. Scale lengths of variation in mean or texture properties will also be seen to have considerable importance in the segmentation procedures developed in Chapters 7 and 8.

When dealing with textured regions, methods for testing stationarity have received little attention as yet, and visual inspection is normally used. The eye is often very good at detecting lack of stationarity. For example, a human interpreter would certainly recognize a dark feature running from top to bottom in the woodland region in Figure 4.1 and so determine that the region is not stationary. However, as noted, statistical tests may prove stronger than human perception in some cases. Nonetheless, later chapters in this book will deal extensively with statistical properties of regions selected to be stationary mainly on the basis of visual inspection. A target will be referred to as *homogeneous* if there are no significant trends in the spatial average properties within the target. Stronger assumptions (e.g., ergodicity) are irrelevant when only single images are available at a given time. The equivalence of ensemble and spatial statistics

is only of importance in those sections of this book dealing with simulation in Chapter 5. Here inferred fluctuations in RCS from observations over a class of objects (e.g., woodland) are used to provide a probabilistic model from which to construct test images with similar properties.

4.11 Limitations in the Speckle Model

The speckle model developed previously is based on (4.1) with the assumption that N is very large at every pixel and that the scatterers within each pixel are statistically identical. However, the same model can also be used to represent other important situations.

1. One scatterer dominates the return, which is the case of interest for target detection when a strong scatterer is embedded in weak clutter. The ensuing PDF of intensity is then a modified Rician distribution [16]

$$P_I(I) = \frac{1}{\sigma} \exp\left(-\frac{I}{\sigma} - \text{SCR}\right) I_0\left(2\sqrt{\frac{I \times \text{SCR}}{\sigma}}\right) \quad I \geq 0 \quad (4.46)$$

where I_0 is a modified Bessel function of the first kind. Then $\langle I \rangle = \sigma(1 + \text{SCR})$ and $\text{var}(I) = \sigma^2(1 + 2 \times \text{SCR})$, so the coefficient of variation is given by

$$\text{CV} = \frac{\sqrt{1 + 2 \times \text{SCR}}}{1 + \text{SCR}}$$

For large values of SCR, $\text{CV} \approx \sqrt{2/\text{SCR}}$, so the target exhibits little fluctuation about its true value. The phase of the target also becomes effectively noisefree for large values of SCR, exhibiting a standard deviation given approximately by $\sqrt{2 \times \text{SCR}}$ [16]. Hence, bright targets in weak clutter do not exhibit speckle fluctuations.

2. In (4.1) not only are the amplitudes A_k and phases ϕ_k random variables, but so also is the number of scatterers N . In some circumstances N may become small (the Rician distribution with a single target and an infinite SCR represents an extreme case of this). For example, very long wavelength radars imaging forests may display behavior appropriate to small varying numbers of scatterers. This situation has been

studied extensively in light scattering [37,38], but its relevance to SAR is still under investigation.

3. A quite different scenario occurs when N is a random variable whose mean value is large. Then the single-channel field distribution becomes indistinguishable from a fluctuating RCS multiplied by a Gaussian speckle term. This model is developed at length in Chapter 11 (Appendix 11A) in the context of polarimetric data. The important point is that for a single channel it can be treated exactly like multiplicative speckle.
4. Mixed families of scatterers can be treated by methods based on extensions of the standard speckle model or of the previous three cases.

4.12 Multidimensional SAR Images

Until now we have been mainly concerned with the formation and properties of single SAR images, but recent developments in SAR technology have made the use of multiple SAR images of the same scene increasingly important. An important distinction is whether the different images are mutually *coherent* or not. By this we mean that the phase relations in the images can be meaningfully compared. We noted in Section 4.3 that the interference effects giving rise to speckle are noiselike but represent true electromagnetic scattering. In the absence of actual system noise, an identical sensor viewing an unchanged scene with the same geometry would measure an identical complex image. Changes in the scene or the sensor geometry, operating frequency, or polarization will cause the complex image to change. However, in certain important cases the changes give rise to images that are correlated and in which the phase properties of image pairs contain useful information. Particularly important are *SAR interferometry* and *SAR polarimetry*.

In SAR interferometry, the same scene is viewed from slightly different directions by a SAR carrying two antennas or by a single-antenna SAR viewing the scene at different times (repeat-pass interferometry). Under certain conditions [39], the phase difference between the scenes can be used to infer the height of scatterers within the image so that a digital elevation model for the scene can be constructed. For repeat-pass interferometry, a requirement is that the geometrical arrangement of scatterers (at the subpixel level) should be essentially unchanged between the times of gathering the two images, otherwise the phase difference between the images will carry no information. Figure 4.9 shows an amplitude (a) and phase difference (b) image produced by the DRA C-band dual antenna system. Interferometric fringes are very well defined over most of the phase difference image, except where coherence is lost in the radar

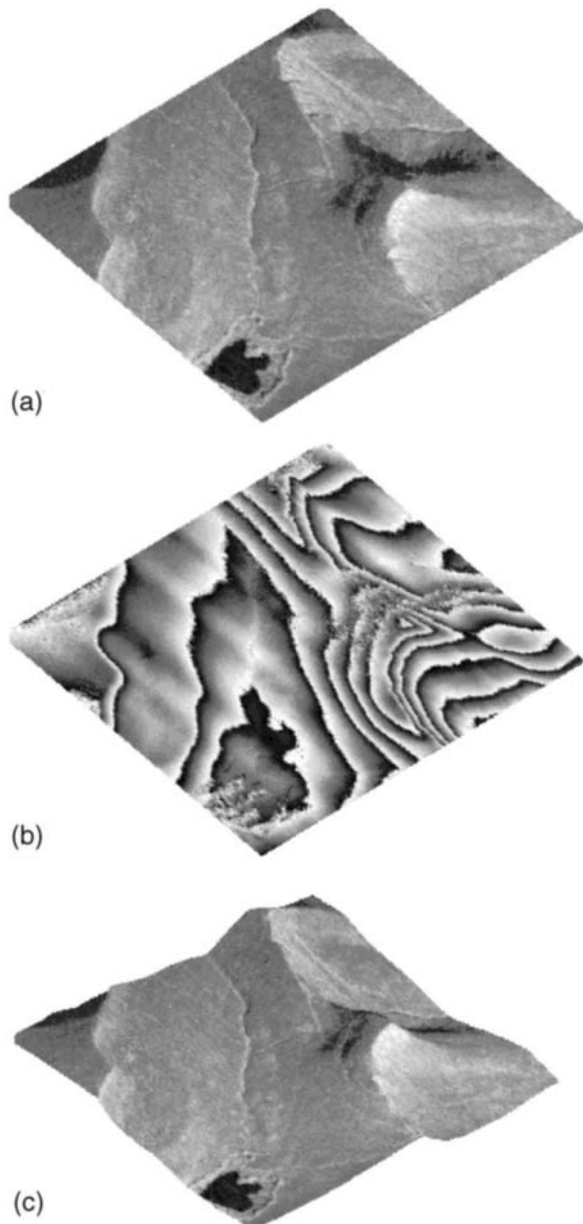


Figure 4.9 Interferometric image of the Brecon Beacons, Wales, produced by the DRA C-band dual antenna SAR: (a) amplitude image, (b) phase difference image with gray-scale cycle corresponding to a change in altitude of 150m, and (c) inferred image of the relief. (British Crown Copyright, 1997/DERA.)

shadow areas (the hill on the right side of the image) and the reservoir (lower left). Each complete cycle of phase corresponds to an altitude change of 150m at the center of the image, allowing the relief in the image to be inferred with an accuracy of $\pm 5\text{m}$, as shown in Figure 4.9(c).

In SAR polarimetry, nearly simultaneous images of the scene are formed with different polarization configurations. Typically the radar transmits and receives radiation that is linearly polarized in the horizontal (H) and vertical (V) planes (relative to the plane defined by the wave vector and the normal to the surface being illuminated), giving rise to four images—HH, HV, VH, and VV, where, for example, HV refers to transmitting horizontally polarized radiation and receiving the vertically polarized component of the backscatter. Depending on the physics of the interactions with the target, the phase differences of polarimetric images can be information bearing (see Chapter 11). There are also several other image types not available for a single image. To illustrate this, in Figure 4.10(a–d), we show L-band amplitude images of a region in Jutland, Denmark, produced by the HH, HV, VH, and VV channels of the *Danish Centre for Remote Sensing* (DCRS) EMISAR polarimetric system. The complex channels can be combined in pairs in a number of ways, but particularly useful prove to be phase difference (e), correlation coefficient (f) (see Chapter 11 for a discussion of this parameter), and amplitude ratio ((g) and (h) show the $|\text{HH}/\text{VV}|$ and $|\text{HV}/\text{VV}|$ ratio images). The images shown as Figure 4.10(e,f) were formed by combining the HH and VV channels. Other useful images can be formed by combining all the polarimetric channels in a variety of ways, as discussed in Chapter 12.

Although system or scene changes may prevent images from being mutually coherent, much information can be gained from incoherent images of the same scene. A particularly important example is *multitemporal* data, which can be used for change detection. As we shall see in Chapter 12, ratio images like those in Figure 4.10(g,h) play an important role for such data but provide only one of numerous possibilities for displaying information when multiple data sets are available.

Although multidimensional SAR data offer new types of information and give rise to new image types, the processing involved is essentially no different from that already described in Sections 2.2 to 2.5. Each image is processed independently and, in isolation, displays the speckle and correlation properties explained in Sections 4.3 to 4.6. In particular, the spatial correlation produced by the system should be identical in the four channels unless the H and V antenna patterns are substantially different. Clearly, when coherence between images is an issue, great care must be taken to preserve phase throughout the processing chain and issues such as system phase noise become relevant. However, this involves no new fundamental concepts.

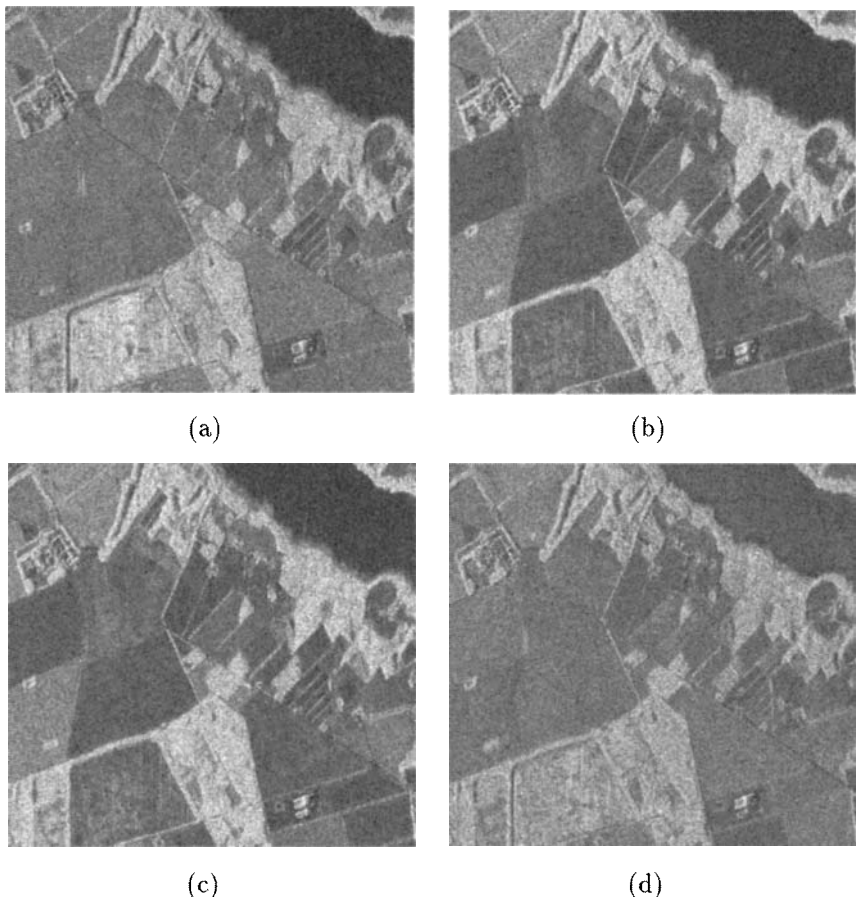


Figure 4.10 (a–d) HH, HV, VH, and VV L-band amplitude images of an agricultural region in Jutland, Denmark, produced by the DCRS EMISAR; (e) HH–VV phase difference; and (f) correlation coefficient images, together with the (g) HH/VV and (h) HV/VV amplitude ratio images.

One other image type deserves to be mentioned in order to indicate the flexibility of the SAR processing. In Chapter 2 it was shown that one way of interpreting the azimuth processing is that the SAR uses Doppler frequencies to achieve enhanced azimuth resolution. This Doppler sensitivity can in some cases be exploited to detect moving objects. In this case, the Doppler spread caused by the different objects in the beam defines the frequency and hence velocity resolution of the *moving target indicator* (MTI) system. In fact, the clutter band (zero Doppler-frequency) in an MTI radar contains the information that is used



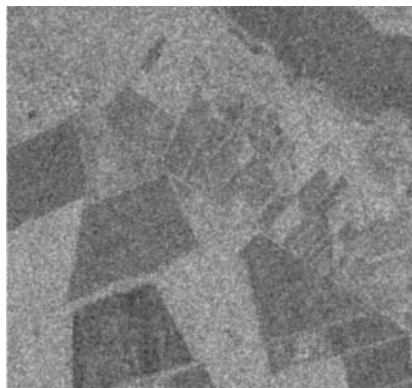
(e)



(f)



(g)



(h)

Figure 4.10 (continued).

in the normal SAR imaging mode. This book will confine its attention to SAR processing of the clutter band alone. Readers with an interest in MTI applications are referred to [40].

4.13 Summary

When trying to infer properties of the world from SAR data, only those properties that leave noticeable or measurable effects in the image are of interest. Our first visual response to these effects is in terms of image structure; armed with experience and our knowledge of the world we can recognize information

carried by shapes, linear features, and objects in the scene. A loose distinction can be made between small and distributed targets. For the latter, coherent speckle caused by interference between elementary scatterers is a dominant aspect of their expression in the image. A well-developed theory and much experimental evidence indicates that, in single-channel data, speckle can be treated as a stationary noiselike quantity multiplying the underlying RCS. The true nature of speckle as a repeatable electromagnetic scattering phenomenon only becomes manifest when multiple channels can be combined, as in SAR interferometry or polarimetry.

For distributed targets, the speckle model (and more refined RCS models developed in Chapter 5) indicates that all the available information is carried by a small number of parameters that characterize the observed distributions. At the simplest level, there is only a single parameter, which is the mean intensity. The viability of this simple speckle model provides a solid basis for the image analysis methods developed in the following chapters. The imaging process complicates the extraction of geophysical properties from the SAR measurements because it induces scaling of the backscattering coefficient, a bias due to system noise and spatial correlation. Post-processing is needed to calibrate the data. Spatial correlation must be accounted for both in parameter estimation and in subsequent image analysis techniques. For the latter, it is often necessary first to decorrelate the data.

Parameter estimation, either locally or over extended targets, plays a central role in extracting information from SAR data, which is a reflection of its function as a bridge between world knowledge (carried both in recognition of image structure and in the empirical basis for describing distributed targets) and physical understanding. Single images provide an important introduction to the issues it raises and give rise to the highly developed theoretical and methodological treatment of Chapters 5 to 10. The understanding gained in this simpler case then helps to bring insight to the more complex task of defining and extracting the information carried by multidimensional SAR data in later chapters.

References

- [1] Ulaby, F. T., R. K. Moore, and A. K. Fung, *Microwave Remote Sensing: Active and Passive*, Vol. 3, Norwood, MA: Artech House, 1986.
- [2] Tsang, L., J. A. Kong, and R. T. Shin, *Theory of Microwave Remote Sensing*, New York: Wiley-Interscience, 1985.
- [3] Fung A. K., *Microwave Scattering and Emission Models and Their Applications*, Norwood MA: Artech House, 1994.

- [4] Kong, J. A. (ed.), *Polarimetric Remote Sensing*, New York, Amsterdam, and London: Elsevier, 1990.
- [5] Kuga, Y., M. W. Whitt, K. C. McDonald, and F. T. Ulaby, "Scattering Models for Distributed Targets," *Radar Polarimetry for Geoscience Applications*, F. T. Ulaby and C. Elachi (eds.), Norwood, MA: Artech House, 1990, pp. 111–190.
- [6] Frison, P. L., E. Mougin, and P. Hiernaux, "Observations and Interpretation of Seasonal ERS-1 Wind Scatterometer Data over Northern Sahel (Mali)," *Remote Sensing of Environment*, submitted 1997.
- [7] Oh, Y., K. Sarabandi, and F. T. Ulaby, "An Empirical Model and an Inversion Technique for Radar Scattering from Bare Soil Surfaces," *IEEE Trans. Geosci. Remote Sensing*, Vol. 30, 1992, pp. 370–381.
- [8] Resnikoff, H. L., *The Illusion of Reality*, New York: Springer-Verlag, 1989.
- [9] Julesz, B., E. N. Gilbert, and J. D. Victor, "Visual Discrimination of Textures with Identical Third-Order Statistics," *Biol. Cybern.*, Vol. 31, 1978, pp. 137–140.
- [10] Julesz, B., H. L. Frisch, E. N. Gilbert, and L. A. Shepp, "Inability of Humans to Discriminate Between Visual Textures That Agree in Second-Order Statistics—Revisited," *Perception*, Vol. 2, 1973, pp. 391–405.
- [11] Brillouin, L., *Science and Information Theory*, New York: Academic Press, 1956.
- [12] Whitt, M. W., F. T. Ulaby, and K. Sarabandi, "Polarimetric Scatterometer Systems and Measurements," *Radar Polarimetry for Geoscience Applications*, F. T. Ulaby and C. Elachi (eds.), Norwood, MA: Artech House, 1990, pp. 191–272.
- [13] Frisch, U., "Wave Propagation in Random Media," *Probabilistic Methods in Applied Mathematics*, Vol. 1, A. T. Bharrucha-Reid (ed.), New York: Academic Press, pp. 75–198.
- [14] Lang, R. H., and J. S. Sidhu, "Electromagnetic Backscattering from a Layer of Vegetation: a Discrete Approach," *IEEE Trans. Geosci. Remote Sensing*, Vol. 21, 1983, pp. 62–71.
- [15] Taylor, J., *Scattering Theory*, New York: Wiley, 1972.
- [16] Goodman, J. W., "Statistical Properties of Laser Speckle Patterns," *Laser Speckle and Related Phenomena*, J. C. Dainty (ed.), New York: Springer-Verlag, 1984, pp. 9–75.
- [17] Arseneault, H. H., and G. April, "Properties of Speckle Integrated with a Finite Aperture and Logarithmically Transformed," *J. Opt. Soc. Amer.*, Vol. 66, 1976, pp. 1160–1163.
- [18] Abramowitz, M., and I. Stegun, *Handbook of Mathematical Functions*, New York: Dover, 1965.
- [19] Kendall, M. G., and A. Stuart, *The Advanced Theory of Statistics*, Vol. 1, London: Charles Griffin and Co., 1958.
- [20] Bush, T. F., and F. T. Ulaby, "Fading Characteristics of Panchromatic Radar Backscatter from Selected Agricultural Targets," *IEEE Trans. Geosci. Electron.*, Vol. 13, 1975, pp. 149–157.
- [21] Lee, J.-S., "A Simple Speckle Smoothing Algorithm for Synthetic Aperture Radar Images," *IEEE Trans. Systems, Man and Cybernetics*, Vol. 13, 1983, pp. 85–89.
- [22] Spiegel, M. R., *Statistics*, New York: McGraw-Hill, 1972.
- [23] Yanasse, C. C. F., S. Quegan, and R. J. Martin, "Inferences on Spatial and Temporal Variability of the Backscatter from Growing Crops Using AgriSAR Data," *Int. J. Remote Sensing*, Vol. 13, 1992, pp. 493–507.

- [24] Beaudoin, A., M. Deshayes, S. Hardy, T. Le Toan, and D. Girou, "Use of Airborne SAR Data for the Mapping of Shifting Cultivation in French Guiana," *Proc. SAREX-92*, ESA WPP-76, 1992, pp. 185–191.
- [25] DeGroot, M. H., *Probability and Statistics*, Reading, MA: Addison-Wesley, 1989.
- [26] Quegan, S., "Parameter Estimation for Polarimetric Measurements from Vegetated Areas," *Proc. Third International Workshop on Radar Polarimetry*, Nantes, 1995, pp. 626–635.
- [27] Wilson, J. J. W., "The Radiometric Resolution for a SAR Employing Correlated Range and Azimuth Looks," *Marconi Research Center Doc. No. ER-TN-MRC-AM-0241*, 1986.
- [28] Davenport, W. B., Jr., and W. L. Root, *An Introduction to the Theory of Random Signals and Noise*, New York: IEEE Press, 1987.
- [29] Papoulis, A., *Signal Analysis*, New York: McGraw-Hill, 1977.
- [30] Papoulis, A., *Probability, Random Variables and Stochastic Processes*, Singapore: McGraw-Hill, 1984.
- [31] Siegert, A. J. F., MIT Rad. Lab. No. 465, 1943.
- [32] Raney, R. K., and R. Bamler, "Comments on SAR Signal and Noise Equations," *Proc. IGARSS '94*, Pasadena, CA, 1994, pp. 298–300.
- [33] Caves, R. G., "Automatic Matching of Features in Synthetic Aperture Radar Data to Digital Map Data," Ph.D. Thesis, University of Sheffield, UK, 1993.
- [34] Keys, R. G., "Cubic Convolution Interpolation for Digital Image Processing," *IEEE Trans. Acoust. Speech, Signal Processing*, Vol. 29, 1981, pp. 1153–1160.
- [35] Quegan, S., "Interpolation and Sampling in SAR Images," *IEEE Trans. on Geoscience and Remote Sensing*, Vol. 28, 1990, pp. 641–646.
- [36] Horgan, G., and H. Meena, "An Investigation of the Variability of SAR Data and Its Effect on Classification," *Proc. Final Workshop on MAESTRO/Agriscatt: Radar Techniques for Forestry and Agricultural Applications*, ESA WPP-31, 1992, pp. 149–153.
- [37] Schaefer, D. W., and P. N. Pusey, "Statistics of Non-Gaussian Scattered Light," *Phys. Rev. Lett.*, Vol. 29, 1972, pp. 843–845.
- [38] Pusey, P. N., D. W. Schaefer, and D. E. Koppel, "Single-Interval Statistics of Light Scattered by Identical Independent Scatterers," *J. Phys. A: Math. Nucl. Gen.*, Vol. 7, 1974, pp. 530–540.
- [39] Rodriguez, E., and J. M. Martin, "Theory and Design of Interferometric Synthetic Aperture Radars," *IEE Proc. F*, Vol. 139, 1992, pp. 147–159.
- [40] Klemm, R., and J. Ender, "New Aspects of Airborne MTI," (FGAN – FFM) *IEEE Int. Radar Conf. Proc.*, 1990, pp. 335–340.

5

Data Models

5.1 Introduction

The nature of information in SAR images was discussed in Chapter 4. Deriving information from these images is a process in which image data are interpreted in light of prior knowledge that is encapsulated in models for both the data and scene properties. In the following chapters we will demonstrate how different data models can be combined with world models in providing optimized information extraction for image interpretation.

To focus the discussion, consider the SAR image in Figure 5.1. The resolution is 1.5m by 1.5m, so details such as a road, clumps of trees, and hedges with associated shadow are clearly visible. In addition, extended areas of clutter, such as the field and woodland areas delineated by white borders are made up of scattering from unresolved objects. Let us start by considering the properties of these two clutter regions.

We have shown in Chapter 4 that speckle arises if the scattering elements within a pixel are randomly distributed. The intensity fluctuations within the field region in Figure 5.1 appear consistent with such a model. We shall discuss the implications of speckle in Section 5.4 in the context of a *product model* that we exploit in Chapters 6 and 7 in deriving information about the underlying cross section in a SAR image, σ . This is estimated from the observed intensity in a pixel and is proportional (rather than identical) to the definitions of RCS or differential cross section in Chapter 2. Nevertheless, we shall (loosely) refer to σ as the RCS.

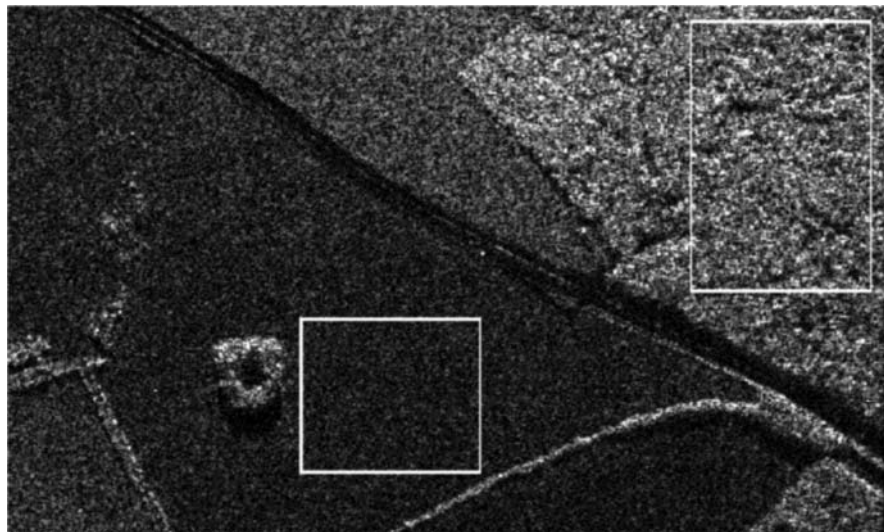


Figure 5.1 DRA C-band SAR image of a rural scene illustrating typical natural clutter, with selected sample regions: (a) field and (b) woodland. Resolution is 1.5 m, single-look.

Speckle itself conveys very little information about a scene other than that it contains many randomly positioned scattering elements. However, in the wooded region it is apparent that there are fluctuations in addition to speckle. Physically, these appear to correspond to strong returns from the crowns of trees with shadows behind them. If we disregard the deterministic positions of these light and dark fluctuations, we can treat this type of natural clutter as a noiselike *texture*. Note that texture is a consequence of fluctuations in the RCS; a clutter sample comprised of speckle alone is not considered textured. Texture measures will take the form of spatial average properties describing the depth of fluctuation of the RCS within the local region. These can be single-point statistics, such as the *probability density function* (PDF). More information is contained in two-point properties such as the power spectrum or ACF. Texture will be exploited in Chapters 8 and 9, both for characterizing the clutter within a homogeneous region and identifying boundaries between regions. The former conveys information that may enable a user to identify cover type, for example, while the latter carries information about the *structure* within the scene.

One of the most important classes of information within an image is contained in its structure. This comprises features such as the boundaries of large areas of texture, for example, fields or woods, as well as discrete objects, such as individual trees, hedges, roads, and buildings. The former can be identified readily by exploiting the texture model. However, a simple noise

model would be an inappropriate description for an urban area that is made up of discrete objects. The relative positions of objects in man-made clutter are constrained by rules; for example, houses lie along streets, or trees in orchards are arranged in rows. It follows that spatial average properties over a region do not encapsulate the relevant information optimally. In this chapter we shall confine our attention largely to data models for natural clutter.

Let us now identify measures that can provide discrimination between such classes of texture. The mean intensities of the field and woodland regions in Figure 5.1 differ by an order of magnitude in RCS, which would certainly enable one to differentiate between them. Suppose, however, that the brightness of the field was the same as the wood, as is often the case in SAR images. A second discriminant could then be the contrast ($\equiv \sqrt{\text{var } I / \langle I \rangle}$), which takes the values 1.003 and 1.41 for the field and woodland regions in Figure 5.1, respectively. The result for the field region is close to unity, as expected for pure speckle, while the woodland region has increased fluctuations. Urban areas typically display even stronger contrast. A third distinguishing characteristic is the spatial extent of image features. In the field region, only speckle fluctuations are observed, with a scale corresponding to the PSF. The woodland sample also includes variation on a scale consistent with tree size and separation. While many objects in urban areas, such as individual houses, are of similar size to isolated trees, some buildings can be on a much larger scale. Each of these general properties might aid image interpretation. The specific measure that optimizes the information about these properties then depends on the detailed form of the data model.

This chapter is concerned with introducing realistic models for SAR image data. The problems inherent in data characterization are considered in Section 5.2, initially restricted to the PDF. A few widely used empirical PDFs are introduced and compared in Section 5.3. The implications of the product model, which separates the physically based speckle model from the phenomenological RCS model, are described in Section 5.4. This extends the basic treatment given in Chapter 4. A comparison of predicted with measured properties for empirical and product models is given in Section 5.5. The product model has the advantage that it contains correlation properties implicitly, as outlined in Section 5.4.1. These are applied in an analysis of the effect of system resolution on measured clutter properties in Section 5.6. This discussion highlights the importance of including the interaction of RCS correlation properties and the PSF in any rigorous clutter analysis. This is an aspect that is omitted from analysis based on fitting clutter PDFs alone and illustrates some of the dangers of artificially restricting the scope of the data model. The discussion of data models then concludes, in Section 5.7, with a summary of circumstances under which they fail.

Having established a reasonable model for natural clutter textures, we then describe techniques for simulating textures with these properties in Section 5.8. Simulation is an important topic in seeking to understand SAR images, for two primary reasons. First, provided simulated textures encapsulate all the properties of the data model, a visual comparison with original textures will reveal failures in that model. For example, a model based on single-point statistics could not reproduce correlation properties. Furthermore, we will demonstrate that one can discriminate between textures with different higher order correlation properties that would not be represented in any model based on the ACF and single-point statistics alone. Second, once a model is validated it can provide a number of sample images that differ randomly but are based on an identical scene. It is clearly not possible to achieve this with real SAR data. There is a danger that image-interpretation algorithms might be designed to provide excellent response to a specific example image but fail to provide robust generic solutions. By allowing a very large number of realizations of the same scene to be investigated, accurate performance statistics can be compiled.

5.2 Data Characterization

Historically, SAR data models have been largely directed at describing single-point statistics through the PDF. Initially, therefore, it is important to consider whether typical SAR images are actually capable of representation in such simple terms. In this section we show that such an approach is at best only an approximation. There are fundamental problems in terms of the nature of the scene being imaged, the physical properties of the imaging process, and finally the analysis of measured data. Let us begin by considering the scene itself. On the coarsest scale the scene is not homogeneous because a map of the area would define boundaries between regions with different properties, such as fields/woodland in Figure 5.1 compared with perhaps land/sea or forest/mountains at lower resolution. Determinism prevails at the limit of fine resolution where it would be possible, in principle, to represent every scattering element within the scene and derive a unique image under defined conditions. Representation in terms of texture can only apply as an approximation on an intermediate scale when the scatterer spatial distribution appears random.

Image formation also introduces variability through physical differences in the imaging process. SAR images depend on the system wavelength due to differing foliage penetration, for example. The response to polarization also varies, as discussed in Chapter 11. Geometrical effects due to the incidence angle will influence the scene through processes such as shadowing. Finally, the resolution of the imaging system will have a strong effect on the appearance of

the clutter because it will average out features on a smaller scale than the resolution while preserving larger ones. In view of the number of processes that contribute to differences between images, it is doubtful whether it is ever worth attempting to define data models with great precision. We need only be concerned with general properties that can be exploited in image interpretation.

Let us next address the issue of the level of complexity needed to represent the data PDF. We are faced with a compromise between choosing a simple model (characterized by few degrees of freedom) that fails to reproduce the observed PDF accurately and a more sophisticated model (with many degrees of freedom) that fits the data. A region of untextured speckle is characterized by a single degree of freedom corresponding to the mean intensity, as discussed in Chapter 4, consistent with the field example in Figure 5.1. However, the associated negative exponential intensity, or Rayleigh amplitude, distribution is not capable of representing some natural clutter, such as the woodland sample in Figure 5.1. A variety of PDFs having two degrees of freedom have been proposed, such as the Weibull, lognormal, and K distributions. The additional degree of freedom allows them to represent different contrasts in the data; contrast has already been identified as a potential texture discriminant. However, there are occasions where even this two-parameter PDF fails to provide a reasonable match to the data and it is necessary to introduce more parameters. We expect this approach to yield a better fit because there are additional degrees of freedom. However, there is often no physical justification, since it merely represents a more complicated parameterization. The process could be repeated indefinitely, using mixture distributions for example, until an exact match to the measured PDF, within statistical errors, was obtained. The resultant PDF would not encapsulate any knowledge about the data but would merely provide a (smoothed) alternative representation. It would provide no indication of how properties might vary as imaging conditions change, for example.

There is a sense, however, in which some classes of PDF have a better phenomenological basis than others. Analysis based on these models should provide a better fit to the observed data with the same number of parameters. The product model in Section 5.4, which separates speckle and RCS properties, provides a physically based factorization of clutter that yields an effective compact representation. Other empirical PDFs, such as the lognormal PDF, have nonphysical properties that restrict their value.

Despite these reservations, let us now consider how to verify the data model. The first requirement is that the test sample should be homogeneous. How is this to be tested? One could adopt a nonparametric approach, such as the Kolmogorov-Smirnov (K-S) test [1]. We will show later that using a test based on the appropriate data model would be more sensitive. However, this model cannot be verified until a suitable homogeneous sample is available.

Thus, the issues of model verification and homogeneity testing cannot be separated. In the absence of a model, the human observer effectively provides the test of homogeneity, as in the selection of the test regions in Figure 5.1.

A second issue concerns region size. It is important that it should be large enough to characterize the statistical properties of the region completely; that is, it must be on a much larger scale than any correlations. This is particularly important if there are large-scale effects, such as ground undulations, that might still be represented by a homogeneous texture if a large enough region is selected. In addition, it needs to contain sufficient independent samples to provide good statistical accuracy. This requirement for large regions conflicts with the observation that the real world does not normally consist of large homogeneous areas. Thus we end up with some compromise choice of region size that approximates homogeneity over a sufficiently large area for adequate statistical accuracy.

Once the sample has been selected the different data models can be investigated. The PDF of the sample intensity, for example, can be compared with the different candidate PDFs. This raises the question of how appropriate parameters to describe the PDF are to be estimated. We might match some arbitrary moment of the measured and theoretical PDFs. However, it is desirable to identify the most sensitive measure for characterizing the data. Since the form of the candidate PDFs is known, we can try to derive the MLE for optimum discrimination. We discuss these issues in detail in Chapter 8 when we consider texture characterization. In any event, the method adopted to estimate parameter values will influence the quality of fit. It is also necessary to select the method for characterizing the goodness of fit between data and model. Initially we derive MLEs for the parameters required by each model, followed by a K-S test to establish if the sample is consistent with that theoretical model. The K-S hypothesis test is not dependent on any model and is determined by the maximum difference between the cumulative probability distributions.

5.3 Empirical Data Distributions

Early distributional measurements on radar data were carried out at low resolution so that objects, such as trees and houses, were much smaller than a resolution cell. Contributions from RCS fluctuations averaged out so that no spatial variations or correlation effects were visible. The resultant complex field PDF was then Gaussian with Rayleigh amplitude and negative exponential intensity PDFs, respectively, as discussed in Chapter 4.

In order to describe higher resolution data, it was necessary to introduce a second parameter to characterize image contrast. The log normal and Weibull are two such distributions that have been widely applied. For example, the

amplitude of low-resolution sea clutter has been fitted to the Rayleigh distribution, corresponding to pure speckle; while the log normal has been applied at a higher resolution [2–4]. A wide range of ocean measurements at different resolutions were shown to be consistent with the Weibull distribution [5–7]. Land clutter was found to be Rayleigh distributed over uniform regions [8] but log normal over built-up areas [8,9]. The Weibull distribution has also been applied extensively to land [5,10,11], weather [12], and sea-ice [13] clutter. These distributions can be fitted to either amplitude or intensity data.

The log normal distribution is given by

$$P(x) = \frac{1}{x\sqrt{2\pi V}} \exp\left[-\frac{(\ln x - \beta)^2}{2V}\right] \quad (5.1)$$

where x is a generic observable, and β and V are the mean and variance of $\ln x$. The mean value and n th normalized moment of this distribution are

$$\langle x \rangle = \exp\left[\beta + \frac{V}{2}\right] \text{ and } x^{(n)} \equiv \frac{\langle x^n \rangle}{\langle x \rangle^n} = \exp\left[n(n-1)\frac{V}{2}\right] \quad (5.2)$$

The log normal distribution predicts zero probability of the observable having a value zero. As such it is a very poor representation of single-look intensity speckle. However, it usually provides a better match to amplitude PDFs, particularly if it is used to represent regions of strong spatial variation such as urban areas [8,9].

The Weibull distribution is given by

$$P(x) = \frac{cx^{c-1}}{b^c} \exp\left[-\left(\frac{x}{b}\right)^c\right] \quad (5.3)$$

where b is a scaling parameter, and c controls the shape. The mean and n th normalized moment of this distribution are

$$\langle x \rangle = b\Gamma\left(1 + \frac{1}{c}\right) \text{ and } x^{(n)} = \frac{\Gamma(1+n/c)}{\Gamma^n(1+1/c)} \quad (5.4)$$

The Weibull distribution is identical to a Rayleigh PDF when $c = 2$ and to a negative exponential when $c = 1$. Thus, it can describe single-look speckle precisely for either amplitude or intensity. Unfortunately, it cannot represent

multilook speckle exactly. The effect of increasing RCS variations is represented by reducing the value of c .

5.4 The Product Model

A significant breakthrough in the understanding of radar image properties was the appreciation that many types of clutter derive from two unrelated processes that can be encapsulated in a product model [14]. In its simplest form, introduced in Chapter 4, this combines an underlying RCS σ , with an uncorrelated multiplicative speckle contribution n ; so the observed intensity I , in a SAR image could be expressed as the product $I = \sigma n$. For L -look intensity data, I can be represented as the product of σ with a speckle contribution n , whose PDF is given by

$$P(n) = \frac{L^n n^{L-1}}{\Gamma(L)} \exp[-Ln] \quad (5.5)$$

This model forms the basis of reconstruction filters and segmentation methods described in Chapters 6 and 7 that are designed to derive specific values of σ associated with an observed value I . Note that, in order to exploit this model, it is essential that the speckle and RCS fluctuations have very different spatial scales. Normally we resample the SAR image so that speckle contributes little correlation between samples, as discussed in Chapter 4. Any RCS fluctuations on a larger spatial scale can then be separated out for further study.

The next component of the product model is to incorporate an *RCS model* that describes the underlying fluctuations. For a given RCS distribution $P(\sigma)$, the product model asserts that the PDF of the observed intensity is given by

$$P(I) \equiv \int_0^{\infty} P(I|\sigma)P(\sigma) d\sigma = \frac{L^L I^{L-1}}{\Gamma(L)} \int_0^{\infty} \frac{d\sigma}{\sigma^L} \exp\left[-\frac{LI}{\sigma}\right] P(\sigma) \quad (5.6)$$

The product model represents an important extension to clutter modeling in that it separates two distinct processes. Speckle is purely a consequence of the random distribution of scattering elements, whereas the RCS depends on the physical properties (such as dielectric constant) of those elements. Notice that this form of product model is only appropriate for single images. It is inadequate for multidimensional sources, such as those encountered in polarimetry or

interferometry, since it ignores correlations between the images in different dimensions. Modifications in describing multidimensional data are introduced in Chapter 11.

5.4.1 The RCS Model

Having defined the speckle contribution to the product model, the next stage is to discuss the RCS model. Studies of sea clutter by Ward [14,15] showed that the detected amplitude was Rayleigh-distributed in regions of negligible swell, corresponding to pure speckle as expected. Swell has a much larger spatial scale than speckle, allowing the speckle contribution to be averaged out without appreciably degrading the swell component. The underlying swell RCS was usually consistent with a gamma PDF, given by

$$P(\sigma) = \left(\frac{\nu}{\langle \sigma \rangle} \right)^{\nu} \frac{\sigma^{\nu-1}}{\Gamma(\nu)} \exp \left[-\frac{\nu \sigma}{\langle \sigma \rangle} \right] \quad (5.7)$$

where ν is an order parameter, with moments given by

$$\langle \sigma^n \rangle = \left(\frac{\langle \sigma \rangle}{\nu} \right)^n \frac{\Gamma(n + \nu)}{\Gamma(\nu)} \quad (5.8)$$

This PDF is completely characterized by two variables: the mean RCS $\langle \sigma \rangle$ and the order parameter ν . The square of the contrast, that is, the normalized variance, is a useful quantity to describe such data and is given by $\text{var } \sigma / \langle \sigma \rangle^2 = 1/\nu$.

Jakeman and Pusey [16] proposed a theoretical model that provided important insight into the basis for this empirical form of clutter PDF. The simple speckle model in Chapter 4 showed that the field within a pixel could be represented as the sum of the contributions from the elementary scatterers

within the resolution cell, so $\mathcal{E} = \sum_{j=1}^N A_j \exp[i\phi_j]$, as in (4.1). Gaussian speckle

then arises from the random interference of many scatterers and corresponds to the limit as $N \rightarrow \infty$. However, Jakeman and Pusey investigated the effect of assuming that the effective number of scatterers N was itself a random number. If the population N is controlled by random processes of birth, death, and migration, the consequent population statistics would be negative binomial [17]. Under these conditions the resultant intensity was shown to be K-distrib-

uted [18–20], rather than the negative exponential form expected from the central limit theorem. This derivation suggests that non-Gaussian clutter statistics can be attributed to the fluctuation in the effective number of scatterers within a resolution cell (see also Appendix 11A).

An equivalent formulation for complex reflectivity could be provided [20,21] using a Fokker–Planck rate equation to describe the RCS. This can be identified as the continuum analogue of a population operated on by processes of birth, death, and migration. The solution to the resulting rate equation yields a gamma-distributed RCS with an order parameter given by the ratio of migration to birth rates and a correlation coefficient at lag X given by [21]

$$\rho_\sigma(X) = \exp[-\gamma X] \quad (5.9)$$

where γ is the migration rate. While this allows all values of order parameter, it restricts the correlation function to a negative exponential form since it is fundamentally a Markov process. However, it is consistent with the choice of a gamma PDF as a description of the RCS [22,23].

The gamma distribution has the convenient mathematical property that it can be regarded as the resultant of a Gaussian random walk process with the final complex reflectivity at a given position expressed as a vector in 2ν dimensions, that is, $S = (S_1, S_2, \dots, S_{2\nu})$, representing independent real and imaginary contributions. Note that each of the contributions $S_1, S_2, \dots, S_{2\nu}$ represents a one-dimensional Gaussian random walk. The total RCS is then given by $\sigma \equiv |S|^2$, which is equivalent to summing ν independent RCS contributions. For simplicity we assume that the correlation properties of each complex reflectivity component are identical. Any form of valid correlation can be adopted, unlike the solution to the Fokker–Planck equation. However, it is only strictly applicable for half-integer values of ν . One consequence of this formalism is that all the higher order correlation properties of S and σ can be derived by exploiting the factorization properties of Gaussian processes [23,24].

Alternatively, these can be derived directly for joint Gaussian processes. For example, the bivariate PDF for correlated RCS samples separated by a distance X is given by [17,25]

$$P_\sigma(X) = \frac{1}{2^{1+\nu}(1 - \rho_\sigma(X))\Gamma(\nu)} \left(\frac{\sigma(0)\sigma(X)}{\rho_\sigma(X)} \right)^{(\nu-1)/2} \times \exp \left[-\frac{\sigma(0) + \sigma(X)}{2(1 - \rho_\sigma(X))} \right] I_{\nu-1} \left[\frac{\sqrt{\sigma(0)\sigma(X)\rho_\sigma(X)}}{1 - \rho_\sigma(X)} \right] \quad (5.10)$$

where $I_n[\cdot]$ is the modified Bessel function of the first kind of order n (Section 9.6 in [26]), and $\rho_\sigma(X)$ is the RCS correlation coefficient at lag X defined by

$$\rho_\sigma(X) \equiv \frac{\langle \sigma(0)\sigma(X) \rangle - \langle \sigma \rangle^2}{\langle \sigma^2 \rangle - \langle \sigma \rangle^2} \quad (5.11)$$

Hence, the n th-order normalized two-point moments are given by [25]

$$\frac{\langle (\sigma(0)\sigma(X))^n \rangle}{\langle \sigma \rangle^{2n}} = 2^{2n} (1 - \rho_\sigma(X))^{v+2n} \frac{\Gamma^2(n+v)}{\Gamma^2(v)} {}_2F_1(n+v, n+v; v; \rho_\sigma(X)) \quad (5.12)$$

where ${}_2F_1(\cdot)$ is the Gaussian hypergeometric function (Section 15.1 in [26]). The results for $n = 1, 2$ are identical to expressions derived by exploiting the factorization properties of the Gaussian random walk [24].

5.4.2 The Intensity PDF

If we now combine the speckle PDF with the gamma RCS PDF, the observed intensity PDF will be given by [27]

$$\begin{aligned} P(I) &= \int_0^\infty P(I|\sigma)P(\sigma) d\sigma = \frac{2}{\Gamma(L)\Gamma(v)} \left(\frac{Lv}{\langle I \rangle} \right)^{(L+v)/2} \\ &\times I^{(L+v-2)/2} K_{v-L} \left[2 \left(\frac{vLI}{\langle I \rangle} \right)^{1/2} \right] \end{aligned} \quad (5.13)$$

for L -look SAR, where $K_{v-L}[\cdot]$ is the modified Bessel function of order $v - L$ (Section 9.6 in [26]). Note that this tends to the gamma distribution for L -look speckle as $v \rightarrow \infty$. The intensity moments are given by

$$\langle I^n \rangle = \langle I \rangle^n \frac{\Gamma(L+n)}{L^n \Gamma(L)} \frac{\Gamma(v+n)}{v^n \Gamma(v)} \quad (5.14)$$

Equation (5.14) can be separated into two, formally similar, parts describing the speckle and cross-section contributions. The normalized variance is given by $\text{var } I/\langle I \rangle^2 = 1/L + 1/v + 1/Lv$, which reduces to $\text{var } I/\langle I \rangle^2 = 1 + 2/v$ for single-look SAR.

The PDF of the amplitude ($A = \sqrt{I}$) is also K-distributed such that

$$\begin{aligned} P(A) &= \int_0^{\infty} P(A|\sigma)P(\sigma) d\sigma = \frac{4}{\Gamma(L)\Gamma(v)} \left(\frac{Lv}{\langle I \rangle} \right)^{(L+v)/2} \\ &\quad \times A^{L+v-1} K_{v-L} \left[2A \left(\frac{vL}{\langle I \rangle} \right)^{1/2} \right] \end{aligned} \quad (5.15)$$

with moments given by

$$\langle A^n \rangle = \langle I \rangle^{n/2} \frac{\Gamma(L + n/2)}{L^{n/2}\Gamma(L)} \frac{\Gamma(v + n/2)}{v^{n/2}\Gamma(v)} \quad (5.16)$$

Hence, $\text{var } A/\langle A \rangle^2 = L\Gamma^2(L)/(\Gamma^2(L + \frac{1}{2})) \times v\Gamma^2(v)/(\Gamma^2(v + \frac{1}{2})) - 1$ is the normalized variance, which reduces to $4v\Gamma^2(v)/(\pi\Gamma^2(v + \frac{1}{2})) - 1$ for single-look SAR.

These derivations for both intensity and amplitude assume that the RCS fluctuations are on a much greater spatial scale than speckle so that multilooking averages speckle without affecting RCS fluctuations. If the contributions were not separable in this way the result would no longer be K-distributed.

The properties of the K-distributed intensity clutter model arising from a gamma-distributed RCS model can be summarized as follows:

- A gamma-distributed RCS can be derived by solving the appropriate rate equation resulting in arbitrary values of v but with a correlation coefficient restricted to a negative exponential form.
- The RCS can also be regarded as the resultant of a $2v$ dimension Gaussian random walk requiring half integer v but allowing arbitrary correlations.
- The gamma PDF has the attractive property that it represents a general noise process, of which thermal noise is the special case when $v = 1$.
- The gamma distribution is the only form of PDF for the RCS discussed in this chapter that yields a closed-form analytic distribution for the detected intensity, that is, the K distribution.

However, the issue that determines the acceptance of this model is the extent to which it is consistent with samples of natural clutter. Previous investigation has shown that the K distribution is consistent with a large number of

coherent scattering experiments, over wavelengths from optical to sonar, and types of scatterer from atmospheric turbulence to natural radar clutter [14–16,23,24,28–33]. In the radar field the K distribution has been used extensively to represent both sea clutter [14–16,18,34–36] and land clutter [22–24,31–33,37–39]. Note that the observed statistics would be modified by any additive input noise in the radar receiver [40,41].

5.5 Comparison of Distributions

Having introduced the K, Weibull, and log normal PDFs, we now establish which provides the best fit to the examples of SAR image data in Figure 5.1. Following the discussion in Section 5.2, we shall determine ML parameter values for the candidate distributions and then perform a K-S test for goodness of fit. The best-fit theoretical PDFs are compared with histograms of the original data in Figure 5.2. The parameter values and fit probability for the different distributions to the field region are summarized in Table 5.1 and those for the woodland region in Table 5.2.

We expect the field sample to correspond to pure speckle with a negative exponential PDF. From Table 5.1 it is apparent that the log normal PDF provides a very poor fit whereas the exponential, Weibull, and gamma distributions have a high probability of being correct. The predicted exponential, Weibull, and gamma distributions are sufficiently close that they can all be represented by the single (exponential) line in Figure 5.2(a). The Weibull shape parameter, c and the gamma order ν , are slightly less than 1.0 (which corresponds to pure speckle). Since the data represent an estimate of the PDF, it would not be expected to have the exact form. Hence, models with an additional parameter, such as Weibull or gamma PDFs, would be expected to yield a higher probability of fit to the estimated histogram, as observed. The distinction between the last three distributions in Table 5.1 is therefore probably insignificant. However, the incorrect form of the log normal in Figure 5.2(a), particularly near the origin, is apparent. Fitting a K distribution to the data was impossible because the estimated PDF actually had a lower contrast than that predicted by the speckle model alone. This would be expected for about half the samples taken over regions of constant RCS. When this condition is observed, it is reasonable to assume that the sample actually contains a constant RCS such that $\nu = \infty$.

The K distribution provides an excellent fit to the example of woodland clutter, as shown by the results of the K-S test in Table 5.2 and the comparison of PDFs in Figure 5.2(b). All other distributions have a negligible probability of being correct over this sample size. Physically, the exponential would be expected to be incorrect since it cannot describe RCS fluctuations with speckle.

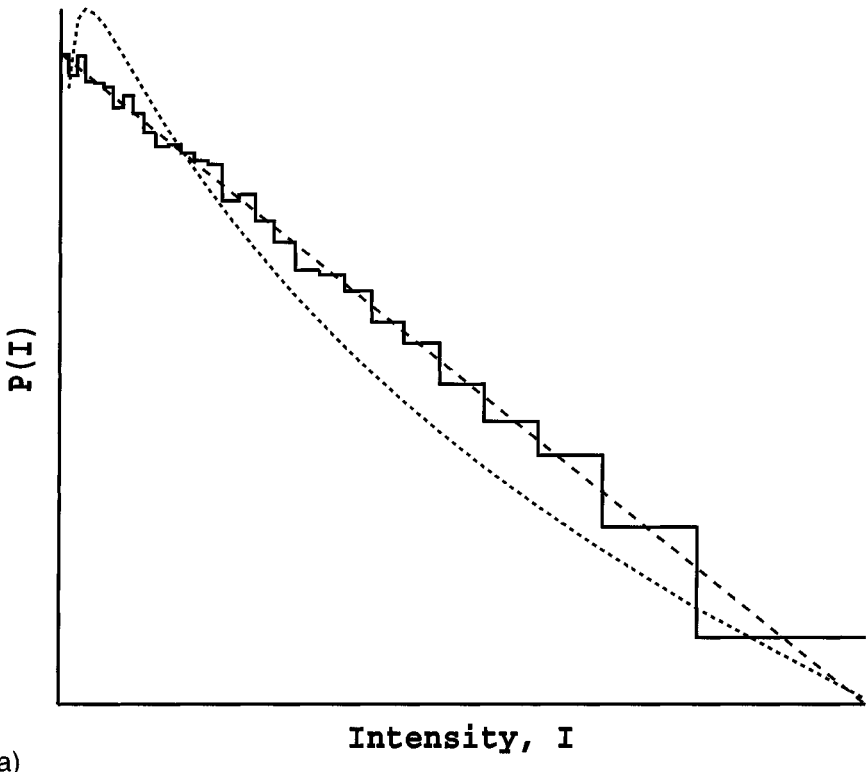


Figure 5.2 Comparison of the intensity PDF with theoretical best fits for (a) field and (b) woodland regions from Figure 5.1. Log plots of data histogram (full); theoretical PDFs for: (a) log normal (short dashes) and exponential (longer dashes); and (b) K, log normal, Weibull, and gamma (progressively increasing dash length) distributions.

The log normal predicts a probability of zero at zero intensity that conflicts with the speckle model. The Weibull PDF, on the other hand, yields an incorrectly large probability for zero intensity. The gamma distribution matches the low intensities well but predicts probabilities for large intensities that are too high.

One might therefore conclude that only the K distribution should be retained as a clutter model, with $\nu = \infty$ assumed where the statistics appear smoother than speckle fluctuations. This would be premature since, while these results are typical of natural clutter at this resolution for a C-band SAR, many other experimental comparisons have been conducted at differing wavelengths, resolutions, and polarizations. The log normal has been found to be appropriate for urban clutter [8,9] while the difference between Weibull and K PDFs is sufficiently small that slight changes in clutter properties make the Weibull

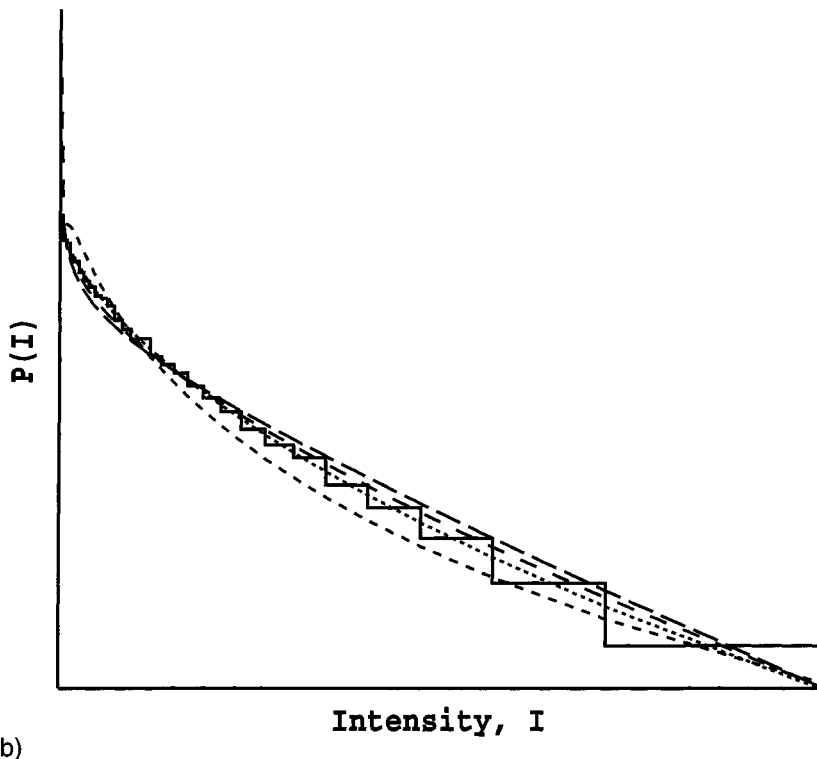


Figure 5.2 (continued).

preferable under some circumstances [5,10–13,39]. The final choice of PDF must depend on the observed statistics in the specific clutter sample. However, we shall retain the product model because of the physical insight it gives into the speckle process, together with a gamma distribution to describe any RCS fluctuations.

Table 5.1
Summary of ML Fit Parameters for Candidate Distributions and K-S Fit
Probability for the Field Region in Figure 5.1

Distribution	Parameter Values	Probability
Log normal	$\beta = 10.689; V = 1.6484$	6.8×10^{-11}
Exponential	$\mu = 78329$	0.572
Weibull	$b = 78227; c = 0.99695$	0.781
Gamma	$\mu = 78329; \nu = 0.99641$	0.683

Table 5.2

Summary of ML Fit Parameters for Candidate Distributions and K-S Fit Probability for the Woodland Region in Figure 5.1

Distribution	Parameter Values	Probability
Log normal	$\beta = 12.668; V = 2.2955$	6.6×10^{-106}
Exponential	$\mu = 737700$	0
Weibull	$b = 641430; c = 0.79237$	2.1×10^{-12}
Gamma	$\mu = 737700; \nu = 0.71488$	1.4×10^{-54}
K	$\mu = 738990; \nu = 2.0335$	1.000

Another reason for not rejecting log normal and gamma distributions for natural clutter is that they can be useful as approximations to the K distribution as sample size becomes small. Thus, in discussing texture edge detection and segmentation in later chapters, which should be applied to the smallest window size possible, analytic log normal and gamma approximations can be applied with only minor degradation, compared with using K distributions that can only be evaluated numerically.

5.6 Imaging RCS Fluctuations With Finite Resolution

In the previous section we ignored the effect of the PSF on the observed intensity; we now deal with this issue. Suppose we image a region of extended clutter, whose RCS is represented by a correlated gamma-distributed process. Following Section 4.6 and retaining a one-dimensional treatment for simplicity, the intensity image at position x , $I(x)$, arising from a scene with complex scattering amplitude, $S(\xi)$, at position ξ is given by

$$I(x) \equiv |\mathcal{E}(x)|^2 = \int_{-\infty}^{\infty} \int_{-\infty}^{\infty} d\xi_1 d\xi_2 S(\xi_1) S^*(\xi_2) b(x - \xi_1) b^*(x - \xi_2) \quad (5.17)$$

Upon taking the ensemble average over all speckle realizations, we observe that the crossterms between the scattered field at different positions average out because of the random phase of scattering elements. Hence,

$$\langle I \rangle = \int_{-\infty}^{\infty} d\xi \langle |S(\xi)|^2 \rangle |b(x - \xi)|^2 = \langle \sigma \rangle \quad (5.18)$$

where the PSF is normalized to unit energy and the ensemble average is assumed to be position-independent. In Chapter 4 we showed that the complex ACF was effectively independent of fluctuations in the RCS. The intensity ACF is given by

$$\begin{aligned} \langle I(x)I(x+X) \rangle &= \int_{-\infty}^{\infty} \int_{-\infty}^{\infty} \int_{-\infty}^{\infty} \int_{-\infty}^{\infty} d\xi_1 d\xi_2 d\xi_3 d\xi_4 \langle S(\xi_1)S^*(\xi_2)S^*(\xi_3)S(\xi_4) \rangle \\ &\times b(x - \xi_1)b^*(x - \xi_2)b^*(x + X - \xi_3)b(x + X - \xi_4) \end{aligned} \quad (5.19)$$

As before, upon taking the ensemble average, crossterms between different scatterers average to zero. The dominant nonzero terms correspond to the special cases $\xi_1 = \xi_2$, $\xi_3 = \xi_4$ and $\xi_1 = \xi_3$, $\xi_2 = \xi_4$. In addition, we note that σ is stationary with an ACF given by

$$\langle \sigma(\xi_1)\sigma(\xi_2) \rangle = \langle \sigma \rangle^2 (1 + \rho_\sigma(\xi_2 - \xi_1)/\nu) \quad (5.20)$$

for the gamma model, so (5.19) becomes

$$\begin{aligned} \langle I(x)I(x+X) \rangle &= \langle \sigma \rangle^2 \left\{ 1 + \left| \int_{-\infty}^{\infty} d\xi b(x - \xi)b^*(x + X - \xi) \right|^2 \right. \\ &+ \int_{-\infty}^{\infty} \int_{-\infty}^{\infty} d\xi_1 d\xi_2 \frac{\rho_\sigma(\xi_2 - \xi_1)}{\nu} |b(x - \xi_1)|^2 \\ &\times |b(x + X - \xi_2)|^2 \\ &+ \int_{-\infty}^{\infty} \int_{-\infty}^{\infty} d\xi_1 d\xi_2 \frac{\rho_\sigma(\xi_2 - \xi_1)}{\nu} b(x - \xi_1) \\ &\times b^*(x + X - \xi_1)b^*(x - \xi_2)b(x + X - \xi_2) \left. \right\} \end{aligned} \quad (5.21)$$

If there are no RCS fluctuations, that is, $\nu = \infty$, only the first two terms remain and (5.21) reduces to the Siegert relation [42], as in Chapter 4, with

$$\langle I(x)I(x+X) \rangle = \langle \sigma \rangle^2 (1 + |\rho(X)|^2) \quad (5.22)$$

The first two terms in (5.21) describe a constant background plus a contribution from the *coherent* imaging of individual point scatterers. The third term yields appreciable contributions for all X , when $\rho_\sigma(X) > 0$, if $\xi_1 \approx x$ and

$\xi_2 \approx x + X$. The fourth term, on the other hand, reduces to zero unless $X \approx 0$. Thus, information about the RCS correlation properties, as well as both order parameter and correlation coefficient, is contained in this third term, which is equivalent to *incoherent* imaging of RCS fluctuations; the fourth term describes *coherent* imaging. Note that the third term describes how imaging modifies the observed intensity properties from those of the RCS. Thus, the intensity resulting from imaging a correlated gamma-distributed RCS with finite resolution would not generally be K-distributed. A similar derivation can be made for the higher order moments of the intensity within a single pixel resulting in

$$\frac{\langle I^n \rangle}{\langle I \rangle^n} = \frac{\Gamma(L+n)}{L^n \Gamma(L)} \int_{-\infty}^{\infty} d\xi_1 \cdots \int_{-\infty}^{\infty} d\xi_n \left(\frac{\langle \sigma(\xi_1) \cdots \sigma(\xi_n) \rangle}{\langle \sigma \rangle^n} \right) |h(\xi_1)|^2 \cdots |h(\xi_n)|^2 \quad (5.23)$$

for L -look images. The integral over the n -point correlation function within a single pixel yields the effect of the PSF on RCS moments. If the RCS is gamma-distributed, only a rectangular PSF yields a K-distributed output, albeit with modified order parameter and correlation properties.

Equations (5.21) and (5.23) represent the effect of the PSF on the ACF and single-point statistics, respectively. Unfortunately no closed analytic form is available for the filtered PDF itself. In common with other forms of RCS, the intensity distribution can only be derived numerically, which removes one of the advantages suggested for the gamma-distribution RCS model [43].

We may use (5.21) to calculate the form of intensity ACF we would expect for the woodland region in Figure 5.1. The two-dimensional correlation coefficient for σ is assumed to be given by

$$\rho_\sigma(x, y) = \exp \left[-\frac{2|x|}{\ell_x} - \frac{2|y|}{\ell_y} \right] \quad (5.24)$$

where x and y denote lag values in azimuth and range directions, respectively, and ℓ_x and ℓ_y are the corresponding $1/e$ correlation lengths. This type of correlation property has been reported for other examples of woodland texture [24,33]. It is also consistent with the previous Markov model derivation that allowed arbitrary values of ν . In addition, the PSF is assumed, for simplicity, to have a two-dimensional Gaussian envelope defined by

$$|h(x, y)| = \exp \left[-\frac{x^2}{w_x^2} - \frac{y^2}{w_y^2} \right] \quad (5.25)$$

with $1/e$ widths of w_x and w_y in azimuth and range directions. While this is an oversimplification, it allows the required integrations to be performed more easily. Appropriate parameter values for the woodland example from Figure 5.1 were estimated from the ACFs of both complex and intensity image leading to $\ell_x = 8.0$ pixels, $\ell_y = 4.5$ pixels, $w_x = 1.36$ pixels, and $w_y = 1.13$ pixels. The predicted form for the intensity ACF was then calculated from (5.21) and is compared with measured data in Figure 5.3. Imaging averages out some of the contrast, so the order parameter for the RCS has to be selected to yield the observed ACF value at zero lag. In this case a value of 1.52 was deduced, which would yield an ACF zero-lag value of 3.32 if there were no averaging effect on imaging, rather than the value of 2.932, which was actually observed. While this comparison is only approximate and is based on oversimplistic assumptions, the consistency indicates the general validity of the product model for natural SAR clutter, based on a correlated gamma-distributed RCS.

The same set of parameters can also be used to predict higher single-point moments based on (5.23) [24]. Values for the second to fourth normalized

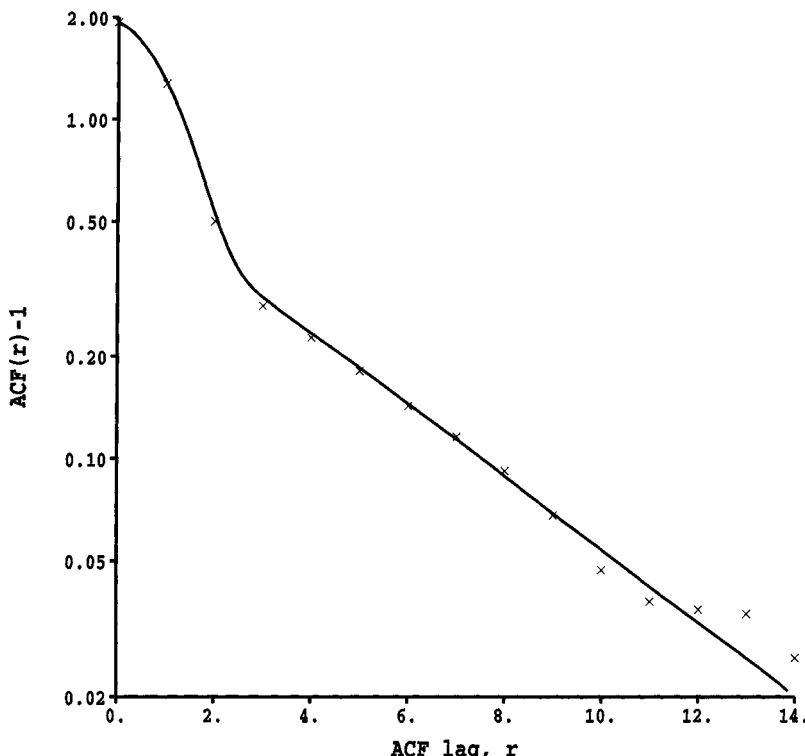


Figure 5.3 Log plot of predicted and measured normalized ACFs for the azimuthal direction of woodland texture in Figure 5.1.

Table 5.3

Comparison of Different Predicted Moments of the Woodland Intensity Distribution

Normalized Intensity Moment	Data	Equivalent Simple K	RCS (Gamma)	Intensity, Delta-Function PSF	Intensity, Gaussian PSF
2	2.932	2.932	1.658	3.32	2.92
3	16.5	17.0	3.84	23.0	17.3
4	147.0	163.0	11.5	276.0	174.0

intensity moments of the woodland texture from Figure 5.1 are shown in column 2 of Table 5.3. In column 3 we show the moments derived by assuming that the observed intensity was K-distributed, as actually indicated by the K-S test. The order parameter could then be estimated directly from the second moment, since $\langle I^2 \rangle / \langle I \rangle^2 = 2(1 + 1/\nu)$, using (5.14), leading to an effective value of 2.15. RCS moments, consistent with the predicted ACF for a correlated RCS in Figure 5.4, are listed in column 4. If these fluctuations were imaged by a system that has a delta-function PSF so that there was no averaging, the expected intensity moments would have the form of column 5. The results in column 6 were obtained using (5.25) to derive the averaged intensity moments after imaging. Comparing columns 5 and 6 it is apparent that the imaging process has reduced the moments as expected, yielding results that are reasonably consistent with the data.

The success of the correlated gamma-distributed RCS model in predicting both the ACF and single-point moments of the image intensity demonstrates that the model provides a valid representation of these samples of natural clutter. A similar approach has been applied to a variety of radar clutter samples [24,33,37], yielding similar consistency between prediction and data. This consideration of the effect of the imaging process demonstrates that it is not sufficient to provide arbitrary parameterized fits of a K distribution to measured single-point statistics. The interaction between the RCS fluctuations and the PSF must be properly estimated. Only this approach can predict the properties of the image of a given scene as the system PSF is changed.

5.7 Limitations of the Data Model

The correlated K-distributed data model is intended to describe extended areas of homogeneous clutter textures, which can be regarded as single realizations of

stationary noise processes. Thus, it was tested against the homogeneous samples identified in Figure 5.1. Of course, the model contains no information about the location of the boundaries of particular textures; this could be provided by independent structural information derived, for example, from a map. Image interpretation based on this model uses spatial average properties, measured over some local neighborhood, to define image properties. While this is appropriate inside extended clutter areas, averaging across boundaries mixes the properties in the overlap region, which is obviously undesirable. We shall demonstrate in Chapters 8 and 9 how detecting texture anomalies can be used to estimate the position of such boundaries.

Despite the success of this correlated noise model, it is important to identify its limitations. The first arises from the fact that there is a large number of individual features in SAR images that cannot be described in terms of homogeneous texture at all. Hedges, isolated trees, and farm buildings, with associated shadows, are best represented as deterministic structures recording the position and cross section of individual objects within the scene, that is, as in a map. In a military context, isolated objects such as vehicles and bridges clearly belong in the same category. These may require a totally deterministic solution that models the full physics of the scattering process. For example, deterministic images of dielectric objects, such as houses, can be simulated based on physical optics combined with the Geometrical Theory of Diffraction [44,45]. While this represents a solution of the Forward Problem, it is not clear to what extent it is useful in image interpretation. Identifying suitable techniques for extracting information about man-made objects against an extended clutter background represents a combination of textural and deterministic properties. We shall provide some discussion of target detection and classification in Chapter 10.

The second limitation emerges when nominally homogeneous regions are analyzed in more detail, particularly as the resolution is increased. For five of the selected regions in Figure 5.4 the probability of being K-distributed is very small ($<10^{-7}$) [46]; only the top region is consistent with a K distribution. Detailed study of the individual textures suggests that, though they appear homogeneous, they contain more than one component. Upon fitting the PDF to a combination of two K distributions, described by five parameters instead of two, the average probability rose to 81% over all samples. Of course, additional degrees of freedom would be expected to improve the fit; nevertheless, this improvement seems significant. These textures were actually represented equally well by a two-component log normal mixture. This differs from the results for the woodland texture in Figure 5.1, where the single-component log normal was markedly poorer. Increasing the number of degrees of freedom tends to make the form of the PDF less critical. This result establishes that a mixture of processes

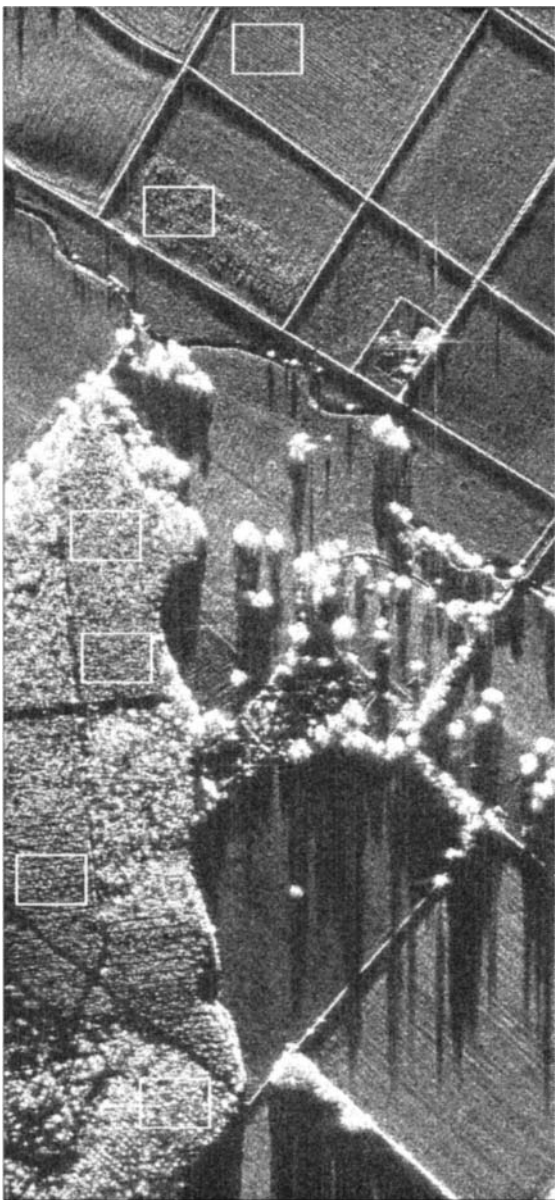


Figure 5.4 High-resolution (< 1m) DRA X-band SAR image.

may be required to describe high-resolution natural SAR clutter where the single-component K distribution model fails.

This demonstrates the importance of representing different populations within a scene individually. While each may be individually K-distributed, their combination may not be. A similar effect has been observed with real aperture radar sea clutter [36]. At grazing incidence the HH polarized return from sea swell is dominated by the phenomenon of sea spikes, so the swell is hardly visible [47–49]. It proves impossible to represent both the ACF and single-point statistics of this process successfully with a single K-distributed correlated component. However, introducing separate components to represent swell and spikes enables both the predicted moments and ACF to be fitted to the data [36]. The sea spikes are represented by a process with a short correlation length, whereas the swell corresponds to a periodic process of longer correlation length. Adopting a physically based description of the process then allows the effect of changed instrument resolution, for example, to be predicted, as discussed in Section 5.6.

5.8 Simulation

An important way to demonstrate that the properties of SAR images are well understood is to simulate them based on the models available. A human observer is often capable of observing differences that tests based on specific models would not detect and so assessing the validity of the model. Furthermore, once a model has been validated, simulation can be used to generate large quantities of statistically identical examples with which to develop and test image-interpretation algorithms. Finally, both structural and textural information could be combined in a SAR simulator that could be used for training both human observers and automatic algorithms. The scene would then be regarded as consisting of regions of homogeneous texture. The edges of these regions might either be defined by structural features, such as known boundaries, or arise from small changes in parameter values. Isolated objects would require a more deterministic approach. In this section we confine our attention to the simulation of homogeneous textures with the required properties.

A set of simulated textures is compared with an original SAR image of a young plantation made up of rows of trees in Figure 5.5, where the original SAR texture is the second from the left. The simulation technique is designed to reproduce the mean and ACF of the original sample. Both the RCS and speckle in each simulation are different realizations with identical parameters. It is difficult to discriminate between the four examples either visually or using statistical tests [33]. Simulation generates a texture in which the underlying

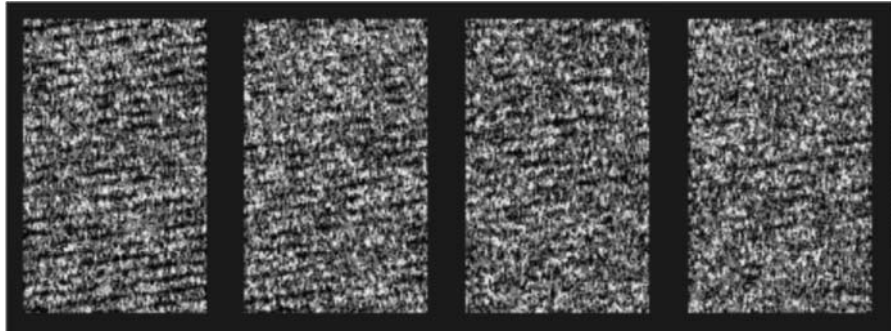


Figure 5.5 Comparison of measured SAR texture from a plantation of young trees (second from left) with three example simulations. Single-look image, 3-m resolution.

positions of bright features, assumed to correspond to trees in the original image, vary randomly. The speckle also varies randomly, so each realization represents a scene that has identical statistics but different detailed structure.

Since the product model describes a SAR image as the result of applying a defined imaging filter to an unknown RCS, it seems intuitively reasonable to design simulation methods to mirror these different processes, though this is not essential [50,51]. Simulation then comprises two stages. In the first a correlated gamma-distributed RCS variable is generated. The second stage, corresponding to introducing speckle in the imaging process, is readily achieved by generating a pair of independent zero-mean Gaussian-distributed samples to represent real and imaginary components, \mathcal{E}_r and \mathcal{E}_i , of a complex image. The variance of the Gaussian random number generator is defined by $\langle \mathcal{E}_r^2(j) \rangle \equiv \langle \mathcal{E}_i^2(j) \rangle \equiv \sigma_j / 2$, where σ_j represents the simulated RCS of the j th pixel. Passing the complex image through a filter defined by the PSF introduces the correct correlated speckle into the final intensity image.

Three different approaches have been proposed for simulating correlated gamma-distributed noise to represent the RCS:

- Filtering uncorrelated gamma-distributed noise;
- Applying the random walk model;
- Resampling methods.

The sample shown in Figure 5.5 is actually derived by an approximate linear filter method [21] in which uncorrelated gamma-distributed noise is convolved with a weighting function designed to reproduce the desired correlation properties in the output. Though this method reproduces the two-point statistics precisely, it fails to reproduce the single-point PDF and higher order statistics and has moments that can be expressed in terms of the original uncorrelated gamma

distribution and the moments of the filter. Only where the weight is rectangular is the output gamma-distributed. This problem can be overcome by representing the desired filter weight as the sum of rectangular components [52,53]. Each component then yields gamma-distributed noise with a triangular autocorrelation function. The combination is gamma-distributed with the desired ACF. However, this approach is limited because of the difficulty of representing arbitrary desired ACFs in terms of sums of rectangular components.

The random walk model, introduced in Section 5.4.2, has the advantage that all the higher order statistical properties of the output can be expressed in terms of the two-point statistics [23]. However, it is only strictly applicable to half-integer values of order parameter and so is of little value for reproducing arbitrary textures.

Resampling from correlated variables that have either exponential or Gaussian distributions forms the basis of the third category of simulation methods. Correlated exponentially distributed random variables can be generated by taking the sum of the squares of two correlated Gaussian random numbers. If the correlation coefficient for the Gaussian process is ρ_G , then that for the exponential variable is given by $\rho_e = |\rho_G|^2$. Thus, only the modulus of the correlation coefficient of the Gaussian process can be derived for a specified negative exponential correlation coefficient. However, this information is all that is required because (5.10) shows that the joint probability for two correlated gamma-distributed samples depends only on the modulus. Armstrong and Griffiths [25] showed that the appropriate resampling scheme to convert a negative-exponential variable y to a gamma variate σ is to invert the expression

$$\gamma(\nu, \sigma) = \Gamma(\nu) \left(1 - \exp \left[-\frac{\nu y}{\mu} \right] \right) \quad (5.26)$$

where $\gamma(\cdot)$ is the incomplete gamma function (Section 6.5 in [26]). The correlation coefficient for the gamma-distributed output ρ_σ , which represents the desired cross section, can be related to that for the negative-exponential input ρ_y by [25]

$$\rho_\sigma = \frac{\langle \sigma_1 \sigma_2 \rangle - \langle \sigma \rangle^2}{\langle \sigma^2 \rangle - \langle \sigma \rangle^2} = \nu \left\{ \left(1 + \rho_y \right)^{\nu+2} {}_2F_1 \left[1 + \nu, 1 + \nu; \nu; \rho_y \right] - 1 \right\} \quad (5.27)$$

where $\langle \sigma_1 \sigma_2 \rangle$ is the ACF of σ for pixels 1 and 2. The modulus of the correlation coefficient of the corresponding Gaussian process $|\rho_G|$, can now be derived from ρ_y . Problems can be encountered in performing the numerical inversions from (5.26) and (5.27), which involve extensive computation. More significantly, the

square root of an arbitrary correlation function is not necessarily itself a valid correlation function (e.g., if ρ_y were triangular).

A limitation of all methods that are based on resampling or filtering negative exponential or gamma processes is that, since both the input and the output must be positive, the correlation coefficients or filter weights must also be positive. This restricts realizable ACFs to those for which $\langle \sigma_1 \sigma_2 \rangle \geq \langle \sigma \rangle^2$, so only positive correlation coefficients can be produced. This inability to reproduce anticorrelations may be significant in attempting to simulate effects such as shadowing, as illustrated in Figure 5.6, which shows a comparison of simulated textures with part of an original SAR image of a mature woodland known to contain well-separated large trees (on the right). A visual inspection reveals that the original texture shows more evidence of dark blobs, presumably associated with shadowing, than the three simulations. Shadows would be expected to correspond to anticorrelations that could be produced by the Gaussian resampling method described next.

Sechtin et al. [54] simulated correlated gamma noise by resampling correlated Gaussian random noise onto a rectangular PDF using the error function. These correlated samples were then mapped onto a gamma PDF using the inverse gamma *cumulative distribution function* (CDF), yielding correlated gamma-distributed random numbers. Both stages involved nonlinear transformations with attendant numerical difficulty. Tough and Ward [55] proposed a similar scheme except that they resampled the correlated Gaussian process directly onto a gamma distribution. Since this comprises only a single nonlinear transformation, it is inherently less numerically complicated. The mapping is defined by equating the CDFs of input and output variables. Thus, for a Gaussian (y_0) to gamma (σ_0) transformation, the mapping is defined by equating random numbers at the same cumulative value. Hence

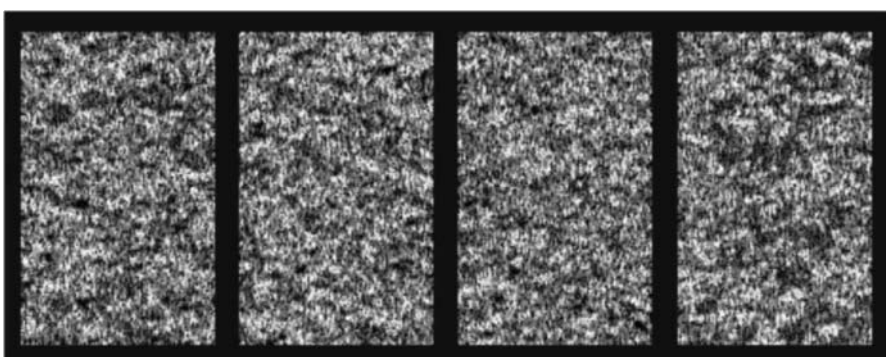


Figure 5.6 Comparison of measured SAR texture from mature woodland (on right) with three sample simulations. Single-look image, 3-m resolution.

$$\frac{1}{\sqrt{2\pi}} \int_{-\infty}^{y_0} \exp\left[-\frac{y^2}{2}\right] dy \equiv \int_0^{\sigma_0} \nu^\nu \frac{\sigma^{\nu-1}}{\Gamma(\nu)} \exp[-\nu\sigma] d\sigma \quad (5.28)$$

This defines both $F(\sigma_0)$, the forward mapping function for $y_0 \rightarrow \sigma_0$, and its inverse $F^{-1}(y_0)$, describing the inversion $y_0 \leftarrow \sigma_0$. In principle, there are no restrictions on the range of order parameter values that can be achieved with this method, although the numerical inversion process has to be handled carefully.

The relationship between the desired correlation coefficient for the gamma-distributed variable ρ_σ , and that for the underlying Gaussian process ρ_y , can then be derived from the single- and two-point moments of σ , defined by

$$\langle \sigma^n \rangle = \int_{-\infty}^{\infty} dy (F^{-1}(y))^n P(y) \quad (5.29)$$

where

$$P(y) = \frac{1}{\sqrt{2\pi}} \exp\left[-\frac{y^2}{2}\right] \quad (5.30)$$

and

$$\langle \sigma_1 \sigma_2 \rangle = \int_{-\infty}^{\infty} \int_{-\infty}^{\infty} dy_1 dy_2 F^{-1}(y_1) F^{-1}(y_2) P(y_1, y_2) \quad (5.31)$$

where

$$P(y_1, y_2) = \frac{1}{2\pi\sqrt{(1 - \rho_y^2)}} \exp\left[-\frac{y_1^2 - 2\rho_y y_1 y_2 + y_2^2}{2(1 - \rho_y^2)}\right] \quad (5.32)$$

The inverse mapping $F^{-1}(y)$ can be solved numerically from (5.28). Hence, the correlation coefficient for the correlated gamma variable, defined in (5.27) can be evaluated from (5.29) to (5.32). This allows the underlying Gaussian correlation coefficients at all lag values to be defined from the desired gamma values. However, this correlation function may again not be valid, so an approximate version that is close to the required form has to be derived. The desired filter amplitude spectrum then corresponds to the square root of the FT of this correlation function.

The simulated correlated K-distributed image is then generated as follows:

1. An image consisting of uncorrelated *Gaussian random variables* (GRV) is formed.
2. Correlated GRVs are generated by multiplying the FT of the uncorrelated data by the filter spectrum and taking the inverse FT.
3. Each correlated GRV is resampled to correlated gamma pixel values using the numerical mapping $F^{-1}(y)$ in (5.28).
4. Speckle is incorporated as described earlier in the section.

In the previous exponential resampling transformations, the output was obtained from the product of a *correlated* gamma variable with an *uncorrelated* speckle contribution. However, simulating correlated exponential variables is generally easier than gamma-distributed variables. Indeed, deriving correlated exponential variables is sometimes a step in the previous methods. An equivalent K-distributed correlated output to represent single-look intensity could be obtained by adopting a new *uncorrelated* gamma variable x , and introducing a new *correlated* negative exponential term z , such that $I = xz$ [50]. Alternatively, I could be represented as the product of an *uncorrelated* beta-distributed variable b , and two *correlated* exponential variables z_1 and z_2 , so that $I = bz_1z_2$ [51]. Both these methods require the derivation of the underlying Gaussian correlation properties previously described. Both fail to model anticorrelations, and both can only be applied to a restricted range of order parameters. Thus, they are generally not as useful as the Gaussian resampling transformation.

The simulation methods described here are designed to reproduce the single-point statistics and the ACF of the original sample texture. This has two important consequences:

- The higher order correlation properties are not specified and so will vary between methods.
- The methods cannot reproduce the directional effect of shadowing because this is not represented in the ACF.

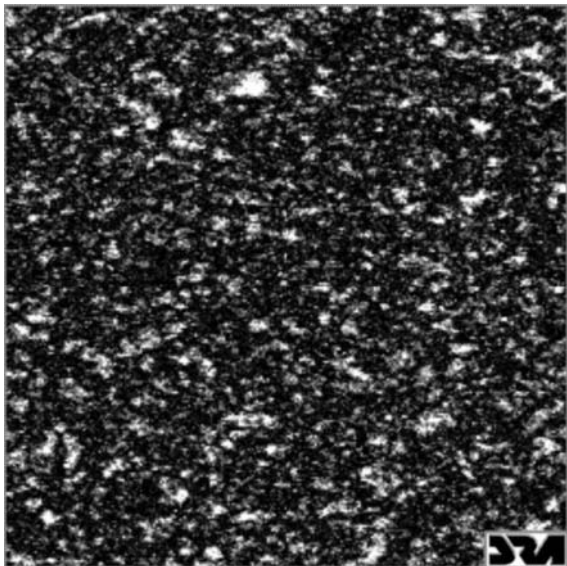
Differences in higher order correlation properties, resulting from the choice of simulation technique, can cause visible differences in the resulting texture [55]. In the random walk simulation method all higher order correlation properties can be expressed in terms of the two-point statistics. This is not true of any other method, so the higher order properties will be determined by the simulation technique. In Figure 5.7 we compare examples of simulated textures with identical gamma PDFs ($\nu = 0.5$) and ACFs (negative exponential). Figure 5.7(a) is the

result of applying the random walk simulation; Figure 5.7(b) corresponds to the Gaussian resampling transformation. A negative exponential PDF ensures an exact filter function, so no approximations are introduced in the resampling method. Though the defined quantities are identical, higher order correlations differ for the two techniques. A visual comparison reveals that Figure 5.7(b) appears to reconstruct distinctive large dark regions that are not visible in Figure 5.7(a). A study of the bivariate histogram reveals differences in the symmetry properties of the two simulations [56]. Thus, the human observer is able to discriminate between simulated textures that have the same PDF and ACF but differing higher order properties. Measurements based on appropriate higher order statistics reveal that tests can be devised to perform this task automatically. Simulation based on a data model is thus capable of revealing inadequacies in that model to the human observer. Establishing which particular high-order moment conveys the appropriate information is more difficult. However, in principle, this could be established and a corresponding constraint built into the clutter model and associated simulation.

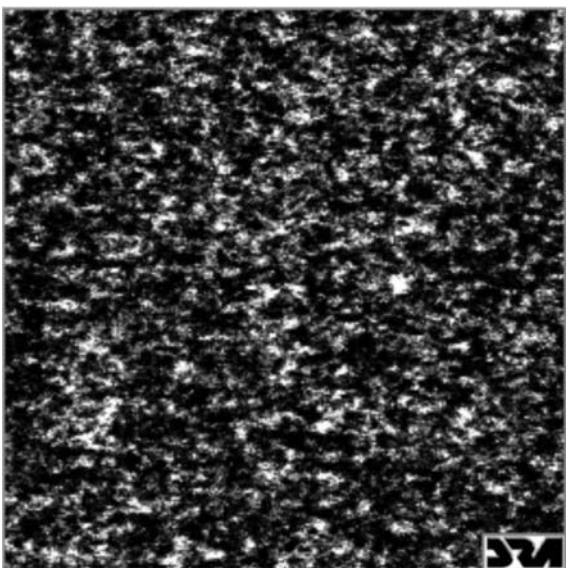
In order to overcome the failure to reproduce directional shadowing, a more deterministic approach to simulating woodland can be used that includes a defined radar direction and probabilistic representation of tree position and size [57]. Figure 5.8 contains a comparison of observed C-band SAR woodland clutter, in Figure 5.8(a), with an example of simulated texture based on a simple deterministic model [58]. Trees with varying sizes and separations make up the simulated scene. The tree crowns intersect to form a canopy that is discretized into facets, each of which is assigned a backscatter coefficient using the mean field/discrete scatterer model. The effects of shadowing for radar illumination at the specified angle of incidence are also introduced. This yields an effective RCS for which simulated imaging is calculated as described earlier. Both simulated and real data yield a probability of 1.0 of being K-distributed when a K-S test is applied. The order parameters of the two textures are 3.58 (real) and 3.70 (simulated). Since no attempt was made to match the properties of the original data precisely, the agreement is striking. In particular, the deterministic modeling of shadowing has overcome the disadvantages of the noise-based simulation in Figure 5.6.

5.9 Conclusions

In this chapter we introduced a correlated K-distributed noise model that seems to represent natural clutter well. The discussion of simulation in Section 5.8 reveals that this model is capable of representing both the single-point statistics and ACF of SAR texture correctly. However, the important physical property of

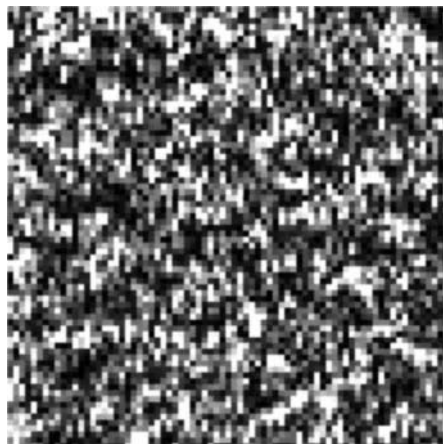


(a)

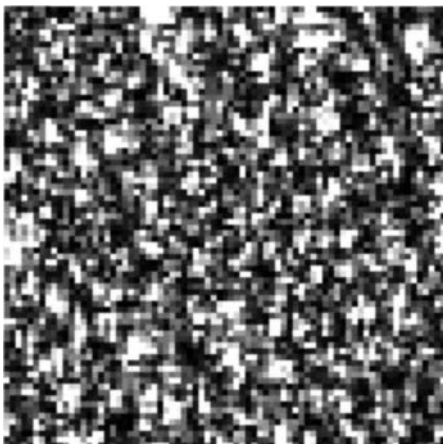


(b)

Figure 5.7 Comparison of different simulation techniques for correlated gamma-distributed noise ($\nu = 0.5$): (a) random walk model and (b) Gaussian resampling transformation.



(a)



(b)

Figure 5.8 Comparison of a sample of (a) C-band SAR woodland clutter with (b) simple deterministic simulation. Resolution 1.5m by 1.5m, single-look.

shadowing is not contained within the ACF and cannot be represented by these noise models. Image interpretation based on texture, described in Chapters 8 and 9, is based on the same model and similarly fails to take account of shadowing. While many important remote sensing properties, such as tree size and spacing, will be contained in the ACF, this cannot represent the optimum description. However, we will demonstrate that much useful information can be extracted even with an incomplete model.

References

- [1] Press, W. H., S. A. Teukolsky, W. T. Vetterling, and B. P. Flannery, *Numerical Recipes in C*, Cambridge, UK: Cambridge University Press, 1994.
- [2] Trunk, G. V., "Radar Properties of Non-Rayleigh Sea Echo," *IEEE Trans.*, Vol. AS-8, 1972, pp. 196–204.
- [3] Trunk, G. V., and S. F. George, "Detection of Targets in Non-Gaussian Sea Clutter," *IEEE Trans.*, Vol. AES-6, 1970, pp. 620–628.
- [4] Schleher, D. C., "Radar Detection in Log Normal Clutter," *Proc. IEEE Int. Radar Conf. Radar '75*, 1975, pp. 262–267.
- [5] Schleher, D. C., "Radar Detection in Weibull Clutter," *IEEE Trans.*, Vol. AES-12, 1976, pp. 736–743.
- [6] Fay, F. A., J. Clarke, and R. S. Peters, "Weibull Distribution Applied to Sea Clutter," *Int. Conf. Radar '77*, IEE Conf. Pub. No. 155, London: IEE, 1977, pp. 101–104.
- [7] Sekine, M., T. Musha, Y. Tomita, T. Hagisawa, T. Irabu, and E. Kiuchi, "Weibull-Distributed Sea Clutter," *IEE Proc. F*, Vol. 130, 1983, p. 476.
- [8] Valenzuela, G. R., and M. B. Laing, "Point-Scatterer Formulation of Terrain Clutter Statistics," Naval Research Laboratory Report 7459, Washington DC, 1972.
- [9] Warden, M. P., "An Experimental Study of Some Clutter Characteristics," *AGARD Conf. Proc. on Advanced Radar Systems*, No. 66, 1970.
- [10] Booth, R., "The Weibull Distribution Applied to the Ground Clutter Backscatter Coefficient," U.S. Army Missile Command, Tech. Report RE-TR-69-15, ASTIA Doc. AD 691109, 1969.
- [11] Sekine, M., S. Ohtani, T. Musha, T. Irabu, E. Kiuchi, T. Hagisawa, and Y. Tomita, "Weibull-Distributed Ground Clutter," *IEEE Trans.*, Vol. AES-17, 1981, pp. 596–598.
- [12] Sekine, M., T. Musha, Y. Tomita, T. Hagisawa, T. Irabu, and E. Kiuchi, "On Weibull-Distributed Weather Clutter," *IEEE Trans.*, Vol. AES-15, 1979, pp. 824–830.
- [13] Ogawa, H., M. Sekine, T. Musha, M. Aota, M. Ohi, and H. Fukushi, "Weibull-Distributed Radar Clutter Reflected from Sea Ice," *Trans. IEICE Japan*, Vol. E70, 1987, pp. 116–120.
- [14] Ward, K. D., "Compound Representation of High Resolution Sea Clutter," *Electron. Lett.*, Vol. 17, 1981, pp. 561–565.
- [15] Ward, K. D., "A Radar Sea Clutter Model and Its Application to Performance Assessment," *Int. Conf. Radar '82*, IEE Conf. Pub. 216, London: IEE, 1982, pp. 203–207.
- [16] Jakeman, E., and P. N. Pusey, "A Model for Non-Rayleigh Sea Echo," *IEEE Trans. Antennas Propagation*, Vol. 24, 1976, pp. 806–814.
- [17] Jakeman, E., "Statistics of Integrated Gamma-Lorentzian Intensity Fluctuations," *Opt. Acta*, Vol. 27, 1980, pp. 735–741.
- [18] Jakeman, E., and P. N. Pusey, "Statistics of Non-Rayleigh Microwave Sea Echo," *Int. Conf. Radar '77*, IEE Conf. Pub. 155, London: IEE, 1977, pp. 105–109.
- [19] Jakeman, E., and P. N. Pusey, "Significance of K Distributions in Scattering Experiments," *Phys. Rev. Lett.*, Vol. 40, 1978, pp. 546–550.

- [20] Jakeman, E., "On the Statistics of K-Distributed Noise," *J. Phys. A: Math. Gen.*, Vol. 8, 1980, pp. 31–48.
- [21] Oliver, C. J., and R. J. A. Tough, "On the Simulation of Correlated K-Distributed Random Clutter," *Opt. Acta*, Vol. 33, 1986, pp. 223–250.
- [22] Oliver, C. J., "A Model for Non-Rayleigh Scattering Statistics," *Opt. Acta*, Vol. 31, 1984, pp. 701–722.
- [23] Oliver, C. J., "Correlated K-Distributed Clutter Models," *Opt. Acta*, Vol. 32, 1985, pp. 1515–1547.
- [24] Oliver, C. J., "The Interpretation and Simulation of Clutter Textures in Coherent Images," *Inu. Problems*, Vol. 2, 1986, pp. 481–518.
- [25] Armstrong, B. C., and H. D. Griffiths, "Modelling Spatially Correlated K-Distributed Clutter," *Electron. Lett.*, Vol. 27, 1991, pp. 1355–1356.
- [26] Abramowitz, M., and I. A. Stegun, *Handbook of Mathematical Functions*, New York: Dover, 1970.
- [27] Oliver, C. J., "Optimum Texture Estimators for SAR Clutter," *J. Phys. D: Appl. Phys.*, Vol. 26, 1993, pp. 1824–1835.
- [28] Jakeman, E., and P. N. Pusey, "Non-Gaussian Fluctuations in Electromagnetic Radiation Scattered by a Random Phase Screen," *J. Phys. A: Math. Gen.*, Vol. 8, 1975, pp. 369–410.
- [29] Jakeman, E., E. R. Pike, and P. N. Pusey, "Photon Correlation Study of Stellar Scintillation," *Nature*, Vol. 263, 1976, pp. 215–217.
- [30] Parry, G., P. N. Pusey, E. Jakeman, and J. McWhirter, "Focusing by a Random Phase Screen," *Opt. Comm.*, Vol. 22, 1977, pp. 195–201.
- [31] Fante, R. L., "Detection of Multiscatter Targets in K-Distributed Clutter," *IEEE Trans. Antennas Propagation*, Vol. 32, 1984, pp. 1358–1363.
- [32] Jao, J. K., "Amplitude Distribution of Composite Terrain Radar Clutter and the K-Distribution," *IEEE Trans. Antennas Propagation*, Vol. 32, 1984, pp. 1049–1062.
- [33] Oliver, C. J., "Representation of Correlated Clutter in Coherent Images," *Inu. Problems*, Vol. 4, 1988, pp. 843–866.
- [34] Sekine, M., T. Musha, Y. Tomita, T. Hagisawa, T. Irabu, and E. Kiuchi, "Log Weibull Distributed Sea Clutter," *IEE Proc. F*, Vol. 127, 1980, pp. 225–228.
- [35] Watts, S., and K. D. Ward, "Spatial Correlation in K-Distributed Sea Clutter," *IEE Proc. F*, Vol. 134, 1987, pp. 526–532.
- [36] Oliver, C. J., "Representation of Radar Sea Clutter," *IEE Proc. F*, Vol. 135, 1988, pp. 497–500.
- [37] Oliver, C. J., Review Article "Information from SAR Images," *J. Phys. D: Appl. Phys.*, Vol. 24, 1991, pp. 1493–1514.
- [38] Yueh, S. H., J. A. Kong, J. K. Jao, R. T. Shin, and L. M. Novak, "K Distribution and Polarimetric Terrain Clutter," *J. Electromagnetic Waves and Appl.*, Vol. 3, 1989, pp. 747–768.
- [39] Kreithen, D. E., S. M. Crooks, W. W. Irving, and S. D. Halversen, "Estimation and Detection Using the Product Model," MIT-Lincoln Lab. Report No. STD-37, 1991.
- [40] Watts, S., "Radar Detection Prediction in K-Distributed Sea Clutter and Thermal Noise," *IEEE Trans. AES*, Vol. 23, 1987, pp. 40–45.

- [41] Lombardo, P., C. J. Oliver, and R. J. A. Tough, "Effect of Noise on Order Parameter Estimation for K-Distributed Clutter," *IEE Proc. Radar Sonar Navig.*, Vol. 142, 1995, pp. 33–40.
- [42] Siegert, A. J. F., MIT Rad. Lab. Report No. 465, 1943.
- [43] Buccarelli, T., P. Lombardo, C. J. Oliver, and M. Perrotta, "A Compound Weibull Model for SAR Clutter Analysis," *Proc. IGARSS '95*, Florence, Italy, 1995, pp. 181–183.
- [44] Tajbakhsh, S., M.-J. Kim, H. M. Berenyi, and R. E. Burge, "Applications of an Extended GTD Model to Synthetic Aperture Radar Simulation," *Europto Conf. on SAR Data Processing for Remote Sensing*, Rome, *SPIE Proc.*, Vol. 2316, 1994, pp. 202–215.
- [45] Tajbakhsh, S., M.-J. Kim, H. M. Berenyi, and R. E. Burge, "Images of Urban Areas by a Synthetic Aperture Radar Simulator," *Europto Conf. on SAR Data Processing for Remote Sensing*, Rome, *SPIE Proc.*, Vol. 2316, 1994, pp. 290–295.
- [46] Blake, A. P., D. Blacknell, and C. J. Oliver, "High Resolution SAR Clutter Textural Analysis and Simulation," *Europto Conf. on Synthetic Aperture Radar and Passive Microwave Sensing*, Paris, *SPIE Proc.*, Vol. 2584, 1995, pp. 101–109.
- [47] Long, M. W., *Radar Reflectivity of Land and Sea*, Lexington, MA: Lexington Books, D. C. Heath and Co., 1975, pp. 77–89.
- [48] Lewis, B. L., and I. D. Olin, "Some Recent Observations of Sea Spikes," *Int. Conf. Radar '77*, IEE Conf. Pub. 155, London: IEE, 1977, pp. 115–119.
- [49] Lewis, B. L., and I. D. Olin, "Experimental Study and Theoretical Model of High Resolution Radar Backscatter from the Sea," *Radio Sci.*, Vol. 15, 1980, pp. 815–828.
- [50] Blacknell, D., A. P. Blake, P. Lombardo, and C. J. Oliver, "A Comparison of Simulation Techniques for Correlated Gamma and K-Distributed Images for SAR Applications," *Proc. IGARSS-94*, Pasadena, CA, 1994, pp. 2182–2184.
- [51] Conte, E., M. Di Biceglie, and C. Galdi, "Modelling and Simulation of Bidimensional Processes for Remote Sensing Applications," *Proc. IGARSS-93*, IEE, 1993, pp. 1993–1995.
- [52] Ronning, G., "A Simple Scheme for Generating Multivariate Gamma Distributions with Non-Negative Covariance Matrix," *Technometrics*, Vol. 19, 1977, pp. 179–183.
- [53] Blacknell, D., "A New Method for the Simulation of K-Distributed Clutter," *IEE Proc. Radar Sonar Navig.*, Vol. 141, 1994, pp. 53–58.
- [54] Sechtin, M. B., L. M. Novak, and M. C. Burl, "Algorithms for Optimal Processing of Polarimetric Radar Data," Project Report TT-73, MIT-Lincoln Lab., 1989.
- [55] Tough, R. J. A., and K. D. Ward, "The Generation of Correlated K-Distributed Noise," DRA Technical Report DRA/CIS/CBC3/WP94001/2.0, 1994, DRA Malvern, St. Andrews Road, Malvern, Worcs.
- [56] Blake, A. P., D. Blacknell, and C. J. Oliver, "Texture Simulation and Analysis in Coherent Imagery," *5th Int. Conf. on Image Processing and Its Applications*, IEE Conf. Publ. 410, London: IEE, 1995, pp. 772–776.
- [57] Garside, J. R., and C. J. Oliver, "Models for Natural Clutter in Coherent Imaging," *SPIE Conf. on Image Processing III*, SPIE, Vol. 1135, 1989, pp. 48–55.
- [58] Williams, M., "Influence of Canopy Shape on SAR Speckle Distributions over Woodland," *IGARSS '97*, Singapore, 1997, pp. 755–757.

6

RCS Reconstruction Filters

6.1 Introduction

The product model for SAR clutter, introduced in Chapters 4 and 5, postulated that the observed intensity in single-channel images comprises an underlying RCS on which speckle is imposed. This speckling process defines the conditional probability of observing an intensity I from RCS σ , which characterizes the Forward Problem. This chapter is concerned with the Inverse Problem of deriving the RCS, given the observed intensity in the image. Even though speckle properties are well understood, the ambiguity introduced by speckle means that there is no unique inversion from I to σ . However, by interpreting data in terms of a series of increasingly sophisticated models, we can produce image reconstructions of continually improving quality.

This chapter is concerned with the development of filters to provide a reconstruction of RCS. Initially, in Section 6.2, we examine the implications of the *speckle model* for reconstructed image quality. In Section 6.3 Bayesian inference is introduced, which provides the basis of most of the filters described. Section 6.4 exploits the speckle model alone, with no information about RCS. Once this model has been exhausted, we introduce and exploit a series of further models, commencing with a *data model* to describe single-point RCS statistics (Section 6.5), followed by *world models* describing scene properties, namely, neighborhood correlation (Section 6.6) and image structure (Section 6.7). Each improves the quality of the despeckled image. Most of these algorithms are adaptive linear processes. However, we demonstrate in Section 6.8 that non-linear iterative processes are capable of offering still further improvement in

image quality. We next apply the concept of a *structure model* in an iterative scheme, analogous to simulated annealing, in Section 6.9.

In passing, it should be noted that a variety of other filters have been proposed for smoothing speckle while retaining strong RCS fluctuations, such as the median [1,2] and sigma [3] filters. While these schemes have desirable aspects, such as computational simplicity, they fail to include the specific properties of SAR speckle. In consequence, they do not perform well enough in practice to aid image interpretation significantly.

Though the data models in Chapter 5 were developed for comparatively high-resolution SAR imagery, many potential applications require algorithms capable of operating on lower resolution (such as satellite) imagery. In principle, there is no reason why image-interpretation methods should depend on resolution; algorithms should be controlled simply by underlying theory and the data themselves. Many algorithm properties, however, will be most evident with high-resolution imagery, and developments in this chapter will primarily be illustrated with the example of 3-m resolution, 2-look DRA X-band airborne SAR imagery shown in Figure 6.1.

A “good” reconstruction filter demonstrates the following properties:

- Speckle reduction in extended uniform regions;
- Feature preservation;



Figure 6.1 DRA X-band airborne SAR image of a rural scene: 3-m resolution, 2-look.

- Absence of artifacts;
- Radiometric preservation.

The first three properties can be observed visually; the last is better verified numerically, as described in Section 6.2. Visual inspection can be used to examine the effectiveness of candidate reconstruction filters in the following manner:

- Speckle reduction in uniform clutter regions should lead to smooth reconstructions without bright or dark flecks where speckle has not been correctly identified by the algorithm.
- Feature preservation, or its lack, is most apparent for small objects. In particular, we shall concentrate on the four weak objects in the dark field near the bottom left of Figure 6.1. Note that these are merely targets of opportunity that are visible in the scene. There is no ground truth confirming their existence or describing their properties. Features such as the hedges between fields provide less stringent visual tests for the algorithms.
- It will be demonstrated that some filters introduce unacceptable artifacts into their reconstruction.

Different applications impose differing penalties if any of these quality issues are violated, so algorithm selection will always be driven by the specific application. Here we shall attempt to identify algorithms that optimize all aspects as far as possible and reject those that obviously fail in some manner.

6.2 The Speckle Model and Quality Measures

In this section we introduce a quantitative image quality measure that includes all the aspects of reconstruction quality discussed earlier. The approach involving the fewest assumptions is to omit any prior knowledge about RCS in the product model and describe the observed intensity in terms of the speckle model alone, as discussed in Chapters 4 and 5. A SAR image can then be thought of as comprised of some variable, corresponding to local RCS, that is combined with speckle to yield the observed intensity at each pixel.

Throughout this chapter we treat speckle in a single image as a multiplicative process, as introduced in Chapter 4, so that the intensity is given by $I =$

σn where n is the speckle contribution. Some useful moments of I for L -look SAR include

$$\langle I \rangle = \langle \sigma \rangle \langle n \rangle \quad \langle I^2 \rangle = \langle \sigma^2 \rangle \langle n^2 \rangle \quad \langle n \rangle \equiv 1 \quad \langle n^2 \rangle = 1 + 1/L$$

and

$$V_I \equiv \frac{\text{var } I}{\langle I \rangle^2} = V_\sigma(1 + V_n) + V_n = V_\sigma \left(1 + \frac{1}{L}\right) + \frac{1}{L} \quad (6.1)$$

where V_I , V_σ , and V_n are the normalized variances of intensity, RCS, and speckle, respectively. This relationship between V_I and V_σ is important because it is not possible to measure V_σ directly; it has to be inferred from V_I .

All the reconstruction methods described require estimates of the sample mean and normalized variance over some window comprising N pixels, defined by

$$\bar{x} \equiv \frac{1}{N} \sum_{j=1}^N x_j \quad \text{and} \quad \bar{V}_x \equiv \frac{\text{var } x}{\bar{x}^2} = \frac{\sum_{j=1}^N (x_j - \bar{x})^2}{N \bar{x}^2} \quad (6.2)$$

where x_j denotes the pixel value. In single-stage filters, x corresponds to intensity I ; with iterative algorithms it should tend toward σ as reconstruction progresses. The size of window depends on the application.

It is important to have some quantitative measure for comparing algorithms, and we will express it in terms of the consistency of the reconstruction and original image with the speckle model. Suppose that the algorithm yields the true RCS σ_j at pixel j . The ratio of the pixel intensity to the derived RCS, $r_j \equiv I_j/\sigma_j$, should then correspond to speckle fluctuations alone with a mean value of one. The sample mean and *standard deviation* (SD) can then be estimated over N pixels, which could comprise the whole scene, and are defined by

$$\bar{r} \equiv \frac{1}{N} \sum_{k=1}^N r_k \quad \text{and} \quad \overline{\text{SD}[r]} \equiv \sqrt{\frac{1}{N} \sum_{k=1}^N (r_k - 1)^2} \quad (6.3)$$

For L -look SAR the expected values for intensity images would be given by $\bar{r} = 1$ and $\overline{\text{SD}[r]} = \sqrt{1/L}$. Similar expressions could be derived for the ratio of the pixel amplitude to the square root of the RCS, for which $\overline{\sqrt{r}} = 1$ and

$\text{SD}[\sqrt{r}] = \sqrt{L\Gamma^2(L)/(\Gamma^2(L + 1/2)) - 1}$. This treatment is too simple since σ_j is *estimated* rather than known, but a rigorous analysis for the statistics of the intensity ratio over uniform regions in segmentation has been reported [4]. When the observed mean value differs significantly from one, it is an indication of radiometric distortion. If the reconstruction follows the original image too closely, the SD would be expected to have a lower value than predicted. It would be larger than predicted if the reconstruction fails to follow genuine RCS variations. This provides a simple test that can be applied to any form of reconstruction, including both despeckling filters and segmentation (see the next chapter). Departures from prediction indicate a failure of the model or of the algorithm attempting to implement it, without specifying the manner in which it fails. For example, the reconstruction may provide an incorrect value for a region of constant RCS or it may fail to register the positions of changes in RCS. The test can be applied over the entire image or to specific regions. Applied globally, it suffers from the problem that it does not indicate if the reconstruction follows speckle fluctuations too closely in some areas but insufficiently closely elsewhere. In spite of these reservations, the test gives two measures of the quality of reconstruction and we will apply it as a numerical test of the algorithms developed in this chapter.

6.3 Bayesian Reconstruction

In most instances, the approach to reconstruction in this chapter will be expressed in terms of the Bayes criterion relating the observed intensity I , to the RCS σ , such that

$$P_{\text{AP}}(\sigma|I) = P(I|\sigma)P_\sigma(\sigma)/P_I(I) \quad (6.4)$$

where $P_{\text{AP}}(\sigma|I)$ is the a posteriori conditional probability of σ , which has a particular value given I , and $P(I|\sigma)$ is the likelihood function, which describes the effect of speckle during imaging. As shown in Chapter 4, this is given by

$$P(I|\sigma) = \left(\frac{L}{\sigma}\right)^L \frac{I^{L-1}}{\Gamma(L)} \exp\left[-\frac{LI}{\sigma}\right] \quad (6.5)$$

for L -look SAR. $P_\sigma(\sigma)$ is the a priori PDF that encapsulates prior knowledge about the RCS. $P_I(I) = \int P(I|\sigma)P_\sigma(\sigma)d\sigma$ only serves to normalize the expression and need not be included specifically in most instances. Generally

we wish to provide an estimate of σ that represents its most likely value given an observed I . This is equivalent to maximizing the log likelihood

$$\lambda \equiv \ln P_{AP}(\sigma|I) \quad (6.6)$$

with respect to σ . Two types of maximum will be considered. If there is no prior knowledge of the form of $P_\sigma(\sigma)$ we can only optimize with respect to the likelihood function in (6.4) leading to the MLE. However, if the form of the a priori PDF is known, the optimum is referred to as the *maximum a posteriori* (MAP) estimate. The latter is more precisely determined since it is based on more specific prior knowledge about the properties of the complete process.

6.4 Reconstruction Using the Speckle Model

6.4.1 Multilook Despeckling

The simplest approach to despeckling is to average the intensity over several pixels within a window centered on a specific pixel. This is tantamount to assuming that the RCS is constant over the filter window. If this assumption is incorrect, the method is fundamentally flawed. The joint probability that all N pixels have this mean value is given by

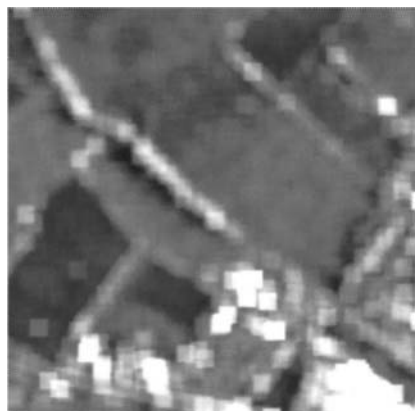
$$P(\sigma|I_1, I_2, \dots, I_N) \propto \prod_{j=1}^N P(I_j|\sigma) = \prod_{j=1}^N \left(\frac{L}{\sigma}\right)^L \frac{I_j^{L-1}}{\Gamma(L)} \exp\left[-\frac{LI_j}{\sigma}\right] \quad (6.7)$$

for L -look SAR, where pixels are assumed independent. The MLE for σ is then given by

$$\sigma_{ML} = \bar{I} \quad (6.8)$$

which is the average intensity over all the pixels in the window, corresponding to multilooking. Note that if this is applied to a single pixel the MLE is equal to the intensity of that pixel, as noted in (4.7). As we will show, different values for the MLE in subsequent algorithms depend on constraints introduced by different world models.

The result of applying this algorithm to the original image in Figure 6.1, using an 11 by 11 window, is shown in Figure 6.2(a). While the method has reduced the SD of the speckle variations in regions of relatively constant RCS



(a)



(b)



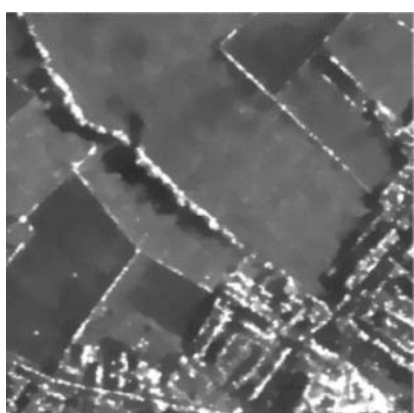
(c)



(d)



(e)



(f)

Figure 6.2 Despeckled versions of Figure 6.1: (a) multilook, (b) MMSE, (c) structural gamma MAP, (d) CML, (e) CMAP, and (f) Crimmins.

by a factor \sqrt{N} , that is, 11, it has also degraded resolution by the same factor resulting in the blurring of small objects. Only if features of interest within the scene occur on a large enough scale can multilook images be effective. An adaptive approach that matches the size of a window to the scale of objects of interest would provide optimum despeckling at the required resolution. Where fluctuations were consistent with a constant RCS the window size can be increased to improve despeckling as far as possible.

6.4.2 Minimum Mean-Square Error Despeckling

Multilook despeckling fails where the assumption of constant RCS within the window breaks down. The filter should then adapt to take account of excess fluctuations compared with speckle within the window. One approach to such an adaptive filter is to provide a model-free *minimum mean-square error* (MMSE) reconstruction based on measured local statistics [5–7]. If the original intensity of the center pixel in a window is I , then its corrected value can be obtained by performing a first-order expansion about the local mean \bar{I} such that

$$\sigma_{\text{MMSE}} = \bar{I} + k(I - \bar{I}) \quad (6.9)$$

where σ_{MMSE} is the MMSE estimate for RCS and k is selected to minimize the mean-square residual between intensity and fit, yielding [7]

$$k = \frac{\overline{V_\sigma}}{\overline{V_I}} = \frac{\overline{V_I} - 1/L}{\overline{V_I}(1 + 1/L)} \quad (6.10)$$

Spatial correlations in σ are neglected in (6.10). However, they can be incorporated in a similar approach, as demonstrated by Frost [6]. Note that σ is no longer constrained to be constant but is specified through the estimates $\bar{\sigma}$ and $\overline{V_\sigma}$ (which is inferred from $\overline{V_I}$ as in (6.1)), which are obtained over the window as defined in (6.2).

A related approach by Lee [5] considers an optimal linear filter that is equivalent to a first-order Taylor expansion. This results in a form similar to (6.9), but the constant k is now given by $k = (\overline{V_I} - 1/L)/\overline{V_I}$. When there is no RCS variation we would expect the estimate $\overline{V_I}$ to be close to $1/L$ so that $k \approx 0$ and $\sigma_{\text{MMSE}} \approx \bar{I}$ for both the MMSE and Lee algorithms. However, speckle fluctuations cause $\overline{V_I}$ to have smaller values about half the time, so k becomes negative. The reconstruction is improved by imposing the condition $k = 0$ where the estimated normalized variance is smaller than predicted by the speckle model, so that $\sigma_{\text{MMSE}} = \bar{I}$. In the opposite limit of large intensity variations the

MMSE solution is $\sigma_{\text{MMSE}} \approx (\bar{I} + LI)/(1 + L)$ for L -look SAR, so the despeckled result is the weighted average of the mean and the individual pixel value. If I is sufficiently large compared with its surroundings, it yields a large value of \bar{V}_I , so $\sigma_{\text{MMSE}} \approx I/(1 + 1/L)$. In this extreme the Lee filter yields $k = 1$ and $\sigma_{\text{Lee}} = I$. Thus, the response to strong targets differs from MMSE in that it ignores the speckle contribution to the target intensity when making the reconstruction, corresponding to treating the bright pixel as a point target that would not give rise to speckle fluctuations. In most applications this form of reconstruction for targets would actually be preferable to MMSE.

The result of applying MMSE over an 11 by 11 window to the image in Figure 6.1 is illustrated in Figure 6.2(b). Speckle is significantly reduced in those regions that are recognized to be homogeneous. However, an artifact of the reconstruction technique is that each bright object is surrounded by a ring of noise. The effect is most obvious for linear features, such as the hedges between fields, where it results in a noisy band on each side of the feature. This problem is common to other forms of adaptive filter, as we will see. It arises from the manner in which the statistics are estimated. Whenever a strong target lies within the window it dominates the statistics, leading to a large normalized variance estimate in (6.2). The algorithm then treats weaker intensities surrounding the target as arising from a widely fluctuating RCS, so the reconstructed value for σ will tend toward $1/(1 + L)$ of the observed intensity. Thus, pixels surrounding a strong target are reconstructed as a dark speckled ring with width equal to the window dimension.

6.5 Reconstruction Using the RCS Model

A better estimate for σ can be obtained if we have prior knowledge about the PDF of the RCS. The Bayes rule in (6.4) shows how this a priori PDF can be used to provide a MAP reconstruction when combined with the likelihood function. We demonstrated in Chapter 5 that the RCS of natural clutter can, in many cases, be well represented by a gamma distribution of the form

$$P_\sigma(\sigma) = \left(\frac{\nu}{\mu} \right)^\nu \frac{\sigma^{\nu-1}}{\Gamma(\nu)} \exp \left[-\frac{\nu\sigma}{\mu} \right] \quad (6.11)$$

where μ and ν are the mean RCS and order parameter, respectively. These cannot be measured directly and must be estimated from the data. The order parameter can be obtained using (6.1) and the fact that the normalized variance

of the RCS is given by $V_\sigma = 1/\nu$. Hence, estimates for μ and ν are obtained by passing a window over the original image and setting

$$\hat{\mu} = \bar{I} \quad \text{and} \quad \hat{\nu} = 1/\bar{V}_\sigma = (1 + 1/L)/(\bar{V}_I - 1/L) \quad (6.12)$$

6.5.1 Gamma MAP Despeckling

The PDF of σ given an intensity I when both likelihood and a priori PDFs are available is given by

$$P_{AP}(\sigma|I) \propto P(I|\sigma)P_\sigma(\sigma) = \left(\frac{I}{\sigma}\right)^L \frac{I^{L-1}}{\Gamma(L)} \exp\left[-\frac{LI}{\sigma}\right] \left(\frac{\nu}{\mu}\right)^\nu \frac{\sigma^{\nu-1}}{\Gamma(\nu)} \exp\left[-\frac{\nu\sigma}{\mu}\right] \quad (6.13)$$

Hence, the log likelihood is given by

$$\begin{aligned} \lambda &\equiv \ln P(I|\sigma) + \ln P_\sigma(\sigma) \\ &= L \ln L - L \ln \sigma + (L-1) \ln I - \ln \Gamma(L) - LI/\sigma \\ &\quad + \nu \ln \nu - \nu \ln \mu + (\nu-1) \ln \sigma - \ln \Gamma(\nu) - \frac{\nu\sigma}{\mu} \end{aligned} \quad (6.14)$$

and the corresponding MAP solution for RCS [8,9] is given by the quadratic

$$\frac{\nu\sigma_{MAP}^2}{\mu} + (L+1-\nu)\sigma_{MAP} - LI = 0 \quad (6.15)$$

where μ and ν are estimated from (6.12).

In regions of pure speckle, we would expect $\bar{V}_I \approx 1/L$ so that, from (6.12), $\nu \approx \infty$ and $\sigma_{MAP} \approx \bar{I}$, as with MMSE. However, as before, statistical fluctuations cause the estimate for \bar{V}_I to be less than $1/L$ about half the time, so $\hat{\nu}$ becomes negative. Again, the reconstruction can be improved when this occurs by setting $\hat{\nu} = \infty$ so that $\sigma_{MAP} = \bar{I}$. In the opposite limit of small ν , provided that $\mu/I \gg 4\nu L/(L+1)^2$, the solution becomes $\sigma_{MAP} \approx I/(1+1/L)$. If a Gaussian PDF is adopted for the a priori PDF the MAP solution is obtained from a cubic equation [8], which is computationally more expensive to solve and is generally not such an appropriate form for SAR.

Both MMSE and gamma MAP reconstructions can be improved by introducing an algorithm that detects and adapts to structural features, such as edges, lines, and points, using gradient masks, and adjusting the shape of the window accordingly [9,10]. A gamma MAP reconstruction of Figure 6.1 over an 11 by 11 window, using structure adaptivity, is illustrated in Figure 6.2(c). Resolution tends to be preserved for bright objects rather better than with the MMSE filter and unlike the multilook reconstruction. There is evidence of structure in the shadows behind the diagonal hedge that was smoothed out in the MMSE reconstruction in Figure 6.2(b). However, the reconstruction again suffers from artifacts around bright objects caused by strong features within the window. This demonstrates the difficulty of constructing an adaptive filter to recognize and correct for the influence of strong features on their surroundings.

It should be noted that the extent of these artifacts in both MMSE and gamma MAP could be reduced by reducing window size, though this would have the effect of increasing speckle fluctuations. Residual artifacts could also be reduced by increasing the number of possible edge orientations tested. The effect would be less apparent where the original scene had less structure, as is generally true for ERS-1 images. Indeed, both methods provide excellent reconstructions over large regions of constant RCS. Gamma MAP reconstruction has been widely and successfully used in image interpretation; see, for example, [11,12].

6.6 Correlated Neighborhood Model

So far we have exploited the speckle model in reconstructing the RCS of a single pixel, combined with the single-point PDF of the RCS in Section 6.5. Surrounding pixels were only involved through estimating the population mean and variance (or order parameter when a gamma a priori PDF was assumed). All the reconstructions illustrated in Figure 6.2 so far suffer from visible defects. Improvement can only result from the introduction of further prior knowledge.

Let us introduce a constraint that relates a pixel intensity to its neighbors via a *correlated neighborhood model* that selects the smoothest possible reconstruction consistent with observed intensity variations in a local region. The conditional probability of observing the intensities within the local neighborhood surrounding a central pixel with RCS σ (illustrated in Figure 6.3) can be expressed through the conditional probability $P_{\text{loc}}(I|\sigma)$. In the absence of a known form for this PDF let us adopt a gamma distribution such that

$$P_{\text{loc}}(I|\sigma) = \left(\frac{\alpha}{\sigma}\right) \frac{I^{\alpha-1}}{\Gamma(\alpha)} \exp\left[-\frac{\alpha I}{\sigma}\right] \quad (6.16)$$

x_1	x_2	x_3
x_4	x_0, σ, I_0	x_5
x_6	x_7	x_8

Figure 6.3 Neighborhood diagram (for $m = 9$ pixels).

The order parameter α is distinct from v since it will have contributions from speckle as well as from fluctuations in the correlated samples of σ within the neighborhood. Its value can be estimated from the normalized variance over the neighborhood as $\alpha = 1/V_I$. The assumption of a gamma PDF is not critical; similar analysis could be performed for a Gaussian PDF.

6.6.1 Correlated Neighborhood ML (CML) Despeckling

Initially we assume that the prior distribution $P(\sigma)$ is unknown. Combining the conditional PDF for the correlated neighborhood model in (6.16) with the speckle conditional PDF in (6.5) yields a constrained ML solution. The joint probability of observing intensity I_0 in the central pixel with surrounding intensities I_1 to I_{m-1} , for RCS σ at the center, is now given by

$$\begin{aligned} P_{\text{ML}}(\sigma | I_0 \cdots I_{m-1}) &\propto P(I_0 | \sigma) \prod_{j=0}^{m-1} P_{\text{loc}}(I_j | \sigma) \\ &= \left(\frac{L}{\sigma}\right)^L \frac{I_0^{L-1}}{\Gamma(L)} \exp\left[-\frac{LI_0}{\sigma}\right] \prod_{j=0}^{m-1} \left(\frac{\alpha}{\sigma}\right)^\alpha \frac{I_j^{\alpha-1}}{\Gamma(\alpha)} \exp\left[-\frac{I_j}{\sigma}\right] \quad (6.17) \end{aligned}$$

Hence, the MLE for the cross section of the center pixel, σ , is given by

$$\sigma_{\text{CML}} = \frac{I_0 + m\alpha\bar{I}/L}{1 + m\alpha/L} \quad (6.18)$$

where α and \bar{I} are estimated over a 3 by 3 neighborhood in the same way as before. This filter can be written in a form similar to the MMSE result, namely,

$$\sigma_{\text{CML}} = \bar{I} + k(I_0 - \bar{I}) \quad \text{where } k = \frac{1}{1 + m\alpha/L} \quad (6.19)$$

This expression assumes that the *intensity* estimates in the neighborhood are uncorrelated even though the *RCS* over the neighborhood is correlated. This assumption must be modified when the process is iterated in Section 6.8.3. From (6.19) we observe that if the neighborhood fluctuations are dominated by speckle, so that $\alpha \approx L$, then $k \ll 1$ and $\sigma_{\text{CML}} \approx \bar{I}$, and the estimate reduces to the local average. In the opposite limit of large variations, $\alpha \ll 1$ and so $k \approx 1$ and $\sigma_{\text{CML}} \approx I_0$, so that the center pixel is unchanged. These represent the same limits as the Lee algorithm [5].

The results of applying this algorithm to the image in Figure 6.1 over a 3 by 3 neighborhood is illustrated in Figure 6.2(d). It is immediately apparent that the despeckling performance over regions of constant RCS is less effective than that achieved by previous algorithms, as expected from the reduced window size. On the other hand, unwanted artifacts surrounding strong objects appear to have been largely removed since the small neighborhood restricts the distance over which the effect of strong features would be evident. As already noted, a similar effect could be obtained by applying MMSE or gamma MAP over this small neighborhood at the expense of degraded speckle reduction.

6.6.2 Correlated Neighborhood Gamma MAP (CMAP) Despeckling

Let us now combine the correlated neighborhood model with the prior PDF for the RCS (6.11) in a MAP reconstruction. The joint PDF for single-look SAR now becomes

$$P_{\text{AP}}(\sigma | I_0 \dots I_{m-1}) \propto P(I_0 | \sigma) P_\sigma(\sigma) \prod_{j=0}^{m-1} P_{\text{loc}}(I_j | \sigma) = \left(\frac{L}{\sigma}\right)^L \frac{I_0^{L-1}}{\Gamma(L)} \times \exp\left[-\frac{LI_0}{\sigma}\right] \left(\frac{\nu}{\mu}\right)^\nu \frac{\sigma^{\nu-1}}{\Gamma(\nu)} \exp\left[-\frac{\nu\sigma}{\mu}\right] \prod_{j=0}^{m-1} \left(\frac{\alpha}{\sigma}\right)^\alpha \frac{I_j^{\alpha-1}}{\Gamma(\alpha)} \exp\left[-\frac{\alpha I_j}{\sigma}\right] \quad (6.20)$$

Hence, the MAP solution for σ is expressed as the positive root of the quadratic equation

$$\frac{\nu\sigma_{\text{CMAP}}^2}{\mu} + \sigma_{\text{CMAP}}(m\alpha + L + 1 - \nu) - LI_0 - m\alpha\bar{I} = 0 \quad (6.21)$$

Estimates for \bar{I} and α are obtained over the local neighborhood. The correlated neighborhood model implies that fluctuations within the neighborhood should be small so that α should be large. The full range of fluctuations would be expected over the larger window that is used to estimate μ and ν as in (6.12).

The results of applying this algorithm to the original image of Figure 6.1 are illustrated in Figure 6.2(e). Upon comparing this result with Figure 6.2(d) we observe that the speckle in uniform regions is further suppressed using the MAP reconstruction. This illustrates the advantage of including more prior knowledge where it is available. However, the algorithm has insufficient speckle reduction performance.

6.7 Structural Adaptive Filtering

With the exception of gamma MAP reconstruction, the filters considered so far have not taken account of any structure. However, we have observed in MMSE and gamma MAP despeckling that the presence of bright objects within the filter window has a deleterious effect via the introduction of artifacts. Results with smaller windows, such as CML and CMAP, show that these artifacts can be reduced at the expense of degraded speckle reduction. It is instructive to enquire whether a structural approach alone could provide useful despeckling performance. Crimmins [2] proposed a geometrical filter based on iterative complementary hulling. This does not incorporate any specific model for speckle statistics but depends on the shape of features in the scene. The image is treated with a set of small (4-pixel) templates that are intended to respond to structural features. At the same time, these templates average over speckle fluctuations. The algorithm is nonlinear, iterating eight times, and actually modifying the image 64 times in the process, leading to speckle reduction. Thus, this filter offers a potential for both adaptive structure enhancement and speckle reduction and can be regarded as an adaptive multilook despeckling method where the window over which averaging is performed is tuned to the scene, albeit imperfectly. This effect is apparent in Figure 6.2(f), which illustrates the result of applying the algorithm to Figure 6.1. The method has provided effective speckle reduction in homogeneous regions and generally appears to

give better speckle reduction, structure preservation, and lack of artifacts than the other methods discussed so far. However, some small-scale structure has been lost, which is to be expected. This tendency to lose or degrade the shape of small objects can be a serious disadvantage. Nevertheless, this reconstruction might be considered to give visually the best reconstruction of those illustrated in Figure 6.2.

6.8 Reconstruction Using Nonlinear Iterated Processing

The reconstructions described so far appear to give limited despeckling performance. Large windows yield good speckle reduction over homogeneous regions but lead to artifacts over a distance equal to the filter dimension in the presence of strong features. This means that background clutter has excess variations in precisely those areas where one would like it accurately defined. Small windows are largely free of these artifacts but give inadequate speckle reduction. In many ways, the Crimmins algorithm gives better reconstruction in spite of degraded resolution. In this method, iteration leads to a considerable reduction in the speckle, which motivates us to consider the effects of iterating the other filters.

6.8.1 Iterated MMSE Despeckling

If we assume that pixel values after iteration are still affected by multiplicative noise, then the same MMSE approach as in (6.9) and (6.10) can be adopted [7]. The iterated MMSE estimate for the RCS now takes the form

$$\sigma_{\text{MMSE}} = \bar{x} + k(x - \bar{x}) \quad (6.22)$$

where x is the current value of the center pixel and

$$k = \frac{\overline{V_x}}{\overline{V_x}} = \frac{\overline{V_x} - 1/L'}{\overline{V_x}(1 + 1/L')} \quad (6.23)$$

Equations (6.22) and (6.23) have a form similar to those for the first iteration. However, the sample estimates \bar{x} and $\overline{V_x}$ are now obtained by applying the filter window to the result of the previous iteration. In addition, the progressively despeckled data have an effective number of looks L' , that increases as iterations proceed. L' is estimated from the normalized variance of the complete image.

An MMSE reconstruction of Figure 6.1, after 8 iterations with an 11 by 11 window, is shown in Figure 6.4(a). Speckle has been smoothed considerably, but excess noise around strong objects is still apparent, though reduced compared with a single look. The primary drawback of the reconstruction, however, is the failure to preserve structure in the scene. Indeed, upon continuing to 200 iterations, nearly all structure is averaged out. It appears that MMSE does not converge to the RCS but continues to smooth out all variation because approximately half of the measurements of the statistics in the window yield a variance lower than that expected for speckle and so the algorithm adopts the local average value, leading to progressively increased smoothing.

6.8.2 Iterated Gamma MAP Despeckling

A similar approach to iteration can be adopted for the gamma MAP algorithm. In principle, it should be possible to base the iteration process on updating the current pixel value, denoted by x , rather than the original intensity I . However, this demands knowledge of the conditional probability $P(x|\sigma)$ relating the current (partially despeckled) pixel value x to the RCS σ . For residual speckle, this PDF would be expected to be gamma-distributed with an order corresponding to an effective number of looks L' . One difficulty encountered in estimating L' is that it will vary across the image. A second is that any degradation in reconstruction will be retained, and probably exacerbated, during subsequent iterations. Thus it seems preferable to insist that the estimated RCS during each iteration should be consistent with the original

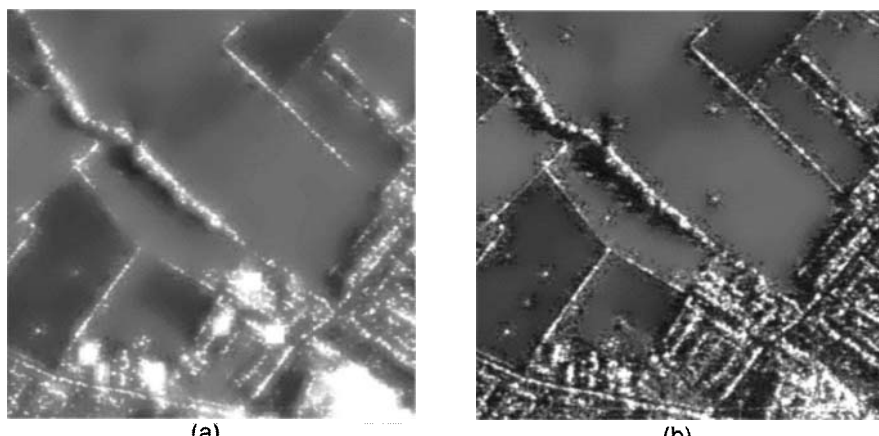


Figure 6.4 Despeckled version of Figure 6.1 after 8 iterations: (a) MMSE and (b) structural gamma MAP.

intensity image described by the speckle conditional probability $P(I|\sigma)$. Though convergence is slower, there is less chance of progressively increasing radiometric distortion. A similar approach will be adopted in all the following iterative reconstruction methods.

As the iterations of the gamma MAP algorithm proceed, we might hope that x converges to σ and the PDF for x converges to (6.11). Hence, the form of the iterated MAP joint probability is identical to (6.13), leading to the same form for the gamma MAP solution for the cross section [13], namely,

$$\frac{\nu\sigma_{\text{MAP}}^2}{\mu} + \sigma_{\text{MAP}}(L - \nu + 1) - LI = 0 \quad (6.24)$$

where I and L are the original intensity and number of looks, respectively, and μ and ν are estimated from the current iteration, so that $\mu = \bar{x}$ and $\nu = 1/V_x$. In fact, x does not converge to σ ; artifacts will be introduced as described earlier that will continue to be reconstructed in the same manner as genuine RCS variations.

The consequences of applying 8 iterations of the structured gamma MAP algorithm within an 11 by 11 window are illustrated in Figure 6.4(b). Homogeneous regions are clearly smoothed without the loss of structure noted with the artifacts around features are still clearly visible as expected. Upon extending to 200 iterations, there is little change in the quality of the reconstruction. Some additional smoothing of uniform regions is apparent, structure is preserved, and the artifacts around features are retained. The spatial extent of these artifacts can be reduced, as mentioned in Section 6.5.1, by reducing window size. As expected, this degrades the despeckling but can be rectified by iteration. However, for a 3 by 3 window, although artifacts are reduced, the structure in the scene is smoothed out to a greater extent than with the larger window. A window dimension could be selected to provide an acceptable compromise between artifact reduction and oversmoothing.

6.8.3 Iterated Correlated Neighborhood ML (CML) Despeckling

When the correlated neighborhood model is invoked, iteration causes the local PDF to become less broad as differences between neighboring pixels due to speckle are removed. However, the joint probability has the same form as before, given by (6.17), resulting in an identical ML solution for σ [13] given by

$$\sigma_{\text{CML}} = \frac{I_0 + m\alpha\bar{x}/L}{1 + m\alpha/L} \quad (6.25)$$

where I_0 and L again correspond to pixel intensity and the number of looks for the original data and \bar{x} and α are estimated from the current iteration over the neighborhood. While (6.25) has the same form as for the first pass in (6.18), iteration causes the pixel values to become increasingly correlated, violating the assumptions of the derivation. Thus, m is now the *effective* number of independent pixels that can be estimated from the ACF within the neighborhood.

The result of applying this algorithm for 8 iterations using a 3 by 3 neighborhood is illustrated in Figure 6.5(a). Speckle is considerably reduced compared with the single-pass result in Figure 6.2(d), though it is still visible, indicating that more iterations are necessary. Detail is also better preserved than with the MMSE reconstruction in Figure 6.4, and artifacts are much less obvious than with either MMSE or gamma MAP. However, increasing to 200 iterations leads to the oversmoothed result in Figure 6.5(c). Notice that shadows behind the hedge, which were clearly visible after 8 iterations, have largely disappeared. Thus, this approach does not appear to converge satisfactorily and must be rejected.

6.8.4 Iterated Correlated Neighborhood Gamma MAP (CMAP) Despeckling

CML made no use of a PDF for the RCS. Upon incorporating the PDF in a full iterated MAP solution, the theoretical description for subsequent iterations of the CMAP algorithm is unchanged from the first iteration (see (6.20)), yielding a solution [13] given by

$$\frac{\nu\sigma_{\text{CMAP}}^2}{\mu} + \sigma_{\text{CMAP}}(m\alpha + L + 1 - \nu) - LI_0 - m\alpha\bar{x} = 0 \quad (6.26)$$

Again the original intensity I_0 , and number of looks L , is used; α , \bar{x} , and m are estimated over the small neighborhood for the current iteration, while μ and ν retain their values from the original image, estimated over the larger window. The general behavior of this algorithm would be expected to be similar to that for the previous ML version in Section 6.8.3, with the exception of an improvement due to the inclusion of the a priori PDF.

Results for 8 and 200 iterations with a 3 by 3 neighborhood and 11 by 11 window are shown in Figure 6.5(b,d). Based on a comparison with CML after 8 iterations (in Figure 6.5(a)), it is apparent that speckle has been smoothed better in homogeneous regions and that detail is better preserved. Both are consequences of the increased prior knowledge being exploited. Upon increasing to

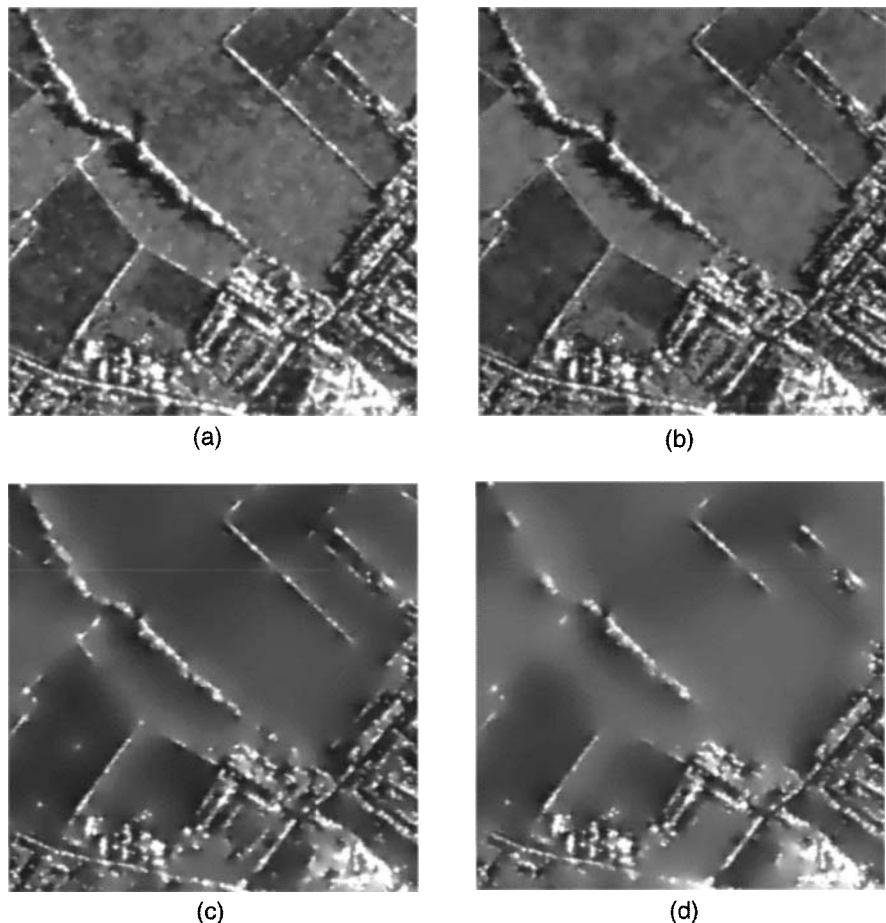


Figure 6.5 Iterated despeckled version of Figure 6.1: 8 iterations of (a) CML and (b) CMAP and 200 iterations of (c) CML and (d) CMAP.

200 iterations (in Figure 6.5(d)), however, the reconstructions display excessive oversmoothing. Thus, both the correlated neighborhood models fail to converge to the RCS as the number of iterations increases and should be rejected.

6.9 Reconstruction by Iterating the Structured Neighborhood Model

The results illustrated in Figures 6.4 and 6.5 indicate that the filters described in Section 6.8 are capable of attaining very good speckle reduction in uniform

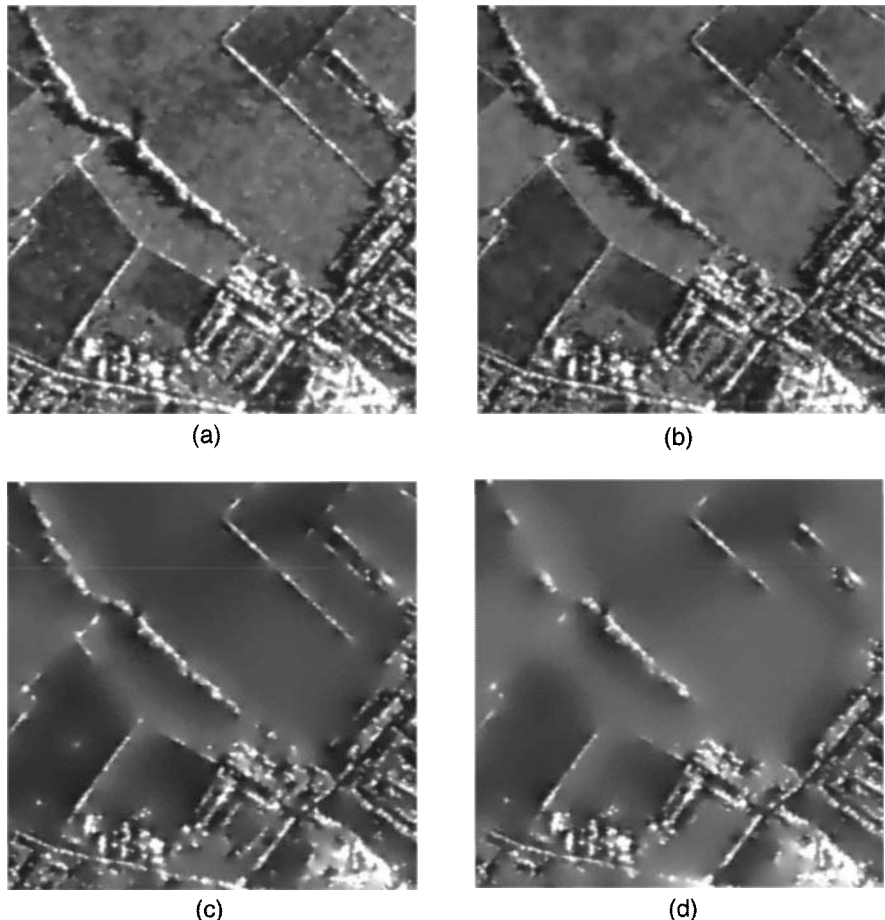


Figure 6.5 Iterated despeckled version of Figure 6.1: 8 iterations of (a) CML and (b) CMAP and 200 iterations of (c) CML and (d) CMAP.

200 iterations (in Figure 6.5(d)), however, the reconstructions display excessive oversmoothing. Thus, both the correlated neighborhood models fail to converge to the RCS as the number of iterations increases and should be rejected.

6.9 Reconstruction by Iterating the Structured Neighborhood Model

The results illustrated in Figures 6.4 and 6.5 indicate that the filters described in Section 6.8 are capable of attaining very good speckle reduction in uniform

regions. However, their symmetrical response tends to smooth out directional features. This suggests that the comparatively good result achieved with the Crimmins filter, shown in Figure 6.2(f), does not stem solely from iteration to reduce speckle but also from its response to structures within the scene. Therefore, in this section we introduce structure sensitivity into the correlated neighborhood model by subdividing the neighborhood into a set of templates that provide directional information [14–16]. Instead of calculating CML or CMAP solutions for the central pixel using all pixels in the neighborhood, a set of 12 different solutions can be produced corresponding to each of the configurations illustrated in Figure 6.6. Structure can then be preserved by selecting the most probable configuration, based on (6.25) or (6.26), respectively. Unlike all the previous filters, which were aimed at providing local optimization, this new approach is intended to derive the global MAP solution for RCS, given the constraints imposed by the different models. As such, it is a member of the well-known class of global optimization problems. A familiar difficulty with attempting analytic optimization is that, if analytic gradient descent techniques are adopted to find the maximum (or minimum), the reconstruction can become trapped in some *local* optimum rather than progressing to the *global* solution. Well-designed optimization methods try to avoid this difficulty and derive the global solution. One such generic technique is simulated annealing. Let us consider how this approach can be combined with the structured neighborhood model to provide a global MAP reconstruction of the RCS.

6.9.1 Simulated Annealing and the Structured Neighborhood Model

Conventional simulated annealing is based on the Metropolis algorithm [17], which is intended to provide a global optimization with respect to an objective function that is defined over the complete image. When applied to despeckling,

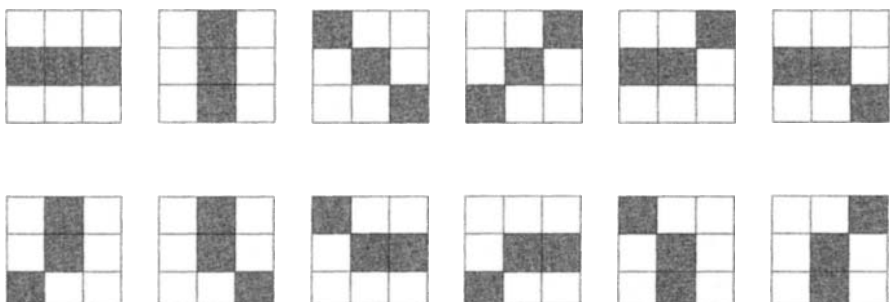


Figure 6.6 The 12 allowed configurations around the central pixel in the structured correlated neighborhood model.

the RCS is modeled as a Markov random field that is governed by the Gibbs distribution describing the conditional probability of the RCS σ , given a noisy estimate x . Thus,

$$P(\sigma|x) = \frac{1}{Z} \exp\left[-\frac{W}{T}\right] \quad (6.27)$$

where Z is a normalizing constant; T is a constant termed the distribution temperature, by analogy with true annealing; and W represents a potential function that encapsulates the data multipoint statistics over the entire image, or at least as much as is feasible. Simulated annealing is guaranteed to find the global minimum of such a system provided that [18]:

- The temperature T tends to zero sufficiently slowly, with

$$T \geq \frac{T_0}{\ln(1 + \beta k)} \quad (6.28)$$

where k is the iteration number, T_0 the starting “temperature” (which controls initial smoothing), and β the convergence rate (which controls the number of iterations over which smoothing occurs).

- Each pixel in the image is visited a very large number of times.

The algorithm proceeds as follows.

1. A particular pixel is randomly perturbed to some different value.
2. The joint probability of all pixels in the image is evaluated, based on the objective function.
3. If the probability of a new configuration is greater than for the previous one, the new pixel value is adopted. If the probability is lower than before, the new value may still be accepted (as described below).
4. A new pixel is selected randomly and the process repeated from 1.

While this scheme is guaranteed to find the values of σ that yield the global minimum of W , both the calculation of the joint probability over the entire image and randomly perturbing the pixel value are extremely time consuming.

Significant speed improvements can be achieved if the objective function is defined locally rather than over the complete image [14–16, 18–20]. There need be no restriction on correlation between pixels, though the general form could be limited to a specific model characterized by variance and correlation length

parameters, for example [20]. Even with this simplification, the algorithm would still be impractical if every pixel could take an arbitrary value of RCS. One way to reduce complexity is to restrict the number of possible values that the intensity can take [18,20]. The output then takes the form of a crude quantization that is unsuitable for RCS estimation. Early methods also encountered difficulty in defining the prior knowledge to be exploited. In particular, it was found that heuristic models for real scenes gave poor results [19]. White [14–16] proposed a novel simulated annealing scheme that restricted the number of configurations for which the potential is defined to those illustrated in Figure 6.6 rather than the total number of possible final states of the entire image. This enables a continuous valued output to be implemented, suitable for RCS estimation.

White [14–16] also proposed a means for overcoming the second time-consuming step. He adopted a deterministic ML solution for the center pixel of each of the 12 candidate configurations corresponding to the prior correlated neighborhood model. This departure from strict annealing means that there is no guarantee of ultimate convergence to the global MAP solution, though it speeds execution considerably. As we will demonstrate, reconstructions are visually satisfactory and also achieve a good quality measure, as defined in Section 6.2.

Let us now examine how the potential function W in (6.27) can be related to the correlated neighborhood model. Following White [14–16] we define W in terms of the log likelihood, λ , for the local neighborhood by

$$-W \equiv -\lambda \equiv -\ln P(I_0|\sigma) - \ln P_\sigma(\sigma) \quad (6.29)$$

Thus, the global MAP solution for λ corresponds to the minimum of W . The structured neighborhood model considers the 12 individual 3-pixel configurations in the neighborhood separately. The original speckle conditional PDF, the intensity of the center pixel, and the number of looks are retained.

In fact, simulated annealing only approximates the global MAP solution. It is therefore important to select operating parameters to derive an effective solution. As noted in (6.27), the algorithm depends on an annealing temperature to prevent convergence on local minima. The choice of initial temperature T_0 and its change per iteration are crucial to the success of the algorithm. If T_0 is too low the solution converges on local minima, whereas if it is too high the reconstruction tends to be too smooth. Similarly, if T decreases too rapidly there is little probability of the 3 pixels in a configuration belonging to the same distribution and the technique fails. On the other hand, if it decreases too slowly convergence is delayed and the image is smoothed too much. It must be appreciated that there is no absolute “best” reconstruction available using this method. In examples that follow we adopt a cooling schedule based on $T_0 = 2.5$ and $\beta = 4$, which preserves details of weak targets within the scene.

The conditional probability for configuration j is then given by (6.27) with $W_j = \lambda_j$ and the CDF of the configuration probability is given by

$$\text{CDF}(K) \equiv \frac{1}{\text{CDF}(12)} \sum_{j=1}^K \exp\left[-\frac{\lambda_j}{T}\right] \quad (6.30)$$

First we identify which configuration out of the 12 has the highest probability and call it K_0 . If this probability is greater than that for the previous iteration, the new configuration is selected. Even if the probability is lower than before, it can still be selected probabilistically if $\text{CDF}(K_0) \leq \text{rnd}(1) < \text{CDF}(K_0 + 1)$, where $\text{rnd}(1)$ denotes a random number selected from a uniform distribution between 0 and 1. This random process prevents convergence on local minima by introducing temperature-dependent noise that allows the reconstruction to select a nonminimum state probabilistically. Cooling progressively allows the reconstruction to settle into an acceptable minimum solution that approximates the true MAP solution. An alternative, rule-based algorithm called TABOO [21] prevents convergence on local minima by making it progressively more difficult to select a state that has been previously selected. Though results of the two methods differ slightly, since neither represents the true global MAP solution, there is no significant difference in image quality and the TABOO algorithm is slightly faster.

Having outlined an approach that combines the structured neighborhood model with annealing we next derive CML and CMAP solutions and compare their performance.

6.9.2 Constant RCS Model

If the RCS within the neighborhood is assumed to have a constant mean, the iterated correlated neighborhood implementations in Sections 6.8.3 and 6.8.4 can be applied directly. Each of the 12 neighborhood configurations has its own probability, depending on the pixel values it contains. Assuming gamma PDFs for both speckle and the local neighborhood fluctuations, the conditional probability of σ_K at the central pixel for the K th configuration using the annealed CML algorithm (ACML), from (6.17), can be expressed as

$$P_K(\sigma_K | I_0, x_1, x_2) \propto \left(\frac{L}{\sigma_K}\right)^L \frac{I_0^{L-1}}{\Gamma(L)} \exp\left[-\frac{LI_0}{\sigma_K}\right] \\ \times \left(\frac{\alpha}{\sigma_K}\right)^{2\alpha} \frac{(x_1 x_2)^{\alpha-1}}{\Gamma^2(\alpha)} \exp\left[-\frac{\alpha(x_1 + x_2)}{\sigma_K}\right] \quad (6.31)$$

where L is the original number of looks for the speckle process, I_0 is the original intensity of the center pixel, and x_1 and x_2 are the outer two pixel estimates for configuration K .

The local order parameter α in (6.31) can be estimated over the whole 3 by 3 neighborhood. The ACML solution for σ_K then has a form similar to (6.18) and (6.25), namely,

$$\sigma_{\text{ACML}}(K) = \frac{I_0 + \alpha(x_1 + x_2)/L}{1 + 2\alpha/L} \quad (6.32)$$

The ML solution with a Gaussian model for both speckle and the local neighborhood fluctuations is given in [14–16]. However, this reconstruction appeared too smooth, so an edge detection stage was introduced, resulting in a segmentation, rather than reconstruction, algorithm.

The equivalent analysis for the ACMAP algorithm yields a conditional probability for the K th configuration similar to (6.31) except that it includes the a priori PDF for σ_K similar to that in (6.20). The MAP solution for σ_K similar to (6.21) and (6.26), is then given by the quadratic expression

$$\frac{\nu\sigma_{\text{ACMAP}}^2(K)}{\mu} + \sigma_{\text{ACMAP}}(K)(2\alpha + L + 1 - \nu) - LI_0 - \alpha(x_1 + x_2) = 0 \quad (6.33)$$

where μ and ν retain their values from the original image, estimated over the larger window, as in Section 6.8.4.

6.9.3 Sloping RCS Model

So far, structure considerations are restricted to the probabilistic selection of that configuration that demonstrates the greatest similarity between the RCS in neighboring pixels. A further refinement is to introduce a local slope in RCS such that the RCS in neighboring pixels in each configuration is in the ratio $\gamma:1:1/\gamma$ [22]. An additive slope is also possible [15,16,22] and yields essentially the same results but with a more complicated formalism. The total probability for the K th configuration in ACML is then given by

$$P_K(\sigma_K | I_0, x_1, x_2) \propto \left(\frac{L}{\sigma_K} \right)^L \frac{I_0^{L-1}}{\Gamma(L)} \exp \left[-\frac{LI_0}{\sigma_K} \right] \\ \times \left(\frac{\alpha}{\sigma_K} \right)^{2\alpha} \frac{(x_1 x_2)^{\alpha-1}}{\Gamma^2(\alpha)} \exp \left[-\frac{\alpha(\gamma x_1 + x_2/\gamma)}{\sigma_K} \right] \quad (6.34)$$

Hence, the MLE for γ becomes

$$\gamma = \sqrt{x_1/x_2} \quad (6.35)$$

while the ACML solution for σ becomes

$$\sigma_{\text{ACML}}(K) = \frac{I_0 + (\alpha/L)(x_1/\gamma + x_2\gamma)}{1 + 2\alpha/L} = \frac{I_0 + (2\alpha/L)\sqrt{x_1 x_2}}{1 + 2\alpha/L} \quad (6.36)$$

A similar derivation can be performed when the a priori PDF for σ_K is introduced. The MLE for γ is the same as (6.35), leading to a quadratic expression for the MAP solution for σ of the form

$$\frac{v\sigma_{\text{ACMAP}}^2(K)}{\mu} + \sigma_{\text{ACMAP}}(K)(2\alpha - v + L + 1) - LI_0 - 2\alpha\sqrt{x_1 x_2} = 0 \quad (6.37)$$

where the parameters are estimated as before.

6.9.4 Discussion of Structured Annealing Results

The result of applying structured annealing to Figure 6.1 using a 3 by 3 neighborhood and an 11 by 11 window are shown in Figures 6.7 and 6.8 for 8 and 200 iterations, respectively. Results for constant RCS with ACML and ACMAP are illustrated in (a) and (b) with the corresponding sloping RCS results in (c) and (d). After 8 iterations, the smoothest reconstruction in uniform regions seems to be obtained in Figure 6.7(d), followed by Figure 6.7(a). The sloping RCS with the ML reconstruction in Figure 6.7(c), and the MAP solution with constant RCS in Figure 6.7(b), both seem to show more fluctuations in uniform speckle regions. There is no significant difference between reconstructed features visible after 8 iterations. After 200 iterations the speckle in uniform regions has been effectively removed with all methods, as shown in Figure 6.8. All methods preserve the four objects in the field at the bottom left. However, the sloping RCS model with ACML, shown in Figure 6.8(c), reconstructs other isolated objects in the vicinity.

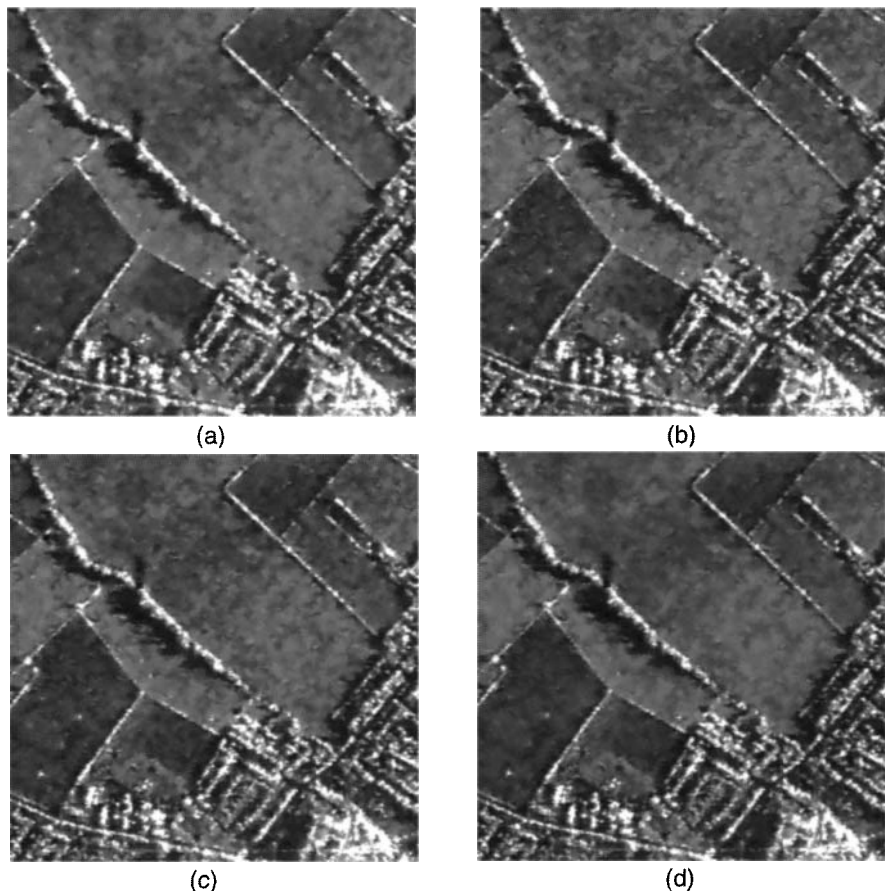


Figure 6.7 Structured neighborhood annealed reconstructions of Figure 6.1 after 8 iterations: constant RCS for (a) ACML and (b) ACMAP, and sloping RCS for (c) ACML and (d) ACMAP.

The ACMAP solution for the sloping RCS model, shown in Figure 6.8(d), removes these. Since all reconstructions approximate to a global optimum, given the slightly differing initial constraints, it is difficult to select one solution in preference to another. However, it is apparent that the fields have been broken up with distinct edges between regions where the constant RCS has been assumed in Figure 6.8(a,b), whereas most of these edges have been removed with the sloping RCS model in Figure 6.8(c,d). This “terracing” effect is an artifact of the constant RCS model, not a property of the data.

Generally, there is little to choose between these annealed reconstructions. All represent a considerable advance visually on any of the techniques described

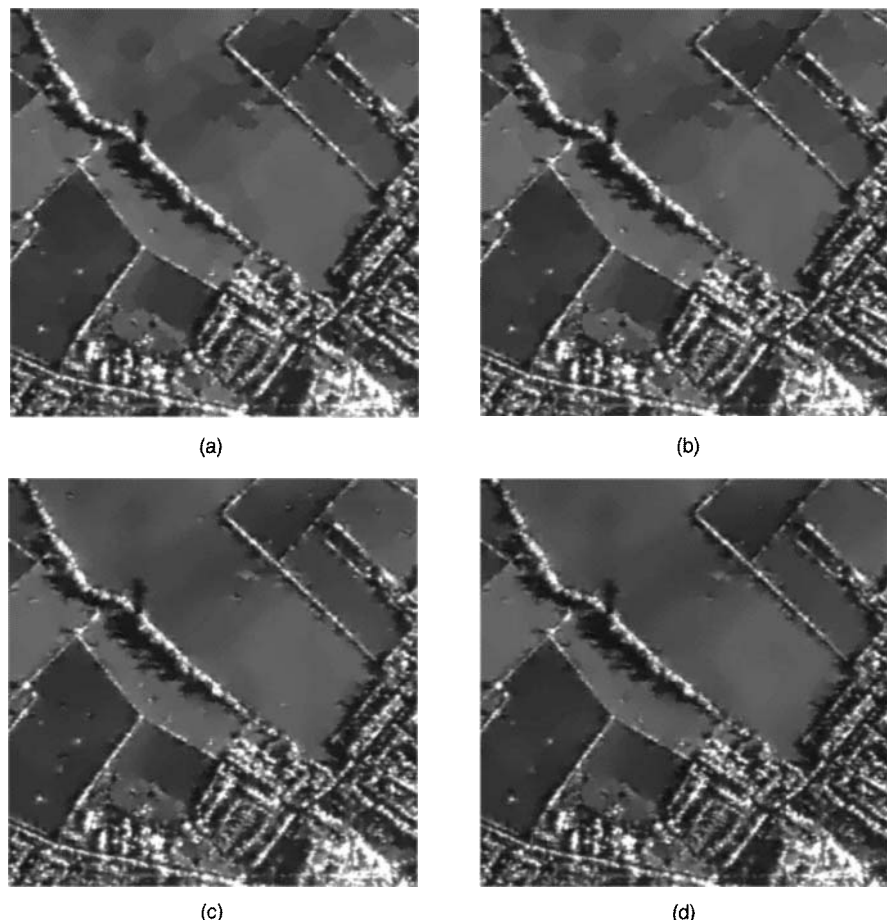


Figure 6.8 Structured neighborhood annealed reconstructions of Figure 6.1 after 200 iterations: constant RCS for (a) ACML and (b) ACMAP, and sloping RCS for (c) ACML and (d) ACMAP.

earlier, in terms of both speckle reduction and feature preservation. ACML with constant RCS or ACMAP with sloping RCS appear to represent uniform speckle regions marginally better, indicated by the results after 8 iterations. The terracing artifact, introduced by the constant RCS model, may be significant in some remote sensing applications where slow variations in RCS are important, in which case the ACMAP with the sloping RCS model is to be preferred. Any difference in radiometric preservation cannot be judged visually and can only be tested quantitatively, as described in the next section.

6.10 Comparison of Reconstruction Algorithms

In assessing the performance of the different despeckling algorithms described in this chapter there are two main considerations:

- Image quality;
- Execution time.

There is little point in implementing a fast algorithm that fails to extract useful information from the image data. On the other hand, it is inadvisable to implement a meticulous reconstruction if the algorithm is so slow that the application becomes impractical. The compromise between these requirements depends on the specific application. The relationship between system resolution and the size of objects of interest is of particular relevance. Pixels can be presumed where objects cover many resolution cells, as in multilook despeckling in Section 6.4.1, without any significant penalty on the definition of the objects involved. In military applications, high resolution must generally be preserved, so this form of speckle reduction is inadvisable and more sophisticated algorithms are required. In this section we will consider both image quality and execution time and identify a good compromise solution yielding high-quality reconstructions with reasonable execution times. It should be borne in mind that execution speeds will increase as computing technology advances. However, the effect of an initial unsuitable choice of algorithm cannot be subsequently rectified.

6.10.1 Image Quality

As discussed in Section 6.2, image quality can be assessed using a global test for consistency of the data with the speckle model. The ratio of the original intensity to the derived RCS enables us to determine the extent to which the reconstruction filter introduces radiometric distortion so that the reconstruction departs from the expected speckle statistics. In Section 6.2 we showed that the ratio image should consist of uniform speckle with a mean value of 1.0 and no trace of structure associated with the original scene. A series of images of this ratio are shown in Figures 6.9 and 6.10, scaled between values of 0.5 and 1.5. These should appear like a speckle image with a mean corresponding to a mid-gray level, similar to the field regions in the annealed reconstructions in Figure 6.10. The fact that the images in Figures 6.9 and 6.10 clearly have differing mean levels reveals bias in the reconstruction. Further, any trace of structure in the ratio indicates a failure of the reconstruction to be consistent with the speckle model. In addition, the depth of modulation of the speckle in

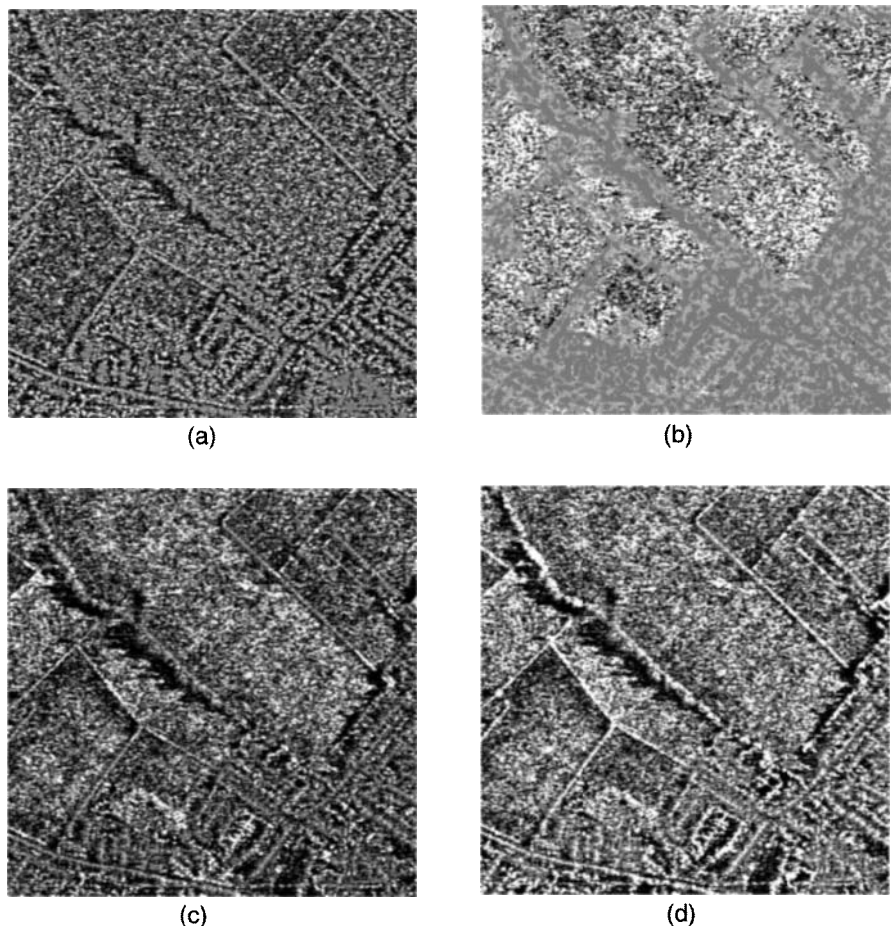


Figure 6.9 Ratio of original image to despeckled reconstruction: (a) Crimmins filter and 200 iterations of (b) gamma MAP, (c) CML, and (d) CMAP.

the ratio image can vary, demonstrating yet another failure of the reconstruction to follow the speckle model. In this comparison we have confined our attention to those algorithms that appear to give a visually satisfactory reconstruction. It is immediately obvious that all fail to yield uncorrelated residual speckle, with the ratio images for CML (Figure 6.9(c)), CMAP (Figure 6.9(d)), and the Crimmins filter (Figure 6.9(a)) showing the greatest depth of modulation by the underlying structure while the annealed reconstructions show considerably less. The ratios for gamma MAP and annealed reconstructions reveal artifacts surrounding any structure in the scene with gamma MAP having the greater spatial extent due to the window size adopted.

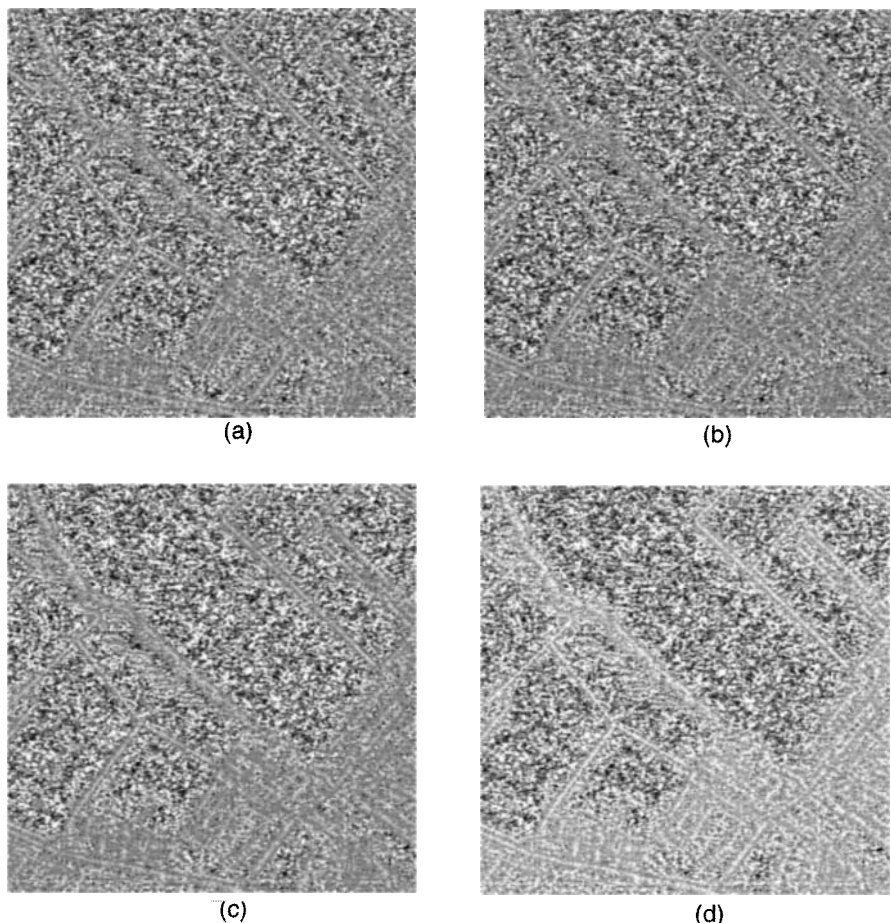


Figure 6.10 Ratio of original image to annealed reconstruction after 200 iterations: constant RCS for (a) ACML and (b) ACMAP, and sloping RCS for (c) ACML and (d) ACMAP.

A numerical comparison of the mean and SD of the intensity ratio over the test image following 200 iterations is listed in Table 6.1. The algorithms have not preserved overall radiometric accuracy because the mean values all differ significantly from 1.0. The original image had 2.2 effective looks, so the expected SD for the intensity ratio image would be 0.674. The bias in the ratio renders it difficult to draw any hard conclusions from the comparison of their SDs. The results suggest that the Crimmins filter follows the intensity too closely, yielding a small value of SD, whereas CMAP appears to smooth the RCS too much, leading to a large value of SD. Other filters appear more consistent with the speckle model.

Table 6.1
 Comparison of Mean and SD for Intensity Ratio Images.
 The expected SD is 0.674

Algorithm	Mean	SD
GMAP	1.270	0.663
Crimmins	0.876	0.575
CML	0.835	0.659
CMAP	1.132	1.144
ACML	1.241	0.648
ACMAP	1.230	0.634
Sloping ACML	1.300	0.666
Sloping ACMAP	1.488	0.727

If we compare these results within separate uniform and structured regions rather than over the whole scene, we find that:

- The bias is approximately independent of scene content and is dominated by the effect of the first iteration; that is, it does not change much as iteration continues. If necessary it can be corrected by scaling the data so that the mean ratio is unity. This is essential for remote sensing applications requiring accurate values of σ^0 .
- The SD in uniform regions is consistent with speckle, whereas in structured regions it is too small. This indicates that the reconstruction of small features is not consistent with the speckle model. This may not necessarily be a disadvantage, however. Most users would prefer small isolated objects to be treated as point targets with $\sigma = I$ (so that the SD is zero) rather than a single realization from a speckle distribution. Structures on an intermediate scale might be expected to require an intermediate value of SD.

6.10.2 Execution Times

Table 6.2 shows comparative timings for several of the reconstruction algorithms obtained over a 512 by 512 pixel image on a Sun Sparc 10 system. Execution times per iteration vary from over 30 sec for the most sophisticated annealing methods to about 4 sec for MMSE. The fastest is MMSE, followed by CML and ACML. Note that the simplest annealing scheme performs each iteration faster than either form of gamma MAP. However, ACML structured annealing typically requires about 50 to 100 iterations to achieve an acceptable

Table 6.2
Execution Times and Speeds for Various Reconstruction Algorithms Applied
to a 512 by 512 Image Using a Sun Sparc 10

Filter Type	Algorithm	Execution Speed (kpixels/s)	Execution Time per Iteration (sec)
Simple	MMSE	66.8	3.9
	Gamma MAP	31.7	8.3
	Structured gamma MAP	9.8	26.6
Correlated neighborhood	CML	50.8	5.2
	CMAP	28.6	9.2
Structured neighborhood (anneal)	ACML: constant RCS	36.3	7.2
	sloping RCS	11.0	23.7
	ACMAP: constant RCS	7.4	35.3
	sloping RCS	7.9	33.0

result, whereas gamma MAP has converged after a few iterations. Thus, ACML requires a total execution time an order of magnitude longer than simple gamma MAP or about three times longer than the structured version.

These timings show that introducing a gamma prior PDF in a MAP reconstruction increases execution time significantly, for example, gamma MAP vs. MMSE, CMAP vs. CML, and ACMAP vs. ACML. The corresponding results for ACML and ACMAP in Figure 6.8 suggest that the most important consideration is whether to adopt the sloping region model to avoid the terracing artifact. This tends to slow down execution, except for ACMAP. Since terracing is only visible after a large number of iterations, it can be ignored in many applications.

6.10.3 Algorithm Selection

We may draw various conclusions about the suitability of the different reconstruction algorithms from this comparison.

With regard to image quality issues discussed in Section 6.10.1:

- Single-stage filters are inadequate; iteration is necessary for effective speckle removal.
- MMSE, CML, and CMAP reconstructions can be rejected because structure is not retained upon iteration.
- The gamma MAP is the best of the nonannealing filters. However, it suffers from artifacts around features. The depth of fluctuation in these

artifacts can be reduced by adopting the structured version, which is therefore preferred. The spatial extent of the artifacts can be reduced by adopting smaller filter windows and performing additional iterations to remove speckle. However, if the window size is reduced too far (e.g., to 3 by 3 pixels), structure tends to be averaged out. A compromise window size of 7 by 7 pixels seems suitable.

- Annealed reconstruction offers still better image quality. The spatial scale and depth of modulation of artifacts is much smaller than from the gamma MAP.
- Introducing further prior knowledge can improve annealed reconstruction. The RCS can be assumed to be gamma-distributed and the MAP solution provided (ACMAP). In addition the sloping RCS model can be employed.

With regard to speed issues discussed in Section 6.10.2:

- Annealed reconstruction (ACML) with constant RCS has an execution time per iteration comparable with the gamma MAP without structure.
- Annealed reconstruction (ACML) with sloping RCS or ACMAP is of comparable speed to the gamma MAP with structure.
- Annealing methods typically require 100 iterations for adequate speckle removal whereas gamma MAP needs about 10. Thus, gamma MAP is about an order of magnitude faster than annealing methods.

This leads to final conclusions:

- If image quality is most important, use annealing with sloping RCS.
- If speed is the overriding consideration, adopt gamma MAP (with structure).
- In either case, the bias introduced in the reconstruction must be corrected to give true RCS values.

6.11 Discussion

This chapter introduced a Bayesian approach to RCS reconstruction. It indicated the advantage of techniques based on annealing, which approximate a global MAP solution. In Section 6.10.1 we quantified image quality in terms of consistency with the speckle model. The most sophisticated reconstruction used a variant of simulated annealing with the structured neighborhood and sloping RCS models. A larger 3-m resolution DRA X-band SAR image near Bedford and its reconstruction using this algorithm are illustrated in Figure 6.11(a,b). The final im-



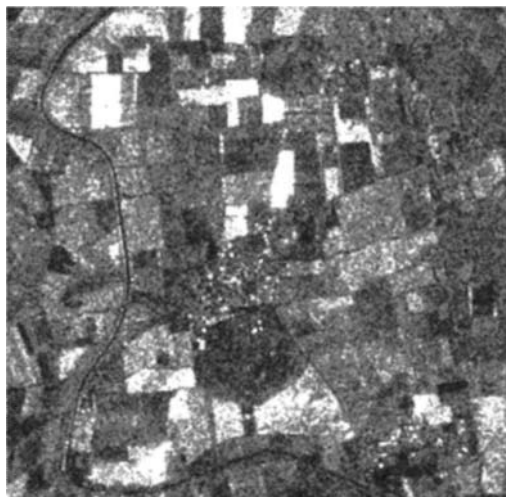
(a)



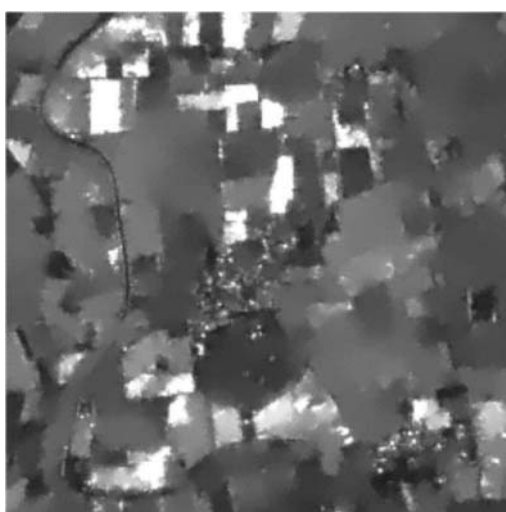
(b)

Figure 6.11 High-resolution (3m) DRA SAR image near Bedford: (a) original image and (b) ACMAP reconstruction using sloping RCS model.

age quality shows little trace of speckle. Clearly this technique presents a very powerful method for removing speckle. By way of contrast, a 24-m resolution ERS-1 PRI image of the Feltwell area in the United Kingdom and its reconstruction are shown in Figure 6.12(a,b). Many of the features that dominated the 3-m resolution image, such as hedges and individual trees, are averaged out, but field



(a)



(b)

Figure 6.12 Low-resolution (24m) ERS-1 SAR image of the Feltwell area: (a) original image (Copyright ESA, 1992) and (b) ACMAP reconstruction using sloping RCS model.

structure shows up quite clearly. It is apparent, however, that the reconstruction in Figure 6.12(b) fails to preserve many of the thin dark features in the original image, such as large sections of the drainage channel and various roads, which are clearly distinguishable to the human observer. The effect is present, though not to so great an extent, in the higher resolution imagery in Figure 6.11. This failure to capture real structure can only be overcome at present by adopting a system resolution with enough pixels at the scale of interest for the filters to respond adequately.

While the theoretical framework of this chapter is essential for a proper understanding of the algorithms, users are principally concerned with selecting the best algorithm for their application. This choice is crucially dependent on the application and differs considerably between (say) a military application concerned with the detection and recognition of small targets and a remote sensing application attempting to classify crops. The former is primarily concerned with structural integrity for recognition purposes, so that bias is less damaging than in remote sensing, which requires accurate RCS estimation. This issue can be highlighted by examining the four small objects visible in the dark field near the bottom left of Figure 6.1. For a military application it would be important that these be clearly reconstructed without any reduction in the SCR in the immediate vicinity. Only iterated ACML and ACMAP with constant or sloping RCS, shown in Figure 6.8, satisfy this requirement. Thus, the other algorithms are probably unsuitable for military applications. On the other hand, most algorithms yield acceptable reconstructions for the RCS of extended clutter away from structure in the scene, once the bias is corrected. Gamma MAP is extensively used in this context [11,12].

References

- [1] Pratt, W. K., *Digital Image Processing*, New York: Wiley, 1978.
- [2] Crimmins, T. R., "Geometric Filter for Reducing Speckle," *Appl. Opt.*, Vol. 24, 1985, pp. 1438–1443.
- [3] Lee, J. S., "A Simple Speckle Smoothing Algorithm for Synthetic Aperture Radar Images," *IEEE Trans. Syst. Man Cybern.*, Vol. 13, 1983, pp. 85–89.
- [4] Caves, R. G., S. Quegan, and R. G. White, "Quantitative Comparison of the Performance of SAR Segmentation Algorithms," *IEEE Trans. Image Proc.*, submitted 1996.
- [5] Lee, J. S., "Digital Image Enhancement and Noise Filtering by Use of Local Statistics," *IEEE Trans. Pattern Anal. Mach. Intell.*, Vol. 2, 1980, pp. 165–168.
- [6] Frost, V. S., J. A. Stiles, K. S. Shanmugan, and J. C. Holtzman, "A Model for Radar Images and Its Application to Adaptive Filtering of Multiplicative Noise," *IEEE Trans. Pattern Anal. Machine Intell.*, Vol. 4, 1982, pp. 157–166.

- [7] Kuan, D. T., A. A. Sawchuk, T. C. Strand, and P. C. Chaval, "Adaptive Restoration of Images with Speckle," *IEEE Trans. Acoust. Speech Signal Process.*, Vol. 35, 1987, pp. 373–383.
- [8] Oliver, C. J., "Review Article—Information from SAR Images," *J. Phys. D: Appl. Phys.*, Vol. 24, 1991, pp. 1493–1514.
- [9] Lopes, A., E. Nezry, R. Touzi, and H. Laur, "Structure Detection and Adaptive Speckle Filtering in SAR Images," *Int. J. Remote Sens.*, Vol. 14, 1993, pp. 1735–1758.
- [10] Lee, J. S., "Refined Filtering of Image Noise Using Local Statistics," *Comp. Graph. Image Proc.*, Vol. 17, 1981, pp. 24–32.
- [11] Le Toan, T., F. Ribbes, L.-F. Wang, N. Flouri, K.-H. Ding, J. A. Kong, M. Fujita, and T. Kuroso, "Rice Crop Mapping and Monitoring Using ERS-1 Data Based on Experiment and Modelling Results," *IEEE Trans. Geosci. Remote Sens.*, Vol. 35, 1997, pp. 41–56.
- [12] Leysen, M. M., J. A. Conway, and A. J. Sieber, "Evaluating Multi-Temporal ERS-1 SAR Data for Tropical Forest Mapping: Regional Mapping and Change Detection Applications," *Proc. of the Second ERS-1 Symposium*, Hamburg, Germany, ESA Vol. SP-361, 1994, pp. 447–452.
- [13] McConnell, I., and C. J. Oliver, "Comparison of Annealing and Iterated Filters for Speckle Reduction in SAR," *Europto Conf. on SAR Image Analysis, Simulation and Modelling*, Taormina, Italy, *SPIE Proc.*, Vol. 2958, 1996, pp. 74–85.
- [14] White, R. G., "Simulated Annealing Applied to Discrete Region Segmentation of SAR Images," DRA Memorandum 4498, 1991.
- [15] White, R. G., "A Simulated Annealing Algorithm for SAR and MTI Image Cross-Section Estimation," *Europto Conf. on SAR Data Processing for Remote Sensing*, Rome, *SPIE Proc.*, Vol. 2316, 1994, pp. 137–147.
- [16] White, R. G., "A Simulated Annealing Algorithm for Radar Cross-Section Estimation and Segmentation," *SPIE Int. Conf. on Applications of Artificial Neural Networks V*, Orlando, FL, *SPIE Proc.*, Vol. 2243, 1994, pp. 231–241.
- [17] Metropolis, N., A. W. Rosenbluth, M. N. Rosenbluth, A. H. Teller, and E. Teller, "Equations of State Calculations by Fast Computing Machines," *J. Chem. Phys.*, Vol. 21, 1953, pp. 1087–1091.
- [18] Geman, S., and D. Geman, "Stochastic Relaxation, Gibbs Distributions and the Bayesian Restoration of Images," *IEEE Trans. Pattern Anal. Mach. Intell.*, Vol. 6, 1984, pp. 721–741.
- [19] Wolberg, G., and T. Pavlidis, "Restoration of Binary Images Using Stochastic Relaxation with Annealing," *Pattern Recog. Lett.*, Vol. 3, 1985, pp. 375–388.
- [20] Kelly, P. A., H. Derin, and K. D. Hartt, "Adaptive Segmentation of Speckled Images Using a Hierarchical Random Field Model," *IEEE Trans. Acoust. Speech Signal Process.*, Vol. 36, 1988, pp. 1628–1641.
- [21] Cvijovic, D., and J. Klinowski, "Taboo Search: an Approach to the Multiple Minima Problem," *Science*, Vol. 267, 1995, pp. 664–666.
- [22] McConnell, I., R. G. White, C. J. Oliver, and R. Cook, "Radar Cross-Section Estimation of SAR Images," *Europto Conf. on SAR Image Analysis, Simulation and Modelling*, Paris, *SPIE Proc.*, Vol. 2584, 1995, pp. 164–175.

7

RCS Classification and Segmentation

7.1 Introduction

In the previous chapter the emphasis was directed toward reconstructing the RCS at each pixel. This was based on exploiting phenomenological models for speckle and RCS combined with a series of world models that introduced constraints into the reconstruction. In this chapter the approach is again based on the product and speckle models but relies on other forms of constraint to derive information. In Section 7.2 we associate each pixel with a particular class, taken from a restricted set representing RCS values. We demonstrate the need to average over many pixels before such classification can be effective, which is only sensible if the boundaries of the averaging window lie within a region of constant RCS in the image. This leads to the cartoon model, described in Section 7.3, and its application in segmentation. Finally, while the principles of these information-extraction techniques may be elegant, most users are primarily concerned with their effectiveness at fulfilling specific image-interpretation functions. Thus, we will consider quantitative image-quality measures for the different algorithms in Section 7.4. In Section 7.5 a discussion of the principles underlying the exploitation of both reconstruction and segmentation is presented.

7.2 RCS Classification

Rather than *estimating* the RCS, as described in the previous chapter, we might attempt to *classify* each pixel in terms of its RCS. Suppose that a restricted set of

possible RCS values is selected and each pixel assigned to the nearest class. Speckle causes uncertainty in this assignment. An optimized classifier for the known speckle model can readily be defined, based on the conditional probability of each RCS class, which is given by (6.5). The log likelihood for L -look SAR therefore has the form

$$\lambda_k = L \ln L - L \ln \sigma_k + (L - 1) \ln I - \ln \Gamma(L) - \frac{LI}{\sigma_k} \quad (7.1)$$

Since L is a known constant for the image, for ML classification we merely need to identify that class k , that maximizes the quantity $-\ln \sigma_k - I/\sigma_k$ for each pixel. Different cross-section classes should be sufficiently separated so that speckle does not cause too many misclassifications. For reasonable error rates, this implies that class spacing should be related to the SD of image intensity, which is σ_k / \sqrt{L} .

An example of this form of ML cross-section classification, applied to the test image in Figure 6.1, is shown in Figure 7.1(a). The image intensity is classified into 12 equally spaced predefined states. It is immediately apparent that the process is dominated by speckle. Upon doubling the spacing so that only 6 states are considered, the result in Figure 7.1(b) is obtained. Even with this coarse quantization, speckle still dominates.

These examples make the point that ML classification based on a single pixel is rendered ineffective by speckle. Under these conditions, the PDF for a

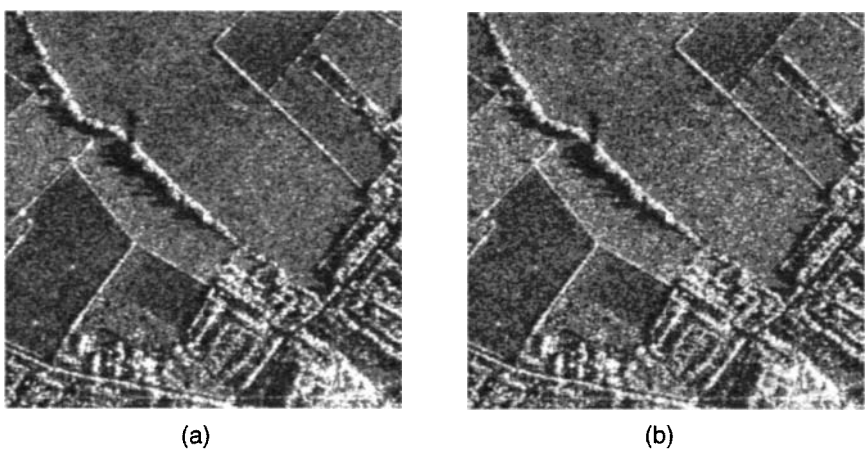


Figure 7.1 ML classification of the individual pixels from Figure 6.1 into RCS values: classified into (a) 12 states and (b) six states, each twice the separation of those in (a).

region of constant RCS extends over a wide range of intensity, so it is mapped into several different classes. Furthermore, any RCS fluctuations that are present tend to be dominated by speckle. Since speckle limits pixel classification, it is reasonable to inquire whether concepts evolved in earlier sections could be relevant. RCS reconstruction was based on exploiting constraints that neighboring pixels were similar. Multilook despeckling introduced this in the form of an average over a window. Though this was unsuccessful in structured regions, it gave satisfactory results in uniform regions. Averaging over neighboring pixels narrows the intensity PDF so that classification may become possible. However, scenes contain structures that may not be aligned with the window defined in this averaging process. It is therefore essential to develop techniques for aligning such averaging windows with image structure. In the next section we consider how this type of approach can yield images that are segmented into regions of the same RCS.

7.3 The Cartoon Model and Segmentation

Segmentation depends upon the introduction of a cartoon model that asserts images are made up of regions, separated by edges, in which some parameter such as the RCS is constant. The number and position of these segments and their mean values are unknown and must be determined from the data. Instead of attempting to reconstruct an estimate of RCS for each pixel, segmentation seeks to overcome speckle by identifying regions of constant RCS. In later sections we show that it provides a powerful tool for image interpretation for two reasons.

1. The cartoon model enables the RCS to be reconstructed without radiometric distortion. This is valuable for pixel-based approaches to information extraction.
2. The structure of the scene should be closely related to the edges found by segmentation that delineate regions of different properties. This offers potential for higher level image interpretation.

Before embarking on a discussion of these approaches, two prerequisites for a successful segmentation algorithm are proposed.

1. All processing must be automatic, with no operator intervention. Only in this way will computation speed be adequate and results reproducible.
2. The algorithm should avoid specific tuning to a particular image. It is permissible to modify a global parameter, such as the false alarm rate

for merging regions or detecting the edge between them, to optimize performance in a given application. Other than that, the algorithm should be capable of accepting any SAR data.

Both these requirements are essential for rapid robust processing. They will only be met when the segmentation process is driven entirely by the data and the theoretical properties of SAR images. Only algorithms that meet these requirements will be discussed here. The examples in this chapter correspond to 2-look high-resolution airborne SAR and lower-resolution 6-look ERS-1 SAR with widely different operating conditions. However, they are processed with identical algorithms and parameter settings.

In principle, segmentation could be addressed as a process of fitting the cartoon model to data with all possible positions of edge, number of regions, and mean value. Such a global fit is feasible in one dimension [1]. However, attempting to follow the same approach with two-dimensional scenes results in a vast computation task, so we resort initially to heuristic methods that have the aim of identifying regions in an image without actually trying every possible configuration [2].

We can be faced with conflicting requirements in segmentation. It is sometimes important to preserve resolution as far as possible, particularly in the military context. Other applications may wish to identify regions that differ by only a small change in RCS. The interplay between these requirements is evident when we consider some previous approaches to segmentation. Many were inadequate for segmenting single-look SAR, so the speckle was first reduced by smoothing. However, smoothing should not precede segmentation but be incorporated into the process [3]. If smoothing does precede segmentation, algorithms can be ineffective either because too small an averaging window leads to inadequate speckle reduction [4] or because an overlarge window yields degraded resolution [5]. The difficulty stems from the adoption of a single-scale smoothing algorithm rather than an adaptive filter of varying region size [6]. High-intensity differences, such as those from targets, can potentially be detected over small regions; whereas low-intensity differences, important in remote sensing applications, require averaging over large regions to attain adequate sensitivity. The conflict between the different requirements is resolved in an adaptive algorithm. This commences with small filters for small-object detection; filter size then increases progressively to give improved sensitivity, at the cost of resolution. In this manner any uniform region is detected at the highest resolution at which sensitivity is adequate.

Three basic classes of segmentation algorithm can be identified that exploit the cartoon model in different ways, namely: edge detection (discussed in Section 7.3.1), region merging (Section 7.3.2), and fitting (Section 7.3.5). In

Section 7.3.3, ML edge detectors are derived for inclusion into segmentation schemes; their implementation is discussed in Section 7.3.4.

7.3.1 Edge Detection

If a scene is made up of uniform regions, a segmentation technique can be based on identifying the presence and position of the edges between these regions. Edge detection algorithms can be subdivided into generic signal-processing techniques or others that exploit both the properties of SAR and the cartoon model specifically. The former category would include edge detectors such as Sobel [7]. Such methods are best suited to low additive-noise scenarios and are totally inappropriate for single-look SAR [8,9].

Frost et al. [8] proposed a hypothesis test to establish whether there was an edge between two different classes at the center of a small window (e.g., 9 by 9 pixels). The problem with such a specific hypothesis is that it might be inappropriate for the actual data, so resulting edge detections are invalid. For example, the test would be inappropriate if more than two regions existed within the window. However, by incorporating the adaptive filter size specified earlier, the problem can be reduced considerably. This form of hypothesis test forms the background for many recent segmentation schemes.

An edge-detection algorithm (RGW) was proposed by White [10,11] that exploited the cartoon model and included adaptive filter size, as illustrated in Figure 7.2(a). Initially the edges within an image are detected. Regions are then grown between these edges. The second stage is not allowed to remove any previous edges, so the first stage is crucial. The process is iterated until some convergence criterion is met, when the current form of the segmentation is output.

The edge-detection stage in RGW proceeds as follows.

1. A series of rectangular windows, varying in size from 3 by 1 to 57 by 13, is constructed around each pixel.
2. The average intensity in each half (\bar{A} and \bar{B}) is calculated.
3. If $|\bar{A} - \bar{B}| > \text{threshold} \times \text{standard error of mean difference}$ then an edge is recorded at the center of the window.

An important feature of this algorithm is that edge-detection criterion (3.) is not based on the standard error within the window but over the regions that the window overlaps. Initially the entire scene is regarded as a single region. As segmentation progresses and segments begin to correspond to regions of constant RCS, edge detection is determined by speckle statistics alone. Note that

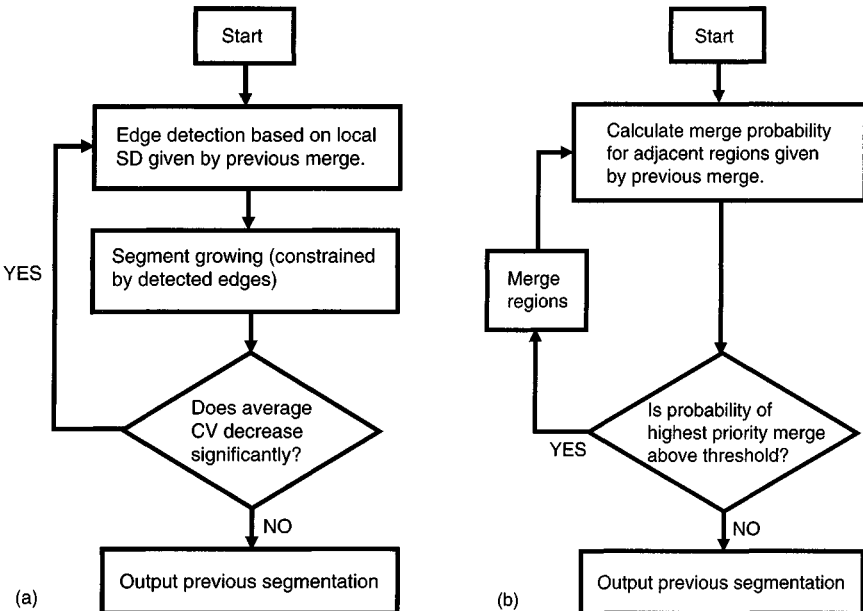


Figure 7.2 Flow diagram for model-based segmentation algorithms: (a) RGW and (b) merge using moments.

bright edges are detected with the smallest masks that are used first, that is, at high resolution. These edges are retained and the pixels excluded from successive stages of edge detection. Weak edges are subsequently detected with larger windows. Thus, the algorithm adapts its resolution to signal strength.

The region-growing stage of the algorithm proceeds as follows.

1. A series of disks is laid on the image so as not to contain any detected edges.
2. Adjacent disks are merged to form larger regions.

Initially disks are large; subsequently, the size of the disks being added is reduced and the same process is repeated. Eventually, every pixel is assigned to a particular region and a complete region map constructed. The full cycle is then repeated, yielding more sensitive edge detection. Iteration continues until the overall coefficient of variation (SD/mean) reaches some preset threshold related to the speckle statistics.

RGW was found to operate more successfully on amplitude rather than intensity images. The result of applying RGW model-based segmentation to Figure 7.3(a) is illustrated in Figure 7.3(b). Here, and throughout the chapter,

each segment is shown with each pixel set to the mean intensity of the segment as calculated from the original pixel values. Figure 7.3(b) contains a large number of small regions. These result from the choice of threshold, which is related to the detection probability and is the only user-selected variable for the process. However, some segments are probably anomalies arising from flaws in the algorithm.

Section 7.3.3 will describe how sensitivity could be improved by introducing an ML hypothesis test for the presence of an edge within the window, based on the speckle and cartoon models. This section will also demonstrate that RGW segmentation is not optimized for the most accurate choice of edge position and will propose a corresponding ML solution.

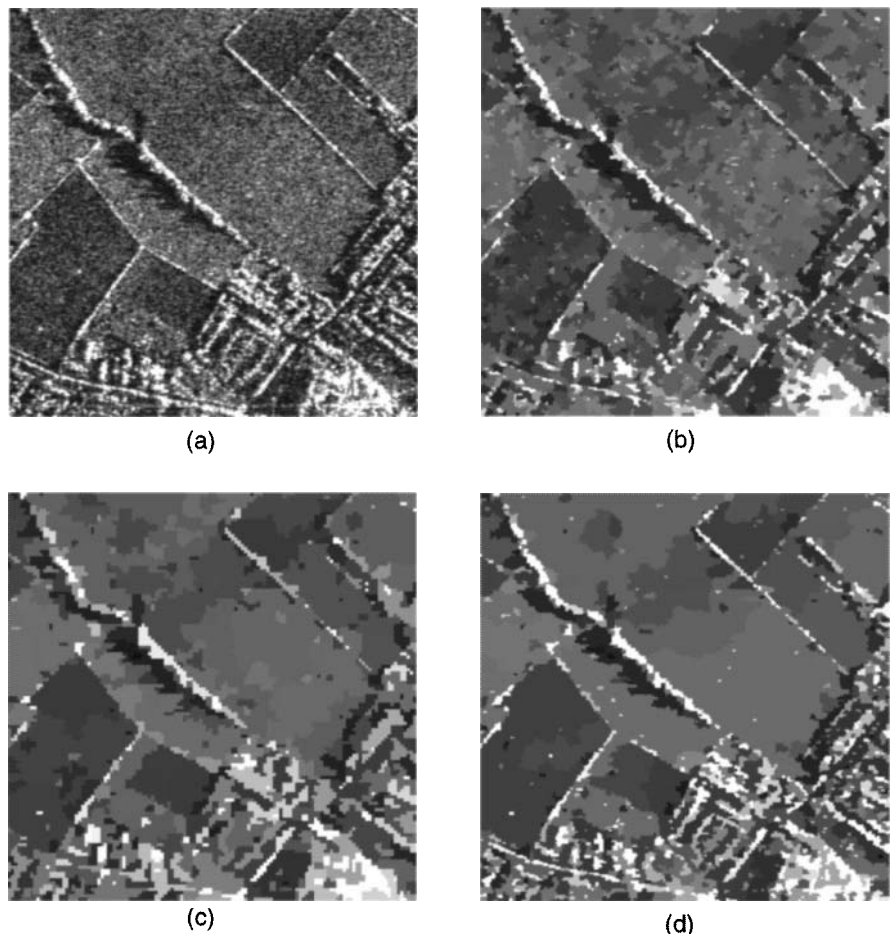


Figure 7.3 Comparison of segmentation methods: (a) original image, (b) RGW, (c) Gaussian MUM, and (d) optimized MUM.

7.3.2 Region Merging

Region merging exploits the cartoon model more directly and attempts to grow large uniform regions by merging neighboring small regions (which might comprise only a single pixel). The crucial issue is whether the decision to merge is reliable, which depends on the statistical criterion adopted to control merging. In fact, an identical criterion can be used to describe both splitting and merging [12,13]. One implementation of merging, *merge using moments* (MUM) [14,15], is based on the Student t test. The sequence of operations, illustrated in Figure 7.2(b), can be summarized as follows.

1. Initialize by subdividing the image into arbitrary small regions, for example, a 2 by 2 or single-pixel grid.
2. For each pair of adjacent subregions A and B calculate the pooled variance defined by

$$\text{var}\{A + B\} = \frac{N_A \text{ var } A + N_B \text{ var } B}{N_A + N_B - 2} \left(\frac{1}{N_A} + \frac{1}{N_B} \right) \quad (7.2)$$

where $\text{var } A$, $\text{var } B$, and $\text{var}\{A + B\}$ are the variances and N_A and N_B are the number of pixels in each region, respectively.

3. Calculate the normalized difference $t \equiv |\bar{A} - \bar{B}| / \sqrt{\text{var}\{A + B\}}$ and apply the Student t test for $N_A + N_B - 2$ degrees of freedom to the data. This evaluates the probability that A and B should be merged.
4. Compile a list in order of priority for merging all pairs of adjacent subregions.
5. Merge the highest priority region and repeat operation for new subregions.

The process is iterated until the false alarm probability for failing to merge a constant region reaches some preset value. Thus, this algorithm has the desirable property that operator controls are restricted to a single parameter, as with RGW. The result of applying MUM to Figure 7.3(a), starting from a 2 by 2 pixel tessellation, is shown in Figure 7.3(c). The effect of the coarse initial tessellation is evident. However, the number of anomalous small regions seems to be lower than with RGW. A more rigorous comparison of segmentation methods can be found in Section 7.7.1.

The Student t test is only rigorous when distinguishing between regions with Gaussian PDFs, which is clearly inappropriate for speckle. Significant performance improvement is possible through an ML derivation using the correct statistics, given in Section 7.3.3.

7.3.3 ML Split/Merge Theory

Both splitting and merging depend on estimating whether two regions belong to the same population or not. In this section we derive an ML test to determine this, given SAR speckle statistics. In fact, there is more than one possible criterion for which the test could be optimized. Either the edge-detection probability in RGW or the merge probability in MUM is maximized or the edge-position accuracy is optimized. We derive the ML estimators for both cases and demonstrate the type of improvement they yield if introduced into existing algorithms.

Let us assume that we retain adaptive window sizes. The cartoon model implies that a window should contain either a single uniform region or two uniform regions with an edge at some unknown position within that window. (Any other possibility will have been eliminated by detecting an edge in an earlier, smaller window). The joint probability of these two states can be expressed in terms of the conditional probability $P(I|\sigma)$ for each. Let us assume that pixels 1 to k are in region A with RCS σ_A , while pixels $k + 1$ to M are in region B with RCS σ_B . We consider a single dimension for simplicity. The results for two dimensions can be easily obtained. The joint probability for the whole window, given single-look intensity I_j at pixel j , is given by

$$\begin{aligned} P_{A,B}(\sigma_A, \sigma_B | I_j, k) &\propto \prod_{j=1}^k P_A(I_j | \sigma_A) \prod_{j=k+1}^M P_B(I_j | \sigma_B) \\ &= \prod_{j=1}^k \frac{1}{\sigma_A} \exp\left[-\frac{I_j}{\sigma_A}\right] \prod_{j=k+1}^M \frac{1}{\sigma_B} \exp\left[-\frac{I_j}{\sigma_B}\right] \end{aligned} \quad (7.3)$$

The probability that the data are consistent with a merged region of mean RCS σ_0 has the same form with $\sigma_A = \sigma_B = \sigma_0$. The log likelihood for split and merged states, $\lambda_{\text{split}}(k)$ and λ_{merge} , can be derived by taking logs of these joint probabilities and a log difference estimator defined such that

$$\begin{aligned} \lambda_D(k) &\equiv \lambda_{\text{split}}(k) - \lambda_{\text{merge}} \\ &= -k \left(\ln \sigma_A + \frac{\bar{I}_A}{\sigma_A} \right) - (M-k) \left(\ln \sigma_B + \frac{\bar{I}_B}{\sigma_B} \right) \\ &\quad + M \left(\ln \sigma_0 + \frac{\bar{I}_0}{\sigma_0} \right) \end{aligned} \quad (7.4)$$

where the mean intensities are estimated over the appropriate windows. The ML estimates of RCS in each region are $\sigma_A = \bar{I}_A$, $\sigma_B = \bar{I}_B$, and $\sigma_0 = \bar{I}_0$. Note

that $\overline{I_A}$ and $\overline{I_B}$ are functions of k , so that the MLE for edge position k is obtained by maximizing [15,16]

$$\lambda_D(k) = -k \ln \overline{I_A} - (M - k) \ln \overline{I_B} + M \ln \overline{I_0} \quad (7.5)$$

An analysis of edge-detection performance based on this likelihood difference, expressed in terms of detection and false alarm probabilities, requires knowledge of its PDF, which is not directly available. However, we shall demonstrate an equivalent formalism based on the intensity ratio defined by $r \equiv \overline{I_A}/\overline{I_B}$. The PDF of r can be shown to be [16,17]

$$P_r(r|R, k, M - k) = \frac{\Gamma(M)}{r \Gamma(k) \Gamma(M - k)} \left\{ \frac{\left(\frac{rk}{R(M - k)} \right)^k}{\left(1 + \frac{rk}{R(M - k)} \right)^M} \right\} \quad (7.6)$$

where R denotes the true ratio of mean values. If an edge is “detected” when r is outside the range $[t_1, t_2]$, the detection probability at position k , given that the true edge is at this position, is given by

$$\begin{aligned} P_d &= 1 - \int_{t_1}^{t_2} P(r) dr \\ &= 1 - \frac{\Gamma(M)}{k(M - k) \Gamma(k) \Gamma(M - k)} \left(\frac{k}{(M - k)R} \right)^k \\ &\quad \times \left\{ {}_2F_1 \left[k, M; k + 1; -\frac{kt_2}{(M - k)R} \right] \right. \\ &\quad \left. - {}_2F_1 \left[k, M; k + 1; -\frac{kt_1}{(M - k)R} \right] \right\} \end{aligned} \quad (7.7)$$

where ${}_2F_1[\cdot]$ is the Hypergeometric function [18]. The false alarm probability P_{fa} corresponds to substituting $R = 1$ into (7.7). The threshold values t_1 and t_2 lie above and below 1 and can be related to the equivalent value of λ_D , which can be derived from (7.5). Hence,

$$\lambda_D(k) = -k \ln t_1 - M \ln M + M \ln[M - k + kt_1] \quad \text{for } t_1 < 1$$

and

$$\lambda_D(k) = k \ln t_2 - M \ln M + M \ln \left[M - k + \frac{k}{t_2} \right] \text{ for } t_2 > 1 \quad (7.8)$$

When the edge is at the center of the window, $k = M/2$ and these combine to the same threshold. This corresponds to the ratio detector proposed by Touzi et al. [19] and Bovik [20], which is given by $r_T \equiv \min[r, 1/r]$. Equivalent numerical solutions for detection probability at other edge positions can also be performed [16].

The equivalence of r_T and r when the test edge is in the center of the window is confirmed by a comparison of the detection probabilities for the ML measure and Touzi ratio as a function of edge position, shown in Figure 7.4. The two regions in these simulations have means of 1 and 8, and the results were obtained over 10^4 samples. At the center both give identical detection probability, while the Touzi ratio is suboptimum elsewhere. The simulated results were also compared with predicted values, showing close agreement [16]. Since the Student t test was employed in the original version of MUM (in Section 7.3.2), we include simulations based on this for comparison. It is apparent that adopting a Gaussian rather than the correct gamma PDF for speckle leads to performance degradation.

This derivation accounts for different numbers of pixels in the two regions and incorporates speckle statistics correctly. It can therefore be used directly in place of the Student t test in the MUM segmentation scheme.

As mentioned earlier, there are two distinct criteria that can be applied to edge detection. The first relates to the accuracy with which edge position is determined and is described by (7.5) and the results of Figure 7.4. The associated filter geometry would be to fix a window position with respect to the scene and scan the test edge, which will be called the *fixed window, scanned edge* (FWSE) configuration. Figure 7.4 demonstrates that the detection probability at a given position is maximized when the central edge in this window is aligned with an edge in the RCS. This suggests that another useful edge-detection geometry would be to scan a window with a fixed central test edge over the data, which will be called the *scanned window, center edge* (SWCE) configuration. Note that SWCE is equivalent to the Touzi ratio test [19].

However, the results of Figure 7.4 depend on knowing the actual edge position in advance. In a real application this would not be the case and the algorithm would determine both the presence and position of any edge. The FWSE window is placed at some arbitrary position in the scene and the test edge scanned. SWCE, on the other hand, scans the window over the scene. In each

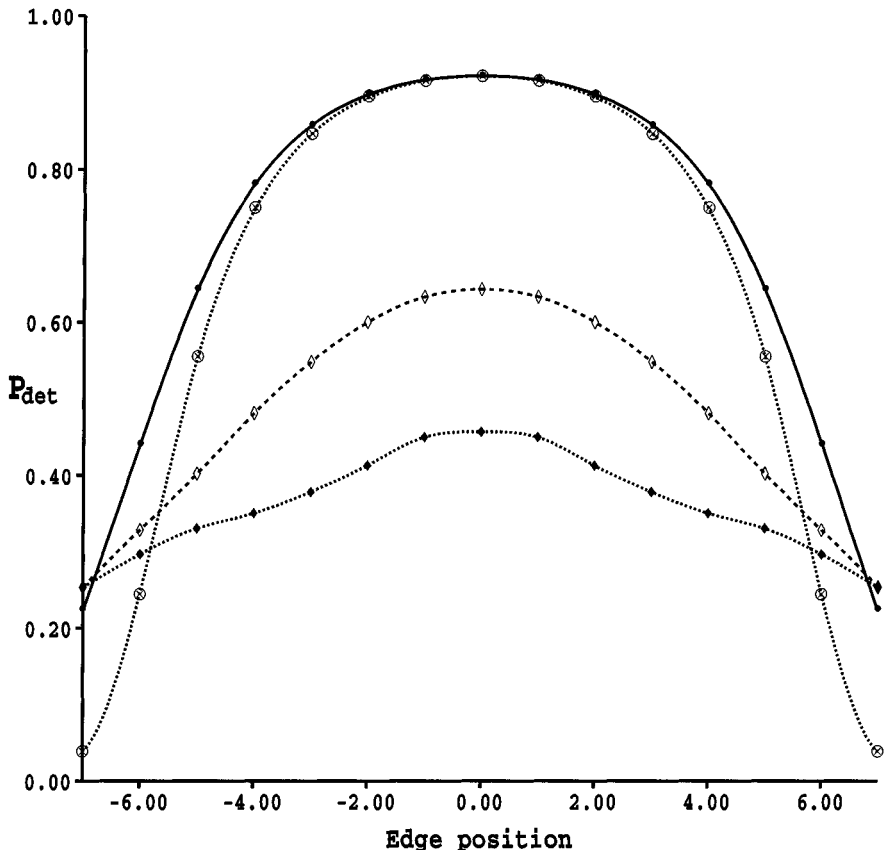


Figure 7.4 The dependence of detection probability on edge position. ML, simulation (●) and prediction (full line); Touzi ratio, simulation (○) and prediction (dotted line); Student *t* measures, simulation only (◊ amplitude, ◆ intensity), joined by smooth curves for clarity.

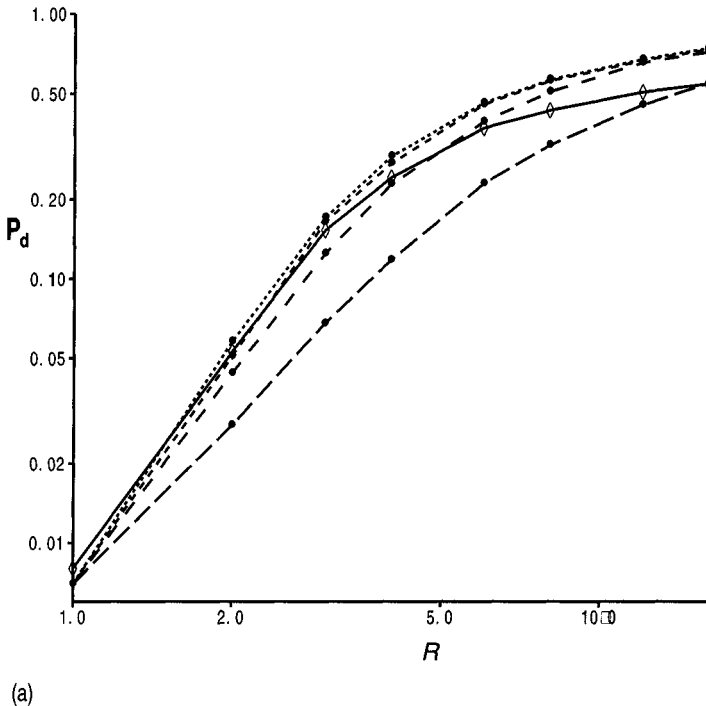
case, the position of greatest likelihood denotes the edge location. The response at this position is then compared with an appropriate threshold to detect whether it is significant, yielding a probability P_d that an edge is detected in the correct position. It is also important to consider whether an edge is detected anywhere in the window, not necessarily in the correct position. This is described by the sum of all the individual values of P_d over the window and is denoted by P_{tot} . We would expect this to be maximized by the SWCE test. However, neither P_d nor P_{tot} can be derived analytically if the edge position is not known and we have to resort to simulation to compare the window configurations [16].

In Figure 7.5(a) we illustrate a comparison of P_d for the two configurations. A 16 by 1 window is used with the ratio of mean values varying between 1 and 16. Offsets of 0, ± 2 , ± 4 , and ± 6 pixels between the true edge position and the center of the window are simulated for FWSE. Alternatively, SWCE scans over the same simulated data. FWSE yields higher values of P_d for small offsets (< 4), whereas SWCE is preferable for larger offsets. Figure 7.5(b) shows the corresponding comparison for P_{tot} . This shows that SWCE always yields greater overall detection probability, as expected from Figure 7.4.

The choice of which configuration to adopt depends on the application. SWCE yields a higher probability of detecting edges in the scene. However, they are less likely to be in the correct position than with FWSE. In order to maximize both performance measures, a two-stage configuration has been proposed [16]. In the first stage the SWCE configuration is applied to optimize P_{tot} . The approximate edge position derived from this defines the fixed window position for FWSE. The edge position is then refined, leading to an improved value for P_d . Provided that the edge position derived in SWCE is mainly within the central half of the fixed window for the second stage, this joint test was shown by simulation [16] to yield optimum results for both performance measures at the expense of slightly increased execution time.

7.3.4 Implementation of ML Split/Merge Theory

The derivation of Section 7.3.3 provides a theoretical framework for ML edge detection, which specifically incorporates the speckle and cartoon models. Let us now inquire whether the proposed window configurations can be incorporated into the existing RGW and MUM segmentation schemes. There is no choice of window configuration in MUM; the regions to be tested are a consequence of the previous merge history. It is only possible to apply the ML merge criterion in (7.6) directly to these existing regions, with consequent improved segmentation performance, as illustrated in Figure 7.3(d) [17], which should be compared with the result for Gaussian MUM in Figure 7.3(c). The new measure provides a more accurate segmentation, containing more detail than the original test. In particular, note that it is able to commence from a single-pixel grid since it is inherently more sensitive. RGW, however, already depends on scanning windows and is designed to handle edges in both dimensions. It is comparatively simple to substitute the optimized split criterion in the existing SWCE mode, which optimizes P_{tot} , followed by edge refinement using the FWSE configuration, which optimizes P_d . This should result in near ML performance for both edge-position accuracy and total-detection probability, suggesting that a modified version of RGW should outperform the improved version of MUM. However, this has not yet been implemented.



(a)

Figure 7.5 Dependence of (a) P_d and (b) P_{tot} on configuration, difference in RCS, and original edge position. Window 16 by 1 pixels; $R = 1, \dots, 16$; overall $P_{\text{fa}} = 10\%$; 10^4 samples. SWCE configuration (full line, \diamond); FWSE configuration (dashed line, \bullet , offsets 0, 2, 4, and 6 pixels with increasing dash length).

7.3.5 Region Fitting

An alternative approach to segmentation can be derived by considering the global problem of segmenting an image into q regions of constant RCS. Assuming a correct segmentation and that the speckle model applies, so that each region is gamma distributed, the log likelihood, or cost, of this configuration is given by a generalization of (7.5), namely [21],

$$\lambda = \sum_{j=1}^q N_j \ln \bar{I}_j \quad (7.9)$$

where N_j and \bar{I}_j are the size and estimated RCS of the j th region, respectively. The segmentation process then corresponds to identifying the MLE for each region position and RCS. As such it is a standard global optimization problem

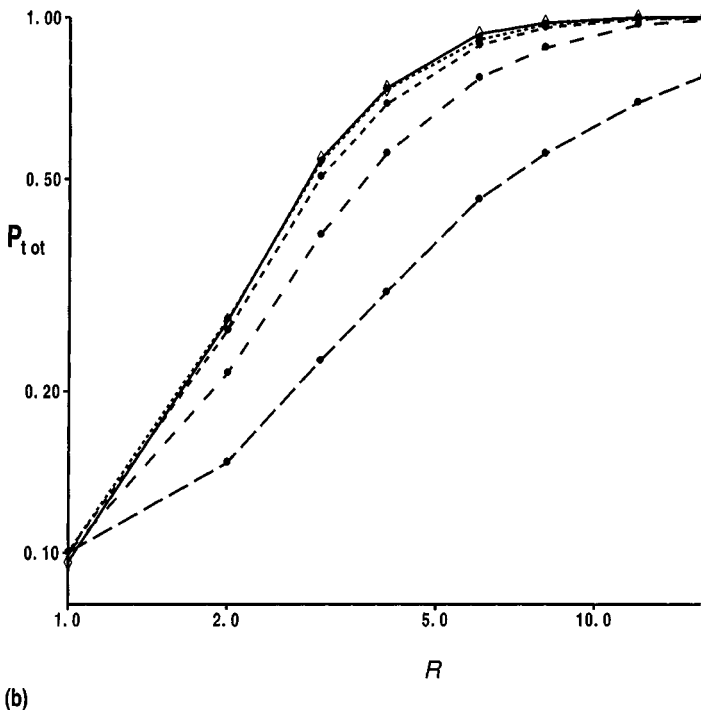


Figure 7.5 (continued).

[22] that can be addressed by simulated annealing as in Section 6.9 by substituting $W \equiv \lambda$ in (6.29).

A flow diagram for the algorithm is shown in Figure 7.6. This form of simulated annealing operates by modifying the boundaries and, hence, the mean values within the q regions. Thus initialization consists of performing some initial segmentation, which is then refined. Notice in the flow diagram that the final stage of the algorithm comprises a stage for merging adjacent regions to some preset value of P_{fa} . Thus, the initial segmentation should generate too many regions that can later be reduced by merging. The initial segmentation is implemented by performing a random square tessellation of the original image with greater region density where the scene has higher contrast. The main simulation loop is then comprised of the following stages:

1. An edge pixel is selected at random, and a temporary change of configuration is made by moving it into an adjoining region.
2. The change in log likelihood is calculated and the standard simulated

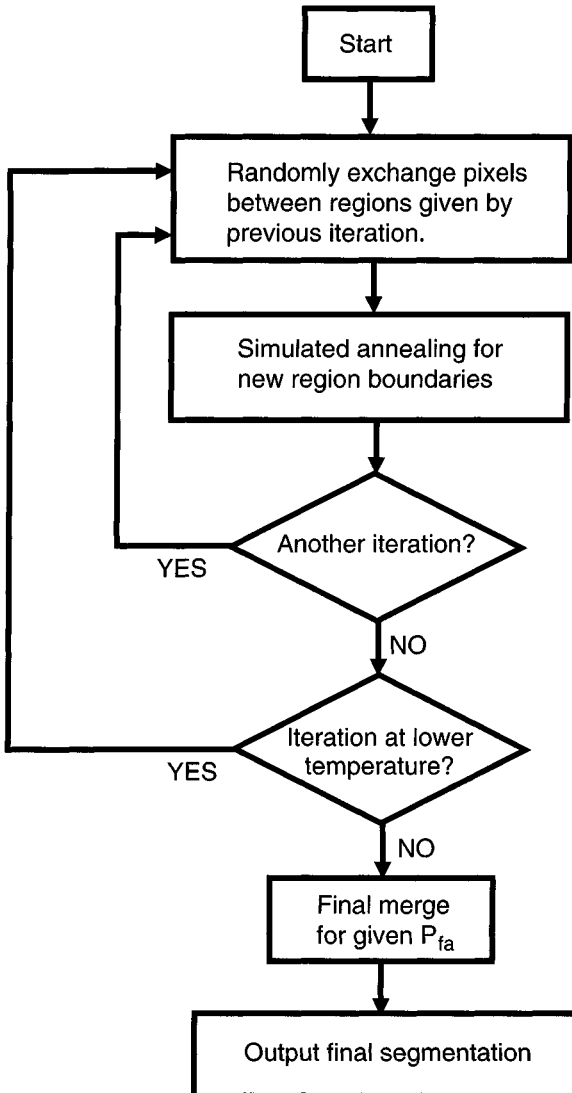


Figure 7.6 Flow diagram for annealed segmentation.

annealing acceptance criterion with temperature T implemented to decide whether to accept or reject the move.

3. The random choice of pixels is repeated for a fixed number of iterations.
4. The annealing temperature is then reduced and the process repeated. The process is terminated after a preset number of iterations.

5. Once the annealing stages have been completed, a final merge is performed for adjacent regions, determined by the false alarm probability P_{fa} , for merging regions of the same RCS.

In the absence of any shape constraint, this approach will tend to separate the image into regions of bright and dark speckle if convergence is unconstrained. This problem is overcome by introducing a curvature penalty term, analogous to surface tension, into the objective function in (6.29), which penalizes irregular shapes. This additional contribution to the objective function is defined by

$$W_S \equiv \sum_i \sum_{j \in N_i} \chi (1 - \delta(f_i - f_j)) \quad (7.10)$$

where f_i denotes the segment label for pixel i , N_i is a set of neighboring pixels (say 8), χ is a constant weighting coefficient, and δ is the Kronecker delta. Hence, if pixels i and j do not have the same segment label, W_S is incremented by χ . Empirically a value of $\chi = 0.05$ seems to offer acceptable edge smoothing and is used in all the examples of annealed RCS segmentation shown.

We illustrate the effect of this term in Figure 7.7. Figure 7.7(a) shows the result of applying the simulated annealing algorithm without the curvature penalty term. The false alarm probability was set at 10^{-5} , which resulted in 1,000 regions being identified. Upon introducing the curvature penalty, the number of regions was reduced to 832 with a segmentation as shown in Figure 7.7(b). The complicated edge structure in Figure 7.7(a), caused by following the

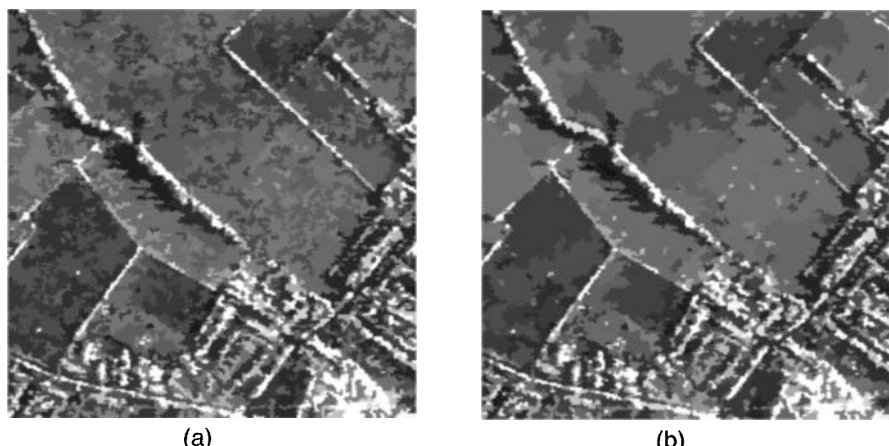


Figure 7.7 Comparison of simulated annealing (a) without and (b) with curvature penalty.

bright and dark speckle, is largely removed in Figure 7.7(b). Small objects appear reasonably well preserved and large areas of constant RCS have been identified, compared with the other segmentation techniques illustrated in Figure 7.3.

In common with other simulated annealing implementations, there are a variety of parameters that have to be determined, such as starting temperature, number of inner loop iterations, cooling schedule, and number of outer loop iterations. In addition, there are questions over the initial tessellation stage that determine both the position and number of initial regions. In principle, simulated annealing will migrate regions to those areas of the image that have a larger density of objects. However, this may involve an excessive number of iterations. Thus, it is advisable to ensure that the original tessellation assigns segments suitably with greater density in regions of high contrast, as noted earlier.

7.4 Comparison of Segmentation Algorithms

Algorithms can be compared in terms of image quality and execution time in the same way as the reconstruction filters in the previous chapter.

7.4.1 Image Quality

A visual assessment of image quality again provides a useful indication of where algorithms fail. As in Chapter 6 we need to check for effective speckle reduction in uniform regions, good feature preservation, and the absence of artifacts. Radiometric preservation is assessed by the quantitative test using the ratio of the original image to its reconstruction as in Section 6.10.1. Once again we will base our visual comparison on features such as the four small objects in the field near the bottom left of the image and some of the weaker hedges between fields.

Different segmented versions of Figure 7.3(a) are illustrated in Figure 7.8. RGW and the original annealing [23–25] segmentation is applied to the amplitude image, whereas optimized MUM and SGAN process the intensity. In Figure 7.8 (a,c,d) the parameters controlling the algorithm were selected to yield a similar number of segments, around 650. Figure 7.8(a) reveals that RGW with only 653 segments fails to provide a visually satisfactory segmentation. It finds three of the four small objects but loses a large number of hedge sections. In addition, it treats a large fraction of the built-up area at the bottom right as a single segment. Small objects and hedges are better preserved in the original implementation in Figures 7.3(b) and 7.8(b), with 2,409 segments. However, this result contains a large number of “flecks” that are almost certainly artifacts, and the buildings again fall predominantly into a single segment. MUM and SGAN, in Figure 7.8(c,d), with 662 and 674 segments, respectively, seem to give similar,

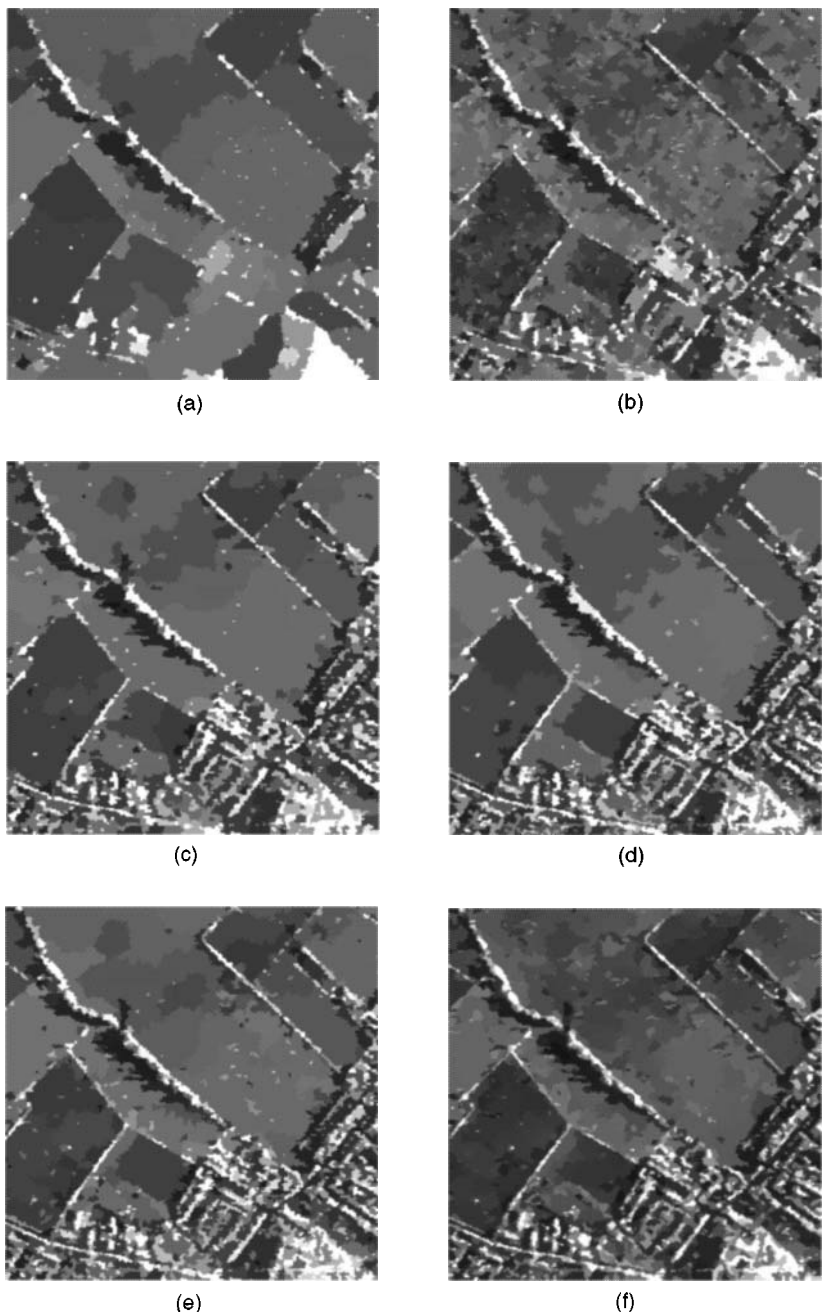


Figure 7.8 Segmented reconstructions of Figure 7.3(a): (a) RGW (653 segments), (b) RGW (2,409 segments; also shown as Figure 7.3(b)), (c) optimized MUM (662 segments; also shown as Figure 7.3(d)), (d) SGAN (674 segments), (e) SGAN (2,389 segments), and (f) original anneal (5,027 segments).

greatly improved, reconstruction quality. There is no evidence of speckle breaking uniform regions into segments, as in Figure 7.8(b). Both techniques reconstruct the hedges and their shadows similarly. In addition, buildings are represented by a large number of segments. However, there are detailed differences in the reconstructions of the four test objects at the bottom left. MUM (c) retains the four expected ones and introduces a fifth, alongside the center of the objects to the right. SGAN (d) includes this fifth object but fails to preserve the fourth object at the top left of the original set. This difference arises from the detailed difference between the heuristics of the *local* MUM operation and *global* SGAN. Upon reducing the threshold level in SGAN so that 2,389 segments are found, as illustrated in Figure 7.8(e), we observe that these same five objects are found. However, additional segments are also detected, which may represent genuine objects or false alarms due to speckle. If Figure 7.8(e) is compared with 7.8(b), which shows the RGW result with approximately the same number of regions, we note that SGAN does not generate “flecks” but concentrates segments in regions with much structure, such as the buildings on the bottom right. Visually, therefore, this algorithm yields a more desirable type of segmentation than RGW.

We observe that the original annealed segmentation [23–25], shown in Figure 7.8(f), contains a large number of segments. Some of these appear to correspond to bright or dark flecks caused by speckle. This suggests that the threshold should be raised to reduce the number of segments. However, even with the original settings, the algorithm fails to reproduce the four objects in the field on the bottom left of the image. Thus, it yields false segments while failing to detect genuine objects. It has therefore been superseded by the more recent version (SGAN) that is optimized for the true speckle statistics.

Without prior knowledge of the true scene content, we cannot make any absolute distinction between the performance of these algorithms. The comparison so far indicates that the original RGW algorithm seems incapable of providing an adequate reconstruction with the same number of regions as MUM or SGAN, suggesting that there is a number of misplaced regions in RGW. Incorporating the optimized split and merge criterion could yield a significant improvement, however. It is probably not the filter architecture that is inadequate but the edge test.

The corresponding ratios of the original image to the segmented versions in Figure 7.8(a–d) are shown in Figure 7.9, plotted over the range 0.5 to 1.5. A visual inspection provides insight into segmentation quality. For a perfect segmentation, the ratio image should appear to be made up of pure speckle. Any sign of structure indicates a failure of the algorithm. It is apparent that RGW with the small number of segments, in Figure 7.9(a), has large departures from pure speckle in regions with structure, such as the hedges and, particularly, the buildings on the bottom left. Even increasing the number of regions still leaves strong evidence of unwanted structure (Figure 7.9(b)). These effects are much

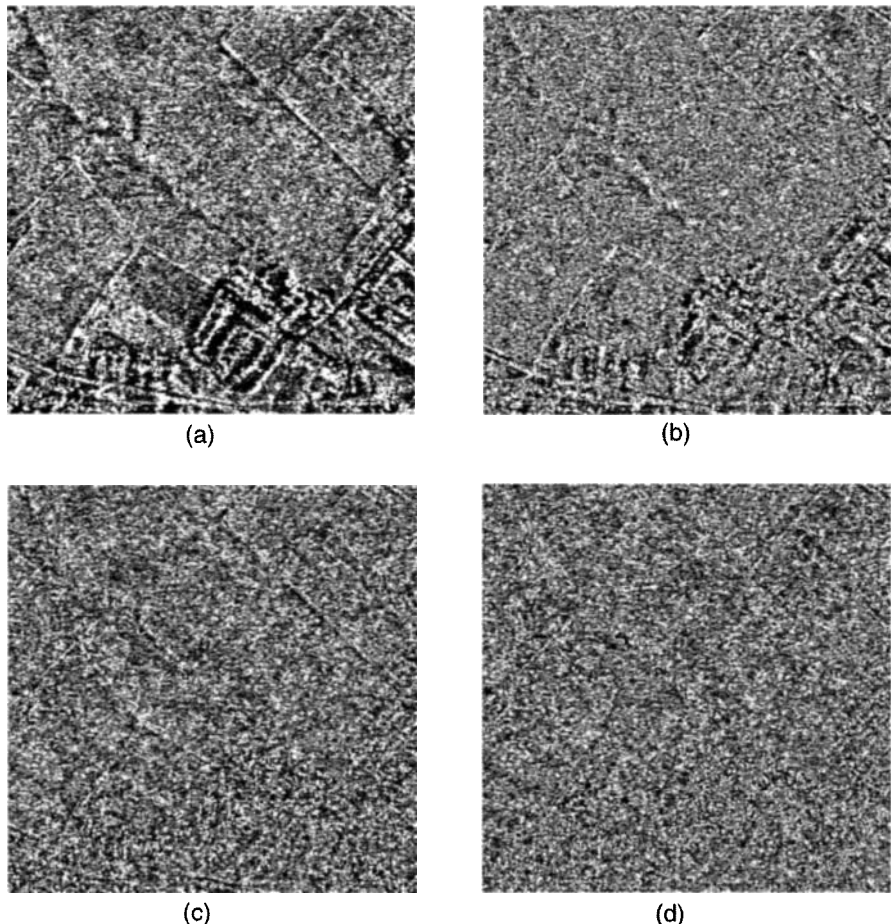


Figure 7.9 Ratio of original image in Figure 7.3(a) to corresponding segmented versions in Figure 7.8 (a–d).

reduced by the optimized MUM segmentation, as shown in Figure 7.9(c); while SGAN yields even less evidence of excess fluctuations (Figure 7.9(d)).

An additional constraint is present when the ratio test is applied to segmentation, since the cartoon model asserts that the RCS is constant over each segment. The estimated cross section within any segment is defined as the local average, unlike the reconstruction filters considered in Chapter 6. Under these conditions, the rigorous theory [26], which accounts for the fact that both the cross section and the ratio are estimated in each segment, can be applied. The mean value of the ratio is unity, by construction, while its variance will be given by

$$\text{var } r = \frac{1}{N - 1} \sum_{j=1}^m \frac{n_j}{L + \frac{1}{n_j}} \quad (7.11)$$

if the segments really consist of uniform regions, where N is the image size, m the number of segments, and n_j the number of pixels in the j th segment. Note that the bias in the variance introduced for a small region can be quite large compared with $1/L$. On the other hand, this contribution makes comparatively little difference to the sum over the whole image that is dominated by the larger regions. In this example, $N = 65536$, $m \approx 660$, $n_j \approx 99$, and $L \approx 2.2$. Substituting these values into (7.11) suggests that the SD of the intensity ratio should be 0.672 instead of the value of 0.674 for the corresponding test in Section 6.10.1. Thus, the estimation correction tends to reduce the observed SD of the ratio slightly. The observed values of SD are much greater than the uncorrected predictions and so we will ignore the correction. It would, of course, be important to retain if making a detailed study of the estimated SD in individual small segments.

Note that a segmentation can fail for two reasons: either the value of σ within a segment is incorrect or an edge between regions of different σ is not recognized or wrongly placed. Both will yield excess values of SD, and it is not possible to differentiate between these causes of failure using this ratio test.

The numerical values of the image quality measure are listed in Table 7.1. Segmentation yields a mean ratio of 1 since every pixel in the segmented scene is assigned the average value over the appropriate segment. Thus, segmentation preserves radiometric accuracy completely, unlike the reconstruction filters. For $L \approx 2.2$ the predicted (uncorrected) SD for pure speckle would be 0.674 for intensity and 0.345 for amplitude. It is clear that SGAN yields results consistent with pure speckle; MUM is slightly worse; but RGW requires many more segments to approach the speckle prediction. Even with 2,409 segments it still gives a considerably larger fractional discrepancy than MUM. Thus, image

Table 7.1
Ratio Measures for Segmentation of the DRA 3-m SAR Image.

Algorithm	Number of Segments	Mean	SD
RGW*	653	1	0.518
RGW*	2,409	1	0.390
MUM	662	1	0.708
SGAN	674	1	0.670

Note: Amplitude segmentation denoted by *; other methods use intensity.

quality considerations suggest that either MUM or SGAN should be used in preference to the present version of RGW.

7.4.2 Execution Times

Table 7.2 shows comparative timings for the three segmentation methods. As an initial comparison we observe that RGW provides the fastest execution time with SGAN the slowest for small images. However, as image size increases SGAN eventually becomes faster than MUM and only a factor of three slower than RGW. Taking 512 by 512 pixels as a standard image size, we note that SGAN is a factor of seven slower than RGW. If we compare SGAN with the structured annealing reconstruction algorithms in Chapter 6, we find that SGAN takes 3.3 times longer than 100 iterations of ACML with constant RCS. The other structured annealing reconstruction techniques are somewhat more time consuming than SGAN.

7.4.3 Algorithm Selection

From this comparison of image quality and execution time we can make the following deductions:

- The present version of RGW yields unacceptable image quality unless excessive numbers of regions are adopted.
- RGW is the fastest algorithm.
- MUM provides reasonable image quality but is slower than RGW. It is preferable to RGW from quality considerations.
- SGAN provides the best image quality but is slowest. It should be used in preference to MUM when image quality is crucial.

Table 7.2

Execution Time (seconds) for the Three Different Segmentation Algorithms as a Function of Image Size (Measurements taken on Sun Sparc 10)

Algorithm	Image Size				
	64 × 64	128 × 128	256 × 256	512 × 512	1,024 × 736
RGW	2.2	15.1	87.4	351.6	1,334.2
MUM	3.6	20.3	134.4	933.8	5,645.0
SGAN	24.8	119.5	515.2	2,388.9	4,043.7

As a final demonstration, we illustrate annealed segmentations of Figures 6.11(a) and 6.12(a) in Figure 7.10(a,b), respectively. The threshold setting for Figure 7.10(a) is identical to that used in Figure 7.8(e). These results can be compared with the equivalent annealed reconstructions shown in Figures 6.12(b) and 6.13(b). In both examples, the segmented image seems to show more detail than the annealed reconstruction. For example, if we compare reconstructions of the dark field just below the center right in Figures 7.10(a) and 6.11(b), it is apparent that segmentation has recovered more objects. Similarly, in the Feltwell scene, the segmentation algorithm has been more successful at reconstructing thin dark features, such as the drainage channel in Figure 7.10(b), than the annealed reconstruction in Figure 6.12(b). However, neither method appears as successful as a human operator at following the course of the drainage channel or the roads in Figure 6.12(a). Methods that specifically search for features such as long thin structures may be the correct way to proceed [27].

7.5 RCS Exploitation

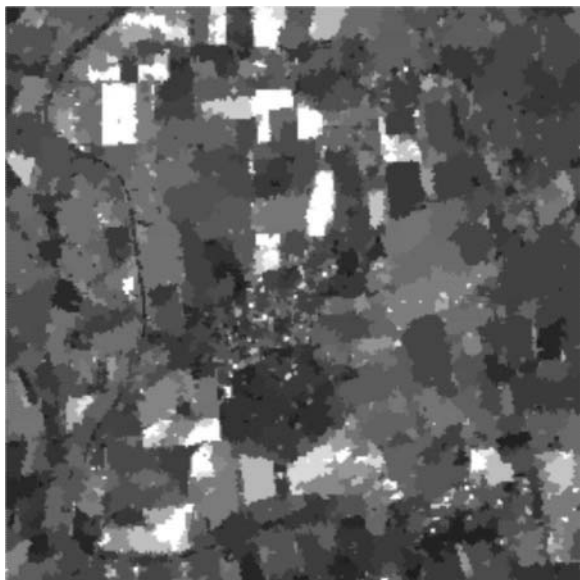
Chapters 6 and 7 introduced a fundamentally Bayesian approach to RCS reconstruction and intensity segmentation. They provided a global MAP solution to both problems that could be most suitably implemented with techniques based on annealing. While this conceptual framework is essential for a proper understanding of the algorithms, users are principally concerned with knowing which algorithm to adopt to solve their particular problem. In this section we attempt to derive some guidelines to aid in this process. In Section 7.5.1 we summarize the behavior of both reconstruction filters and segmentation algorithms, identify the types of information they each generate, and select the most suitable implementation of each type. However, it must be appreciated that the entire discussion is crucially dependent on the application itself. This includes both the properties of the image and, importantly, the category of information required by the application. In Section 7.5.2, therefore, we discuss a possible application example as a means of focusing the discussion. We identify the type of information the user wishes to derive from the data and how it might be contained in it. We draw conclusions about the best choice of algorithm based on quantitative radiometric image-quality comparison and indicate how the quality of the structural information might be assessed.

7.5.1 Algorithm Properties

Figure 7.11 shows a flow diagram for the selection of the most suitable algorithm for RCS exploitation. Let us first summarize what information is gener-



(a)



(b)

Figure 7.10 Annealed segmentation applied to (a) high-resolution DRA image of Figure 6.11(a) and (b) low-resolution ERS-1 image of Figure 6.12(a).

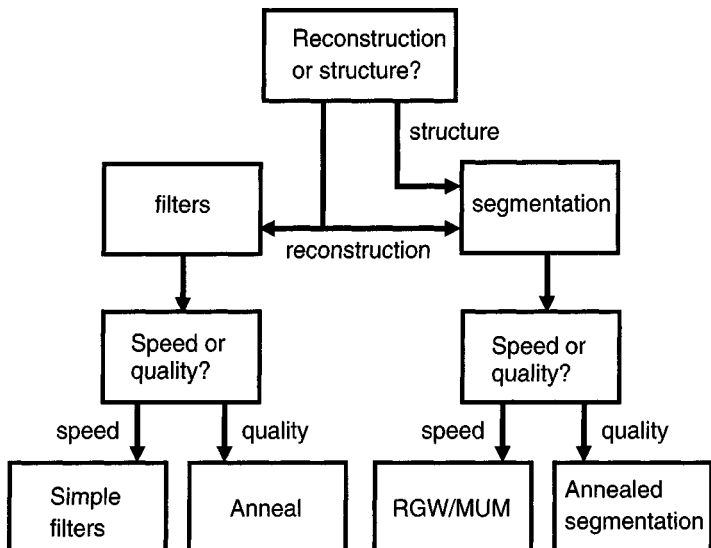


Figure 7.11 Flow diagram for selection of algorithms for RCS exploitation.

ated by the reconstruction filters, described in Chapter 6, and the segmentation techniques discussed in this chapter. Reconstruction provides estimates of the RCS at every pixel, depending on the constraints introduced as models into the MLE. Segmentation, on the other hand, performs a dual role. It provides another form of RCS estimate, subject to the cartoon model, but also contains structural information from knowledge of the edges between the segments it has identified. In terms of Figure 7.11, applications that require knowledge of the RCS on a pixel-by-pixel basis could use either approach. If the information is expected to reside in region structure, then segmentation must be employed.

The high quality of the RCS reconstructions suggests that it might be possible to perform effective segmentation on these output images rather than as one would for optical images. Qualitatively this is correct. The problem resides in the choice of the criterion for recognizing an edge. This depends on the original speckle and the size of the region over which the estimate of RCS has been obtained. If this information were retained, in addition to the reconstructed image, it should be possible to devise post-reconstruction segmentation rigorously based on the image properties. However, since this would depend on identical criteria to those adopted in the direct segmentation algorithms, it is difficult to see that it can offer any advantage.

Whichever class of algorithm is selected, it is important to identify a suitable compromise between the quality of reconstruction and the speed of execution. Annealing methods result in higher quality but longer execution times. However,

the annealing filter ACML appears to be a suitable compromise for a reconstruction filter. MUM seems a reasonable compromise for segmentation, though SGAN is only a factor of 2.5 slower (over a 512 by 512 scene) with improved image quality. The choice of algorithm will depend on the application, which will determine the level of speckle reduction required to achieve the desired exploitation result. It also depends on the computing power available. It is ineffective to perform sophisticated analysis if results only appear after a deadline for using the information has expired. If a simpler algorithm is capable of providing the necessary information, it should be adopted. On the one hand, several applications in remote sensing, such as ice-floe monitoring, can be handled satisfactorily with comparatively simple filters. On the other hand, there is little value in producing a rapid output that cannot contain the necessary information due to inadequate speckle reduction. If both speed and sophistication are required for an application, it may be essential to provide more computing power.

7.5.2 Application Example

As an informative example, we will consider the problem of identifying and classifying fields in the ERS-1 PRI image introduced in Figure 6.12(a). Results for annealed reconstruction and segmentation of this image are shown in Figures 6.12(b) and 7.10(b), respectively, as the “best” implementation of each approach. The type of information required might then be the boundaries of all the fields, together with values for the RCS within each field. Ideally this information should be contained in the SAR image. However, there is no guarantee that information required by the user actually corresponds to a change in RCS that can be observed in the SAR image. For example, a hedgerow would probably be represented by the user as a single line delineating the boundary between two fields. The corresponding SAR image will contain bright returns, with associated shadows, due to the trees and bushes in the hedge, with weaker scattering in between. Thus, continuous features in a map data base may be broken up in an SAR image.

The principles underlying the selection of the best implementation can be summarized as follows:

- Both reconstruction filters and segmentation can be used for RCS estimation.
- Segmentation yields ML estimates of RCS for every size of region.
- With reconstruction filters, large regions will be given the correct value of RCS after the bias is removed; however, small regions will not (see Section 6.10.1).
- Thus, σ^0 measurements over extended regions of uniform clutter from

both methods are reliable, but only segmentation offers accurate values of RCS for a small object.

- In addition, segmentation provides structural information through the edge maps it constructs.

In many applications ancillary information about the scene is available, such as the position of field boundaries. The normal procedure is then to average over each field to derive σ^0 . However, this suffers from two weaknesses.

- σ^0 may not be constant over the field, caused by crop variability, ground slope change, or varying soil moisture, for example. Many applications wish to determine whether this is the case. Both RCS reconstruction and segmentation provide an optimum smoothed reconstruction of σ^0 as a function of position.
- The map from which the boundaries are derived may be incorrect. The edge maps generated by segmentation offer the potential for identifying such changes and therefore updating the map.

This discussion indicates that segmentation is potentially the most useful technique for extracting information from SAR images because it is radiometrically undistorted over the entire image and includes important additional information about the position of edges. The increase by a factor of about three in processing time is probably not a serious penalty.

Let us now address the issue of the image quality achieved in the segmentation of the ERS-1 Feltwell scene from Figure 6.12(a). In Figure 7.12 we compare RCS reconstructions generated by RGW, MUM, and SGAN. A visual comparison indicates that the scene appears to be adequately represented by MUM (809 segments) and SGAN (827 segments). Many of the general field structures seem to be common to all reconstructions. However, the RGW segmentation (805 segments), in Figure 7.12(a), completely fails to reconstruct the drainage channel on the left of the image or the buildings in Feltwell village in the center, as well as other buildings on the bottom right. Upon increasing the number of segments in RGW to 2,305, the results in Figure 7.12(b) show more evidence of the drainage channel as well as reconstructing some of the buildings. However, the quality of reconstruction in both MUM and SGAN reconstructions, in Figure 7.12(c,d), respectively, still appears appreciably better.

The quality of the reconstructions is also indicated by the measure defined in Section 6.2 as summarized in Table 7.3. The effective number of looks for the data was found to be 6.0, leading to predicted SDs of 0.206 and 0.408 for amplitude and intensity data, respectively. The correction implied by the rigor-

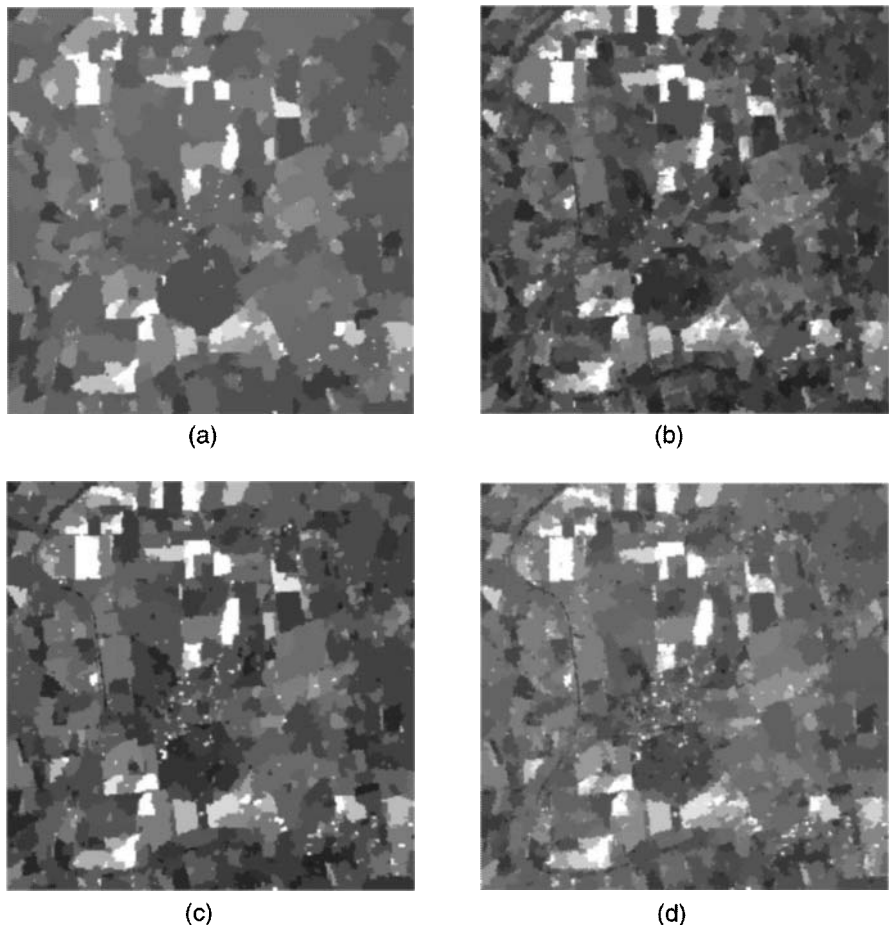


Figure 7.12 Comparison of the RCS reconstructions achieved when different segmentation algorithms are applied to Figure 6.12(a): (a) RGW (805 segments), (b) RGW (2,305 segments), (c) MUM (809 segments), and (d) SGAN (827 segments).

ous theory [26] can again be neglected. In common with the earlier segmentations on higher resolution data (see Table 7.1) SGAN appears closest to consistency with the speckle model.

If the information required is contained in the edge maps, then it is instructive to inquire whether the different segmentation routines would yield a similar ordering of effectiveness from the point of view of edge structure. Edge maps generated by RGW, MUM, and SGAN are shown in Figure 7.13. One indication of the relative quality can be obtained by following the drainage

Table 7.3
Ratio Measures for ERS1 Feltwell Image

Algorithm	Number of Segments	Mean	SD
RGW*	805	1	0.305
RGW*	2,305	1	0.248
MUM	809	1	0.458
SGAN	827	1	0.409

Note: Amplitude segmentation denoted by *; other methods use intensity.

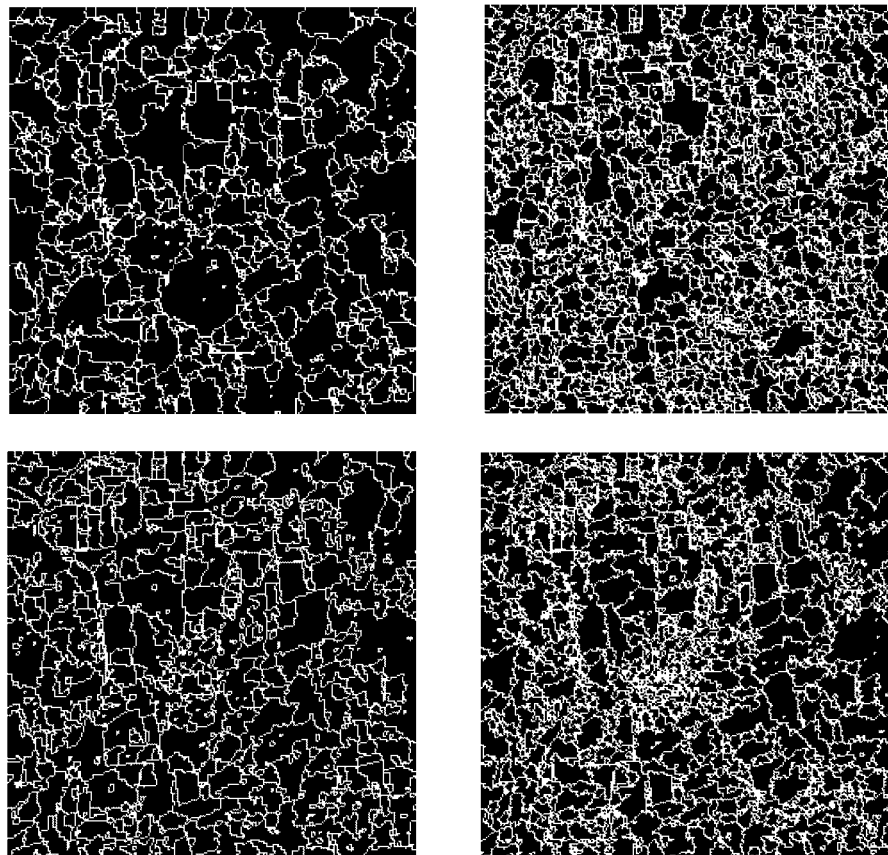


Figure 7.13 Comparison of the edge maps corresponding to the segmentations of Figure 7.12.

channel on the left. Only in SGAN is its presence evident over most of its course. If we reject RGW, we observe that the details of the edge maps generated by MUM and SGAN differ considerably, even though they give similar global quality measures. SGAN appears to contain more small segments. Since the total number of segments is similar, this indicates that it must also contain more large ones. The impression is that these images contain more edges than the user would like. Since these reconstructions are consistent with both speckle and cartoon models, these excess edges are due to real features in the scene, implying that a high-level scene description in terms of, for example, field boundaries, overrides or rejects information present in the image. It is also possible to see real features in the original image that have been lost in these reconstructions, in particular some of the long, thin, dark features, such as roads and the drainage channel. The human observer is obviously capable of exploiting additional forms of prior knowledge about possible feature types, such as long, thin lines. No equivalent capability is currently available for segmentation, though an approach based on simulated annealing has been recently reported [27].

In the absence of ground truth it is impossible to make quantitative statements about the quality of the edge maps generated by segmentation routines. This type of consideration can be dealt with by designing a suite of tests [26,28] to measure the response of different algorithms to important features for the application. These might be long, thin structures or small targets, for example. If the user's requirements could be adequately represented, this test suite could be used to optimize the response of the different algorithms. This is an area that requires considerable future development if the requirements of different applications are to be represented in a quantifiable fashion.

References

- [1] Delves, L. M., R. T. McQuillan, and C. J. Oliver, "A One-Dimensional Despeckling Algorithm for SAR Images," *Inverse Problems*, Vol. 4, 1988, pp. 471–484.
- [2] Delves, L. M., R. T. McQuillan, R. Wilkinson, J. B. E. Sandys-Renton, and C. J. Oliver, "A Two-Dimensional Segmentation Algorithm for SAR Images," *Inverse Problems*, Vol. 7, 1991, pp. 203–220.
- [3] Freitag, B. J., B. Guindon, A. J. Sieber, and D. G. Goodenough, "Enhancement of High Resolution SAR Imagery by Adaptive Filtering," *Int. Geoscience Remote Sensing Symp., IGARSS '83*, Paris: ESA, 1983.
- [4] Oddy, C. J., and A. J. Rye, "Segmentation of SAR Images Using a Local Similarity Rule," *Pattern Recog. Lett.*, Vol. 1, 1983, pp. 443–449.
- [5] Ali, S. M., and R. E. Burge, "New Automatic Techniques for Smoothing and Segmenting SAR Images," *Signal Process.*, Vol. 14, 1988, pp. 335–346.

- [6] Rosenfeld, A., and M. Thurston, "Edge and Curve Detection for Visual Scene Analysis," *IEEE Trans. Computers*, Vol. 20, 1971, pp. 562–569.
- [7] Abdou, I. E., and W. K. Pratt, "Quantitative Design and Evaluation of Enhancement/Thresholding Edge Detectors," *Proc. IEEE*, Vol. 67, 1979, pp. 753–763.
- [8] Frost, V. S., K. S. Shanmugan, and J. C. Holtzman, "Edge Detection for Synthetic Aperture Radar and Other Noisy Images," *Int. Geoscience and Remote Sensing Symp., IGARSS '82*, Paris: ESA, 1982.
- [9] Grimsom, W. E. L., and T. Pavlidis, "Discontinuity Detection for Visual Surface Reconstruction," *Comp. Vision Graphics Image Proc.*, Vol. 30, 1985, pp. 316–330.
- [10] White, R. G., "Low Level Segmentation of Noisy Imagery," DRA Memorandum 3900, 1986.
- [11] White, R. G., "Change Detection in SAR Imagery," *Int. J. Remote Sensing*, Vol. 12, 1991, pp. 339–360.
- [12] Horowitz, S. L., and T. Pavlidis, "Picture Segmentation by a Tree Traversal Algorithm," *J. ACM*, Vol. 17, 1976, pp. 368–388.
- [13] Gerbrands, J. J., and E. Backer, "Split and Merge Segmentation of SLAR Imagery: Segmentation Consistency," *IEEE 7th Int. Conf. Pattern Recognition*, Vol. 1, 1984, pp. 284–286.
- [14] Cook, R., and J. B. E. Sandys-Renton, "A Parallel Segmentation Algorithm (Merge Using Moments) for SAR Images," *Appls. of Transputers*, Vol. 1, 1991, pp. 311–316.
- [15] Cook, R., I. McConnell, and C. J. Oliver, "MUM (Merge Using Moments) Segmentation for SAR Images," *Europto Conf. on SAR Data Processing for Remote Sensing*, Rome, *SPIE Proc.*, Vol. 2316, 1994, pp. 92–103.
- [16] Oliver, C. J., D. Blacknell, and R. G. White, "Optimum Edge Detection in SAR," *IEE Proc. Radar Sonar Navig.*, Vol. 143, 1996, pp. 31–40.
- [17] Oliver, C. J., I. McConnell, D. Blacknell, and R. G. White, "Optimum Edge Detection in SAR," *Europto Conf. on SAR Image Analysis, Simulation and Modelling*, Paris, *SPIE Proc.*, Vol. 2584, 1995, pp. 152–163.
- [18] Abramowitz, M., and I. A. Stegun, *Handbook of Mathematical Functions*, New York: Dover, 1970, Section 15.1.
- [19] Touzi, R., A. Lopes, and P. Bousquet, "A Statistical and Geometrical Edge Detector for SAR Images," *IEEE Trans. Geosci. Remote Sens.*, Vol. 26, 1988, pp. 764–773.
- [20] Bovik, A. C., "On Detecting Edges in Speckled Imagery," *IEEE Trans. Acoust. Speech Signal Process.*, Vol. 36, 1988, pp. 1618–1627.
- [21] Cook, R., I. McConnell, D. Stewart, and C. J. Oliver, "Segmentation and Simulated Annealing," *Europto Conf. on SAR Image Analysis, Simulation and Modelling II*, Taormina, Italy, *SPIE Proc.*, Vol. 2958, 1996, pp. 30–37.
- [22] Geman, S., and D. Geman, "Stochastic Relaxation, Gibbs Distributions and the Bayesian Restoration of Images," *IEEE Trans. Pattern Anal. Mach. Intell.*, Vol. 6, 1984, pp. 721–741.
- [23] White, R. G., "Simulated Annealing Applied to Discrete Region Segmentation of SAR Images," DRA Memorandum 4498, 1991.
- [24] White, R. G., "A Simulated Annealing Algorithm for SAR and MTI Image Cross-Section Estimation," *Europto Conf. on SAR Data Processing for Remote Sensing*, Rome, *SPIE Proc.*, Vol. 2316, 1994, pp. 137–147.

- [25] White, R. G., "A Simulated Annealing Algorithm for Radar Cross-Section Estimation and Segmentation," *SPIE Int. Conf. on Applications of Artificial Networks V*, Orlando, FL, *SPIE Proc.*, Vol. 2243, 1994, pp. 231–241.
- [26] Caves, R. S., S. Quegan, and R. G. White, "Quantitative Comparison of the Performance of SAR Segmentation Algorithms," *IEEE Trans. Image Proc.*, submitted 1996.
- [27] Hellwich, O., "Line Extraction from Synthetic Aperture Radar Scenes Using a Markov Random Field Model," *Europto Conf. on SAR Image Analysis, Simulation and Modelling II*, Taormina, Italy, *SPIE Proc.*, Vol. 2958, 1996, pp. 107–113.
- [28] Delves, L. M., R. Wilkinson, C. J. Oliver, and R. G. White, "Comparing the Performance of SAR Image Segmentation Algorithms," *Int. J. Remote Sensing*, Vol. 13, 1992, pp. 2121–2149.

8

Texture Exploitation

8.1 Introduction

Techniques for removing speckle from SAR images and deriving the RCS were described in Chapters 6 and 7. Information is then carried at the single-pixel level. However, this is not the only type of information contained in a SAR image. We illustrate this in Figure 8.1 with an example of airborne SAR imagery from the Tapajos region of the Amazon rain forest, obtained with the CCRS C-band system, as part of the SAREX program [1–3]. These 6-m resolution, 5-look data were obtained with illumination from the right at an incidence angle of about 60 degrees. A highway runs diagonally from top right to bottom left. The region to the left of this is comprised of primary forest; while that to the right is made up of a mixture of primary forest, secondary forest, and clearings with pasture and crops.

Suppose that the remote sensing task is to distinguish those regions that correspond to primary forest from secondary forest and clearings. It is apparent that the radar return in this image falls into two categories. One, corresponding to secondary forest and clearings, has no fluctuations above those expected for 5-look speckle. This is caused by the fact that vegetation is sufficiently dense and uniform so that the RCS is effectively constant. The other, corresponding to primary forest, has appreciable excess fluctuations caused by tall trees penetrating the canopy and resulting in bright tree crowns with associated shadow. Visually, it appears that there is no relevant information in the mean RCS. Some regions of primary forest have a larger RCS than the secondary forest and clearings; others have a smaller value. This follows from the fact that both

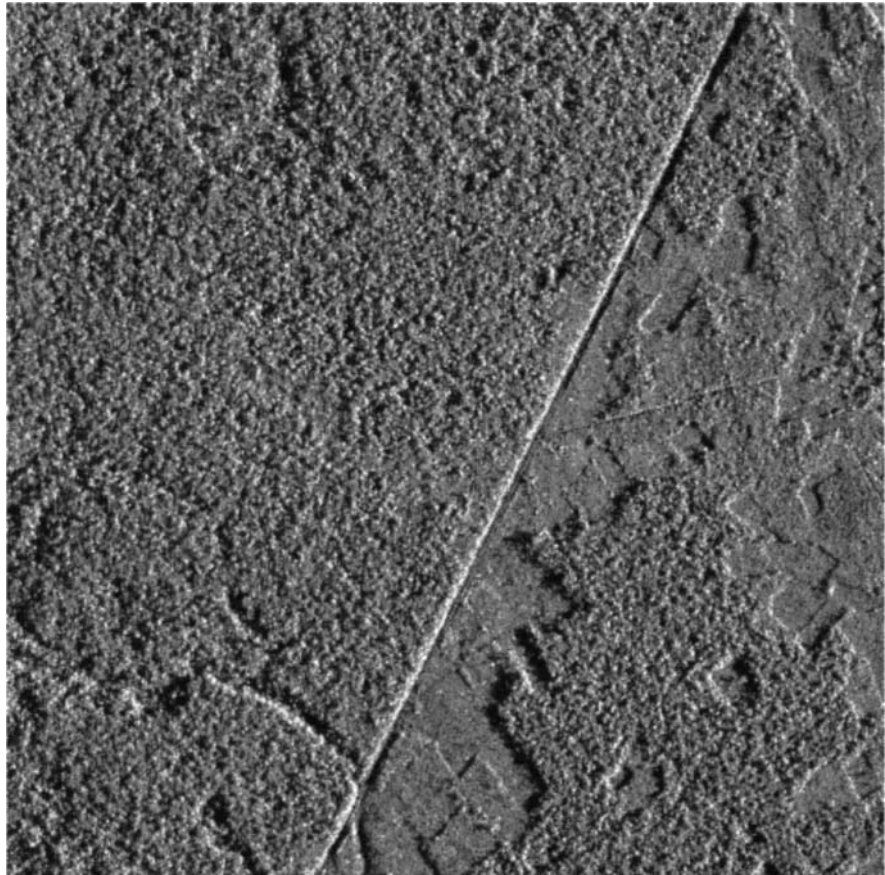


Figure 8.1 SAREX image of part of the Amazon rain forest in the Tapajos region.

returns correspond to wet vegetation canopies with essentially the same water content, having the same RCS at the 6-cm wavelength used. Thus, the information required to discriminate between the two clutter types resides in image texture. This cannot be estimated from a single pixel but requires a finite window to characterize local statistics. The situation is further complicated if the texture is correlated, as we will show in Chapter 9.

We demonstrated in Chapter 5 that clutter textures could be described by the normalized variance. Thus, single-point texture statistics can be utilized as a means of characterizing clutter in image interpretation. This chapter is concerned with establishing optimum means for extracting and exploiting this textural information.

In Section 8.2 we discuss how texture information can be derived without any knowledge of the data distribution. However, where prior knowledge of the form of PDF is available, it should be exploited. Model-based texture parameter estimation is discussed in Section 8.3. ML texture estimators for various forms of PDF are derived in Section 8.3.1, leading to texture measures that can be used in texture characterization. Assuming that clutter textures are actually K-distributed, the associated statistical uncertainty in the estimation of the order parameter for the different measures is derived in Section 8.3.2. The normalized log measure is then exploited in a texture analysis of rain forest data in Section 8.3.3. The issue of texture classification into regions of different parameter values is addressed in Section 8.4. Section 8.5 provides an analysis and discussion of techniques for optimum texture segmentation. Finally, we compare the quality and speed of algorithms for texture exploitation in Section 8.6.

8.2 Model-Free Texture Exploitation

It is not possible to select texture measures that optimize the information content without a specific model for the data. However, suboptimal results can be obtained with noncommittal approaches. For example, the K-S test, introduced in Section 8.2.1, compares the CDF of two data sets. Alternatively, moments of the data PDF might be compared. The ability to discriminate between textures would then depend on the accuracy with which these moments were estimated, as discussed in Section 8.2.2. The selection of which particular moment to adopt is crucial. If the form of the PDF is known, then those moments that optimize the information about the texture can be selected. In Section 8.2.3 we demonstrate how some simple moments are optimized for particular forms of PDF. In Section 8.2.4 we discuss how the form of the data PDF can be approximated in terms of a mixture of simple analytic distributions, each of which possesses an analytic solution.

8.2.1 The Kolmogorov–Smirnov Test

The K-S test investigates the null hypothesis that two data sets are taken from the same distribution and depends on the maximum value of the absolute difference between their CDFs. The probability that the K-S measure exceeds that observed is approximately independent of the size of the sample (provided this is greater than four) and the form of the data PDF and can be readily calculated [4,5]. The test can be applied to classification, as described in Section 8.4.2, with one input provided by theoretical or trained CDFs for the different classes. In segmentation, discussed in Section 8.5, our interest is in determining

whether two data samples are members of the same (unknown) distribution and no analytic PDF or training data are necessary. In both situations, if the analytic form of the PDF is known a priori, it is better that it should be incorporated into model-based exploitation methods rather than using the noncommittal K-S test.

8.2.2 Estimating Moments

In Chapter 5 we showed that the normalized variance (the square of the contrast) of intensity provided a means of discriminating between examples of field and woodland. Performance is then determined by the statistical uncertainty in these estimates. Consider the variance of an uncorrelated random intensity I with an estimate, defined over a window of N pixels, by

$$\overline{\text{var } I} \equiv \overline{I^2} - \bar{I}^2 \equiv \frac{1}{N} \sum_{j=1}^N I_j^2 - \left(\frac{1}{N} \sum_{j=1}^N I_j \right)^2 \quad (8.1)$$

where the bars denote sample averages. Though both \bar{I} and $\overline{I^2}$ are unbiased, since $\langle \bar{I} \rangle = \langle I \rangle$ and $\langle \overline{I^2} \rangle = \langle I^2 \rangle$, the estimated variance $\overline{\text{var } I}$ is biased since $\langle (\bar{I})^2 \rangle \neq \langle I \rangle^2$. In fact, the mean and variance of this estimator are given by

$$\langle \overline{\text{var } I} \rangle = \left(1 - \frac{1}{N} \right) \text{var } I \quad (8.2)$$

exactly, and

$$\begin{aligned} \text{var}[\overline{\text{var } I}] &= \frac{1}{N} \left(\langle I^4 \rangle - 4\langle I^3 \rangle \langle I \rangle - \langle I^2 \rangle^2 \right. \\ &\quad \left. + 8\langle I^2 \rangle \langle I \rangle^2 - 4\langle I \rangle^4 \right) \end{aligned} \quad (8.3)$$

to $O(1/N)$, respectively. For “true” normalization this estimate is divided by the square of the true mean.

Alternatively, a self-normalized estimate is obtained by dividing the estimated variance by the square of the estimated mean. Hence,

$$\frac{\overline{\text{var } I}}{\bar{I}^2} \equiv \frac{\overline{I^2}}{\bar{I}^2} - 1 \quad (8.4)$$

The uncertainty in this estimator depends on errors in both numerator and denominator, which are clearly not independent. The expected value of this estimator can be derived by perturbing both numerator and denominator about their mean value [6] leading to

$$\left\langle \frac{\overline{\text{var } I}}{\bar{I}^2} \right\rangle \approx \frac{\langle I^2 \rangle}{\langle I \rangle^2} \left(1 - \frac{1}{N} \left(\frac{2\langle I^3 \rangle}{\langle I \rangle^2 \langle I \rangle} - \frac{3\langle I^2 \rangle}{\langle I \rangle^2} + 1 \right) \right) - 1 \quad (8.5)$$

which is biased to $O(1/N)$. The variance of the quantity can be derived following a similar process leading to

$$\text{var} \left[\frac{\overline{\text{var } I}}{\bar{I}^2} \right] \approx \frac{1}{N} \left(\frac{\langle I^4 \rangle}{\langle I \rangle^4} - \frac{4\langle I^3 \rangle \langle I^2 \rangle}{\langle I \rangle^5} + \frac{4\langle I^2 \rangle^3}{\langle I \rangle^6} - \frac{\langle I^2 \rangle^2}{\langle I \rangle^4} \right) \quad (8.6)$$

Let us examine the difference between true and self normalizations for a K-distributed intensity with order parameter ν , by substituting appropriate moments from (5.14). With true normalization the bias is

$$\text{Bias} \equiv \frac{\langle \overline{\text{var } I} \rangle}{\langle I \rangle^2} - \frac{\text{var } I}{\langle I \rangle^2} = \frac{1}{N} \left(1 + \frac{2}{\nu} \right) \quad (8.7)$$

while the variance is

$$\frac{\text{var} [\overline{\text{var } I}]}{\langle I \rangle^4} \approx \frac{4}{N} \left(2 + \frac{20}{\nu} + \frac{53}{\nu^2} + \frac{36}{\nu^3} \right) \quad (8.8)$$

The self-normalized quantity, on the other hand, has a bias of

$$\text{Bias} \equiv \left\langle \frac{\overline{\text{var } I}}{\bar{I}^2} \right\rangle - \frac{\text{var } I}{\langle I \rangle^2} \approx -\frac{2}{N} \left(1 + \frac{1}{\nu} \right) \left(1 + \frac{6}{\nu} \right) \quad (8.9)$$

and a variance of

$$\text{var} \left[\frac{\overline{\text{var } I}}{\bar{I}^2} \right] \approx \frac{4}{N} \left(1 + \frac{1}{\nu} \right) \left(1 + \frac{4}{\nu} \right) \left(1 + \frac{5}{\nu} \right) \quad (8.10)$$

With no RCS variation ($\nu \rightarrow \infty$) the variance with true normalization has a bias of $1/N$ compared with $2/N$ for the self-normalized variance. In the opposite limit with strong RCS fluctuations ($\nu \rightarrow 0$), the biases are $2/N\nu$ and $12/N\nu^2$, respectively. This shows that the bias of the self-normalized estimate is greater than that with true normalization. If we consider the variance of the estimators, we find that the estimator with true normalization has a variance of $8/N$, for $\nu \rightarrow \infty$, whereas that for the self-normalized estimator is $4/N$. In the opposite limit ($\nu \rightarrow 0$), the variances are $144/N\nu^3$ and $80/N\nu^3$, respectively. Thus, the variance of the self-normalized estimator varies monotonically between a factor of 2 and 1.8 less than that with true normalization. Though self-normalized estimators introduce more bias, they have smaller uncertainties and so are generally a more useful quantity to measure. They will be adopted for all the discussion that follows.

8.2.3 Optimum Selection of Moments

In texture exploitation, measures generally have to be estimated over as small an area as possible in order to retain high resolution. This restricts the accuracy with which the data moments can be estimated. If the PDF of the data is known, an optimized measure for the parameters which characterize the distribution provides greater sensitivity than an arbitrary moment, such as the variance discussed in the previous section. If only two moments are to be determined, an important issue is which two should be measured for optimum sensitivity. This question can be addressed from *maximum entropy* (ME) considerations [7].

ME analysis shows [7] that the mean and variance of the intensity would correspond to an optimum measure if $P(I)$ were Gaussian. The unknown mean μ_K and order ν_K of the equivalent K distribution could then be evaluated from the mean μ , and normalized variance V_I of I , since $\mu = \mu_K$ and $V_I = 1 + 2/\nu_K$, for single-look images. Another option would be to measure the first two moments of the natural logarithm of the data for which the ME solution would be the log normal PDF. The mean and order of the equivalent K distribution could then be evaluated from the mean β , and variance $V_L (\equiv \langle \ln^2 I \rangle - \langle \ln I \rangle^2)$ of $\ln I$, since $\beta = \psi^{(0)}(\nu_K) - \ln \nu_K - \gamma_E + \ln \mu_K$ and $V_L = \psi^{(1)}(\nu_K) + \pi^2/6$ for single-look clutter, where $\psi^{(0)}(.)$ is the digamma function, $\psi^{(1)}(.)$ the trigamma function, and γ_E Euler's constant [8]. Third, the mean and the mean log of intensity could be measured, in which case the ME solution would be the gamma PDF. The relationships $\mu_\gamma = \mu_K$ and $\psi^{(0)}(\nu_\gamma) - \ln \nu_\gamma = \psi^{(0)}(\nu_K) - \ln \nu_K - \gamma_E$ would then relate the gamma distribution parameters for mean and order, μ_γ and ν_γ , to those for the corresponding K distribution, μ_K and ν_K . The difference between these texture estimates indi-

cates the importance of selecting optimum measures determined by the actual form of the intensity PDF.

8.2.4 Estimating the PDF

In an ideal situation, an analytic form for the data PDF would be known a priori. In the absence of such a model it is useful to deduce an approximate analytic form for the PDF made up of a mixture of simple analytic contributions. If these component PDFs have a form similar to the data, then it is possible for a small number of contributions to provide a reasonable representation.

For a mixture distribution, we represent the estimated PDF, $\hat{P}(I)$, as a weighted sum of a set of test distributions having the form

$$\hat{P}(I) = \sum_{i=1}^q w_i P(I, s_i) \quad (8.11)$$

where $P(I, s_i)$ is the i th constituent of the mixture, s_i is the vector of parameters for the i th distribution, w_i is its weight, and q the number of components in the mixture. The estimated PDF is fitted, using ML methods based on expectation maximization [9], to determine appropriate weights, parameter values, and number of components for the mixture distributions. In principle, increasing the number of components improves the fit; however, individual parameter values are less accurately determined.

As an example, we show a three-component mixture distribution fit to the PDF of the log of a K-distributed variable in Figure 8.2 [10]. The original distribution is far too asymmetric to be represented by a single Gaussian component. However, after three components have been summed the resultant is close to the original shape. Note that the quality of the representation was improved considerably by taking the log of the data. It would require many more components to represent the PDF of the original data.

8.3 Model-Based Texture Parameter Estimation

So far we have not exploited any model for the data in attempting to derive information from the texture. However, Section 8.2.3 indicates that an optimum texture measure is determined by the form of the data. For the remainder of this chapter we shall assume that a data model is known, characterized by its single-point PDF. This PDF then determines optimum measures for texture parameters (in Section 8.3), classification (in Section 8.4), and segmentation (in Section 8.5).

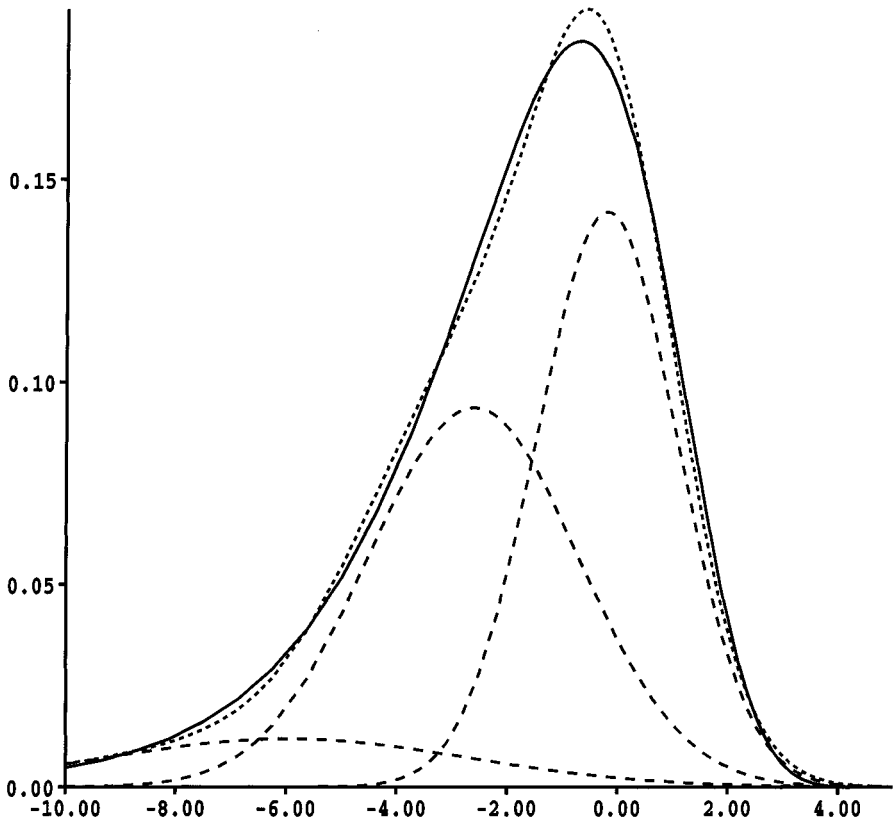


Figure 8.2 Mixture distribution fit (short dashes) to the PDF of the log of a K distribution (full curve) made up of three Gaussian contributions (long dashes).

8.3.1 Derivation of MLEs for Different PDFs

In this section we derive MLEs for the parameter values implied by assuming different forms of PDF to characterize the data. These different PDFs lead to a variety of texture measures.

8.3.1.1 Gaussian Distribution

Suppose the data have a Gaussian PDF of the form

$$P(x) = \frac{1}{\sqrt{2\pi}V} \exp\left[-\frac{(x-\mu)^2}{2V}\right] \quad (8.12)$$

where μ and V represent the mean and variance of x . The resulting log likelihood over N pixels is given by

$$\lambda = -\frac{N \ln(2\pi V)}{2} - \frac{\overline{(x - \mu)^2}}{2V} \quad (8.13)$$

with MLEs for mean and variance given by

$$\mu = \bar{x} \quad \text{and} \quad V = \overline{x^2} - \bar{x}^2 \quad (8.14)$$

This Gaussian PDF could represent either the intensity or the amplitude of the data. Self-normalized texture measures of the form

$$V_I \equiv \frac{\overline{I^2}}{\bar{I}^2} - 1 \quad (8.15)$$

and

$$V_A \equiv \frac{\overline{A^2}}{\bar{A}^2} - 1 = \frac{\bar{I}}{\overline{A^2}} - 1 \quad (8.16)$$

have been proposed [11–13] for intensity and amplitude data, respectively, which would therefore be ML measures when the appropriate PDF was Gaussian.

8.3.1.2 Log Normal Distribution

Suppose the data follow a log normal distribution of the form

$$P(x) = \frac{1}{x\sqrt{2\pi W}} \exp\left[-\frac{(\ln x - \beta)^2}{2W}\right] \quad (8.17)$$

where β and W are the mean and variance of $\ln x$. The associated log likelihood is given by

$$\lambda = -\frac{N}{2} \ln(2\pi W) - N \overline{\ln x} - \frac{N \overline{(\ln x - \beta)^2}}{2W} \quad (8.18)$$

and the MLEs for β and W by

$$\beta = \overline{\ln x} \quad \text{and} \quad W = \overline{\ln^2 x} - (\overline{\ln x})^2 \quad (8.19)$$

The variance of log measure for intensity, defined by

$$V_L \equiv \overline{\ln^2 I} - (\overline{\ln I})^2 \quad (8.20)$$

has also been proposed as a suitable texture measure [14].

8.3.1.3 The K Distribution

Chapter 5 showed that natural clutter can often be represented by a K distribution of the form

$$P(I) = \frac{2}{\Gamma(L)\Gamma(\nu)} \left(\frac{L\nu}{\mu} \right)^{\frac{(L+\nu)}{2}} I^{\frac{L+\nu-2}{2}} K_{\nu-L} \left[2\sqrt{\frac{\nu LI}{\mu}} \right] \quad (8.21)$$

for L -look SAR, where μ and ν are the mean and order of the intensity PDF, respectively. In this case the associated log likelihood is

$$\begin{aligned} \lambda = & N \ln \left[\frac{2}{\Gamma(L)} \right] - N \ln \Gamma(\nu) + \frac{N}{2} \ln \left[\frac{L\nu}{\mu} \right] \\ & + N \left(\frac{L + \nu - 2}{2} \right) \overline{\ln I} + N \left\{ \overline{\ln K_{\nu-L} \left[2\sqrt{\frac{\nu LI}{\mu}} \right]} \right\} \end{aligned} \quad (8.22)$$

Unfortunately, there is no exact analytic form for the partial derivatives of the last term in (8.22) which prevents a derivation of the MLEs. These have to be determined by a numerical search over μ and ν to find the largest value of λ ; the corresponding values of μ and ν are the MLEs. Since this is very time consuming, it is useful to provide approximate forms for the K distribution that have analytic solutions.

8.3.1.4 Approximations to the K Distribution

An analytic approximation for a K-distributed intensity in the limit of large L is [11]

$$P(I) = \frac{\sigma^{\nu-1}}{\Gamma(\nu)} \left(\frac{\nu}{\mu} \right) \exp \left[-\frac{\nu I}{\mu} \right] \\ \times \left\{ 1 + \frac{\nu}{L} \left(1 + \nu - \frac{2I(1+\nu)}{\mu} + \frac{\nu I^2}{\mu^2} \right) \right\} \quad (8.23)$$

leading to a log likelihood over N samples given by

$$\lambda = N\nu \ln \nu - N\nu \ln \mu - N \ln \Gamma(\nu) + N(\nu - 1) \overline{\ln I} - \frac{\nu \bar{I}}{\mu} \\ + \frac{1}{2L} \left\{ N\nu(1 + \nu) - \frac{2N\nu(1 + \nu)\bar{I}}{\mu} + \frac{\nu^2 \bar{I}^2}{\mu^2} \right\} \quad (8.24)$$

The MLEs for mean and order are then given by

$$\mu = \bar{I} \left(1 + \frac{1}{L} \left(1 + \nu - \frac{\nu \bar{I}^2}{\bar{I}^2} \right) \right) \quad (8.25)$$

and

$$\ln \nu - \psi^{(0)}(\nu) + \frac{\nu}{L} \left(\frac{\bar{I}^2}{\bar{I}^2} \right) = \ln \bar{I} - \overline{\ln I} + \frac{1}{2L} \quad (8.26)$$

These reduce to the results for a gamma distribution as $L \rightarrow \infty$, when speckle contributions would be averaged out [15]. Note that the right-hand side of (8.26) involves a normalized log measure, defined by

$$U \equiv \overline{\ln I} - \ln \bar{I} \quad (8.27)$$

which has been used as a texture measure [7,11]. When (8.26) is inverted it provides a close approximation to the ML solution for the order parameter for K distributions with large numbers of looks, and is exact for a gamma distribution. However, the normalized log in (8.27) provides a poorer approximation to an ML estimate for ν for single-look images. Nevertheless, we shall demonstrate that adopting this measure yields little performance degradation. It corresponds to approximating a K distribution by a gamma distribution, as proposed by Raghavan [16], and has been applied widely in texture analysis [7,12,17–19].

8.3.2 Uncertainty in Order Parameter Estimates

In the previous section we derived ML texture measures V_b , V_A , V_L , and U corresponding to particular PDFs. In this section we apply the same texture measures to characterize data that we assume to be K-distributed. Obviously, we would expect a texture measure arising from a PDF that was close to a K distribution to yield the greatest statistical accuracy. For example, we would expect V_b defined in (8.15), to be a poor measure whereas U , defined in (8.27), and V_L , defined in (8.20), should represent considerable improvements.

From this point on we will confine our attention to single-look SAR since it yields maximum resolution and retains all the texture information available to the sensor. The expected values of the texture estimators can be related to the order parameter, in the limit of large N , by evaluating appropriate moments of the K distribution. Thus,

$$\langle V_I \rangle = \frac{\langle I^2 \rangle}{\langle I \rangle^2} - 1 = 1 + \frac{2}{\nu} \quad (8.28)$$

$$\langle V_A \rangle = \frac{\langle I \rangle}{\langle A \rangle^2} - 1 = \frac{4\nu\Gamma^2(\nu)}{\pi\Gamma^2\left(\nu + \frac{1}{2}\right)} - 1 \quad (8.29)$$

$$\langle V_L \rangle = \langle \ln^2 I \rangle - \langle \ln I \rangle^2 = \psi^{(1)}(\nu) + \frac{\pi^2}{6} \quad (8.30)$$

and

$$\langle U \rangle = \langle \ln I \rangle - \ln \langle I \rangle = \psi^{(0)}(\nu) - \ln \nu - \gamma_E \quad (8.31)$$

The value of ν can be estimated by inverting (8.28)–(8.31).

These texture measures are estimated over a window of N pixels. Approximate values for their mean and variance can be derived by performing perturbation expansions of V_b , V_A , V_L , and U about their expected values. The bias is derived by taking the expectation value of these expansions. The variance is obtained by squaring the expansion before taking the expectation value. Both bias and variance to first order in $1/N$ have been derived [11,12]. For small windows (< 200 pixels) the second-order term is also required [13].

In describing K-distributed texture, we are concerned with the bias and variance of the estimate for ν rather than the measure from which it is obtained. The relation between small changes in the texture measures and the estimates for order can be derived by differentiating (8.28) to (8.31). Following the

methods of Section 8.2.2, the bias in the order is derived by taking ensemble averages of these differentiated expressions and substituting for the bias in the texture estimators. Similarly, the variance is derived by squaring the differentials of the expectation values before taking ensemble averages and substituting for the variance of the texture estimators. The most convenient way to present the results is in the form of relative bias and variance, denoted by $\langle \Delta v \rangle / v$ and $\langle \delta v^2 \rangle / v^2$, respectively, where a subscript denotes the mean from which the estimate was obtained. Summarizing the results we obtain [11–13]

$$\frac{\langle \Delta v \rangle_{V_L}}{v} = \frac{v}{N} \left(1 + \frac{1}{v} \right) \left(1 + \frac{6}{v} \right) \quad (8.32)$$

$$\begin{aligned} \frac{\langle \Delta v \rangle_{V_A}}{v} &= \frac{\pi \Gamma^2 \left(v + \frac{1}{2} \right)}{4 N v \Gamma^2(v) \left(1 + 2v \left(\psi^{(0)}(v) - \psi^{(0)} \left(v + \frac{1}{2} \right) \right) \right)} \\ &\times \left(\frac{12v\Gamma^2(v)}{\pi \Gamma^2 \left(v + \frac{1}{2} \right)} - 4 - \frac{3}{2v} \right) \end{aligned} \quad (8.33)$$

$$\frac{\langle \Delta v \rangle_{V_L}}{v} = - \frac{\psi^{(1)}(v) + \frac{\pi^2}{6}}{N v \psi^{(2)}(v)} \quad (8.34)$$

where $\psi^{(2)}(.)$ is the tetragamma function [8], and

$$\frac{\langle \Delta v \rangle_U}{v} = \frac{1 + \frac{2}{v}}{2N(v\psi^{(1)}(v) - 1)} \quad (8.35)$$

for the relative bias in order parameter from V_B , V_A , V_L , and U , respectively. The corresponding expressions for relative variance are

$$\frac{\langle \delta v^2 \rangle_{V_L}}{v^2} = \frac{v^2}{N} \left(1 + \frac{1}{v} \right) \left(1 + \frac{4}{v} \right) \left(1 + \frac{5}{v} \right) \quad (8.36)$$

$$\frac{\langle \delta\nu^2 \rangle_{V_A}}{\nu^2} = \frac{1}{N \left(1 + 2\nu \left(\Psi^{(0)}(\nu) - \Psi^{(0)}\left(\nu + \frac{1}{2}\right) \right) \right)^2} \times \left(\frac{16\nu\Gamma^2(\nu)}{\pi\Gamma^2\left(\nu + \frac{1}{2}\right)} - 5 - \frac{1}{\nu} \right) \quad (8.37)$$

$$\frac{\langle \delta\nu^2 \rangle_{V_L}}{\nu^2} = \frac{\Psi^{(3)}(\nu) + 2\Psi^{(1)2}(\nu) + \frac{2\pi^2}{3}\Psi^{(1)}(\nu) + \frac{11\pi^4}{90}}{N(\nu\Psi^{(2)}(\nu))^2} \quad (8.38)$$

where $\Psi^{(3)}(.)$ is the pentagamma function [8], and

$$\frac{\langle \delta\nu^2 \rangle_U}{\nu^2} = \frac{\Psi^{(1)}(\nu) + \frac{\pi^2}{6} - 1}{N(1 - \nu\Psi^{(1)}(\nu))^2} \quad (8.39)$$

The uncertainty in the estimated order parameter is greater than the bias, since the latter is of order $1/N$ whereas its standard deviation is of order $1/\sqrt{N}$. It is therefore possible to ignore the effects of bias for simplicity, particularly for large N . In order to compare the performance of different measures, a plot of their predicted relative standard deviation is shown in Figure 8.3. These predictions are compared with numerical results for the exact K distribution. Some simulated results are also included.

The first conclusion that can be drawn is that there is good agreement between theory and simulation, except for V_I with small values of order parameter where the discrepancy can be partially resolved by introducing the second-order term [13], with still higher orders needed for $\nu \leq 0.4$.

Let us next compare the performance of the different measures. The numerical ML calculation for the exact K distribution [12], denoted by the full curve, effectively represents the envelope of the optimum performance of the approximate analytic measures. It can be seen that U is best for $\nu < 3$, whereas V_A is best for $3 < \nu < 10$. Hence, some combination of U and V_A should yield a closer approximation to the true ML solution over the range $0.1 < \nu < 10$ [20]. Equation (8.24) suggests that the MLE for a K distribution should combine both U and V_I (rather than V_A). Joughin et al. [21] used numerical simulation to show that the variance of the estimate of ν is exponentially related to its mean value. In the limit of large ν , the minimum variance for unbiased

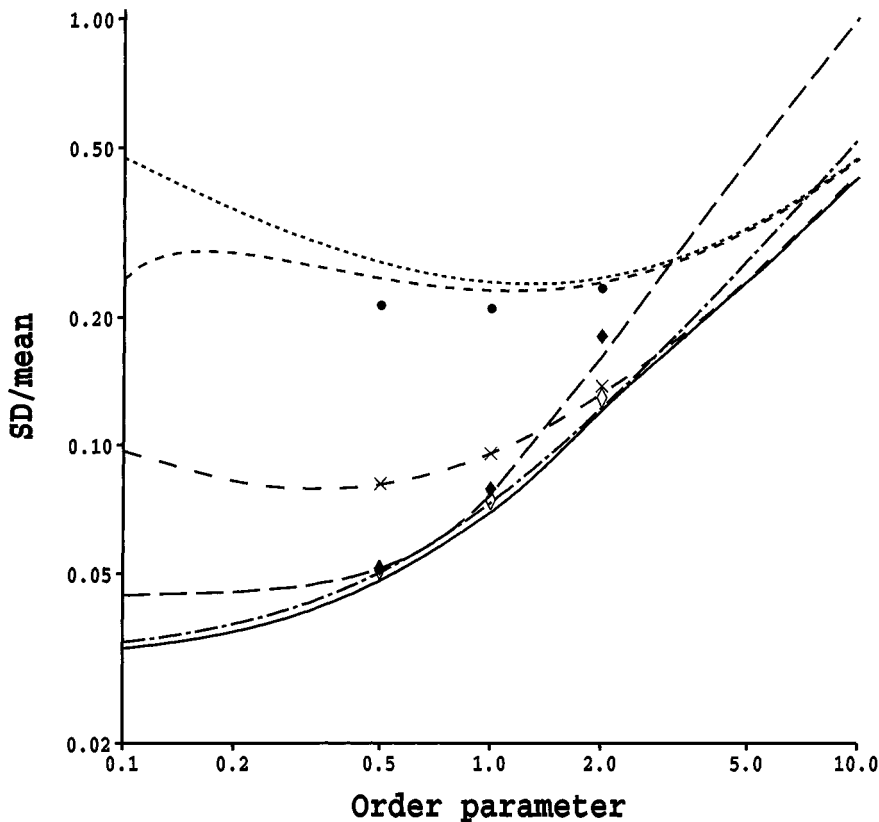


Figure 8.3 Comparison of predicted relative standard deviation in order parameter from different measures. Window 32 by 32 pixels; simulation over 10^3 samples. Exact numerical ML solution for K distribution (full). Theoretical results for approximations denoted by increasing dash length: V_f : first-order theory, second-order theory and simulation (●); V_A : theory and simulation (✕); V_L : theory and simulation (♦); U : theory (long and short dashes), simulation (◇).

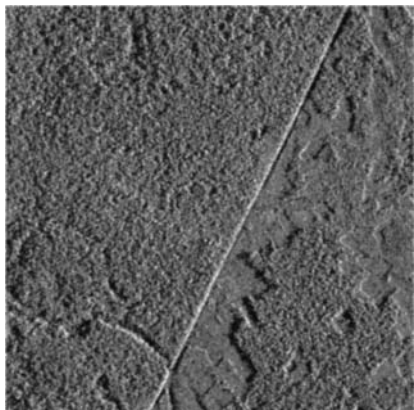
estimators is approximately given by the Cramer–Rao bound that has the value v^2/N [13]. The errors in all the measures considered here have this form, with constants of proportionality taking the value 1.0, 1.63, 11.9, and 2.58 for V_f , V_A , V_L , and U , respectively. Thus, V_f is asymptotically the optimum estimator for large v where it attains the Cramer–Rao bound. However, it is the worst estimator in the opposite limit where U appears best.

For large values of v the texture fluctuations are very weak and the intensity distribution tends to the negative exponential speckle PDF for single-

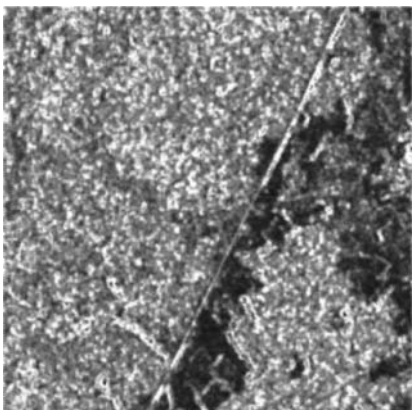
look imagery. Strong texture is of more interest, corresponding to smaller values of ν , where U or V_L provide reasonable approximations to the true MLE. Subsequent discussion on texture classification and edge detection will generally be based on these texture measures.

8.3.3 Texture Estimation Example

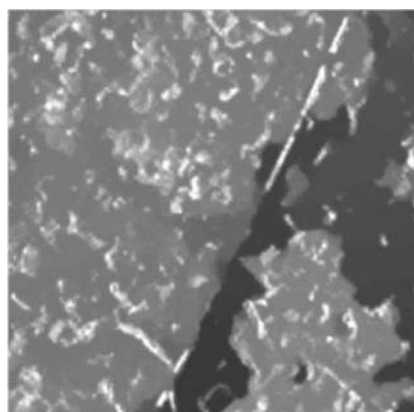
In this section we apply texture estimates to the Amazon rain forest example in Figure 8.1, repeated as Figure 8.4(a). The normalized log measure U , was evaluated over a window size of 8 by 8 pixels, leading to the result in Figure



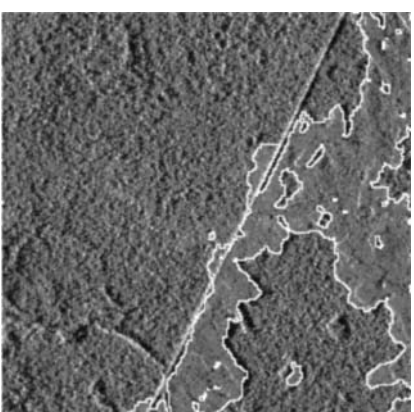
(a)



(b)



(c)



(d)

Figure 8.4 Texture analysis of SAREX image from Figure 8.1: (a) original image, (b) normalized log texture measure output for 8 by 8 pixel window, (c) annealed version of (b) to reduce speckle, and (d) overlay of derived edges on original image.

8.4(b) [18,19]. Note that in this instance the measure was not inverted to estimate the order parameter. This texture image is corrupted by the effects of speckle, which can be reduced considerably using the simulated annealing filter, described in Chapter 6. After suitable resampling to overcome correlations introduced by the scanning window, the despeckled texture image is shown in Figure 8.4(c). Regions corresponding to clearings in the original image appear dark, with primary forest generally lighter. This indicates that the texture measure could be applied to discriminate between the different classes in the scene. Indeed, the distributions of texture measures for primary forest and clearings are so well separated in this example that it is possible to apply a simple threshold to the texture measure to distinguish between the two classes. The edges obtained in this manner are overlaid on the original image in Figure 8.4(d). It is apparent that this provides successful delineation of the region boundaries.

8.4 Texture Classification

Classification is intended to determine the closest match between a data sample and a set of samples representing the different classes. The example in Figure 8.4 indicates that texture estimators can sometimes be used for classification in terms of region type, that is, clearing or primary forest. Classification can also be used to discriminate between regions having the same form of PDF, for example, a K distribution with different parameter values (even though the physical meaning of these differences may be unknown). In this section we compare a method based on fitting texture parameters with one in which a hypothesis test is applied directly to the data. The direct method, which is based on log likelihood or K-S tests, is more reliable than fitting, since one can always identify the closest class, whereas fitting procedures are not very robust.

For simplicity we will confine our attention to K-distributed textures with the same mean value and discuss classification based on differences in order parameter alone. This can be achieved by fitting the order parameter and classifying on the basis of the distribution of errors in this estimate, as described in Section 8.4.1. Alternatively, the texture can be classified directly by calculating the likelihood that the data are consistent with each K distribution (characterized by its order parameter) within the reference set, as described in Section 8.4.2. This likelihood measure is then applied in a simulated annealing classification in Section 8.4.3.

8.4.1 Classification by Fitting

In this approach each texture sample is represented by an estimated order parameter $\hat{\nu}$, obtained by fitting. These estimates are compared with reference values and

the sample assigned to a class. This process can be optimized if $P(\hat{\nu})$ is known, when it would be possible to calculate the log likelihood of a sample belonging to each class. To establish the form of $P(\hat{\nu})$, we simulated a set of uncorrelated K-distributed textures, over a window of 16 by 16 pixels, having order parameter values of 0.5, 1.0, and 2.0. The order parameter was estimated in each example and the overall PDF compared with theoretical Gaussian, gamma, and log normal distributions with appropriate ML values for their parameters. We found that a log normal distribution provided the closest resemblance to the PDF of estimated order in all cases, followed by a gamma distribution [22]. Thus, classification by fitting should assume that $P(\hat{\nu})$ is log normal, with MLE parameter values given by $\beta = \ln \hat{\nu}$ and $W = \ln^2 \hat{\nu} - (\ln \hat{\nu})^2$. Appropriate values of β and W for the three classes and each of the measures discussed in Section 8.3.1 were derived from the training data.

Classification is then performed over the same size region and order parameter values using the training results as reference. The average probability for correct classification of the three textures for the V_I , V_A , V_L , and U measures are compared in Table 8.1. V_I is clearly the worst while U is best, as expected from the plots of errors in the different estimators in Figure 8.4. Not surprisingly, these results demonstrate that one should classify using the measure that has the smallest statistical uncertainty.

8.4.2 Direct Classification

There are many occasions when determining estimator values as part of the classification process is not required. For example, the K-S test, introduced in Section 8.2.1, provides a nonparametric method that classifies the data directly. If the form of the distribution is known, it is better to test directly whether the data is consistent with the candidate PDFs. In this section we compare numerical evaluation of the log likelihood for the exact K distribution with analytic

Table 8.1
Comparison of the Average Probability of Correct
Classification for the Three Textures Using the V_I , V_A ,
 V_L , and U Measures

Texture Measure			
V_I	V_A	V_L	U
0.764	0.951	0.962	0.978

Note: the SD in each result is approximately ± 0.001

results for the approximate gamma and log normal PDFs, as summarized in Section 8.3.1. A set of simulations was performed for uncorrelated textures with order parameter values of 0.5, 1.0, and 2.0 over a window of 16 by 16 pixels [22]. The average probabilities for correct classification, using appropriate likelihood tests, are compared with the results of the K-S test in Table 8.2. Approximate forms of PDF again lead to a slight reduction in the probability of correct classification, though that introduced by the gamma PDF is only just outside the statistical uncertainty of 0.001 in each result. The K-S test, which is not matched to the form of the data PDF, yields significantly poorer classification, as we would expect. This again reinforces the importance of using any information available in exploiting image data. In fact, these results show that it is better to use any one of these theoretical forms for the PDF than to be noncommittal. Since most data can be represented within this span of possible distributions, one of the approximations can be applied for all data without significant degradation.

If the results from fitting the order parameter estimated from the normalized log estimator in Table 8.1 are compared with the results in Table 8.2, it is apparent that the dominant factor in classification performance is the choice of an appropriate distribution to represent the data. The gamma approximation to a K distribution yields the best performance, regardless of whether it is then used to classify by fitting or directly.

8.4.3 Annealed Texture Classification

We now apply the texture likelihood classification technique in a data-driven annealing scheme similar to that described for RCS in the previous chapter. Let us assume for simplicity that the PDF of the intensity can be approxi-

Table 8.2
Comparison of the Average Probability of Correct Classification
of the 12 Correlated Textures Using K-S or Likelihood Tests
Based on the Exact K and Approximate Gamma and Log normal PDFs

Likelihood Test			
K-S Test	Log Normal	Gamma	K
0.962	0.972	0.977	0.979

Note: the SD in each result is approximately ± 0.001

mately represented by a gamma distribution, as in (8.23) in the limit of large L . The log likelihood that the N pixels have mean and order of μ and ν , respectively, is then given by (8.24). In this application the values of mean and order for each class are not known *a priori* but have to be *estimated* from the data. The log likelihood of N_q pixels then belonging to class q is given by

$$\lambda_q = N_q \left[\hat{\nu}_q \ln \hat{\nu}_q - \hat{\nu}_q \ln \bar{I}_q - \ln \Gamma(\hat{\nu}_q) \right. \\ \left. + (\hat{\nu}_q - 1) \overline{\ln I_q} - \hat{\nu}_q \right] \quad (8.40)$$

where \bar{I}_q and $\overline{\ln I_q}$ represent the average intensity and average log of intensity within the pixels assigned to class q and $\hat{\nu}_q$ is the MLE for the order parameter derived from (8.26). This expression for the texture likelihood can be incorporated into an annealing scheme comprised of the following stages:

1. Initialize by tessellating the image into square blocks and assign each block randomly to some class q out of m possible classes.
2. Calculate \bar{I}_q , $\overline{\ln I_q}$, and $\hat{\nu}_q$ over the pixels belonging to each class and evaluate the total configuration likelihood from $\lambda = \sum_{q=1}^m \lambda_q$.
3. Transfer one randomly selected edge pixel into a neighboring segment.
4. Repeat step 2.
5. If λ increases, then preserve the change. If not, use annealing probability, as in Section 6.9.1, to determine whether to retain the change.
6. Iterate steps 2 to 5 until the improvement is negligible.

The penalty for edge curvature is again included to override the effects of speckle, as described in Section 7.3.5.

The result of classifying the rain forest image in Figure 8.4(a) into five classes with initial segments of 7 by 7 pixels and a curvature penalty parameter of 0.01 is illustrated in Figure 8.5(a). Applying a threshold to separate into primary and secondary forest/clearing classes leads to the boundaries shown as an overlay in Figure 8.5(b). This demonstrates the potential of combining annealing techniques with ML estimates for texture.

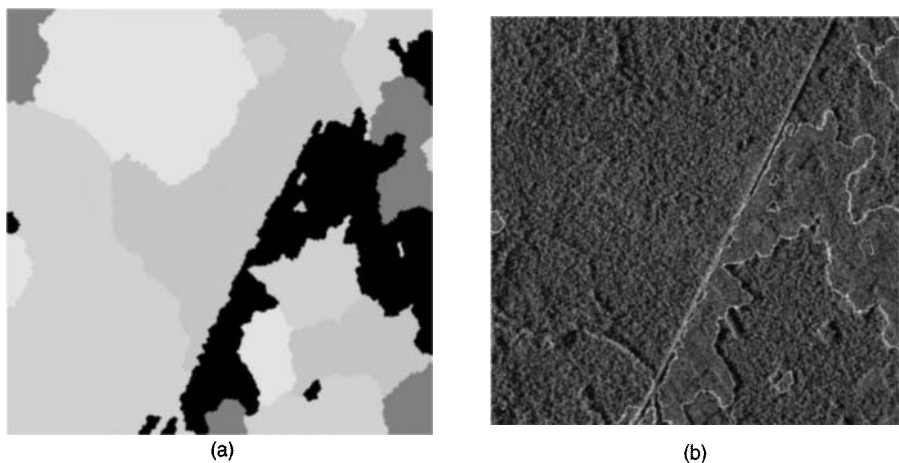


Figure 8.5 Annealed classification of the Tapajos rain forest image from Figure 8.4(a):
 (a) five-class classification and (b) overlay when thresholded into two classes.

8.5 Texture Segmentation

The texture estimation and classification examples in Sections 8.3.3 and 8.4.3 suggest that the position of edges within texture can be estimated accurately. Here we analyze the limiting performance for texture edge detection, and hence segmentation [23,24], following the approach for RCS segmentation described in Section 7.10.3.

Edge detection, based on both the noncommittal K-S test and the specific likelihood test, is discussed in Section 8.5.1. The latter adopts the analytic gamma PDF approximation for the K distribution. This ML edge detector is then incorporated into model-based segmentation in Section 8.5.2 and annealed segmentation in Section 8.5.3.

8.5.1 Edge Detection

Let us consider the same edge-detection window geometry as in Chapter 7. Again, there are two possible optimization criteria [25]. First, we may wish to maximize the total detection probability. Second, we may wish to optimize the determination of edge position, which may be particularly important when comparing segmented images [26]. In Chapter 7 we showed that total detection probability is optimized using the SWCE configuration while the FWSE geometry optimizes edge detection at the correct position.

The K-S test can be applied to both configurations. It tests the hypothesis that the region is split at each position of the window or edge. The probability

that the region is homogeneous will be smallest when the test edge is aligned with the real edge. Thus, an edge is identified as occurring at the position for which this test probability is a minimum. In addition to estimating potential edge position, it is also necessary to detect this edge against some threshold to restrict false alarm edge detections. This does not relate directly to the probability generated by the K-S test because we adopt the minimum over many possible edge positions. However, the dependence on edge position is incorporated correctly so that a single threshold value can be applied throughout.

The likelihood test can also be applied to determine whether the pixels in a window should be merged into a single region, with mean μ_0 and order ν_0 , or split into two regions, with pixels 1 to k having mean μ_1 and order ν_1 while pixels $k+1$ to M have μ_2 and ν_2 . We construct the log likelihood difference, as in Section 7.3.3, from the likelihoods in each region, defined as in (8.40). Hence, the log likelihood difference is given by

$$\begin{aligned}\lambda_D = & k[\hat{\nu}_1 \ln \hat{\nu}_1 - \hat{\nu}_1 \ln \bar{I}_1 - \ln \Gamma(\hat{\nu}_1) + (\hat{\nu}_1 - 1)\overline{\ln I_1} - \hat{\nu}_1] \\ & + (M - k)[\hat{\nu}_2 \ln \hat{\nu}_2 - \hat{\nu}_2 \ln \bar{I}_2 - \ln \Gamma(\hat{\nu}_2) + (\hat{\nu}_2 - 1)\overline{\ln I_2} - \hat{\nu}_2] \\ & - M[\hat{\nu}_0 \ln \hat{\nu}_0 - \hat{\nu}_0 \ln \bar{I}_0 - \ln \Gamma(\hat{\nu}_0) + (\hat{\nu}_0 - 1)\overline{\ln I_0} - \hat{\nu}_0]\end{aligned}\quad (8.41)$$

Let us again define the probability that the edge is detected in the correct position by P_d and that the overall detection probability within the window is P_{tot} . Unfortunately, the threshold required for a specific value of false alarm probability for the FWSE configuration is a function of position, mean, order, and P_{fa} [23,24]. No analytic dependence is available, so the threshold has to be derived from simulation. Once correct values are available, a comparison of K-S and ML edge detection can be made for both FWSE and SWCE configurations. This reveals that the ML edge detector yields higher detection probability than that based on the K-S test, demonstrating that the introduction of a more specific model leads to better performance. As in RCS segmentation, we find that the FWSE configuration yields higher values of P_d than SWCE, whereas SWCE gives larger values of P_{tot} than FWSE.

The theoretical expression for ML edge detection can be incorporated into segmentation algorithms, such as RGW or MUM, as discussed in Section 8.5.2. Alternatively, it can be introduced into a global optimization procedure (annealing) in the form of a cost function, as described in Section 8.5.3, in a similar manner to that described for intensity segmentation in Chapter 7. In each case the theoretical framework is the same. However, the first types of segmentation rely on a model-based approach testing for edges while the annealing approach considers all possible region states and should be inherently more effective.

8.5.2 Model-Based Segmentation

In this section we examine the effect of modifying the merge criterion in the MUM algorithm, described in Chapter 7, to apply to texture following the analysis of Section 8.5.1. Figure 8.6(a) illustrates the estimated order parameter in each segment resulting from applying ML order parameter and mean segmentation simultaneously, based on the likelihood difference measure in (8.41). The distributions of order parameter for clearing and primary forest regions are sufficiently well separated for a single threshold to discriminate between them, leading to the regions identified by the overlay in Figure 8.6(b). The method clearly provides accurately defined edges with a sensitivity of about 2 pixels. There seem to be more false alarms in the primary forest on the right side of the scene than were found in Figure 8.4(d). However, this is a real property of the data, not a failure of the algorithm. It indicates that the data statistics do not map exactly into the two classes. Theory suggests [22–24] that the potential resolution of texture segmentation is on a finer scale than the 2 by 2 limit imposed by the initial MUM segmentation. Therefore, we require a scheme in which a fixed window with a sliding edge is adopted to refine the edge position once maximum total detection has been achieved with a scanning window [23,25]. This appears to be compatible with the two-stage form of RGW suggested in Section 7.3.4.

8.5.3 Annealed Segmentation

While the segmentation schemes described in Section 8.5.2 are reasonably effective, a global optimization process, such as simulated annealing (SGAN) is not so dependent on the heuristics required in model-based segmentation. The log likelihood can be obtained by generalizing (8.40) for q regions such that [27]

$$W = -\lambda = -\sum_{j=1}^q N_j \left(\hat{\nu}_j \ln \hat{\nu}_j - \hat{\nu}_j \ln \bar{I}_j - \ln \Gamma(\hat{\nu}_j) \right) + (\hat{\nu}_j - 1) \overline{\ln I_j} - \hat{\nu}_j \quad (8.42)$$

The method then follows the procedure described for RCS annealed segmentation in Section 7.3.5 except that two variables need to be estimated. The curvature penalty term, introduced in Chapter 7, is again incorporated into the annealing algorithm. The result of applying annealed texture segmentation to Figure 8.4(a) is illustrated in Figure 8.6(c). As previously, we fix the number of regions to be produced by the segmentation. An average region size of 2,000 pixels and a curvature penalty parameter of 0.4 were adopted. When the order

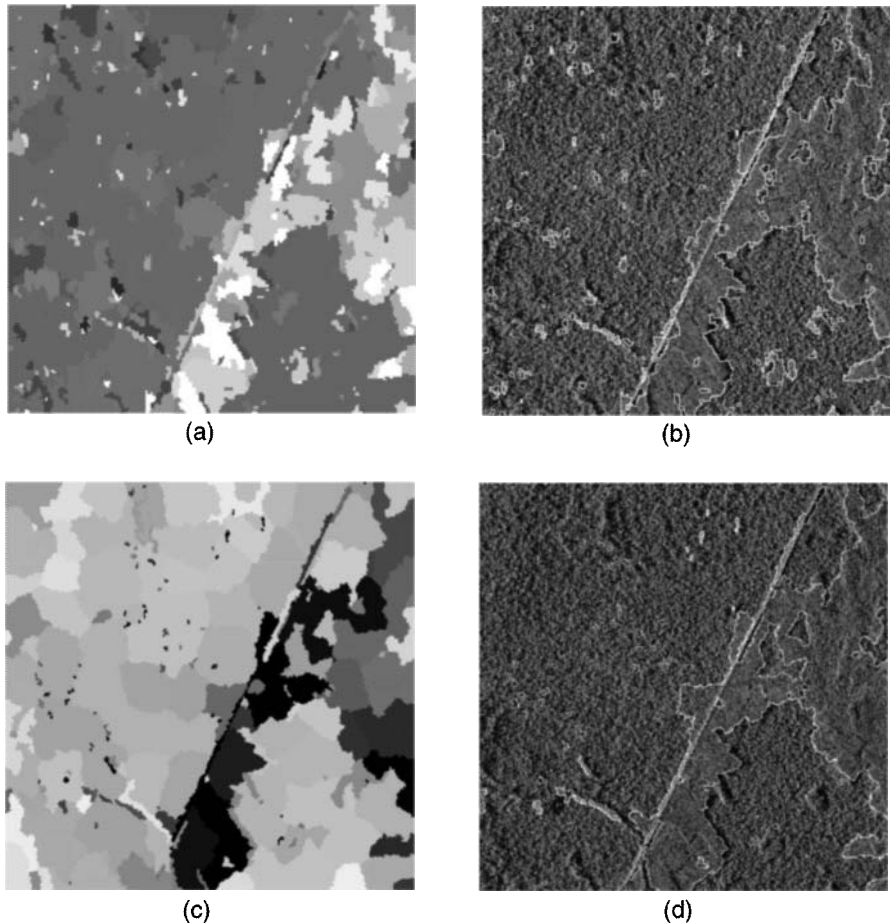


Figure 8.6 Joint mean and order parameter texture segmentation of Tapajos rain forest image from Figure 8.4(a): (a) and (b) MUM and (c) and (d) SGAN. Note that (a) and (c) display the order parameter in each segment and that (b) and (d) show an overlaid edge map on the original image.

parameter values in the different segments were thresholded into two classes, the overlay in Figure 8.6(d) was obtained. These results are similar to those in Figure 8.6(b) while avoiding the 2-pixel quantization of the MUM implementation. These results can only be regarded as preliminary, though they are obviously promising. Further research is required into the derivation of false alarm probability for texture edge detection.

8.6 Discussion

In this chapter a theoretical framework has been developed that enables approximate ML solutions to be obtained for exploiting texture. It is important to consider the kinds of applications and data types for which texture measures would be relevant. In exploiting RCS information, the value of RCS has direct physical significance. However, the connection between the value of a texture measure and a physical property of the scene is ambiguous. Clearly texture describes the depth of fluctuation, which depends on both physical RCS and spatial relationships between objects in the scene. Thus, discriminating between regions of different texture allows us to distinguish between different scene categories. The difference in contrast between fields, woods, and built-up areas has already been mentioned as an example. A texture measure can be used either to classify into regions of different textures, which either depend on a prior reference data base or may be learned from the data, or in a segmentation process that determines uniform regions of significantly different texture properties. The former approach identifies a texture sample with the nearest member of a reference set, while the latter provides data-driven separation into an unknown number of regions. Both may become part of a higher level classification process that attempts to label the texture (e.g., as woodland or urban areas) depending on the value of the texture measure.

A flow diagram for texture exploitation is shown in Figure 8.7. The initial question is whether information is contained in texture or in intensity values. If the latter, the data should be processed following the RCS exploitation techniques described in Chapters 6 and 7. If the former, we require prior knowledge of the PDF of the data. This PDF in turn defines MLEs that encapsulate the information about that texture. We have already demonstrated in Sections 8.4 and 8.5 that either a gamma or log normal distribution provides near-optimum discrimination. The second issue to resolve is whether classification or segmentation is the most suitable way to proceed in the given application. Classification has the advantage that data are assigned to the nearest of a fixed number of classes. Segmentation, on the other hand, is totally data-driven, so its statistical uncertainty is greater. However, it will not be deceived if an unexpected sample, inconsistent with the reference set, is encountered.

If the classification route is selected, the log likelihood for each reference is calculated as in (8.24) (for predefined references) or (8.40) (for data-driven processing) and the largest value taken to denote the class. Section 8.4.3 demonstrated the power of simulated annealing in data-driven classification.

In comparing segmentation algorithms, issues of image quality and execution time have to be addressed, as in Chapter 7, with basically the same algorithm options. We already established that annealing (SGAN) approximates a global optimum segmentation if the initial conditions are set correctly. At

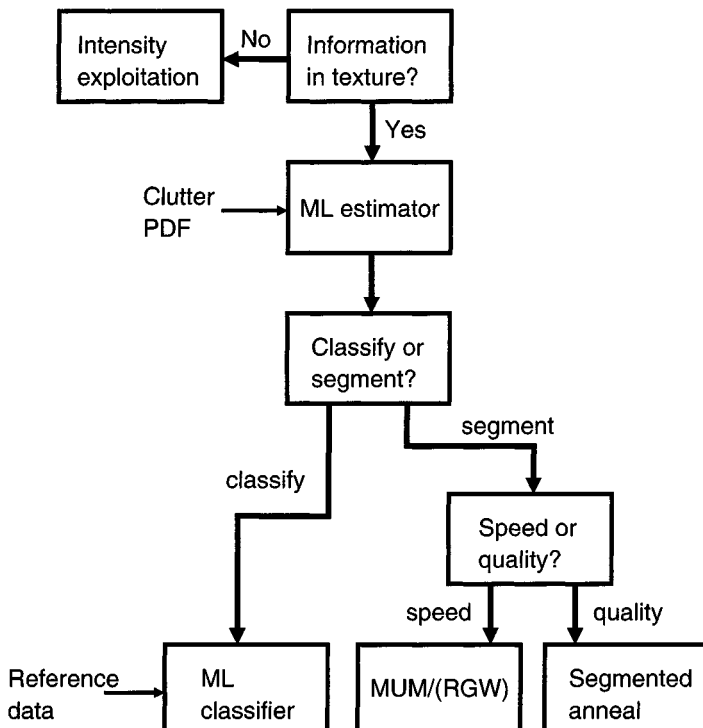


Figure 8.7 Flow diagram for selection of algorithms for texture exploitation.

present MUM is the only model-based segmentation algorithm that has been applied to texture, though we indicated in Section 8.5.2 that a modified version of RGW should do better. However, both model-based techniques adopt heuristics that render them suboptimum, so SGAN is potentially the best. Further development of SGAN is required for both classification and segmentation. The form of the curvature penalty term needs further investigation as does the “best” choice of average region size. Quality comparison should be used to verify that SGAN is operating correctly and to quantify the extent to which MUM (or RGW) is less effective. Unfortunately, image-quality assessment is more complicated than for RCS segmentation because it is not possible to define an equivalent simple measure to the ratio adopted there. Probably the best approach is via a test suite using patterns of simulated textures. The user can then impose his own cost function for the different types of segmentation error.

Comparative execution times for MUM and SGAN segmentation are listed in Table 8.3. The MUM results are for an initial 3 by 3 tessellation of the image; SGAN was set to provide 500 regions. Both methods have execution

Table 8.3

Comparison of Execution Times for MUM and SGAN Texture Segmentation
on Test Image as Function of Size

Image Size	Execution Time (sec)			
	64 × 64	128 × 128	256 × 256	512 × 512
MUM	0.4	1.5	8.0	38.7
SGAN	48.0	202.0	836.0	3,313.0

times proportional to window size, but annealed segmentation is about two orders of magnitude more expensive than MUM. It is instructive to compare these results with those achieved for RCS segmentation in Chapter 7. For the same size image MUM had an execution time of 934 seconds for RCS, compared with 38.7 seconds for texture. RCS segmentation operates on single pixels, which increases the work load considerably. In addition, it generates many more segments since the algorithm is more sensitive. On the other hand, the execution time for SGAN is somewhat greater for texture (3,313 sec) than for RCS (2,389 sec) due to a similar number of regions being found in both examples (about 500), while the texture likelihood calculation is more complicated.

In conclusion, the execution time of SGAN is much greater than MUM and seems to yield similar results at present. Unless further development indicates otherwise, there seems little to be gained by using annealing for texture segmentation. This conclusion differs from that for cross-section segmentation where the execution times of the two algorithms are more comparable. At present annealed classification is about three times slower than annealed segmentation (SGAN). However, these results are only very preliminary and should improve with further development.

References

- [1] Shimabukuro, Y. E., F. Ahern, and P. F. Hernandez, "Initial Evaluation of Airborne and ERS-1 SAR Data for the Tapajos National Forest, Brazil," *Proc. SAREX-92*, ESA Vol. WPP-76, 1993, pp. 87–94.
- [2] Quegan, S., and K. D. Grover, "Change Detection and Backscatter Modelling Applied to Forest Modelling by SAR," *Proc. European Symp. on Satellite Remote Sensing II*, Paris, September, 1995, pp. 241–251.
- [3] Grover, K. D., and S. Quegan, "Image Quality, Statistical and Textural Properties of

- SAREX Data from the Tapajos Test Site," *Proc. SAREX-92 Workshop*, ESA Vol. WPP-76, 1994, pp. 15–23.
- [4] Stephens, M. A., "Use of the Kolmogorov-Smirnov, Cramér-von Mises and Related Statistics Without Extensive Tables," *J. Royal Statistical Soc. B*, Vol. 32, 1970, pp. 115–122.
 - [5] Press, W. H., S. A. Teukolsky, W. T. Vetterling, and B. P. Flannery, *Numerical Recipes in C*, Cambridge, UK: Cambridge University Press, 1994, Chap. 14.
 - [6] Oliver, C. J., "The Interpretation and Simulation of Clutter Textures in Coherent Images," *Inv. Problems*, Vol. 2, pp. 481–518.
 - [7] Lombardo, P., and C. J. Oliver, "Simultaneous Segmentation of Texture Properties of K-Distributed SAR Images," *Europto Conf. on SAR Data Processing for Remote Sensing*, Rome, *SPIE Proc.*, Vol. 2316, 1994, pp. 104–114.
 - [8] Abramowitz, M., and I. A. Stegun, *Handbook of Mathematical Functions*, New York: Dover, 1970, Chap. 6.
 - [9] Luttrell, S. P., "An Adaptive Bayesian Network for Low-Level Image Processing," *Proc. 3rd Int. Conf. on Artificial Neural Networks*, London: IEE, pp. 313–316.
 - [10] Blacknell, D., "Texture Anomaly Detection in Radar Imagery," *Europto Conf. on SAR Data Processing for Remote Sensing*, Rome, *SPIE Proc.*, Vol. 2316, 1994, pp. 125–136.
 - [11] Oliver, C. J., "Optimum Texture Estimators for SAR Clutter," *J. Phys. D: Appl. Phys.*, Vol. 26, 1993, pp. 1824–1835.
 - [12] Blacknell, D., "A Comparison of Parameter Estimators for the K Distribution," *IEE Proc. Radar Sonar Navig.*, Vol. 141, 1994, pp. 45–52.
 - [13] Lombardo, P., and C. J. Oliver, "Estimation of Texture Parameters in K-Distributed Clutter," *IEE Proc. Radar Sonar Navig.*, Vol. 141, 1994, pp. 196–204.
 - [14] Kreithen, D. E., S. M. Crooks, W. W. Irving, and S. D. Halversen, "Estimation and Detection Using the Product Model," MIT-Lincoln Lab. Report No. STD-37, 1991.
 - [15] Harter, H. L., and R. S. Moore, "Maximum Likelihood Estimation of the Parameters of Gamma and Weibull Populations from Complete and from Censored Samples," *Technometrics*, Vol. 7, 1965, pp. 639–643.
 - [16] Raghavan, R. S., "A Method for Estimating Parameters of K-Distributed Clutter," *IEEE Trans.*, Vol. AES-27, 1991, pp. 238–246.
 - [17] Lombardo, P., C. J. Oliver, and R. J. A. Tough, "Effect of Noise on Order Parameter Estimation for K-Distributed Clutter," *IEE Proc. Radar Sonar Navig.*, Vol. 142, 1995, pp. 533–540.
 - [18] Oliver, C. J., A. P. Blake, and R. G. White, "Optimum Texture Analysis of SAR Images," *SPIE Conf. Algorithms for Synthetic Aperture Radar Imagery*, Orlando, FL, *SPIE Proc.*, Vol. 2230, 1994, pp. 389–398.
 - [19] Oliver, C. J., "Edge Detection in SAR Segmentation," *Europto Conf. on SAR Data Processing for Remote Sensing*, Rome, *SPIE Proc.*, Vol. 2316, 1994, pp. 80–91.
 - [20] Jahangir, M., D. Blacknell, and R. G. White, "Accurate Approximation to the Optimum Parameter Estimate for K-Distributed Clutter," *IEE Proc. Radar Sonar Navig.*, Vol. 143, 1996, pp. 383–390.
 - [21] Jougin, I. R., D. B. Percival, and D. P. Winebrenner, "Maximum Likelihood Estimation

- of K Distribution Parameters for SAR Data," *IEEE Trans. Geo. Remote Sens.*, Vol. 31, 1993, pp. 989–999.
- [22] Oliver, C. J., "Optimum Classification of Correlated SAR Textures," *Europto Conf. on SAR Image Analysis, Simulation and Modelling II*, Taormina, Italy, *SPIE Proc.*, Vol. 2958, 1996, pp. 64–73.
- [23] Oliver, C. J., I. McConnell, and D. Stewart, "Optimum Texture Segmentation of SAR Clutter," *Proc. EUSAR 96*, Konigswinter, 1996, pp. 81–84.
- [24] Oliver, C. J., and P. Lombardo, "Simultaneous Mean and Texture Edge Detection in SAR Clutter," *IEE Proc. Radar Sonar Navig.*, Vol. 143, 1996, pp. 391–399.
- [25] Oliver, C. J., D. Blacknell, I. McConnell, and R. G. White, "Optimum Edge Detection in SAR," *Europto Conf. on SAR Image Analysis, Simulation and Modelling*, Paris, *SPIE Proc.*, Vol. 2584, 1995, pp. 152–163.
- [26] Caves, R. G., and S. Quegan, "Matching Segmentation Algorithms to ERS-1 SAR Applications," *Europto Conf. on SAR Data Processing for Remote Sensing*, Rome, *SPIE Proc.*, Vol. 2316, 1994, pp. 148–158.
- [27] Cook, R., I. McConnell, D. Stewart, and C. J. Oliver, "Segmentation and Simulated Annealing," *Europto Conf. on SAR Image Analysis, Simulation and Modelling II*, Taormina, Italy, *SPIE Proc.*, Vol. 2958, 1996, pp. 30–37.

9

Correlated Textures

9.1 Introduction

In the previous chapter we demonstrated how the information contained in textured clutter could be exploited for both classification and segmentation. However, it is clear from studying SAR images, such as the rain forest example in Figure 8.1, that texture information is not only contained in the single-point statistics but also in the correlation (and spectral) properties. This chapter provides the background for incorporating correlation properties into techniques for extracting information from texture. We shall assume, as in Chapter 8, that the RCS can be regarded as a single realization of a stationary gamma-distributed noise process. The discussion will be centered on the set of simulated correlated textures illustrated in Figure 9.1. These correspond to single-look SAR intensity images of a gamma-distributed RCS with a symmetrical Gaussian ACF of the form

$$r_\sigma(X, Y) \equiv \frac{\langle \sigma(0,0)\sigma(X,Y) \rangle}{\langle \sigma \rangle^2} = 1 + \frac{1}{\nu} \exp\left[-\frac{X^2 + Y^2}{\ell^2}\right] \quad (9.1)$$

where X and Y are the lags in each dimension, ν the order parameter and ℓ the correlation length. In Figure 9.1 ν takes values of 0.5, 1.0, and 2.0 while ℓ corresponds to 1, 2, 4, and 8 pixels. These textures can be simulated exactly since they have half-integer order parameters and thus obey the random walk model of Section 5.8. For this simulation the imaging process did not introduce any further correlations. Real data would have to be resampled to match this behavior by removing PSF correlations, as described in Chapter 4.

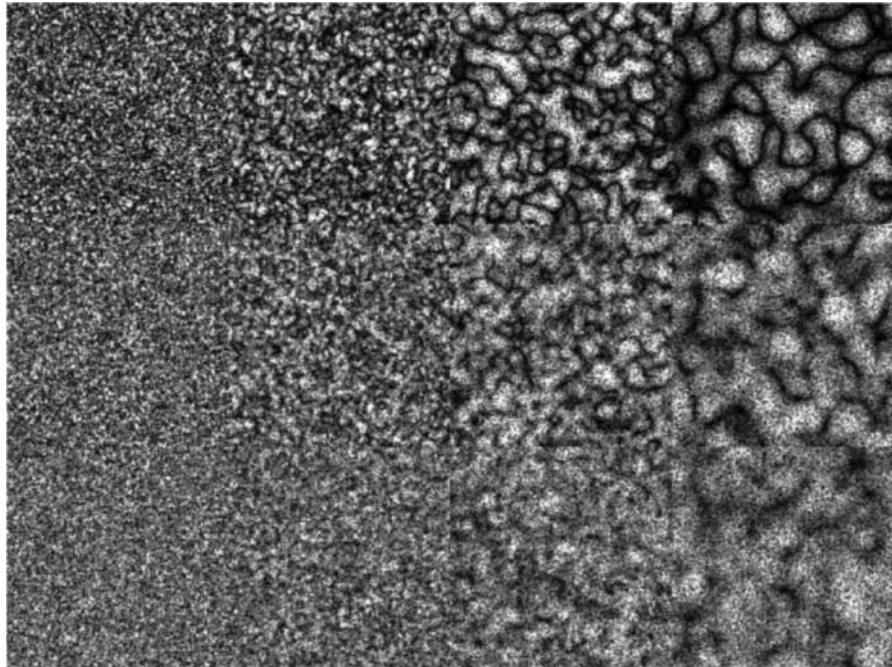


Figure 9.1 Montage of 128 by 128 pixel regions of simulated correlated textures, shown as amplitude images. The textures, characterized by (ν, ℓ) are labeled from 1 to 12 and have positions in the montage denoted by:

1 (0.5,1)	2 (0.5,2)	3 (0.5,4)	4 (0.5,8)
5 (1.0,1)	6 (1.0,2)	7 (1.0,4)	8 (1.0,8)
9 (2.0,1)	10 (2.0,2)	11 (2.0,4)	12 (2.0,8)

From Figure 9.1 it appears comparatively easy to distinguish visually the boundary between textures with different correlation length. However, the distinction between textures with different ν and small ℓ (i.e., textures 1, 5, 9 on the left of Figure 9.1) is not so clear. A visual determination of the edges between regions is aided considerably by the large area of each texture sample. Indeed, one of the lessons of Chapter 8 was that it is possible to detect the position of an edge between textures with single-pixel accuracy provided that large enough regions of each texture are available to define their properties sufficiently accurately.

However, for effective exploitation it is necessary to determine the texture properties from a comparatively small region of texture so as to maintain as high a resolution as possible. Typically a window of about 32 by 32 pixels has been shown to yield reasonable accuracy in estimating ν and ℓ [1–4] and will be

employed in the succeeding discussion. A random selection of such samples is shown in Figure 9.2. It is apparent that identifying the properties of each sample is now considerably more difficult. Experience shows that a typical observer would classify about 50% of these examples correctly.

In this chapter we consider a variety of methods for extracting textural information from such small regions. Initially we consider parameter estimation for these textures in Section 9.2. Classification will be discussed in Section 9.3 and edge detection in Section 9.4. Classification and edge detection can be performed on the parameter estimates arising from Section 9.2, which demand a specified form of ACF. Alternatively, fitting can be avoided and the processes can be carried out directly using the spectral properties. The latter approach has the advantage that any form of spectrum or ACF can be treated.

9.2 Model-Based Parameter Estimation

As discussed in Chapter 5, the mean and ACF provide a complete description of the simulated stationary noise process in Figure 9.1. Parameter values can be estimated by fitting the normalized intensity ACF, which has the form [1]

$$r_I(X, Y) \equiv \frac{\langle I(0,0)I(X, Y) \rangle}{\langle I \rangle^2} = \delta_{X,0}\delta_{Y,0} \left(1 + \frac{1}{v}\right) + r_o(X, Y) \quad (9.2)$$

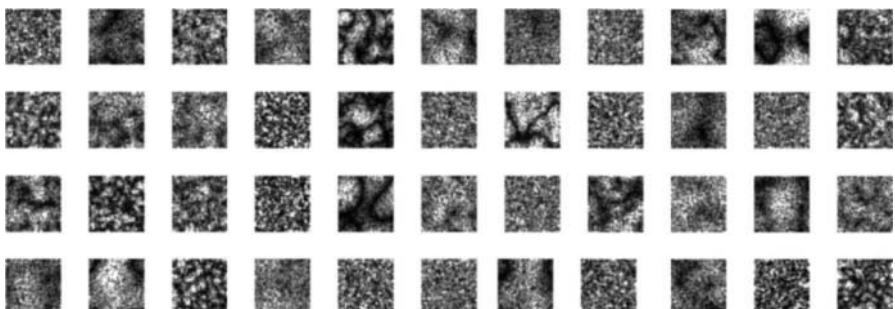


Figure 9.2 Random selection of 32 by 32 pixel regions of the different correlated textures. The different textures are laid out in positions given by:

5	8	6	12	3	8	10	9	7	4	6
6	11	11	1	3	9	3	5	10	9	6
7	2	6	1	4	11	9	7	12	8	11
12	4	2	10	5	9	4	5	8	1	2

for the process described by (9.1), where $\delta_{X,0}$ is the Kronecker delta. As shown in Section 5.6, the contribution at zero lag includes coherent interference terms arising from individual random scatterers and RCS fluctuations. The RCS correlation properties are contained in the nonzero lag ACF coefficients, $r_\sigma(X, Y)$, which include a constant background of 1. In order to derive information about these we have to remove the peak at the origin, which is caused by speckle alone.

The statistical uncertainty in the ACF coefficients in (9.2) determines the error with which order and correlation length are estimated. We would not expect a least-squares fit to provide MLEs unless the errors had a Gaussian PDF and were uncorrelated from lag to lag. Early work was confined to fitting the intensity ACF [1,4]. However, in Chapter 8 we demonstrated that determining the order parameter by fitting intensity contrast was much poorer than fitting either normalized log, variance of log, or amplitude contrast [2]. Similarly, we would expect that correlation length determination would be improved by fitting ACF measures that have inherently smaller statistical errors. In Chapter 8 we demonstrated that the normalized log measure approximates the MLE for order parameter, but there is no corresponding definition of ACF. Therefore, we adopt the ACF of the log of intensity (which has the variance of the log as its value at the origin) and the ACF of amplitude to compare with the intensity ACF. Unfortunately, theoretical derivations of the errors in these ACF coefficients and the resultant correlation lengths are more cumbersome than those for the intensity ACF. The amplitude ACF is given by [2]

$$r_A(X, Y) = \delta_{X,0}\delta_{Y,0} \left(1 - \frac{\pi}{4}\right) \frac{4\nu\Gamma^2(\nu)}{\pi\Gamma^2(\nu + \frac{1}{2})} + r_{\sqrt{\sigma}}(X, Y) \quad (9.3)$$

where

$$\begin{aligned} r_{\sqrt{\sigma}}(X, Y) &= \left(1 - \nu(r_\sigma(X, Y) - 1)\right)^{\nu+1} \\ &\times {}_2F_1\left[\nu + \frac{1}{2}, \nu + \frac{1}{2}; \nu; \nu(r_\sigma(X, Y) - 1)\right] \end{aligned} \quad (9.4)$$

and ${}_2F_1(\cdot)$ is the Gaussian hypergeometric function (Section 15.1 in [5]). The log ACF is [2]

$$\begin{aligned} r_{\ln f}(X, Y) &= 1 + \delta_{X,0}\delta_{Y,0} \frac{\pi^2}{6(\psi^{(0)}(\nu) - \ln \nu + \ln \mu - \gamma_E)^2} \\ &+ \frac{(\psi^{(0)}(\nu) - \ln \nu + \ln \mu)^2}{(\psi^{(0)}(\nu) - \ln \nu + \ln \mu - \gamma_E)^2} (r_{\ln \sigma}(X, Y) - 1) \end{aligned} \quad (9.5)$$

where

$$r_{\ln \sigma}(X, Y) = 1 + \frac{(1 - \nu(r_\sigma(X, Y) - 1))^v}{(\psi^{(0)}(\nu) - \ln \nu + \ln \mu)^2} \sum_{k=0}^{\infty} \frac{(\nu(r_\sigma(X, Y) - 1))^k}{k!} \frac{\Gamma(k + \nu)}{\Gamma(\nu)} \\ \times [\psi^{(0)}(k + \nu) - \psi^{(0)}(\nu) + \ln(1 - \nu(r_\sigma(X, Y) - 1))]^2 \quad (9.6)$$

$\psi^{(0)}(\cdot)$ is the digamma function, and γ_E is Euler's constant (Chapter 6 in [5]). A comparison of these ACFs is shown as a log plot in Figure 9.3 for a symmetrical Gaussian ACF with $\ell = 4$ pixels and $\nu = 1.0$. It is apparent that the amplitude and intensity ACFs have similar form but that the log ACF decays more rapidly and has a smaller spike at the origin. The statistical uncertainty in the estimated ACF coefficients determines the accuracy with which parameters can then be estimated.

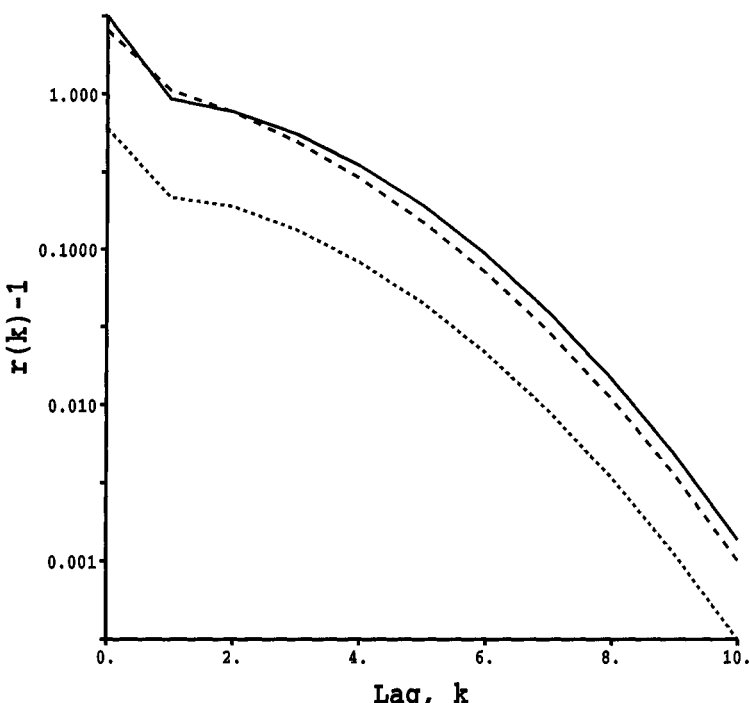


Figure 9.3 Comparison of a log plot of the predicted intensity (full), amplitude (short dashes), and log (long dashes) ACFs, $r(k) - 1$, for texture 4, in which $\nu = 1.0$ and $\ell = 4$ pixels.

Initially let us consider the determination of the order parameter from single-point statistics. Expressions for the errors in ν for uncorrelated textures were given in (8.36) to (8.38). Figure 8.3 showed that simulation and prediction were in good agreement [3,4,6–8]. No general theoretical form for correlated processes is available, so the behavior has to be deduced from simulation. The fractional errors in order parameter, as a function of correlation length, are shown in Table 9.1 [9]. The results for textures with $\ell = 0$ can be compared with the uncorrelated theory from Chapter 8 and show reasonable agreement. The simulated results for small ℓ show slightly increased errors, with the log ACF providing the best estimate of order. As correlation lengths increase the errors increase, showing the effect of correlation between pixels reducing the number of independent estimates within the sample. The fractional error in ν is then approximately the same for all three ACF estimates. The amplitude ACF could well be a more appropriate estimate than the log ACF over the typical range of values encountered with real SAR clutter. It consistently offers better performance than the ACF of intensity, without the sensitivity to correlation length and order shown by the log ACF.

Table 9.1

Dependence of Fractional Error in Order Parameter on Correlation Length for Sample Size of 32 by 32 Pixels

Measure	ν	Prediction ($\ell = 0$)	Simulation			
			$\ell = 0$	$\ell = 2$	$\ell = 4$	$\ell = 8$
Intensity	0.5	.27 (.23)	.21	.24	.31	.51
	1.0	.24 (.22)	.21	.24	.31	.64
	2.0	.25 (.24)	.23	.26	.33	1.27
Amplitude	0.5	.08	.08	.10	.19	.48
	1.0	.10	.10	.13	.21	.50
	2.0	.13	.14	.17	.24	.49
Log	0.5	.05	.05	.06	.08	.51
	1.0	.08	.08	.09	.14	.57
	2.0	.16	.18	.20	.29	.59

Note: Results for ACFs of intensity, amplitude, and log are shown. Simulation was performed over 10^3 samples. Predictions for uncorrelated data are included for comparison. The predictions in brackets refer to the second-order correction for the intensity ACF. Uncertainty ± 0.01 .

A rigorous derivation of the error in estimated correlation length is extremely complicated. Previous approximate theory for fitting the intensity ACF [1,3,4,10] makes assumptions that lead to predictions that are qualitatively reasonable. Rigorous derivations have been presented for a negative exponential ACF only; even these require numerical evaluation [2]. Again we can only determine behavior by simulation, as summarized in Table 9.2 [9]. It is apparent that the fractional error in correlation length does not show much dependence on ν , ℓ , or the choice of ACF measure. There is evidence that adopting the amplitude or log ACF yields a slight advantage for small ℓ , though none for larger ones. Over all ν and ℓ considered, the amplitude ACF seems to offer the smallest error in determining ℓ .

In general, one might conclude that the amplitude ACF provides the most robust estimator on which to base order parameter and correlation length fitting. The simulated errors can be regarded as guide to the accuracy with which any specific value of ν and ℓ could be determined for different forms of ACF. Indeed, in many instances fitting a Gaussian profile to the ACF might be regarded as a means of determining some characteristic correlation length. Certainly, where only small windows are used to calculate the ACF and determine ℓ , errors in ACF coefficients are likely to dominate over the discrepancy between the true shape and a Gaussian of similar width.

It should be noted that the drawback to fitting either amplitude or log ACFs for determining correlation length is that the theoretical form of ACF has to be re-evaluated continually during the fitting process. While this is simple for

Table 9.2
The Fractional Error in Correlation Length With a Sample Size of 32 by 32 Pixels

Measure	ν	$\ell = 2$	$\ell = 4$	$\ell = 8$
Intensity	0.5	0.18	0.18	0.21
	1.0	0.19	0.17	0.20
	2.0	0.23	0.19	0.21
Amplitude	0.5	0.14	0.18	0.23
	1.0	0.14	0.16	0.20
	2.0	0.18	0.18	0.20
Log	0.5	0.14	0.18	0.25
	1.0	0.14	0.17	0.21
	2.0	0.20	0.18	0.21

Note: Results for intensity, amplitude, and log ACFs for different ν and ℓ are compared. Simulation was performed for 10^3 samples. The uncertainty is about ± 0.01 .

the intensity ACF, the other two measures represent a considerable computing task; this suggests that ℓ might be most readily determined by fitting the intensity ACF.

9.3 Texture Classification

Let us now consider the problem of classifying samples of 32 by 32 pixels for the set of correlated textures in Figure 9.1. Parameter estimates can themselves be used in classification [1, 3, 4], as described in Section 8.5.1. Alternatively, a direct classification process can be derived, analogous to that in Section 8.5.2.

9.3.1 Classification by Fitting

In this method each estimate of ν and ℓ is compared with reference values and the sample assigned to a class, as described in Section 8.5.1. Simulation reveals that both the order parameter and correlation length estimates for correlated textures are better fitted on the basis of an assumed log normal or gamma PDF, with a Gaussian distribution giving significantly worse results [9]. Adopting the MLE parameter values for a log normal PDF from Section 8.5.1, the average probability of correct classification over all 12 textures for ACFs of intensity, amplitude, and log intensity is summarized in Table 9.3. The amplitude ACF is shown to give the best classification, with the log slightly poorer and intensity the worst. This contrasts with the uncorrelated results in Chapter 8 where both the normalized log and variance of log were better than the amplitude measure.

9.3.2 Direct Spectrum Classification

Parameter fitting need not form part of the classification process. Instead, in this section, we derive a direct approach to classification using the log likelihood as a distance measure. In order to do this, it is essential that the data should be

Table 9.3

The Average Probability of Correct Classification of the 12 Test Textures Using Intensity and Amplitude Contrast and Variance of Log Measures

Intensity	Amplitude	Log
.697	.814	.790

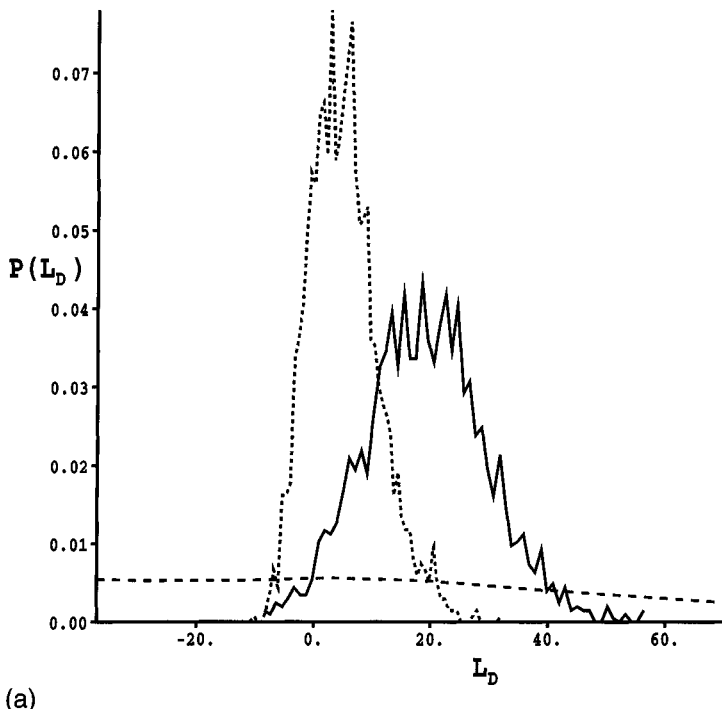
independent (so that the total likelihood can be formed by taking the sum of the logs of individual PDFs) and that the form of the PDF should be known. To this end we base this approach on the FT of the image [11], which includes all information present in the original data. The Fourier coefficients would be independent if the window was infinite; for a 32 by 32 pixel window they should be approximately uncorrelated [11]. This was not true for fitting the ACF in Section 9.3.1 where errors in ACF coefficients were correlated.

Initially we investigate the PDF of the spectral coefficients for intensity, amplitude, and log data. Simulation reveals that the distributions appear to be approximately zero-mean Gaussian with identical variances for the real and imaginary components. In Chapter 8 we showed that estimates of texture parameters could be improved by normalizing images by their estimated mean [1,2,6]. When texture samples are normalized in this fashion, the complex spectral components are found to become more nearly Gaussian. However, significant differences emerge when we calculate the relevant log likelihoods. As an example, we illustrate in Figure 9.4 distributions of estimated likelihood differences between examples of simulated textures from classes 7 and 11 in Figure 9.1. Unnormalized (a) and normalized (b) results for spectra derived from intensity, amplitude, and log data are shown. For good classification these likelihood difference distributions should be predominantly positive. It is clear that intensity data yield very poor discrimination, whereas amplitude data are more effective and further improved by normalization. The spectrum of the log data provides the best result and so is adopted for subsequent study. Its performance is not affected by normalization. This comparison indicates the high sensitivity of likelihood methods to the form of the distribution of the spectral coefficients.

Let us, therefore, represent the PDF of the complex spectrum coefficients by a single-component Gaussian mixture distribution [11]. The joint PDF of the j th component of the real and imaginary spectral coefficients, $a_r(j)$ and $a_i(j)$, then has the form

$$P_A(a_r(j), a_i(j)) = \frac{1}{2\pi\sqrt{V_r(j)V_i(j)}} \exp \left[-\frac{(a_r(j) - \mu_r(j))^2}{2V_r(j)} - \frac{(a_i(j) - \mu_i(j))^2}{2V_i(j)} \right] \quad (9.7)$$

where $\mu_r(j)$ and $\mu_i(j)$ are the mean real and imaginary values for the j th component and $V_r(j)$ and $V_i(j)$ are the corresponding variances. The PDFs of the spectral coefficients derived from simulation suggest that the means are



(a)

Figure 9.4 PDF of likelihood difference estimate between classes 7 and 11 for simulated texture 7: (a) unnormalized and (b) normalized. Intensity (dashed), amplitude (dotted), and log (full) PDFs compared.

approximately zero and the variance of each component is the same. However, consideration of the log likelihoods shows that approximating the mean by zero degrades classification performance appreciably. Instead, it is preferable to assume that the means and variances are identical, in which case (9.7) can be modified to

$$P_A(a_r(j), a_i(j)) = \frac{1}{2\pi V(j)} \exp \left[-\frac{(a_r(j) - \mu(j))^2 + (a_i(j) - \mu(j))^2}{2V(j)} \right] \quad (9.8)$$

where $\mu = \mu_r = \mu_i$ and $V = V_r = V_i$. It should be noted that the spectrum has special cases for the components at $(0, 0)$, $(0, n_y/2)$, $(n_x/2, 0)$, and $(n_x/2, n_y/2)$, where the window dimensions are $n_x \times n_y$. The joint PDF of the spectrum over the whole window for texture from class p is then given by

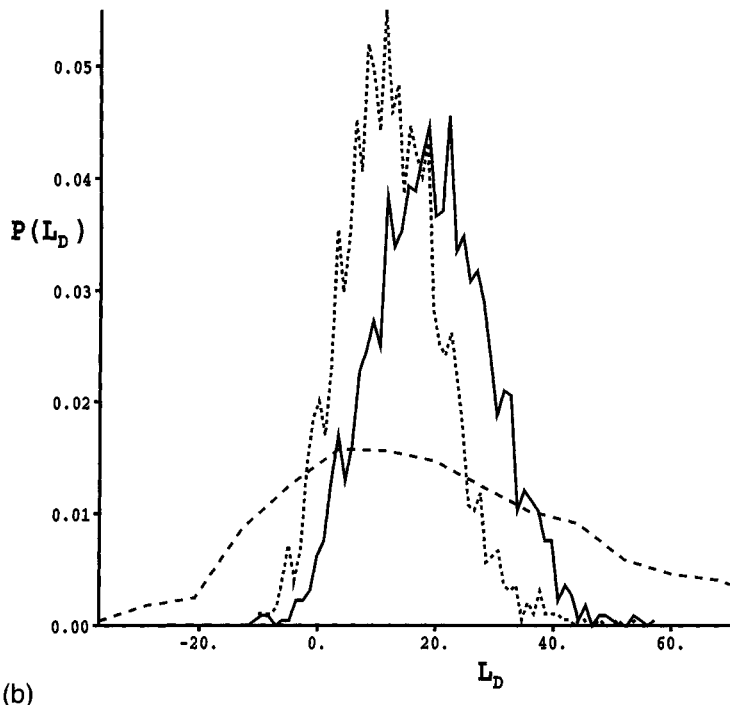


Figure 9.4 (continued).

$$P_p(a_r(1), a_i(1), \dots, a_r(M), a_i(M))$$

$$= \frac{1}{\pi^M} \prod_{j=1}^M \frac{1}{2V_p(j)} \exp \left[-\frac{(a_r(j) - \mu_p(j))^2 + (a_i(j) - \mu_p(j))^2}{2V_p(j)} \right] \quad (9.9)$$

where $M = n_x \times n_y$, and the log likelihood of class p by

$$\lambda_p = -M \ln 2\pi - \sum_{j=1}^M \left\{ \ln V_p(j) + \frac{(a_r(j) - \mu_p(j))^2 + (a_i(j) - \mu_p(j))^2}{2V_p(j)} \right\} \quad (9.10)$$

For classification we calculate the log likelihood of each class, based on previous training for the mean and variance of the Gaussian spectral components. The sample is then assigned to the class with greatest likelihood.

Having established the basis for classification of correlated textures in terms of complex spectral components, let us next assess the extent to which this approach falls short of an exact solution for K-distributed noise. As shown in Section 8.5.2, a numerical classification is required for *uncorrelated* K-distributed noise. A set of uncorrelated sample textures with $\nu = 0.5, 1.0$, and 2.0 was simulated (over a window of 16 by 16 pixels) and classified using the complex spectrum. The average probability of classifying the three textures correctly was 0.976 ± 0.001 . A comparison with Tables 8.1 and 8.2 demonstrates that this performance is comparable with fitting the order parameter derived from the normalized log measure and classification based on the approximate gamma PDF. All are slightly worse than exact classification.

We now make an equivalent comparison for the correlated textures shown in Figure 9.1. Sets of 10^4 samples of each class were simulated (over a window of 32 by 32 pixels) to train the means and standard deviations of the complex spectra. Next an equivalent set was simulated to provide a measure of classification performance. The average probability of correct classification for all twelve textures using spectrum classification and ACF parameter fitting (from the previous section) are compared in Table 9.4. This shows that the ACF fit is considerably worse than the complex spectral method for correlated textures. Since the two methods were identical for uncorrelated textures, this indicates that the fitting process must be degraded by the effect of correlations, probably attributable to the oversimplistic assumption that order and correlation length effects could be treated separately.

We have shown that applying an ML likelihood classifier to the complex spectrum of the log intensity yields better performance than parameter fitting. Spectral classification has the additional advantage that the ACF fit method relies on knowing the analytic form of the ACF *a priori* and estimating appropriate parameter values, whereas the spectral method does not. Provided that the log of the data retains a Gaussian profile for each complex spectral component, the method is viable. Note that this method can be used with data that do not have an analytic ACF if trained reference spectra can be provided.

Table 9.4
Comparison of Average Probability of
Correct Classification for the 12
Correlated Textures Based on ACF Fit
and Spectrum Classification

ACF Fit	Spectrum
0.814	0.946

9.4 ML Correlated Texture Edge Detection

9.4.1 ML Edge-Detection Theory

Classification of the complex spectrum generally depends on a large training set to yield accurate values for the mean and variance of each Gaussian component. However, in segmentation or data-driven classification (as in Section 8.4.3), decisions have to be based solely on the real and imaginary components of a single estimate of each spectral coefficient. Thus, the number of degrees of freedom cannot be more than two for each component. The assumption that the means and variances of the real and imaginary parts are identical satisfies this requirement. Assuming that the mean values were both zero yielded poorer *classification* performance against predefined references in Section 9.3.2. However, we can establish by simulation that it improves *edge detection*. Making this assumption we find that, if all M pixels in a window are taken from the same spectral component distribution with (known) j th power spectral component $S_p(j)$ from class p , the log likelihood simplifies from (9.10) to

$$\lambda_p = -M \ln \pi - \sum_{j=1}^M \left\{ \ln S_p(j) + \frac{\hat{S}(j)}{S_p(j)} \right\} \quad (9.11)$$

where $\hat{S}(j) \equiv a_r^2(j) + a_i^2(j)$ and $S_p(j) = 2V_p(j)$ are the observed and reference power spectral densities, respectively. Note that the special cases identified in the previous section have to be treated separately.

The treatment of edge detection for uncorrelated textures in Section 8.6 can now be extended to include correlation by incorporating the texture spectrum into the edge-detection scheme in place of single-point statistics. We adopt the same window geometry with k pixels in region 1 and $M - k$ in region 2. The log likelihood for each region is obtained from (9.11), and the joint likelihood that the region is split at position k is then given by [9,12]

$$\begin{aligned} \lambda_{\text{split}}(k) \equiv \lambda_{p_1} + \lambda_{p_2} &= -M \ln \pi - \sum_{j=1}^k \left\{ \ln S_{p_1}(j) + \frac{\hat{S}_1(j)}{S_{p_1}(j)} \right\} \\ &\quad - \sum_{j=k+1}^M \left\{ \ln S_{p_2}(j) + \frac{\hat{S}_2(j)}{S_{p_2}(j)} \right\} \end{aligned} \quad (9.12)$$

where the j th components in region 1, $\hat{S}_1(j)$ and $S_{p_1}(j)$, denote the observed power spectrum and reference for class p_1 in region 1 comprising pixels 1 to k ,

for example. This form relies on prior definition of the reference spectra. These are unknown in segmentation, so the spectrum has to be estimated from the data themselves. In this case the ML values of the spectral components are identical to their observed values, so $S_{p_1}(j)$ is replaced by $\hat{S}_1(j)$. Hence, the log likelihood for a split at position k becomes

$$\lambda_{\text{split}}(k) = -M(1 + \ln \pi) - \sum_{j=1}^k \ln \hat{S}_1(j) - \sum_{j=k+1}^M \ln \hat{S}_2(j) \quad (9.13)$$

This can be compared with the log likelihood that the merged region is consistent with a single overall spectrum estimate $\hat{S}_0(j)$, denoted by the subscript 0. The log likelihood λ_{merge} is then derived from (9.13) by summing over the complete region. The region is split if the log likelihood difference,

$$\lambda_D(k) = \lambda_{\text{split}}(k) - \lambda_{\text{merge}} = \sum_{j=1}^M \ln \hat{S}_0(j) - \sum_{j=1}^k \ln \hat{S}_1(j) - \sum_{j=k+1}^M \ln \hat{S}_2(j) \quad (9.14)$$

exceeds some threshold value.

9.4.2 Edge-Detection Performance

It has been shown in Chapters 7 and 8 that the SWCE configuration maximizes the total detection probability P_{tot} , whereas FWSE maximizes the probability of detecting an edge in the correct position P_d [12–15]. We adopt the same configurations for edge detection in correlated textures.

Selecting the threshold level is a complicated process because it depends on edge position, mean, order, correlation length, false alarm probability (P_{fa}), and window size. Simulation indicates that the threshold is approximately independent of mean, order, and correlation length but proportional to the square root of window size and the log of P_{fa} . It also depends on the position of the test edge within the window, being approximately constant over the central region and reducing by about 10% toward the ends of the window [9,12]. Unfortunately, P_{fa} is strongly dependent on the threshold, so a small change in the setting leads to large changes in P_{fa} . Thus, if a well-defined P_{fa} is demanded, the threshold must be selected by simulation for the specific conditions.

We comment only on selected aspects of detection performance [9,12]. It is important to establish whether the spectral method makes as effective use of the texture information as the PDF-based technique described in the previous chapter. Therefore, we start by considering edge detection between textures with

short correlation lengths of 0.5 pixels (so that samples are approximately uncorrelated). Initially we consider the dependence of P_d and P_{tot} on window height n_y for a fixed width $n_x = 16$ as the edge position in the x -direction is tested. The following observations can be made:

- FWSE yields a greater value of P_d than the SWCE configuration.
- SWCE yields a greater value of P_{tot} than the FWSE configuration.
- The window height n_y needs to be about four times greater to give similar performance to that achieved with PDF-based edge detection.

The first two conclusions are the same as previous results for uncorrelated texture (in Chapter 8) and differences in mean only (in Chapter 7). Since both PDF-based and spectrum-based edge detection are derived from MLEs, it is not immediately clear why the latter is less effective. However, it should be appreciated that the spectral method makes no assumption about the relationship between different spectral coefficients; each is separately determined from the data. The PDF technique, on the other hand, assumes that the data are completely described by a single texture parameter, the order, which is determined from the data. This representation makes use of more specific prior knowledge about the texture and so would be expected to yield greater accuracy.

We next comment on the dependence of P_d and P_{tot} on order parameter for approximately uncorrelated textures. Again, we compare both spectral and PDF-based performance for both FWSE and SWCE configurations. The results for P_d lead to the following observations:

- FWSE yields a greater value of P_d than the SWCE configuration.
- The difference is more marked with spectral-based than PDF-based methods.
- PDF-based performance is better than spectral-based results.

The corresponding comparison for P_{tot} leads to the same conclusions. Note that the difference between the FWSE and SWCE configurations is much greater for the spectral-based method than for the PDF-based one.

Finally, when we apply the spectral technique described in this chapter to assess the dependence of P_d and P_{tot} on correlation length, we find that:

- FWSE again yields a greater value of P_d than the SWCE configuration.
- SWCE again yields a greater value of P_{tot} than the FWSE configuration.

No comparison with the PDF-based edge detector is possible since this cannot use any information derived from texture correlations.

9.5 Discussion

Introducing correlations into texture representation renders exploitation considerably more complicated. The single-point statistics can be well represented by a K distribution, as demonstrated in Chapter 5. Gamma and log normal PDFs were shown in Chapter 8 to provide convenient analytic approximations with little loss in performance. These PDFs are also capable of representing a wide range of data types. Thus, characterization in terms of the single parameter representing order should be a robust approach. However, we require a very large number of parameters to describe the spectrum at all possible spatial frequencies, which prevents any simple characterization of the spectral properties.

It is essential to have prior knowledge of the specific form of the texture ACF for model-based parameter estimation. The order parameter of a simple texture characterized by order and symmetrical Gaussian correlation length seems most robustly estimated from the normalized variance of amplitude. The log ACF yields poor results for large order parameters and correlation lengths, but fitting the normalized log, as in Chapter 8, leads to smaller errors if texture correlations are ignored. Estimating the correlation length reveals little difference between fitting the intensity, amplitude, and log ACFs. However, the intensity ACF has a simple analytic form that lends itself readily to the fitting process and is probably to be preferred.

In Section 9.3 we conclude that parameter estimation should not be employed as a stage in texture classification. It is less sensitive than the spectral method and requires knowledge of the analytic form of the ACF. The spectral method can be based on assuming that each component of the complex spectrum of the log of the image is Gaussian. The PDFs of the spectra from intensity or amplitude data are not sufficiently close to Gaussian. Classification performance for uncorrelated textures is comparable with results from the PDF-based technique in Chapter 8. At present there is no analysis for correlated textures. However, the results with uncorrelated textures suggest that the method might also provide a sensitive classifier for correlated textures.

There are additional problems in edge detection. Each spectral coefficient has a real and imaginary component from which both the mean and variance of its Gaussian PDF have to be estimated. Edge-detection performance is improved if it is assumed that the mean is identically zero, which reduces the statistical uncertainty in the estimates of the variances. However, this assumption was demonstrated to degrade classification performance, which also raises

some doubt about its impact on edge detection. The probability of detecting the edge in the correct position, P_d , was shown to be greater with the FWSE configuration than with the SWCE configuration. The total detection probability within the window, P_{tot} , on the other hand, was greater with SWCE. Thus, the general properties of edge-detection configurations discussed in Chapters 7 and 8 still apply. In particular, the two-stage scheme that initially optimized P_{tot} using SWCE, followed by edge refinement using FWSE with the window placed at the edge position estimated by SWCE, is shown to be nearly optimum for both correlated and uncorrelated textures as well as for differences in the mean [12–14,16].

Significantly, edge-detection performance for uncorrelated textures using the spectral method was found to be poorer than that based on the single-point statistics, requiring about four times the window size for comparable results. This has considerable impact on how we might exploit the spectrum in deriving information from texture analysis. Rather than attempting to segment simultaneously into an unspecified number of regions of uniform order and spectral properties, it suggests that two other options should be considered:

- Simpler spectrum representation;
- Data-driven classification into a restricted number of classes.

A simpler spectrum representation in which the number of spectral coefficients is only a small fraction of the number of pixels within the window would improve the accuracy of the parameter estimates. This might result in segmentation accuracy comparable with classification against a similarly restricted number of predefined classes, as in Section 9.3.2. Alternatively, data-driven classification into a small number of classes, similar to Section 8.4.3, should have a similar effect, since the accuracy with which the coefficients are estimated improves rapidly as we move away from the one-to-one mapping described in Section 9.4.2.

Further development of methods for extracting information from correlated textures is required to clarify these issues. However, note that even when the additional richness implied by correlation is successfully exploited, the increased complexity of spectral analysis will demand considerably more processing than the single-point texture exploitation described in the previous chapter.

References

- [1] Oliver, C. J., “Review Article—Information from SAR Images,” *J. Phys. D: Appl. Phys.*, Vol. 24, 1991, pp. 1493–1514.

- [2] Lombardo, P., and C. J. Oliver, "Estimating the Correlation Properties of K-Distributed SAR Clutter," *IEE Proc. Radar Sonar Navig.*, Vol. 142, 1995, pp. 167–178.
- [3] Oliver, C. J., "Clutter Classification Based on a Correlated Noise Model," *Inv. Problems*, Vol. 6, 1990, pp. 77–89.
- [4] Oliver, C. J., "Parameter Estimation with Correlated Textures," *Inv. Problems*, Vol. 5, 1989, pp. 903–914.
- [5] Abramowitz, M., and I. A. Stegun, *Handbook of Mathematical Functions*, New York: Dover, 1970.
- [6] Oliver, C. J., "Optimum Texture Estimators for SAR Clutter," *J. Phys. D: Appl. Phys.*, Vol. 26, 1993, pp. 1824–1835.
- [7] Lombardo, P., and C. J. Oliver, "Estimation of Texture Parameters in K-Distributed Clutter," *IEE Proc. Radar Sonar Navig.*, Vol. 141, 1994, pp. 196–204.
- [8] Blacknell, D., "A Comparison of Parameter Estimators for the K Distribution," *IEE Proc. Radar Sonar Navig.*, Vol. 141, 1994, pp. 45–52.
- [9] Oliver, C. J., "Optimum Classification of Correlated SAR Textures," *Europto Conf. on SAR Image Analysis, Simulation and Modelling*, Taormina, Sicily, *SPIE Proc.*, Vol. 2958, 1996, pp. 64–73.
- [10] Oliver, C. J., "The Sensitivity of Texture Measures for Correlated Radar Clutter," *Inv. Problems*, Vol. 5, 1989, pp. 875–901.
- [11] Blacknell, D., "Texture Anomaly Detection in Radar Imagery," *Europto Conf. on SAR Data Processing for Remote Sensing*, Rome, *SPIE Proc.*, Vol. 2316, 1994, pp. 125–136.
- [12] Oliver, C. J., "Correlated Texture Information in SAR," DRA Tech. Memorandum DRA/LS2/TR96020, 1997.
- [13] Oliver, C. J., D. Blacknell, and R. G. White, "Optimum Edge Detection in SAR," *IEE Proc. Radar Sonar Navig.*, Vol. 143, 1996, pp. 31–40.
- [14] Oliver, C. J., I. McConnell, D. Blacknell, and R. G. White, "Optimum Edge Detection in SAR," *Europto Conf. on SAR Image Analysis, Simulation and Modelling*, Paris, *SPIE Proc.*, Vol. 2584, 1995, pp. 152–163.
- [15] Oliver, C. J., I. McConnell, and D. Stewart, "Optimum Texture Segmentation of SAR Clutter," *Proc. EUSAR 96*, Konigswinter, 1996, pp. 81–84.
- [16] Oliver, C. J., and P. Lombardo, "Simultaneous Mean and Texture Edge Detection in SAR Clutter," *IEE Proc. Radar Sonar Navig.*, Vol. 143, 1996, pp. 391–399.

10

Target Information

10.1 Introduction

The concept of an object being a target reflects military terms of reference in which the scene is regarded as consisting of background clutter and a small number of significant objects (i.e., targets), which are generally man-made, such as buildings, bridges, or vehicles. These cannot be treated as homogeneous, like natural clutter, but are characterized by local *structure* rather than texture, which is position dependent. Indeed, the scattered radiation requires a deterministic coherent treatment in which the relative phase of each scatterer is retained.

In Figure 10.1(a) we show a simulated image of a tanklike vehicle at a resolution of 3m with no background. Though there is little evidence of structure at this resolution, the image is clearly asymmetric. Forming an equivalent image at a resolution of 0.75m, as shown in Figure 10.1(b), illustrates that the target return is dominated by four major scatterers, clearly resolved under these conditions. Since targets are dominated by a few well-separated scatterers, essential information is contained in the phase and amplitude relationships between them.

In addition to targets, each scene comprises a majority of pixels containing clutter that provides the background against which targets must be detected. The result of adding a uniform speckle background (20 dBs below the target peak) is shown in Figure 10.1(c). In addition to distorting the target shape, the single-look speckle completely destroys the regular sidelobe structure by interfering with the target return. In target detection we are concerned with discriminating this target from the neighboring background. In subsequent recognition

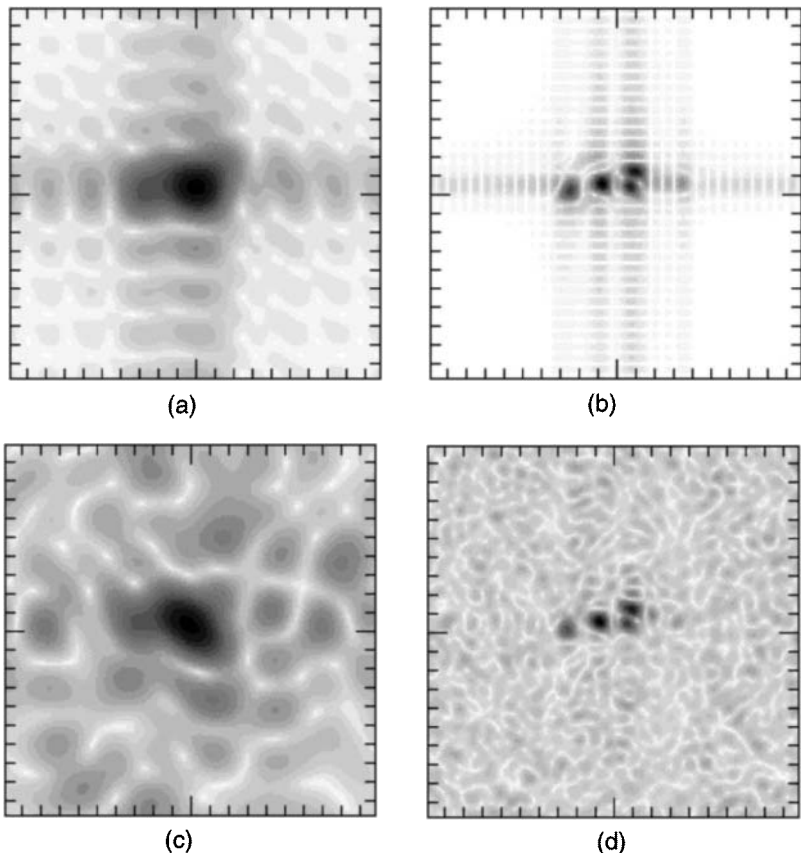


Figure 10.1 Simulated images of a tanklike object at different resolutions showing the effects of introducing a weak background with an SCR of 20 dB: (a) 3-m resolution, no background; (b) 0.75-m resolution, no background; (c) 3-m resolution with background; and (d) 0.75-m resolution with background.

we are involved with characterizing the target based on the structure of the return. Both these processes are degraded by the speckle background. Adding the same background level to the high-resolution image in Figure 10.1(b) leaves the brighter returns largely unchanged, as shown in Figure 10.1(d), but the sidelobe structure is again destroyed.

In Section 10.2 we introduce a Bayesian approach to target detection and show the relationships between different detection criteria. Since targets occupy only a very small fraction of the pixels within the image, the simultaneous minimization of false detections and maximization of genuine detections is extremely important. In Sections 10.3 and 10.4 we discuss how the nature of

target and background properties affects the detection process and the influence of uncertainties introduced by estimating target and background parameters. Section 10.5 then addresses further refinements associated with problems encountered in *constant false alarm rate* (CFAR) detection. Once targets have been detected, target recognition is introduced in Section 10.6. The issues of discrimination and classification are addressed in Sections 10.7 and 10.8. In Section 10.9 we outline an approach to target super-resolution that allows targets to be reconstructed with increased spatial resolution by introducing prior knowledge into the imaging process. This can provide a useful processing stage before classification is attempted.

10.2 Introduction to Target Detection

Let us initially explore a Bayesian approach to target detection [1]. The problem is one of testing two hypotheses for the data vector \mathbf{x} , namely, that a target is present or not. Detection performance can then be characterized in terms of the probability of false alarm, P_{fa} , that the data \mathbf{x} will be interpreted as denoting the presence of a target when one is not present, and the probability of detection, P_d , that a target will be detected when one is indeed present. The Bayes criterion for detecting a target states that

$$P(T|\mathbf{x}) = P(\mathbf{x}|T)P(T)/P(\mathbf{x}) \quad (10.1)$$

where $P(T|\mathbf{x})$, the a posteriori PDF, describes the probability of a target given the data; $P(\mathbf{x}|T)$, the likelihood function, describes the probability of data \mathbf{x} when a target is present; $P(T)$ is the a priori probability that a target is present; and $P(\mathbf{x})$ is the probability of obtaining that data. Similarly for the background hypothesis,

$$P(B|\mathbf{x}) = P(\mathbf{x}|B)P(B)/P(\mathbf{x}) \quad (10.2)$$

The MAP criterion implies that a target should be considered *present* when

$$\frac{P(T|\mathbf{x})}{P(B|\mathbf{x})} > 1$$

from which

$$\frac{P(\mathbf{x}|T)}{P(\mathbf{x}|B)} > \frac{P(B)}{P(T)} \quad (10.3)$$

where the left-hand side of (10.3) is the likelihood ratio. Notice in (10.3) that as the ratio of background to target probabilities increases, causing targets to become scarcer, the threshold level is increased to reduce the number of potential false alarms.

The MAP detection criterion is usually impractical since it requires prior knowledge of the relative probabilities of target and background. If we assume that clutter and target are equally likely, (10.3) reduces to

$$\frac{P(\mathbf{x}|T)}{P(\mathbf{x}|B)} > 1$$

which is the ML detection criterion. However, this is an unreasonable assumption for target detection, and thus, we adopt an intermediate criterion, the Neymann–Pearson observer [2], for which a target is detected if [3]

$$\frac{P(\mathbf{x}|T)}{P(\mathbf{x}|B)} > t \quad (10.4)$$

The threshold t is selected to give a defined false alarm probability. The detection conditions in (10.3) and (10.4) now depend on knowing the correct target and background likelihood functions.

In practice, only the background PDF is characterized. Under these conditions we are forced to adopt anomaly detection, a suboptimum approach. The data are assigned to the background if they appear consistent with the known background distribution, so

$$P(\mathbf{x}|B) > t \quad (10.5)$$

otherwise a target is declared present.

Consider a single pixel with value x , which is assumed positive. The probability of a false alarm in a background region is given by

$$P_{fa} = \int_t^{\infty} P(x|B) dx \quad (10.6)$$

where the threshold t can be selected to yield a certain CFAR. The corresponding detection probability for a target is

$$P_d = \int_t^{\infty} P(x|T) dx \quad (10.7)$$

An example of how estimates of the relevant quantities can be obtained is illustrated in Figure 10.2. The average target intensity can be estimated over the central *region of interest* (ROI) of m pixels, that is, $\bar{I}_T \equiv \sum_{j=1}^m I_j / m$. The ROI is surrounded by a guard ring a few pixels wide to prevent any leakage from the target into the boundary ring of M pixels, which is used to estimate the average background level \bar{I}_B , as well as the normalized background variance V_B . A conventional two-parameter CFAR [4] applied to image intensity is defined by the criterion that “detection” occurs when

$$\frac{\bar{I}_T / \bar{I}_B - 1}{\sqrt{V_B}} > t \quad (10.8)$$

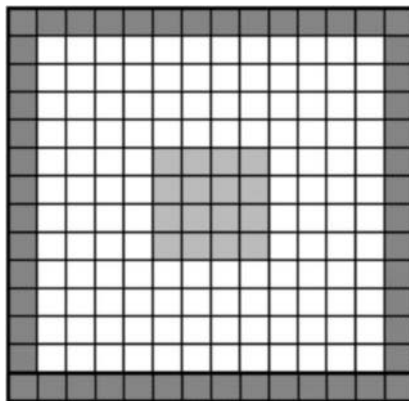


Figure 10.2 Diagram of target detection configuration comprising an ROI for a target in the center, a guard ring to avoid leakage from the target into the background, and a boundary ring to estimate the background level.

In the simplest implementation of (10.8) we assume that the background RCS is constant, so for single-look SAR, $\sqrt{V_B} = 1$, resulting in the one-parameter CFAR condition

$$\frac{\bar{I}_T}{\bar{I}_B} - 1 > t \quad (10.9)$$

which forms the basis of conventional cell-averaging CFAR. We shall refer to the term on the left-hand side of (10.8) and (10.9) as the CFAR statistic. Note, however, that these estimated parameter values may be suboptimal, contributing to CFAR loss [5].

This discussion shows that where the target PDF is not known it is not possible to provide an optimum Bayesian classification. One can only set a CFAR threshold and detect targets as anomalies in the specified background distribution. If the target PDF is known, P_d could then be derived from (10.7). However, this would be a suboptimal use of the information. The Neymann–Pearson criterion, in which the CFAR threshold is defined in terms of the likelihood ratio, should be used instead. Indeed, Blacknell and Tough [6] have suggested that it is preferable to adopt weak prior knowledge about the target, encapsulated in a broad PDF, and then *classify* into target/background, using (10.4), rather than perform *anomaly detection* into background/not background, based on (10.5), which is all that is possible without a target model.

10.3 Constant Target and Background RCS

The simplest scattering scenario corresponds to a constant RCS background, leading to a negative exponential background intensity PDF when speckle is included. In this section we adopt this model and further assume a Swerling 1 target [7], which also has a negative exponential intensity distribution.

10.3.1 Standard CFAR Target Detection

Initially let us assume that a target fills a single pixel. Standard CFAR target detection then consists of inspecting individual pixels and assigning each to background or target classes on the basis of the RCS and prior knowledge of the

background distribution for a single pixel. Since the background PDF is negative exponential, the false alarm rate is given by

$$P_{fa} = \frac{1}{\sigma_B} \int_t^\infty \exp\left[-\frac{I}{\sigma_B}\right] dI = \exp\left[-\frac{t}{\sigma_B}\right] \quad (10.10)$$

where σ_B is the background RCS. Hence, the required t for a given false alarm probability is given by

$$t = -\sigma_B \ln P_{fa} \quad (10.11)$$

and the detection probability for a Swerling 1 target by

$$P_d = \exp\left[-\frac{t}{\sigma_T}\right] = \exp\frac{\ln P_{fa}}{R} \quad (10.12)$$

where $R \equiv \sigma_T/\sigma_B$ is the SCR.

On averaging the background over the ROI, \bar{I} will be gamma-distributed with mean σ_B and order parameter m so that

$$P_B(\bar{I}) = \frac{1}{m} \left(\frac{m}{\sigma_B} \right)^m \frac{\bar{I}^{m-1}}{\Gamma(m)} \exp\left[-\frac{m\bar{I}}{\sigma_B}\right] \quad (10.13)$$

and the appropriate false alarm probability is given by the incomplete gamma function (Section 6.5 in [8])

$$P_{fa} = \Gamma\left(m, \frac{t}{\sigma_B}\right) / \Gamma(m) \quad (10.14)$$

This enables the threshold level t for the incoherent average \bar{I} to be derived numerically for a specific CFAR. Similarly, the detection probability for a Swerling 1 target filling the ROI would be

$$P_d = \Gamma\left(m, \frac{t}{\sigma_T}\right) / \Gamma(m) \quad (10.15)$$

A typical result for the dependence of P_d on the SCR is illustrated in Figure 10.3 for windows of 1, 4, 9, 16, and 36 pixels. P_{fa} was set to 10^{-3} throughout. It is apparent that P_d is considerably increased by incoherent averaging over many pixels. Thus, it is advantageous to increase resolution as far as possible so that the image of the target is spread over as many pixels in the ROI as possible, with consequent reduction in speckle.

This analysis is, however, misleading because, in practice, both target and background RCS are unknown and have to be estimated from the data, leading to CFAR loss [5]. In addition, real targets would be unlikely to have uniform RCS over the window.

10.3.2 Optimized Target Detection

CFAR loss can be minimized by adopting a target detection scheme that incorporates ML parameter estimates. The probability that the target and background estimates are consistent with belonging to the same or different PDFs

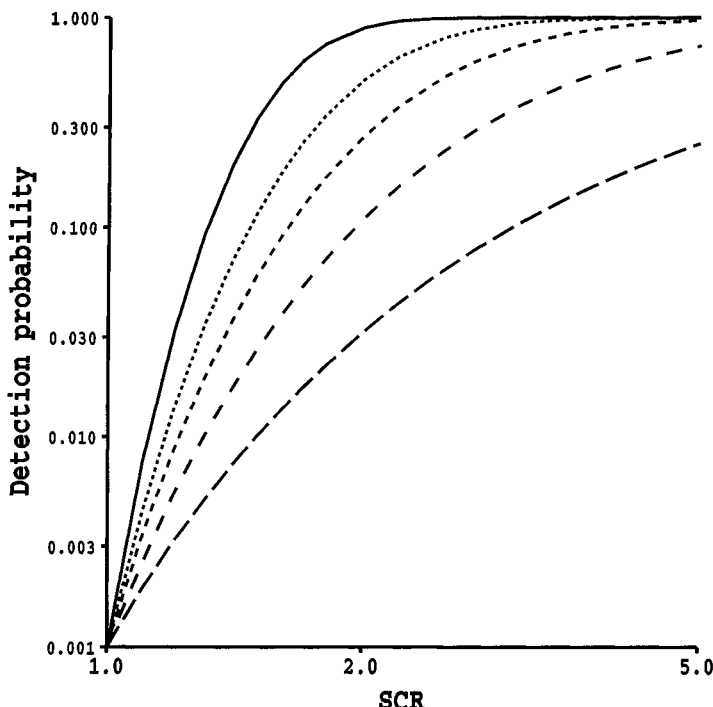


Figure 10.3 Variation of P_d with SCR for negative exponential statistics; dependence on region size $m = 1, 4, 9, 16$, and 36 from right to left.

follows the same description as the segmentation theory summarized in Chapter 7, with a log likelihood difference similar to (7.5), such that

$$\lambda_D = -m \ln \bar{I}_T - M \ln \bar{I}_B + (M + m) \ln \bar{I}_0 \quad (10.16)$$

where

$$\bar{I}_0 = \frac{m\bar{I}_T + M\bar{I}_B}{M + m} \quad (10.17)$$

A target is detected when λ_D exceeds some threshold t . As described in Chapter 7, the detection probability as a function of the SCR, R , can now be expressed in terms of the observed ratio r ($\equiv \bar{I}_T/\bar{I}_B$), with the additional constraint that $r > 0$. Hence,

$$\begin{aligned} P_d &= 1 - \int_0^t P_r(r|R, m, M) \\ &= 1 - \frac{\Gamma(M+m)}{m\Gamma(m)\Gamma(M)} \left(\frac{mr}{MR} \right)^m {}_2F_1 \left[m, M+m; m+1; -\frac{mr}{MR} \right] \end{aligned} \quad (10.18)$$

where ${}_2F_1[.]$ is the Gaussian hypergeometric function (Section 15.1 in [8]).

P_{fa} is obtained by setting $R = 1$, which allows the numerical derivation of t for a given P_{fa} . The detection probability can then be calculated for different values of R . The simple analytic theory for known means is compared with the results for estimated means in Figure 10.4. This shows that the uncertainty attendant on introducing estimated, rather than known, values for the means demands an increase of between 10% and 15% in the SCR for a fixed P_d . Note also in Figure 10.4 the advantage of performing incoherent averaging to reduce speckle fluctuations, when both target and clutter have constant RCS with statistics determined by speckle.

10.4 Effect of Background and Target Statistics

So far, both clutter and target intensity PDFs have been treated as negative exponential. Any fluctuation in underlying RCS will influence detection that is based on the RCS alone. An underlying gamma-distributed cross section, leading to a K-distributed intensity, has been demonstrated to provide a close fit to

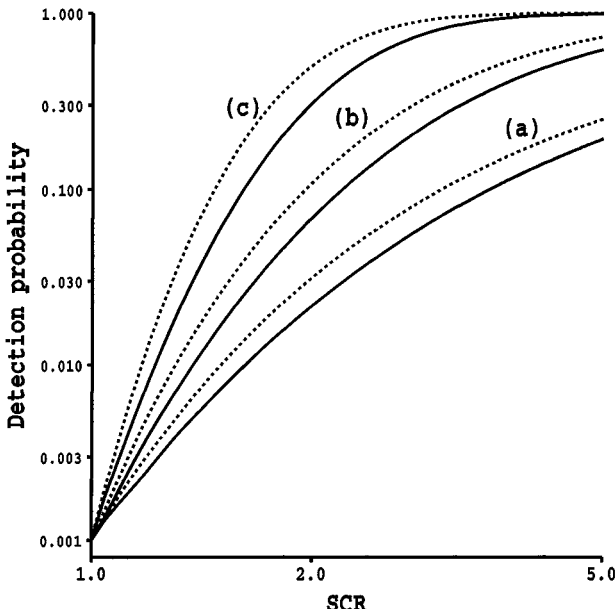


Figure 10.4 Variation of P_d with SCR for negative exponential statistics; the effect of estimation errors. Three configurations are compared with: (a) $m = 1, M = 16$; (b) $m = 4, M = 28$; and (c) $m = 16, M = 52$. Results for known means are denoted by dashed curves, those for estimated means by full curves.

observed clutter in Chapter 5 and exploited in texture segmentation in Chapter 8. Let us now examine the effect of a K-distributed background with a PDF

$$P(I) = \frac{2}{\Gamma(\nu_B)} \left(\frac{\nu_B}{\mu_B} \right)^{(1+\nu_B)/2} I^{(\nu_B-1)/2} K_{\nu_B-1} \left[2 \sqrt{\frac{\nu_B I}{\mu_B}} \right] \quad (10.19)$$

for single-look SAR, where μ_B and ν_B are the background mean and order, respectively. In Section 10.4.1 we describe standard CFAR detection, based on the RCS, for a Swerling 1 target against this type of textured clutter. If the target ROI subtends several pixels it is possible to characterize higher order properties of the target region, such as an order parameter, in addition to the average RCS. In Section 10.4.2 we take advantage of this additional degree of freedom in proposing a texturelike target model representing the interference between scattering centers in a single target. We show how this can result in a target detection algorithm that again uses the Neymann–Pearson criterion with ML parameter estimates.

10.4.1 Standard CFAR Target Detection

If a target occupies a single pixel, the RCS is the only measurable quantity. For a K-distributed background, the false alarm probability, from standard CFAR theory on a single pixel, is given by (10.6) as

$$P_{fa}^{(K)} = \frac{2}{\Gamma(\nu_B)} \left(\frac{\nu_B t}{\mu_B} \right)^{\nu_B/2} K_{\nu_B} \left[2 \sqrt{\frac{\nu_B t}{\mu_B}} \right] \quad (10.20)$$

The appropriate value of threshold t can be derived numerically by inverting (10.20) for a given $P_{fa}^{(K)}$. If the threshold is derived assuming negative exponential rather than K-distributed clutter, as in (10.11), the modified false alarm rate P'_{fa} is given by

$$P'_{fa} = \frac{2}{\Gamma(\nu_B)} (-\nu_B \ln P_{fa})^{\nu_B/2} K_{\nu_B} \left[2 \sqrt{-\nu_B \ln P_{fa}} \right] \quad (10.21)$$

Figure 10.5 illustrates the effect the K-distributed background has on the predicted false alarm rate. As ν_B increases, the background PDF tends toward a negative exponential so that the two values of false alarm rate become the same. In the opposite limit of small ν_B , corresponding to a spiky background distribution, P'_{fa} increases by between one and two orders of magnitude compared with $P_{fa}^{(K)}$. This demonstrates the crucial importance of adopting a realistic background clutter model for target-detection theory. Ward [9] demonstrated the consequences of ignoring background RCS variations in maritime target detection. Theoretical studies of corrected CFAR algorithms for Weibull [4,10–14] and K-distributed [15] clutter have been reported.

If a target subtends many pixels, we can estimate the CFAR conditions over more than the single pixel discussed previously. We have already demonstrated that it is advantageous to perform incoherent averaging over many pixels. Unfortunately, there is no analytic relationship between the single-pixel K distribution and the result of performing incoherent averaging when the cross section itself varies between pixels. (Note that multilook imaging discussed in Chapter 4 assumes that the cross section is constant and that only the speckle fluctuates.) For simplicity we adopt the same gamma distribution approximation to the K distribution proposed in Chapter 8. The mean of the two PDFs is the same and the order parameters are related by

$$\psi^{(0)}(\nu_\gamma) - \ln \nu_\gamma = \psi^{(0)}(\nu) - \ln \nu - \gamma_E \quad (10.22)$$

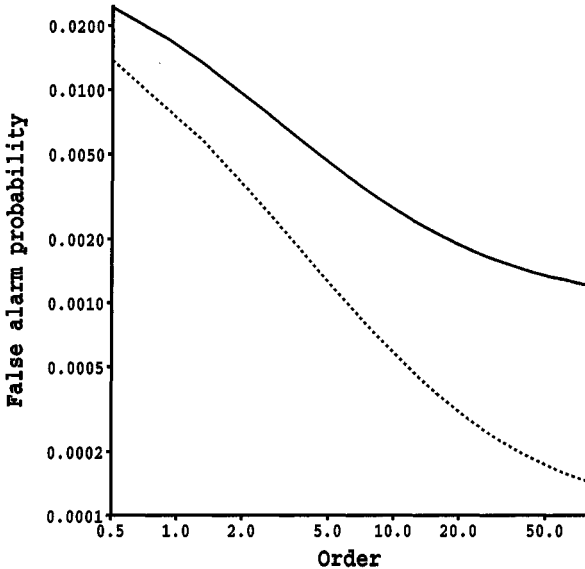


Figure 10.5 Dependence of false alarm probability for a single pixel of K-distributed background, incorrectly assumed to be negative-exponentially distributed, on clutter order parameter. Results for nominal negative exponential false alarm probabilities of 10^{-3} (full curve) and 10^{-4} (dashed curve) are shown.

where ν is the order of the K distribution, ν_γ is that for the approximating gamma distribution, $\psi^{(0)}(\cdot)$ is the digamma function, and γ_E is Euler's constant (Chapter 6 of [8]). Thus, the approximate form for the single-pixel intensity PDF is

$$P(I) \approx \left(\frac{\nu_\gamma}{\mu_B} \right)^{\nu_\gamma} \frac{I^{\nu_\gamma - 1}}{\Gamma(\nu_\gamma)} \exp \left[-\frac{\nu_\gamma I}{\mu_B} \right] \quad (10.23)$$

Upon performing incoherent averaging over the ROI we obtain

$$P(\bar{I}) \approx \frac{1}{m} \left(\frac{m\nu_\gamma}{\mu_B} \right)^{m\nu_\gamma} \frac{\bar{I}^{m\nu_\gamma - 1}}{\Gamma(m\nu_\gamma)} \exp \left[-\frac{m\nu_\gamma \bar{I}}{\mu_B} \right] \quad (10.24)$$

The false alarm probability is then derived in the same way as (10.14), yielding

$$P_{fa} = \Gamma \left(m\nu_\gamma, \frac{\nu_\gamma t}{\mu_B} \right) / \Gamma(m\nu_\gamma) \quad (10.25)$$

Equation (10.25) can be inverted numerically to yield the appropriate value of threshold for a given P_{fa} .

To derive the target-detection probability we retain the Swerling 1 target model, adopted in Section 10.3, with uniform RCS over the ROI. The threshold setting, derived by inverting (10.25), is inserted into (10.12) to yield P_d .

The dependence of P_d on region size and background order parameter is illustrated in Figure 10.6(a,b). In each case $P_{fa} = 10^{-3}$ and the SCR varies from 1.0 to 5.0. In Figure 10.6(a) we show the dependence on region size for a K-distributed background order parameter of 1.0. If these results are compared with those in Figure 10.2 (with no background cross-section fluctuations), it is obvious that additional fluctuations degrade performance. As region size increases, both speckle and cross-section fluctuations are averaged out, improving P_d as before. In Figure 10.6(b) we illustrate the effect of ν_B on P_d , for $m = 16$, as the SCR varies from 1.0 to 5.0 and $P_{fa} = 10^{-3}$. This illustrates the increase in SCR that is required to keep P_d constant as ν_B decreases and background texture becomes more spiky.

10.4.2 Optimized Detection for the Textured Target Model

This analysis was directed entirely at providing target detection with a constant false alarm rate for K-distributed clutter with a uniform target RCS. However, high-resolution target images, as shown in Figure 10.1(b), tend to consist of a few dominant scatterers. The strength and position of these scatterers are strong functions of orientation, as we shall discuss in Section 10.8. Indeed images from different viewing angles bear little resemblance to each other. We therefore introduce a *textured target model* that includes strong noiselike RCS fluctuations with no knowledge of the positions of high intensity. In particular, we assume that both the target intensity and the clutter are K-distributed. The wide spatial variation in target RCS manifests itself through small values of order parameter, typically less than 1. We already investigated the effect of this form of background PDF on the CFAR threshold. Let us now examine how a target PDF of this form modifies conventional detection based on the RCS alone. The theoretical form of P_d now corresponds to (10.25) with μ_T and ν_T substituted for μ_B and ν_B , allowing also for the gamma PDF approximation as in (10.23). Figure 10.7 shows the effect of the target order parameter on P_d when $\nu_B = 1$ and ν_T ranges from 1.0 to 0.1. For small target strengths, with $SCR \approx 1.0$, more spiky targets have a better chance of detection due to the possibility of high-intensity data in the tail of the distribution. However, as the SCR increases, the spiky target PDF leads to a large probability of obtaining a low intensity resulting in a missed detection. A comparison of these results with those for the negative exponential target and background in Figure 10.6(b) indicates the

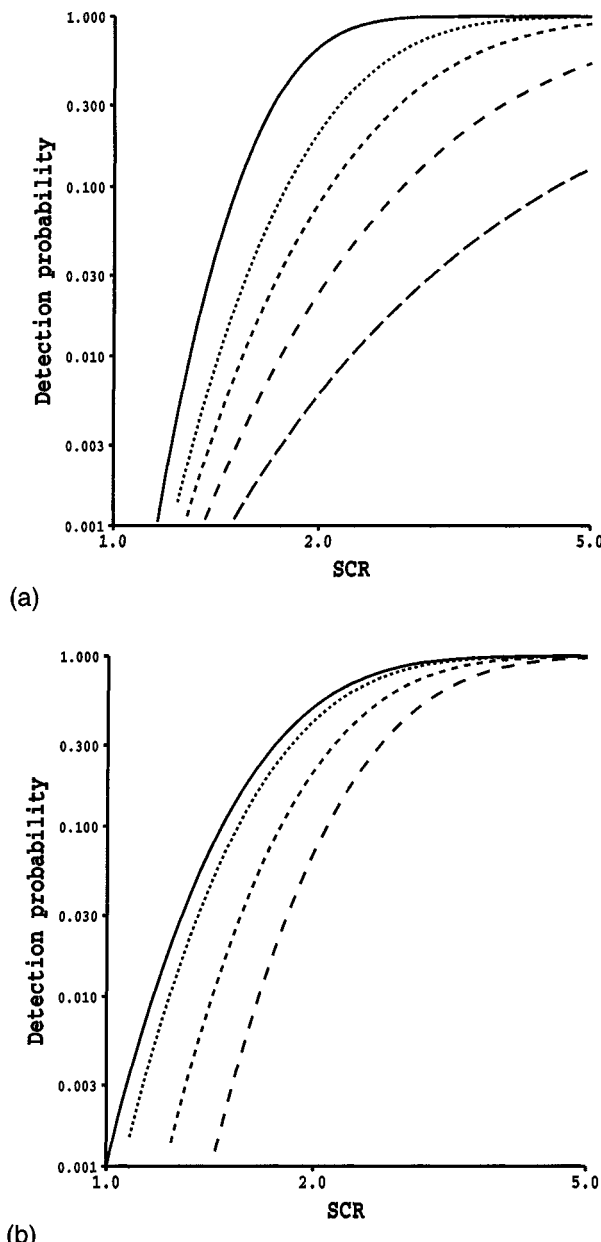


Figure 10.6 Variation of P_d with SCR for Swerling 1 target and K-distributed background; $P_{fa} = 10^{-3}$. (a) $v_B = 1$, dependence on $m = 1, 4, 9, 16, \text{ and } 36$ pixels from right to left. (b) $m = 16$, dependence on $v_B = 0.5, 1, 4, \text{ and } 16$ from left to right.

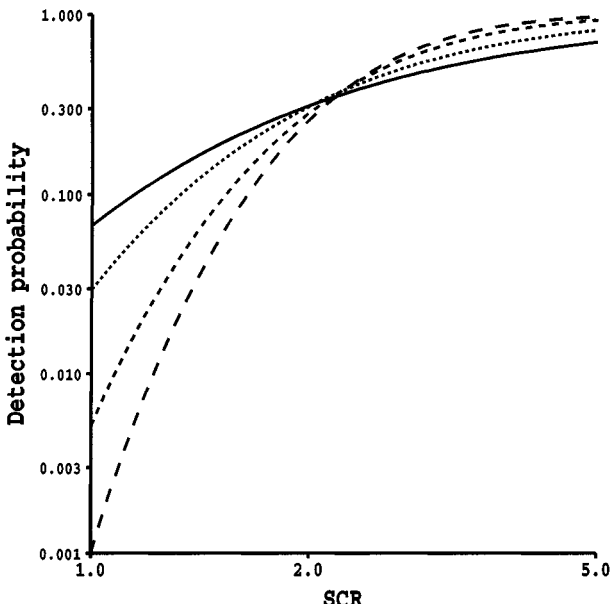


Figure 10.7 Variation of P_d with SCR for $P_{fa} = 10^{-3}$, $m = 16$, and $\nu_B = 1$. Dependence on $\nu_T = 0.1, 0.2, 0.5$, and 1 from top to bottom on the left-hand side.

considerable reduction in P_d as ν_T is reduced, that is, the target spikiness increases.

Is this performance degradation as target and clutter RCS depart from uniformity fundamental or does it stem from inadequate exploitation of the information in the signal? So far, target detection has been treated as depending solely on the difference in RCS between regions. The textured target model implies that both target and background have the same form of PDF, characterized by different values of both mean and order parameter. Optimized detection must be based on both parameters through the likelihood ratio, so detection based on RCS alone would be expected to be suboptimum. The full exploitation of texture properties in detection is closely related to textured segmentation, analyzed in Chapter 8. Unfortunately, there is no analytic solution, so we resort to simulation to determine threshold values and detection probabilities. The approach is similar to that adopted for Figure 10.4 except that both order and mean are estimated using the approximate ML estimators from (8.25) and (8.26), with $L = \infty$, namely,

$$\hat{\mu} = \bar{I} \equiv \frac{1}{N} \sum_{j=1}^N I_j \quad \text{and} \quad \ln \hat{\nu} - \psi^{(0)}(\hat{\nu}) = \ln \bar{I} - \ln \bar{I} \quad (10.26)$$

These estimates are then substituted into the expression for the log likelihood difference, similar to (8.41), leading to an ML log likelihood difference given by [16]

$$\begin{aligned}\lambda_D = & m \left[\hat{\nu}_T \ln \hat{\nu}_T - \hat{\nu}_T \ln \bar{I}_T - \ln \Gamma(\hat{\nu}_T) + (\hat{\nu}_T - 1) \overline{\ln I_T} - \hat{\nu}_T \right] \\ & + M \left[\hat{\nu}_B \ln \hat{\nu}_B - \hat{\nu}_B \ln \bar{I}_B - \ln \Gamma(\hat{\nu}_B) + (\hat{\nu}_B - 1) \overline{\ln I_B} - \hat{\nu}_B \right] \\ & - (M+m) \left[\hat{\nu}_0 \ln \hat{\nu}_0 - \hat{\nu}_0 \ln \bar{I}_0 - \ln \Gamma(\hat{\nu}_0) + (\hat{\nu}_0 - 1) \overline{\ln I_0} - \hat{\nu}_0 \right] \quad (10.27)\end{aligned}$$

where the target region is denoted by the subscript T, the background by B, and merged regions by 0; $\hat{\nu}$ denotes the order parameter estimated from (10.26). Detection occurs when λ_D exceeds the threshold t . Initially simulation is performed with target and background regions that have the same input properties to determine the appropriate threshold value for a given P_{fa} . Further simulations with varying mean and order parameters can then be performed based on this threshold to derive the performance characteristics.

Note that we no longer exploit the prior knowledge that either target or background has a negative exponential PDF (with $\nu \equiv \cdot$). In each case, both the mean and order parameter are *estimated* for each region.

Initially, in Figure 10.8(a), we vary ν_B between ∞ and 0.5, while ν_T is maintained at ∞ , corresponding to a negative exponential PDF. Threshold settings are determined by simulation over 10^5 samples, whereas results for P_d are obtained over 10^4 samples. These results should be compared with equivalent results for detection of RCS differences when parameter values are known in advance, shown in Figure 10.6(b). First, it should be noted that including the effect of texture in target detection now yields the best detection for a given SCR when the two order parameters differ most. Second, if we consider results for $\nu_B = \infty$, we see that having to estimate both mean and order has led to considerable reduction in detection performance compared with the original situation where these were known a priori.

In the second comparison, in Figure 10.8(b), we set $\nu_B = 1.0$ but allow ν_T to vary between 1.0 and 0.1. This represents the expected situation, with target fluctuations more marked than background ones. If we compare results for $\nu_B = \nu_T = 1.0$ in Figure 10.8(b) with those for $\nu_B = \nu_T = \infty$ in Figure 10.8(a), it is clear that reducing both ν_B and ν_T increases the uncertainty in the determination of parameter values and degrades detection. However, as ν_T falls below ν_B in Figure 10.8(b), detection improves considerably, which should be compared with Figure 10.7 where detection was based on RCS alone. Though reducing ν_T increases detection for small SCRs in Figure 10.7, the results for

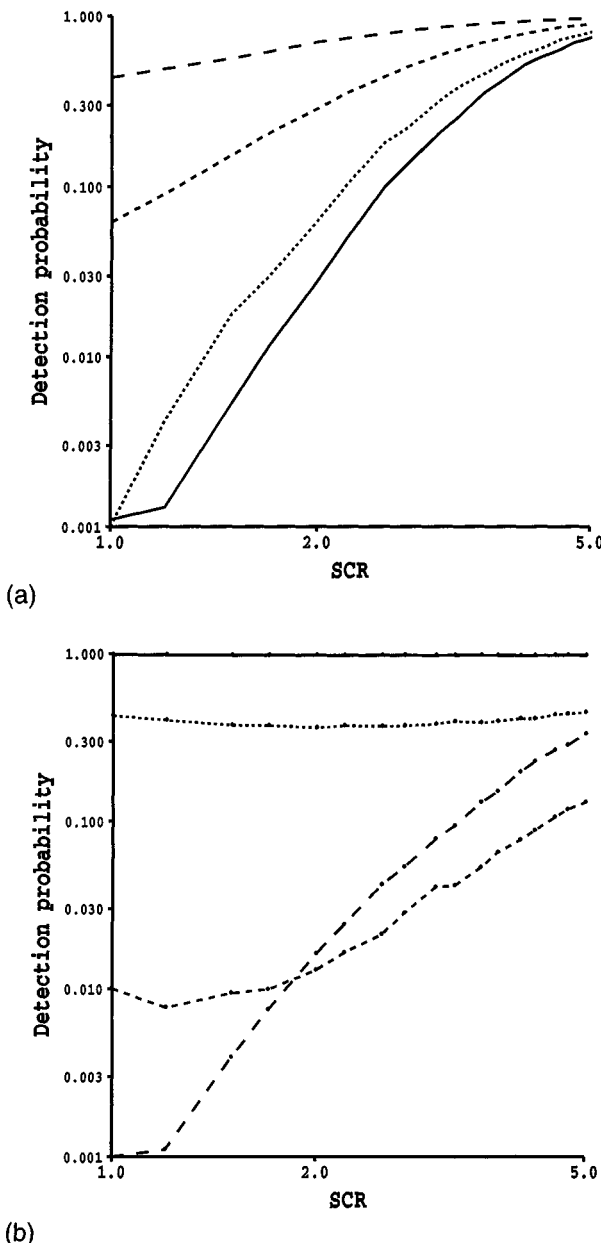


Figure 10.8 Variation of P_d with SCR for K-distributed target and background with parameters estimated over $m = 16$ and $M = 52$; $P_{fa} = 10^{-3}$. (a) $\nu_T = \infty$; curves correspond to $\nu_B = \infty, 4, 1$, and 0.5 ordered from bottom to top. (b) $\nu_B = 1.0$; curves correspond to $\nu_T = 1, 0.5, 0.2$, and 0.1 ordered from bottom to top on the left-hand axis.

larger SCRs are degraded. In the present results, the effect of reducing ν_T is that it becomes the dominant factor in detection and the performance is essentially independent of SCR for small ν_T . Texture alone provides target discrimination under these conditions. Thus, introducing the textured target model leads to a considerable improvement in detection capability.

Note that this method provides an optimized balance between differences in mean and order parameter as it corresponds to the Neymann–Pearson observer [2]. It uses ML estimates of parameters and overcomes the degradation where detection is based solely on differences in the RCS, which is all that is possible if the target merely subtends one pixel. The analysis shows that if the target occupies many pixels it is advantageous to use both RCS and texture in the detection process. Note that the analysis only approximates the K-distribution by a best-fit gamma distribution, as described earlier, resulting in slightly suboptimum performance.

A more sophisticated model which identifies the actual positions of strong scatterers should provide even better detection. Indeed, the goal of such an approach would be to provide a filter matched to a target with which to scan the scene. This is tantamount to omitting a distinct target detection stage and proceeding directly to a recognition mode, which will be addressed later. At present it should be noted that the textured target model achieves significant improvement in detection if the target extends over several pixels and shows strong fluctuations, consistent with a K distribution.

10.5 Further Refinements to Target Detection

Sections 10.3 and 10.4 dealt with comparatively simple target-detection scenarios. There are two areas in which this simple treatment should be extended:

- Obtaining more accurate estimates of background properties;
- Handling inhomogeneous backgrounds.

Since the determination of the background properties is governed by speckle, it is attractive to investigate methods for reducing this uncertainty. Combining different wavelength or polarization images could be considered. However, this has to be undertaken with care because properties are usually a strong function of both wavelength and polarization, as described in Chapter 11. Even if multipolarization images, for example, are combined using the polarization whitening filter [17–19], an improvement of only about 2.7 dB is obtained compared with a single-channel image, corresponding to 1.9 independent contributions. In Chapters 6 and 7 we demonstrated that the RCS could be estimated with an accuracy equivalent to averaging many more pixels than the boundary ring in Figure 10.2, leading to greatly improved estimation; so these methods can supersede conventional CFAR [20].

The major drawback of the target-detection configuration of Figure 10.2 is its response when either unwanted targets occur within the background ring or there are discontinuities in the background. In the presence of unwanted targets the estimates of both the background mean and variance are increased. For one-parameter CFAR, the increase in \bar{I}_B reduces P_d . In addition, the unwanted targets may themselves be detected. For two-parameter CFAR, the increase in the variance reduces the detection probability for both genuine and unwanted targets. If the background is textured, we showed in Section 10.4 that P_d for one-parameter CFAR is as expected, since the mean background is unchanged; however, P_{fa} is increased [9,21]. Two-parameter CFAR yields reduced P_{fa} because the variance is increased, at the expense of a reduction in P_d . Finally, the presence of a discontinuity in the background increases the variance and yields an estimate of the mean between the high and low background levels on either side of the discontinuity. This renders target detection and false alarm probabilities with both one- and two-parameter CFAR unreliable, depending on the true background value in the ROI.

Rohling [22] proposed that the order statistics within the boundary ring could be used to overcome the effects of unwanted targets. The PDF within the ring is attributed to many pixels containing a constant RCS (with associated speckle PDF), combined with a few isolated strong returns from the unwanted targets. The average constant background can be estimated by omitting the unwanted targets within the background ring. The choice of how to reject unwanted targets is therefore crucial. It could be implemented rigorously by testing the hypothesis that the ring contains $M - k$ constant background pixels and k unwanted targets. Following the description of annealed segmentation in Chapter 7, k could then be varied to find its optimum value. If the same scheme is applied to a textured background, it removes strong fluctuations, which increases P_d but will also increase P_{fa} .

Different types of CFAR detector have been proposed to cope with a step discontinuity in the background. These are based on detecting either the high [23] or low [24] regions in the background ring. However, the methods fail to provide a reliable estimate of the background surrounding the potential target.

In fact, the problem of both unwanted targets and discontinuous background can be largely overcome using segmentation methods, as described in Chapters 7 to 9. Since segmentation identifies all the regions that differ statistically from each other, regardless of shape, it provides the most sensitive method for identifying the true background level at each potential target, undistorted by neighboring unwanted targets or changes in background level.

The detection process is also influenced by variation in target type. We can describe objects that are comparable with or smaller than the system resolution as pointlike. At higher resolution (and for larger targets) the scattering elements making up that object become visible in the form of "texture," which may be

described in terms of either single-point statistics, correlation properties, or even deterministic target structure. The first category formed the basis of the target texture model in Section 10.4.2, while the latter two types can be regarded as part of target classification, discussed in Section 10.8. As we show in Section 10.7, other simple characteristics of targets can be used to discriminate between genuine and unwanted targets.

10.6 Introduction to Target Recognition

Since SAR images contain enormous numbers of pixels, it is desirable to provide *automatic target recognition* (ATR) functions in any image-understanding system. In the next few sections we will spell out some of the principles that underlie such a system and discuss the different compromises that have to be made in its design.

It is instructive to consider the main differences between SAR and optical images. These are illustrated in Figure 10.9, which compares (a) a side-view photograph of a tank with (b) a high-resolution simulated SAR image of a tanklike object, with the same orientation as in (a), imaged from the right. The optical photograph is instantly recognizable; the interpretation of the SAR image is more difficult. Not only is the resolution of the SAR image much poorer than the optical one, but its appearance differs dramatically. Though the gun barrel is visible to the right in both images, it is very difficult to associate other features in Figure 10.9(b) with those in Figure 10.9(a). Thus, recognition methods that have been developed to deal with optical images are inappropriate for SAR. Many recognition processes with optical images are feature-based. Recognition is then expressed in terms of the combination of these individual features. Thus, if an object has a roof, door, windows, and chimney, for example, it is a house. Alternatively, if it has tracks and a gun-barrel, it is a tank or self-propelled gun. This approach is feasible for the optical but not the SAR image. As a final complication there is the effect of speckle, which serves to disguise features in the image, as illustrated in Figure 10.1.

Recognition with SAR images must be a property of the complete target signature. However, the size of reference data base required to represent all the information within such an image is very large. In Figure 10.10 we illustrate simulated SAR images for a tanklike target over a variety of orientations in the horizontal plane, where the top left image corresponds to head-on illumination with strong backscatter from the front of the tank [25]. Images are then sequentially rotated by about 1.4 degrees per step. The image changes significantly as this occurs. There are strong returns from the broadside views on the left of rows 5 and 13 as well as from the back view, on the left of row 9. As the

(a)



(b)

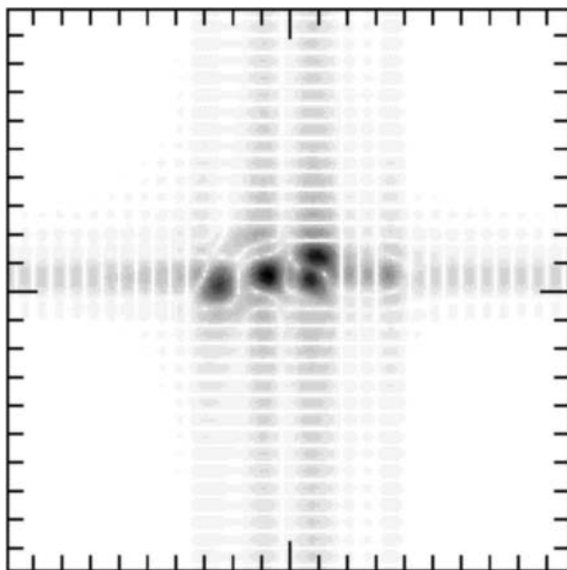


Figure 10.9 Comparison of (a) optical photograph and (b) simulated SAR image of tank.

image evolves with angle the strength and position of the dominant scattering centers change, due to broadside flashes, obscuration, and interference effects. However, the general image properties appear consistent with the textured target model in Section 10.4.2. In order to provide a reference set for such a target, about 256 separate orientations, each comprising (say) 32 by 32 elements, are required. However, this only represents horizontal rotations; pitch and roll must also be taken into account. If we allow for 20 different roll and pitch angles,

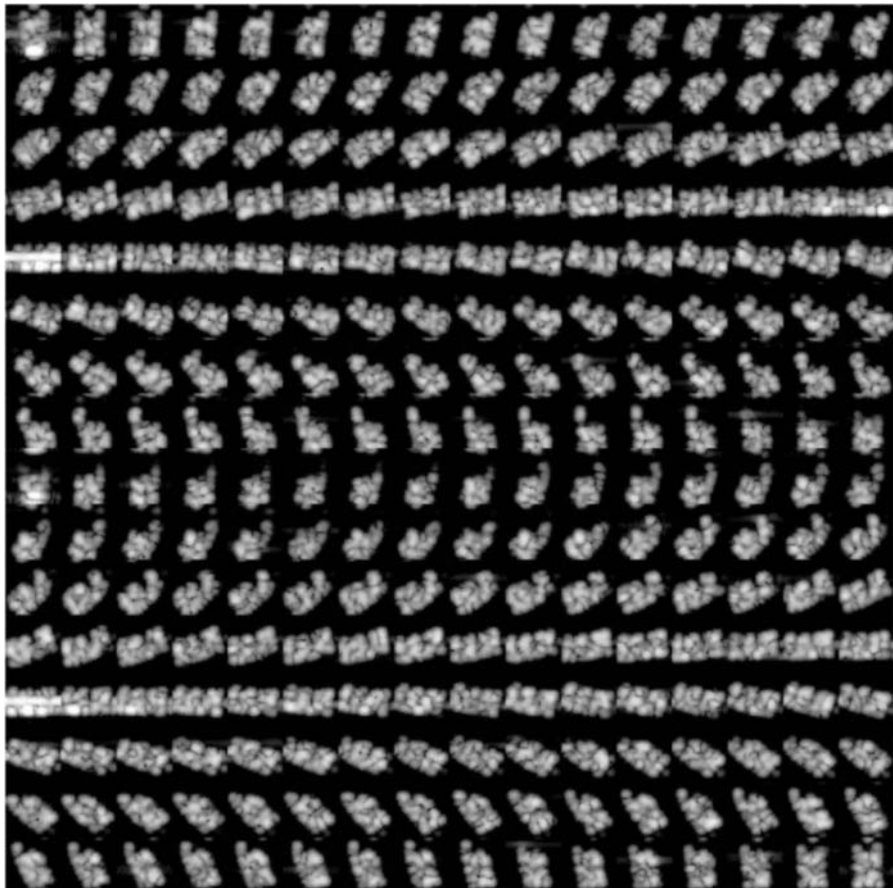


Figure 10.10 Variation of simulated SAR image of model tank with orientation over 360 degrees.

then the total data base for a single target class would comprise about 10^8 elements. Add to this the fact that we require reference sets for all potential targets (say 50) and the total data base consists of 5×10^9 elements.

Next consider discriminating between the simulated tank, with the reference set shown in Figure 10.10, and an *armored infantry fighting vehicle* (AIFV), with a corresponding set of simulated training data shown in Figure 10.11 [25]. For 100% classification, *all* the orientations of the tank image must be distinct from *any* for the AIFV. Once receiver noise and background speckle are included, it is by no means obvious from Figures 10.10 and 10.11 that this condition can be satisfied. A reduction in resolution with an increase in background clutter would certainly degrade the ability to distinguish between them.

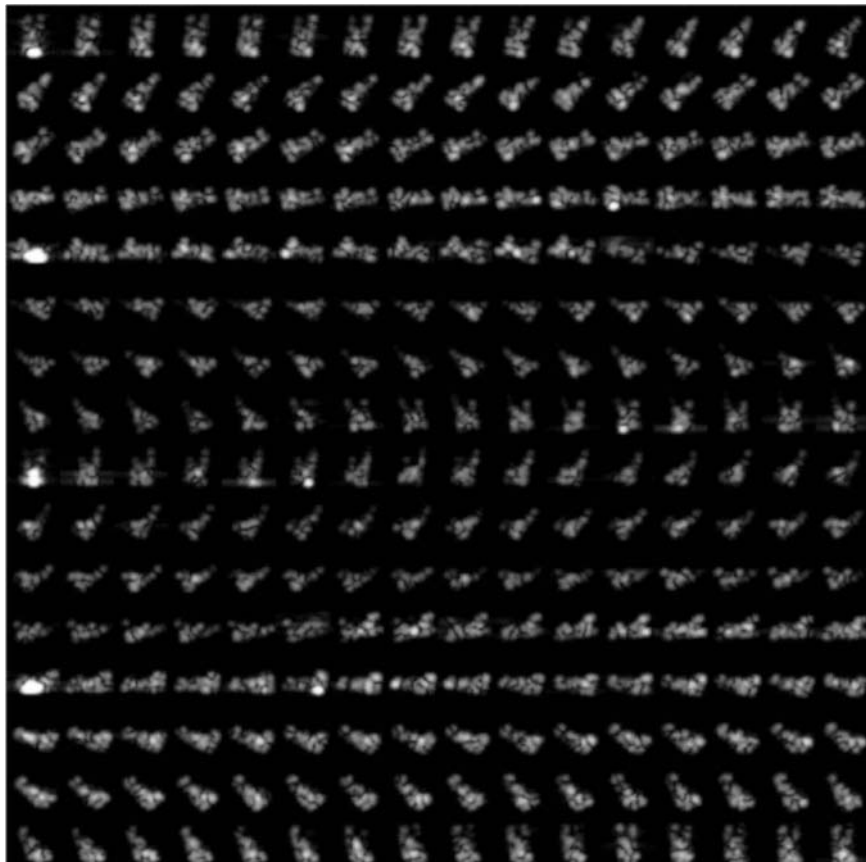


Figure 10.11 Variation of simulated SAR image of model AIFV with orientation over 360 degrees.

Given the scale of the computation load for real-time ATR based on such a set of references, it is essential to minimize the number of images to which full classification is applied.

10.7 Target Discrimination

An ATR scheme that factorizes target recognition into a variety of sequential steps of increasing complexity and sensitivity could be based on the processing chain illustrated in Figure 10.12. The entire SAR image is first scanned for targets in a *detection* stage [25]. This requires, at least, knowledge of the background clutter model but could be optimized by incorporating a target model into a Bayesian classifier, as described in Section 10.3.2 or 10.4.2. Detection

yields a large number of false alarms in addition to identifying potential targets. Most false alarms derive from man-made objects, though some arise from natural clutter. The detection stage retains only about one in 10^3 pixels for further processing. Improving resolution and using polarimetric despeckling techniques can increase the effectiveness of the target-detection stage, as indicated earlier. For example, Novak et al. [26] report experiments that achieved a false alarm probability of about one in 1.4×10^5 , divided approximately equally between natural and man-made clutter, using a polarization whitening filter [17–19] on fully polarized SAR images at 1-ft resolution.

Potential targets identified in the detection stage are then passed to a *discrimination* stage, which is intended to reject further false targets based on some simple properties of the potential target, including both geometrical and electromagnetic effects. A list of possible features is given in Table 10.1. We wish to identify a subset of independent tests that extract all information in the image. Though we cannot satisfy these requirements from such an ad hoc list,

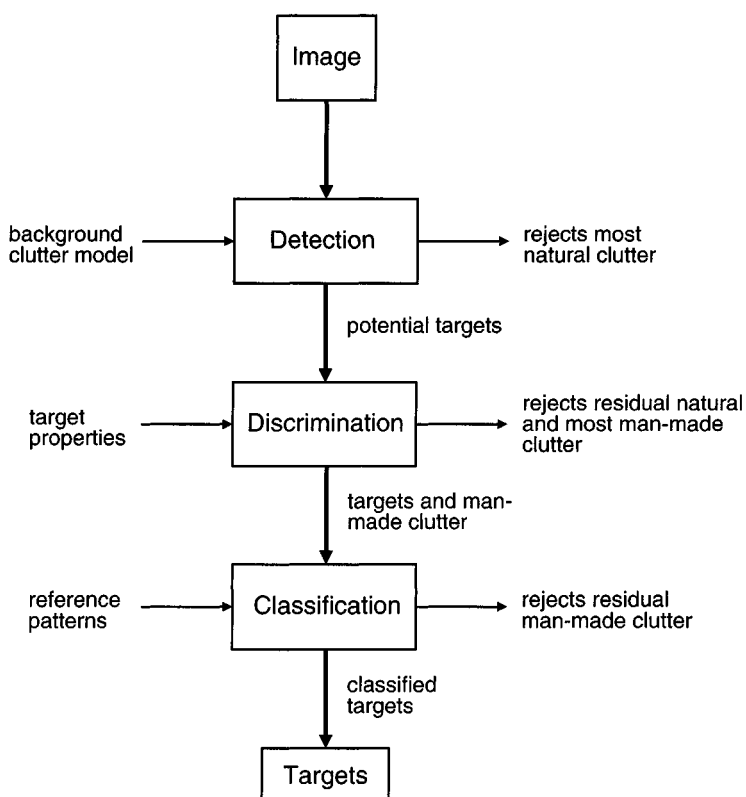


Figure 10.12 Processing chain for ATR.

an effective selection should include an independent test from each of the feature types. Some of the features in Table 10.1 [27] are estimated over a target-shaped binary region derived by applying morphological operations to the data—these include mass, diameter, and rotational inertia; the three CFAR contrast tests; and the three polarimetric tests. Three other tests—the standard deviation, fractal dimension, and weighted fill ratio [28]—apply to the original intensity within a rectangular ROI, which has been scaled, rotated, and translated to lie optimally around the target.

Let us now examine the features in more detail, commencing with the size-based examples. Mass is defined as the total number of pixels within a target region, diameter as its longest dimension. The ratio is that for major and minor axes of the enclosing ROI or target region, while the perimeter is the number of pixels around the edge. Rotational inertia describes how cross section is distributed within the target region.

An example of simple size-based target discrimination is shown in Figure 10.13 [25]. A SAR image of an airfield area is shown in Figure 10.13(a). Several vehicles along one of the runways provide the targets of interest. Apart from these, the image contains returns from a large number of buildings, fences, and even

Table 10.1
List of Features Used in Discrimination Stage of Target Recognition

Feature Type	Feature	Success
Size	Mass	
	Diameter	•
	Ratio	
	Perimeter	
Texture	Rotational inertia	•
	Standard deviation	•
	Weighted fill ratio	
Contrast	Fractal dimension	•
	Peak CFAR	
	Mean CFAR	•
Polarization (where applicable)	% bright CFAR	
	% pure	
	% pure even	•
Time dependence	% bright even	
	Change detection	

runway lights. Following target detection using a one-parameter CFAR with $P_{fa} = 10^{-3}$, many detections are visible in Figure 10.13(b). In Figure 10.13(c) we illustrate the effect of applying a simple discriminant such that only vehiclelike objects are retained [25], characterized by major and minor axis lengths and total RCS. The first two tests are equivalent to the diameter and ratio tests in Table 10.1, while the total RCS is related to the mean CFAR statistic. The majority of unwanted objects, such as the buildings, fences, and runway lights, fail to meet these criteria; and we are left with a high detection rate on the targets of interest and a very small number of residual incorrect targets.

Discriminants based on texture in Table 10.1 measure the variation of RCS within the target region. The standard deviation describes the single-point statistics and is generally applied to the log of the data [26], which would be optimal if the target had a lognormal PDF, as discussed in Chapter 8. We also showed there that the normalized log measure, from which the order parameter could be derived, would be preferable for a K-distributed target. The weighted fill ratio measures the fraction of total energy contained in the brightest 5% (say) of the scatterers within the ROI, and the fractal dimension provides a measure of the spatial dimensionality of the detected object [29]. Contrast features are all related to values of the CFAR statistic (see (10.8)) within the ROI. Peak and mean CFAR statistics are self-explanatory; the percentage bright measure is the fraction of pixels whose CFAR statistic exceeds some threshold.

Polarimetric features, where available, introduce another dimension into discrimination and are discussed in more detail in Chapters 11 and 12. Used in the context of discrimination we are concerned with classifying returns in terms of the number of reflections they have undergone. If the received fields E_{hh} , E_{hv} , E_{vv} in the different polarization states are measured, then the energy corresponding to odd and even bounce mechanisms is given by [26]

$$E_{\text{odd}} = \frac{|E_{hh} + E_{vv}|^2}{2} \quad \text{and} \quad E_{\text{even}} = \frac{|E_{hh} - E_{vv}|^2}{2} + 2|E_{hv}|^2 \quad (10.28)$$

Natural clutter returns dominated by surface scattering correspond to a single bounce, and in many cases scattering from vegetation has the characteristic of diffuse scattering with no preference for even or odd numbers of reflections [30]. The return from man-made objects, on the other hand, can result from reflections by a flat plate (one-bounce), a dihedral (two-bounce), or a trihedral (three-bounce). The energy in the different polarizations depends on whether an odd or even number of reflections has occurred. This allows two-bounce returns from dihedral structures to be identified, which has been proposed as a test for man-made objects [26,27]. However, scattering from forest at longer wave-

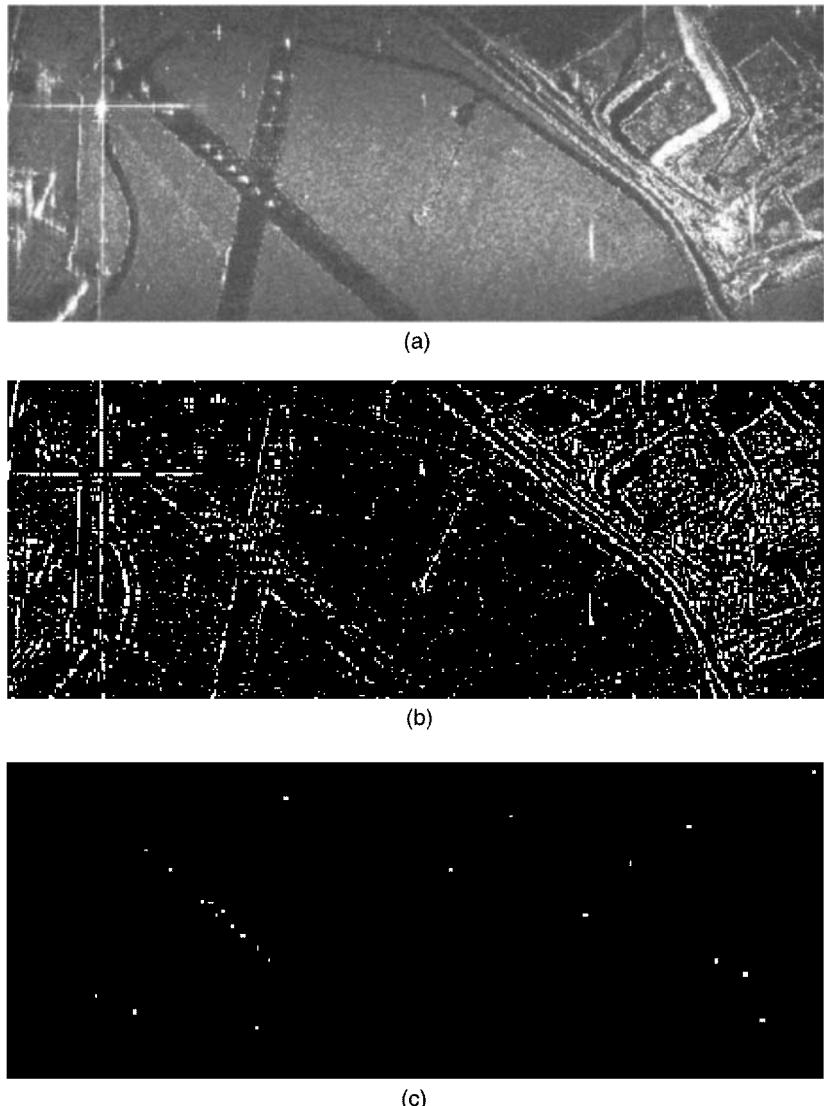


Figure 10.13 Example of target detection applied to airborne X-band SAR image: (a) original multilook SAR image, (b) detections based on assumed negative exponential background PDF, and (c) discriminated result when a simple size constraint is placed on targets.

lengths, particularly over a wet or flooded surface, also shows very clear signatures of double-bounce scattering [30]. This means that it is important to apply this test in a suitable context. Further discussion of polarization effects can be found in later chapters.

The percentage pure measure is defined as that fraction of pixels within the ROI for which some fraction of the energy can be attributed to either the even- or odd-bounce category. The percentage pure even measure describes the fraction of pixels for which the energy in the even-bounce channel exceeds some threshold. The percentage bright even measure corresponds to the fraction of bright pixels in the image that are mainly even-bounce scatterers.

Once individual features have been measured the results for each can be combined using a specific criterion, such as a quadratic distance measure of the form [26]

$$d(\mathbf{x}) \equiv \frac{1}{n} (\mathbf{x} - \mathbf{m})^T C^{-1} (\mathbf{x} - \mathbf{m}) \quad (10.29)$$

where \mathbf{x} is the vector of features from the detected object; \mathbf{m} and C are the mean and covariance of these features, estimated from training on another set of targets; and n is the number of features.

Upon comparing the performance of the different measures for a set of three types of target, namely a tank, a self-propelled gun, and an armored personnel carrier, Novak et al. [26] found that the best set of discriminants to use were those indicated by • in the third column of Table 10.1. This includes two size-based measures, one of which involves the distribution of RCS, which introduces independent information. The texture features carry independent information about the spikiness of the distribution (through the standard deviation of the log) and the space-filling property (through the fractal dimension). The total RCS is included through the mean CFAR measure. A single polarimetric measure is also included (the percentage pure even); other polarimetric measures are correlated with this feature and do not provide independent information. Applying these discrimination tests to fully polarimetric high-resolution data, Novak et al. [26] report that the total false alarm rate was reduced from one in 1.4×10^5 , after the polarization whitening filter was applied, to one in 7×10^5 . False alarms from natural clutter were reduced nearly twice as much as those from man-made clutter. This clutter rejection was achieved with no appreciable loss in detection probability for genuine targets.

A different type of approach to discriminating targets from false alarms is based on their time dependence, as listed in the final row of Table 10.1. Identifying objects within the scene that have changed since previous images were acquired allows us to keep track of objects, such as vehicles, which are likely to be most

significant as targets. Target change detection exploits the high degree of geometrical accuracy that can be achieved following the methods described in Chapter 3, so it is possible to register individual pixels precisely in different scenes. This enables a direct comparison of detections in each scene in order to identify changes [31,32]. Figure 10.14(a,b) shows a region of about 1.5-km square on consecutive days. Figure 10.14(c) identifies those targets that were detected in the first image, but not the second; while Figure 10.14(d) shows the opposite. The probability of detecting genuine changes, primarily in the two formations of vehicles visible in Figure 10.14(c), is high, while the false alarm probability elsewhere in the scene is very low.

10.8 Target Classification

Once the detection and discrimination stages have rejected as much clutter as possible, the final stage of the ATR scheme consists of target classification. Potentially this could be based on pattern-matching techniques using all the information in the data. A theoretical framework can be devised similarly to that used for homogeneous correlated textures in Chapter 9. Section 9.3.2 showed that the required textural information is contained in the complex spectrum. For deterministic targets the assumption of homogeneity is no longer applicable and it is necessary to estimate the likelihood for each relative shift d of reference and data. Taking the logarithm of the random texture results in the distributions of the estimated complex spectral coefficients being approximately Gaussian [33,34]. Even if this assumption is not correct for targets, it should be possible to treat the spectrum as if it consisted of a Gaussian mixture distribution of sufficient terms [35]. The reference data then depend on the mean and variance of the real and imaginary components at each spectral coefficient for each mixture contribution. For homogeneous textures the mean and variance in the real and imaginary components were the same. For simplicity, we make the same assumption for targets so that the likelihood for target class p and shift d , related to (9.10), is given by

$$\lambda_p(d) = -M \ln \pi - \sum_{j=1}^M \left\{ \ln S_p(j+d) + \frac{(a_r(j) - \mu_p(j+d))^2 + (a_i(j) - \mu_p(j+d))^2}{S_p(j+d)} \right\} \quad (10.30)$$

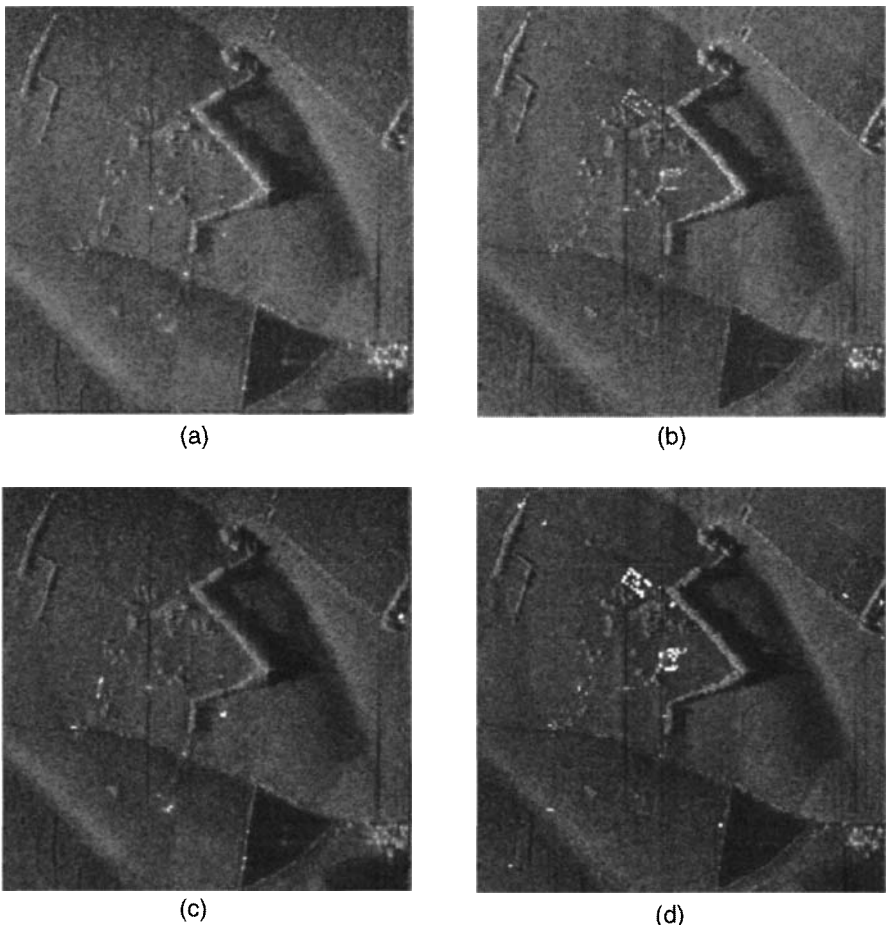


Figure 10.14 Target change detection: (a) first image, (b) second image, (c) targets detected in (a) but not (b), and (d) targets detected in (b) but not (a).

where $S_p(j) = 2V_p(j)$ is the power spectral density of the j th component of the p th target class. The overall maximum value of $\lambda_p(d)$, then identifies both target position and class.

It should be noted that (10.30) provides a *theoretical framework* for ML target recognition. However, such an approach is time consuming and it is important to examine compromise solutions offering slightly degraded performance but reduced cost. Pattern matching for deterministic structures depends on orientation and displacement, unlike the correlated texture classification approach described in Section 9.3. Nevertheless, the latter can provide a description of ML classification. The correct orientation of the rectangular ROI, as described

in the previous section, reduces the alignment problem to one of two-dimensional translation [36]. A variety of slightly different pattern-matching techniques such as eigenimage classification [37,38], shift-invariant two-dimensional pattern matching [38], and quadratic distance correlation classification [36,39,40] can then be applied; these all offer similar performance. Though they are not truly ML methods, they can be related to these through (10.30). The last term of (10.30), corresponding to the square modulus of the difference of the data and reference components, contains a contribution from the crosscorrelation between reference and data. Thus, it is related to the quadratic distance correlation classifier or shift-invariant two-dimensional pattern-matching classifier proposed by Novak et al. [36]. Note, however, that minimum mean-square and correlation measures are only optimal if the variances of the classes are the same, which is not the case.

A variety of other simplified classifiers have been proposed, but they all lead to degraded performance. Therefore, these should be rejected in favor of the two-dimensional pattern-matching methods. Though somewhat suboptimal, the minimum mean-square error and crosscorrelation measures have been refined and realistically implemented. Classification results for the shift-invariant two-dimensional pattern matcher over a restricted number of targets are shown in Table 10.2 [36]. Very similar results were reported also for the quadratic distance correlation classifier [36] and, more recently, for the eigenimage approach [38]. The probability of detection was reduced to about 90% after this classification stage rather than the 100% performance achieved after detection and discrimination stages [36].

These results show promise but are only preliminary, gathered over a restricted range of geometries. Including more target classes and imaging con-

Table 10.2
Confusion Matrix for Classification of Tank, APC,
and Self-Propelled Gun Against Clutter for 1-ft Resolution Polarimetric Data

Object	Percentage Classified as:			
	Tank	APC	Gun	Clutter
Tank	100			
APC		100		
Gun			100	
Clutter		2	4	94

Source: [36]. Copyright 1994, reprinted with kind permission from Elsevier Science Ltd., The Boulevard, Langford Lane, Kidlington OX5 1GB, UK.

figurations would tend to degrade classification. It is not clear what performance this factorized approach with a discrimination stage could achieve under these circumstances. Nevertheless, at present it provides the only realistic option to bridge the gap between the enormous number of initial detections and final target recognition.

10.9 Target Super-Resolution

Both detection and classification can be significantly enhanced by improved resolution. This can be attained by introducing prior knowledge about the object that is being imaged. A variety of techniques have been developed for exploiting this type of processing under the general heading of super-resolution, which can be regarded as performing an extrapolation in spatial frequency to higher frequencies than those defined by the Rayleigh resolution criterion.

The imaging process is described in detail in Chapter 2. Ignoring receiver noise, we can represent the SAR image as a (speckle-free) target added to a uniform speckled clutter background. For discretely sampled data we can represent it by the matrix equation

$$\mathbf{g} = H\mathbf{f} + \mathbf{b} \quad (10.31)$$

where \mathbf{g} , \mathbf{f} , and \mathbf{b} are vectors representing the complex image samples, the field scattered by the target, and additive zero-mean Gaussian background speckle, respectively; H is a matrix representing the imaging process. The inverse scattered field problem of recovering \mathbf{f} from \mathbf{g} represents the normal reconstruction process. The inverse cross-section problem of recovering the samples of σ from \mathbf{g} [41,42] is closer to the real requirement but is considerably more complicated.

10.9.1 Super-Resolution Theory

A popular method for solving the inverse scattering problem is based on a least-squares reconstruction. This is equivalent to the Moore–Penrose pseudo-inverse and performs a perfect reconstruction where there is no background. The least-squares solution is defined by

$$\mathbf{f}_{LS} = (H^\dagger H)^{-1} H^\dagger \mathbf{g} = \mathbf{f} + (H^\dagger H)^{-1} H^\dagger \mathbf{b} \quad (10.32)$$

where H^\dagger denotes the adjoint of H . The effect of the additive background can be appreciated by considering a *singular value decomposition* (SVD) of the imaging matrix H [43]. Suppose that \mathbf{u}_i and \mathbf{v}_i are the i th components of the

orthonormal basis vector in the scattered field and image, respectively. Each component of \mathbf{u}_i passes through the imaging system to give an output component \mathbf{v}_i attenuated by λ_i , the corresponding eigenvalue of the SVD. The least-squares reconstruction can then be expressed as

$$\mathbf{f}_{\text{LS}} = (H^\dagger H)^{-1} H^\dagger \mathbf{g} = \left(\sum_{i=1}^n \frac{1}{\lambda_i} \mathbf{v}_i \mathbf{u}_i^* \right) \mathbf{g} = \mathbf{f} + \left(\sum_{i=1}^n \frac{1}{\lambda_i} \mathbf{v}_i \mathbf{u}_i^* \right) \mathbf{b} \quad (10.33)$$

If the singular values are arranged in order of decreasing magnitude, there comes a point where the background term becomes very large and dominates the reconstruction. Under these conditions the problem is said to be "ill-posed." One way to overcome this problem is to truncate the singular values used in the reconstruction so that those with eigenvalues below the background level are rejected [43]. However, it has been shown [44] that the quality of such reconstructions is not significantly improved compared with a matched filter. In contrast to this ad hoc method, a Bayesian approach is ideally suited to treating such ill-posed problems because it is explicitly formulated to provide a consistent means of performing inferences from limited information [45]. The inverse scattered field problem can be represented by the Bayes relation

$$P(\mathbf{f}|\mathbf{g}) \propto P(\mathbf{g}|\mathbf{f})P(\mathbf{f}) \quad (10.34)$$

where $P(\mathbf{f})$ encapsulates the prior knowledge about the scattered field, which itself depends on prior knowledge about the RCS. $P(\mathbf{g}|\mathbf{f})$ is the likelihood function which incorporates information about the imaging process itself. If the PDFs are assumed to be Gaussian, the peak value of the a posteriori PDF, $P(\mathbf{f}|\mathbf{g})$, corresponds to the minimum mean-square error estimate of \mathbf{f} given \mathbf{g} . Thus, the MAP solution can be adopted as a suitable reconstruction, \mathbf{f}_{rec} , from the entire range of possible solutions.

Let us assume a Gaussian a priori PDF for the scattered field [46] given by

$$P(\mathbf{f}) \equiv \frac{1}{\det(\pi C_s)} \exp[-\mathbf{f}^\dagger C_s^{-1} \mathbf{f}] \quad (10.35)$$

where C_s denotes the covariance matrix of the object. If we assume for simplicity that the two-point statistics described by the covariance matrix are in fact delta-correlated, then the matrix contains diagonal terms only, corresponding to a weighting function profile or underlying cross section [47]. The background clutter is modeled as in Chapter 4 by the Gaussian likelihood PDF defined by

$$P(\mathbf{g}|\mathbf{f}) \equiv \frac{1}{\det \pi C_b} \exp \left[-(\mathbf{g} - H\mathbf{f})^\dagger C_b^{-1} (\mathbf{g} - H\mathbf{f}) \right] \quad (10.36)$$

where C_b denotes the covariance matrix of the background in the imaging process, which is also assumed to be uncorrelated. We may now derive the MMSE reconstruction by substituting from (10.35) and (10.36) into (10.34). After manipulation we obtain

$$P(\mathbf{f}|\mathbf{g}) \equiv \frac{1}{\det \pi C_{s,\text{rec}}} \exp \left[-(\mathbf{f} - \mathbf{f}_{\text{rec}})^\dagger C_{s,\text{rec}}^{-1} (\mathbf{f} - \mathbf{f}_{\text{rec}}) \right] \quad (10.37)$$

where the mean and covariance are given by

$$\mathbf{f}_{\text{rec}} \equiv \langle \mathbf{f} \rangle = C_s H^\dagger (H C_s H^\dagger + C_b)^{-1} \mathbf{g} \quad (10.38)$$

and

$$C_{s,\text{rec}}^{-1} = H^\dagger C_b^{-1} H + C_s^{-1} \quad (10.39)$$

Note that \mathbf{f}_{rec} is derived from \mathbf{g} by applying a linear operator. A Wiener filter leads to an identical result by calculating the MMSE between the reconstruction and data [42]. This equivalence follows from the use of mean and covariance as completely specifying the process. The Bayesian approach has the advantage in that it can be generalized to non-Gaussian PDFs.

Although this method reconstructs the scattered field at a higher resolution than the original data, it is incomplete because the information is carried by the RCS (see Chapters 6 and 7) rather than the scattered field, which merely transforms this information. (Note that this in turn is an oversimplification, based on the assumption that the field is delta-correlated, as described previously.) A solution is therefore required for the inverse cross-section problem. The appropriate Bayes theorem relating the complex image \mathbf{g} , to the underlying cross section $\boldsymbol{\sigma}$, is

$$P(\boldsymbol{\sigma}|\mathbf{g}) \propto P(\mathbf{g}|\boldsymbol{\sigma})P(\boldsymbol{\sigma}) \quad (10.40)$$

Note that the relationship between \mathbf{g} and $\boldsymbol{\sigma}$ is carried through the scattered field \mathbf{f} . Thus, one means of solving (10.40) is to solve for \mathbf{f} given \mathbf{g} for various estimates of $\boldsymbol{\sigma}$. The global maximum then corresponds to the desired solution. In order to avoid a global search, a hill-climbing routine can be used to

determine the direction in which to change σ . Unfortunately, $P(\sigma|g)$ does not exhibit Gaussian behavior amenable to linear techniques. However, the behavior for small changes can be developed in terms of a Taylor expansion [42], depending on the first derivative, which can be incorporated into an iterative approach to super-resolution [48].

10.9.2 Super-Resolution Example

Figure 10.15(a) is the simulated image of a tanklike object embedded in uniform clutter with an SCR of 20 dB, taken from Figure 10.1(c). Initially we need to deduce an appropriate form for the weighting function corresponding to diagonal elements of C_s in (10.35). The key component of this process is to incorporate the same model as that applied in target detection. We assert that the image in question can be represented as a *target* superimposed on a uniform clutter *background* [47]. The target region can be identified by conventional target detection, as in Sections 10.3 and 10.4. If desired, target change detection, from Section 10.7, can also be applied to indicate that a target is likely to be significant rather than an object that is always present in the scene. The mean intensity of those pixels that lie below the threshold is taken as the estimated background, while the intensity of those pixels that exceed the threshold is taken as an estimate of target cross section. This process for generating prior knowledge may seem circular. However, it is important to realize that the prior knowledge is not contained in the data but in the description of the image as comprised of localized *targets* set against a uniform *speckled* background and in the rules that are used to identify them. When this process is applied to Figure 10.15(a), the estimated underlying cross section is as shown in Figure 10.15(b). Note that two regions of clutter at the top and bottom of the image have been identified as *target* since they exceed the threshold. This weighting function with its flat background is adopted as the covariance function C_s . Upon solving the inverse scattered field problem we then obtain the result in Figure 10.15(c). Comparison with Figure 10.15(a) indicates increased structure in the target due to improved resolution.

The inverse cross-section problem can be solved by repeating the process, for different cross-section weightings, to identify the global optimum [47]. As a rudimentary approach to this, suppose we apply the same target-selection rules to Figure 10.15(c) as originally applied to Figure 10.15(a) to yield an “improved” estimate of the underlying cross section, in Figure 10.15(d). This in turn can be used as an a priori PDF to solve the inverse scattered field problem once more, leading to the result shown in Figure 10.15(e). Apparent resolution has now been significantly improved, with target structure showing distinct evidence for four dominant scattering regions. Note also that the false target

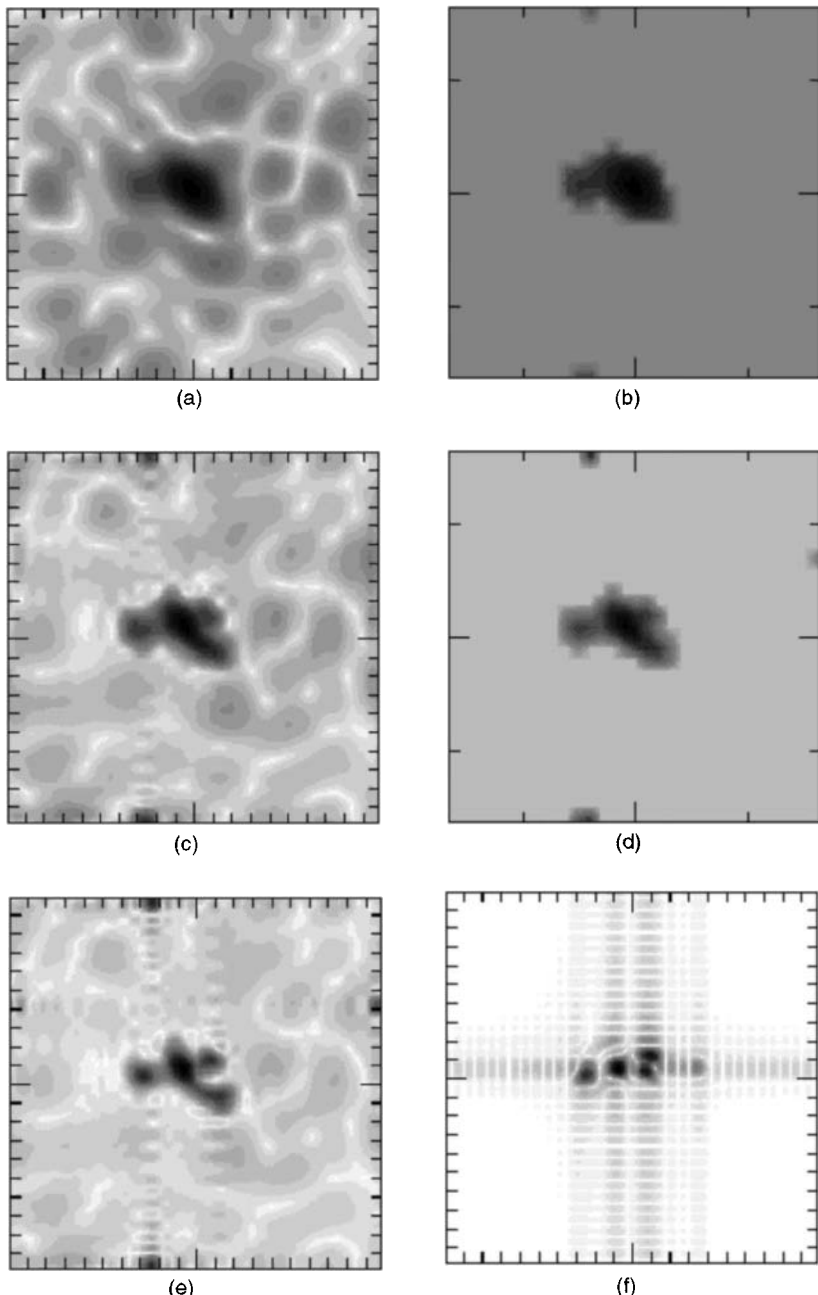


Figure 10.15 Stages in super-resolution reconstruction: (a) original 3-m resolution image with background, (b) derived background and target cross sections, (c) reconstructed image, (d) derived background and target cross section for second iteration, (e) reconstructed image, and (f) original 0.75-m resolution image without background for comparison.

detections in Figure 10.15(b) have been reconstructed more strongly, as has a new false detection on the right of Figure 10.15(d).

The acid test of such a reconstruction is to compare it with the known target model. Figure 10.15(f) shows a simulated image of a tank with no background at a resolution four times better in each direction. It seems that three of the four scattering centers in the super-resolved image (Figure 10.15(e)) have approximately the correct position and RCS. However, the scatterer on the lower right is significantly displaced. Reconstructions with different speckle realizations consistently reproduce the three “correct” scatterers while the fourth varies appreciably. This illustrates that background speckle prevents further iterations being useful. While these early results are somewhat crude, a more sophisticated iterative approach [48] yields similar consequences. In this case, reconstruction is automatically terminated when the effect of speckle begins to dominate.

10.9.3 Conclusions About Super-Resolution

Improved resolution would be expected to lead to enhanced detection and recognition. Novak et al. [49] reported that super-resolution has the same effect. However, there are two issues that have to be addressed. The first is the experimental problem associated with residual errors in the PSF, which depends on how accurately motion-compensation and autofocus (as described in Chapter 3) characterize the sensor motion. Studies suggest that these residual errors are equivalent to injecting noise with a signal-to-noise ratio of about 30 dB [50]. Super-resolution on the scale illustrated in Figure 10.15 should therefore be successful. Furthermore, Luttrell [41] showed that a joint autofocus, super-resolution algorithm can be devised to solve for residual errors in the instrument function as well as solving the inverse scattered field problem. The second issue is more conceptual. Since the information contained in the output reconstruction is only a composite of prior knowledge and data, it could, in principle, be used directly in classification without an intermediate reconstruction. On the other hand, super-resolution represents an optimum way of combining data and prior knowledge and so may still provide an effective route. More experience with super-resolution methods is required to quantify their performance in real systems.

10.10 Summary

This chapter has been devoted to deriving information about targets from SAR images. Three principal stages were described: detection, discrimination, and classification. In each case the aim was to develop optimum techniques for extracting the relevant information.

Detection was treated in Bayesian terms based on the Neymann–Pearson observer (Section 10.2). Following a conventional CFAR analysis for a Swerling 1 target against constant RCS clutter (Section 10.3), we demonstrated:

- Performance degradation caused by textured clutter (Section 10.4.1);
- Performance improvement if targets could also be treated as textured (Section 10.4.2);
- Performance improvement for higher resolution imagery (Sections 10.3.2 and 10.4.2).

A discussion of the effects of unwanted targets and background discontinuities in the CFAR process revealed the advantage of using RCS segmentation (from Chapter 7) in place of conventional CFAR as a means for characterizing the background around a potential target in a way that is unaffected by details in the scene.

Following detection, it is important to include a *discrimination* stage during which a variety of simple target features characterizing size, texture, contrast, and polarization are used to reject unwanted detections (Section 10.7). Though the list of features is ad hoc, a selection of independent measures was shown to yield good discrimination. An example of the use of target change detection to reject all events except those corresponding to changes in the scene was demonstrated. All these discrimination stages further restrict the number of candidate targets for which higher level recognition processes are required.

Target *classification* can be described in the same terms as the classification of correlated textures. It assumes that the PDF of the complex spectral coefficients can be represented by a Gaussian PDF (Section 10.8). While it is not permissible to assume homogeneity for targets, a suboptimum treatment that ignores this restriction leads to a simple theoretical expression. Other suboptimum classifiers can be devised that compromise the optimum solution in different ways. Experimental tests have demonstrated that these offer promise for future development.

Target detection, discrimination, and classification are all improved if the system resolution is improved. In Section 10.9 we described an approach to target super-resolution, based on similar models representing targets and clutter to those used earlier, that enables appreciable resolution improvement without modifying the radar system. Development of this type of postprocessing technique may well offer significant performance improvement in the future.

References

- [1] Woodward, P. M., *Probability and Information Theory with Applications to Radar*, New York: McGraw-Hill, 1953.
- [2] Neyman, J., and E. S. Pearson, "The Problem of the Most Efficient Tests of Statistical Hypothesis," *Phil. Trans. Roy. Soc. (London)*, Vol. A231, 1933, pp. 289–333.
- [3] Galati, G., and R. Crescimboni, "Basic Concepts on Detection, Estimation and Optimum Filtering," *Advanced Radar Techniques and Systems*, G. Galati (ed.), London: IEE, 1991, Chap. 1.
- [4] Goldstein, G. B., "False-Alarm Regulation in Lognormal and Weibull Clutter," *IEEE Trans.*, Vol. AES-9, 1973, pp. 84–92.
- [5] Musha, T., and M. Sekine, "CFAR Techniques in Clutter," *Advanced Radar Techniques and Systems*, G. Galati (ed.), London: IEE, 1991, Chap. 3.
- [6] Blacknell, D., and R. J. A. Tough, "Clutter Discrimination in Polarimetric SAR Imagery," *Europto Conf. on SAR Data Processing for Remote Sensing II*, Paris, *Proc. SPIE*, Vol. 2584, 1995, pp. 179–187.
- [7] Marcum, J. I., and P. Swerling, "Studies of Target Detection by Pulsed Radar," *IRE Trans.*, Vol. IT-6, 1960, pp. 59–308.
- [8] Abramowitz, M., and I. A. Stegun, *Handbook of Mathematical Functions*, New York: Dover, 1970.
- [9] Ward, K. D., "Compound Representation of High Resolution Sea Clutter," *Electron. Lett.*, Vol. 17, 1981, pp. 561–565.
- [10] Sekine, M., T. Musha, Y. Tomiyata, and T. Iraba, "Suppression of Weibull-Distributed Clutter," *Electron. Comm. Japan*, Vol. K62-B, 1979, pp. 45–49.
- [11] Cole, L. G., and P. W. Chen, "Constant False Alarm Detector for a Pulse Radar in a Maritime Environment," *Proc. IEEE, NAECON*, 1987, pp. 1101–1113.
- [12] Clarke, J., and R. S. Peters, "Constant False Alarm Detector Adaptive to Clutter Statistics," RSRE Memo. (UK) No. 3150, 1978.
- [13] Farina, A., A. Russo, F. Scannapieco, and S. Barbarossa, "Theory of Radar Detection in Coherent Weibull Clutter," *IEE Proc. F*, Vol. 134, 1987, pp. 174–190.
- [14] Hansen, V. G., "Constant False Alarm Rate Processing in Search Radars in Radar—Present and Future," *IEE Conf. Publ.*, Vol. 105, 1973, pp. 325–332.
- [15] Kreithen, D. E., S. M. Crooks, W. W. Irving, and S. D. Halversen, "Estimation and Detection Using the Product Model," MIT-Lincoln Lab. Report No. STD-37, 1991.
- [16] Oliver, C. J., and P. Lombardo, "Simultaneous Mean and Texture Edge Detection in SAR Clutter," *IEE Proc. Radar Sonar Navig.*, Vol. 143, 1966, pp. 391–399.
- [17] Novak, L. M., and M. C. Burl, "Optimal Speckle Reduction in POL-SAR Imagery and Its Effect on Target Detection," *Millimetre Wave and Synthetic Aperture Radar, Proc. SPIE*, Vol. 1101, 1989, pp. 84–115.
- [18] Novak, L. M., and M. C. Burl, "Optimal Speckle Reduction in Polarimetric SAR Imagery," *IEEE Trans. Aerospace Electron. Systems*, Vol. AES-26, 1990, pp. 293–305.
- [19] Novak, L. M., and C. M. Netishen, "Polarimetric Synthetic Aperture Radar Imaging," *Int. J. Imaging Sci. Tech.*, Vol. 4, 1992, pp. 306–318.

- [20] White, R. G., "A Simulated Annealing Algorithm for Radar Cross-Section Estimation and Segmentation," *SPIE Int. Conf. on Applications of Artificial Networks V*, Orlando, FL, *SPIE Proc.*, Vol. 2243, 1994, pp. 231–241.
- [21] Watts, S., "Radar Detection Prediction in Sea Clutter Using the Compound K-Distribution Model," *IEE Proc. F*, Vol. 132, 1985, pp. 613–620.
- [22] Rohling, H., "Radar CFAR Thresholding in Clutter and Multiple Target Situations," *IEEE Trans. Aerospace Electron. Systems*, Vol. AES-19, 1983, pp. 608–621.
- [23] Hansen, V. G., and J. H. Sawyers, "Detectability Loss Due to Greatest-of-Selection in a Cell Averaging CFAR," *IEEE Trans. Aerospace Electron. Systems*, Vol. AES-16, 1980, pp. 115–118.
- [24] Weiss, M., "Analysis of Some Modified Cell Averaging CFAR Processors in Multiple Target Situations," *IEEE Trans. Aerospace Electron. Systems*, Vol. AES-18, 1982, pp. 102–114.
- [25] Horne, A. M., R. G. White, and C. J. Baker, "Extracting Militarily Significant Information from SAR Imagery," *Battlefield Systems International 96*, Chertsey, UK, 1996.
- [26] Novak, L. M., S. D. Halversen, G. J. Owirka, and M. Hiett, "Effects of Polarisation and Resolution on the Performance of a SAR Automatic Target Recognition System," *Lincoln Laboratory J.*, Vol. 6, 1995, pp. 49–67.
- [27] Environmental Research Institute of Michigan (ERIM) study under Strategic Target Algorithm Research (STAR) contract.
- [28] Kreithen, D. E., and S. D. Halversen, "A Discrimination Algorithm and the Effect of Resolution," *IEEE National Radar Conf.*, 1993, pp. 128–133.
- [29] Butterfield, J., "Fractal Interpolation of Radar Signatures," *IEEE/NTC Proc.*, 1991, pp. 83–87.
- [30] van Zyl, J. J., "Unsupervised Classification of Scattering Behaviour Using Radar Polarimetry Data," *IEEE Trans. Geoscience Remote Sens.*, Vol. 27, 1989, pp. 36–45.
- [31] Finley, I. P., C. J. Oliver, R. G. White, and J. W. Wood, "Synthetic Aperture Radar—Automatic Change Detection," UK Patent No. GB 2,234,130B, 1988; US Patent No. 4,963,877, 1990.
- [32] Wood, J. W., R. G. White, and C. J. Oliver, "Distortion-Free SAR Imagery and Change Detection," *Proc. US National Radar Conf.*, Ann Arbor, MI, 1988, pp. 95–99.
- [33] Blacknell, D., "Texture Anomaly Detection in Radar Imagery," *Europto Conf. on SAR Data Processing for Remote Sensing*, Rome, *Proc. SPIE*, Vol. 2316, 1994, pp. 125–136.
- [34] Oliver, C. J., "Optimum Classification of Correlated SAR Textures," *Europto Conf. on SAR Image Analysis, Simulation and Modelling I*, Taormina, Sicily, *SPIE Proc.*, Vol. 2958, 1996, pp. 64–73.
- [35] Blacknell, D., "A Mixture Distribution Model for Correlated SAR Clutter", *Europto Conf. on SAR Image Analysis, Simulation and Modelling II*, Taormina, Sicily, *SPIE Proc.*, Vol. 2958, 1996.
- [36] Novak, L. M., G. J. Owirka, and C. M. Netishen, "Radar Target Identification Using Spatial Matched Filters," *Pattern Recognition*, Vol. 27, 1994, pp. 607–617.
- [37] Turk, M., and A. Pentland, "Eigenfaces for Recognition," *J. Cognitive Neuroscience*, Vol. 3, 1991, pp. 71–86.

- [38] Novak, L. M., and G. J. Owirka, "Radar Target Identification Using an Eigen-Image Approach," *Proc. IEEE National Radar Conf.*, Atlanta, GA, 1994, 1996, pp. 129–131.
- [39] Mahalanobis, A., A. V. Forman, M. Bower, N. Day, and R. Cherry, "A Quadratic Distance Classifier for Multi-Class SAR ATR Using Correlation Filters," *SPIE Conf. on Ultrahigh Resolution Radar*, Los Angeles, *SPIE Proc.*, Vol. 1875, 1993, pp. 84–95.
- [40] Mahalanobis, A., A. V. Forman, N. Day, M. Bower, and R. Cherry, "Multi-Class SAR ATR Using Shift-Invariant Correlation Filters," *Pattern Recognition*, Vol. 27, 1994, pp. 619–626.
- [41] Luttrell, S. P., "A Bayesian Derivation of an Iterative Autofocus/Super-Resolution Algorithm," *Inverse Problems*, Vol. 6, 1990, pp. 975–996.
- [42] Luttrell, S. P., "The Theory of Bayesian Super-Resolution of Coherent Images: a Review," *Int. J. Remote Sensing*, Vol. 12, 1991, pp. 303–314.
- [43] Bertero, M., and E. R. Pike, "Resolution in Diffraction Limited Imaging, a Singular Value Analysis. Part 1: The Case of Coherent Illumination," *Opt. Acta*, Vol. 29, 1982, pp. 727–746.
- [44] Guglielmi, V., F. Castanie, S. Puechmorel, and P. Piau, "Comparison of Super-Resolution Techniques for SAR Pre-processing," *Europto Conf. on SAR Image Analysis, Simulation and Modelling*, Paris, *SPIE Proc.*, Vol. 2584, 1995, pp. 252–263.
- [45] Cox, R. P., "Probability, Frequency and Reasonable Expectation," *American J. Physics*, Vol. 17, 1946, pp. 1–13.
- [46] Luttrell, S. P., "Prior Knowledge and Object Reconstruction Using the Best Linear Estimate Technique," *Opt. Acta*, Vol. 32, 1985, pp. 703–716.
- [47] Luttrell, S. P., and C. J. Oliver, "Prior Knowledge in Synthetic-Aperture Radar Processing," *J. Phys. D: Appl. Phys.*, Vol. 19, 1986, pp. 333–356.
- [48] Pryde, G. C., L. M. Delves, and S. P. Luttrell, "A Super-Resolution Algorithm for SAR –Images," *Inverse Problems*, Vol. 4, 1988, pp. 681–703.
- [49] Novak, L. M., G. R. Benitz, G. J. Owirka, and L. A. Bessette, "ATR Performance Using Enhanced Resolution," *SPIE Conf. on Algorithms for Synthetic Aperture Radar Imagery III*, Orlando, FL, *SPIE Proc.*, Vol. 2757, 1996, pp. 332–337.
- [50] Oliver, C. J., "The Limits on SAR Resolution Imposed by Autofocus Uncertainty," *Int. J. Remote Sensing*, Vol. 14, 1993, pp. 485–494.

11

Information in Multichannel SAR Data

11.1 Introduction

Up to this point, we have been concerned only with the information carried by a single SAR image. Of increasing importance are SAR systems that provide multidimensional information via multiple frequencies or polarizations. Such systems provide a much enhanced capacity for investigating Earth terrain because different frequencies and polarizations allow the probing of different scattering mechanisms and different components of the scattering layers. For example, in forest imaging, modeling suggests that for shorter wavelengths the backscatter from mature conifers is dominated by direct crown backscattering at all polarizations but that at long wavelengths the main component of the return depends on the polarization: trunk-ground interactions dominate at HH, for VV the major contribution to the return is direct crown backscatter, while the HV return is predominantly due to the primary branches in the crown layer [1,2].

As for single-channel data, a primary step in extracting information from such images is to develop a model of the image statistics for distributed scatterers because in many applications, such as agriculture, forestry, and hydrology, such targets are the objects of interest. Even when we are concerned with small scatterers, their detection and classification is crucially affected by their clutter surroundings. Hence, the main goal of this chapter is to establish statistical models appropriate to multichannel data, especially polarimetric data. We will find that much of the structure already developed in earlier parts of this book transfers naturally into higher dimensions and provides a clear guide as to what

is meant by information. In particular, the Gaussian data model again plays a central role in the analysis but with an added richness provided by the extra data channels and the enhanced range of useful parameters.

A key concern when handling multichannel data is the correlation between channels, and radar polarimetry provides an ideal vehicle to discuss the issues this raises. As a result, we initially concentrate on this data type before applying the lessons learnt more generally. The basic concepts of polarimetric measurement are introduced in Section 11.2. The treatment is at a sufficient level to appreciate what is described by polarimetric data, but any reader intending to make serious use of such data would be well advised to consult a more comprehensive treatment, such as that provided in [3]. Given that polarimetric data are inherently multidimensional, an immediate concern is to elucidate which of the many possible combinations of channels carry information and, hence, are useful to display as images. To deal with this we must have some knowledge of which parameters convey physical information about the scene and/or describe the statistical distributions characterizing the data. Accordingly, in Section 11.3 we develop an argument based on collections of point scatterers that suggests the multidimensional Gaussian model is crucial in describing polarimetric data, but with modifications caused by fluctuations in the numbers of scatterers. The Gaussian model described in Section 11.4 leads naturally to the image types that display the information carried by the polarimetric data. The associated single-look distributions are developed in Section 11.5, and their properties are discussed in Section 11.6. Section 11.7 is concerned with parameter estimation and its attendant problems. This leads us to consider multilook data and provides a natural bridge to the Stokes vector formulation of scattering in Section 11.8. Texture in polarimetric data is discussed in Section 11.9. Finally, Section 11.10 discusses how the results of this chapter are applicable to other forms of multidimensional data, especially interferometric SAR.

11.2 Polarimetric Measurements

Here we deal only with the most common form of polarimetric SAR, in which a linearly polarized signal is transmitted and two orthogonal polarizations of the backscattered signal are measured. When a horizontally polarized wave is transmitted, the signals received in the horizontal (H) and vertical (V) channels undergo separate SAR processing to produce measurements S_{hh} and S_{vh} of the local copolarized and crosspolarized complex scattering amplitudes. By interleaving H and V polarized transmitted pulses, the corresponding terms S_{vv} and S_{hv} can also be measured to give the full polarimetric response of a scatterer.

These four measurements allow the response to an *arbitrary* transmitted polarization to be calculated (for a fixed frequency, incidence angle, resolution, and time), as follows. Any polarization state of the transmitted wave can be uniquely described by an electric field vector of the form

$$\mathbf{E} = E_{ih}\hat{\mathbf{h}} + E_{iv}\hat{\mathbf{v}} \quad (11.1)$$

where the subscript i denotes incident and $\hat{\mathbf{h}}$ and $\hat{\mathbf{v}}$ are unit vectors defined by $\hat{\mathbf{h}} = \hat{\mathbf{z}} \times \hat{\mathbf{k}} / |\hat{\mathbf{z}} \times \hat{\mathbf{k}}|$ and $\hat{\mathbf{v}} = \hat{\mathbf{h}} \times \hat{\mathbf{k}}$. Here $\hat{\mathbf{z}}$ is a unit normal to the Earth's surface and $\hat{\mathbf{k}}$ is a unit vector parallel to the wave vector \mathbf{k} . The backscattered wave observed at a distance R in the far field of the scatterer is then given by

$$\begin{pmatrix} E_{sh} \\ E_{sv} \end{pmatrix} = \frac{e^{ikR}}{R} \begin{pmatrix} S_{hh} & S_{hv} \\ S_{vh} & S_{vv} \end{pmatrix} \begin{pmatrix} E_{ih} \\ E_{iv} \end{pmatrix} \quad (11.2)$$

where the subscript s denotes scattered. Note that in this expression the coordinate system is throughout defined relative to the direction of the *transmitted* wave (the backscatter alignment convention); the transformations needed if the scattered wave is defined relative to its propagation direction (the forward scattering alignment convention) are discussed in [3]. Notice also that a single-channel SAR measures only one of the complex scattering amplitudes S_{pq} , which is normally one of the copolarized responses S_{hh} or S_{vv} .

Implicit in this formulation are the conditions:

- Adequate sampling for the returns from both the H and V transmitted pulses;
- Preservation of phase coherence between pulses;
- Correct sampling so that all responses are measured at the same position;
- Preservation of the internal state of the scatterers between pulses.

While the first three of these conditions are concerned with the system and can be treated as an engineering problem, the last depends on the physics of the target. For targets whose internal state is unaltered by the polarization of the probing wave, *reciprocity* will hold [4], that is,

$$S_{hv} = S_{vh} \quad (11.3)$$

This is expected to be the case for most naturally occurring scatterers. However, targets can be constructed for which this condition is violated, and (11.2) may then become meaningless except for pure H and V inputs.

Even when the targets are reciprocal, measured values of S_{hv} and S_{vh} may not be equal, because of system imperfections. In fact, polarimetric SAR can be affected by a number of forms of distortion, in addition to those due to uncorrected spatial or temporal variations in power or gain discussed in Chapter 2. These include:

- Crosstalk due to coupling of orthogonal polarizations on transmit and/or receive;
- Channel imbalance caused by different transmitted powers in the H and V channels, differing gains on receive and/or system-induced phase shifts between channels.

Of these the first is the most pernicious because it scrambles the information in the different channels. Fortunately, methods to correct for crosstalk are well developed [5–7] although incomplete because of the inadequate treatment of PSF effects [8,9]. Channel imbalance can be separated into correction of phase and amplitude distortions. Calibration targets or internal calibration tones are needed to remove these effects [10,11]. In this chapter we assume that all corrections have been made and that targets are reciprocal. The data at each pixel can then be represented by a three-vector:

$$\mathbf{S} = \begin{pmatrix} S_{hh} \\ S_{hv} \\ S_{vv} \end{pmatrix} \equiv \begin{pmatrix} S_1 \\ S_2 \\ S_3 \end{pmatrix} \quad (11.4)$$

An alternative representation of the data in terms of Stokes vectors and Stokes scattering operators will be described in Section 11.8.

11.3 Polarimetric Data Distributions

With single-channel data, only one of the copolarized quantities S_{hh} or S_{vv} is normally available and, as we have seen in Chapter 4, for distributed targets the phase carries no useful information. Hence, taken in isolation, each channel provides only one useful number per pixel, viz. an estimate of σ^o in that channel. When multiple channels are available, the true basis of speckle in electromagnetic scattering becomes manifest. Phase (or rather, phase difference) now

provides information both as a useful statistical parameter and in the physical sense of corresponding to dielectric and geometric properties of the scattering medium. Hence, for polarimetric data the potential information per pixel is five real numbers, given by the intensities and the phase differences of the three channels. However, when dealing with distributed scatterers, we showed that the actual information per pixel is much lower because individual pixels are simply random samples from distributions characterized by a small number of parameters. In fact, large areas of single-channel SAR images are completely characterized by the mean σ^0 (if untextured) or the mean σ^0 and an order parameter (and possibly spatial correlation properties) if textured.

If there exist similar simple models for the distributions observed in polarimetric data they would clearly be of great value because they would do the following:

- Define the information content of the data.
- Isolate the set of measurements needed to characterize the scattering properties of distributed targets and, hence, that need to be explained by physical theory.
- Permit an estimation theory for polarimetric parameters to be developed.
- Provide a sound basis for image analysis operations, such as filtering, classification, target detection, and segmentation.

With these aims in mind, we now present an argument indicating the form of statistical model likely to be appropriate for describing polarimetric data.

As described in Chapter 4, the observations from a distributed target in single-channel SAR can be explained by interference of waves scattered from many point sources in the target. Such a treatment arises naturally from scattering models dealing with discrete scattering events, such as the finite-order Born or distorted Born approximations. In this way a link can be established between the statistical distributions displayed by SAR measurements and the numerical values of the parameters involved in these distributions [12]. When the number of scatterers is very large in each resolution cell, the complex signal is circular mean-zero Gaussian, the phase is uniformly distributed, and the signal amplitude and intensity display Rayleigh and exponential distributions (see (4.2) to (4.4)).

Many SAR observations exhibit such behavior, but significant departures occur at high resolutions [13] (see also references in Chapter 5) and at longer wavelengths [14]. Jakeman [15] made a fundamental contribution to understanding such phenomena by noting that if the number of scatterers in the

resolution cell is treated as a random variable, non-Gaussian behavior could result. He placed particular emphasis on negative binomial number fluctuations, which give rise to K-distributed intensity observations. This model has been adopted by numerous authors as a model for radar data, with much success [13,16]. It has also been extended to polarimetric data [17], although in this case its comparison with data gave mixed results at long wavelengths (see Section 11.9 and [14]). In addition, the multivariate K distribution has been shown to be equivalent to a product model in which the observation at a point can be regarded as the product of two independent processes, one Gaussian and one representing local fluctuations in a texture variable [17].

In this section we generalize these treatments. In doing so we establish the links between arbitrary number distributions of statistically identical scatterers (but for which the mean number is large) and the observed polarimetric data. A crucial result is that any number fluctuation model gives rise to data that is multivariate Gaussian at each pixel. This has strong implications for the measurements relevant to radar polarimetry.

11.3.1 Theoretical Formulation

Since the results developed here have relevance beyond single-frequency polarimetric data, they will be set in the more general context of measurements made in M channels. For calibrated polarimetric data, $M = 3$, but other interesting cases include $M = 4$ for uncalibrated data and $M = 2$ for two-channel interferometric data. It is also useful to compare the multichannel results with the single-channel case, for which $M = 1$. Assuming that N independent scatterers contribute to the observed signal in each of the M channels, the processed signal is the complex data vector

$$\mathbf{S} = \begin{pmatrix} a_1 + ib_1 \\ \vdots \\ a_M + ib_M \end{pmatrix} = \sum_{k=1}^N \begin{pmatrix} r_{k1}e^{i\theta_{k1}} \\ \vdots \\ r_{kM}e^{i\theta_{kM}} \end{pmatrix} e^{i\phi_k} \quad (11.5)$$

This equation represents the observed complex reflectivity in channel j , $a_j + ib_j$, as the sum of contributions from N elementary scatterers, where N is treated as a random variable. The k th scatterer has a complex reflectivity in channel j whose amplitude and phase are r_{kj} and θ_{kj} , while the phase ϕ_k is a propagation variable dependent on the distance of scatterer k from the sensor. The resolution cell is typically many wavelengths across, and scatterers are considered randomly placed in it. Hence, ϕ_k will be uniformly distributed and independent of the scatterer properties. This, therefore, represents the multidimensional version of the single-channel speckle model introduced in Section 4.3.

The analysis of this data model is complicated and is deferred to Appendix 11A, but the crucial result is as follows.

If the mean number of scatterers $\langle N \rangle$ contributing to the measurement at each pixel is large, then whatever the PDF of the number fluctuations, the data S can be represented by a *product* of two independent processes T and G ,

$$S = TG \quad (11.6)$$

where T is a positive scalar *texture* variable; the moments of T^2 are determined by the number fluctuations via the relation

$$\langle T^{2k} \rangle = \langle N^k \rangle / \langle N \rangle^k \quad (11.7)$$

so $\langle T^2 \rangle = 1$. The random variable G is a multivariate Gaussian, with the same covariance structure as S because

$$\langle S_i S_j^* \rangle = \langle TG_i T G_j^* \rangle = \langle T^2 \rangle \langle G_i G_j^* \rangle = \langle G_i G_j^* \rangle \quad (11.8)$$

The observations will be pure Gaussian (so that we can set $T \equiv 1$) only for number distributions in which $\langle N^k \rangle / \langle N \rangle^k \rightarrow 1$ as $\langle N \rangle \rightarrow \infty$.

This result places the multivariate Gaussian distribution at the heart of polarimetric data analysis, for two reasons.

1. In many cases the observations would be expected to be pure Gaussian, for example, if the number fluctuations obey a binomial or Poisson distribution. An important case where this is *not* true is when the fluctuations obey a negative binomial distribution. Then, as $\langle N \rangle \rightarrow \infty$,

$$\frac{\langle N^k \rangle}{\langle N \rangle^k} \rightarrow \prod_{n=0}^{k-1} \left(1 + \frac{n}{\nu}\right) \quad (11.9)$$

where ν is an order parameter. The equivalent continuous random variable T^2 with moments determined by (11.7) is a gamma distribution with mean 1 and order parameter ν . This then leads to the multidimensional K distribution [17] whose one-dimensional form is discussed in Chapter 5.

2. As we shall see, most of the key polarimetric parameters are derived from *ratios* of channels. Hence, by (11.6), they are independent of T

and depend only on the corresponding ratios for the Gaussian variable \mathbf{G} .

11.3.2 Relation to the One-Dimensional Multiplicative Noise Model for Speckle

Before exploring the consequences of the multivariate product model, we will relate it to the one-dimensional treatment found in earlier chapters and in much of the literature on single-channel SAR data. There the product model for one-dimensional SAR data is expressed (see (4.17)) as

$$S = \sqrt{\sigma} m \quad (11.10)$$

where S represents the observed complex data, m (the speckle) is a circular zero-mean complex Gaussian with unit variance, and σ is the local RCS (to be understood in the sense discussed in Section 4.3 as proportional to the backscattering coefficient, so we omit the 4π normalizations present in (2.24) and (2.29)). The phase of S is completely randomized by the uniform phase distribution associated with m . The intensity data is then given by

$$I = |S|^2 = \sigma|m|^2 = \sigma n \quad (11.11)$$

In this data model the speckle is seen as a multiplicative stationary noise corrupting the true information carried by σ .

Ignoring for the moment the argument given in Appendix 11A, the most obvious way to extend this to M dimensions appears to be to describe the complex reflectivity in channel k , $1 \leq k \leq M$, as

$$S_k = \sqrt{\sigma_k} e^{i\theta_k} m_k \quad (11.12)$$

where the speckle vector $\mathbf{m} = (m_1, \dots, m_M)^t$, with superscript t denoting transpose, has a jointly Gaussian distribution and we associate a phase θ_k with each true observation. Then

$$\langle S_k S_l^* \rangle = \langle \sqrt{\sigma_k \sigma_l} e^{i(\theta_k - \theta_l)} \rangle \langle m_k m_l^* \rangle \quad (11.13)$$

The multidimensional equivalent of (11.11) requires the mean of the measured covariance to be the true covariance of the data; the speckle should average out. In order to retain this property we are forced to set $\langle m_k m_l^* \rangle = 1$ for all k, l (unless the channels are uncorrelated). A Gaussian random variable with such a covariance structure is degenerate in the sense that the joint PDF of the speckle vector, $P(\mathbf{m})$, is only nonzero when all the m_k are identical. In other words, (11.12) must have the form

$$S_k = m \sqrt{\sigma_k} e^{i\theta_k} \quad (11.14)$$

where m is a circular zero-mean Gaussian variable with unit variance, which is *independent* of k . Although apparently similar to (11.10), this decomposition is of little value for a number of reasons.

- Unlike (11.10) it provides no separation of texture and covariance structure—this is all still encapsulated in the behavior of the σ_k and θ_k .
- It contains no information on the joint distribution of the σ_k and θ_k .
- The jointly Gaussian nature of \mathbf{m} has turned out to be spurious.
- It asserts that the speckle contribution is identical in each channel, which would lead us to expect images formed from ratios of channels to appear quite smooth, contrary to observations (see, for example, Figure 11.7).

Other methods to force a stationary speckle model onto polarimetric data are equally unsatisfactory. Fundamentally this is because, except for a single channel, we cannot ignore the electromagnetic basis of speckle. Hence, the stationary multiplicative noise model does not extend in any natural way to more than one dimension. Instead, casting (11.6) into its one-dimensional form, we can write

$$S = TG \quad (11.15)$$

In this formulation, G carries the covariance structure, so that $\langle |G|^2 \rangle$ describes the mean RCS, and T controls the fluctuation about the mean, with $\langle T^2 \rangle = 1$. This should be compared with (11.10) in which $\langle |m|^2 \rangle = 1$, m is thought of as a noise term, and the single variable σ carries the information about both the RCS and its fluctuations.

11.4 The Multidimensional Gaussian Distribution

Section 11.3 indicated the importance of the multidimensional Gaussian distribution in describing polarimetric data, and we now develop its implications. The fundamental fact about a homogeneous Gaussian-distributed target is that *all* the information is carried by the covariance matrix C , which can be expressed in the form

$$C = \begin{pmatrix} \sigma_1 & \sqrt{\sigma_1\sigma_2}\rho_{12} & \sqrt{\sigma_1\sigma_3}\rho_{13} \\ \sqrt{\sigma_1\sigma_2}\rho_{12}^* & \sigma_2 & \sqrt{\sigma_2\sigma_3}\rho_{23} \\ \sqrt{\sigma_1\sigma_3}\rho_{13}^* & \sqrt{\sigma_2\sigma_3}\rho_{23}^* & \sigma_3 \end{pmatrix} \quad (11.16)$$

where

$$C_{kl} = \langle S_k S_l^* \rangle \quad (11.17)$$

$$\sigma_k = \langle |S_k|^2 \rangle \quad (11.18)$$

is the backscattering coefficient in channel k and

$$\rho_{kl} = \frac{\langle S_k S_l^* \rangle}{\sqrt{\sigma_k \sigma_l}} \quad (11.19)$$

is the complex correlation coefficient of channels k and l . If we have accurate estimates of these nine real parameters (three real backscattering coefficients and three amplitudes and phases of the correlation coefficients) we know everything there is to know about the measurable properties of the target. This at last allows us to display images that describe the information content of the data.

Figures 11.1 to 11.3 show estimates of these parameters from the NASA/JPL AirSAR system [18] at C-, L-, and P-bands for an agricultural region in East Anglia, UK, acquired during the MacEurope campaign in 1992 [19]. The detailed properties of these images will be discussed later, but certain features are immediately obvious.

1. The dynamic range and image contrast increase with wavelength.
2. The copolarized correlation coefficient appears to carry more information than the crosspolarized, both in its amplitude and phase, especially at C-band.

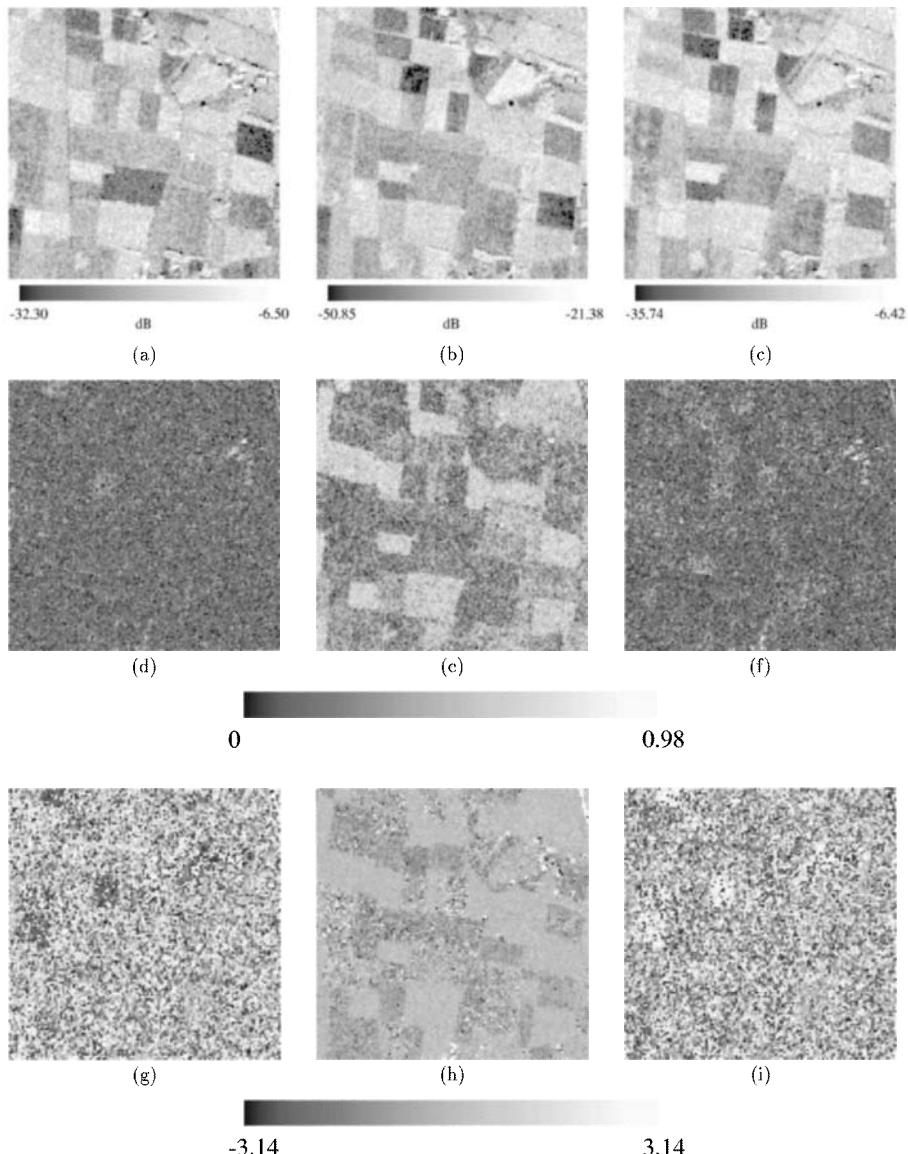


Figure 11.1 Estimated C-band polarimetric parameters from Feltwell, UK, imaged by the NASA/JPL AirSAR system: (a) σ_{hh} , (b) σ_{hv} , (c) σ_{vv} , (d) $|\rho_{hh, hv}|$, (e) $|\rho_{hh, vv}|$, (f) $|\rho_{hv, vv}|$, (g) $\angle\rho_{hh, hv}$, (h) $\angle\rho_{hh, vv}$, and (i) $\angle\rho_{hv, vv}$. The channel powers σ_{pq} are indicated by the dB scales. The scaling of the amplitude and phase of the correlation coefficients is from 0 to 1 and from $-\pi$ to π , respectively.

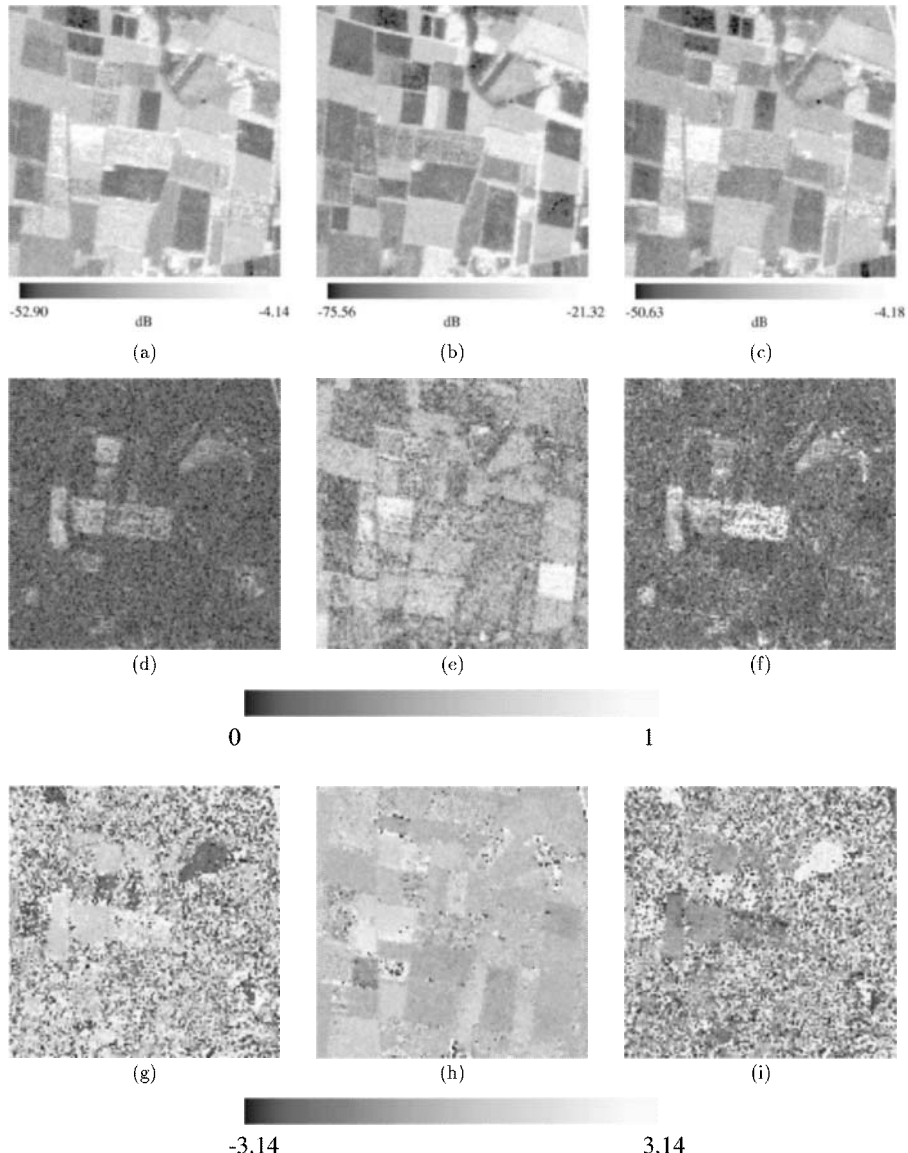


Figure 11.2 As for Figure 11.1 but for L-band.

3. Correlation phase is better defined when the correlation amplitude is larger and appears noiselike when the correlation amplitude is low.

The second of these is related to the fact that for azimuthally symmetric targets, the cross-polarized correlation coefficients will be zero [20], so the

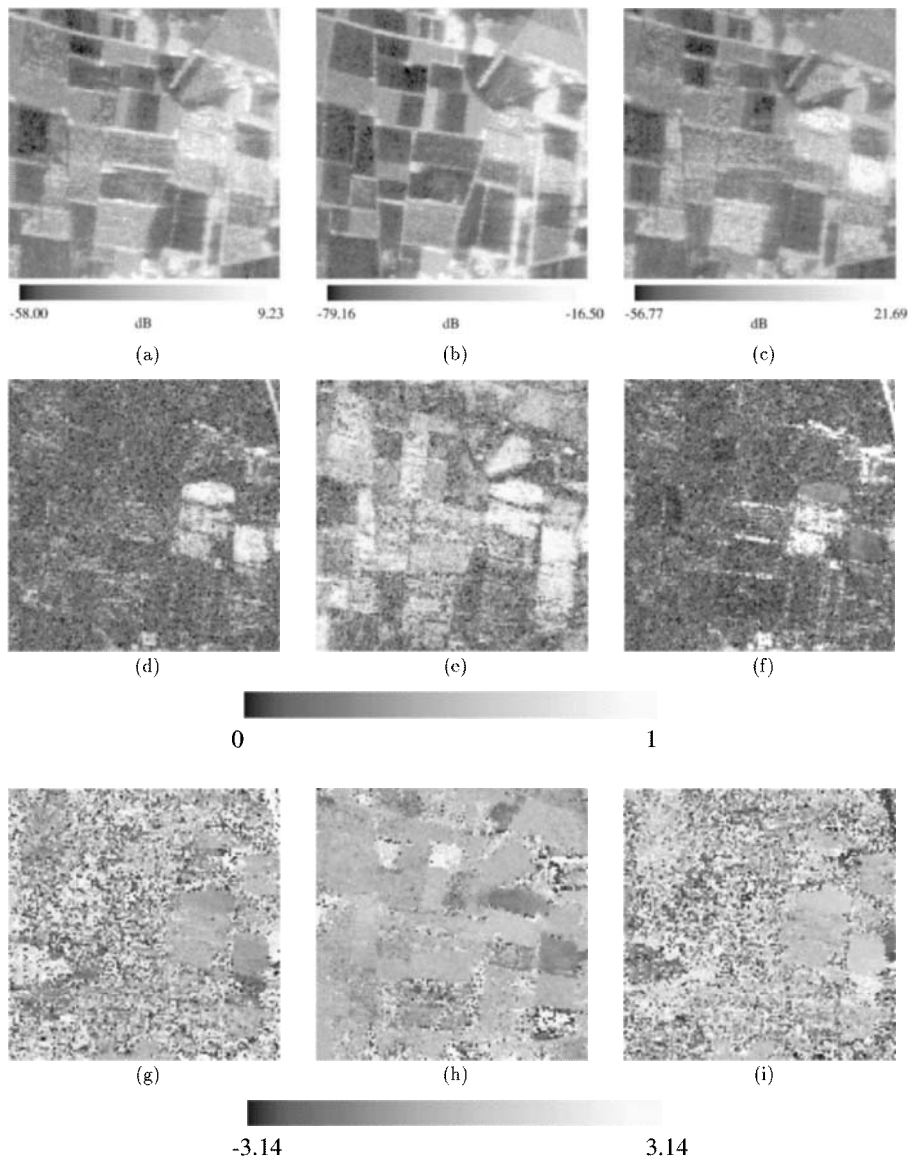


Figure 11.3 As for Figure 11.1 but for P-band.

covariance matrix (11.16) contains only five real parameters. This condition would be expected to hold for the shorter wavelengths if the canopy appears isotropic, but row effects in the soil could rise to the observed asymmetry due to the greater penetrating power at longer wavelengths. Additionally, we will show in Section 11.9 that the longer wavelength data need further parameters

for a full description, because they are not pure Gaussian and exhibit texture. Hence Figures 11.1 to 11.3 do not tell the full story.

11.4.1 Real and Complex Gaussian Distributions

In order to derive the basic properties of the complex Gaussian distribution and its various marginal distributions, it is useful to have available its equivalent real and complex forms. As in Section 11.3, we denote the k th complex channel by $S_k = a_k + i b_k$, $1 \leq k \leq M$. Under the multiple independent scatterer model (11.5), the uniform distribution of the total phase term ϕ_k implies that

$$\langle S_k S_l \rangle = \sum_p \sum_q \langle r_{pk} r_{ql} \exp i(\theta_{pk} + \theta_{ql}) \rangle \langle \exp i(\phi_k + \phi_l) \rangle = 0 \quad (11.20)$$

for all k, l . Using $a_k = \frac{1}{2}(S_k + S_k^*)$ and $b_k = -\frac{i}{2}(S_k - S_k^*)$, we then have

$$\langle a_k a_l \rangle = \langle b_k b_l \rangle = \frac{1}{2} \operatorname{Re} \langle S_k S_l^* \rangle = \frac{1}{2} \operatorname{Re} (C_{kl}) \quad (11.21)$$

and

$$\langle a_k b_l \rangle = -\langle a_l b_k \rangle = -\frac{1}{2} \operatorname{Im} \langle S_k S_l^* \rangle = -\frac{1}{2} \operatorname{Im} (C_{kl}) \quad (11.22)$$

These equations relate the covariance matrix C_R of the real data vector $S_R = (a_1, b_1, \dots, a_M, b_M)^t$ to the corresponding complex covariance matrix C .

The Gaussian PDF is completely defined by its covariance matrix and in the real case is given by

$$P(S_R) = \frac{1}{\sqrt{(2\pi)^{2M} |C_R|}} \exp\left(-\frac{1}{2} S_R^t C_R^{-1} S_R\right) \quad (11.23)$$

where $|C_R|$ is the determinant of C_R . It can be shown that $|C_R| = 2^{-2M} |C|^2$ and $S_R^t C_R^{-1} S_R = 2 S^\dagger C^{-1} S$, where S^\dagger is the conjugate transpose of S . Hence,

$$P(S) = \frac{1}{\pi^N |C|} \exp(-S^\dagger C^{-1} S) \quad (11.24)$$

11.4.2 Moments

All the moments of a Gaussian distribution can be derived once the second-order moments (11.17) and (11.20) are known. For our purposes, only moments up to the fourth order will be needed, and it is convenient to summarize these. From (11A.14), any odd moment of the field is zero. The fourth-order moments are easy to calculate from the well-known relation for arbitrary jointly distributed Gaussian variables X_p, X_j, X_k, X_l [21]:

$$\langle X_i X_j X_k X_l \rangle = \langle X_i X_j \rangle \langle X_k X_l \rangle + \langle X_i X_k \rangle \langle X_j X_l \rangle + \langle X_i X_l \rangle \langle X_j X_k \rangle \quad (11.25)$$

An important special case arises when $X_i = S_i$, $X_j = S_i^*$, $X_k = S_k$, and $X_l = S_k^*$. Since the intensity of channel i is given by $I_i = |S_i|^2$, we then have

$$\langle I_i I_k \rangle = \langle S_i S_i^* S_k S_k^* \rangle = \langle I_i \rangle \langle I_k \rangle + |C_{ik}|^2 \quad (11.26)$$

We know from the elementary properties of speckle described in Chapter 4 that for single-channel data, $\text{var}(I_i) = \langle I_i \rangle^2$ and $\text{var}(S_i) = \langle I_i \rangle$. Hence, (11.26) is equivalent to

$$\rho_{ik}^{(I)} = |\rho_{ik}|^2 \quad (11.27)$$

where $\rho_{ik}^{(I)}$ is the correlation coefficient of intensity between channels i and k . This important connection between the correlation structures of the fields and intensities, known as the Siegert relationship [22], has already been encountered in a different guise as (4.34).

It should also be noted that for polarimetric data all fourth-order field moments are zero unless they are of the form $\langle S_i S_j S_k S_l^* \rangle$, otherwise each corresponding term on the right-hand side of (11.25) contains a factor that is zero. For moments of this form, we can write

$$\langle S_i S_j S_k S_l^* \rangle = C_{ik} C_{jl} + C_{il} C_{jk} \quad (11.28)$$

11.5 Single-Look Distributions Involving Two Polarimetric Channels

Of particular importance for polarimetric data are parameters formed from pairs of channels, for which the PDF is jointly Gaussian with $M = 2$ (see, for example, the images formed from the correlation coefficients in Figures 11.1 to

11.3). We will denote these channels as $S_k = r_k e^{i\theta_k}$ with $k = 1, 2$, and their complex correlation by

$$\rho = \frac{C_{12}}{\sqrt{\sigma_1 \sigma_2}} \quad (11.29)$$

where σ_k is the RCS of channel k . Here 1 and 2 can stand for any of hh, hv, or vv.

Pairs of channels can be combined in a variety of ways, but for single-look data, two combinations have particular importance. These are the complex Hermitian product $S_1 S_2^*$ and the channel ratio S_1/S_2 . Since the phases of these two quantities are the same, only three real quantities are involved, viz. $r_1 r_2$, r_1/r_2 and $\theta_1 - \theta_2$. The distributions of these quantities have been discussed by a number of authors [17, 23–25], and we only briefly indicate their derivations. A first step is to set $M = 2$ and transform coordinates in (11.24) by

$$S_1 = \sqrt{\sigma_1} E \cos \psi e^{i\theta_1} \quad (11.30a)$$

$$S_2 = \sqrt{\sigma_2} E \sin \psi e^{i\theta_2} \quad (11.30b)$$

where $E \geq 0$, $0 \leq \psi \leq \pi/2$, and $-\pi < \theta_k \leq \pi$. This transformation has Jacobian $|J| = \sigma_1 \sigma_2 E^3 \sin \psi \cos \psi$ leading to the joint PDF

$$P(E, \psi, \theta_1, \theta_2) = \frac{E^3 \sin 2\psi}{2\pi^2 (1 - |\rho|^2)} \times \exp\left(\frac{-E^2 [1 - |\rho| \sin 2\psi \cos(\theta_1 - \theta_2 - \angle \rho)]}{1 - |\rho|^2}\right) \quad (11.31)$$

It is straightforward to integrate E out of this expression, yielding

$$P(\psi, \theta_1, \theta_2) = \frac{1 - |\rho|^2}{4\pi^2} \frac{\sin 2\psi}{(1 - Y \sin 2\psi)^2} \quad (11.32)$$

where $Y = |\rho| \cos(\theta_1 - \theta_2 - \angle\rho)$. Substituting $t = \tan \psi$ and using partial fractions allows ψ to be integrated out. The joint distribution $P(\theta_1, \theta_2)$ is then obtained as

$$P(\theta_1, \theta_2) = \frac{1}{4\pi^2} \left(\frac{1 - |\rho|^2}{1 - Y^2} \right) \left(1 + \frac{Y}{\sqrt{1 - Y^2}} \cos^{-1}(-Y) \right) \quad (11.33)$$

from which the distribution of the phase difference $\theta_d = \theta_1 - \theta_2 (\text{mod } 2\pi)$ is

$$P(\theta_d) = \frac{1}{2\pi} \left(\frac{1 - |\rho|^2}{1 - Y^2} \right) \left(1 + \frac{Y}{\sqrt{1 - Y^2}} \cos^{-1}(-Y) \right) \quad (11.34)$$

where $-\pi < \theta_d \leq \pi$ and $Y = |\rho| \cos(\theta_d - \angle\rho)$.

To derive the amplitude ratio distribution, first integrate (11.32) over θ_1 and θ_2 to obtain the PDF of ψ

$$P(\psi) = \frac{\sin 2\psi}{\left(1 - |\rho|^2 \sin^2 2\psi\right)^{3/2}} \quad (11.35)$$

Since the amplitude ratio is given by $Q = |S_2/S_1| = r_2/r_1 \sqrt{\sigma_2/\sigma_1} \tan \psi$, a change of variables yields its PDF as

$$P(Q) = \frac{2\gamma(1 - |\rho|^2)Q(\gamma + Q^2)}{\left[(\gamma + Q^2)^2 - 4\gamma|\rho|^2Q^2\right]^{3/2}} \quad (11.36)$$

where $\gamma = \sigma_2/\sigma_1$.

For the amplitude product, we return to (11.31) and integrate out θ_1 and θ_2 to yield the joint PDF

$$P(E, \psi) = \frac{2E^3 \sin 2\psi}{1 - |\rho|^2} e^{-E^2/(1 - |\rho|^2)} I_0\left(\frac{|\rho|E^2 \sin 2\psi}{1 - |\rho|^2}\right) \quad (11.37)$$

where $I_0(\cdot)$ is a modified Bessel function (Section 9.6 of [26]).

Defining the amplitude product A by $A = |S_1 S_2| = r_1 r_2 = \frac{1}{2} E^2 \sqrt{\sigma_1 \sigma_2} \sin 2\psi$ gives a joint PDF

$$P(A, \psi) = \frac{4A}{X} \frac{1}{\sin 2\psi} \exp\left(-\frac{2A}{X \sin 2\psi}\right) I_0\left(\frac{2|\rho|A}{X}\right) \quad (11.38)$$

where $X = \sqrt{\sigma_1 \sigma_2} (1 - |\rho|^2)$. The integral over ψ assumes a standard form with the substitution $u = \operatorname{cosec} \psi$ and leads to

$$P(A) = \frac{4A}{X} K_0\left(\frac{2A}{X}\right) I_0\left(\frac{2|\rho|A}{X}\right) \quad (11.39)$$

where $K_0(\cdot)$ is a modified Bessel function (Section 9.6 of [26]).

11.6 Properties of the Distributions

The distributions (11.34), (11.36), and (11.39) each depend on two real parameters. For the phase difference distribution these are the amplitude and phase of the complex correlation coefficient, $|\rho|$ and $\angle\rho$; for the amplitude ratio they are $|\rho|$ and $\gamma = \sigma_2/\sigma_1$ while the amplitude product has a distribution involving $|\rho|$ and $\sigma_1 \sigma_2$. For single-look data, the phase difference and amplitude ratios are particularly important, and their properties are discussed in this section. The significance of the Hermitian product becomes clearest in the context of parameter estimation and then in its multilook form. This is treated in Section 11.7, although a detailed treatment of the single-look form is given in [24].

11.6.1 The Phase Difference Distribution

This distribution is unimodal and symmetric ($\bmod 2\pi$) about its mode, which occurs at $\theta_d = \angle\rho$. Its minimum is at $\angle\rho + \pi$ ($\bmod 2\pi$). The width of the distribution is controlled by $|\rho|$. If $|\rho|$ is near 1, the distribution is sharply peaked about $\angle\rho$; in the limiting case, as $|\rho| \rightarrow 1$, (11.34) tends to a δ -function centered on $\angle\rho$. As $|\rho|$ decreases, the distribution becomes flatter and is uniform if $|\rho| = 0$. As a result, phase difference images will appear noisier in areas where the correlation coefficient is low. This is clear in the multilook images in Figures 11.1 to 11.3 and is illustrated for single-look data by Figure 11.4, which shows L-band EMISAR images of (a) $\angle S_{hh} S_{vv}^*$ and (b) $\angle S_{hh} S_{hv}^*$ over an agricultural region in Jutland, Denmark. Figure 11.4(c,d) shows histograms of the phase difference for a single field of winter wheat at the bottom right of the image,

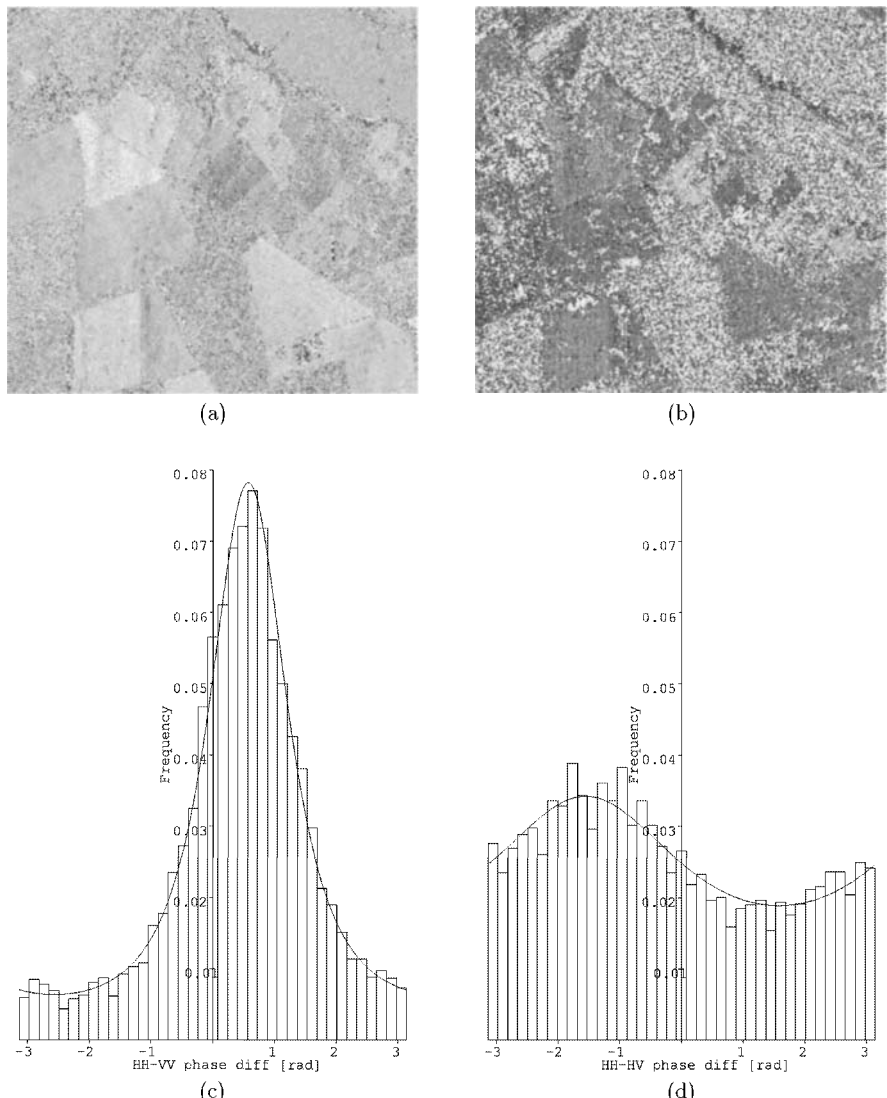


Figure 11.4 L-band EMISAR phase difference images from an agricultural area: (a) HH-VV and (b) HH-HV. Observed and theoretical phase difference distributions for a single winter wheat field of 5,537 pixels in the above images: (c) HH-VV, $|l_p| = 0.67$, $\angle \rho = 33$ degrees; and (d) HH-HV, $|l_p| = 0.19$, $\angle \rho = -89$ degrees.

together with the associated theoretical distributions (shown by the solid curves) using values of ρ estimated from the field. For the HH-VV data, $| \rho | \sim 0.67$ and $\angle \rho \sim 33$ degrees while the corresponding values for HH-HV are 0.19 and -89 degrees, respectively. The good fit between theory and measurement is clear, as is the dependence of the width of the distribution on $| \rho |$.

Quantitative measures of fit are much aided by the fact that the phase difference distribution has an analytic CDF given by

$$\begin{aligned} F(\phi) &= \int_{-\pi}^{\phi} P(\theta_d) d\theta_d \\ &= f(\phi - \angle \rho) + f(\pi + \angle \rho) \quad -\pi < \phi \leq \pi \end{aligned} \quad (11.40a)$$

where

$$f(\phi) = \frac{1}{2\pi} \left(\phi + \frac{| \rho | \sin \phi \cos^{-1}[-| \rho | \cos \phi]}{\sqrt{1 - | \rho |^2 \cos^2 \phi}} \right) \quad (11.40b)$$

This greatly simplifies the use of the K-S test of fit (see [14], for example).

It is clear that the natural measures of centrality and width for the single-look phase difference distribution are $\angle \rho$ and $| \rho |$, but it is common in the literature to find phase statistics described in terms of mean and standard deviation. These quantities can be expressed in terms of ρ since [24]

$$\langle \theta_d \rangle = \angle \rho + \frac{| \rho | \sin \angle \rho}{\sqrt{1 - | \rho |^2 \cos^2 \angle \rho}} \cos^{-1}(| \rho | \cos \angle \rho) \quad (11.41)$$

and

$$\begin{aligned} \text{var}(\theta_d) &= \frac{1 - | \rho |^2}{1 - | \rho |^2 \cos^2 \angle \rho} \left(\frac{\pi^2}{4} - \pi \sin^{-1}(| \rho | \cos \angle \rho) + [\sin^{-1}(| \rho | \cos \angle \rho)]^2 \right) \\ &\quad + \frac{1}{2} \sum_{n=1}^{\infty} \frac{1 - | \rho |^{2n}}{n^2} \end{aligned} \quad (11.42)$$

Both have serious flaws as summary statistics that arise from the circular nature of the phase measurement. These are easily demonstrated by a simple example. Consider the two phase difference distributions indicated in Figure 11.5. These are identical apart from a π phase shift, with that on the left

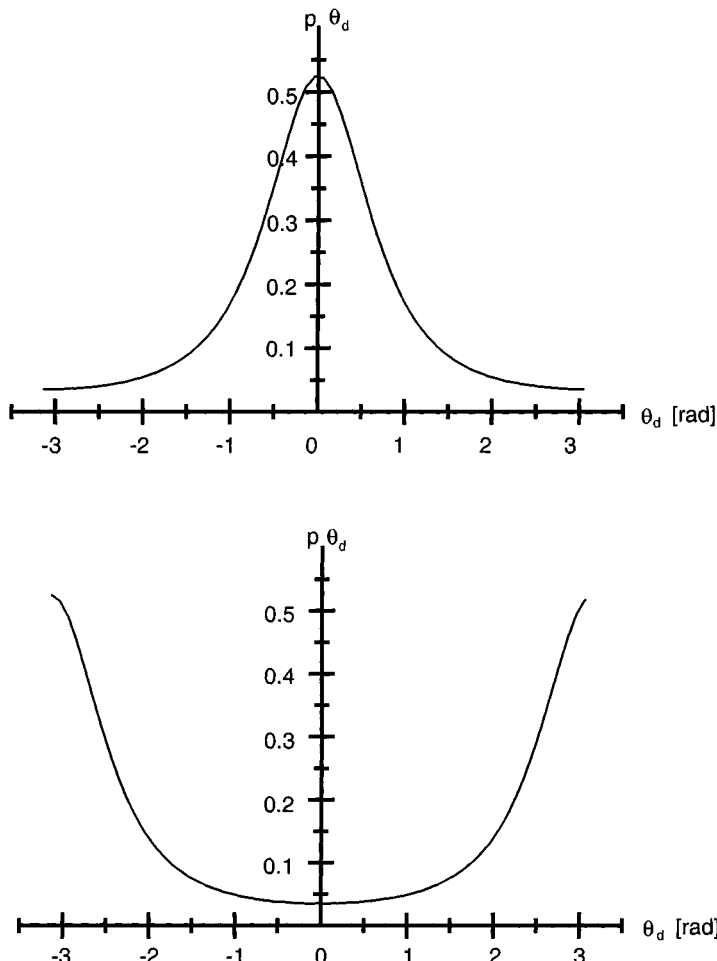


Figure 11.5 Examples of two phase difference distributions, identical except for a phase shift of π radians.

centered on zero and that on the right centered on π radians. Note that both distributions have mean zero but the variance is much larger for the distribution on the right. Hence, the mean and variance can provide a very misleading way of summarizing the distributional shape unless the modal phase difference is near zero. However, it is not uncommon in polarimetric data for modes well in excess of $\pi/2$ to occur (e.g., in woodland at longer wavelengths [14]). A thorough quantitative analysis of this issue is given in [27].

Avoiding the use of mean and variance presents no problem when the distribution is given by (11.34), but alternative measures are needed for more

general cases (including multilook data; see Section 11.7). Such measures, described in [28,29], are based on assigning to each observed phase θ_d a unit vector $(\cos \theta_d, \sin \theta_d)$. Taking the average of all these vectors yields a vector $\bar{R}(\cos \bar{\theta}, \sin \bar{\theta})$. The *mean direction* θ is independent of choice of origin; the *resultant length* lies in the range $[0,1]$, with 1 indicating coincident points. The quantity $V = 1 - \bar{R}$ is known as the *sample circular variance*. It is easy to see that with these definitions the distributions illustrated in Figure 11.5 would have the same sample circular variance and have mean direction zero and π as desired.

Examples of the use of these measures are shown in Figure 11.6 for L-band AirSAR data for regions of two different cover types. In Figure 11.6(a) the measured values of $\angle(S_{hh} S_{vv}^*)$ are plotted on a circular dial for regions of wheat; while Figure 11.6(b) shows the same quantity for coniferous woodland. The arrows indicate the vector $\bar{R}(\cos \bar{\theta}, \sin \bar{\theta})$ and the circles are each of radius 1. The mean direction is similar for both cover types (26 degrees for wheat and 19.8 degrees for conifer), but there is much greater dispersion in the wheat measurements. This is reflected in the sample circular variance measures of 0.206 for wheat and 0.003 for conifers.

11.6.2 The Amplitude Ratio Distribution

The amplitude ratio has a number of important uses, both as a means of inferring physical properties of a medium and as a way of removing terrain effects. As an example of the former, we note that since scattering models predict that the copolarized ratio depends only on surface dielectric and not on surface roughness, this ratio can be used to estimate soil moisture [30]. In [31], the crosspolarized ratio is also used to mask out vegetated areas when retrieving soil moisture. For terrain effects, uncorrected variations in local incidence angle cause changes in the effective scattering area [32]. This multiplicative geometrical factor applies equally to all channels and, hence, can be removed by taking channel ratios [33]. The price paid is to lose one degree of freedom in describing the data.

Although the distribution (11.36) has an analytic CDF given by

$$F(Q) = \frac{1}{2} \left(1 + \frac{Q^2 - \gamma}{[(\gamma + Q^2)^2 - 4|\rho|^2 \gamma Q^2]^{\frac{1}{2}}} \right) \quad (11.43)$$

making distributional fitting easy, its moments have no simple form. Figure 11.7 shows results corresponding to Figure 11.4, where now (a) and (b) are the $|HH/VV|$ and $|HV/VV|$ images while (c) and (d) show a comparison between theory and data. As in Figure 11.4, the theoretical curves use estimated parame-

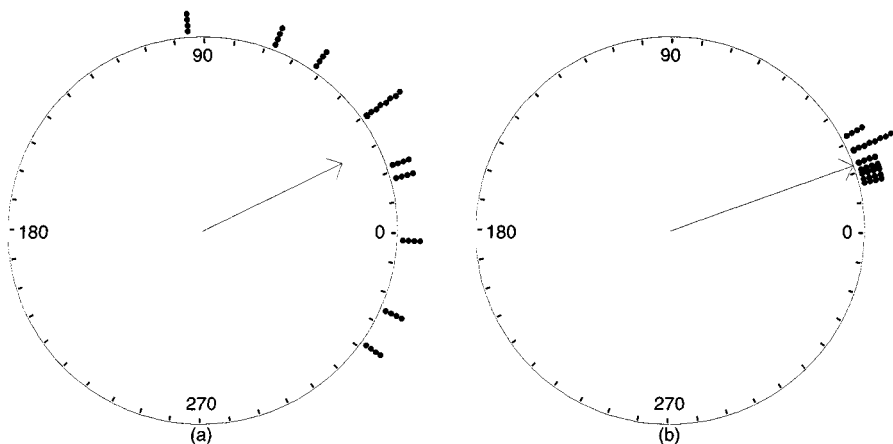


Figure 11.6 Circular plots of the HH-VV phase difference for L-band AirSAR data from (a) 10 wheat fields and (b) 10 conifer regions. The arrows indicate the mean vector, and the circles are of unit radius.

ters, in this case $|p| = 0.67$ and $\gamma = 0.9$ for the $|HH/VV|$ data and $|p| = 0.195$, $\gamma = 0.056$ for $|HV/VV|$. It is noticeable in this figure that the $|HV/VV|$ ratio (b) gives better defined structure, but the $|HH/VV|$ ratio in (a) picks out a region at lower left that is not obvious in (b). This probably indicates a crop with vertical structure, such as standing cereal [31]. The widths of the curves are not as easy to interpret as for the phase difference because the amplitude ratio distribution gets narrower as $|p|$ increases and wider as γ increases [34]. Hence, in the two plots shown as (c) and (d) there are competing effects (note the difference in scales).

11.7 Estimation of Polarimetric Parameters

The properties of a homogenous region in a SAR image that is made up of independent normally distributed pixels are completely described if we can provide an accurate estimate of the covariance matrix. For single-channel data this is straightforward, since the in-phase and quadrature channels are uncorrelated Gaussian variables with the same variance $\sigma^2/2$. Hence, only σ need be estimated, and it is easy to show that, given N observations of *spatially uncorrelated* data, the MLE of σ is given by multilooking, as discussed in Section 4.4.

For Gaussian polarimetric data the MLE of the covariance matrix C is similarly shown to be [35]

$$\hat{C} = \frac{1}{N} \sum_{k=1}^N \mathbf{S}^{(k)} \mathbf{S}^{(k)\dagger} \quad (11.44)$$

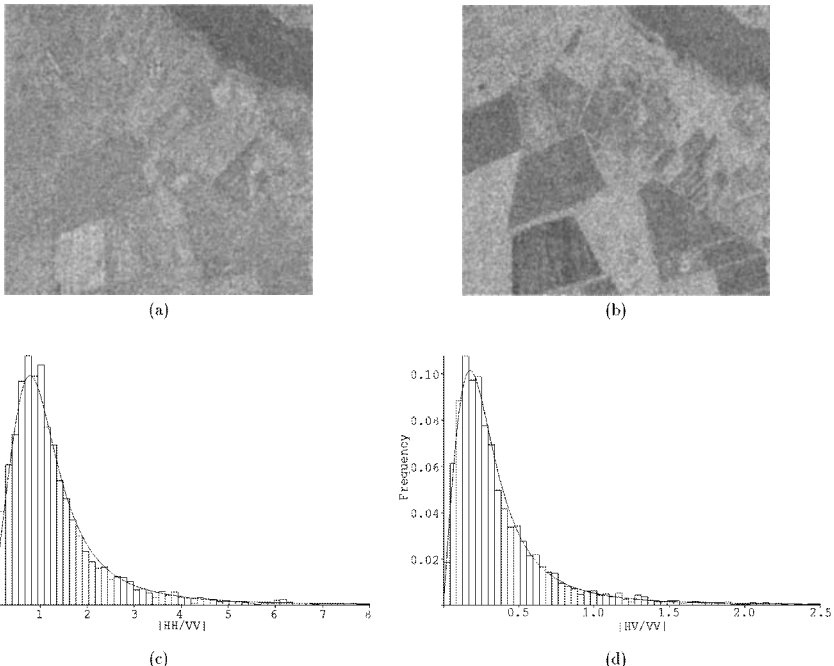


Figure 11.7 L-band EMISAR amplitude ratio images from an agricultural area: (a) |IHH/VVI| and (b) |IHV/VVI|. Observed and theoretical amplitude ratio distributions for a single winter wheat field in the previous images: (c)|IHH/VVI|, $|p_1| = 0.67$, $\gamma = 0.9$; and (d) |IHV/VVI|, $|p_1| = 0.19$, $\gamma = 0.056$.

where $S^{(k)}$ denotes the k th complex data vector. In other words, the sample covariance matrix is the MLE of the true covariance matrix. In the case of two channels, the covariance matrix has the form

$$C = \begin{pmatrix} \sigma_1 & R \\ R^* & \sigma_2 \end{pmatrix} \quad (11.45)$$

so the MLE estimates are the multilook averages

$$\hat{\sigma}_1 = \frac{1}{N} \sum_{k=1}^N |S_1^{(k)}|^2 \quad (11.46a)$$

$$\hat{\sigma}_2 = \frac{1}{N} \sum_{k=1}^N |S_2^{(k)}|^2 \quad (11.46b)$$

and

$$\hat{R} = \hat{Z}e^{i\hat{\Phi}} = \hat{A} + i\hat{B} = \frac{1}{N} \sum_{k=1}^N S_1^{(k)} S_2^{(k)*} \quad (11.46c)$$

The joint PDF of the estimates has the form of a *complex Wishart distribution* [35] given by

$$P(\hat{\sigma}_1, \hat{\sigma}_2, \hat{A}, \hat{B}) = \frac{N^{2N} (\hat{\sigma}_1 \hat{\sigma}_2 - |\hat{R}|^2)^{N-2}}{\pi \Gamma(N) \Gamma(N-1) \Delta^N} \times \exp \left\{ -N \frac{[\sigma_2 \hat{\sigma}_1 + \sigma_1 \hat{\sigma}_2 - 2\sqrt{\sigma_1 \sigma_2} \operatorname{Re}(\rho \hat{R}^*)]}{\Delta} \right\} \quad (11.47)$$

where $\Delta = \sigma_1 \sigma_2 (1 - |\rho|^2)$ and $\hat{\sigma}_1 \hat{\sigma}_2 \geq |\hat{R}|^2$. The marginal distributions of $\hat{\sigma}_1$ and $\hat{\sigma}_2$ are gamma distributions identical to the multilook distribution (4.9) and need no further discussion. The specific polarimetric parameters are conveyed by \hat{R} , the PDF of whose amplitude and phase is found by integrating $\hat{\sigma}_1$ and $\hat{\sigma}_2$ out of (11.47) and making the change of variable $\hat{A} = \hat{Z} \cos \hat{\Phi}$, $\hat{B} = \hat{Z} \sin \hat{\Phi}$, yielding

$$P(\hat{Z}, \hat{\Phi}) = \frac{2N(N\hat{Z})^N}{\pi \Delta \Gamma(N) (\sqrt{\sigma_1 \sigma_2})^{N-1}} \exp \left\{ \frac{2N\sqrt{\sigma_1 \sigma_2} |\rho| \hat{Z} \cos [\hat{\Phi} - \angle \rho]}{\Delta} \right\} \times K_{N-1} \left(\frac{2\sqrt{\sigma_1 \sigma_2} N\hat{Z}}{\Delta} \right) \quad (11.48)$$

where $K_{N-1}(.)$ is a modified Bessel function (Section 9.6 of [26]). From the joint distributions (11.47) and (11.48) we can derive the marginal distributions of three parameters, detailed in the following subsections, which are of particular interest (see also [24]).

11.7.1 The Multilook Phase Difference Distribution

The first of these is the phase difference, whose marginal distribution has the form [24,36]

$$P_{\hat{\Phi}}(\hat{\Phi}) = \frac{(1 - |\rho|^2)^N}{2\pi} \left\{ \frac{(2N - 2)!}{[(N - 1)!]^2 2^{2(N-1)}} \right. \\ \times \left[\frac{(2N - 1)Y}{(1 - Y^2)^{N+\frac{1}{2}}} \cos^{-1}(-Y) + \frac{1}{(1 - Y^2)^N} \right] + \frac{1}{2(N - 1)} \\ \times \left. \sum_{r=0}^{N-2} \frac{\Gamma(N - \frac{1}{2})}{\Gamma(N - \frac{1}{2} - r)} \frac{\Gamma(N - 1 - r)}{\Gamma(N - 1)} \frac{1 + (2r + 1)Y^2}{(1 - Y^2)^{r+2}} \right\} \quad (11.49)$$

where $Y = |\rho| \cos(\hat{\Phi} - \angle\rho)$. Other formulations of the phase distribution have been derived [34,37,38] involving a hypergeometric function, which must be evaluated by numerical quadrature. By contrast, (11.49) involves only a finite summation that is more convenient for data analysis. Note that when $N = 1$ the summation contains no terms and the distribution reduces to the single-look case (11.34).

Examples of theoretical distributions for different values of N and $|\rho|$ and comparison with observations will be found in [34,38], while practical applications of multilooking are shown in Chapter 12 (see Figure 12.1). As one would expect, the distribution (11.49) becomes narrower as N increases, but around its *mode*, $\angle\rho$, which is conserved by multilooking. The invariance of the mode confirms its value as the best representative of the phase difference distribution. No analytic expressions for the mean and variance of the phase exist except in the case $N = 1$ (see (11.41) and (11.42)), although limiting cases are discussed in [36,24]. The arguments given in Section 11.6.1 again apply here: the mean and variance have defects as representative statistics unless the mode is near zero or the measurements are defined relative to the mode. A complete treatment of the estimation problem including correction for the estimated mode has not yet been carried out.

The distribution of $\hat{\Phi}$ also becomes narrower as $|\rho|$ increases. This is clearly seen in Figures 11.1 to 11.3, which are for 16-look data; regions for which the estimated value of $|\rho|$ (panels (d–f) in the figures) is large show much less variation in $\hat{\Phi}$ (panels (g–i)).

11.7.2 The Multilook Coherence Distribution

From the PDF (11.48) it is straightforward to derive the marginal PDF and estimation properties of $\hat{Z} = |\hat{R}|$ [24], but this is of limited value. Of much greater importance in applications is the estimate of $|\rho|$, the magnitude of the complex correlation coefficient, which is often called the interchannel *coherence*. Since $|\rho|$ is a function of the polarimetric parameters, its MLE, \hat{r} , is given by replacing each parameter by its MLE [39]; hence,

$$\hat{r} = |\hat{\rho}| = \frac{|\hat{R}|}{\sqrt{\hat{\sigma}_1 \hat{\sigma}_2}} \quad (11.50)$$

The distribution of \hat{r} is given in [35] as

$$\begin{aligned} P(\hat{r}) &= 2(N-1)\left(1 - |\rho|^2\right)^N \hat{r}(1 - \hat{r}^2)^{N-2} {}_2F_1\left(N, N; 1; |\rho|^2 \hat{r}^2\right) \\ &= \frac{2\left(1 - |\rho|^2\right)^N \hat{r}(1 - \hat{r}^2)^{N-2}}{\Gamma(N)\Gamma(N-1)} \sum_{l=0}^{\infty} \left[\frac{\Gamma(l+N)}{\Gamma(l+1)} \right]^2 (|\rho|\hat{r})^{2l} \end{aligned} \quad (11.51)$$

where $0 \leq \hat{r} \leq 1$ and the second inequality arises by writing the hypergeometric function as an infinite sum (Section 15.1 of [26]). Plots of the theoretical PDFs for different values of N and ρ are available in [40,41], with practical applications in Chapter 12 (see Figure 12.1).

From (11.51) it is easy to calculate the moments of \hat{r} as

$$\begin{aligned} \langle \hat{r}^m \rangle &= \frac{\left(1 - |\rho|^2\right)^N}{\Gamma(N)} \sum_{l=0}^{\infty} \left[\frac{\Gamma(l+N)}{\Gamma(l+1)} \right]^2 \frac{\Gamma(l + \frac{m}{2} + 1)}{\Gamma(l + \frac{m}{2} + N)} |\rho|^{2l} \\ &= \left(1 - |\rho|^2\right)^N \Gamma(N) \frac{\Gamma(\frac{m}{2} + 1)}{\Gamma(\frac{m}{2} + N)} {}_3F_2\left(\frac{m}{2} + 1, N, N; 1, \frac{m}{2} + N; |\rho|^2\right) \end{aligned} \quad (11.52)$$

where

$${}_3F_2(a, b, c; d, e; z) = \frac{\Gamma(d)\Gamma(e)}{\Gamma(a)\Gamma(b)\Gamma(c)} \sum_{l=0}^{\infty} \frac{\Gamma(l+a)\Gamma(l+b)\Gamma(l+c)}{\Gamma(l+d)\Gamma(l+e)} \frac{z^l}{l!}$$

is a generalized hypergeometric function. Since \hat{r} is the MLE of $|\rho|$, it is asymptotically unbiased, so that $\hat{r} \rightarrow |\rho|$ as N increases. However, setting $m = 1$ allows

us to calculate the bias in \hat{r} for a finite sample. This bias is positive and increases as $|\rho|$ decreases [40]; for small values of $|\rho|$ it can be significant even for quite large N . In fact, for $\rho = 0$,

$$\langle \hat{r} \rangle = \frac{2^{2(N-1)} \Gamma^2(N)}{\Gamma(2N)} \approx \frac{1}{2} \sqrt{\pi/N} \quad (11.53)$$

where the approximation is for large N using Stirling's formula (Section 6.1 of [26]), so at least 314 samples would be needed to reduce the bias to less than 0.1. This bias can be seen in Figures 11.1 to 11.3, where panels (d–f) show \hat{r} with $N = 16$. Very few pixels take values less than 0.1; for the large areas in the crosspolarized channels that are essentially featureless, most of the pixels lie in the range 0.1 to 0.3. Perhaps more important than (11.51) is the a posteriori PDF $P(|\rho| \|\hat{r})$, which is proportional to the PDF given in (11.51) if $|\rho|$ is equally likely to take any value in the range [1, 0]. However, it is now considered as a function of $|\rho|$; the constant of proportionality normalizes the expression to have unit area as it is integrated over the range $0 \leq |\rho| \leq 1$. Plots of this PDF and a discussion of its use in estimating confidence intervals for $|\rho|$ are given in [41,42].

11.7.3 The Multilook Intensity Ratio

As discussed in Section 11.6.2, the amplitude or intensity ratio of channels can be important both as a direct measure of physical effects or to remove topographic effects. The multilook intensity ratio $Q = \hat{\sigma}_1/\hat{\sigma}_2$ has a PDF given by

$$P(Q) = \left(\frac{\sigma_1}{\sigma_2} \right)^L \frac{\Gamma(2L)}{\Gamma^2(L)} \frac{(1 - |\rho|^2)^L (\sigma_1/\sigma_2 + Q) Q^{L-1}}{\left([\sigma_1/\sigma_2 + Q]^2 - 4|\rho|^2 \sigma_1 Q / \sigma_2 \right)^{L+1/2}} \quad (11.54)$$

which yields the single-look expression (11.36) when we set $L = 1$. (Note that (11.36) gives the *amplitude* ratio, so a simple change of variables is also involved.) The derivation of this result together with theoretical plots and a comparison with data can be found in [34,38]. The result is identical to the single-channel form in (7.6) (with $M = 2L$, $k = L$, and $R = \sigma_1/\sigma_2$) if the channels are uncorrelated, so $|\rho| = 0$.

11.8 The Stokes Scattering Operator Formulation of Polarized Scattering

The previous section showed that, for Gaussian polarimetric data, multilooking provides the best estimates of the information-bearing parameters. Here we provide another description of the scattering behavior, originally developed for optical data, which provides a useful route to forming such data.

Radar systems can make direct phase measurements on the received data, permitting the scattering matrix to be measured. Essential to this is the availability of stable local oscillators providing a reference phase over the period of the measurement. By contrast, in optical data, the time scales for coherence of the individual wave packets making up the signal are so short that phase measurements must be inferred. This provides the basic motivation for the description of polarization state introduced by Rayleigh, using the *Stokes vector* [3,43]. The Stokes vector corresponding to a completely polarized wave with polarimetric field vector $(E_v, E_h)^t$ is a four-component real vector given by

$$\mathbf{F} = \begin{pmatrix} |E_v|^2 + |E_h|^2 \\ |E_v|^2 - |E_h|^2 \\ 2 \operatorname{Re}(E_v E_h^*) \\ 2 \operatorname{Im}(E_v E_h^*) \end{pmatrix} \quad (11.55)$$

The incident and scattered complex field vectors, \mathbf{E}^i and \mathbf{E}^s , are related by the scattering matrix S according to (see 11.2)

$$\mathbf{E}^s = \frac{e^{ikR}}{R} S \mathbf{E}^i \quad (11.56)$$

This corresponds to a transformation of Stokes vectors given by

$$\mathbf{F}^s = \frac{2}{r^2} Q M \mathbf{F}^i \quad (11.57)$$

where the matrix M is known as the *Stokes scattering operator*, and Q is the matrix

$$Q = \begin{pmatrix} 1 & 0 & 0 & 0 \\ 0 & 1 & 0 & 0 \\ 0 & 0 & 1 & 0 \\ 0 & 0 & 0 & -1 \end{pmatrix} \quad (11.58)$$

For reciprocal scattering, S and M are symmetric, and the terms in M are given by

$$M_{11} = \frac{1}{4} (|S_{vv}|^2 + 2|S_{hv}|^2 + |S_{hh}|^2) \quad (11.59a)$$

$$M_{12} = \frac{1}{4} (|S_{vv}|^2 - |S_{hh}|^2) \quad (11.59b)$$

$$M_{13} = \frac{1}{2} \operatorname{Re}(S_{vv} S_{hv}^* + S_{hh} S_{hv}^*) \quad (11.59c)$$

$$M_{14} = -\frac{1}{2} \operatorname{Im}(S_{vv} S_{hv}^* - S_{hh} S_{hv}^*) \quad (11.59d)$$

$$M_{22} = \frac{1}{4} (|S_{vv}|^2 - 2|S_{hv}|^2 + |S_{hh}|^2) \quad (11.59e)$$

$$M_{23} = \frac{1}{2} \operatorname{Re}(S_{vv} S_{hv}^* - S_{hh} S_{hv}^*) \quad (11.59f)$$

$$M_{24} = -\frac{1}{2} \operatorname{Im}(S_{vv} S_{hv}^* + S_{hh} S_{hv}^*) \quad (11.59g)$$

$$M_{33} = \frac{1}{2} (|S_{hv}|^2 + \operatorname{Re}(S_{vv} S_{hh}^*)) \quad (11.59h)$$

$$M_{34} = -\frac{1}{2} \operatorname{Im}(S_{vv} S_{hh}^*) \quad (11.59i)$$

$$M_{44} = \frac{1}{2} (|S_{hv}|^2 - \operatorname{Re}(S_{vv} S_{hh}^*)) \quad (11.59j)$$

These definitions and other associated formulations of the scattering description are given, for example, in [3]. Note that:

- The Stokes scattering operator contains only Hermitian products of field terms, so absolute phase has been lost, but phase differences are preserved.
- S can be recovered from M , up to a single unknown phase.
- Swapping the roles of h and v causes M_{12} , M_{14} , M_{23} , and M_{34} to change sign but leaves the other coefficients unchanged (this is relevant because the values supplied by the JPL AirSAR system contain this modification).

For a distributed target, M is a random matrix, whose mean value is the relevant quantity. As can be seen, the expected value of each term in M is formed from sums of terms from the covariance matrix, so the MLE of M is given by combining terms from the sample covariance matrix. Hence, in applications where parameter estimation for distributed targets is more important than resolution, it is common to pre-average Stokes scattering operators to form multilook data. This provides an important method of reducing the data volume. Note that averaging scattering matrix data is of no value because this would not improve the estimates of the covariance terms that carry the actual information (see the discussion in Section 4.4). As discussed in Chapter 4, multilooking can be carried out within the processor, or by spatial averaging of pixels. Multilook Stokes scattering operators can be further averaged within homogeneous regions to provide ML estimates of the covariance parameters with greater accuracy.

Although scattering information may be supplied in the form of multilook Stokes scattering operator terms (this is normal for the JPL AirSAR system), from the point of view taken in this chapter, the primary object of interest is the sample covariance matrix. This can be estimated from the Stokes scattering operator by the relations

$$\hat{C}_{11} = M_{11} + M_{22} + 2M_{12} \quad (11.60a)$$

$$\hat{C}_{22} = M_{33} + M_{44} \quad (11.60b)$$

$$\hat{C}_{33} = M_{11} + M_{22} - 2M_{12} \quad (11.60c)$$

$$\hat{C}_{12} = (M_{13} + M_{23}) - i(M_{14} + M_{24}) \quad (11.60d)$$

$$\hat{C}_{32} = (M_{13} - M_{23}) + i(M_{14} - M_{24}) \quad (11.60e)$$

$$\hat{C}_{13} = M_{33} - M_{44} - 2iM_{34} \quad (11.60f)$$

Here, the subscripts 1, 2, and 3 on the covariance terms correspond to VV, HV, and HH, respectively, while the Stokes scattering operator terms are as defined in (11.59). The results derived in Section 11.7 can now be applied.

11.9 Texture in Polarimetric Data

In Appendix 11A we establish that a number fluctuation model leads to a description of the scattering matrix data as

$$\mathbf{S} = T\mathbf{G} \quad (11.61)$$

where T is a positive real texture variable and \mathbf{G} is a multivariate Gaussian variable independent of T . The properties of the Gaussian component, \mathbf{G} , can be estimated from the data since $\langle S_i S_j^* \rangle = \langle G_i G_j^* \rangle$ (see (11.8)). Hence \mathbf{S} and \mathbf{G} have the same covariance matrix. Also, since $S_i/S_j = G_i/G_j$ is independent of T , the single-look amplitude ratio and phase difference distributions are exactly the same as for the Gaussian case. Tests confirming this have been reported [14]. The Hermitian product $S_i S_j^* = T^2 G_i G_j^*$ will, however, show evidence for the departure from Gaussian behavior either through its real and imaginary parts or through its amplitude (though not through its phase, since this is the phase difference distribution discussed in Section 11.6.1); the corresponding analysis is given in [44].

For the particular case of negative binomial number fluctuations, T^2 is gamma-distributed with mean 1; hence, T has a square-root gamma distribution given by

$$P(T) = 2 \frac{\nu^\nu}{\Gamma(\nu)} T^{2\nu-1} e^{-\nu T^2} \quad (11.62)$$

where ν is an order parameter. In this case we can derive the PDF of the scattering matrix data for the M -dimensional product model as

$$\begin{aligned} P_s(\mathbf{S}) &= \int_0^\infty \frac{1}{T^{2M}} P_G(\mathbf{S}/T) P_T(T) dT \\ &= \frac{1}{\pi^M |C| \Gamma(\nu)} \int_0^\infty T^{2\nu-2M-1} e^{-\nu T^2} \exp\left(-\frac{\mathbf{S}^\dagger C^{-1} \mathbf{S}}{T^2}\right) dT \\ &= \frac{2}{\pi^M |C| \Gamma(\nu)} (\nu \mathbf{S}^\dagger C^{-1} \mathbf{S})^{\frac{\nu-M}{2}} K_{\nu-M}\left(2\sqrt{\nu \mathbf{S}^\dagger C^{-1} \mathbf{S}}\right) \end{aligned} \quad (11.63)$$

This is a multidimensional K distribution. In similar fashion, any of the other PDFs arising from the product model can be derived by integrating over T .

11.9.1 Multilook Textured Data

When considering multilook data, two cases are relevant. In the first, the texture variable is assumed constant over each area for which the pixels are being averaged. Hence, any vector or scalar quantity X known in the Gaussian case to have the conditional PDF $P(X|T)$ gives rise to the corresponding PDF in the texture model

$$P(X) = \int_0^{\infty} P(X|T)P(T) dT \quad (11.64)$$

Since in this case the multilook phase difference, amplitude ratio, and sample coherence are all independent of T , they are also independent of texture. In the second case, the texture variable fluctuates between the samples being averaged. Few, if any, analytic results are available in this case. For example, even the PDF of a sum of samples has no analytic form.

11.9.2 Parameter Estimation

For the product model with gamma-distributed texture, 10 real parameters need to be estimated in the general case (the three channel powers, the phase and amplitude of the three interchannel correlation coefficients, and the order parameter). As already observed in Section 8.3, the ML estimation problem has no analytic solution even for single-channel data. Following the analysis in [45], an approximate ML estimate of the covariance matrix is given by

$$\hat{C}_{ij} = \frac{1}{N} \sum_{n=1}^N S_i^{(n)} S_j^{(n)*} = \frac{1}{N} \sum_{n=1}^N T_n^2 G_i^{(n)} G_j^{(n)*} \quad (11.65)$$

Using (11.8) and the fact that $\langle T^2 \rangle = 1$ implies that \hat{C}_{ij} is an unbiased estimate of C_{ij} . For each single channel, the analysis described in Section 8.3 indicates that a reasonable estimate of the order parameter ν (see (11.62)) is given by solving the equation

$$\ln \hat{\nu} - \psi^{(0)}(\hat{\nu}) + \gamma_E = \ln \bar{I} - \overline{\ln I} = \overline{\ln(\bar{I}/I)} \quad (11.66)$$

where, for any quantity x , \bar{x} denotes $\frac{1}{N} \sum_{i=1}^N x_i$. If all three channels have the same order parameter, there are effectively $3N$ (correlated) samples. Two possible approaches to using all the information would be to estimate v for each channel and average the results or instead to solve [24]

$$\ln \hat{v} - \psi^{(0)}(\hat{v}) + \gamma_E = \frac{1}{3N} \sum_{k=1}^N \ln \left(\frac{\hat{\sigma}_1}{I_1^{(k)}} \right) + \ln \left(\frac{\hat{\sigma}_2}{I_2^{(k)}} \right) + \ln \left(\frac{\hat{\sigma}_3}{I_3^{(k)}} \right) \quad (11.67)$$

where $\hat{\sigma} = \hat{I}$ (see (11.46)). The relative merits of these two approaches is at present unknown.

11.9.3 Texture Observations in Polarimetric Data

Data from the NASA/JPL AirSAR polarimetric system acquired during the 1991 MacEurope campaign from the Feltwell, UK, agricultural site provided a surprising opportunity to examine texture in polarimetric data [14]. The surprise was that at the low resolutions used (15.5m in azimuth by 11m in slant range), texture was observed at all, since it is normally associated with higher resolutions (see Chapters 5 and 8). Figures 11.1 to 11.3 have already shown the channel powers and correlation terms for 16-look C-, L-, and P-band images for a section of the test site. Figure 11.8 shows the estimated value of v^{-1} for the same region at HH polarization for all three wavelengths, using single-look data. All the images are shown with the same gray scale and the calculated values are per segment values, based on an image segmentation (see Chapters 7 and 12), in order to improve estimation accuracy. The occurrence of negative values indicated by the scale is a result of estimation error in some of the small segments. The increased texture at longer wavelengths is very obvious. The field structure observed in Figures 11.1 to 11.3 becomes progressively clearer as we move from C- to P-band. Most of the C-band image exhibits low values, corresponding to large values of v and hence near-Gaussian behavior. As wavelength increases, the data progressively depart from being Gaussian; measurements of the observed distributions and reasons for this behavior are discussed in the following paragraphs.

A crop map compiled for the day of the data acquisition (July 28, 1991) facilitated an investigation of how the polarimetric distributions and parameters varied with crop type and frequency. For this purpose, measurements were made on 10 regions of conifer forest, barley, grass, wheat, potatoes, and sugarbeet, giving 60 regions in total. The broader classification into conifers, cereals

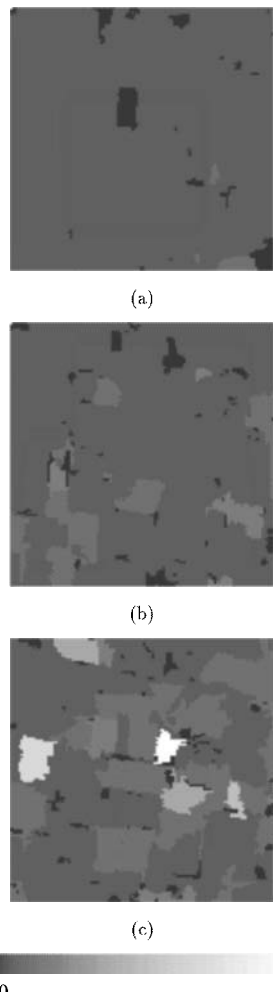


Figure 11.8 Estimated values of ν^{-1} calculated over the same region as in Figures 11.1 to 11.3, using single-look HH data from the NASA/JPL AirSAR at (a) C-band, (b) L-band, and (c) P-band.

(barley, grass, and wheat), and root crops (potatoes and sugarbeet) gave rise to very clear distributional differences, as summarized in Table 11.1. It was found that the Gaussian model appeared viable for all vegetation types at C-band. While conifers and root crops remained Gaussian, cereal crops became non-Gaussian at L-band, in most cases being reasonably well fitted by a K distribution. At P-band only the conifer forest appeared Gaussian. Root crops were better fitted by K distributions; cereal crops, although modeled better by K distributions, in many cases gave a poor fit [14].

Table 11.1
Distributional Forms Observed as a Function of Wavelength and
Cover Type for the Feltwell Region in AirSAR Data

	Cereals	Root Crops	Conifer
C	Gaussian	Gaussian	Gaussian
L	K	Gaussian	Gaussian
P	K?	K	Gaussian

The Gaussian behavior of the C-band data is as expected, since at the low resolution of the imagery we would expect many independent scatterers per resolution cell, with the backscatter arising predominantly from volume scattering in the vegetation canopy. In contrast, no satisfactory physical interpretation of the results at the longer wavelengths is currently available. It is hard to see how scattering in the canopy could produce the spatial variability implied by the measurements: the data were gathered in late July, so in most cases the fields would exhibit full ground cover with crops at a late stage of development. Alternatively, we may see a soil effect because significant penetration to the soil surface and even some penetration into the ground will occur at L-band and particularly at P-band. However, the soil surface would appear comparatively smooth at these wavelengths. Hence, it may not contribute greatly to the backscatter nor be able to give rise to the fluctuations in backscattering coefficient needed to explain the observed behavior. A possibility is that agricultural treatment gave rise to long-scale variations in surface slope. However, these are likely to be greater for the root crops than the cereals, whereas the cereals show the greatest degree of non-Gaussian behavior. In these circumstances, we should perhaps regard these data as providing a good example of where image analysis outstrips our current understanding of the underlying physics.

An attractive aspect of these data is that they allowed us to test whether the phase difference and amplitude ratio distributions were independent of whether the data are Gaussian or K-distributed, as predicted by the product model for texture. To this end, K-S fits were performed for all frequencies and regions using the CDFs given as (11.40) and (11.43). The results confirmed the robustness of these distributions, particularly at C- and L-bands; at P-band, a few of the cereal fields gave poor fits, associated with the departure from the K distribution [14]. A further aspect of the model that was investigated was the behavior of the order parameter between channels. (The order parameter was calculated by inverting (8.31), but it should be noted that the interpretation of this parameter is clear only for those regions displaying a K distribu-

tion.) According to the product model, the order parameter should be the same for all channels; this was observed in the C- and L-band data. However, at P-band, significant differences between the estimated order parameters in the three channels were observed for cereal crops, especially for the grass fields [14]. This suggests a breakdown in the simple texture model, which could occur because at the long wavelengths the assumption of a large mean number of scatterers is no longer valid or because the different polarizations are effectively not seeing the same scatterers due to different attenuation properties. The theoretical basis for differences in texture variables between polarizations is discussed in [12], and observed differences are also described in [46]. In the latter case, the significance of the differences is unclear, because we currently do not have a well-developed theory to establish confidence intervals for the order parameter.

11.10 Interferometric, Multifrequency, and Multitemporal Data

Although the developments in this chapter have been principally motivated by the properties of polarimetric data, they are applicable to other forms of multi-dimensional data, with some simplifications and modifications. Closest in spirit to polarimetric data is interferometric data, since this is critically dependent on correlation between channels, where now the channels are distinguished by their viewing angle of the scene [47]. In fact, all the information characteristic of interferometry is carried by the complex correlation of channels, from which can be inferred, *inter alia*, a terrain map of the scene [48,49], disturbances to the surface due to agricultural treatment [50], and surface motion or deformation [51]. Hence, from the point of view of image statistics, interferometric data have the same properties as polarimetric data because the channels will be jointly Gaussian (possibly with texture) and the quantities of interest are the complex correlation coefficients. The MLEs of interferometric phase and coherence are as described in Section 11.7. As noted there, accurate estimates of phase require high coherence or large numbers of samples. This has a direct impact on the properties of the information that can be extracted from interferometry. For example, accurate measurements of phase in areas of low coherence require a lot of spatial averaging, with consequent loss of spatial resolution. Since phase is the quantity used to infer topography, this affects the quality of any inferred digital elevation model; consistent height accuracy across a scene implies differing spatial resolution. Although the local estimation problem is essentially the same as that for polarimetry, a rather important difference is that phase measurements are often of most interest where there is a phase gradient. Hence, there is the

problem of trade-off between local homogeneity (in order to measure an unbiased local phase) and acceptable variance (the precision of the measurement). This has given rise to methods of adaptive filtering, as described in [52]. In many cases the statistical model for interferometric data can be simplified compared to that for polarimetry because only two channels are used (although more are needed in differential interferometry [48,53]) and often the channel powers will be the same. However, cases have been reported for repeat-pass interferometry where significant changes in σ^o have occurred between the acquisition of the images, but coherence is still obtained [53].

For multifrequency polarimetric or single-channel SAR, the data will be independent between frequencies; hence, the covariance matrix will simply consist of blocks down the leading diagonal, with zeroes elsewhere. This means that there is no value in forming crossfrequency parameters as far as extracting information goes, and each channel can be considered separately. In particular, texture is likely to be different between channels, as already observed in Section 11.9.

For multitemporal data exhibiting no coherence (and hence of no value for interferometry), the situation becomes simpler still. Since the data are uncorrelated between dates, the covariance matrix is diagonal and all the information is carried in the σ^o values at each date, together with any texture parameters.

11.11 Summary

Despite the apparent complexity introduced when multichannel data are available, simple models provide a viable means of describing the information available from distributed targets. For a single frequency, physical reasoning and measurement support descriptions based on local Gaussian behavior modulated by a scalar texture, which can be interpreted as a number fluctuation effect. This interpretation cannot be pushed too far, because, for example, the differing penetration depths of H and V polarized waves into media that show preferred horizontal or vertical structures (e.g., cereals) indicate that not all scatterers receive the same incident wave. Nonetheless, distributions derived from this model appear consistent with observations, except in some cases at the longest wavelengths.

Because such simple models can be used, the information-bearing parameters in the data are readily identified. When the data are Gaussian, there is a well-developed estimation theory for these parameters. In principle, few difficulties arise in applying this theory. In practice, the complicated expressions for the sample coherence and phase difference distributions have at present pre-

vented the development of a simple treatment for confidence intervals and moments, for example. For textured data, the estimation theory runs into the problems identified in Chapter 8, preventing analytic MLE solutions; only approximate solutions are currently available. The success of a simple tractable model for the data provides a sound basis for our investigations of filtering, classification, and segmentation in later chapters. However, it must be remarked that the empirical basis for this model is currently very incomplete. Comparatively few studies over a limited set of terrain types have attempted to validate it. We have indicated that problems occur at long wavelengths, but more investigation is needed to establish the effects of, for example, resolution and cover type. Nonetheless, we will adopt the product model as our basic descriptor of single-frequency multichannel data in the following chapters, with data gathered at different frequencies being considered independent.

References

- [1] Le Toan, T., A. Beaudoin, S. Goze, J. A. Kong, C. C. Hsu, H. C. Han, and R. T. Shin, "Microwave Interaction and Analysis of Polarimetric Data: Retrieval of Forest Biomass," Final report to ESA ESTEC on Contract No. 9352/91/NL/LC(SC), 1992.
- [2] Le Toan, T., A. Beaudoin, J. Riom, and D. Guyon, "Relating Forest Biomass to SAR Data," *IEEE Trans. Geosci. Remote Sensing*, Vol. 30, 1992, pp. 403–411.
- [3] Ulaby, F. T., and C. Elachi, *Radar Polarimetry for Geoscience Applications*, Norwood, MA: Artech House, 1990.
- [4] Tsang, L., J. A. Kong, and R. T. Shin, *Theory of Microwave Remote Sensing*, New York: Wiley Interscience, 1985.
- [5] Quegan, S., "A Unified Algorithm for Phase and Crosstalk Calibration—Theory and Observations," *IEEE Trans. Geosci. Remote Sensing*, Vol. 32, 1994, pp. 89–99.
- [6] van Zyl, J. J., "Calibration of Polarimetric Radar Images Using Only Image Parameters and Trihedral Corner Reflector Responses," *IEEE Trans. Geosci. Remote Sensing*, Vol. 28, 1990, pp. 337–348.
- [7] Freeman, A., J. J. van Zyl, J. D. Klein, H. A. Zebker, and Y. Shen, "Calibration of Stokes and Scattering Matrix Format Polarimetric SAR Data," *IEEE Trans. Geosci. Remote Sensing*, Vol. 30, 1992, pp. 531–539.
- [8] Quegan, S., and I. Rhodes, "Problems in the Linear Distortion Model for Polarimetric Calibration," *Proc. CEOS Calibration Workshop*, ESA WPP-048, 1993, pp. 127–132.
- [9] Sarabandi, K., L. E. Pierce, and F. T. Ulaby, "Calibration of a Polarimetric Imaging SAR," *IEEE Trans. Geosci. Remote Sensing*, Vol. 30, 1992, pp. 540–549.
- [10] Sheen, D. R., A. Freeman, and E. S. Kasischke, "Phase Calibration of Polarimetric Radar Images," *IEEE Trans. Geosci. Remote Sensing*, Vol. 27, 1989, pp. 719–730.
- [11] Zebker, H. A., and Y. Lou, "Phase Calibration of Imaging Radar Polarimeter Stokes Matrices," *IEEE Trans. Geosci. Remote Sensing*, Vol. 28, 1990, pp. 246–252.

- [12] Williams, M. L., S. Quegan, and D. Blacknell, "Intensity Statistics in the Distorted Born Approximation: Application to C-band Images of Woodland," *Waves in Random Media*, 1997 (in press).
- [13] Oliver, C. J., "A Model for Non-Rayleigh Scattering Statistics," *Opt. Acta*, Vol. 6, 1984, pp. 701–722.
- [14] Quegan, S., and I. Rhodes, "Statistical Models for Polarimetric Data: Consequences, Testing and Validity," *Int. J. Remote Sensing*, Vol. 16, 1995, pp. 1183–1210.
- [15] Jakeman, E., "On the Statistics of K-Distributed Noise," *J. Phys. A: Math. Gen.*, Vol. 13, 1980, pp. 31–48.
- [16] Jao, J. K., "Amplitude Distribution of Composite Terrain Radar Clutter and the K Distribution," *IEEE Trans. Geosci. Remote Sensing*, Vol. 22, 1984, pp. 1049–1062.
- [17] Yueh, S. H., J. A. Kong, J. K. Jao, R. T. Shin, H. A. Zebker, T. Le Toan, and H. Ottl, "K-Distribution and Polarimetric Radar Clutter," *Polarimetric Remote Sensing*, J. A. Kong (ed.), Amsterdam: Elsevier, 1990.
- [18] Held, D. N., W. E. Brown, A. Freeman, J. D. Klein, H. Zebker, T. Sato, T. Miller, Q. Nguyen, and Y. Lou, "The NASA/JPL Multifrequency Multipolarisation Airborne SAR System," *Proc. IGARSS '88 Symp.*, Edinburgh, 1988, pp. 345–349.
- [19] Wooding, M., F. Lodge, and E. Attema, (eds.), *MAC-Europe 91: Final Results Workshop Proc.*, ESA WPP-88, 1995.
- [20] Nghiem, S. V., S. H. Yueh, R. Kwok, and F. K. Li, "Symmetry Properties in Polarimetric Remote Sensing," *Radio Sci.*, Vol. 27, pp. 693–711.
- [21] Papoulis, A., *Probability, Random Variables and Stochastic Processes*, Singapore: McGraw-Hill, 1984.
- [22] Siegert, A. J. F., MIT Rad. Lab. No. 465, 1943.
- [23] Davenport, W. B., and W. L. Root, *Random Signals and Noise*, New York: McGraw-Hill, 1958.
- [24] Tough, R. J. A., D. Blacknell, and S. Quegan, "A Statistical Description of Polarimetric and Interferometric Synthetic Aperture Radar Data," *Proc. Roy. Soc. London A*, Vol. 449, 1995, pp. 567–589.
- [25] Middleton, D., *Introduction to Statistical Communication Theory*, New York: McGraw-Hill, 1960.
- [26] Abramowitz, M., and I. Stegun, *Handbook of Mathematical Functions*, New York: Dover, 1965.
- [27] Quegan, S., L. V. Dutra, and K. D. Grover, "Phase Measurements in MAESTRO Polarimetric Data from the UK Test Sites," *Int. J. Remote Sensing*, Vol. 15, 1994, pp. 2719–2736.
- [28] Mardia, K. V., *Statistics of Directional Data*, New York: Academic Press, 1972.
- [29] Fisher, N. I., *Statistical Analysis of Circular Data*, Cambridge: Cambridge University Press, 1993.
- [30] Oh, Y., K. Sarabandi, and F. T. Ulaby, "An Empirical Model and an Inversion Technique for Radar Scattering from Bare Soil Surfaces," *IEEE Trans. Geosci. Remote Sensing*, Vol. 30, 1992, pp. 370–381.

- [31] Dubois, P. C., J. J. van Zyl, and T. Engman, "Measuring Soil Moisture with Imaging Radars," *IEEE Trans. Geosci. Remote Sensing*, Vol. 33, 1995, pp. 915–926.
- [32] Schreier, G., "Geometrical Properties of SAR Images," *SAR Geocoding: Data and Systems*, G. Schreier (ed.), Karlsruhe: Wichmann, 1993, pp. 103–134.
- [33] Shi, J., J. Dozier, and H. Rott, "Snow Mapping in Alpine Regions with Synthetic Aperture Radar," *IEEE Trans. Geosci. Remote Sensing*, Vol. 32, 1994, pp. 152–158.
- [34] Joughin, I. R., D. P. Winebrenner, and D. B. Percival, "Probability Density Functions for Multilook Polarimetric Signatures," *IEEE Trans. Geosci. Remote Sensing*, Vol. 32, 1994, pp. 562–574.
- [35] Goodman, N. R., "Statistical Analysis Based on a Certain Multivariate Gaussian Distribution (an Introduction)," *Ann. Math. Stat.*, Vol. 34, 1963, pp. 152–177.
- [36] Tough, R. J. A., "Interferometric Detection of Sea Surface Features," DRA Memorandum 4446, 1991.
- [37] Barber, B. C., "The Phase Statistics of a Multichannel Radar Interferometer," *Waves in Random Media*, Vol. 3, 1993, pp. 257–266.
- [38] Lee, J.-S., K. W. Hoppel, S. A. Mango, and A. R. Miller, "Intensity and Phase Statistics of Multilook Polarimetric and Interferometric SAR Imagery," *IEEE Trans. Geosci. Remote Sensing*, Wichmann, Vol. 32, 1994, pp. 1017–1028.
- [39] de Groot, M. H., *Probability and Statistics*, Reading, MA: Addison-Wesley, 1989.
- [40] Touzi, R., and A. Lopes, "Statistics of the Stokes Parameters and of the Complex Coherence Parameters in One-Look and Multi-Look Speckle Fields," *IEEE Trans. Geosci. Remote Sensing*, Vol. 34, 1996, pp. 519–531.
- [41] Giani, M., C. Prati, and F. Rocca, "Study on SAR Interferometry and Its Applications," ESRIN Contract No. 8928/90/F/BZ, 1992.
- [42] Foster, M. R., and J. Guinzy, "The Coefficient of Coherence, Its Estimation and Use in Geophysical Data Processing," *Geophys.*, Vol. 32, 1967, pp. 602–616.
- [43] Born, M., and E. Wolf, *Principles of Optics*, New York: Pergamon Press, 1965.
- [44] Quegan, S., and I. Rhodes, "Statistical Models for Polarimetric Data," *Proc. IEE Seminar on Texture Analysis in Radar and Sonar*, IEE Digest No. 1993/207, London, 1993, pp. 8/1–8/8.
- [45] Oliver, C. J., "Optimum Texture Estimators for SAR Clutter," *J. Phys. D*, Vol. 26, 1993, pp. 1824–1835.
- [46] Sheen, D. R., and L. P. Johnston, "Statistical and Spatial Properties of Forest Clutter with Polarimetric Synthetic Aperture Radar," *IEEE Trans. Geosci. Remote Sensing*, Vol. 30, 1992, pp. 578–588.
- [47] Rodriguez, E., and J. M. Martin, "Theory and Design of Interferometric Synthetic Aperture Radars," *IEE Proc.-F*, Vol. 139, 1992, pp. 147–159.
- [48] Zebker, H. A., and R. M. Goldstein, "Topographic Mapping from Interferometric Synthetic Aperture Radar Observations," *J. Geophys. Res.*, Vol. 91, 1986, pp. 4993–4999.
- [49] Kwok, R., and M. A. Fahnestock, "Ice Sheet Motion and Topography from Radar Interferometry," *IEEE Trans. Geosci. Remote Sensing*, Vol. 35, 1996, pp. 189–200.
- [50] Wegmuller, U., and C. Werner, "Retrieval of Vegetation Parameters with SAR Interferometry," *IEEE Trans. Geosci. Remote Sensing*, Vol. 35, 1996, pp. 18–24.

- [51] Massonnet, D., M. Rossi, C. Carmona, F. Adraga, G. Peltzer, K. Feigi, and T. Rabaute, "The Displacement Field of the Landers Earthquake by SAR Interferometry," *Nature*, Vol. 364, 1993, pp. 138–142.
- [52] Werner, C. L., P. Rosen, S. Hensley, E. Fielding, and E. Chapin, "Detection of Aseismic Creep Along the San Andreas Fault Near Parkfield, California with ERS-1 Radar Interferometry," *Proc. Third ERS Scientific Symp.*, Florence, Italy, March 18–22, 1997.
- [53] Gabriel, A. K., R. M. Goldstein, and H. A. Zebker, "Mapping Small Elevation Changes over Large Areas: Differential Radar Interferometry," *J. Geophys. Res.*, Vol. 94, 1989, pp. 9183–9191.

Appendix 11A Number Fluctuations and the Generalized Product Model

Assume that N independent scatterers contribute to the observed M -channel signal, \mathbf{S} . The complex reflectivity of the k th scatterer in channel j is $r_{kj}e^{i\theta_{kj}}$, and propagation between the scatterer and the sensor causes a phase change, ϕ_k assumed uniformly distributed on $(0, 2\pi)$ and independent of scatterer properties. The data vector \mathbf{S} is then given by

$$\mathbf{S} = \begin{pmatrix} a_1 + ib_1 \\ \vdots \\ a_M + ib_M \end{pmatrix} = \sum_{k=1}^N \begin{pmatrix} r_{k1} e^{i\theta_{k1}} \\ \vdots \\ r_{kM} e^{i\theta_{kM}} \end{pmatrix} e^{i\phi_k} \quad (11A.1)$$

(see (11.5)) and has characteristic function

$$\begin{aligned} \chi(\mathbf{u}) &= \langle \exp i(\mathbf{u} \cdot \mathbf{S}_R) \rangle \\ &= \prod_{k=1}^N \left\langle \exp \left(i \sum_{p=1}^M v_p r_{kp} \cos(\theta_{kp} + \phi_k - \alpha_p) \right) \right\rangle \quad (11A.2) \end{aligned}$$

where $\mathbf{S}_R = (a_1, b_1, \dots, a_M, b_M)^t$ is the real vector corresponding to \mathbf{S} , $\mathbf{u} = (u_1, \dots, u_{2M})$, and we have set $u_{2p-1} = v_p \cos \alpha_p$ and $u_{2p} = v_p \sin \alpha_p$. The angle brackets indicate averaging over the joint PDF of r_{kp} , θ_{kp} , and ϕ_k .

Expanding the cosine in terms of $\cos \phi_k$ and $\sin \phi_k$ allows us to write (Section 9.1 of [26])

$$\chi(\mathbf{u}) = \prod_{k=1}^N \langle J_0(R_k) \rangle \quad (11A.3)$$

where $J_0(.)$ is the zero-order Bessel function and

$$\begin{aligned} R_k^2 &= \left(\sum_{p=1}^M v_p r_{kp} \cos(\theta_{kp} - \alpha_p) \right)^2 + \left(\sum_{p=1}^M v_p r_{kp} \sin(\theta_{kp} - \alpha_p) \right)^2 \\ &= \sum_{p=1}^M \sum_{q=1}^M v_p v_q r_{kp} r_{kq} \cos(\theta_{kp} - \theta_{kq} - \alpha_p + \alpha_q) \end{aligned} \quad (11A.4)$$

If the scatterers are identically distributed, $\langle J_0(R_k) \rangle$ is independent of k and we can write

$$\chi(\mathbf{u}) = \langle J_0(R) \rangle^N \quad (11A.5)$$

Now consider N as a random variable with PDF P_N and mean value \bar{N} and impose the condition that for large \bar{N} the second-order moments of S are finite, that is, $\bar{N} \langle r_p r_q \rangle < \infty$ as $\bar{N} \rightarrow \infty$. Renormalizing the r_k by $\sqrt{\bar{N}}$ implies that $\langle r_p r_q \rangle < \infty$ as $\bar{N} \rightarrow \infty$. With this renormalization the expected characteristic function has the form

$$\bar{\chi}(\mathbf{u}) = \sum_{N=0}^{\infty} P_N \left\langle J_0 \left(\frac{R}{\sqrt{\bar{N}}} \right) \right\rangle^N \quad (11A.6)$$

The Bessel function can be expanded as a power series in the form

$$\left\langle J_0 \left(\frac{R}{\sqrt{\bar{N}}} \right) \right\rangle = 1 + \frac{\langle y \rangle}{\bar{N}} \quad (11A.7)$$

where $y = \frac{R^2}{4} \sum_0^{\infty} \frac{(-1)^{k+1}}{(k+1)!} \left(\frac{R^2}{4\bar{N}} \right)^k$, so

$$\begin{aligned} \bar{\chi}(\mathbf{u}) &= \sum_0^{\infty} P_N \left(1 + \frac{\langle y \rangle}{\bar{N}} \right)^N \\ &= \sum_0^{\infty} P_N \left(1 + N \frac{\langle y \rangle}{\bar{N}} + \frac{N(N-1)}{2!} \frac{\langle y \rangle^2}{\bar{N}^2} + \dots \right) \end{aligned}$$

As $\bar{N} \rightarrow \infty$, $\langle y \rangle \rightarrow -\langle R^2 \rangle / 4$ since R^2 stays finite, and

$$\bar{\chi}(\mathbf{u}) \rightarrow \sum_0^{\infty} \frac{(-1)^k}{k!} \frac{\langle N^k \rangle}{\bar{N}^k} \left(\frac{\langle R^2 \rangle}{4} \right)^k \quad (11A.8)$$

The apparently complicated expression for $\langle R^2 \rangle$ given by averaging (11A.4) has, in fact, a simple form. If the k th scatterer contributes a field vector $(a_{k1}, b_{k1}, \dots, a_{kM}, b_{kM})^t$ with covariance matrix C_R , then in the notation of (11A.2), but dropping subscripts,

$$\begin{aligned} \mathbf{u}^t C_R \mathbf{u} &= \langle (\mathbf{u} \cdot \mathbf{S}_R)^2 \rangle \\ &= \left\langle \left(\sum_{p=1}^M v_p r_p \cos(\theta_p - \alpha_p + \phi) \right)^2 \right\rangle \\ &= \sum_{p,q=1}^M \langle v_p v_q r_p r_q \cos(\theta_p - \alpha_p + \phi) \cos(\theta_q - \alpha_q + \phi) \rangle \\ &= \sum_{p,q=1}^M \frac{v_p v_q}{2} \langle r_p r_q \cos(\theta_p - \theta_q - \alpha_p + \alpha_q) \rangle \end{aligned}$$

where the last equality arises from averaging over the uniformly distributed phase, ϕ . Hence,

$$\langle R^2 \rangle = 2 \mathbf{u}^t C_R \mathbf{u} \quad (11A.9)$$

and

$$\bar{\chi}(\mathbf{u}) \rightarrow \sum_0^{\infty} \frac{(-1)^k}{k!} \frac{\langle N^k \rangle}{\bar{N}^k} \left(\frac{\mathbf{u}^t C_R \mathbf{u}}{2} \right)^k \quad (11A.10)$$

A crucial result is that (11A.10) is equivalent to a representation of the data, \mathbf{S}_R , as a product

$$\mathbf{S}_R = T \mathbf{G}_R \quad (11A.11)$$

in which T is a positive real scalar (texture) variable, \mathbf{G}_R is a mean-zero Gaussian variable with covariance matrix C_R , and T and \mathbf{G}_R are independent.

To establish this, note that if (11A.11) is the case, then the characteristic function of \mathbf{S}_R is given by

$$\begin{aligned}\chi(\mathbf{u}) &= \langle \exp(i\mathbf{T}\mathbf{u} \cdot \mathbf{G}_R) \rangle \\ &= \iint \exp(i\mathbf{T}\mathbf{u} \cdot \mathbf{G}_R) P(T)P(\mathbf{G}_R) dT d\mathbf{G}_R \\ &= \int \sum_{k=0}^{\infty} \frac{\langle T^k \rangle}{k!} (i\mathbf{u} \cdot \mathbf{G}_R)^k P(\mathbf{G}_R) d\mathbf{G}_R\end{aligned}\quad (11A.12)$$

For Gaussian \mathbf{G}_R , the characteristic function is

$$\chi_{G_R} = \exp\left\{-\frac{1}{2} \mathbf{u}^\top C_R \mathbf{u}\right\} = \sum_{k=0}^{\infty} \frac{(i\mathbf{u} \cdot \mathbf{G}_R)^k}{k!} P(\mathbf{G}_R) d\mathbf{G}_R \quad (11A.13)$$

Expanding the exponential in (11A.13) and equating terms yields

$$\langle (\mathbf{u} \cdot \mathbf{G}_R)^{2k+1} \rangle = 0 \quad (11A.14)$$

and

$$\frac{\langle (\mathbf{u} \cdot \mathbf{G}_R)^{2k} \rangle}{(2k)!} = \frac{1}{k!} \left(\frac{\mathbf{u}^\top C_R \mathbf{u}}{2} \right)^k \quad (11A.15)$$

so

$$\chi(\mathbf{u}) = \sum_{k=0}^{\infty} \frac{(-1)^k}{k!} \langle T^{2k} \rangle \left(\frac{\mathbf{u}^\top C_R \mathbf{u}}{2} \right)^k \quad (11A.16)$$

Comparing (11A.10) and (11A.16), it is immediately clear that *any* model based on number fluctuations of scatterers where the mean number of scatterers is large has an equivalent representation as a product model. The form of the number fluctuations only affects the texture variable T , which must be chosen to have the moments

$$\langle T^{2k} \rangle = \langle N^k \rangle / \bar{N}^k \quad (11A.17)$$

Since (11A.17) provides all of the moments of T^2 , this allows the PDF of T^2 to be constructed; a change of variable will then yield the PDF of T .

Note that in the multichannel case, this model relies on all channels seeing the same scatterers, so that the random walk in each channel has the same number of steps. The model would therefore be valid if the scattering is accurately described by a first-order Born approximation from a uniform layer of scatterers. However, both multiple scattering and differing penetration depths of different polarizations weaken the argument and its validity [12].

12

Analysis Techniques for Multidimensional SAR Images

12.1 Introduction

Multidimensionality arises in SAR data whenever the same scene is imaged in several channels, which may be separated by differences in polarization, frequency, time, aspect angle, or incidence angle. All of these can be exploited to provide extra information. A fundamental distinction between multidimensional data types is whether the channels are *correlated* at the pixel level or not. When correlation is present, the correlation parameters provide possible extra information about the scene. However, as we shall see, correlation can reduce our ability to remove speckle by combining channels. Images gathered in nonoverlapping frequency bands are expected to be uncorrelated. Multitemporal images of many types of terrain are correlated over short time scales (and hence can be exploited for interferometry) but decorrelate if the images are gathered a long time apart. The decorrelation time is highly dependent on the frequency and the terrain type (essentially because it depends on significant changes in the relative positions of the scatterers contributing to the return at a particular frequency). Interchannel correlation is an essential feature of polarimetric SAR but, as noted in Chapter 11, is nonzero only for the copolarized channels when the target displays azimuthal symmetry.

In this chapter, we discuss a variety of ways to extract the information present in multidimensional data. Here another important distinction is needed between the *statistical* information available from a distributed target and the

structural information that defines the shapes and boundaries that mark out those distributed targets. In the first case our main concern is to estimate the parameters describing the target accurately. In the second case, we wish to bring out the structure as clearly as possible. Reflecting this distinction, Section 12.2 is primarily concerned with single-frequency polarimetric data and with filters that locally estimate the parameters of the product model set out in Chapter 11. The treatment is very close in spirit to that in Chapter 6, but with significant differences due to the extra mathematical richness of the statistical model. In particular, the concept of a speckle term that is stationary and noiselike only appears meaningful in one dimension (see the discussion in Section 11.3.2). Hence “removing the speckle,” which formed the essential theme of Chapter 6, has no obvious meaning here.

In Section 12.3 we describe methods to combine channels in order to produce a single intensity image with reduced speckle compared with the separate channels. Such speckle reduction is intended to improve our ability to extract structural information from the data. For polarimetric data we consider methods starting with scattering matrix, full Stokes scattering operator, or with only intensity data. The latter methods are equally relevant to combining uncorrelated channels, such as those gathered with different frequencies, different geometries, or with time separations exceeding the decorrelation time of the scene.

A specific problem that arises in multitemporal data is the detection of areas of change. Changes can be in the internal parameters of distributed targets or in scene structure. In Section 12.4, we deal with the first of these, which is closely related to problems of edge detection (see Chapter 7) and the properties of channel amplitude ratios discussed in Section 11.5.

Extraction of structural information and changes in structure are discussed in Section 12.5. Figures 11.1 to 11.3 illustrate clearly that images of the same scene can show marked differences in the features they display when polarization or frequency is changed. Equally obvious effects occur due to changes in aspect angle [1], incidence angle [2], or time [3–7]. Hence, the recovery of true scene structure may be aided by combining information from multiple channels. For example, some field boundaries are only obvious in a single channel of the polarimetric data shown in Figures 11.1 to 11.3 even though they are certainly present in the other images. Once a boundary is established, however, it allows more sensitive parameter estimation and enables us to bring out subtle differences between segments. Methods for carrying out segmentation using multiple channels are developed in this section.

Although they are developed separately in this chapter, the different methods discussed are highly interrelated when it comes to applications. This is illustrated via a case study concerned with discriminating forest from nonforest

in Brazilian Amazonia in Section 12.6. Here filtering and segmentation techniques are compared in the context of a change detection problem using ERS-1 SAR data, in the process weaving together many of the strands encountered in this and earlier chapters.

12.2 Polarimetric Reconstruction Filters

In the most general context, the purpose of a reconstruction filter is to recover the “true” signal from data in which this signal has been corrupted by system effects and/or noise. This requires a statistical model for the data that includes some definition of what constitutes the true signal. In the context of polarimetric data, our approach to this is through the product model developed in Chapter 11, in which the observed data S from a distributed target can be written as

$$S = TG \quad (12.1)$$

with T a positive real scalar for which $\langle T^2 \rangle = 1$ and G a zero-mean Gaussian variable specified completely by its complex covariance matrix.

In one dimension, S and G are simply complex scalars and only intensity data need be considered because phase carries no information about distributed targets. In this case, the product model has an alternative form given by

$$I = |S|^2 = T^2|G|^2 = T^2\langle|G|^2\rangle \times G^2/\langle|G^2|\rangle = \sigma n \quad (12.2)$$

This form is useful because, for any distributed target, it decomposes the data into an RCS term σ , and a unit mean speckle term n , that is *target-independent*. Hence, we can think of the data as a process σ affected by stationary multiplicative noise, n . The RCS, σ , is made up of a mean intensity term (since $\langle I \rangle = \langle |G|^2 \rangle$) and a texture term T^2 . The local estimation of σ formed the theme of Chapters 6 and 7, while separation out of the texture was discussed in Chapter 8.

It was shown in Section 11.3.2 that, in polarimetric data, there is no useful way to make a similar separation into a stationary “noise” term and an “information” term unless all the channels are uncorrelated. Instead, it is more fruitful to consider estimation of the information-bearing quantities, of which a key element is the covariance matrix characterizing G . The information carried by the texture T is not defined a priori unless we assume some prior PDF for T .

Despite this change in perspective, we find that several of the filters developed in Chapter 6 have polarimetric equivalents, as we now describe.

12.2.1 Multilook Reconstruction

When we assume that a collection of N polarimetric pixels is drawn from the same Gaussian population (so that the texture variable is constant over the collection), the MLE for the covariance matrix is the sample covariance matrix, as discussed in Section 11.7 [8]. This is the multidimensional version of (6.8). Because we are now dealing with multichannel data, a visual assessment of the effects of this filter requires that all the information-bearing parameters be displayed. However, Figure 6.2(a) illustrates what happens in the intensity channels, with smoothing being gained at the expense of resolution. To illustrate the effect of multilooking on the other elements in the covariance matrix, we use L-band data from the DCRS airborne EMISAR system.

Figure 12.1 is the result of adding single-look HH and VV intensity images for an agricultural region in Jutland, Denmark. Figure 12.2(a) is the corresponding HH-VV phase difference image, while Figure 12.2(b) displays the modulus of the two-look HH-VV correlation coefficient (notice that the modulus of the one-look coefficient is not useful because it is identically unity). In Figure 12.2(c,d) the corresponding 16-look images are shown, with a striking decrease in the noisiness of the parameters but loss of resolution. An exact description of the effects of multilooking on the output distributions was given in Section 11.7. Although the PDFs of both correlation phase (equivalent to phase difference) and amplitude are known for L -look data (see (11.49) and (11.51)), only the correlation amplitude has an analytic expression for its moments; this is given as (11.52). However, as expected, both distributions become narrower as L increases; this is what causes the reduced noise evident in Figure 12.2(c,d). To exemplify this, the observed phase difference distributions of the single-look and 16-look data for a single rye field are shown as Figure 12.2(e,f). Note the conservation of the mode and the marked narrowing of the distribution in the multilook data.

12.2.2 MMSE Reconstruction

We can derive the MMSE of covariance by treating T as a perturbing “noise” variable to be smoothed out. This leads to a filter that is quite different from the one-dimensional MMSE filter discussed in Section 6.4.2. It is not attempting to reduce the speckle but to remove textural effects that will hinder the recovery of the local covariance structure. Neither MMSE filter requires a specific statistical model for the texture PDF.

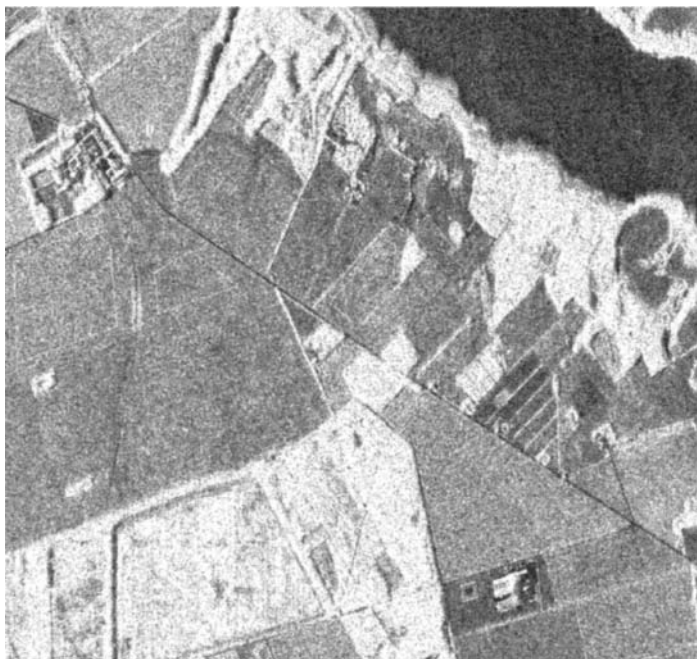


Figure 12.1 EMISAR L-band image of an agricultural region in Jutland, Denmark, formed by the summation of the HH and VV intensity images.

For calibrated fully polarimetric data, it is helpful to describe the information carried by the covariance in terms of the real nine-vector [9]

$$\mathbf{z}_c = \left(|z_1|^2, |z_2|^2, |z_3|^2, \operatorname{Re}(z_1 z_2^*), \operatorname{Im}(z_1 z_2^*), \operatorname{Re}(z_1 z_3^*), \operatorname{Im}(z_1 z_3^*), \operatorname{Re}(z_2 z_3^*), \operatorname{Im}(z_2 z_3^*) \right)^t \quad (12.3)$$

associated with any complex three-vector $\mathbf{z} = (z_1, z_2, z_3)^t$. More generally, if there are M channels, the corresponding vector requires M^2 terms. (For $M = 1$, \mathbf{z}_c is simply the channel power.) By the product model,

$$\mathbf{S}_c = T^2 \mathbf{G}_c \quad (12.4)$$

Although (12.4) is ostensibly in single-look form, \mathbf{S}_c only involves Hermitian products, and (12.4) is still valid for L -look data as long as the texture variable T^2 does not vary between looks. The following treatment is then applicable to L -look data, with the elements of \mathbf{S}_c derived from the Stokes

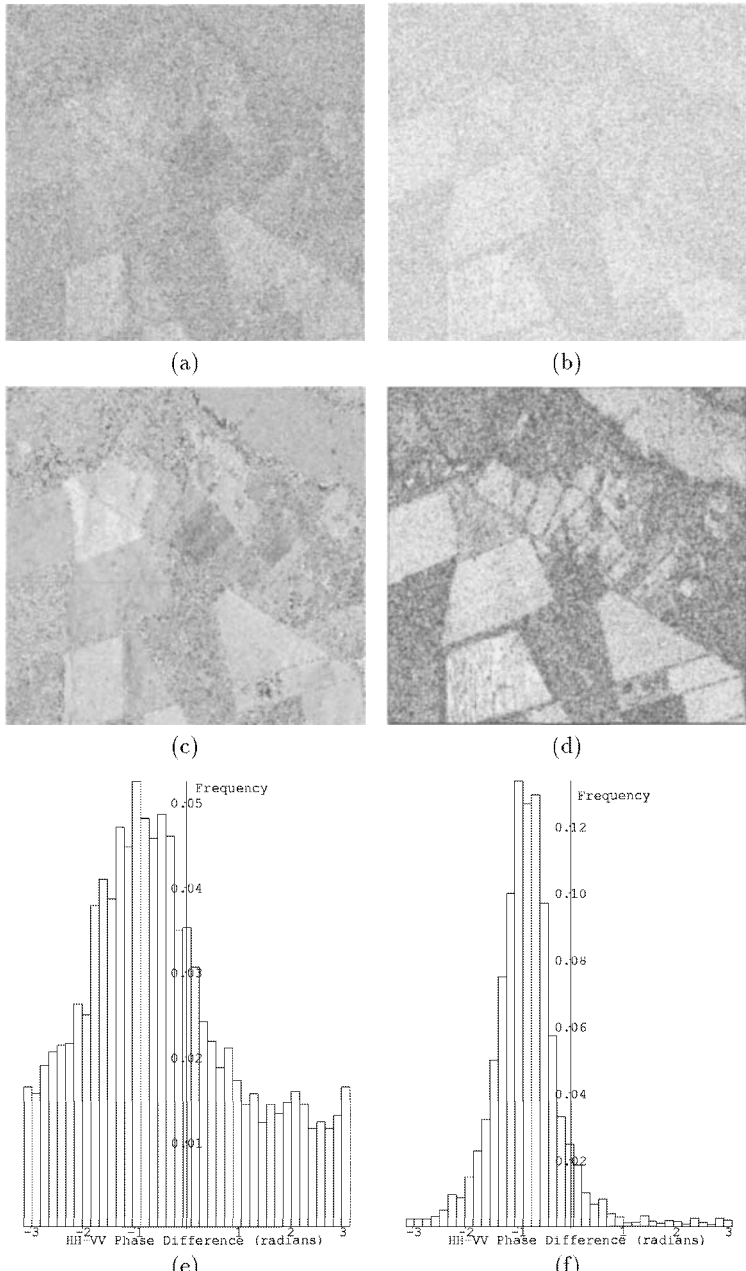


Figure 12.2 (a) The HH-VV phase difference image corresponding to Figure 12.1; (b) the modulus of the two-look HH-VV correlation coefficient; (c,d) the 16-look images corresponding to (a,b); (e,f) observed phase difference distributions from a field of rye for single-look and 16-look data, respectively.

scattering operator rather than from the scattering matrix. This is more general than the MMSE filter described in [9] using single-look data. The treatment in [9] is also much complicated because it deals with uncalibrated data. However, calibration can be carried out in an optimized way as a separate step [10]. It is also simpler than the filter derived in [11], which is based on a concept of speckle that, as argued in Section 11.3.2, does not seem appropriate for polarimetric data.

A linear estimate of \mathbf{G}_c from the data \mathbf{S} is given by

$$\hat{\mathbf{G}}_c = A + B\mathbf{S}_c \quad (12.5)$$

where A and B are matrices to be determined. For $\hat{\mathbf{G}}_c$ to be unbiased requires

$$\langle \mathbf{G}_c \rangle = \langle \hat{\mathbf{G}}_c \rangle = A + B\langle \mathbf{S}_c \rangle \quad (12.6)$$

Hence,

$$\hat{\mathbf{G}}_c = \langle \mathbf{G}_c \rangle + B(\mathbf{S}_c - \langle \mathbf{S}_c \rangle) \quad (12.7)$$

The MMSE filter chooses B to minimize $\langle e \rangle$, where $e = \|\mathbf{G}_c - \hat{\mathbf{G}}_c\|^2$ and $\|\cdot\|^2$ is the Euclidean norm. Writing

$$e = (\mathbf{G}' - B\mathbf{S}')^t(\mathbf{G}' - B\mathbf{S}') \quad (12.8)$$

where $\mathbf{G}' = \mathbf{G}_c - \langle \mathbf{G}_c \rangle$ and $\mathbf{S}' = \mathbf{S}_c - \langle \mathbf{S}_c \rangle$, and differentiating with respect to the coefficients of B yields a minimum for $\langle e \rangle$ when

$$B = C_{GS} C_S^{-1} \quad (12.9)$$

Here C_S is the autocovariance matrix of \mathbf{S}_c and C_{GS} is the crosscovariance matrix of \mathbf{G}_c and \mathbf{S}_c . Using (12.4),

$$C_{GS}(i, j) = \langle G'(i)S'(j) \rangle = \langle T^2 \rangle \langle G'(i)G'(j) \rangle = C_G(i, j) \quad (12.10)$$

so the MMSE filter is

$$\hat{\mathbf{G}}_c = \langle \mathbf{G}_c \rangle + C_G C_S^{-1}(\mathbf{S}_c - \langle \mathbf{S}_c \rangle) \quad (12.11)$$

We can express C_G in terms of the observed covariance C_S using

$$\begin{aligned} C_S(i, j) &= \langle S_c(i)S_c(j) \rangle - \langle S_c(i) \rangle \langle S_c(j) \rangle \\ &= \langle T^4 \rangle (C_G(i, j) + \langle G_c(i) \rangle \langle G_c(j) \rangle) - \langle G_c(i) \rangle \langle G_c(j) \rangle \end{aligned} \quad (12.12)$$

The MMSE filter therefore has the form

$$\hat{G}_c = \langle G_c \rangle + \frac{1}{\langle T^4 \rangle} (I_9 - [\langle T^4 \rangle - 1] \langle G_c \rangle \langle G_c^T \rangle C_S^{-1}) (\mathbf{S}_c - \langle \mathbf{S}_c \rangle) \quad (12.13)$$

where I_9 is the 9×9 identity matrix. In this form, all the terms can be directly estimated from the observed data. The mean vector $\langle \mathbf{S}_c \rangle = \langle G_c \rangle$ can be estimated from a window surrounding the pixel of interest. In order to estimate $\langle T^4 \rangle$, note that

$$\frac{\langle S_c(i)S_c(j) \rangle}{\langle S_c(i) \rangle \langle S_c(j) \rangle} = \langle T^4 \rangle \frac{\langle G_c(i)G_c(j) \rangle}{\langle G_c(i) \rangle \langle G_c(j) \rangle} \quad (12.14)$$

Since G is Gaussian, the normalized moment on the right-hand side of (12.14) can be readily calculated using (11.2). It is most convenient to set $i = j$ with $1 \leq i \leq 3$, whereupon it takes the value $1 + 1/L$ for L -look data. A problem in using (12.14) was already encountered in Section 6.4.2: finite sampling effects may cause the estimate of $\langle T^4 \rangle$ to be less than 1, despite the fact that $\langle T^4 \rangle \geq 1$ in the population. This can have nonphysical consequences, such as leading to negative estimates of the powers in the channels. Since this occurrence indicates an artifact of the sampling, $\langle T^4 \rangle$ should be constrained to be the maximum of 1 and the value supplied by (12.14).

The one-dimensional version of the MMSE filter reduces to

$$\widehat{|G^2|} = \langle I \rangle + \frac{(I - \langle I \rangle)}{LV_I} \quad (12.15)$$

where I is the measured intensity and $V_I = \text{var}(I)/\langle I \rangle^2$. Without estimation error, in an untextured region $V_I = 1/L$, so the original data value is returned. However, with significant texture, V_I becomes large and the filter returns the local average intensity $\langle I \rangle$. However, the above sampling problems are very clear in this case, since if $I < \langle I \rangle (1 - LV_I)$, the estimator will be negative.

This cannot occur if V_1 is not allowed to be less than $1/L$, which is equivalent to forcing $\langle T^4 \rangle \geq 1$.

Assessing the performance of this filter is not easy because it is trying to reconstruct the whole covariance matrix. It can be seen from (12.13) that in an untextured region (for which $\langle T^4 \rangle = 1$) the MMSE output should be the original data, up to estimation error. This has been confirmed [12]. Figure 12.3 shows the effects of the filtering on the phase difference distribution for single-look L-band AirSAR data from a forest region for different sizes of the window used to estimate the local mean value of G_c and T^4 . The original distribution (solid line) is progressively sharpened about the mode (which is almost unchanged) as the window size increases; results are shown for 3 by 3 and 7 by 7 windows.

12.2.3 Gamma MAP Estimation

In the previous section we considered the problem of estimating the Gaussian component in the product model. If instead we are interested in the texture variable, we can perform an analysis similar to that in Section 6.5 and [13] if

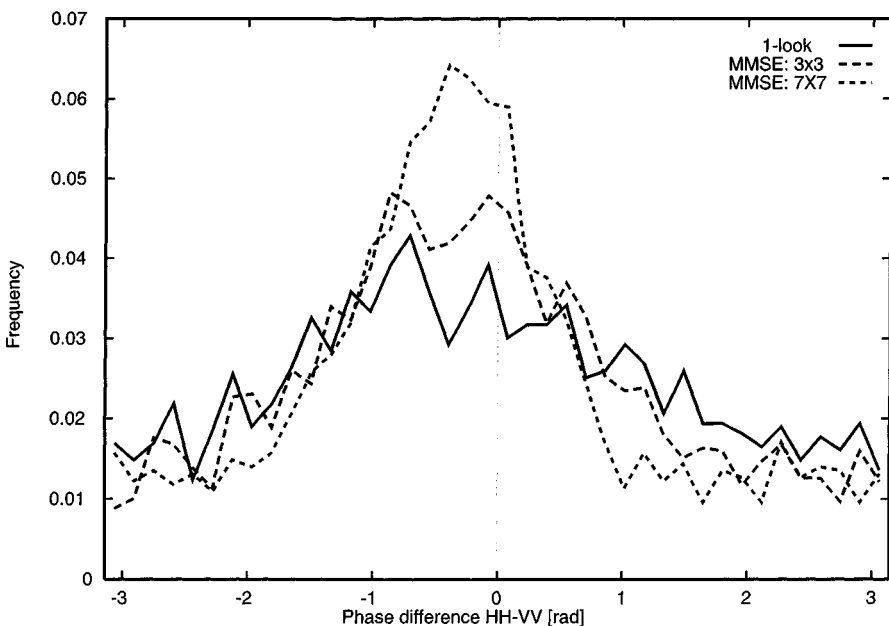


Figure 12.3 Histograms of the HH-VV phase difference for single-look L-band AirSAR data from a forest region before and after MMSE filtering using window sizes of 3 by 3 and 7 by 7 pixels to estimate the population parameters (see plot for key).

the texture variable T^2 is assumed to be gamma-distributed with mean 1. For single-look M -channel data with covariance matrix C , the actual covariance matrix at a particular pixel is T^2C . Given the observed data S , we can therefore write, by Bayes theorem,

$$\begin{aligned} P(T|S) &\propto P(S|T)P(T) \\ &= \frac{1}{\pi^M |T^2 C|} \exp\left\{-\text{tr}\left[\left(T^2 C\right)^{-1} S S^\dagger\right]\right\} \cdot 2\nu^\nu \frac{T^{2\nu-1}}{\Gamma(\nu)} e^{-\nu T^2} \end{aligned} \quad (12.16)$$

where \dagger denotes complex conjugate and tr denotes trace. The log likelihood is then given by

$$\lambda = \frac{\text{tr}(C^{-1} S S^\dagger)}{T^2} + (2\nu - 2M - 1) \ln T - \nu T^2 \quad (12.17)$$

where terms not involving T have been omitted. Setting $\delta\lambda/\delta T = 0$ leads to the MAP solution for T as

$$\nu T^4 + (M - \nu + \frac{1}{2})T^2 - \text{tr}(C^{-1} S S^\dagger) = 0 \quad (12.18)$$

This treatment can be cast into multilook form by noting that the expression for $P(T|S)$ would be unchanged if one-look Stokes scattering operator data were available, since $P(T|S) = P(T|SS^\dagger)$. For data in multilook Stokes form, we instead have an L -look average covariance matrix \bar{C} at each point (SS^\dagger is the one-look form of \bar{C}). Then $P(T|\bar{C}) \propto P(\bar{C}|T)P(T)$. As before, the actual covariance matrix at the point is T^2C . The multilook data \bar{C} are known to obey a complex Wishart distribution [8], given by

$$P(\bar{C}|T) = \frac{|\bar{C}|^{L-M} \exp(-L \text{tr}(C^{-1} \bar{C})/T^2)}{K(L, M) T^{2ML} |C|^L} \quad (12.19)$$

where $K(L, M) = \pi^{M(M-1)/2} \Gamma(L) \cdots \Gamma(L - M + 1) L^{-ML}$ and $P(\bar{C})$ refers to the joint PDF of $\text{Re}(\bar{C}_{ij})$ and $\text{Im}(\bar{C}_{ij})$ for $1 \leq i, j \leq M$. Forming $\lambda = \ln(P(\bar{C}|T)P(T))$, assuming gamma-distributed T^2 as before, and differentiating with respect to T yields

$$\nu T^4 + (ML - \nu + \frac{1}{2})T^2 - L \text{tr}(C^{-1} \bar{C}) = 0 \quad (12.20)$$

This is the multilook version of (12.18).

If we had chosen to find the MAP solution for T^2 instead of T , we would arrive at the same equations but with $1/2$ replaced by 1 in the coefficient of T^2 . For single-channel data, this yields a solution identical to (6.15) when we set $M = 1$; note that in (6.15) $\bar{C} = I$, $C^{-1} = 1/\mu$, and $\sigma_{\text{MAP}} = \mu T^2$.

Note that the explicit model for the PDF of texture used in Section 12.2.3 should be more powerful than the model-free approach used in Section 12.2.2 as long as the model is correct. In fact, a model-based approach to estimating the texture variable for use in MMSE filtering gave better results [12]. The relation of this approach to texture estimation in polarimetric data and that discussed in Section 11.9.2 has not yet been investigated.

12.3 Speckle Reduction by Polarimetric or Multichannel Filtering

In Section 12.2 we considered the problem of filtering polarimetric data in order to estimate the *parametric* information that characterizes the local statistical distribution. Alternatively, multiple channels can be used to improve our ability to recognize the *structural* information in the data by forming a single intensity image in which the speckle fluctuations are reduced. The treatment here deals with a general situation that can include multiple frequencies and multitemporality as well as polarimetric data. Hence, the data vector will be written as \mathbf{z} rather than \mathbf{S} .

12.3.1 Using Covariance Matrix Data

The principle of multilooking was discussed in Section 4.4, where it was noted that if M uncorrelated identically distributed looks or pixels are incoherently averaged (i.e., averaged in intensity), then the normalized variance decreases by a factor M . More generally, the complex data vector $\mathbf{z} = (z_1, \dots, z_M)^t$ at each pixel may have correlated channels, or channels drawn from different distributions (due to different polarizations or frequencies). Then a simple addition of the intensities does not produce optimum speckle reduction. Instead, a linear transformation

$$\mathbf{w} = P\mathbf{z} \quad (12.21)$$

that decorrelates (prewhitens) the channels should first be employed [14,15]. To see this, we observe that the incoherent addition of the channels in the vector \mathbf{w} gives an intensity

$$J = \sum_{i=1}^M |w_i|^2 = \mathbf{w}^\dagger \mathbf{w} = \mathbf{z}^\dagger A \mathbf{z} = \text{tr}(A \mathbf{z} \mathbf{z}^\dagger) \quad (12.22)$$

where $A = P^\dagger P$ is Hermitian. It is straightforward to show that

$$\langle J \rangle = \text{tr}(AC) = \text{tr}(CA) \quad (12.23)$$

where $C = \langle \mathbf{z} \mathbf{z}^\dagger \rangle$ is the covariance matrix of \mathbf{z} , since $\langle \mathbf{z} \rangle = 0$. Furthermore,

$$\langle J^2 \rangle = \sum_{jklm} A_{jk} A_{lm} \langle z_j^* z_k z_l^* z_m \rangle \quad (12.24)$$

When \mathbf{z} is Gaussian, (11.28) shows that

$$\langle z_j^* z_k z_l^* z_m \rangle = C_{kj} C_{ml} + C_{mj} C_{kl} \quad (12.25)$$

so

$$\langle J^2 \rangle = \text{tr}(AC)^2 + (\text{tr}(AC))^2 \quad (12.26)$$

and

$$\text{var}(J) = \text{tr}(AC)^2 \quad (12.27)$$

Note that any orthogonal transformation P gives the same mean and variance as the original data \mathbf{z} , since A is then just the identity matrix. Note also that, for each component of \mathbf{w} , $\langle |w_i|^4 \rangle = 2\langle |w_i|^2 \rangle$. Hence, the intensity $|w_i|^2$ in channel i always has normalized variance 2. This follows by setting P to be a matrix containing a single nonzero row and is independent of texture.

The trace of a matrix is equal to the sum of the eigenvalues; and clearly, if λ is an eigenvalue of AC , then λ^2 is an eigenvalue of $(AC)^2$. Hence,

$$\langle J \rangle = \sum_i \lambda_i \quad (12.28)$$

and

$$\text{var}(J) = \sum_i \lambda_i^2 \quad (12.29)$$

where λ_i are the eigenvalues of AC . Hence, the normalized variance of J is given by $V_J = \sum \lambda_i^2 / (\sum \lambda_i)^2$.

A more general result is available when single-frequency polarimetric data are used and texture is described by a product model. Then \mathbf{z} can be written as $\mathbf{z} = TG$ with T a real scalar and G Gaussian. In this case, the mean value of J given by (12.23) is unchanged, but

$$\langle J^2 \rangle = \langle T^4 \rangle \text{tr}(AC)^2 + (\langle T^4 \rangle - 1)(\text{tr}(AC))^2 \quad (12.30)$$

(Here, as in earlier sections, we assume $\langle T^2 \rangle = 1$ and that T and G are independent.) Hence, in this case the normalized variance is

$$V_J = \frac{\text{var}(J)}{\langle J \rangle^2} = \langle T^4 \rangle \frac{\sum \lambda_i^2}{(\sum \lambda_i)^2} + \langle T^4 \rangle - 1 \quad (12.31)$$

For both the Gaussian and product model, V_J is minimized when the ratio $\sum \lambda_i^2 / (\sum \lambda_i)^2$ is minimum. Lagrange multiplier methods immediately show that this occurs when all the λ_i are equal, so $A = C^{-1}$ (up to a scalar multiple). This implies that the minimum value of normalized variance is given by

$$V_J(\min) = \left\langle T^4 \left(1 + \frac{1}{M} \right) \right\rangle - 1 \quad (12.32)$$

for the textured case, which reduces to just $1/M$ in the Gaussian case. Experimental verification of this result is reported in [12,14,16].

From (12.21), the covariance matrix of the transformed data \mathbf{w} is given by

$$C_w = \langle P \mathbf{z} \mathbf{z}^\dagger P^\dagger \rangle = PCP^\dagger \quad (12.33)$$

If \mathbf{q} is an eigenvector of CA with eigenvalue λ , then

$$C_w(P\mathbf{q}) = PCP^\dagger P\mathbf{q} = PCA\mathbf{q} = \lambda(P\mathbf{q}) \quad (12.34)$$

so that C_w has the same eigenvalues as CA and the eigenvalues of C_w are related to those of CA by the transformation P . In the particular case of optimum speckle reduction, CA is the identity matrix and so the eigenvalues are all unity. Also, from (12.33)

$$C_w = PA^{-1}P^\dagger = P(P^\dagger P)^{-1}P^\dagger = I_M \quad (12.35)$$

where I_M is the $M \times M$ identity matrix, so the individual components in w are uncorrelated with unit variance. J is then formed by the incoherent addition of M independent channels, each with the same variance. Hence, if we start from correlated Gaussian data, $V_J(\min) = 1/M$, as already noted.

Although the matrix A is completely determined by the condition $A = C^{-1}$, this leaves considerable freedom in P . In fact, since A is Hermitian, it is defined by M^2 real numbers, whereas the matrix P satisfying $P^\dagger P = A$ contains $2M^2$ real numbers. However, as shown in (12.22), only A is needed to form the desired intensity image.

Notice that this filter relies on a local estimate of the covariance matrix (or, more precisely, its inverse), which will suffer from the estimation errors discussed in Chapter 11. Notice also that, as defined, the mean value of the output image, that is, the mean value of J , is M at all positions. The preservation of image structure requires some other constraint to be applied, for example, that the total average power $\langle z^\dagger z \rangle$ should be unchanged at each pixel. The averaging could, for example, be performed over the same window as that used to estimate C . Figure 12.4(a) shows the output of the full polarimetric filter when applied to the scene shown as Figure 12.1. In this case, we display the quantity $(C_{11} + C_{33})\text{tr}(C^{-1}zz^\dagger)$, that is, the quantity J defined in (12.22) multiplied by the sum of the copolarized powers. All the terms in C are estimated from a 3 by 3 window surrounding the current pixel of interest.

The need to estimate C locally impacts on the resolution achievable by the filter. In the ideal case, the resolution of the output is the same as that of each channel. In practice, energy spreads out in the filtered image. This is illustrated in Figure 12.5, which shows the original EMISAR intensity data along a range profile containing a trihedral corner reflector and the corresponding profile after filtering using full polarimetric data (for filtering using intensity data only, see next section). The data points are joined by interpolated curves (hence the negative values shown are artifacts), and the different amplitudes of the trihedral response are a result of the local weighting. (No attempt has been made to correct for this since it improves the clarity of the figure.) As can be seen, the filtering causes some widening of the trihedral response, due to the 3 by 3 window used to estimate the filter coefficients. Optimal filtering requires better estimates of the local covariance, implying larger windows (see [16] for a discussion of the best window size), with obvious impacts on the final resolution in the filtered image.

Finally, we observe from (12.22) that the filter does not need the scattering matrix data, only the terms in zz^\dagger , which can be obtained from the Stokes



(a)



(b)

Figure 12.4 (a) The output from full polarimetric filtering of the scene shown in Figure 12.1 and (b) the corresponding output using intensity data only.

scattering operator. A similar analysis is therefore possible using Gaussian or textured multilook data as long as the texture variable is assumed constant over the averaged looks. In (12.31) this simply causes the first term on the right-hand side to be multiplied by a factor $1/L$, so $A = C^{-1}$ as before. The optimum speckle-reducing filter therefore takes the form

$$J = \text{tr}(C^{-1}\bar{C}) \quad (12.36)$$

where \bar{C} is the multilook average covariance matrix extracted from the Stokes scattering operator data. As shown in the discussion in the next section, practical implementation of this filter produces speckle reduction consistent with theory. The impact of the polarimetric whitening filter on target detection is discussed

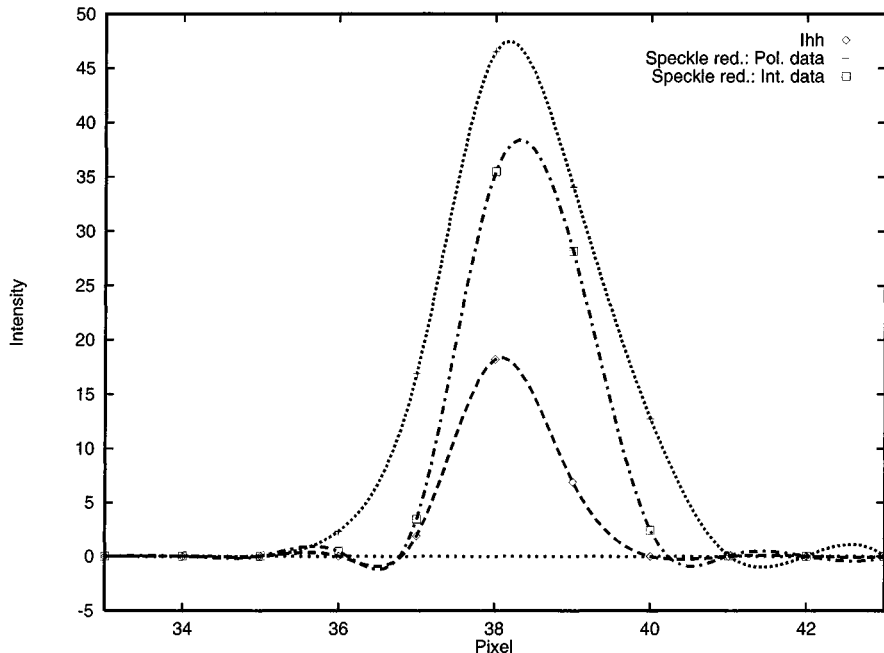


Figure 12.5 Profile of intensity in the range direction through a trihedral corner reflector in an original HH EMISAR image and after filtering using full polarimetric data or only intensity data.

in [17] in which it was found that the local estimate of the covariance matrix required by (12.36) had little effect on target detection and that a fixed value of C could be used. However, in the dataset used, the correlation coefficients showed little variation with cover type. More general investigation of this issue is needed.

12.3.2 Using Intensity Data Only

The speckle-reducing filter described in Section 12.3.1 uses all the local Hermitian products $z_i z_j^*$ in order to minimize speckle fluctuations. If only the intensities in each channel are used, the problem becomes one of finding the linear combination $J = \sum A_i |z_i|^2$ that minimizes the normalized variance. This can be treated as in Section 12.3.1, but for A a diagonal matrix whose diagonal terms are given by the vector $\mathbf{A}^\dagger = (A_1, \dots, A_M)$. The single-look case can be absorbed into that for L looks, where we have an average covariance matrix \bar{C} whose one-look form is zz^\dagger . Again using Lagrange multiplier methods (but in this case

directly, without involving eigenvalues) we find the normalized variance is minimized in the Gaussian case when

$$\mathbf{A} \propto C_I^{-1}\boldsymbol{\sigma} \quad (12.37)$$

where $\boldsymbol{\sigma}^t = (C_{11}, \dots, C_{MM})$ and C_I is the covariance matrix of one-look intensity

$$C_I(i, j) = \langle I_i I_j \rangle - \langle I_i \rangle \langle I_j \rangle = |C(i, j)|^2 \quad (12.38)$$

This last equality is the Siegert relationship (see (4.34) and (11.27)). The constant of proportionality in (12.37) is arbitrary and can be chosen locally.

For L -look textured data obeying the product model, the minimizing vector is again given by (12.37) and the value of the minimum normalized variance is

$$\begin{aligned} V_j(\min) &= \frac{\langle T^4 \rangle}{L} \frac{\mathbf{A}^t C_I \mathbf{A}}{(\mathbf{A}^t \boldsymbol{\sigma})^2} + \langle T^4 \rangle - 1 \\ &= \langle T^4 \rangle \left(1 + \frac{1}{L \boldsymbol{\sigma}^t C_I^{-1} \boldsymbol{\sigma}} \right) - 1 \end{aligned} \quad (12.39)$$

The minimum value in the Gaussian case is given by setting $\langle T^4 \rangle = 1$.

Unlike the full polarimetric filter described in Section 12.3.1, when the constant of proportionality in (12.37) is independent of position, the output of the filter has a varying mean value dependent on the local correlation coefficients (but is independent of the individual channel powers). However, unless there are strong variations in the interchannel correlation coefficients, features will be lost in the filtered image; so it is again necessary to weight the filter output by some local property, such as the mean total power. Figure 12.4(b) shows the effect of filtering using only intensity data on the same scene as Figure 12.4(a), again using a weighting by the sum of the local copolarized powers. Although not visually very different from Figure 12.4(a), we record in Table 12.1 the values of normalized variance obtained in the two filtered images for a number of fields. Values for the full polarimetric filter lie around $1/3$, as expected (see the discussion following (12.35)). For the intensity-only filter, values are higher (since the filtering is not optimal) and show slightly more variation, since the minimum value depends on the local value of the interchannel correlation coefficients. The effects of this filter on resolution are indicated

Table 12.1
Normalized Variance for a Selection of Fields in the Scene of Figure 12.1 After Full
Polarimetric and Intensity-Only Filtering

Field Number	Polarimetric Filtering	Intensity-Only Filtering
77	0.2932	0.4041
19	0.3383	0.4958
63	0.3187	0.4667
48	0.3314	0.4720
65	0.3116	0.4601
61	0.3689	0.4717

in Figure 12.5. Some resolution is lost, but this appears less marked than for the full polarimetric filter.

While this treatment was concerned with finding the filter giving minimum normalized variance, it is instructive to consider arbitrary weighted sums of intensities in the special case where the like and crosspolarized channels are uncorrelated. Setting $\langle |S_i|^2 \rangle = \sigma_i$ for $1 \leq i \leq 3$ and $\langle S_1 S_3^* \rangle = \sqrt{\sigma_1 \sigma_3} \rho$, the normalized variance of a weighted sum of intensities for untextured data is then given by

$$V_J = \frac{\text{var}(J)}{\langle J \rangle^2} = \frac{1}{L} \times \frac{1 + 2\gamma|\rho|^2 A_3 + \gamma^2 A_3^2 + \epsilon^2 A_2^2}{(1 + \epsilon A_2 + \gamma A_3)^2} \quad (12.40)$$

where A_1 is set to 1, $\gamma = \sigma_3/\sigma_1$, and $\epsilon = \sigma_2/\sigma_1$. Figure 12.6 indicates regions in the (A_2, A_3) plane where $V_J < L^{-1}$ (so speckle is reduced) or $V_J > L^{-1}$ (so speckle is enhanced). The boundary between the two regions occurs when

$$A_3 = -\frac{\epsilon A_2}{\gamma(\epsilon A_2 + 1 - |\rho|^2)} \quad (12.41)$$

and is indicated in Figure 12.6 by the solid curves, separating two regions in which V_J is reduced and a single region in which V_J is enhanced. Also marked on the figure is the line along which V_J takes infinite values. The global minimum has the value

$$V_J(\min) = \frac{1}{L} \times \frac{1 + |\rho|^2}{3 + |\rho|^2} \quad (12.42)$$

which is achieved when \mathbf{A} is any multiple of the vector $(1/\sigma_1, (1 + |\rho|^2)/\sigma_2, 1/\sigma_3)^T$. Under these circumstances, these are precisely the values given by (12.37) and (12.39). When we set $A_1 = 1$, the minimum therefore occurs at $A_2 = (1 + |\rho|^2)\epsilon^{-1}$, $A_3 = \gamma^{-1}$ as noted on Figure 12.6.

From (12.42) it is clear that when only intensity data are used, the possible degree of speckle reduction depends on the local correlation structure. Only in the case where the channels are all uncorrelated can the value of V_J be reduced to $1/(3L)$, which is the value achievable in all cases when full polarimetric data are used. From Figure 12.6, we can see that the global minimum lies in the first quadrant but that any pair of positive values (A_2, A_3) gives speckle reduction. Hence, a good estimate of the local correlation structure is needed if the global minimum is to be achieved, but some degree of speckle reduction will still be obtained even if there are errors in this estimate. Also clear is that filtering schemes that allow negative coefficients (such as can arise, for example, in principal components analysis) run the risk of creating very noisy images or image sections.

12.3.3 Principal Components Analysis in Multichannel SAR Data

When correlated multichannel data are available, a standard procedure to compress the information and eliminate redundancy between channels is to apply an orthogonal transformation (equivalent to a set of linear filters), which decorrelates the data. This is effected by the *principal components transformation* (PCT), which projects the data onto the eigenvectors of the covariance matrix. The variance of the i th component of the transformed data is λ_i , where λ_i is the associated eigenvalue. Hence, by ordering the eigenvalues in decreasing value, the components of the transformed data successively exhibit less variance. Typically, for optical data the images generated by the first few principal component images tend to carry most of the information, whereas the later principal components become noisy. (This reflects the fact that the signal-to-noise ratio decreases as λ_i decreases.)

This method can be applied to multifrequency polarimetric data, but with significant limitations. Since images produced at different frequencies are statistically uncorrelated, the only scope for information compression is within the polarimetric channels at each frequency. When the like and crosspolarized channels are uncorrelated, the PCT will in fact operate only on the two copo-

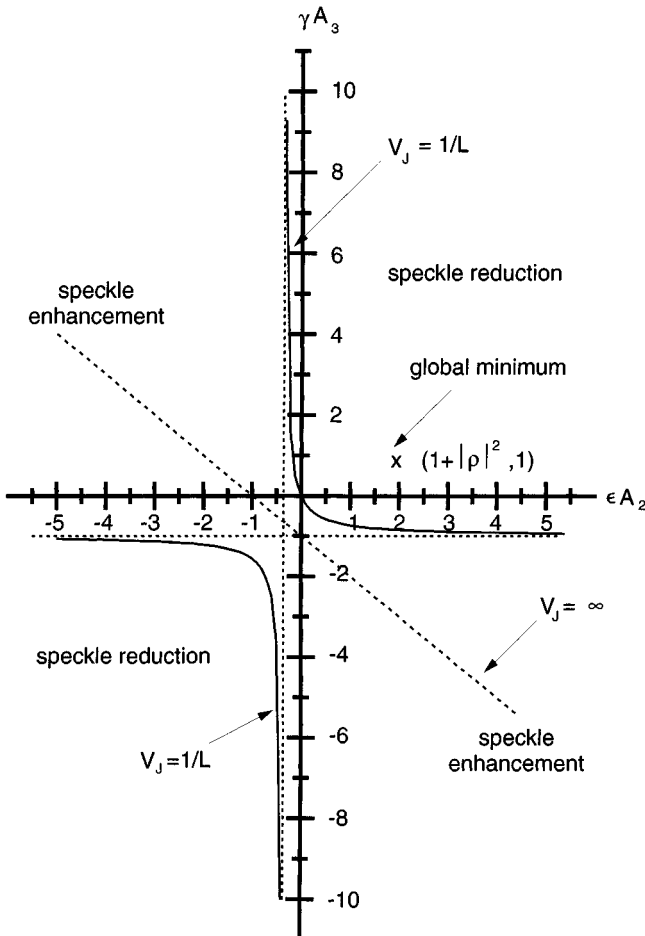


Figure 12.6 Plot of regions in the (A_2, A_3) plane where linear filtering of polarimetric intensity data with uncorrelated like and crosspolarized components gives rise to speckle reduction or enhancement. Boundaries between these regions (where $V_J = L^{-1}$) are marked as solid curves. The axes are normalized in terms of ϵA_2 and γA_3 , and the global minimum of normalized variance is marked in the first quadrant.

larized channels. In SAR data, the variance is proportional to the mean intensity, so ordering principal components by variance causes the frequencies that carry most power to have the larger eigenvalues and thus apparently carry more information. Finally, the noise concepts applicable to optical data (with additive noise) do not apply in any simple way to SAR data. A thorough analysis of the

PCT is given in the context of scattering matrix data in [18], where it is shown that for azimuthally symmetric targets or scenes the PCT effectively attempts to remove the phase difference between the two copolarized channels, so this information is lost in the displayed image of each principal component. The phase information is embedded in the eigenvectors. It is not clear, therefore, that the PCT performs a useful function in terms of bringing out information. Similar reservations about its value are raised in [19] when it is applied simply to the channel powers. In particular, the great sensitivity to channel scaling is demonstrated (see also [20]).

Despite these negative impressions of the utility of the PCT for SAR data, it should be noted that it forms a central concept in [21], where the eigenvectors of the covariance matrix are interpreted as representing different scattering mechanisms with the eigenvalues corresponding to probabilities. A type of nonorthogonal transform referred to as a generalized form of the PCT is also developed in [22], based on the concept of speckle in polarimetric data as a nonstationary noise. It appears to give degenerate results in the context of the product model, and there has been no in-depth assessment of its value for image analysis purposes.

12.4 Measuring and Detecting Differences Between Two Images

When dealing with pairs of images of the same scene, produced at different times or by different frequencies or polarizations, it is often necessary to describe differences between the images. Such differences can be in the structure apparent in the different images (see Figures 11.1 to 11.3) or in the parameters describing a distributed target present in both images. Particular importance attaches to images gathered at different *times*, so differences correspond to *change*. In this section (and Section 12.5) we will develop the tools needed to carry out this task, but defer examples of their use to Section 12.6.

12.4.1 Pixel-Based Change Detection

Here, we will consider the problem of measuring and detecting change at the pixel level between two multilook intensity images and, in particular, its dependence on the number of looks. It will be assumed that the images are registered, calibrated, and have the same geometry (as would be the case for repeat-pass satellite images).

A possible approach, and that normally adopted for optical data, is pixel-wise subtraction of images. Whatever the data type, if the observed value at a

given position in the two images is I_1 and I_2 , respectively, then the difference $d = I_1 - I_2$ has mean value and variance given by

$$\langle d \rangle = \langle I_1 \rangle - \langle I_2 \rangle \quad (12.43)$$

and

$$\text{var}(d) = \text{var}(I_1) + \text{var}(I_2) - 2\sqrt{\text{var}(I_1)\text{var}(I_2)}\rho_i \quad (12.44)$$

where ρ_i is the correlation coefficient of the intensity images at that point. For uncorrelated image pairs, the variance is simply the sum of the variances of each image pixel. As an example, for optical data with uncorrelated identically distributed additive noise in the two images, the difference image would have a mean giving the true difference but with double the noise variance of a single image. For uncorrelated L -look SAR intensity images, detailed descriptions of the distribution and first two moments of d are given in [23,24]. For our purposes it is sufficient to observe that if the true values of the RCS at a point in the images are σ_1 and σ_2 , respectively, then d is an unbiased estimator of $\sigma_1 - \sigma_2$ but

$$\text{var}(d) = \frac{\sigma_1^2 + \sigma_2^2}{L} \quad (12.45)$$

(using (4.10)). This means that simple thresholding of the difference image will yield bigger errors for a given change in a bright area than a darker area. This is a familiar problem, encountered in various guises when dealing with speckled data.

To counter this problem, an alternative approach is to consider the ratio image, $Q = I_2/I_1$ (which is equivalent to the difference of the log of the images). The ratio image has the advantages of being unaffected by multiplicative calibration errors (as long as they are the same for both images) and by slope-induced effects on the backscattering coefficient (such effects are multiplicative and identical for images with the same imaging geometry [25]).

For image regions in which there is an underlying complex correlation with value ρ between the two times, the distribution of Q is given by (11.54). When the channels are uncorrelated this takes the simple form

$$P(Q) = \frac{\Gamma(2L)}{\Gamma^2(L)} \frac{\gamma^L Q^{L-1}}{(\gamma + Q)^{2L}} \quad (12.46)$$

where $\gamma = \sigma_2/\sigma_1$ is the true change in RCS. This result also follows directly from (7.6). For a given L and γ , the probability that the ratio exceeds a threshold T is therefore the detection probability

$$\begin{aligned} P_d(T, L) &= p\{Q > T\} = \int_T^{\infty} P(Q) dQ \\ &= \frac{\Gamma(2L)}{\Gamma^2(L)} \sum_{k=0}^{L-1} \binom{L-1}{k} \frac{(-1)^{L-k-1}}{2L-k-1} \left(1 + \frac{T}{\gamma}\right)^{k-2L+1} \end{aligned} \quad (12.47)$$

A convenient reduction formula for computation is

$$P_d(T, L+1) = P_d(T, L) + X(R, L) \quad (12.48a)$$

where $R = T/\gamma$, $P_d(T, 1) = (1 + R)^{-1}$, and

$$\begin{aligned} X(R, L) &= \binom{2L-1}{L} \frac{R^L (1-R)}{(1+R)^{2L+1}} \\ &= \frac{2}{L} (2L-1) \frac{R}{(1+R)^2} X(R, L-1) \end{aligned} \quad (12.48b)$$

with $X(R, 1) = R(1-R)/(1+R)^3$.

From (12.48) it can be seen that if a region in which the true change is γ is thresholded with $T = \gamma$, so that $R = 1$, then the detection probability is $1/2$, whatever the number of looks. Since useful detection probabilities would normally exceed 50%, the threshold required is less than the change to be detected, so $R < 1$. Then P_d increases as L increases.

As in other detection problems, a second important quantity is the false alarm probability P_{fa} , which is the probability of exceeding the threshold if no change has occurred. This can be calculated from (12.47) by setting $\gamma = 1$ or from (12.48) by setting $R = T$.

Given γ , T , and L , (12.47) tells us how to calculate P_d and P_{fa} . In practical applications, it is often more important to know how to select T and L in order to generate a defined value of P_d and P_{fa} for a given γ . In order to do this, note that, if γ is fixed, (12.47) defines for each L a threshold level T_L needed to meet a given detection probability. This then fixes P_{fa} for each L , and L can be chosen so that P_{fa} does not exceed some specified value. This procedure is most easily carried out using graphical methods. As an illustration, plots of T_L and P_{fa} against L for detection of a 3-dB change ($\gamma = 2$) with probabilities of detection

$P_d = 0.9$, 0.95 , and 0.99 are shown as Figure 12.7(a–c), respectively. We can see, for example, that for $P_d = 0.95$, a 1% false alarm rate requires the data to be pre-averaged in order to give an equivalent number of looks $L \sim 67$ and a threshold to be set at $T \sim 1.5$ (1.76 dB). Note that this approach is the converse to that normally adopted in detection theory where the probability of false alarm is selected first. This then determines the threshold level and the ensuing probability of detection (see, for example, Sections 10.3 and 10.4).

12.4.2 Area-Based Difference Measures

When an image is segmented (manually or automatically) so that segments represent homogeneous statistical populations, area-based rather than pixel-based measures of difference or change can be adopted. This involves comparisons of averages from regions normally containing different numbers of independent pixels. The same region in two different images can also involve different numbers of pixels if the imaging geometry has changed. In both these circumstances we would expect the regions being compared to be statistically uncorrelated.

As discussed in the previous section, measures based on differences will give false alarm probabilities that are dependent on the local intensity, so that it is more useful to consider ratios. Given two independent speckle populations of size L_1 and L_2 pixels, characterized by mean intensities σ_1 and σ_2 with ratio $\gamma = \sigma_2/\sigma_1$, the MLE of γ is given by

$$\hat{\gamma} = \frac{\frac{1}{L_2} \sum_{k=1}^{L_2} I_2^{(k)}}{\frac{1}{L_1} \sum_{l=1}^{L_1} I_1^{(l)}} \quad (12.49)$$

where k and l are pixel labels. This estimate has a PDF (a generalized form of (12.46)) given by (7.6) with the replacements $r \rightarrow \hat{\gamma}$, $R \rightarrow \gamma$, $k \rightarrow L_2$, and $M \rightarrow L_1 + L_2$, with moments

$$m_k = \langle \hat{\gamma}^k \rangle = \begin{cases} \frac{\Gamma(L_2 + k)\Gamma(L_1 - k)}{\Gamma(L_1)\Gamma(L_2)} \left(\frac{L_1}{L_2}\gamma\right)^k & L_1 > k \\ \infty & L_1 \leq k \end{cases} \quad (12.50)$$

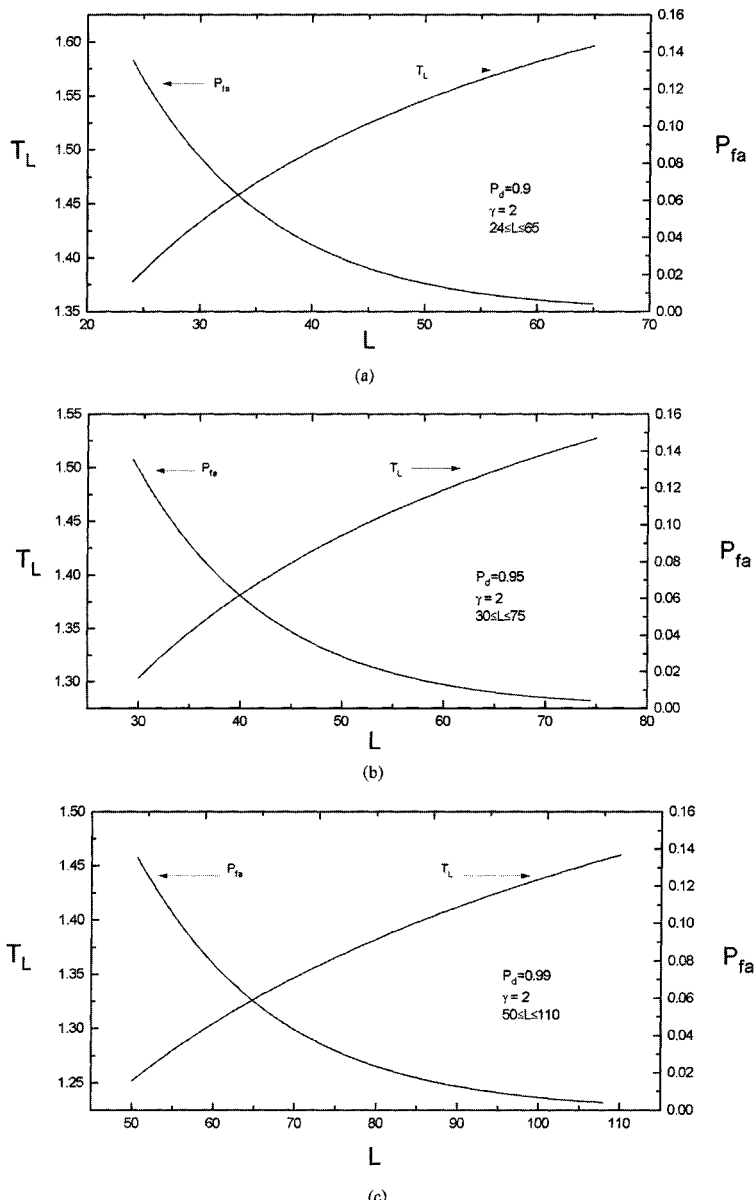


Figure 12.7 Plots of the threshold value, T_L , needed for detection of a 3-dB change as a function of L and the corresponding false alarm probability, P_{fa} , at three levels of detection probability: (a) $P_d = 0.9$, (b) $P_d = 0.95$, and (c) $P_d = 0.99$.

If L_1 is small, $\hat{\gamma}$ is significantly biased, since

$$\langle \hat{\gamma} \rangle = m_1 = \frac{L_1}{L_1 - 1} \gamma \text{ if } L_1 > 1 \quad (12.51)$$

An unbiased estimate is therefore given by $\hat{\gamma}_c = L_1^{-1} L_1 (L_1 - 1) \hat{\gamma}$; this estimate has variance

$$\text{var}(\hat{\gamma}_c) = \frac{L_1 + L_2 - 1}{L_2(L_1 - 2)} \gamma^2 \text{ if } L_1 > 2 \quad (12.52)$$

Given an observed value of $\hat{\gamma}_c$, an exact confidence interval for γ can be calculated making use of the exceedance probability

$$\begin{aligned} P_E(T) &= \{ \hat{\gamma}_c > T \} \\ &= \frac{\Gamma(L_1 + L_2)}{\Gamma(L_1)\Gamma(L_2)} \sum_{k=0}^{L_2-1} \binom{L_2 - 1}{k} \frac{(-1)^{L_2-k-1}}{L_1 + L_2 - k - 1} \\ &\times \left(1 + \frac{L_2 T}{(L_1 - 1)\gamma} \right)^{-(L_1 + L_2 - k - 1)} \end{aligned} \quad (12.53)$$

Hence, the probabilities that γ is at least a factor δ_u greater than $\hat{\gamma}_c$ and δ_l less than $\hat{\gamma}_c$ are given by

$$p\{\gamma > \delta_u \hat{\gamma}_c\} = p\{\hat{\gamma}_c < \gamma/\delta_u\} = 1 - P_E(\gamma/\delta_u) \quad (12.54a)$$

and

$$p\{\gamma < \delta_l \hat{\gamma}_c\} = p\{\hat{\gamma}_c > \gamma/\delta_l\} = P_E(\gamma/\delta_l) \quad (12.54b)$$

Both of these are independent of γ , so that for chosen confidence values, δ_u and δ_l can be determined.

Less accurate but more convenient estimates of the confidence interval for γ can be made for large values of L_1 and L_2 by assuming that $\hat{\gamma}_c$ is normally distributed. Then

$$p\{\gamma > \delta_u \hat{\gamma}_c\} \approx 0.5 - F\left((1 - \delta_u^{-1}) \sqrt{\frac{L_2(L_1 - 2)}{L_1 + L_2 - 1}}\right) \quad (12.55)$$

where $F(z) = \frac{1}{\sqrt{2\pi}} \int_0^z e^{-t^2/2} dt$. The lower confidence value is found using a similar expression, but with $(1 - \delta_u^{-1})$ replaced by $(\delta_l^{-1} - 1)$ in the argument of $F(\cdot)$.

These expressions can also be used to estimate the number of independent looks required to measure a ratio to a specified level of precision. For example, taking $L_1 = L_2 = L$, estimating γ to within 3 dB with 95% confidence involves setting $\delta_u = 2$, $\delta_l = 0.5$, and both probabilities to 0.05. The argument of F in both cases will then be 1.645, yielding $L \geq 23$ to put an upper limit on γ or $L > 7$ for the lower limit. If the precision is increased to 1 dB, the required numbers of independent looks increase to 129 and 82, respectively.

The number of independent pixels required based on the Gaussian approximation is in fact bigger than is indicated by an exact calculation based on (12.53). This is illustrated by Figure 12.8, which shows the exact and approximate probabilities that γ exceeds $\delta_u \hat{\gamma}_c$, based on (12.54a) and (12.55). In both cases, $\gamma = 2$. Figure 12.8(a) shows the two probabilities as a function of L for $\delta_u = 1.259$ (1 dB), while Figure 12.8(b) gives the same information for $\delta_u = 1.995$ (3 dB). From Figure 12.8(b) it can be seen that, in fact, only 11 looks are needed for a 3-dB 95% upper confidence limit, not the 23 inferred from the Gaussian approximation. Similarly, Figure 12.8(a) shows that 102 looks are required for a 1-dB confidence limit, not 129.

Note that these methods allow a quantitative answer to the question of whether two regions are different: if 1 is not within the confidence interval for γ , then they are statistically different. Equivalently, this question can be addressed using the normalized ratio

$$r_T = \min[\hat{\gamma}, \hat{\gamma}^{-1}] \quad (12.56)$$

which deals only with the size of a change, not whether it is an increase or decrease (see Section 7.3.3 and [23,26]).

12.5 Multichannel Segmentation

The estimates of the intensity ratio discussed in Section 12.4.2 relied on a prior segmentation in order to define homogeneous areas in two images (or different areas in the same image). That segmentation can be based on:

- Visual inspection;
- Transfer of a known segmentation from elsewhere (e.g., using a registered field map);
- Using the data themselves to learn the segmentation.

where $F(z) = \frac{1}{\sqrt{2\pi}} \int_0^z e^{-t^2/2} dt$. The lower confidence value is found using a similar expression, but with $(1 - \delta_u^{-1})$ replaced by $(\delta_l^{-1} - 1)$ in the argument of $F(\cdot)$.

These expressions can also be used to estimate the number of independent looks required to measure a ratio to a specified level of precision. For example, taking $L_1 = L_2 = L$, estimating γ to within 3 dB with 95% confidence involves setting $\delta_u = 2$, $\delta_l = 0.5$, and both probabilities to 0.05. The argument of F in both cases will then be 1.645, yielding $L \geq 23$ to put an upper limit on γ or $L > 7$ for the lower limit. If the precision is increased to 1 dB, the required numbers of independent looks increase to 129 and 82, respectively.

The number of independent pixels required based on the Gaussian approximation is in fact bigger than is indicated by an exact calculation based on (12.53). This is illustrated by Figure 12.8, which shows the exact and approximate probabilities that γ exceeds $\delta_u \hat{\gamma}_c$, based on (12.54a) and (12.55). In both cases, $\gamma = 2$. Figure 12.8(a) shows the two probabilities as a function of L for $\delta_u = 1.259$ (1 dB), while Figure 12.8(b) gives the same information for $\delta_u = 1.995$ (3 dB). From Figure 12.8(b) it can be seen that, in fact, only 11 looks are needed for a 3-dB 95% upper confidence limit, not the 23 inferred from the Gaussian approximation. Similarly, Figure 12.8(a) shows that 102 looks are required for a 1-dB confidence limit, not 129.

Note that these methods allow a quantitative answer to the question of whether two regions are different: if 1 is not within the confidence interval for γ , then they are statistically different. Equivalently, this question can be addressed using the normalized ratio

$$r_T = \min[\hat{\gamma}, \hat{\gamma}^{-1}] \quad (12.56)$$

which deals only with the size of a change, not whether it is an increase or decrease (see Section 7.3.3 and [23,26]).

12.5 Multichannel Segmentation

The estimates of the intensity ratio discussed in Section 12.4.2 relied on a prior segmentation in order to define homogeneous areas in two images (or different areas in the same image). That segmentation can be based on:

- Visual inspection;
- Transfer of a known segmentation from elsewhere (e.g., using a registered field map);
- Using the data themselves to learn the segmentation.

Note that, in general, all three approaches will produce different answers and problems. A visual inspection can input much greater world knowledge into the process, to the extent of ignoring data that conflict with what is expected. It, however, performs differently in bright and dark areas, despite similar statistical conditions. Transferring a segmentation carries a number of problems: map data can often be erroneous; different structures on a map may produce similar responses in the image; and registration and matching of geometries are essential. Using the data to learn the image structure relies on an image model, which

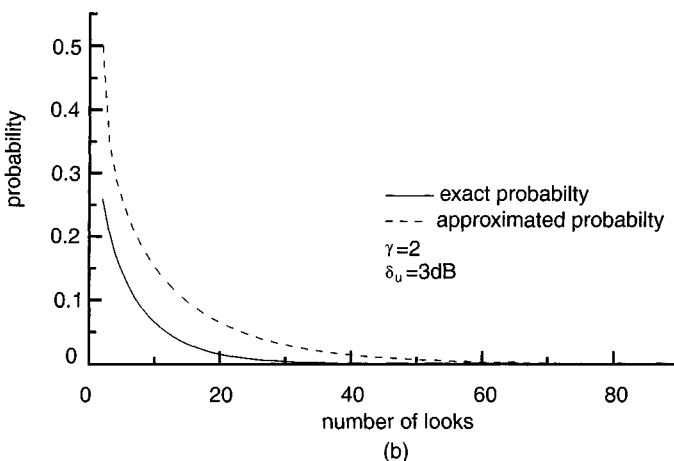
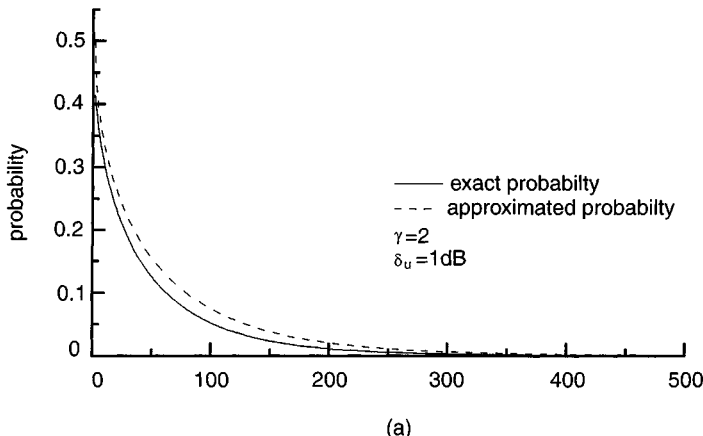


Figure 12.8 Approximate and exact probabilities that the true intensity ratio exceeds the observed unbiased ratio by a factor δ_u , as a function of the number of looks (a) $\delta_u = 1 \text{ dB}$ and (b) $\delta_u = 3 \text{ dB}$.

must be complete enough and realistic enough to produce meaningful segmentations that conform with known properties of typical scenes. Resistance to speckle is an important concern in such methods.

Methods for learning image structure were discussed in Chapter 7 for single-channel data. However, a glance at Figures 11.1 to 11.3 makes clear that increased information on scene structure is provided by combining images acquired with different frequencies, polarizations, or at different times. In this section we discuss how the methods developed in Chapter 7 can be extended to multidimensional data.

When multiple channels are available, an immediate concern is the definition of what is meant by a segmentation and the parameters on which it is to be based. In the context of single-frequency polarimetric data, the simplest data model is that segments are statistically homogeneous and completely characterized by a covariance matrix. This is the polarimetric version of the cartoon model developed in Section 7.3. Two segments are distinct if any of the nine parameters (three channel powers and three amplitudes and phases of the correlation coefficients) differs significantly between them. Hence, in principle, segmentation of polarimetric data should be based on estimates of all nine parameters. In practice, the sampling properties of the correlation coefficient terms render them less useful than the channel powers when making decisions about edges and merging of regions. For example, there are no easily applicable rigorous tests for when the phases or amplitudes of the correlation coefficients of two regions are significantly different. We, therefore, consider only algorithms based on the powers in the three channels. Multitemporal and polarimetric segmentation can, therefore, be treated similarly.

12.5.1 Multidimensional RGW Segmentation

Given a multichannel image, the simplest way to segment it is apparently to segment each channel separately and combine the results. Unfortunately, the different speckle patterns in the different channels tend to cause random “jitter” in edge location, so features present in all channels give rise to thickened edge features. To illustrate this, Figure 12.9(a,c,e) shows the L-band HH, HV, and VV intensity channels of an agricultural region imaged by the NASA/JPL AirSAR system; while Figure 12.9(b,d,f) shows the individual segmentations using the RGW algorithm [27,28] described in Section 7.3.1. Figure 12.9(g) shows the effects of overlaying the segmentations of each separate channel. (Segments are shown filled with their mean HH intensity.) The thickening and fragmentation of edges is obvious. Better performance would be expected if the optimum edge-detection strategy set out in Section 7.3.3 was adopted, but it is unlikely that this would remove the problem entirely.

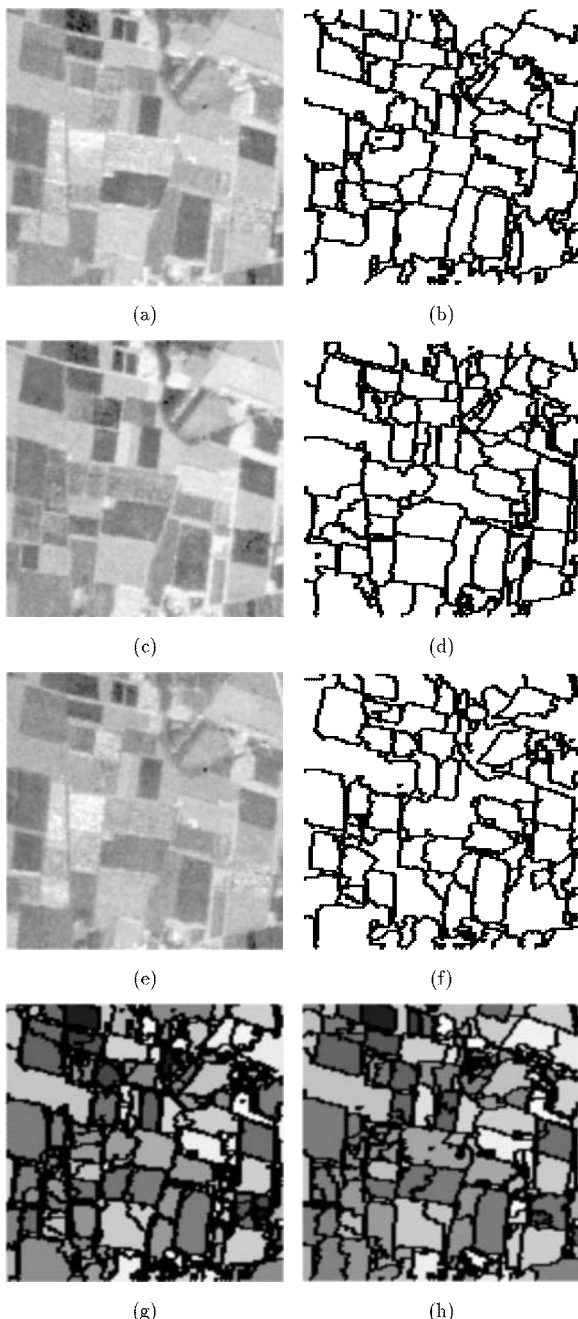


Figure 12.9 (a) L-band HH intensity image acquired by the NASA/JPL AirSAR system; (b) single-channel segmentation using the RGW algorithm; (c,d) same as for (a,b) but for the HV channel; (e,f) same as for (a,b) but for the VV channel; (g) segmentation formed by retaining any edge found in (b), (d), or (f); and (h) multidimensional segmentation using modified RGW.

The alternative is to treat the multichannel image as a single entity and make decisions on the existence and position of an edge using information from all channels simultaneously. In order to do this, both the edge-detection and region-growing components of RGW have been modified [29,30]. As described in Section 7.3.1, for edge detection RGW uses a threshold applied to the normalized gradient calculated from the two halves of a series of windows of various sizes. In the multichannel case, the threshold is instead applied to the rms value of the normalized gradient in all channels. This produces a single edge map that can be used to control segment growing. Similarly, merging disks uses an rms measure of the difference between the mean values of disks in each channel. The average contrast in each channel is calculated after each iteration, and the algorithm stops when there is an increase in the rms average contrast. Figure 12.9(h) shows the result of applying this process (again indicating the mean HH intensity in each segment). Note the clear visual improvement in edge structure as compared with Figure 12.9(g). Notice also possible loss of information; for example, an edge detected only in the HV image in the top right of the image is lost in the multidimensional segmentation.

The edge map generated by this procedure can be used to test whether a given segment boundary occurs in all or only some of the channels. For each channel, the probability that the test edge is due purely to speckle can be calculated. Those edges for which this probability exceeds a given threshold are thus ascribed to speckle and considered not to be present in that channel. The result of applying this operation to each of the intensity images in Figure 12.9(a,c,e) is shown as Figure 12.10(a–c). Clearly this provides a means of interrogating the data to establish the contribution to overall structure provided by each channel. This is most easily illustrated using color overlays (so that edges present in different combinations of channels can be identified). However, in Figure 12.10 we instead show (a) the edges present in HH alone; (b) the edges in both HH and VV (shown in black), in HH but not VV (dark gray), and in VV but not HH (light gray); (c) the edges present in HH, VV, and HV (black), in HH or VV but not HV (dark gray), and in HV but not in either HH or VV (light gray). We can see that much of the structure is common to all channels but that there are significant differences and each channel adds information about the overall field structure. In addition, use of multichannel segmentation to improve the estimates of polarimetric or texture parameters is discussed in Section 11.9.3 and [29,30].

12.5.2 Multidimensional Annealed Segmentation

Although the combination of channels by RGW as described appears to produce reasonable results, the way in which the information is combined between channels is not ideal. An obvious objection is that the use of an rms criterion to locate edges means that an edge detection that is significant in only one channel



Figure 12.10 (a) Edges in the multidimensional segmentation shown in Figure 12.9(h) that are present in the HH channel. (b) Edges present in both the HH and VV channels (black), HH but not VV (dark gray), and VV but not HH (light gray). (c) Edges present in HH, VV, and HV (black); HH or VV but not HV (dark gray), and HV but not HH or VV (light gray).

may not be strong enough to put the rms measure above threshold. However, this is by design, otherwise problems of edge jitter would not be eased by combining channels. The price paid for an image that is easier to interpret is therefore a potential loss of information that is carried in only one or a small number of the available channels. A more rigorous approach when the images are uncorrelated is to extend the annealed segmentation algorithm described in Section 7.3.5. This is possible because, if the boundaries in the different images of the scene are expected to lie in the same position, the log likelihoods for each image for given boundaries can be summed to form the total log likelihood. The optimization can then proceed as for single-channel data. However, as yet there is no rigorous criterion for the false alarm probability, so a postprocessing merge stage to yield a defined P_{fa} is not possible.

The three ERS-1 PRI images in Figure 12.11(a–c) were gathered on April 16, June 9, and August 18, 1992, respectively, from the Feltwell area, UK. The same display conditions are adopted for each, revealing the markedly different multitemporal behavior of the backscattering coefficient in different fields during the year. Crop development and soil moisture changes give rise to images that have very different structures (see Section 13.2 for a further discussion of this point). Field definition appears better in the two earlier images due to significant changes in crop state over the growing period. The August image exhibits generally low contrast, probably reflecting the fact that many of the fields have already been harvested by this date so that the image is dominated by soil effects.

Each individual image was first segmented using annealed segmentation with an average region size chosen to be 50 pixels, corresponding to 1,310 segments [31]. The average intensities within each segment for the three individual images are shown in Figure 12.11(d–f). Figure 12.11 (d,e) yields reasonable evidence of field boundaries, whereas the segments in (f) are more fragmented. The corresponding edge maps are shown in Figure 12.11(g–i). They seem to have little detailed structure in common except for the drainage channel on the left of the image, parts of which are visible in the different scenes. In contrast, the edge map from multidimensional annealed segmentation shown as Figure 12.11(j) appears distinctly superior to any of the individual cases shown as (g–i). The structure of the fields and the river appears much cleaner, more complete, and better defined in this composite result.

The average intensities within the multidimensional segments for each of the original images are shown in Figure 12.12(a–c). If Figure 12.12(a) is compared with (b), the very different behavior of the backscattering coefficient of different fields is dramatically evident. Moreover, we can use the inferred structure to examine the more subtle differences present in the August image of Figure 12.12(c). The statistical significance of these spatial and temporal changes can then be assessed using the analysis developed in Section 12.4. The

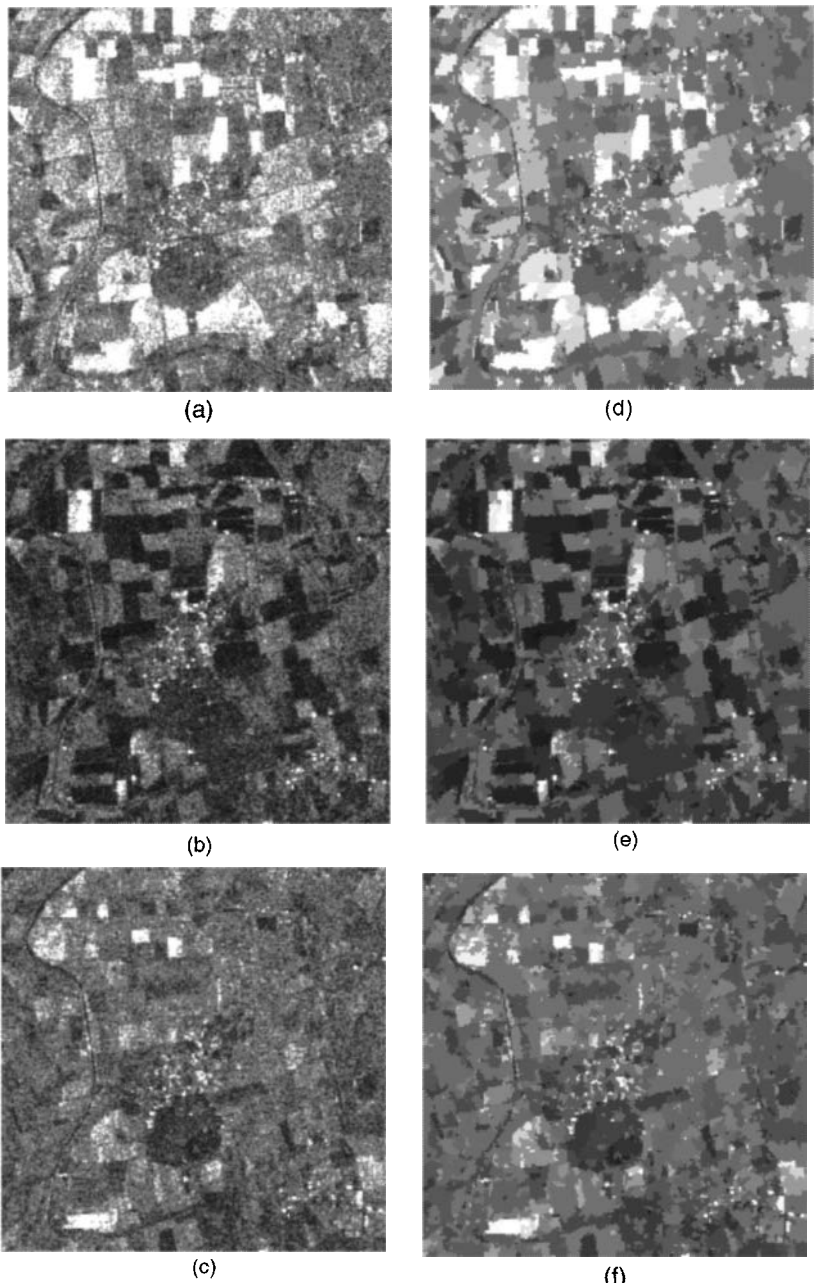


Figure 12.11 (a–c) ERS-1 PRI images of an agricultural area near Feltwell, UK, gathered on (a) April 16, (b) June 9, and (c) August 18, 1992 (Copyright ESA). (d–f) The corresponding one-dimensional annealed segmentations; (g–i) the associated edge maps; and (j) the edge map resulting from multidimensional annealed segmentation. (British Crown Copyright, 1997/DERA.)

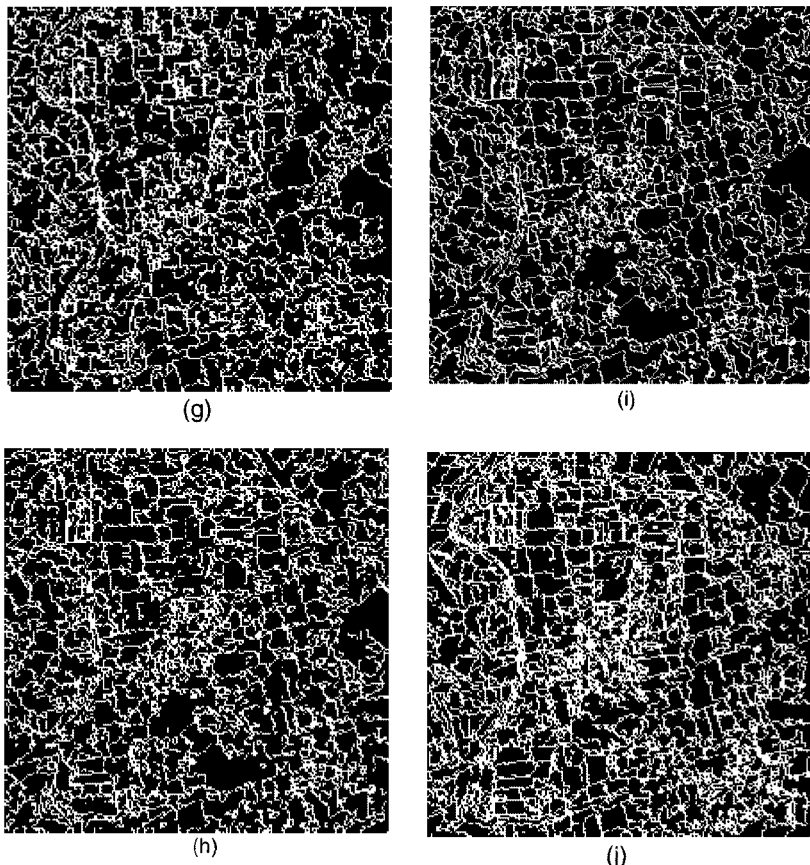


Figure 12.11 (continued).

importance of such tools for monitoring large agricultural areas is made much clearer in Section 13.2, where we discuss some of the empirical background relevant to analyzing the multitemporal behavior of σ^o for crops.

Before closing this section, it should be remarked that in addition to the currently inadequate treatment of false alarm probabilities noted previously, another shortcoming is that multidimensional annealed segmentation provides a rigorous approach only when the channels are independent. Further development is needed to provide optimal methods when channels are correlated, as in polarimetric data.

12.6 Comparison of Algorithms—A Case Study

Quantitative methods for assessing algorithm performance based on internal properties of the imagery have been discussed in Chapters 6 and 7. In this

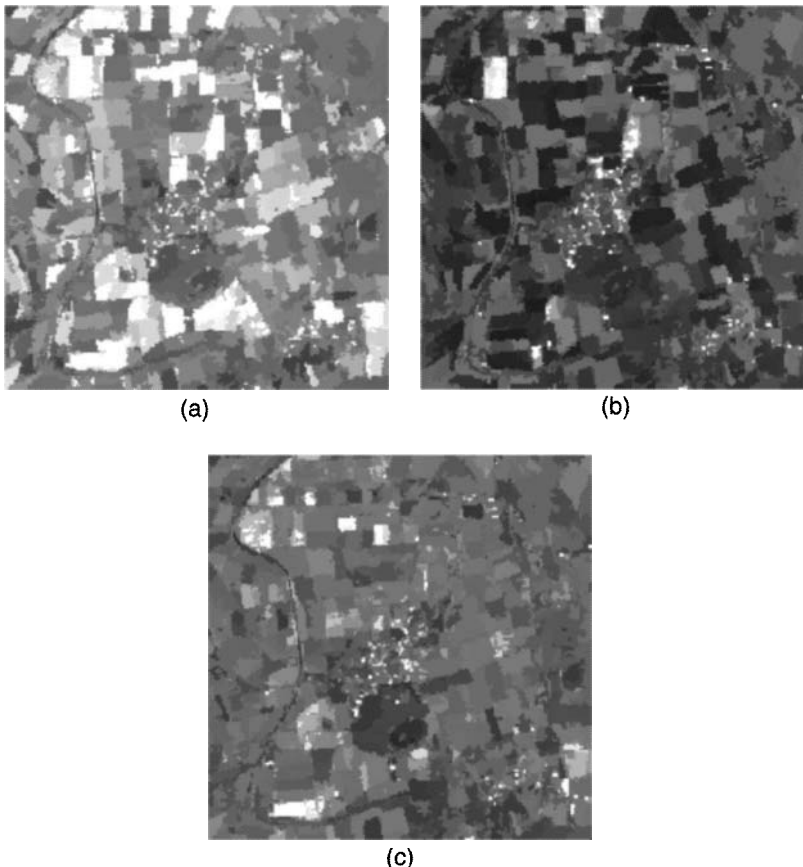


Figure 12.12 Mean intensities within the segments indicated by Figure 12.11(j) for the individual images shown as Figure 12.11(a–c). (British Crown Copyright, 1997/DERA.)

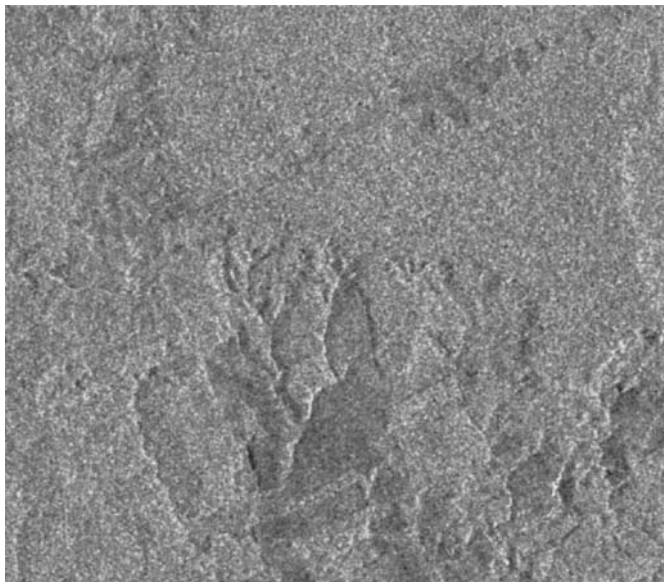
section we instead start from an application and use it to evaluate several of the tools described in this and earlier chapters. This evaluation is based on an excellent dataset gathered over the Tapajos National Forest in Brazilian Amazonia including airborne SAR, ERS-1, JERS-1, Radarsat, and TM data [32,33] (for examples of airborne SAR and Radarsat data from this region see Chapters 8 and 13, respectively). For the purposes of this section, our main interest will be in a multitemporal ERS-1 dataset gathered in 1992. The three acquisitions (May 22, July 31, and December 18) are all from the 35-day repeat cycle and, hence, provide images with almost identical viewing geometries. We also make use of a cloudfree Landsat TM image of the test site acquired on July 29, 1992.

The particular problem discussed here is an assessment of the extent to which the C-band ERS data will permit a discrimination of forest from non-forest. It must be stressed that ERS is not expected to be ideal for this application since both modeling and observations indicate that low, wet vegetation canopies may give similar responses to fully developed forest canopies [4]. Essentially, the C-band signature saturates at low levels of biomass, and longer wavelengths are needed for forest monitoring [34,35]. Therefore, we do not expect particularly good results from ERS-1. However, we can explore how the data should be treated to best effect. Hence, the case study is less to evaluate ERS-1 for this application than to compare a range of image analysis approaches.

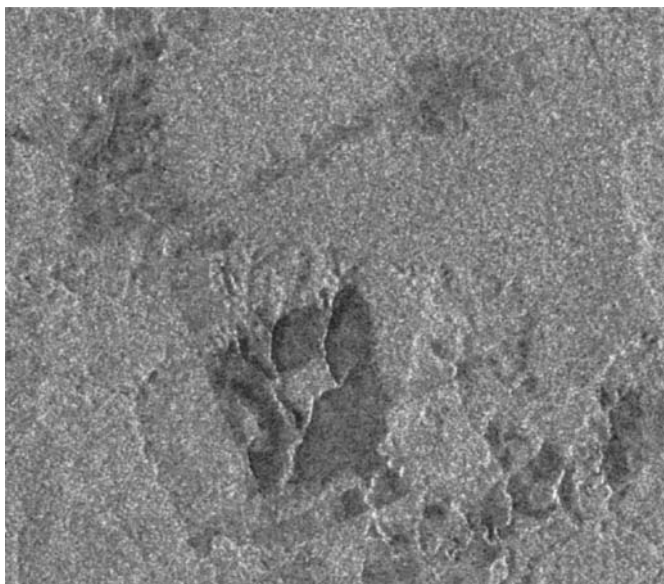
The primary factor underlying the analysis is the temporal and spatial stability of the RCS of the tropical forest [36]. By contrast, other areas tend to exhibit temporal variability. This is illustrated in Figure 12.13 (a,b) and shows the July and December images of a region on the edge of the Tapajos forest. The July image exhibits very low contrast; while in December more image structure is clear, dominated by a roughly square area of pasture in the lower part of the image. Also visible are areas of settlement and shifting agriculture along the Santarem-Cuiaba highway (running roughly top to bottom) and along two roads perpendicular to this highway, one at the top and one at the bottom of the image. In addition, areas of relief associated with drainage patterns are clear in both images.

On the basis of backscatter models, the differences in backscattering coefficient between the two images can be ascribed to soil moisture changes in areas of little vegetation or bare soil, with the December image corresponding to drier conditions (despite this being in the rainy season). This is supported by field work and meteorological data [4]. In areas of higher vegetation (including the forest canopy) the soil moisture signature is effectively masked, so there is little response to rainfall and the backscattering coefficient is approximately constant.

One approach to forest discrimination would be to try to detect areas of reduced backscatter compared to the known level of the primary forest after dry periods, as occurs in Figure 12.13(b). The disadvantage of this approach in a general context is that topographic effects (which are significant in many tropical forest areas, though not of major impact for Tapajos) will cause significant misclassification. To prevent this, *change* between wet and dry periods can be measured using ratio images, as discussed in Section 12.4. Simple ratioing of the two images produces Figure 12.14(a), which, after applying a 1.5-dB threshold, gives rise to Figure 12.14(b). It can be seen that topographic effects have been suppressed (though not entirely removed, perhaps due to slight misregistration). However, both images appear very noisy, as would be expected from the analysis of Section 12.4.1, since the ERS data are only 3-look.



(a)



(b)

Figure 12.13 ERS-1 PRI images of a region bordering the Tapajos National forest on (a) July 31 and (b) December 18, 1992. (Copyright ESA.)

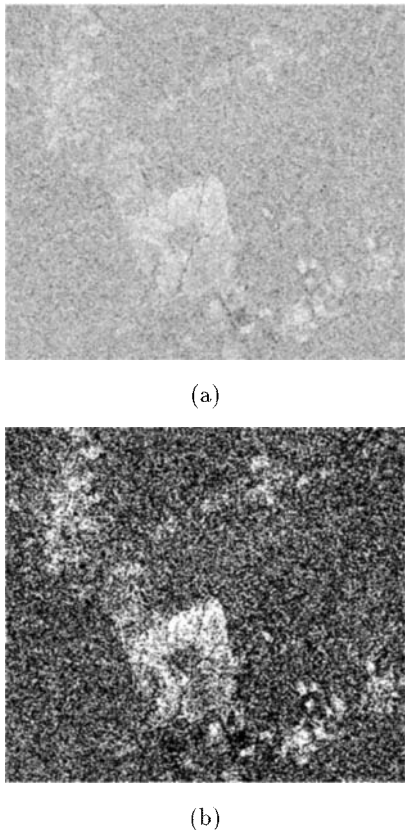


Figure 12.14 (a) Ratio of the images shown as Figure 12.13(a,b) and (b) thresholding of the ratio image at 1.5 dB.

Reasonable performance clearly requires speckle suppression. Following Section 12.4.1, this could be achieved by averaging pixels before ratioing, at the expense of resolution. Another alternative is to apply adaptive feature-preserving filters before taking ratios (in order to preserve resolution); here we use gamma MAP reconstruction (see Section 6.5.1 and [13]) and annealed despeckling (Section 6.9). We also use multichannel RGW segmentation (Section 12.5.1) to provide homogeneous regions; this allows ratioing of the average backscattering coefficient within the confines of detected segments. Related work over a tropical forest area in Sumatra is reported in [37]; this makes use of both temporal [15] and gamma MAP filtering [13].

The result of carrying out an 18 by 18 average of the July and December images is shown in Figure 12.15(a,b) with their ratio (in decibels) shown in Figure 12.15(c) and the histogram of the ratio given as Figure 12.15(d). (The

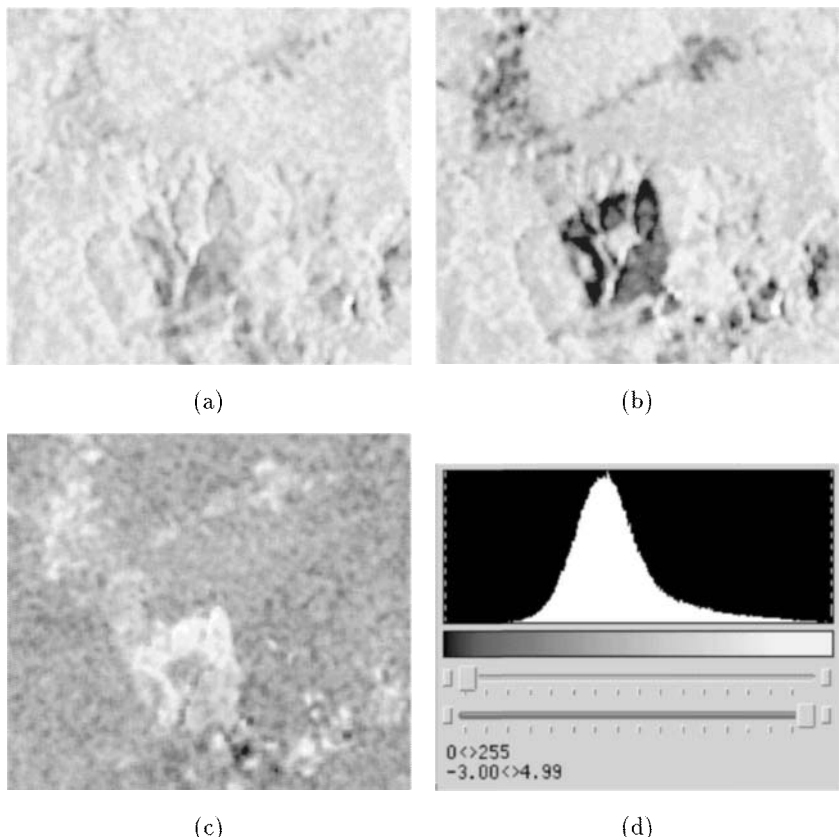


Figure 12.15 (a,b) Images formed by 18×18 block averaging of the images shown in Figure 12.13; (c) ratio of the images shown in (a,b); and (d) histogram of values in the ratio image, truncated at -3 and 4.99 dB.

range of -3 to 4.99 dB indicated on the histogram includes a clipping of extreme values.) Relief effects (which are obvious in the averaged images) are clearly suppressed by ratioing, although the stream beds running through the area of pasture are still visible. In the histogram the modal value is 0 dB and there is a long positive tail, but we observe no separation of classes.

The corresponding ratio images and histograms for the other techniques are shown in Figure 12.16(a-f). In all these cases, the data were first block-averaged using a 2 by 2 window in order to reduce spatial correlation, giving rise to speckle distributions close to 5-look [26]. In Figure 12.16(a) the July and December images were filtered with a structure-preserving 9 by 9 gamma MAP filter before ratioing. The histogram (b) is wider than in all other cases, indicat-

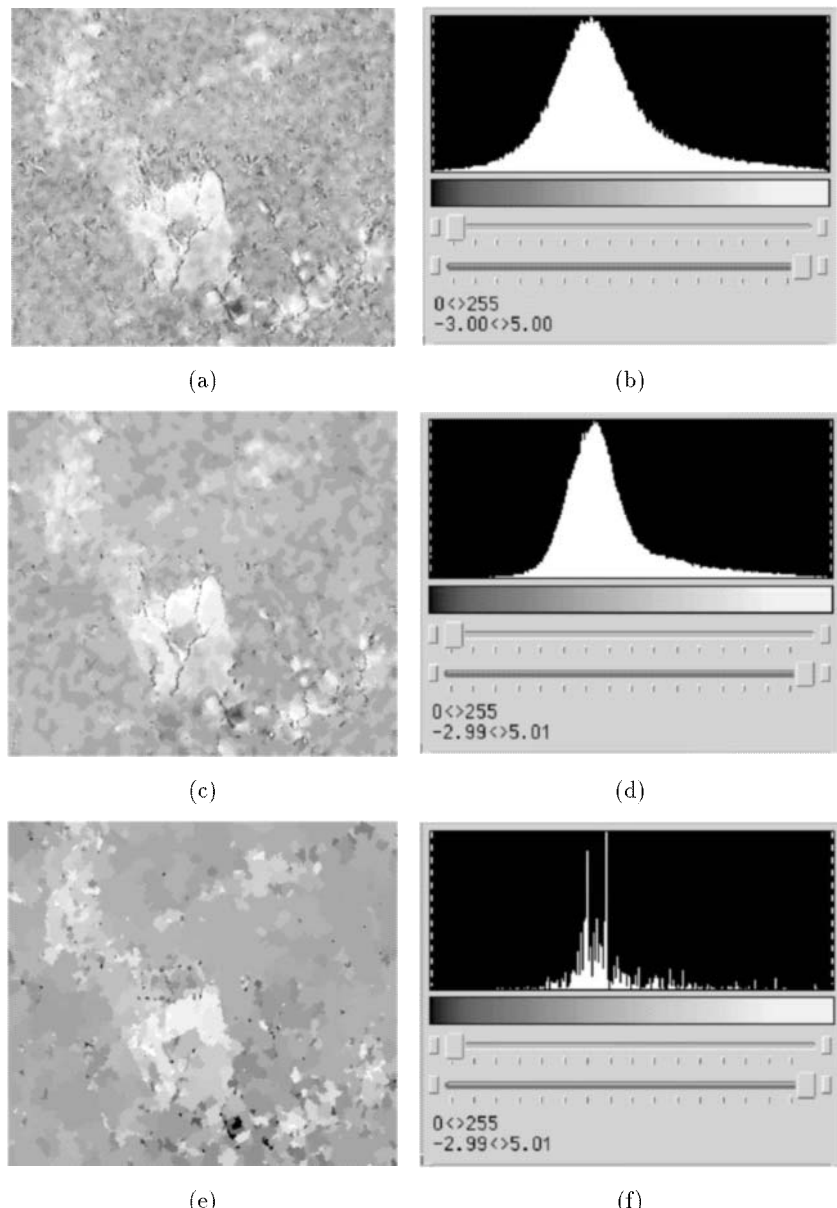


Figure 12.16 Images and histograms corresponding to Figure 12.15(c,d) for postprocessing by: (a,b) gamma MAP filtering, (c,d) annealed despeckling, and (e,f) multidimensional RGW segmentation.

ing less smoothing. The global MAP result (implemented by annealed despeckling) is shown in Figure 12.16(c,d), with a comparatively narrow histogram. Finally, the effect of performing a multidimensional segmentation and ratioing mean values within segments is shown in Figure 12.16(e,f). Each spike in the histogram indicates the ratio values within one or a small number of segments.

To carry out a classification requires a threshold to be chosen, but the lack of structure in the histograms means that this choice is not clear-cut. Classifications based on a 1.5-dB threshold are shown as Figure 12.17(a–d) for the four methods employed, together with the results for a ratio image that has not been preprocessed (Figure 12.17(e)). Based on the theory in Section 12.4.1, this threshold corresponds to a false alarm rate of 4.74×10^{-5} in Figure 12.17(a) when we make allowance for the correlation of samples in the ERS-1 data. This correlation means that the 18 by 18 3-look averages are equivalent to approximately 257 looks (see Section 4.8, especially the discussion following (4.43)).

The preprocessed images all pick out the main structural blocks of the data. The blurring produced by the large averaging window is clear in Figure 12.17(a). Annealing preserves the edge structures much better, while segmentation displays an intermediate behavior. Very noticeable in the gamma-MAP filtered data is the noisiness of the image, with many random false detections in the forest areas. By contrast, the other three algorithms produce little random noise; detections in the forest areas tend to occur as coherent regions.

Also shown as Figure 12.17(f) is a forest/nonforest classification based on a threshold applied to band 5 of the TM data. Under the assumption that this is a reliable classification (this is discussed in detail in [4]), we can carry out a quantitative comparison of the various methods. Table 12.2 shows the classification accuracies for the different methods. The first and second columns indicate the proportions of correctly detected nonforest and forest pixels, respectively. The third column indicates the area of false nonforest detections as a proportion of the true nonforest area, which in this image forms 22.3% of the total area.

As expected, the table indicates that ERS-1 is not ideal for forest discrimination, with less than 50% of the nonforest areas being correctly detected. Missed detections are clear when comparing Figure 12.17(f) with any of Figure 12.17(a–d). For example, the nonforest area protruding from the right side of the square pasture region is not picked out in the radar image by any of the methods. This reflects the fact that even low vegetation canopies can have a backscattering coefficient similar to that of primary forest at C-band. Longer wavelengths are more appropriate to this application, such as the L-band data provided by JERS-1; a comparison of ERS-1 and JERS data for Tapajos will be found in [4]. Two other comments are relevant here. First, a more complete temporal coverage of the region may have given better per-

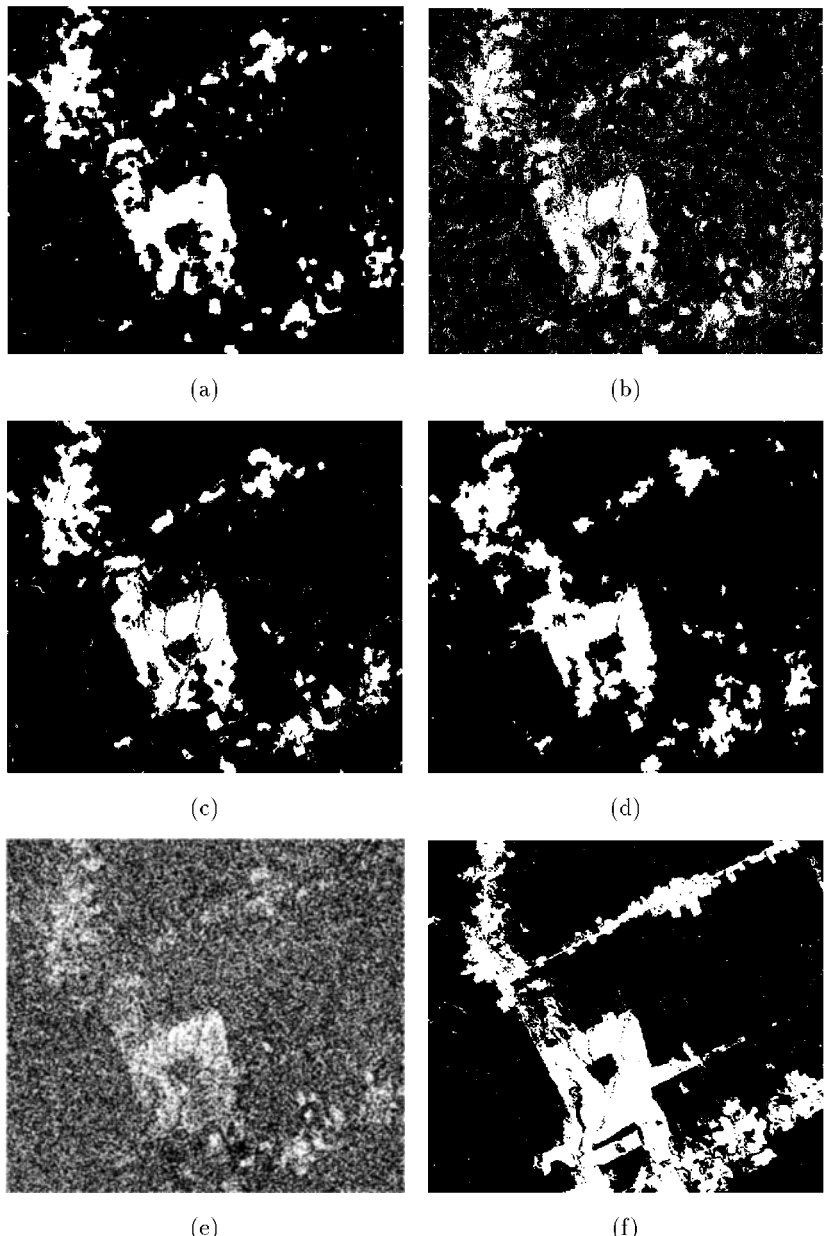


Figure 12.17 (a-d) One-bit images formed by thresholding the images shown as Figures 12.15(c), 12.16(a), 12.16(c), and 12.16(e), respectively; (e) the corresponding image using the ratio of the original (unprocessed) ERS-1 images; and (f) a forest/nonforest template prepared by thresholding band 5 of a TM image acquired on July 29, 1992.

Table 12.2
Classification Accuracies of the Preprocessing Methods

	$p\{N NF\}$	$p\{F F\}$	$p\{F\}p\{N F\}/p\{N\}$
Averaging (18×18)	0.420	0.942	0.156
GMAP (9×9)	0.467	0.931	0.180
Anneal	0.457	0.942	0.157
Segmentation	0.453	0.940	0.164

formance. Long time sequences of ERS images gathered over temperate forests, which also show very stable behavior, allow good forest discrimination using change-detection techniques. We do not have enough images from Tapajos to test this. Second, C-band systems are capable of good forest discrimination in the tropics if they have sufficient resolution (preferably combined with not too steep an incidence angle). This has been demonstrated in Chapter 8 for airborne data and will also be illustrated using spaceborne data from Radarsat in Chapter 13.

Nonetheless, Table 12.2 does provide a means by which to compare the performance of the different algorithms. The removal of small areas of change and the poor definition of edges cause simple averaging to give the lowest percentage of correct nonforest detections. The highest detection rate is that which uses the gamma MAP filter, but at the expense of significantly increased false detections (18%) that also have a highly random noiselike quality, as noted previously. Overall, annealed despeckling gives the best performance, while segmentation performs a little worse than annealing, with a slightly lower detection rate and more false detections.

These results illustrate once more the importance of algorithm selection discussed in Sections 6.10 and 7.4. In this application, annealing appears to provide the best performance of the algorithms tested. However, it requires considerably more computing power than the simplest method based on block averaging. For large-area estimates, or an initial assessment of overall pattern, this suggests that averaging may provide the most useful approach. However, because large windows must be used for averaging to give adequate performance, this is at the price of lost boundary detail, failure to detect small areas, and underestimation of nonforest areas. When a higher level of performance is required, a more sophisticated and powerful method such as annealing must be used, possibly in a selective manner to regions identified to be of interest by averaging.

12.7 Concluding Remarks

This chapter has covered a wide range of techniques for extracting information from multidimensional SAR images. It is very much based on foundations built in earlier chapters, extending techniques developed for single-channel data to this more general and demanding environment. Other aspects of multichannel filtering for which there are no useful one-dimensional analogies (e.g., polarimetric matched filtering) are discussed in the next chapter, since these are closer to classification techniques.

What should be clear here and from Chapter 11 is that the development in this area is far from complete. Among a variety of areas of weakness, we note that there has been comparatively little testing of algorithms, objective methods for algorithm performance are not established, and there are known limitations in the data model used by the segmentation algorithms in the context of polarimetric data. In a more general context, the state of development of these algorithms is such that large-scale assessment of their value to selected applications is now timely but has not yet been carried out. Section 12.6 indicated an approach to this problem. In doing so, it raises the difficult issue of separating the possible contribution of radar images to a given application (what information is potentially available?) from the information provided after postprocessing (has an algorithm destroyed or misrepresented the available information?). This is perhaps the central issue in methods for image understanding because it requires us to ensure that our data models are true representations of information sources in radar data and that the algorithms correctly embody these models. There is little doubt that on both counts our current level of understanding is not complete.

References

- [1] Quegan, S., A. Hendry, and J. Wood, "The Visibility of Linear Features in SAR Images," *Proc. IGARSS 88*, Edinburgh, 1988, pp. 1517–1520.
- [2] Greeley, R., and D. G. Blumberg, "Preliminary Analysis of Shuttle Radar Laboratory (SRL-1) Data to Study Aeolian Features and Processes," *IEEE Trans. Geosci. Remote Sensing*, Vol. 33, 1995, pp. 927–933.
- [3] Quegan, S., R. G. Caves, K. D. Grover, and R. G. White, "Segmentation and Change Detection in ERS-1 Images over East Anglia," *Proc. of the First ERS-1 Symp.*, Cannes, ESA SP-359, 1993, pp. 617–622.
- [4] Grover, K. D., S. Quegan, and C. C. F. Yanassee, "Quantitative Estimation of Tropical Forest Cover by SAR," *IEEE Trans. Geosci. Remote Sensing*, in press 1997.
- [5] Borgeaud, M., J. Noll, and A. Bellini, "Multitemporal Comparisons of ERS-1 and JERS-1 SAR Data for Land Applications," *Proc. IGARSS 94*, Pasadena, 1994, pp. 1603–1605.

- [6] Schmullius, C., J. Nithack, and M. Kern, "Comparison of Multitemporal ERS-1 and Airborne DLR E-SAR Image Data for Crop Monitoring," *Proc. Second ERS-1 Symp.*, Hamburg, ESA SP-361, 1994, pp. 79–84.
- [7] Wooding, M. G., A. D. Zmuda, and G. H. Griffiths, "Crop Discrimination Using Multitemporal ERS-1 SAR Data," *Proc. Second ERS-1 Symp.*, Hamburg, ESA SP-361, 1994, pp. 51–56.
- [8] Goodman, N. R., "Statistical Analysis Based on a Certain Multivariate Gaussian Distribution (an Introduction)," *Ann. Math. Stat.*, No. 34, 1963, pp. 152–177.
- [9] Goze, S., and A. Lopes, "A MMSE Speckle Filter for Full Resolution SAR Polarimetric Data," *J. Elect. Waves and Appns.*, No. 7, 1993, pp. 717–737.
- [10] Quegan, S., "A Unified Algorithm for Phase and Crosstalk Calibration—Theory and Observations," *IEEE Trans. Geosci. Remote Sensing*, Vol. 32, 1994, pp. 89–99.
- [11] Touzi, R., and A. Lopes, "The Principle of Speckle Filtering in Polarimetric SAR Imagery," *IEEE Trans. Geosci. Remote Sensing*, Vol. 32, 1994, pp. 1110–1114.
- [12] Schou, J., "Validation of Filters and Statistical Models," Short Course report, University of Sheffield, 1996.
- [13] Lopes, A., E. Nezry, R. Touzi, and H. Laur, "Structure Detection and Adaptive Speckle Filtering in SAR Images," *Int. J. Remote Sensing*, Vol. 14, 1993, pp. 1735–1758.
- [14] Novak, L. M., and M. C. Burl, "Optimal Speckle Reduction in Polarimetric SAR Imagery," *IEEE Trans. Aerospace Elect. Sys.*, Vol. 26, 1990, pp. 293–305.
- [15] Bruniquel, J., and A. Lopes, "Multi-variate Optimal Speckle Reduction in SAR Imagery," *Int. J. Remote Sensing*, Vol. 18, 1997, pp. 603–627.
- [16] Lee, J., M. R. Grunes, and S. A. Mango, "Speckle Reduction in Multipolarisation, Multi-frequency SAR Imagery," *IEEE Trans. Geosci. Remote Sensing*, Vol. 29, 1991, pp. 535–544.
- [17] Novak, L. M., M. C. Burl, and W. W. Irving, "Optimal Polarimetric Processing for Enhanced Target Detection," *IEEE Trans. Aerospace Elect. Sys.*, Vol. 29, 1993, pp. 234–244.
- [18] Quegan, S., and L. V. Dutra, "SAR Calibration and Principal Component Analysis," *Proc. Third Airborne SAR (AIRSAR) Workshop*, Jet Propulsion Lab, Pasadena, 1991, pp. 138–146.
- [19] Quegan, S., "Application of Principal Components Analysis to Quadpolarised Data," *GEC-Marconi Research Centre: Studies of Multi-frequency and Multi-polarisation SAR Applications*, Appendix E, MTR 93/73, Contract RAE 1B/89, 1993.
- [20] Singh, A., and A. Harrison, "Standardised Principal Components," *Int. J. Remote Sensing*, Vol. 6, 1985, pp. 883–896.
- [21] Cloude, S. R., and E. Pottier, "An Entropy Based Classification Scheme for Land Applications of Polarimetric SAR," *IEEE Trans. Geosci. Remote Sensing*, Vol. 35, 1997, pp. 68–78.
- [22] Lee, J.-S., and K. W. Hoppel, "Principal Components Transformation of Multifrequency Polarimetric SAR Imagery," *IEEE Trans. Geosci. Remote Sensing*, Vol. 30, 1992, pp. 686–696.
- [23] Touzi, R., A. Lopes, and P. Bousquet, "A Statistical and Geometrical Edge Detector for SAR Images," *IEEE Trans. Geosci. Remote Sensing*, Vol. 26, 1988, pp. 764–773.
- [24] Rignot, E. J. M., and J. J. van Zyl, "Change Detection Techniques for ERS-1 SAR Data," *IEEE Trans. Geosci. Remote Sensing*, Vol. 31, 1993, pp. 896–906.

- [25] Schreier, G., "Geometrical Properties of SAR Images," *SAR Geocoding: Data and Systems*, G. Schreier (ed.), Karlsruhe: Wichmann, 1993, pp. 103–134.
- [26] Caves, R. G., "Automatic Matching of Features in Synthetic Aperture Radar Data to Digital Map Data," Ph.D. Thesis, University of Sheffield, UK, 1993.
- [27] White, R. G., *Low Level Segmentation of Noisy Imagery*, Tech. Report 3900, Roy. Signals and Radar Estab., Malvern, 1986.
- [28] White, R. G., "Change Detection in SAR Imagery," *Int. J. Remote Sensing*, Vol. 12, 1991, pp. 339–360.
- [29] Caves, R. G., and S. Quegan, "The Role of Segmentation in Multi-channel SAR Image Analysis," *Proc. RSS '95: Remote Sensing in Action*, Southampton, Remote Sensing Society, 1995, pp. 1171–1178.
- [30] Caves, R. G., and S. Quegan, "Multi-channel SAR Segmentation: Algorithm and Applications," *Proc. European Symp. on Satellite Remote Sensing II*, Paris, 1995, pp. 241–251.
- [31] McConnell, I., and D. Stewart, "Multi-dimensional Annealed Segmentation," N.A. Software Rpt. No. 10, DRA Contract No. CSM1/072, 1997.
- [32] Quegan, S., K. D. Grover, and C. C. F. Yanasse, "Use of C Band SAR for Quantitative Estimation of Tropical Forest Cover—Methods and Limitations," *Proc. International Symp. on Retrieval of Bio- and Geophysical Parameters from SAR Data for Land Applications*, Toulouse, 1996, pp. 167–178.
- [33] Sant'Anna, S. J., C. C. F. Yanasse, and A. C. Frery, "Estudo Comparativo de Alguns Classificadores Utilizando-se Imagens Radarsat da Regiao de Tapajos," *Proc. First Latino-American Seminar on Radar Remote Sensing: Image Processing Techniques*, ESA SP-407, 1997, pp. 187–194.
- [34] Le Toan, T., A. Beaudoin, J. Riom, and D. Guyon, "Relating Forest Biomass to SAR Data," *IEEE Trans. Geosci. Remote Sensing*, Vol. 30, 1992, pp. 403–411.
- [35] Dobson, M. C., F. T. Ulaby, T. Le Toan, E. S. Kasischke, and N. L. Christensen, "Dependence of Radar Backscatter on Coniferous Forest Biomass," *IEEE Trans. Geosci. Remote Sensing*, Vol. 30, 1992, pp. 412–415.
- [36] Lecomte, P., and E. P. Attema, "Calibration and Validation of the ERS-1 Wind Scatterometer," *Proc. of the First ERS-1 Symp.*, Cannes, ESA SP-359, 1993, pp. 19–29.
- [37] Le Toan, T., F. Ribbes, N. Flouri, and U. R. Wasrin, "Use of ERS-1 SAR Data for Forest Monitoring in South Sumatra," Final Report, TREES Project, 1997.

13

Classification of SAR Imagery

13.1 Introduction

A central theme throughout earlier chapters is that the information in a SAR image is embodied in image structure (objects) together with a statistical description of the properties of these objects. Our major drive was to derive, test, and exploit progressively more highly developed data models and consequently find optimal methods to infer this structure and to characterize the objects. The endpoint of most of the work described up to now is an estimate of the relevant model parameters at each pixel based either on image reconstruction or in the context of an image segmentation. Arriving at this description of the image relies on two types of knowledge about the world: (1) semiempirical inferences about the types of statistical data likely to be needed in describing the observations from distributed targets and (2) general descriptors of scene structure carried in such concepts as the cartoon model (Chapter 7). Essentially we were concerned with *measurement*: what should be measured in a SAR image, which methods should be used, and how accurate are the results? At a fundamental level, these measurements are all we have. A theory of measurement that is complete tells us everything there is to know about a pixel or object in the scene and circumscribes what needs to be explained about it. Nonetheless, to make measurements *useful*, we need to assign high-level meanings to them, which requires considerably more world knowledge. A ubiquitous requirement is one of of objects in the scene. This can be at the object level (this is a field or a village or a tank, for example) or at the pixel labeling level (e.g., crop type, water, or single-year ice). When segmentation or target-detection techniques are used,

both aspects can be combined. A general approach to the first level is well beyond the scope of this book, but in this chapter we deal with the second, which is a problem of *classification*. Essentially we try to make the links between a low-level classification into parameter values at a pixel or within a segment (as dealt with in Chapters 7 to 9, 11, and 12) and a high-level classification into specific cover types.

It must be recognized that there may be a significant disparity between the classes of interest in a given application and the ability of the sensor to discriminate them. At one extreme, unless the desired classes can produce measurable differences in the available parameters (such as texture parameter and covariance), they are indistinguishable. In this case, no classification is possible. At the other extreme, the complex nature of the microwave interaction with natural media may cause an individual desired class to contain subclasses with different behavior (e.g., different parts of a body of water can display a radically different backscattering coefficient as a result of local wind patterns). When the number of these disturbing effects becomes large, it becomes hard to find a robust classifier that maps onto application needs. Any form of robust classification, therefore, depends not only in knowing what parameters to measure but on an appreciation of the physical factors likely to affect those measurements. In other words, the decision rules by which we distinguish objects must be firmly based in the information provided by the imaging system.

A realistic assessment of the role of SAR in any classification scheme must also take account of other available information sources. In some cases SAR may be all we have. This can occur because of cloud cover or darkness (examples include agricultural monitoring in Northern Europe, rain forest mapping, and sea ice mapping). SAR may be the only sensor available at a given location and/or time or that can provide a repetitive time series to observe a process (only ERS-1 data provided observations of the break-up of the Larsen ice shelf [1]). In addition, the special properties of microwave images may mean that they are the only way to observe a phenomenon (e.g., canopy penetration at longer wavelengths and polarimetric capabilities allow us to detect inundated forest and measure biomass; sensitivity to geometric and dielectric properties can be used to distinguish different soil roughnesses and to estimate soil moisture). In other circumstances, SAR may supplement or complement other data. In agricultural monitoring, for example, the data provided by optical sensors is in most cases preferred over SAR because of the comparative stability and predictability of the spectral response of many cover types (although affected by such factors as atmospheric transmission, sun angle, season, and natural variability of the crop). Information is also available in several spectral bands, and, of course, there are none of the problems in image interpretation that arise from speckle. However, for early season estimates, radar may be an important information

source because of its sensitivity to agricultural treatment of the soil. In addition, as already noted, it can provide a monitoring capability when cloud cover prevents optical data acquisition.

The potential contribution of SAR to classification therefore needs us to understand how the system configuration (polarization, wavelength, incidence angle, and revisit time) and the choice of measurement (such as phase difference, backscattering coefficient, texture parameter, and amplitude ratio) impact on characterizing the objects of interest and their properties. Considerable progress in this direction has been made as the number and type of radar systems supplying reliable measurements over diverse regions has grown. Numerous parameters related to the radar system and the medium being observed are now known to affect the information encoded in the SAR image. In the context of natural surfaces covered by vegetation, factors affecting the radar signal include:

- The geometric and dielectric properties of the vegetation cover, which are related to the structure and biomass distribution in the canopy. Within one vegetation type, these parameters are strongly dependent on the density, growth stage, and moisture content of the plants.
- The geometric and dielectric properties of the underlying soil; these are related to the soil roughness and moisture, which in turn are related to agricultural practices and weather conditions.

The relative importance to the radar response of these different properties of the scattering medium depends on the frequency, polarization, and incidence angle of the radiation.

As a result, the backscatter from a given terrain type may have a “within class” variability due to the variation of one or more of the parameters determining the dominant scattering mechanisms (e.g., differing row directions, soil moisture variations due to irrigation, and biomass and structure change due to variations in crop calendar may all cause significant variability in the backscattering coefficient observed from a single crop class). There may also be large temporal variations due to evolution in the characteristics of the medium. Taken in combination, this means that in many cases of interest not only will a given class exhibit internal variation, but there will also be significant overlap in the observed backscatter from different classes for a given set of radar characteristics.

While the world may contain much variability when seen at radar wavelengths, classification relies on (1) objects of a given class having repeatable behavior that is known or can be inferred from the data and (2) objects from different classes exhibiting distinguishing behavior under some circumstances.

Identifying those circumstances needs physical understanding combined with observation. To this end, in Section 13.2 we survey some of the empirical evidence concerning the conditions under which SAR data meet these two criteria. Dealing with the full range of applications of SAR data would not be appropriate, so we restrict ourselves to issues related to land use, agriculture, and forestry. Related information on other areas can be found in [2–9]. However, the concerns raised here are of general relevance.

The empirical evidence indicates what may be possible with the data, but in order to turn this into reality we need to define procedures for handling the data. In Section 13.3 general issues in defining classification procedures are discussed and three main categories of approach to this problem are set out. These are then described in more detail in Sections 13.4 (data-driven methods), 13.5 (methods based on identifying scattering mechanisms), and 13.6 (rule-based methods based on physical insight). In Section 13.7 we move one step beyond taxonomy and use the ability of SAR to discriminate biophysical properties within a single class. This refinement of a broad classification uses capabilities specific to SAR and is an indicator of how SAR may be used within a wider classification framework.

Unlike many of the issues dealt with in earlier chapters, it will become clear that the problem of classification does not permit a single optimal solution except in an idealized world. The real world exhibits great variability at radar wavelengths; and conceptually simple classes, such as wheat or water, may show vastly different responses even within a local area. Equally, different desired classes may exhibit very similar behavior. Understanding why this happens, learning how to account for it, and designing systems that give the best possible capability to provide the information needed present major challenges to the use of SAR data. To a large extent, then, this chapter presents an overview of a wide range of possible techniques; only in a few cases are preferred methods becoming clear.

13.2 The Empirical Basis for Classification

Effective classification requires the desired classes to have distinguishing features. Hence, a first approach to classification is to examine representative data to see if such features exist. The choice of features is dictated by the statistical structure of the data because, as we have seen, in many cases distributed targets can be described by a small number of parameters, which describe all the available information (Chapters 4, 5, and 11). We have also seen that there are known optimal or near-optimal estimators (in a maximum likelihood or maximum a posteriori sense) for these parameters (Chapters 6 to 9 and 11). An

investigation of the classification potential of SAR would therefore seem to be comparatively straightforward.

In practice, this has not proved to be the case. A primary reason is that it requires large, comprehensive, well-calibrated radar datasets accompanied by extensive ground data. Considerable effort has been devoted to the acquisition of such datasets, initially from ground-based scatterometers in the case of agricultural crops and soils [10–20]. Early attempts to develop equivalent datasets from airborne SAR and scatterometer systems were beset by system defects and calibration problems [21–23]. Even for modern systems, radiometric calibration is still a major concern, although focusing and geometric fidelity need not be a problem, as is made clear in Chapter 3. High-quality data are being produced by several current systems; in this book we make extensive use of data from the NASA/JPL AirSAR system and the DCRS EMISAR systems, for both of which data calibration and image quality are given the utmost importance. Similar care is typical of most of the numerous civilian systems currently deployed or under development. (For military systems concerned with target detection, calibration is normally not a major concern.) However, at the time of writing the supply of well-documented, high-quality airborne data is still fairly limited and restricted to a small number of test sites.

The flexibility and comparative ease of deployment of airborne SAR has made it the main vehicle for technical development. All the available polarimetric and multifrequency data, other than that from the Shuttle Imaging Radar (SIR-C/X-SAR) mission, have been produced by airborne sensors. However, a major drawback in these airborne datasets at present is that almost no high-quality multitemporal data are available. Instead, much of our knowledge of the dynamics of scattering from natural targets has been provided by the regular revisit time offered by orbital SAR. The excellent stability of the ERS-1 SAR has allowed long time series of reliable σ^0 measurements to be assembled; this is likely to continue to be the case with ERS-2 and the follow-up ENVISAT mission. For the JERS-1 SAR, image radiometry is fairly stable and of satisfactory quality, although affected by artifacts [24,25]. The Radarsat data calibration and evaluation phase is presently ongoing.

A major contrast between the data acquired by orbital SAR and data from airborne or Shuttle missions is in the range of system configurations available. The ERS, JERS, and Radarsat satellites carry single-frequency, single-polarization systems operating with C-VV, L-HH, and C-HH characteristics, respectively. For ERS and JERS only a narrow range of incidence angles is available (19.3 to 26.4 degrees for ERS and 32 to 38 degrees for JERS). Radarsat offers considerable flexibility in its operating modes, with possible incidence angles from 17 to 55 degrees and a variety of swath widths and resolutions. ENVISAT is planned to have similar flexibility, but with the addition of polarization

diversity (although it is not intended to acquire full polarimetric data). Another important difference is in the resolutions available. Typically, airborne systems provide data with a resolution of the order of a few meters, although higher resolution systems are not uncommon, particularly in a military context. Of the spaceborne systems, only Radarsat operating in fine mode currently offers comparable resolution, of about 6m (slant range) by 8.9m (azimuth). The ERS satellites can give this order of resolution only in the azimuth direction.

It will be observed that the available SAR data fall into two complementary (and incomplete) categories. Orbital SARs offer a multitemporal capability and large area coverage, but with only a limited range of system configurations. Airborne SARs and the Shuttle Imaging Radar provide a wide range of parameters but little in the way of multitemporal data. Airborne data in most cases cover limited spatial areas. In addition, spaceborne data (including those provided by the Shuttle) are in most cases of lower resolution than those from airborne sensors. Hence, a comprehensive assessment of the impacts of resolution, frequency, polarization, incidence angle, and time on the classification potential of SAR is not possible from the existing data alone. Modeling and simulation combined with inferences from ground-based experimental facilities, therefore, are essential in extrapolating the available results. However, a large international effort is devoted to exploring what is possible with current data; relevant publications geared toward gaining such an overview are found in [2–9]. Here we do not attempt to summarize all this activity but instead highlight main themes and issues using examples from spaceborne and airborne data.

13.2.1 Spaceborne Multitemporal Data

The use of ERS data for agricultural and forest applications has attracted much attention ([26] and references therein). Although interferometry provides a potential information source in this regard [27,28], its use for monitoring is limited when only single satellites are operating with long repeat times (as at present). As a result, the primary information source for European agriculture is a time series of field-averaged σ^0 values. (As shown in Chapter 4, averaging provides the MLE of σ^0 within a field, assuming that it comprises a uniform target.) An example of the observed behavior of sugarbeet and winter wheat is shown in Figure 13.1 for a collection of fields in the Flevoland region of the Netherlands [26].

Two features of these data are immediately obvious.

1. The two crop types only become separable in this case during the period from June to August, with a peak separation between signatures of around 5 to 7 dB. This corresponds to the period between sugarbeet

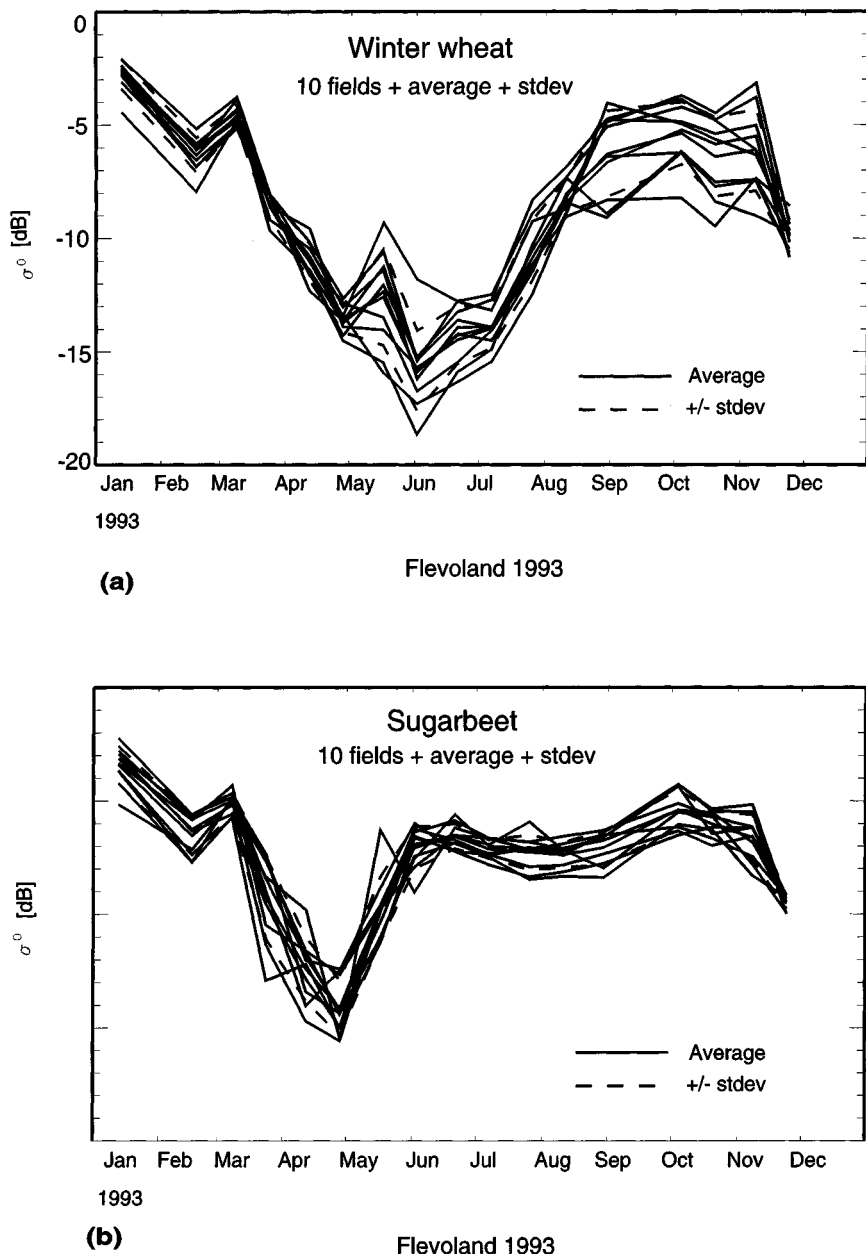


Figure 13.1 Time series of field-averaged σ^0 values measured by ERS-1 in Flevoland, the Netherlands, in 1993: (a) winter wheat and (b) sugarbeet [26].

attaining full coverage and wheat being harvested. In the early part of the year the signatures are practically the same in both cases, dominated by soil effects. For sugarbeet, the comparatively rapid development of full ground cover is marked by a rapid rise in σ^0 , which then remains effectively constant throughout the rest of the year until harvesting. This behavior is indicative of volume scattering in the canopy, which rapidly saturates as the canopy density increases. For wheat, plant development gives rise to a much wider trough in σ^0 , which can be explained, given the low-volume fraction occupied by the vegetation, in terms of increasing attenuation of the soil response as the vegetation grows. Values become comparable to those for sugarbeet around September, when the behavior of both crops is again soil-dominated.

2. Within each crop type there is considerable variation in σ^0 at a fixed time, perhaps due to slight variations in plant growth stage and (in the case of wheat) different soil roughness states. For our sample there is no overlap in the signatures during the critical period.

This example indicates that for these two crop types (more generally, for large-leaved root crops and cereals) there is reasonable expectation of good classification performance, as long as the data acquisitions occur at the right time and enough pixels can be averaged to give sufficient statistical separability. Note that only data for 1993 are shown here. Other years show similar behavior, although with time shifts possibly related to weather conditions, location, or sowing times [26].

When discrimination of crop types with similar structure is desired, the empirical evidence is less encouraging. Figure 13.2 shows a comparison of time series for winter wheat and barley. It is obvious that the behavior of the two crop types is closely related. The best conditions for separating them occur during the reproductive stage when the difference in the two plant structures results in different attenuation of the soil response at VV polarization. Since this difference is small, viable classification relies on large fields and accurate calibration (in order to minimize the uncertainty in σ^0). A further important consideration relevant to many areas (but not Flevoland) is correction for topographic effects. Slopes of even a few degrees can induce apparent σ^0 changes that are significant in relation to the small dynamic range covering different crops. While this macroscale variation in slope is a disturbing factor, the sensitivity of SAR to microscale structure can be turned to an advantage. In particular, its ability to detect changes and differences in soil roughness can provide information on early season soil preparation, from which a broad crop type may be inferred [29]. Similar inferences can be made from interferometric data [27].

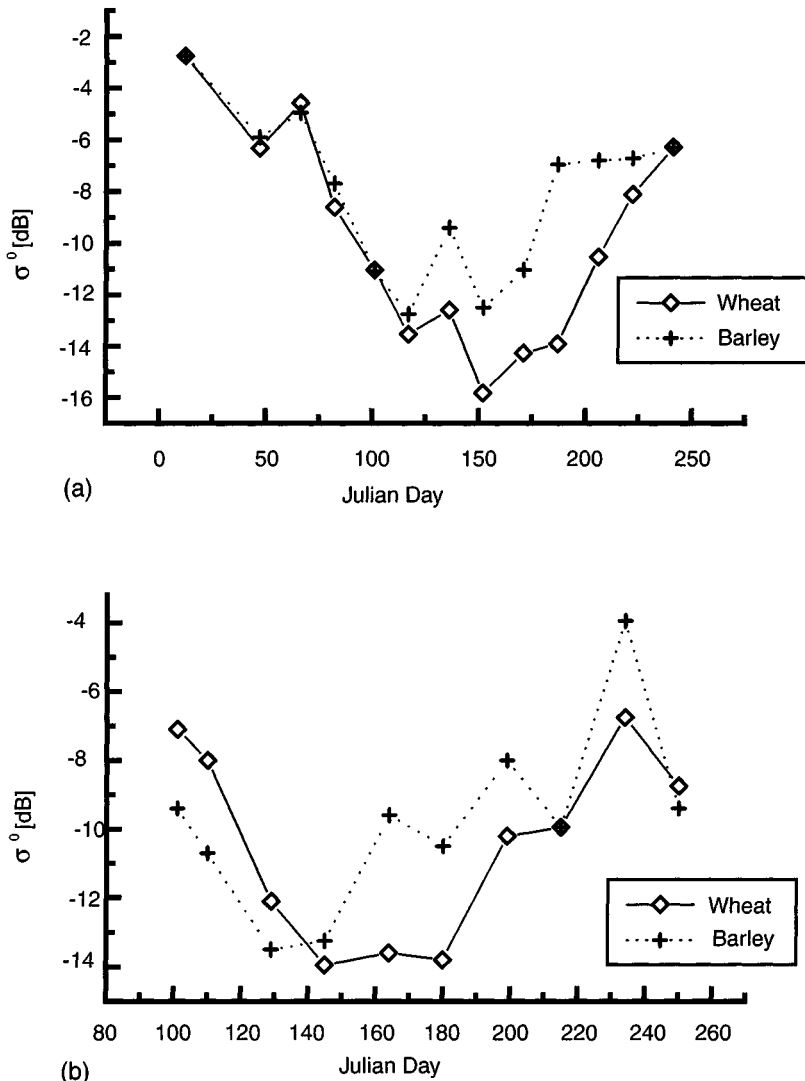


Figure 13.2 Time series of mean field-averaged σ^0 values for winter barley and winter wheat for the 1993 growing season: (a) Netherlands data and (b) Feltwell, UK, data [26].

13.2.2 Polarimetric Data

Figures 11.1 to 11.3 indicate that AirSAR polarimetric data can provide at least five useful parameters per region with which to classify vegetation types. These are the three channel powers and the phase and amplitude of the copolarized complex correlation coefficient (see Section 11.4). Extra potential information

is available in the correlation coefficient of the like and crosspolarized channels when the target does not display azimuthal symmetry at the probing wavelength [30]. Examples can be seen in the L- and P-band data of Figures 11.2 and 11.3 but we will not discuss this here. In addition, texture may show variation with vegetation type (see Chapter 8 and Section 11.9). The impact of texture on classification is dealt with in Sections 13.2.3 and 13.6.

Many studies of the empirical behavior of these five polarimetric parameters have been performed for vegetation targets [31–42]. Here we first describe observations from the Feltwell region, UK, gathered in late July 1991 by the AirSAR system during the MacEurope campaign [31], since they illustrate very well some important issues in classification using polarimetric data, before examining the classification methods to which they give rise. The SAR analysis was supported by crop data for the study area, and the results described in this section are for ten areas from each of six different vegetation types (barley, grass, wheat, potatoes, sugarbeet, and coniferous woodland). The first three of these we will refer to generically as cereals, the fourth and fifth as (large-leaved) root crops. A full description of the data is given in [31]. Figures 13.3 and 13.4 show the C- and L-band measurements, respectively, for the 60 regions and correspond to region-based averages to form the MLEs of the five polarimetric parameters. Notice that in the correlation plots the phase (indicated by crosses) has been normalized by a factor π in order to lie in the range $[-1, 1]$; the correlation amplitude (coherence) is marked by circles and lies between 0 and 1.

Several important features of these results are obvious.

1. Coniferous woodland shows stable behavior in all parameters. (This is characteristic of mature stands of trees of the same species, for which the backscatter exhibits saturation at C- and L-bands for all polarizations.) Potatoes are stable at C-band but show more variation at L-band. This may reflect a row direction effect that is only visible at L-band because of the greater penetration depth. The cereal and sugarbeet fields exhibit significantly higher variability in all parameters except the C-band phase difference, which is close to 0 degrees for all vegetation types.
2. The dynamic range increases with wavelength.
3. The conifers and root crops tend to give brighter responses in all channels; this is most marked at L-band, where conifer woodland separates out as the brightest return.
4. Except for conifers at L-band, there is much overlap between the powers observed for different vegetation types.

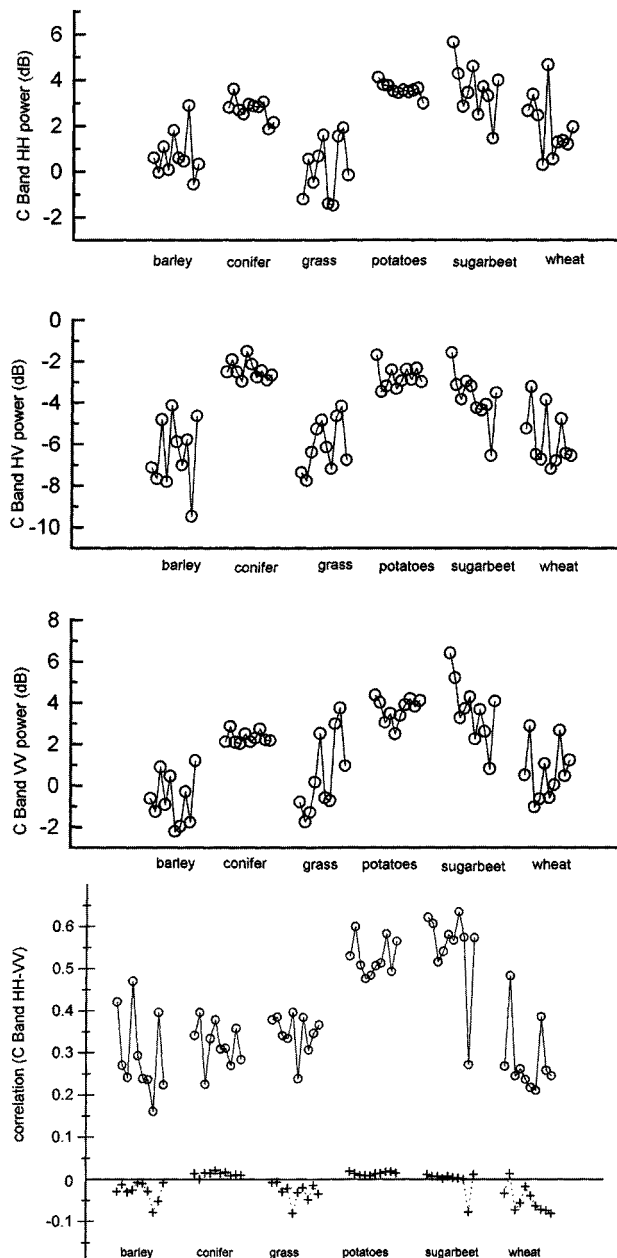


Figure 13.3 Plots of the HH, HV, and VV backscattering coefficients and the amplitude (circles) and phase (crosses) of the HH-VV correlation coefficient for C-band AirSAR data gathered over Feltwell, UK.

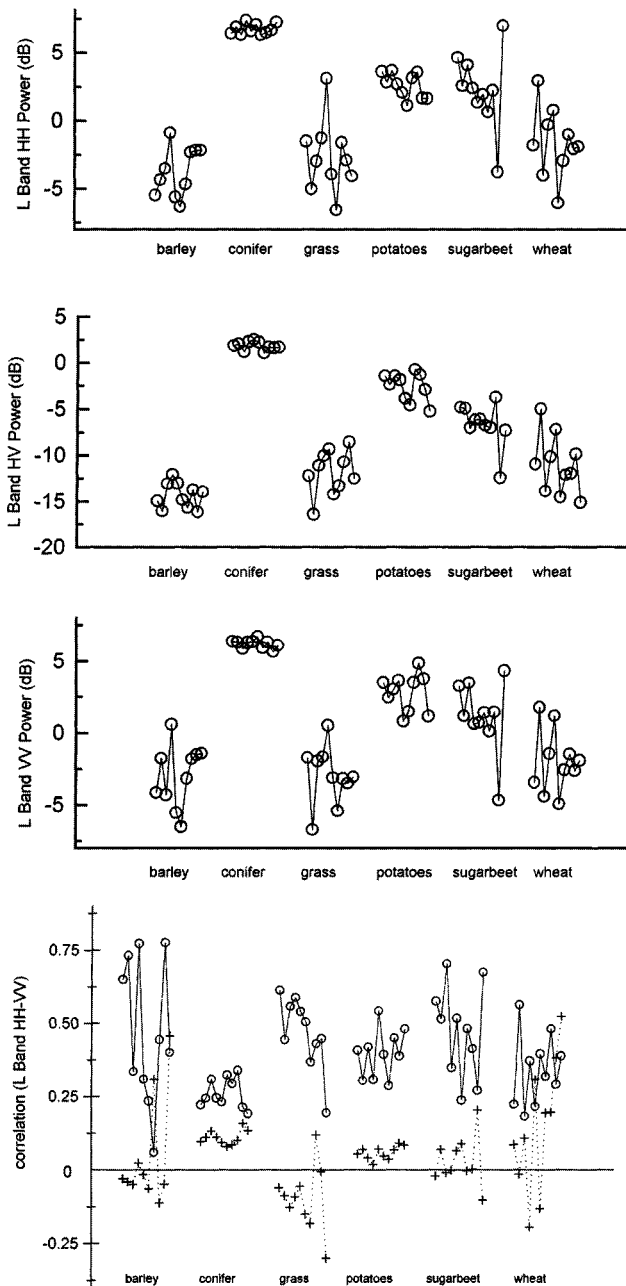


Figure 13.4 As Figure 13.3 but for L-band.

5. There is useful information in the correlation coefficient. At C-band, phase differences tend to be small, but Figure 11.1 shows that much of the field pattern can be seen. Conifers and root crops exhibit a stable phase difference close to 0 degrees (except for one anomaly); whereas the cereals display a noisy negative phase, around -10 degrees on average. Such differences are probably connected with the dominant vertical orientation of the stalks in the cereal canopies, while the other vegetation types have no such preferred orientation in their constituents. Root crops tend to show higher coherence, and in our dataset can be separated from other vegetation types on this basis (except for one exceptional sugarbeet field). At L-band the reduced value of coherence and positive phase difference of conifers are notable, but the variability within the other vegetation types weakens the value of this trend as a classifier. (It should be noted, however, that a large positive phase difference is a very clear indicator of conifer forest at P-band for this test site [31].) Unlike C-band, the cereals and root crops have similar average values of coherence, but this is very variable (extremely so for barley). The correlation phase of the cereals is also very variable but more stable for the root crops.

On the basis of these observations it would be expected that the three broad classes of vegetation should be separable, but individual crop types within each class would be hard to distinguish. An extensive study of fields from the Feltwell area based on the Jeffries–Matsushita separability measure [43], in fact, indicated good separability within the cereal type fields when C- and L-band data are used [32]; the associated classification accuracies are not, however, available. It should also be noted that these conclusions are based on a single acquisition; strategies for separating classes may be clearer when multitemporal data are available.

13.2.3 Texture in Classification

Sections 13.2.1 and 13.2.2 were concerned only with properties of the mean backscattering coefficient or covariance matrix. However, Chapters 8, 9, and 11 showed that texture is certainly present and is a potential information source in at least two circumstances: high-resolution and long-wavelength data. Most of our knowledge about texture, therefore, has been gained from airborne SAR because spaceborne data have not been available at wavelengths longer than L-band and have been of comparatively low resolution. (An exception is the fine mode of Radarsat, as will be discussed in Section 13.6.) As a result, we have little knowledge of its multitemporal behavior.

In addition, most of our understanding of texture is phenomenological: it is a measured parameter whose physical meaning is obscure. Tentative explanations for its occurrence in various circumstances include number fluctuations, and RCS fluctuations (in both cases of unknown physical origin) or, in the case of forest texture, patterns imposed by radar highlights and shadow connected with tree spacing and shape. Inferences in this latter case have been used to explain the increase of texture with incidence angle [44] and to predict conditions under which texture will become measurable for a given forest type [45]. The connection between these different points of view is only just beginning to be made [46]. Despite this uncertain theoretical basis for texture, it plays an important role in several of the classification schemes described in Section 13.6. In particular, it is critical in distinguishing regenerating from primary tropical forest in Radarsat data.

13.3 Decision Rules for Classification

In order to carry out classification we need to define a procedure or a set of decision rules to apply to the data. The approach to defining the decision rules varies widely and is dependent on the amount of knowledge about the nature of SAR statistics and the physics of scattering that goes into their definition. At one end of the spectrum we have purely statistical, data-driven methods, in which some parameters are measured on a given dataset and used in a supervised or unsupervised scheme. A variety of such schemes is discussed in Section 13.4. The most powerful methods to date make full use of the expected statistical models for SAR data to drive a global MAP approach. However, all such schemes have unknown generalizability in time and/or space and rely on large, well-validated, comprehensive datasets if they are to have more than local interest. At the other end of the spectrum, polarimetric data can be classified in terms of the dominant scattering mechanism, as discussed in Section 13.5. This provides a robust approach (if the rules for identifying the different mechanisms are well founded) but suffers from two operational weaknesses: classes in which we are interested may have similar dominant scattering mechanisms and thus be indistinguishable by these means and the relation of the scattering mechanism to a given terrain type is not yet clearly understood. Between these purely statistical and the purely physical approaches lies a range of techniques combining empirical knowledge with physical reasoning. Several viable classification schemes of this type are discussed in Section 13.6.

All these approaches rely to a greater or lesser extent on statistical properties of the data. They also rely on the data from different classes occupying different regions in feature space without much overlap. For a given dataset, this

may not always be the case, as indicated in Section 13.2. A final issue is whether to apply classification procedures at the pixel or region level. In the former case some form of image reconstruction is normally needed to reduce statistical variability. The latter case requires image segmentation. Both approaches have been used and will be met in the following sections.

13.4 Data-Driven Methods of Classification

A purely statistical, data-driven approach to classifying an M -channel data vector \mathbf{A} into one of N classes can be based on Bayesian methods by means of the relation

$$P(n|\mathbf{A}) \propto P(\mathbf{A}|n)P(n) \quad (13.1)$$

where the prior probability of class n occurring is given by $P(n)$ and $P(\mathbf{A}|n)$ is the likelihood that \mathbf{A} occurs, given that the measurement is from class n . The MAP classifier selects that n for which $P(n|\mathbf{A})$ is maximal. This is equivalent to minimizing $(\ln P(\mathbf{A}|n) + \ln P(n))$, which is often a more convenient expression to handle. In order to use MAP classification, both the likelihood $P(\mathbf{A}|n)$ and the prior probabilities $P(n)$ must be available. If the $P(n)$ are unknown, they are often assumed equal for all classes, in which case this approach reduces to ML classification.

For multichannel SAR data, we have seen that there are three basic models for $P(\mathbf{A}|n)$ in which the underlying complex single-look data:

- Are jointly Gaussian;
- Obey a product model for which the texture is the same in all channels (single-frequency polarimetric data);
- Have independently textured channels.

Only for jointly Gaussian data has the classification theory been well-developed (although an approach for single-channel textured SAR data has been proposed in [47]) and we concentrate on this case.

13.4.1 Gaussian MAP Classification

When the multichannel data are Gaussian, all the information is carried by the covariance matrix. Each class is therefore identified by a single covariance matrix or possibly by a range of covariance matrices. The need for considering a range

is well illustrated by Figure 13.1. In this figure, the temporal spacing of the data is large enough to remove any correlation between the measurements (so that they would be of no value for interferometry) and texture is not expected to be present in data from agricultural crops at the ERS-1 resolution of around 24m. Hence, the temporal sequence can be thought of as an M -vector of field-averaged 3-look measurements where the underlying complex data consist of M independent Gaussian channels. It can be seen that although the wheat and sugarbeet classes display different characteristic temporal behaviors, there is considerable variation within each class. This natural variation corresponds to a range of covariance matrices describing a single class.

The basic tool for deriving the properties of M -channel multilook Gaussian data is the complex Wishart distribution [48,49] described in Section 11.6. If A is the observed L -look sample covariance matrix for a class n with fixed covariance matrix C_n , we can associate with it a real vector \mathbf{A} , as in (13.1), whose elements are $\text{Re}(A_{ij})$ and $\text{Im}(A_{ij})$. Then,

$$P(\mathbf{A}|n) = \frac{|A|^{L-M} \exp\{-L\text{tr}(C_n^{-1}A)\}}{K(L, M)|C_n|^L} \quad (13.2)$$

where $K(L, M) = \pi^{M(M-1)/2}\Gamma(L)\cdots\Gamma(L-M+1)L^{-ML}$ and $|\cdot|$ is the determinant. Since A is Hermitian, A_{ii} is real and $A_{ji} = A_{ij}^*$, so the random vector \mathbf{A} contains only M^2 real terms. The MAP classifier will therefore assign an observed \mathbf{A} to the class for which

$$d_n = -\ln P(n) + L[\text{tr}(C_n^{-1}A) + \ln(|C_n|)] \quad (13.3)$$

is minimized. (Note that this measure can be negative since we omitted terms not involving n in $\ln P(\mathbf{A}|n)$). The expression (13.3) is clearly linear in the variables $\text{Re}(A_{ij})$ and $\text{Im}(A_{ij})$, which implies that the decision boundaries (that is, where $d_n = d_m$) are hyperplanes in M^2 dimensions. The one-dimensional version of (13.3) is given as (7.1) for gamma distributed RCS values. This makes clear that the term $\ln(|C_n|)$ corresponds to a measure of the overall spread of values within the population of class n .

Although representing an optimal classifier, (13.3) relies for its success on having known values for $P(n)$ and C_n and the fact that C_n is uniquely defined for class n . In practice, neither condition may hold. Typically $P(n)$ and C_n have to be inferred from the data, in the latter case either by use of training sets (supervised classification) or from clusters inferred from the data (unsupervised classification). Iterative learning of the C_n is possible and gives performance that has been

reported to improve on that of supervised classification in a limited study of sea ice classification [49]. The prior probabilities $P(n)$ present more of a problem because they are rarely known a priori. However, they can have a significant impact on pixel-based classification. This is demonstrated in [50], where it is shown that adaptive learning of the prior probabilities can give markedly improved performance. Notice that if the classes of interest are homogeneous enough to be well represented by a single known covariance matrix, then (13.3) implies that the prior probabilities $P(n)$ become less important as L increases. (Equivalently, as L increases, the MAP and MLE classifiers become equivalent.) Hence, an alternative to learning the prior probabilities is instead to minimize their impact by making L large. However, for large L , mixed populations will often occur within an arbitrary classification window, which indicates that the full power of the classification is best attained within a segmentation where homogeneous regions are first identified, as described in Chapters 7, 8, and 12.

A bigger obstacle to applying (13.3) in practical applications is the variability of the covariance matrix describing a single desired class. This intrinsic variability (rather than variability as a consequence of estimating the class covariance) is obvious from Figures 13.1, 13.3, and 13.4. In some cases this does not represent a fundamental difference in covariance structure and can be dealt with using a normalization by the power in one of the channels [51]. This cannot, however, remove the effects of the highly fluctuating phase differences observed for some cover types in Figure 13.4(b), for example. Where a given class n must be described by a distribution of covariance matrices $P(C_n)$, the likelihood function of class n takes the form

$$P(\mathbf{A}|n) = \int P(\mathbf{A}|C_n)P(C_n) dC_n \quad (13.4)$$

Currently no useful results have emerged from this generalization except in the trivial case where $P(C_n)$ consists of a set of weighted δ -functions (i.e., class n is made up of a set of well-defined subpopulations). However, a procedure based on fuzzy c -means optimization has been reported in [38], which may provide the best approach to this problem, since it allows the data itself to define clusters with adequate separability (which may or may not correspond to desired classes).

The classifier based on (13.3) is very general because:

1. It can be applied to data with any number of looks (including single-look complex, from which an estimate of the covariance matrix would be formed).

2. The decision criterion is applicable to areas of different sizes within the same image.
3. The data type can be polarimetric, interferometric, uncorrelated multichannel (multifrequency, multitemporal), or any combination of these.

The forms of the classifiers for some of these special cases are now discussed.

13.4.2 Single-Frequency Polarimetric Classification

In the special case where only the like-polarized channels have significant correlation, the covariance matrix in each class has the form

$$C = \begin{pmatrix} \sigma_1 & 0 & \sqrt{\sigma_1 \sigma_3} \rho \\ 0 & \sigma_2 & 0 \\ \sqrt{\sigma_1 \sigma_3} \rho^* & 0 & \sigma_3 \end{pmatrix} \quad (13.5)$$

For notational simplicity the subscript n appropriate to class n has been omitted from the parameters σ_i and ρ . Then

$$|C| = \sigma_1 \sigma_2 \sigma_3 (1 - |\rho|^2) \quad (13.6a)$$

and

$$\text{tr}(C^{-1} A) = \frac{A_{22}}{\sigma_2} + \frac{1}{1 - |\rho|^2} \left\{ \frac{A_{11}}{\sigma_1} + \frac{A_{33}}{\sigma_3} - \frac{2}{\sqrt{\sigma_1 \sigma_3}} \text{Re}(\rho A_{13}^*) \right\} \quad (13.6b)$$

13.4.3 Repeat-Pass Interferometry

For classification based on a single interferometric pair the expressions developed in Section 13.4.2 can be used with all terms in σ_2 omitted and subscripts 1 and 3 referring to the two times of image acquisition. Here the classifier tells us how to exploit both the intensity and correlation properties in the image in an optimal way. Notice that in the Gaussian case the Bayesian classifier is linear in terms of the sample covariance matrix. Other linear combinations of these terms or any nonlinear treatment (e.g., based on the log of the data) will not be optimal.

13.4.4 Uncorrelated Channels

When the channels are uncorrelated, the covariance matrix of class n is diagonal

$$C_n = \text{diag}[\sigma_{1n}, \sigma_{2n}, \dots, \sigma_{Mn}]$$

with inverse

$$C_n^{-1} = \text{diag}[\sigma_{1n}^{-1}, \sigma_{2n}^{-1}, \dots, \sigma_{Mn}^{-1}]$$

Then

$$d_n = -\ln P(n) + L \left\{ \sum_{i=1}^M \left(\frac{A_{ii}}{\sigma_{in}} + \ln \sigma_{in} \right) \right\} \quad (13.7)$$

with the decision boundary between class m and n defined by

$$\sum_{i=1}^M A_{ii} \left(\frac{1}{\sigma_{im}} - \frac{1}{\sigma_{in}} \right) = \frac{1}{L} \ln \left(\frac{P(m)}{P(n)} \right) - \sum_{i=1}^M \ln \left(\frac{\sigma_{im}}{\sigma_{in}} \right) \quad (13.8)$$

As expected, the decisions are based just on the sample intensities because any observed correlations between channels are simply due to finite sampling effects. In such circumstances, we can instead consider only the measured intensities in our data vector. The joint PDF, therefore, is a product of independent L -look gamma distributions, and the distance measure between classes is exactly the same as that given by (13.3). An advantage of taking this approach is that it is applicable when the number of looks in different channels is different. This can arise, for example, if the observing geometries for a given region are different between channels because the flight lines of the sensor varied between observations. In this more general case,

$$P(A_{11}, A_{22}, \dots, A_{MM}|n) = \prod_{i=1}^M \left(\frac{L_i}{\sigma_{in}} \right)^{L_i} \frac{A_{ii}^{L_i-1}}{\Gamma(L_i)} \exp \left(-\frac{L_i A_{ii}}{\sigma_{in}} \right) \quad (13.9)$$

and

$$d_n = -\ln P(n) + \sum_{i=1}^M L_i \left(\frac{A_{ii}}{\sigma_{in}} + \ln \sigma_{in} \right) \quad (13.10)$$

13.4.5 Applications of MAP Classification

The data type that has attracted most attention for the application of MAP classification methods is multifrequency polarimetric data, in most cases ignoring the correlation of the like and crosspolarized terms, as described in Section 13.4.2. As would be expected, different levels of performance are recorded, dependent on the problem. Very high levels of accuracy are found in a three-class separation into urban, vegetation, and ocean classes using iterative learning of the prior probabilities [50]; other approaches applied to the same dataset using nonadaptive methods do not perform as well [51–54]. Of these latter studies [51] is noteworthy because it demonstrates the improvement in performance as the number of looks increases. This is also demonstrated in [52] in a two-class separation into grassland and forest; 16 looks were required to reduce the overall probability of error to less than 10% in this case. Our own experience with MAP crop classification in the Feltwell area gave poor results, in our view due to the overlap of classes and the large variability within classes (see Figures 13.3 and 13.4). Similar poor performance was noted in [35] for a mixed agricultural and forested test site.

However, the most refined assessments of MAP methods are those described in [38,55,56], where they are embedded in a global MAP approach using simulated annealing. Very good classification accuracies are recorded for agricultural and geological applications in [55]. This study noted the importance of reducing within-class variability by restricting the range of incidence angles encountered in the data. (Associated problems caused by relief are noted in [38].) As a result of this restriction, the limited area considered, or the intrinsic homogeneity of the areas considered, class clusters were both compact and well separated, leading to the observed good performance. The application of these techniques to a sea-ice classification in [38] provides good visual results, although not quantitatively assessed due to absence of in situ data.

These techniques also provided classification accuracies exceeding 90% for different Alaskan forest types, as reported in [56]. Interestingly, this study clearly illustrates that the best results were obtained for this purpose using crosspolarized data only at two frequencies. Results got worse when full polarimetric data were employed, because the addition of channels that provide no discriminating capability acts as a noise source to the classifier [56]. Although requiring

considerable computing power, such techniques currently appear to provide the most promising approach to data-driven classification.

13.4.6 Other Data-Driven Approaches

In addition to the global MAP approach, other data-driven methods have been reported, using rules derived from inspection of the data or clustering techniques. The examples given in this section are completely data-driven and hence suffer from the risk of particularity implicit in using a single dataset. We also include in this section a brief review of classification methods based on image filtering. These are data-driven in the sense that they rely entirely on estimated or predefined covariance properties of the scene constituents. Rule-based systems with a more explicit physical content that therefore possess greater generalization capabilities will be introduced in Section 13.6.

A typical example of a rule-based approach is given in [36], where SIR-C data of the Amazon floodplain (C- and L-band σ^0 values in the three channels but no correlation parameters) were used in a hierarchical scheme to distinguish flooded and nonflooded forest, clearings, floating vegetation, and open water, with very good classification accuracies. The study of agricultural classification using AirSAR data reported in [33] also made use of a hierarchical decision tree. In this case thirteen different classes including relevant crop types were identified, with good classification accuracies reported, except for confusion between cereal type crops (as might be expected from the results reported in Section 13.2.2). However, the decision rules were not recorded, and it was noted that they were not transportable in time or space.

Cluster-based approaches simply attempt to identify types of pixels or regions that clump together in feature space and then to mark in decision boundaries that separate clusters in some way, usually on the basis of a distance measure. Clusters can be identified in an unsupervised (use the data to identify clusters) or supervised (use the desired classes to identify cluster centers and properties) manner. Both methods have been used for SAR data, including those making use of global MAP methods and simulated annealing reported previously [38,55,56]. Another example of such an approach is given in [39] that used the same dataset as in [33], but no indication of comparative performance was given. Three-channel C-band polarized powers were combined with texture in an agricultural study [40]; here it was shown that row direction must be included in the class descriptor for cereal crops. Neural nets have also been used to carry out this process [41,42]; in [42] they were combined with a more direct maximum likelihood classifier that was applied iteratively after cluster centers were identified.

The statistical classification schemes described previously and in Sections 13.4.1 to 13.4.4 make a direct class assignment based on the observed properties

of the covariance data. A different approach instead uses a particular feature or set of features extracted from the data to make a decision [57–59]. Such features can be displayed in image form and, hence, readily used for visual image analysis. In essence, this approach is a target-detection problem, particularly when only a two-class separation is performed. Since this problem is well-reported elsewhere, here we only briefly review the work in this area. It is particularly relevant to polarimetric data, and we describe it within this context.

In Section 12.3 we considered linear filters of the form $\mathbf{w} = P\mathbf{z}$ from which an intensity image

$$J = \sum_i |w_i|^2 = \mathbf{z}^\dagger A \mathbf{z} = \text{tr}(A \mathbf{z} \mathbf{z}^\dagger)$$

could be formed. Here $A = P^\dagger P$. For a two-class separation, the problem is then to determine the matrix A giving the maximum mean intensity ratio between the *target* class and the *clutter* class, that is, to maximize $r_{tc} = \text{tr}(AC_t)/\text{tr}(AC_c)$ where C_t and C_c are the covariance matrices of target and clutter classes, respectively. This is known as *polarimetric matched filtering* [52,60,61]. As noted in [60], a possibly more useful approach is to maximize the *contrast* between the two classes. In this case, the matrices A_{\max} and A_{\min} , which give rise to the maximum and minimum values of r_{tc} , are found; if $r_{tc}(\max) > r_{tc}^{-1}(\min)$, A_{\max} provides the maximum contrast filter; otherwise A_{\min} is selected. Both forms of filtering can be translated into optimum transmit and receive polarizations [52,53]. Explicit solution schemes for these problems and examples of the use of this approach for distributed target discrimination in polarimetric data will be found in [52,53]. However, the value of the full polarimetric approach has been called into question by Novak et al. [61] when detecting man-made targets in clutter. Here it was found that simpler detectors using only intensity information provided comparable or better performance than the polarimetric matched filter (for the same number of transmitted pulses), without requiring the exact knowledge of target and clutter covariance needed for the polarimetric matched filter. (By contrast, Novak et al. [62] note the value of the polarimetric *whitening* filter in target detection; see Section 12.3.1.) Since target detection is the most usual example of where a simple binary classification is sufficient, the real value of such techniques in remote sensing is therefore still unclear.

13.5 Classification Based on Scattering Mechanism

The previous section considered the problem of classification in terms of the experimental data available from different systems and for different types of land

cover. When applied blind, such an approach is necessarily limited by the data in hand; it is essentially about correlation and its conclusions are local. Only by dealing with very large, diverse datasets can general conclusions emerge. In recognition of this, several of the studies reported previously did not take a purely data-related approach and used physical reasoning to explain the observed properties of the classification.

While providing a normal and necessary first step in assessing the information carried by the data, a correlative approach cannot explain its own limitations or be generalized in any reliable way outside the conditions defined by the existing observations. It is also constrained by the structuring of the data. Unless all the significant controlling variables are recorded, variations in the measurements (e.g., due to row direction, soil moisture, and slope) may simply appear as unexplained factors causing scatter in the observations.

For this reason, there has been an increased use of physically based reasoning and models both to interpret the observations and to guide the nature of the classification. In its purest form, this approach seeks a classification based on scattering *mechanism* (in other words, what physically gives rise to the different properties of the observed signal?), which we can then attempt to map onto more familiar target descriptions by an understanding of how these targets interact with microwaves. Classification by mechanism can be further refined by detailed treatment of targets exhibiting similar broad scattering properties. One of its major advantages, as noted in [63], is that this approach is completely general. It requires no training or knowledge of the scene, only an understanding of the signatures of different scattering mechanisms. A disadvantage is that it provides no information in regions dominated by single scattering mechanisms; for an example drawn from geology, see [38].

Polarimetric data provide the clearest example of this approach. As shown in [63], polarimetry can distinguish scattering events in which an even or odd number of reflections occur as well as a further class of diffuse scattering with mixtures of even and odd reflections. These descriptions can be related to deterministic scatterers but also to random surfaces and random media through the use of scattering models. Figure 13.5 shows an example of this classification applied to a region of mixed forest and agriculture near Feltwell, UK, using AirSAR polarimetric data at C-, L-, and P-bands, with white and gray denoting odd and even numbers of reflections, respectively, and black indicating diffuse scattering. A comparison with a map indicates that the diffuse scattering regions in the L-band data are forest and provide a very good discrimination of forest from agricultural fields; the latter are characterized by an odd number of reflections at this frequency. The C-band results indicate that some of the forest regions give rise to diffuse scattering, but most areas provide single reflection signatures. The P-band results are hardest to interpret. Even number reflection

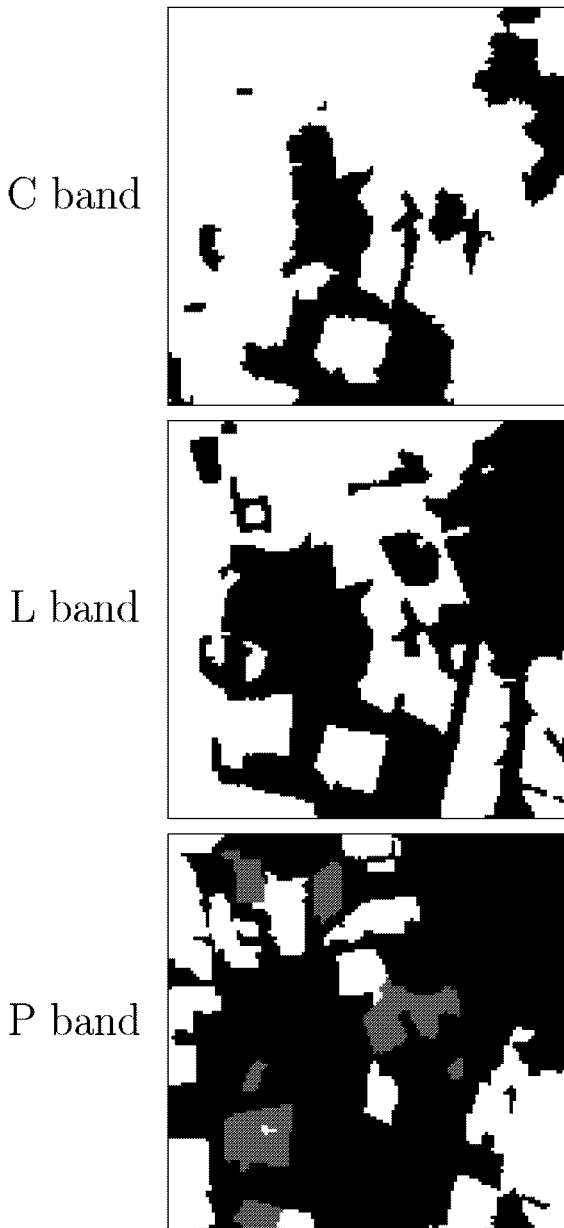


Figure 13.5 Classification of C-, L-, and P-band AirSAR data by scattering mechanism for an area consisting of mixed forest and agricultural fields. White denotes an odd number of reflections, gray an even number, and black corresponds to diffuse scattering.

signatures are found in several agricultural fields (unfortunately, we do not have a detailed description of the cover types or region characteristics for these areas), and diffuse scattering is encountered in many areas other than the forest. (In at least some cases, these correspond to regions with low shrubs.) These results are found even though the P-band forest data in particular show the large HH-VV phase differences expected for an even number of reflections.

Recognition of a dominant scattering mechanism within each region also forms the basis of the classification scheme described in [64]. In this case the eigenvectors of the covariance matrix are interpreted as evidence of different scattering processes and the degree of mixing or randomness of the mechanism is quantified by an entropy measure. Two examples of resulting classifications will be found in [64]: in one case applied to distinguishing urban, ocean and vegetated areas, and in the other for discriminating forest from clear cut areas. However, whether this approach provides new insights into the information carried by polarimetric data needs further investigation, since it relies on post-processing of the covariance matrix, which is the primary information source (and is directly provided by scattering models, for example). Also, in moving to quantities derived from the covariance matrix, the estimation theory for the extracted parameters loses the well-known structure available for the covariance matrix itself (see [48] and Chapter 11).

13.6 Knowledge-Based Classification

In a knowledge-based approach, generic characteristics of different cover types are derived, based on the available empirical evidence, and combined with physical reasoning to define classification rules. Because of their emphasis on the physical content of the SAR data, they attempt to generate robust, widely applicable methods that nonetheless have to take into account local conditions. An important and spectacular example of the power of this approach is in the use of the ERS-1 SAR for monitoring wetland rice. In contrast to the well-structured field pattern, large fields (in many areas), and season-related crop calendar characteristic of European agriculture that informed our discussion in Section 13.2, tropical areas often have small fields with diverse crops and overlapping growing cycles. Under these circumstances, spaceborne SAR monitoring may seem unlikely to be useful. However, one can exploit the large dynamic range of the C-band σ^0 signature of wetland rice through its growing cycle, of the order of 10 dB, together with understanding of how this change is related to the crop state [65,66]. In particular, the dominant scattering mechanism that gives rise to the observed backscattering behavior is provided by the vegetation/water

interaction, which increases as plant biomass increases. Without the underlying water, this scattering mechanism would be replaced by a much weaker interaction of the canopy and soil surface and the characteristic multitemporal signature displayed by wetland rice would be lost.

Change detection on images from different dates can therefore provide a classification into early rice, late rice, and nonrice areas, as demonstrated in a study of a test site in Indonesia [65]. As in the Tapajos forest study described in Section 12.6, the data required preprocessing to reduce the effects of speckle on classification performance, in this case based on multitemporal filtering [67] followed by maximum a posteriori (gamma MAP) spatial filtering [68]. Figure 13.6 shows ERS-1 PRI images acquired on (a) February 16, 1994 and (b) March 6, 1994; while (c) displays the filtered ratio image and (d) the classified image. In (d) the dark regions correspond to early rice, light gray to late rice, and white to nonrice. Separability is made much clearer by the use of color [65].

Although the methods used are closely related to those for tropical forest/nonforest separation described in Section 12.6, some points of difference must be noted if the results are to be compared.

1. The changes for wetland rice are much larger than the 3 dB observed for nonforest regions at Tapajos, in principle allowing greater classification accuracy.
2. The gamma MAP filter did not perform very well for the forestry example given in Chapter 12 (see Figure 12.17(b)) but produces acceptable results here. This may be because no postprocessing was performed in Figure 12.17(b). In Figure 13.6, however, a last stage reclassifies isolated pixels to be consistent with their neighbors [65].
3. No extensive ground data or corroborative evidence were available to validate the classification in Figure 13.6(d), whereas in Section 12.6 TM data was used to provide a reference. (SPOT data were available over the study area but were unable to provide a useful discrimination of the growth stage of the rice.) The justification for the classification is therefore primarily on the basis of the known relation of RCS to rice growth stage [65].

Physical insight combined with examination of data has lead to a number of other viable rule-based classification schemes, in a variety of contexts. In [35] a hierarchical scheme was used to classify image pixels from combined L- and C-band AirSAR data into four classes: tall vegetation (trees), short vegetation, urban, and bare surfaces, using polarimetric parameters (but not phase difference) and texture. Accuracies between 91% and 100% were recorded.

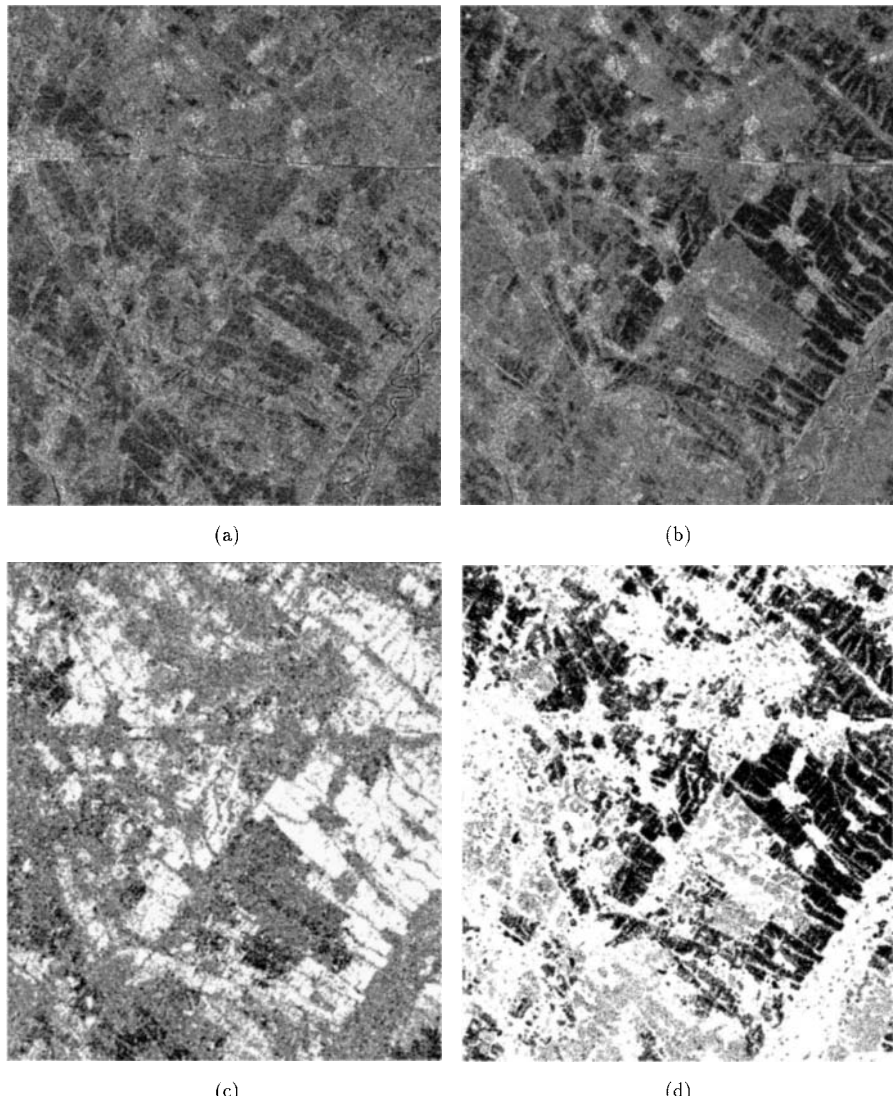


Figure 13.6 (a) ERS-1 PRI image of the Demak area, Indonesia, for February 16, 1994; (b) corresponding image for March 6, 1994 (Copyright ESA). (c) Ratio image formed after preprocessing; (d) image classification: early rice (black); late rice (mid-gray); nonrice (white) (*From: [65]. © 1997 IEEE.*)



(a)



(b)

Figure 13.7 (a) Radarsat fine-mode image from Tapajos, Brazilian Amazonia (© Canadian Space Agency/Agence Spatiale Canadienne, 1997). (b) Image in (a) after application of 5 by 5 Frost filter. (c) Coefficient of variation in (a) using a 7 by 7 sliding window. (d) Order parameter in (a) within an 11 by 11 sliding window [69].



(c)



(d)

Figure 13.7 (continued).

Similar principles were used in [37] (which also includes a survey of previous classification studies) for ERS-1/JERS-1 coregistered images, where now the tree class was further broken down into structural form and leaf type (broad leaf or needles). Another hierarchical scheme combined AirSAR and SIR-C data to distinguish agricultural crops and other sorts of land cover using pixel-based methods [34], with reasonable accuracies obtained.

Texture in SIR-C L-band data was one of the parameters used in [35] to make a separation between forest and low vegetation. Its value as a discriminator of forest from nonforest in tropical regions was also clearly demonstrated using airborne data in Chapter 8. A further striking example of how it may provide the most important information source in tropical forest monitoring is illustrated by Figure 13.7 [69]. The four panels in the figure show (a) a fine-mode Radarsat image (resolution of the order 6m by 8.9m) from the Tapajos region of Brazilian Amazonia (which is the same region as that shown in Figure 12.13); (b) the image in (a) after applying a 5 by 5 Frost filter [70]; (c) the coefficient of variation in image (a) calculated within a 7 by 7 sliding window; (d) the estimated order parameter in image (a), assuming K-distributed data, calculated within an 11 by 11 sliding window. The data were obtained under the Radarsat Announcement of Opportunity under a Principal Investigatorship held by Dr. C. C. F. Yanasse of INPE. This set of images illustrates a number of important issues. First, the resolution and incidence angle afforded by the Radarsat fine mode clearly allows texture to be discriminated from space and as predicted for the Tapajos region in [45]. Second, as expected from airborne data gathered during the SAREX campaign [44,71], texture is perhaps the most important discriminator for distinguishing cover types in tropical regions (and probably other forested regions of the world) if C-band data are to be used. Third, and of great significance, is that texture allows us to distinguish regions of regenerating and primary forest. This can be seen at the upper left of the roughly rectangular area of pasture in the middle of the image, which is an area of regenerating forest. It displays comparatively low values in the coefficient of variation image, which are equivalent to large order parameters. Hence it is dark in Figure 13.7 (c) and bright in Figure 13.7(d). We can interpret this as indicating that in the regenerating forest there is a more uniform canopy than in the primary forest; in the latter, emergent trees create a much “rougher” canopy topography, leading to greater variation in backscatter due to radar shadows and highlights.

13.7 Using SAR Properties To Refine a Classification

In Section 13.1, we discussed how the sensitivity of SAR to biophysical parameters such as plant structure, biomass, and soil moisture can complicate its use in

classification. This sensitivity can, of course, be turned to an advantage when interpreting a classified image (with classification derived from a map or optical data or from the SAR itself) because it may permit internal properties of each class to be inferred. This type of refined classification may in some cases provide the most telling contribution of SAR to monitoring and understanding the dynamics of vegetated surfaces.

As an example, we show in Figure 13.8 a biomass map inferred from SIR-C data acquired on October 1994, from the Nezer test site in the Landes Forest, France. In this case both the classification and the biomass are inferred from the SAR data alone by a two-step process. The *discrimination* of forest from nonforest (clear cut) is achieved by use of the C-band HH-VV correlation coefficient, estimated from the 8-look data by means of a 3 by 3 sliding window. This provides

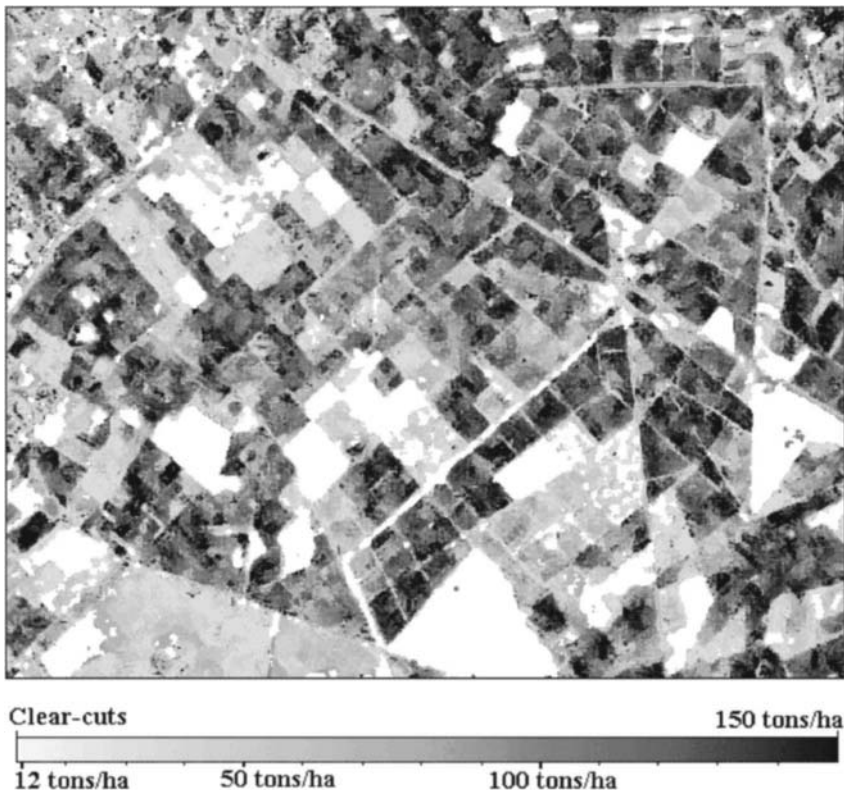


Figure 13.8 Biomass map of the Nezer test site, les Landes, France, derived from SIR-C data [72].

a robust classifier because it is consistently higher for soil surfaces than for forest, whatever the soil moisture or roughness state. It is also insensitive to miscalibration and slope effects because it is formed by channel ratios, as discussed in Chapter 11. The accuracy of the forest/nonforest separation is around 87% [72].

The *mapping of forest biomass* relies on the L-band HV backscattering coefficient, estimated after applying the Kuan et al. filter [73] over a 9 by 9 window. This parameter is known to be sensitive to biomass in the range of 0 to 65 tonnes/ha [74]. A strong relationship between the two can be established in les Landes because of the dominance of maritime pine in this area, with ensuing regularity of tree structure [74]. Training stands indicate an accuracy of about 80% for classification into five biomass ranges (clear cut, 8 to 20 tonnes/ha, 21 to 33 tonnes/ha, 34 to 50 tonnes/ha, and greater than 50 tonnes/ha).

13.8 Concluding Remarks

Classification is a requirement for many applications of SAR data, both as an end in itself and as a precursor to bringing other knowledge to bear. As an example, once an object is recognized as a field of wheat or rice, knowledge of its multitemporal or polarimetric signature may permit us to infer its state of development or its health. Many approaches to classification are possible, ranging from those making extensive use of the scattering physics of different kinds of terrain, which are inherently transportable and capable of generalization, to limited studies that are purely data based and of little general value. Most informed studies to date lie somewhere between these two extremes, with physical argument being used to comment on the interpretation and generalizability of statistical or rule-based approaches.

Because of the diversity of data types, test sites, and applications, there are few areas in which preferred or optimal methods are clear. Equally, rigorous evaluation of methods has only been attempted in a small number of cases. What does seem clear is that in order to minimize the within-class variability and hence to provide a well-defined description of the classes, disturbing effects must be accounted for or steps taken to mitigate them (e.g., in an agricultural context, there are known effects on a single crop type from such factors as incidence angle, row direction, soil type variations, differing crop calendars, and crop variety). The extent to which this will prevent the development of widely applicable reliable methods is not known. The fundamental issue is whether the classes desired for a given application show the degree of stability, homogeneity, and separability in the available radar data to be accurately identified. As indicated in this chapter, this is a focal point at which experiment, physical

modeling, data models, parameter estimation, statistical methods, computational techniques, and applications all meet.

References

- [1] Rott, H., P. Skvarca, and T. Nagler, "Rapid Collapse of Northern Larsen Ice Shelf, Antarctica," *Science*, Vol. 271, 1996, pp. 788–792.
- [2] New Views of the Earth: Scientific Achievements of ERS-1, ESA SP-1176/I, 1996.
- [3] New Views of the Earth: Applications Achievements of ERS-1, ESA SP-1176/II, 1996.
- [4] Second ERS Applications Workshop, London, ESA SP-383, 1996.
- [5] Special Issue on SIR-C/X-SAR, *IEEE Trans. Geosci. Remote Sensing*, Vol. 33, 1995.
- [6] Elachi, C., *Spaceborne Radar Remote Sensing: Applications and Techniques*, New York: IEEE Press, 1987.
- [7] *Proc. of the First ERS-1 Symp.*, Cannes, ESA SP-359, 1993.
- [8] *Proc. of the Second ERS-1 Symp.*, Hamburg, ESA SP-361, 1994.
- [9] *Proc. of the Third ERS-1 Symp.*, Florence, ESA SP-414, 1997.
- [10] Le Toan, T., "Scatterometer Measurements on Crop and Soil Surfaces," *Proc. ESA-EARSeL Workshop*, Alpbach, ESA SP-166, 1981, pp. 99–110.
- [11] Le Toan, T., A. Lopes, and M. Huet, "On the Relationships Between Radar Backscattering Coefficient and Vegetation Canopy Characteristics," *Proc. IGARSS 84 Symp.*, Strasbourg, ESA SP-215, 1984, pp. 155–160.
- [12] Lopes, A., and T. Le Toan, "Effet de la Polarisation d'une Onde Electromagnetique dans l'Atténuation de l'Onde dans un Couvert Végétal," *Proc. Third Int. Symp. on Spectral Signatures of Objects in Remote Sensing*, Les Arcs, ESA SP-247, 1985, pp. 117–122.
- [13] Alphonse, and T. Le Toan, "Retrieving Vegetation and Soil Parameters from Radar Measurements," *Proc. Fourth International Symp. on Spectral Signatures of Objects in Remote Sensing*, Aussois, ESA SP-287, 1988, pp. 105–111.
- [14] Bush, T. F., and F. T. Ulaby, "Fading Characteristics of Panchromatic Radar Backscatter from Selected Agricultural Targets," *IEEE Trans. Geosci. Electronics*, No. 13, 1976, pp. 149–157.
- [15] Ulaby, F. T., "Radar Response to Vegetation," *IEEE Trans. Antennas and Propagation*, Vol. 23, 1975, pp. 36–45.
- [16] Ulaby, F. T., T. F. Bush, and P. P. Batlivala, "Radar Response to Vegetation II: 8–18 GHz Band," *IEEE Trans. Antennas and Propagation*, No. 23, 1975, pp. 608–618.
- [17] Bush, T. F., and F. T. Ulaby, "An Evaluation of Radar as a Crop Classifier," *Remote Sensing of Environment*, Vol. 7, 1978, pp. 15–36.
- [18] Ulaby, F. T., C. Allen, G. Eger, and E. Kanemasu, "Relating the Radar Backscattering Coefficient to Leaf Area Index," *Remote Sensing of Environment*, Vol. 14, 1984, pp. 113–133.
- [19] Hoekman, D. H., L. Krul, and E. P. W. Attema, "A Multi-Layer Model for Backscattering

- from Vegetation Canopies," *Proc. IGARSS 82 Symp.*, Munich, IEEE Pub., 1982, pp. 41–47.
- [20] Ulaby, F. T., R. K. Moore, and A. K. Fung, *Microwave Remote Sensing: Active and Passive*, Vol. 2, Reading, MA: Addison-Wesley, 1982.
- [21] Yanasse, C. C. F., S. Quegan, and R. J. Martin, "Inferences on Spatial and Temporal Variability of the Backscatter from Growing Crops Using AgriSAR Data," *Int. J. Remote Sensing*, Vol. 13, 1992, pp. 493–507.
- [22] Snoeij, P., and P. J. F. Swart, "Processing and Calibration of the DUTSCAT Data During the AGRISCATT Campaigns," *Proc. MAESTRO/AGRISCATT Final Workshop: Radar Techniques for Forestry and Agricultural Applications*, ESA WPP-31, 1992, pp. 160–164.
- [23] Hawkins, R. K., and L. D. Teany, "SAREX 1992 Data Calibration," *Proc. SAREX-92 Workshop: South American Radar Experiment*, ESA WPP-76, 1993, pp. 41–53.
- [24] Shimada, M., and M. Nakai, "Inflight Evaluation of L Band SAR of Japanese Earth Resources Satellite-1," *Adv. Space Res.*, Vol. 14, 1994, pp. 231–240.
- [25] Rossi, M., B. Rognon, and D. Massonnet, "JERS-1 SAR Image Quality and Interferometric Potential," *IEEE Trans. Geosci. Remote Sensing*, Vol. 34, 1996, pp. 824–827.
- [26] Satellite Radar in Agriculture: Experience with ERS-1, ESA SP-1185, 1995.
- [27] Wegmuller, U., and C. Werner, "Retrieval of Vegetation Parameters with SAR Interferometry," *IEEE Trans. Geosci. Remote Sensing*, Vol. 35, 1997, pp. 18–24.
- [28] Hagberg, J. O., L. M. H. Ulander, and J. Askne, "Repeat-pass SAR Interferometry over Forested Terrain," *IEEE Trans. Geosci. Remote Sensing*, Vol. 33, 1995, pp. 331–340.
- [29] Lemoine, G., H. de Groot, and H. J. C. Leeuwen, "Monitoring Agricultural Land Preparation Activities with ERS-1 to Complement and Advance Early Season Crop Estimates in the Framework of the MARS Project," *Second ERS Applications Workshop*, London, ESA SP-383, 1996, pp. 7–12.
- [30] Nghiem, S. V., S. H. Yueh, and R. Kwok, "Symmetry Properties in Polarimetric Remote Sensing," *Radio Sci.*, Vol. 27, 1992, pp. 693–711.
- [31] Quegan, S., and I. Rhodes, "Statistical Models for Polarimetric Data: Consequences, Testing and Validity," *Int. J. Remote Sensing*, Vol. 16, 1995, pp. 1183–1210.
- [32] Cordey, R. A., J. T. Macklin, P. A. Wright, P. J. Saich, S. Quegan, A. Wielogorska, and W. P. Loughlin, "Studies of Multi-frequency and Multi-polarisation SAR Applications," Final Report on DRA Contract RAE 1B/89, GEC-Marconi Research Centre Doct. MTR 93/73A, Vol. 3, 1993.
- [33] Freeman, A., J. Villasensor, J. D. Klein, P. Hoogeboom, and J. Groot, "On the Use of Multi-Frequency and Polarimetric Radar Backscatter Features for Classification of Agricultural Crops," *Int. J. Remote Sensing*, Vol. 15, 1994, pp. 1799–1812.
- [34] Ferrazoli, P., S. Paloscia, P. Pampaloni, G. Schiavon, S. Sigismondi, and D. Solimini, "The Potential of Multifrequency Polarimetric SAR in Assessing Agricultural and Arboreous Biomass," *IEEE Trans. Geosci. Remote Sensing*, Vol. 35, 1997, pp. 5–17.
- [35] Pierce, L. E., F. T. Ulaby, K. Sarabandi, and M. C. Dobson, "Knowledge-based Classification of Polarimetric SAR Images," *IEEE Trans. Geosci. Remote Sensing*, Vol. 32, 1994, pp. 1081–1086.
- [36] Hess, L. L., J. M. Melack, S. Filoso, and Y. Wang, "Delineation of Inundated Area and

- Vegetation Along the Amazon Floodplain with the SIR-C Synthetic Aperture Radar," *IEEE Trans. Geosci. Remote Sensing*, Vol. 33, 1996, pp. 896–904.
- [37] Dobson, M. C., L. E. Pierce, and F. T. Ulaby, "Knowledge-based Land-Cover Classification Using ERS-1/JERS-1 SAR Composites," *IEEE Trans. Geosci. Remote Sensing*, Vol. 34, 1996, pp. 83–99.
- [38] Rignot, E. J. M., R. Chellappa, and P. Dubois, "Unsupervised Classification of Polarimetric Data Using the Covariance Matrix," *IEEE Trans. Geosci. Remote Sensing*, Vol. 30, 1992, pp. 697–705.
- [39] Wong, Y.-F., and E. C. Posner, "A New Clustering Algorithm Applicable to Multispectral and Polarimetric SAR Images," *IEEE Trans. Geosci. Remote Sensing*, Vol. 31, 1993, pp. 634–644.
- [40] Anys, H., and D.-C. He, "Evaluation of Textural and Multipolarisation Radar Features for Crop Classification," *IEEE Trans. Geosci. Remote Sensing*, Vol. 33, 1995, pp. 1170–1181.
- [41] Chen, K. S., W. P. Huang, D. H. Tsay, and F. Amar, "Classification of Multifrequency Polarimetric SAR Imagery Using a Dynamic Learning Neural Network, *IEEE Trans. Geosci. Remote Sensing*, Vol. 34, 1996, pp. 814–820.
- [42] Hara, Y., R. G. Atkins, S. H. Yueh, R. T. Shin, and J. A. Kong, "Application of Neural Networks to Radar Image Classification," *IEEE Trans. Geosci. Remote Sensing*, Vol. 32, 1994, pp. 100–109.
- [43] Swain, P. H., and S. M. Davis, *Remote Sensing: The Quantitative Approach*, New York: McGraw-Hill, 1978.
- [44] Beaudoin, A., M. Deshayes, S. Hardy, T. Le Toan, and D. Girou, "Use of Airborne SAR Data for the Mapping of Shifting Cultivation in French Guiana," Proc. SAREX-92 Workshop, ESA WPP-76, 1994, pp. 185–191.
- [45] Oliver, C. J., A. Blake, and R. G. White, "Optimum Texture Analysis of SAR Images," *SPIE Conf. on Algorithms for Synthetic Aperture Radar Imagery*, Orlando, FL, *SPIE Proc.*, Vol. 2230, 1994, pp. 389–398.
- [46] Williams, M. L., "The Influence of Canopy Shape on SAR Speckle Distributions over Woodland," *Proc. IGARSS 97*, Singapore, 1997, pp. 755–757.
- [47] Nezry, E., A. Lopes, D. Ducrot-Gambart, C. Nezry, and J.-S. Lee, "Supervised Classification of K-Distributed SAR Images of Natural Targets and Probability of Error Estimation," *IEEE Trans. Geosci. Remote Sensing*, Vol. 34, 1996, pp. 1233–1242.
- [48] Goodman, N. R., "Statistical Analysis Based on a Certain Multivariate Gaussian Distribution (an Introduction)," *Ann. Math. Stat.*, Vol. 34, 1963, pp. 152–177.
- [49] Lee, J.-S., M. R. Grunes, and R. Kwok, "Classification of Multi-look Polarimetric SAR Imagery Based on Complex Wishart Distribution," *Int. J. Remote Sensing*, Vol. 15, 1994, pp. 2299–2311.
- [50] van Zyl, J. J., and C. F. Burnette, "Bayesian Classification of Polarimetric SAR Images Using Adaptive a Priori Probabilities," *Int. J. Remote Sensing*, Vol. 13, 1992, pp. 835–840.
- [51] Yueh, H. A., A. A. Swartz, J. A. Kong, R. T. Shin, and L. M. Novak, "Bayes Classification of Terrain Cover Using Normalized Polarimetric Data," *J. Geophys. Res.*, Vol. 93, 1988, pp. 15261–15267.
- [52] Kong, J. A., H. A. Yueh, H. H. Lim, R. T. Shin, and J. J. van Zyl, "Classification of Earth Terrain Using Polarimetric Radar Images," *Progress in Electromagnetics Research: Polarimetric*

- Remote Sensing*, J. A. Kong (ed.), New York, Amsterdam, and London: Elsevier, 1990, pp. 327–370.
- [53] van Zyl, J. J., H. A. Zebker, and C. Elachi, “Polarimetric SAR Applications,” *Radar Polarimetry for Geoscience Applications*, F. T. Ulaby and C. Elachi (eds.), Norwood, MA: Artech House, 1990, pp. 315–360.
- [54] Lim, H. H., A. A. Swartz, H. A. Yueh, J. A. Kong, R. T. Shin, and J. J. van Zyl, “Classification of Earth Terrain Using Polarimetric Synthetic Aperture Radar Images,” *J. Geophys. Res.*, Vol. 94, 1989, pp. 7049–7057.
- [55] Rignot, E. J. M., and R. Chellappa, “Segmentation of Polarimetric Synthetic Aperture Radar Data,” *IEEE Trans. Image Processing*, Vol. 1, 1992, pp. 281–299.
- [56] Rignot, E. J. M., C. L. Williams, J. B. Way, and L. A. Viereck, “Mapping of Forest Types in Alaskan Boreal Forests Using SAR Imagery,” *IEEE Trans. Geosci. Remote Sensing*, Vol. 32, 1994, pp. 1051–1059.
- [57] Evans, D. L., T. G. Farr, J. J. van Zyl, and H. A. Zebker, “Radar Polarimetry: Analysis Tools and Applications,” *IEEE Trans. Geosci. Remote Sensing*, Vol. 26, 1988, pp. 774–789.
- [58] Zebker, H. A., J. J. van Zyl, and D. N. Held, “Imaging Radar Polarimetry from Wave Synthesis,” *J. Geophys. Res.*, Vol. 92, 1987, pp. 683–701.
- [59] Touzi, R., S. Goze, T. Le Toan, and A. Lopes, “Polarimetric Discriminators for SAR Images,” *IEEE Trans. Geosci. Remote Sensing*, Vol. 30, 1992, pp. 973–980.
- [60] Swartz, A. A., H. A. Yueh, J. A. Kong, L. M. Novak, and R. T. Shin, “Optimal Polarisations for Achieving Maximum Contrast in Radar Images,” *J. Geophys. Res.*, Vol. 93, 1988, pp. 15252–15260.
- [61] Novak, L. M., M. B. Sechtin, and M. J. Cardullo, “Studies of Target Detection Algorithms that Use Polarimetric Radar Data,” *IEEE Trans. Aerosp. Elect. Systems*, Vol. 2, 1989, pp. 150–165.
- [62] Novak, L. M., G. J. Owirka, and C. M. Netishen, “Radar Target Identification Using Spatial Matched Filters,” *Pattern Recognition*, Vol. 27, 1994, pp. 607–617.
- [63] van Zyl, J. J., “Unsupervised Classification of Scattering Behaviour Using Radar Polarimetry Data,” *IEEE Trans. Geosci. Remote Sensing*, Vol. 27, 1989, pp. 36–45.
- [64] Cloude, S. R., and E. Pottier, “An Entropy Based Classification Scheme for Land Applications of Polarimetric SAR,” *IEEE Trans. Geosci. Remote Sensing*, Vol. 35, 1997, pp. 68–78.
- [65] Le Toan, T., F. Ribbes, L.-F. Wang, N. Flouri, K.-H. Ding, J. A. Kong, M. Fujita, and T. Kurosu, “Rice Crop Mapping and Monitoring Using ERS-1 Data Based on Experiment and Modelling Results,” *IEEE Trans. Geosci. Remote Sensing*, Vol. 35, 1997, pp. 41–56.
- [66] Kurosu, T., M. Fujita, and K. Chiba, “Monitoring of Rice Crop Growth from Space Using ERS-1 C-band SAR,” *IEEE Trans. Geosci. Remote Sensing*, Vol. 33, 1995, pp. 1092–1096.
- [67] Bruniquel, J., and A. Lopes, “Multi-variate Optimal Speckle Reduction in SAR Imagery,” *Int. J. Remote Sensing*, Vol. 18, 1997, pp. 603–627.
- [68] Lopes, A., E. Nezry, R. Touzi, and H. Laur, “Structure Detection and Adaptive Speckle Filtering in SAR Images,” *Int. J. Remote Sensing*, Vol. 14, 1993, pp. 1735–1758.
- [69] Sant’Anna, S. J. S., C. C. F. Yanasse, and A. C. Frery, “Estudo Comparativo de Alguns Classificadores Utilizando-se Imagens Radarsat da Regiao de Tapajos,” *Proc. First Latino-*

American Seminar on Radar Remote Sensing: Image Processing Techniques, Buenos Aires, ESA SP-407, 1997, pp. 187–194.

- [70] Frost, V. S., J. A. Stiles, K. S. Shanmugan, and J. C. Holtzman, “A Model for Radar Images and Its Application to Adaptive Filtering of Multiplicative Noise,” *IEEE Trans. Pattern Anal. Machine Intell.*, Vol. 4, 1982, pp. 157–166.
- [71] Grover, K. D., and S. Quegan, “Image Quality, Statistical and Textural Properties of SAREX Data from the Tapajos Test Site,” *Proc. SAREX-92 Workshop*, ESA WPP-76, 1994, pp. 15–23.
- [72] Souyris, J. C., T. Le Toan, N. Flouri, C. C. Hsu, and J. A. Kong, “Inversion of Forest Biomass Using SIR-C/X-SAR Data,” *IEEE Trans. Geosci. Remote Sensing*, submitted 1997.
- [73] Kuan, D. T., A. A. Sawchuk, T. C. Strand, and P. C. Chaval, “Adaptive Restoration of Images with Speckle,” *IEEE Trans. Acoust. Speech Signal Process.*, Vol. 35, 1987, pp. 373–383.
- [74] Le Toan, T., A. Beaudoin, J. Riom, and D. Guyon, “Relating Forest Biomass to SAR Data,” *IEEE Trans. Geosci Remote Sensing*, Vol. 30, 1992, pp. 403–411.

14

Current Status and Future Prospects

14.1 Introduction

Perhaps the most remarkable feature of our understanding of SAR images is that very simple, approximate models can provide good representations of the properties of the images. Almost all of the developments described in this book flow from four such models.

1. The complex SAR image is formed by linear filtering of the complex reflectivity of the scene; this linear filter (the SAR PSF) is divisible into the product of a range and azimuth PSF.
2. The complex reflectivity of the scene can be described by a set of discrete scatterers, envisaged as point scatterers, facets, or volume scattering elements. For distributed targets, these scatterers are randomly positioned in the resolution cell.
3. Within distributed scatterers, the properties of the underlying scatterers change slowly in comparison with the resolution length.
4. Image structure arises from discontinuities in one or more measurable image properties.

From the first of these, we can immediately infer the behavior of single point targets, or small clusters of targets, with correct representations of the interference between them. The sampling properties of the data are also immediate. From the second, in combination with the first, the properties of speckle arise. When there

are very many scatterers in every resolution cell, the complex reflectivity can be represented as a white Gaussian process, so the complex image is a correlated Gaussian process where correlation is determined by the PSF. All the elementary properties of distributed and point targets follow and allow us to quantify the role of targets, distributed scatterers, and system noise in the observed image.

This basic model needs only to include number fluctuations in the scatterer populations between resolution cells in order to provide viable representations of texture. Both single-point PDFs and the correlation properties of textured regions are explained consistently within this simple structure. It also extends readily to deal with the multidimensional SAR images produced by polarimetry and interferometry.

A crucial but not obvious consequence is that, for most purposes, the information contained in the *scene* only becomes available when products of channels are formed. For a single channel, this means generation of the intensity image; while for correlated multichannel data we must include quantities such as phase difference, amplitude ratio, or correlation coefficient. From the complex image itself we can mainly infer only properties of the *sensor*, such as the PSF. The principal exception to this is for isolated point targets, where the phase signature is given by the SAR PSF and can be used as a detector, as well as being critical in super-resolution.

While the first two models are central in *explaining* what we see in SAR images, the third is crucial in *recovering* the information they contain. Interference between scatterers manifests itself as speckle in single-channel images and more generally in the multivariate Gaussian distribution encountered for higher dimensional images. In order to deal with these high-frequency fluctuations we assume that they mask a real-world complex reflectivity that changes on much slower scales (except at edges and near isolated targets). All the approaches to filtering, reconstruction, and segmentation described in earlier chapters have at their root this assumption of a comparatively smooth reflectivity, punctuated by structural elements in the scene. The fourth model allows us to build this knowledge about discontinuities into our algorithms and to make them adaptive to local structure. The validation of these methods takes us back, at least for single-channel data, just to the properties of one-dimensional speckle.

Expressed in these terms, the physical content of much of the material in this book is low because we made little use of electromagnetic theory, the dielectric properties of materials, or the nature of the scattering medium. Equally, only the most general concepts about the nature of a scene were introduced. Instead, we principally concerned ourselves with the processes by which the arrays of numbers corresponding to digital SAR images need to be treated in order to isolate the information-bearing components of the data. It is through these components that the links to deeper physical theories can be

made: by characterizing the data, we bring into focus what physical theory needs to explain. Equally, the structure we see in an image, on which we can bring our knowledge of the world to bear, relies on the choice of what to display and how to display it. This means we must deal properly with situations where more than a single parameter is needed to capture the information in the data, either because of multidimensionality or texture.

In this sense, we were concerned with providing the bridge that connects the physics of scattering, through measurement, to investigation of real world processes, as illustrated in Figure 14.1. Notice that the arrows connecting the boxes in this figure are two-way, due to the fact that, in some cases, we can measure an effect (e.g., texture) without having any clear idea of the physical phenomenon causing it (indeed, we may have several theories, but be unable to decide which, if any, is correct). An examination of many of the images in this book reveals numerous effects that we cannot currently explain. Image analysis then acts as a stimulus to physical understanding. Equally, the need to apply images places requirements on the performance of image analysis methods in order for them to be useful. For example, the loss of much of the prominent drainage channel shown in Figure 6.12(a) in the reconstruction of Figure 6.12(b) and to a lesser extent in the segmentation shown as Figure 7.10(b) indicates that neither algorithm is currently reliable in a mapping context at this spatial resolution. Such failures motivate new and more powerful methods.

In order to make this bridge as safe as possible, we tried to establish firm foundations and rigorous developments based on data models. However, as with all attempts to represent complex phenomena by models (and hence make them susceptible to mathematical treatment), it is critical to assess the extent to which the models are complete, accurate, tractable, and useful. By surveying these highly interrelated issues, we will summarize what was achieved, identify failings, and indicate directions where further efforts are required.

14.2 Are the Models Complete?

A model can be considered complete in a statistical sense if measurements made on the data are consistent with that model. For parametric statistical models,



Figure 14.1 Image analysis bridges the gap between physical theory and the high-level understanding required to apply the images.

which form the backbone of most of the analysis in the earlier chapters, completeness needs to be coupled with economy. We tried to identify a minimal set of parameters from which all other measurements can be inferred. Striking success was demonstrated over a variety of systems for the Gaussian model and the K distribution model. By measuring a covariance matrix and an order parameter, all the information is captured. However, we also identified situations where these models begin to break down, including:

- Very high resolution data (< 1m), where mixture distributions or other types of distribution become necessary to describe the data (see Section 5.7);
- Long wavelength data (50 to 100 cm), where for some cover types the distribution may not be properly characterized by either of these models (see Section 11.9);
- Very long wavelength data (tens of meters) provided by systems such as CARABAS [1] in which the assumption of many comparable scatterers per resolution cell is likely to be violated;
- Urban areas, where semideterministic structures violate the conditions leading to the local Gaussian model.

In the first three of these cases, the amount of data that is available and has been thoroughly examined is very limited. Very high resolution data are likely to remain of most relevance in the military context, so clutter models for target detection will drive the developments. The second two data types have both military and civilian applications but are unlikely to become widely available in the near future, not least because of problems of interference with other systems. Where this problem can be circumvented, an important application for both types is likely to be in forestry. Particularly for the very long wavelengths, the data distributions will then need better characterization since they may carry information on the number density of scatterers and hence tree spacing. (This is currently very speculative.) Urban areas present special problems due to corner reflector and specular effects but represent possibly important target types for application of SAR [2].

If we inquire whether the models are complete in the physical sense, our answer must be no, for a number of reasons. Perhaps the most pertinent is that the linear imaging model and the speckle model both rely to some extent on a representation of the world as a collection of discrete scatterers whose interaction with the incident wave is by single scattering. The product model for polarimetric data (Appendix 11A) effectively made the further assumption that all scatterers see the same field. In scattering theory terms, this

corresponds to the Born approximation, while the inclusion of attenuation effects can be described by the distorted Born approximation. This simplification may seem unreasonable, since it ignores multiple scattering and situations, such as surface scattering, for which a continuous model of the medium seems more appropriate. We nonetheless find that the predictions based on it are often consistent with the data. For example, since different polarizations penetrate to different depths in forest canopies, measured order parameters in the HH and VV channels could, in principle, be different. The few measurements that address this question seem to indicate otherwise. In theoretical terms, [3] also indicates that, at least for one formulation of surface scattering, the continuous medium model effectively reduces to a discrete single scattering model.

Another gap in our physical description is in texture modeling. At various points we discussed texture as a number fluctuation effect, a shadowing/high-light effect, or a random variation in the underlying continuous RCS. The links between these points of view are only just becoming established [4,5]. This physical understanding of texture is important in our statistical modeling of the process, since Section 5.8 indicated that only by inserting such knowledge can we produce textures corresponding to those observed in woodland. It is also crucial in fully exploiting texture because it indicates the geophysical parameters controlling texture. This insight also indicates the sensor and target conditions under which texture is likely to be observable [6]. However, no such insight is available for the texture distributions observed at very high resolutions. Indeed, at these resolutions the world appears to become progressively more complex. Simple statistical models break down and the links of more complicated models to physical parameters become tenuous.

At the other end of the spatial scale, all of the algorithms described in this book acquire their information locally and only build up long-range spatial correlations by iteration. They contain no a priori knowledge, for example, about linear structures or corners, despite these having very high information content in human perception of scenes [7]. This is reflected in the failure, noted previously, to detect some structural scene elements that are obvious to a human observer. Some algorithms that can make use of long-range information exist, such as the Hough transform for detecting extended linear features [8]. However, their integration into the Bayesian approach adopted in this book does not seem straightforward. Indeed, it is questionable whether the type of information inherent in scene structure is susceptible to any form of Bayesian analysis. Nonetheless, work by Hellwich [9] demonstrated that line finding can be introduced into a simulated annealing scheme, as mentioned in Chapter 7. Also, some aspects of shape can be controlled within a Bayesian treatment, for example, through the curvature penalty involved in annealed segmentation

(Section 7.3.5). The extent to which such methods can fully capture our prior knowledge of the properties of scenes has yet to be established.

14.3 Are the Models Accurate?

Accuracy is highly coupled with completeness and economy. We observed that very close approximations to the distributions observed in SAR scenes are possible using simple models, and in Section 14.2 we indicated where these break down. However, an accurate model does not necessarily imply accurate conclusions or measurements unless it can be applied. This has three aspects. First, the model may need to be approximated because it requires the solution of nonanalytic equations, numerical methods, or techniques that are too time consuming for the available computing power and application. As an example, a rigorous process of fitting regions to a two-dimensional image to optimize a cost function is computationally prohibitive. The impact of such considerations on algorithm selection was dealt with in Sections 6.10 and 7.4 (see also Figure 7.11). This issue is closely connected with the questions of tractability, as discussed in the next section. Second, the result of an algorithm derived from an optimization principle may not be consistent with the model on which it is based. For example, it is readily shown that the single-channel MAP filter, which assumes a K-distributed input in its reconstruction, does not generate the expected gamma distribution on output. Similarly, the reconstruction filters discussed in Chapter 6 were all shown to cause radiometric distortion. Third, if the accurate model leads to a solution that is itself too complicated for exploitation, then either a simpler model or a way to degrade the solution needs to be found. This is well illustrated by some of the very complex edge maps shown in Figure 7.13, which do not map readily onto map features or human perceptions of structure in the image. Hence, accuracy may in some circumstances have to be placed in the context of what is needed to represent the *desired* information rather than the *available* information. Similar issues arise in classification, where the complexity of the world at radar wavelengths must be taken into account in order to arrive at robust methods.

14.4 Are the Models Tractable?

The model-based development throughout this book relied mainly on developing statistical distributions involving small numbers of parameters that can successfully describe a wide range of target types encountered in SAR images. These were used to identify the measurements and image types that convey the

information content of the data. Two-point distributions also entered the picture mainly through their spatial correlation properties, involving the interaction between spatial properties of the scene and the SAR PSF.

The existence of viable parameterized models together with simple structure models for the scene allowed us to follow a Bayesian approach to information extraction. This led to a range of optimization problems of varying degrees of complexity. Much of the theory and analysis was concerned with investigating the properties of the distributions or solving the optimization problems.

For the Gaussian model a nearly complete treatment applicable to multilook and multichannel data is possible. All the important distributions are derivable, difficulties being encountered only for the moments of multilook phase difference and Hermitian product amplitude (see Chapter 11 and [10]). There is a very well-developed sampling theory, based on the complex Wishart distribution. From it, the estimation properties of the ML estimators of such important parameters as coherence and phase difference can be derived, providing a firm basis for estimating bias and establishing confidence intervals, for example.

The introduction of a product model changes the picture completely, even in the simplest and most widely applicable case of a K distribution. Now, even for single-look, single-channel data, the ML solution for the parameters is not analytic and approximate methods must be used. Good progress was made in this simplest case (see Chapter 7) and the required approximations shown not to degrade performance significantly. However, we do not currently have a readily applicable analysis of confidence intervals for order parameters. Hence, questions concerned with discrimination of textures and even the existence of texture within a data sample cannot be adequately resolved at present. For multilook, single-channel data, useful methods are only available when the texture is effectively constant across the looks. (In the case of multilooking by averaging image pixels, this means that the texture must vary on scales longer than that of the averaging window.) When this condition holds, the product model still applies and approximate methods are available. When this condition does not hold, there are few results available, since little work has been reported on the distributions arising from sums of K-distributed pixels. For multichannel data obeying the product model, optimal methods to estimate texture parameters still await thorough investigation, but sensible approaches to this problem are available (see Section 11.9 and [10]).

14.5 Are the Models Useful?

It must be recognized that the need for powerful methods depends on the application. Very useful information can in some cases be inferred from SAR

images simply by looking at them. A very good example of this is the analysis of the break-up of the Larsen iceshelf reported in [11], which effectively treated the series of ERS-1 images like a set of photographs. For this purpose, all the relevant information was carried in the structure (the iceshelf margin, icefloes, and fixed features) and there was sufficient radiometric contrast to pick these out. Many of the images in this book contain structural information that is obvious to a human being and, therefore, may be all that is needed for mapping.

However, once we go beyond treating the SAR image purely as a picture, the machinery developed in this book becomes relevant. Parameter estimation (e.g., in agricultural applications) and all aspects of handling multidimensional data (e.g., EMISAR or AirSAR multifrequency polarimetric data) require proper knowledge of the underlying distributions. Detecting small or weak targets in a clutter background or rapid, consistent handling of large amounts of data requires automatic or semiautomatic image analysis tools. To carry out these tasks effectively it is essential to understand how information about the scene is encoded in the data. The development of such understanding was an underlying theme throughout this book.

However, the acid test of usefulness is whether these developments can aid applications. There has, in fact, been little large-scale validation of any of the methods in this book. We can attribute this to a number of factors:

1. Methods have been reported in a piecemeal fashion in a large variety of journals, and it is hard for a potential user to get an overview of the corpus of work. Basically, much of this work is not well-known to the user community.
2. Many of the reports of algorithms have paid little attention to validation or assessment of their real value to applications. This in some sense reflects a separation between the community that develops algorithms and those with a remote sensing task.
3. Many of the algorithms reported here are comparatively sophisticated, not easily implemented, and require considerable computing power. Hence, there is a tendency to rely on simple methods, even if they are not particularly effective.
4. Much of the analysis of SAR data has been on small datasets over local areas where human interaction is a more efficient means to carry out the task required. Where large-scale applications are underway, uncertainties about the reliability of automatic methods may still make it preferable for images to be handled by large numbers of human analysts. The trade-off of accuracy against cost has yet to be done. It is essential that the ability of the methods reported here to emulate or

improve on the performance of human analysts be properly assessed if they are to have serious impact on applications. (This does not apply to the selection of data features that carry the relevant information, since this is common to both human and automatic analysis. It does apply to image analysis tasks such as reconstruction or segmentation.)

5. The methods reported here are comparatively new and continually evolving. Very significant strides have been made in algorithm development and validation inside the last few years (e.g., compare the results described in [12] with those in earlier chapters in this book).
6. Very many civilian applications need the coverage and repeatability provided by satellite data. Because of the lower resolution, the information available to recover objects of interest is less. Hence, the local methods on which all the reconstruction and segmentation algorithms are based may not be sufficient to recover all the image structure. This is particularly true when thin, dark features are important scene elements. A clear example of this is the prominent drainage channel in the ERS-1 image shown as Figure 6.12(a). It is poorly defined in the reconstructions shown in Figures 6.12(b) and 7.10(b) and in the single-channel segmentations displayed as Figure 12.11(d–f). Only when several multitemporal images are combined does this feature become well reproduced by segmentation (Figure 12.12). Notice that even in this case the channel is represented as many different segments and does not have the integrity that would be assigned to it by a human being.
7. Only in some cases are robust methods for classification based on SAR data alone available, as described in Chapter 13. Since this is a critical step for many applications, the role of SAR in the information required for the application may then be subordinate or ill-defined. The whole question of how to combine SAR data with other data types in the context of a variety of applications needs much further work. A related issue is the availability of data; classification methods may be known but the SAR systems required to carry them out may not yet be in operation.

14.6 Future Developments

Perhaps the most important issues with which to end this book are an assessment of whether we have gone as far as is necessary along the road we have been following and whether we can fruitfully try to go further. Our aim throughout has been to try to identify the information in SAR images and to devise methods

that display it to best advantage. For single-channel data we followed both reconstruction and segmentation routes, and our best current efforts are epitomized by Figures 6.11 and 7.10(a) for high-resolution airborne data and Figures 6.12 and 7.10(b) for lower resolution satellite data. Visually the reconstructed airborne data are of very high quality but are known to contain radiometric distortion (see Section 6.10) and not to conform to the speckle model in regions of the image with small-scale structure (see Figures 6.9 and 6.10). The segmented data, on the other hand, are visually less attractive, largely because of the steps in brightness forced by the cartoon model. However, they are radiometrically unbiased and conform closely to the speckle model (see Figure 7.9). This suggests that the lack of such conformity in the reconstructions is a failure of the algorithms, where there is small-scale structure, not a failure of the speckle model.

Images like Figures 6.11, 6.12, and 7.10 represent the state of the art, and we need to question whether the techniques that produced them are good enough and whether there is any scope for them to be bettered. Although we have described objective tests of algorithm performance and are currently working to improve these tests (e.g., to evaluate the shape preservation aspects of the segmentation algorithms), the first question can only be answered by assessing how they perform in applications. As in all aspects of SAR imaging, this interplay between technique and purpose will drive progress. Shortcomings of the algorithms become immediately obvious from failures to emulate tasks that can be carried out by a human being. However, it is not necessary (and is almost certainly unachievable) that all aspects of image understanding should be automatically reproducible; only those relevant to the task are needed. The failure to reconstruct faithfully the drainage channel in Figure 6.12 or 7.10(b) may not prevent these images from being used effectively in crop classification, for example.

A Bayesian, MAP treatment implemented through simulated annealing appears to provide the most powerful approach to image analysis currently available. For single-channel data, the only way this is going to be improved is by embedding improved prior knowledge in the process. One form of knowledge known to be omitted is the existence of thin linear features, as was already noted. For many civilian applications, however, multichannel (especially multitemporal) data is likely to be more important. For polarimetric and interferometric data, there are inadequacies in the segmentation methods, since they ignore interchannel correlation and texture. The existing MAP approach with annealing extends correctly to multitemporal data in which interchannel correlation is negligible, though again texture is not yet represented. The real challenges that seem likely to arise will be the incorporation, if possible, of new forms of knowledge into the Bayesian framework, particularly other types of data (such as map information and optical images).

Finally, the methods and results described here provide a yardstick against which other algorithms and further improvements must be measured. We tried to make clear the continual development of the algorithms and why the currently preferred methods are judged to be the most powerful available. We also tried to indicate the relative merits of other approaches so that users of SAR imagery can make an informed choice in their selection of image analysis tools. In the final analysis, it is the fitness of the tool to the task that decides its real value.

References

- [1] Israelsson, H., L. M. H. Ulander, J. I. H. Askne, P. F. Fransson, A. Gustavsson, and H. Hellsten, "Retrieval of Forest Stem Volume Using VHF SAR," *IEEE Trans. Geosci. Remote Sensing*, Vol. 35, 1997, pp. 36–40.
- [2] Henderson, F. M., and Z.-G. Xia, "SAR Applications in Human Settlement Detection, Population Estimation, and Urban Land Use Patterns: a Status Report," *IEEE Trans. Geosci. Remote Sensing*, Vol. 35, 1997, pp. 79–85.
- [3] Jakeman, E., and P. N. Pusey, "Non-Gaussian Fluctuations in Electromagnetic Radiation Scattered by a Random Phase Screen. I. Theory," *J. Phys. A: Math Gen.*, Vol. 8, 1975, pp. 369–391.
- [4] Williams, M. L., S. Quegan, and D. Blacknell, "Distribution of Backscattered Intensity in the Distorted Born Approximation: Application to C-band SAR Images of Woodland", *J. Electromagnetic Waves and Their Appls.*, 1997 (in press).
- [5] Williams, M. L., "Influence of Canopy Shape on SAR Speckle Distributions over Woodland," *Proc. IGARSS 97*, Singapore, 1997, pp. 755–757.
- [6] Oliver, C. J., A. P. Blake, and R. G. White, "Optimum Texture Analysis of Synthetic Aperture Radar Images," *SPIE Conf. on Algorithms for Synthetic Aperture Radar*, Orlando, FL, *SPIE Proc.*, Vol. 2230, 1994, pp. 389–398.
- [7] Resnikoff, H. L., *The Illusion of Reality*, New York; Springer-Verlag, 1989.
- [8] Murphy, L. M., "Linear Feature Detection and Enhancement in Noisy Images Via the Radon Transform," *Pattern Recog. Letts.*, Vol. 4, 1986, pp. 279–284.
- [9] Hellwich, O., "Line Extraction from Synthetic Aperture Radar Scenes Using a Markov Random Field Model," *Europto Conf. on SAR Image Analysis, Simulation and Modelling II*, Taormina, *SPIE Proc.*, Vol. 2958, 1996, pp. 107–113.
- [10] Tough, R. J. A., D. Blacknell, and S. Quegan, "A Statistical Description of Polarimetric and Interferometric Synthetic Aperture Radar Data," *Proc. Roy. Soc. London A*, Vol. 449, 1995, pp. 567–589.
- [11] Rott, H., P. Skvarca, and T. Nagler, "Rapid Collapse of Northern Larsen Ice Shelf, Antarctica," *Science*, Vol. 271, 1996, pp. 788–792.
- [12] Quegan S., R. G. Caves, K. D. Grover, and R. G. White, "Segmentation and Change Detection in ERS-1 Images over East Anglia," *Proc. First ERS-1 Symposium*, Cannes, France, 1992, pp. 617–622.

Index

<u>Index terms</u>	<u>Links</u>
A	
Adaptive feature-preserving filters	403
Agricultural monitoring	414
Airborne SAR	17 30 68 418
2-look	198
DRA X-band image	26 80
geometry	13
high-resolution data	460
<i>See also</i> SAR; SAR images	
AirSAR system	2 349 352 353
	373 393 394 417
data classes	438
polarimetric data	421 435
SIR-C combined with	442
Amplitude modulation (AM)	43 44
Amplitude product	335
Amplitude ratio distribution	335 340
analytic CDF	340
EMISAR images	342
uses	340
<i>See also</i> Phase difference distribution	
Annealed CMAP (ACMAP)	186 189
iterated	192
for sloping RCS model	182
<i>See also</i> CMAP	

<u>Index terms</u>	<u>Links</u>
Annealed CML (ACML)	179 186 221
analysis	180
with constant RCS	182
execution time	189
iterated	192
Kth configuration in	180
with sloping RCS	189
<i>See also</i> CML	
Annealed segmentation	208 408
application of	219
comparison	211
flow diagram	210
loop stages	209
multidimensional	395
texture	251
<i>See also</i> Segmentation	
Annealed texture classification	247
Antenna	
pattern	37 59
stabilization	59
Area-based difference measures	388
Armored infantry fighting vehicle (AIFV)	298
Atmospheric refractive index	45
Autocorrelation function (ACF)	22
amplitude	262 266
coefficients	262 263
of complex data	111
Gaussian	259 263
intensity	140 262 263 266
log	262 274
normalized	141 261
parameter fitting	270

Index terms**Links**

Autocorrelation function (ACF) (<i>Continued</i>)				
results	264			
texture	274			
Autofocus				
accuracy of	52			
CO method	48	51	52	
correction estimation	65			
implementation	51			
iterated	63			
method choice	52			
MLR method	48	50		
PD method	48	49		
PG method	48	49		
PPP	48	49	51	
residual acceleration power spectrum	68			
scatterer properties effect on	53			
techniques	5	48		
<i>See also</i> Defocus				
Automatic methods	458			
Automatic target recognition (ATR)				
defined	296			
processing chain	300			
target classification and	305			
<i>See also</i> Target detection				
Average intensity	89			
Azimuth	12	25		
beamwidth	26			
intensity correlation coefficients	103	108		
processing	28	33		
processing parameters	28			
PSF	32	69		
resolution	27			

Index termsLinksAzimuth (*Continued*)

strip	31
<i>See also</i> Range	
Azimuthal distortion	56 58
geometric	56
residual	61

B

Background

distribution	280
effect of	285
Gaussian, speckle	308
K-distributed	287 290
PDF	280
properties	279 294
RCS	282 283
region, false alarm	280
speckled	311
weak	278

Backscattering coefficient

33 401 403

Bandwidth	12
-----------	----

Doppler	94
---------	----

spatial	27
---------	----

Bayesian approach

classifier	430
MAP treatment	460
reconstruction	7 161 189
target detection	278 279 314

Beam weighting

Bessel function

expanded	361
----------	-----

zero-order	361
------------	-----

<u>Index terms</u>	<u>Links</u>
Binomial distribution	325
Biomass map	443
Blurring	406
Born approximations	323
Boundaries	
decision	431
establishing	366
between regions	124
of texture	124
C	
Calibration	5 34
errors	386
inadequate	5
internal, tones	322
necessity of	91
targets	322
Cartoon model	197 198 202
Change detection	8
on images from different dates	438
pixel-based	385
target	305 306
<i>See also</i> Target detection	
Channels	
in-phase (I)	36 93
polarimetric	333 341
quadrature (Q)	36 93
uncorrelated	431
Chirp pulse	21 24
Classification	
accuracies	408 432 433
based on scattering mechanism	434

Index terms**Links***Classification (Continued)*

of C-, L-, and P-band AirSAR data	436
crop	432
data-driven methods	427 433
decision rules for	426
effective	416
empirical basis for	416
Gaussian MAP	427
image	8
knowledge-based	437
MAP	432
ML	196
object	79
RCS	195
refined	443
SAR image	413
SAR properties to redefine	442
sea-ice	432
single-frequency polarimetric	430
target	305
texture	245 425
threshold and	406

Clutter

class	434
K-distributed	287 289
natural	302

Clutter-to-noise ratio (CNR)

102 104	102 104
CMAP	170 185
annealed (ACMAP)	182
despeckling	169
iterated, despeckling	174

See also Correlated neighborhood model

Index terms**Links**

CML	170	185
annealed (ACML)	179	
despeckling	168	
iterated, despeckling	173	
<i>See also</i> Correlated neighborhood model		
Coefficient of variation (CV)	88	
Coherent imaging	139	140
Complex (field) correlation coefficient	101	
Complex image	85	86
Complex of reflectivity	29	
Complex scattering amplitude	29	
Complex Wishart distribution	343	428 457
Compression ratio	23	
Constant false alarm rate (CFAR) detection	279	282 314
cell-averaging	282	
condition estimation	287	
contrast tests	301	
corrected algorithms	287	
one-parameter	295	302
standard	282	287
statistic	302	
threshold	282	
types of	295	
<i>See also</i> Target detection		
Constant RCS model	179	182
Contrast optimization (CO)	48	
defined	51	
focus parameter effects on	51	
objects in	54	
post-use illustration	52	
Correlated neighborhood model	167	
defined	167	

Index termsLinks

Correlated neighborhood model (<i>Continued</i>)	
diagram	168
gamma MAP. <i>See</i> CMAP	
ML. <i>See</i> CML	
Correlated textures	259
average probability comparison	270
classification	266
ML correlated edge detection	271
ML edge-detection theory	271
model-based parameter estimation	261
random region selection of	261
<i>See also</i> Textures	
Correlation	76
coefficient	102 386 422
local, structure	383
reducing	109
removing	110
spatial	99 105 119 164
Correlation length	
fractional error dependence on	264
fractional error in	265
increase	264
Covariance matrix	
data, using	375
distribution of	429
L-look	428
measuring	454
ML estimate of	351
postprocessing of	437
of transformed data	377
Cramer-Rao bound	243
Crimmins algorithm	171 185

Index terms**Links**

Crop					
cereal	433				
classification	432				
types	420				
Cumulative distribution function (CDF)	148				
amplitude ratio	340				
of configuration probability	179				
trained	231				
 D					
Data					
characterization	126				
covariance matrix	375				
empirical distributions	128				
intensity	380				
interferometric	355				
multifrequency	356				
multilook textured	351				
multitemporal	356				
polarimetric	7 30 322 350 421				
SAR	34 98 319				
Data model	76 123 157				
advantages	82				
correlated K-distributed	142 151				
homogeneity testing	128				
interrelation flowchart	82				
limitations of	142				
parameter dependency	82				
product model	123 130				
verification	128				
Defocus	45				
cause of	46				

Index terms**Links**

Defocus (<i>Continued</i>)		
illustrated	46	
<i>See also</i> Autofocus		
Depth-of-focus (DOF) limit	64	68
Despeckling		
CMAP	169	
CML	168	
gamma MAP	166	
illustrations	163	
iterated CMAP	174	
iterated CML	173	
iterated gamma MAP	172	
iterated MMSE	171	
MMSE	164	
multilook	162	
<i>See also</i> Speckle		
Deterministic RCS	6	
Differential backscattering coefficient	31	
Dirac delta function	32	
Direct classification	246	
Direct measurements	34	
Direct spectrum classification	266	
Distortion	45	55
across-track	61	
along-track	55	
azimuthal	56	58
geometric	55	
minimizing	60	
over aperture	61	
physical causes and	55	
radiometric	55	

<u>Index terms</u>	<u>Links</u>
Distributed scatterer	87
Distributed targets	38 91 99
speckle model for	119
uniformly	102
Distributions	128
amplitude ratio	335 340
binomial	325
comparison of	135
complex Wishart	343
Fischer-Tippett	88
gamma	133 137 138 239
Gaussian	236 325 328
intensity	140
K	134 135 136 138
log normal	127 128 129 136
marginal	237
343 344	
multilook coherence	345
multilook phase difference	344
phase difference	336
Poisson	325
polarimetric data	322
Rayleigh	89 129
sampling	112
single-look	333
theoretical	90
Weibull	126 127 128 129
Doppler centroid parameter	47 50
Doppler sensitivity	117
Doppler shift	28 31 33

Index termsLinks**E**

Edge detection	199
analysis	204
comparison	201
for correlated textures	271
defined	199
edge-detection criterion	199
flow diagram	200
improving	271
ML theory	271
operation of	200
PDF-based	274
performance	272
RGW	199 395
texture segmentation	249
<i>See also</i> RGW; Segmentation	
Eigenimage classification	307
Elevation antenna pattern	30
EMISAR	368 417
amplitude ratio images	342
HH image	380
images	336
intensity data	378
L-band image	369
polarimetric system	116
stability	417
ENVISAT satellite system	1 417
Equivalent number of looks (ENL)	95
ERS-1	1
6-look, SAR	198
azimuth correlation coefficients	102
azimuth resolutions	27
data	18 20 401 414

Index terms**Links***ERS-1 (Continued)*

forest discrimination and images	406	408	19	191	458	459
multitemporal dataset	400					
parameters	17					
PRI images	29	397	398	402		
	439					
PSF	35					
SLC imagery	5	89				
for wetland rice monitoring	437					
ERS-2 satellite	1					
Estimating						
autofocus correction	65					
intensity	169					
MAP	162					
model-based parameters	231	235				
moments	232					
PDF	235					
RCS	93	99	178			
spatial correlation	110					
Euler's constant	263	288				
Execution times						
ACML	189					
reconstruction	187					
segmentation algorithm	217					
Exponential variables	150					

F

False alarm probability	211					
dependence of	288					
derivation	288					
pixel-based detection	387					

Index termsLinks

False alarms	
discriminating targets from sources of	304 300
Fast Fourier transform (FFT)	109
Fischer-Tippett distribution	88
Fitting	
classification by regions	245 208
Fixed windows, scanned edge (FWSE)	
configuration	205 249 250 273
edge-detection probability	272 275
SWCE vs.	273
Flat-Earth approximations	16
Focus parameter	27 47 66
Fokker-Planck rate equation	132
Forest	
biomass, mapping of	444
discrimination	406 408 443
Forward mapping	149
Forward Problem	
defined	77
requirement	79
solution of	79
<i>See also</i> Inverse Problem	
Fourier transform (FT)	49
Frequency modulation (FM)	21 32
Furrows	6

G

Gain	36 37
Gamma-distributed RCS	6 133 134 140 259

<u>Index terms</u>	<u>Links</u>
Gamma distribution	137 239
as approximations	138
L-look	133 431
Gamma MAP	166 185
algorithm	173
comparison	187
detection rate	408
estimation	373
filtered data	406
iterated, despeckling	172
reconstruction	166
selection	188
<i>See also</i> Maximum a posteriori (MAP)	
Gamma variables	150
Gaussian background speckle	308
Gaussian distribution	236
complex	332
moments	333
multidimensional	328
multivariate	325
real	332
Gaussian hypergeometric function	133
Gaussian MAP classification	427
Gaussian random number generator	146
Gaussian random variables (GRV)	150 327
Gaussian resampling transformation	151
Geometrical Theory of Diffraction	143
Geometric distortion	55
azimuthal	56
minimizing	60
residual	60
Global Positioning System (GPS)	56 62

Index terms**Links**

Ground range	15
data	17
resolution	17
<i>See also</i> Range	

H

Histograms	404
Hough transform	455
Hughes Map Drift technique	48
Huygens wavelets	92

I

Image classification. *See* Classification

Images. *See* SAR images

Image texture. *See* Texture

Imaging

coherent	139	140		
consequences of	102			
contrast averaging	141			
incoherent	140			
RCS fluctuations	138			
Incoherent averaging	93			
Incoherent imaging	140			
Inertial Navigation System (INS)	56	57	62	
In-phase (I) channel	36	93		
Integrated sidelobe ratio (ISLR)	62	68		
Intensity				
ACF	140	262	263	266
data	380			
distribution	140			
estimates	169			
fluctuations	123			

Index terms**Links**

Intensity (<i>Continued</i>)			
HH	368		
K-distributed	233	238	
moments	133	142	
PDF	133	136	
uncorrelated random	232		
VV	368		
Intensity correlation coefficients	20	103	108
calculated in azimuth direction	103	108	
calculated in range direction	20		
Intensity ratio			
approximate/exact probabilities	392		
multilook	346		
SD of	216		
Interchannel coherence	345		
Interferometry			
data	355		
images	115		
repeat-pass	114	430	
SAR	114		
Interpolation	109		
Inverse mapping	149		
Inverse Problem	78		
defined	78		
requirement	79		
solving methods	78	79	
<i>See also</i> Forward Problem			
Iterated autofocus	63		
Iterated CMAP despeckling	174		
Iterated CML despeckling	173		
Iterated gamma MAP despeckling	172		
Iterated MMSE despeckling	171		

Index termsLinks**J**

Jeffries-Matsushita separability measure	425
JERS-1 satellite system	1 406 417

K

K distribution	134 135 138 143
	150 151 238 354
approximations to	238
background	287 290
clutter	238 287 289
intensity	233 238
log likelihood	239 246
ML calculation for	242
MLE for	242
moment evaluation	240
multivariate	324
pixels	457
texture	240
uncorrelated noise	270
Knowledge-based classification	437
Kolmogorov-Smirnov (K-S) test	127 128 151 231
	246 249 338 354

L

Lagrange multiplier methods	377
L-band amplitude images	116 117 118
Linear systems theory	100
L-look	93 94 160 162
average intensity	94
covariance matrix	428
gamma distributions	431
intensity data	130
log likelihood	196

Index terms**Links***L-look (Continued)*

speckle, gamma distribution	133
textured data	381
uncorrelated intensity images	386

Log likelihood

calculation	253	269
of classes	269	
difference	250	
as distance measure	266	
K distribution	239	246
L-look	196	
log normal distribution	237	
ML, difference	292	
for regions	271	272
total	397	

Log normal distribution

127	128	129	136
-----	-----	-----	-----

237

log likelihood	237
----------------	-----

PDF	127	234	266
-----	-----	-----	-----

Looks

29

M

Mapping

of forest biomass	444
forward	149
inverse	149

Marginal distributions

343 344

Match filtering

23

Maximum a posteriori (MAP)

classification, applications of	432
crop classification	432
detection criterion	279 280
estimate	162

Index terms**Links**

Maximum a posteriori (MAP) (<i>Continued</i>)	
gamma, despeckling	166
global	406 426 432
global reconstruction	176 178
reconstruction	165
solution	166
Maximum entropy (ME)	234
Maximum likelihood estimate (MLE)	93 238 342
defining	253
derivation of	236
identifying	208
of interferometric phase	355
for K distribution	242
for mean and order	239
for mean and variance	237
Maximum likelihood (ML)	5
calculation for K distribution	242
classification	196
covariance matrix estimate	351
detection criterion	280
edge-detection theory	271
estimation problem	351
likelihood classifier	270
log likelihood difference	292
parameter estimates	284
<i>See also</i> ML split/merge theory	
Mean direction	340
Mean-square error	53
Measurements	82
C-band	423
covariance matrix	454
imaging model and	102
information and	84

Index terms**Links**

Measurements (<i>Continued</i>)			
interrelation of	82		
L-band	424		
polarimetric	320		
RCS	83		
texture	91		
useful	413		
Merge using moments (MUM)	222	251	254
application of	202		
comparative execution times	254		
comparison	201		
edge maps	224		
Gaussian	207		
local	214		
optimized	212	213	215
selecting	217		
<i>See also</i> Segmentation			
Metropolis algorithm	176		
Minimum mean-square error (MMSE)			
applying	165		
despeckling	164		
iterated, despeckling	171		
one-dimensional filter	368	372	
output	373		
reconstruction	164	172	368
ML split/merge theory	203		
implementation of	207		
<i>See also</i> Maximum likelihood (ML); Segmentation			
Model-based segmentation	251		
Model-based texture parameter estimation	231	235	
correlated texture	261		
example	244		
uncertainty in	240		

Index terms**Links**

Model-free texture exploitation	231
Models	
accuracy of	456
breakdown of	454
completeness of	453
correlated neighborhood	167
data	76 123 157
Gaussian	454 457
parametric statistical	453
product	123 130 360 369 457
RCS	131 165 179 180
speckle	113 157 159
textured target	289 455
tractability of	456
usefulness of	457
Moments	
estimating	232
evaluating	240
fourth-order field	333
of Gaussian distribution	333
optimum selection of	234
<i>See also</i> Merge using moments (MUM)	
Moore-Penrose pseudo-inverse	308
Motion-compensation (MOCO)	44 45 57
conventional combined with signal-based	66
extended, system	58
focus parameter	66
high-frequency tracking	64
iterated autofocus	63
signal-based	58 63 71
techniques	2

<u>Index terms</u>	<u>Links</u>
Moving target indicator (MTI) system	117
Multichannel SAR data	319 427
channel correlation	320
multidimensional Gaussian distribution and	328
polarimetric data distributions	322
polarimetric measurements	320
principal components analysis in	383
<i>See also</i> SAR data	
Multichannel segmentation	391
annealed	395
average intensities	397 400
basis of	391
edges in	396
of polarimetric data	393
RGW	393
transferring	392
<i>See also</i> Segmentation	
Multidimensional annealed segmentation	395
Multidimensional Gaussian distribution	7 328
Multidimensional RGW segmentation	393 403
Multidimensional SAR images	114
algorithm comparison	399
analysis techniques	365
data types	365
<i>See also</i> SAR images	
Multifrequency data	356
Multilook	29
coherence distribution	345
data	93
despeckling	162
intensity ratio	346

Index terms**Links**

Multilook (<i>Continued</i>)		
phase difference distribution	344	
reconstruction	368	
spatial effects on	105	
Stokes scattering operators	349	
textured data	351	
Multilook registration (MLR)	48	
defined	50	
objects in	54	
two-look	50	
Multiplicative noise	76	96
Multitemporal data	356	

N

Neumann series expansion	87	
Neural nets	433	
Neymann-Pearson criterion	286	294
Noise		
effects of	99	
Gaussian	100	
multiplicative	76	96
speckle and	85	
Nyquist condition	28	

O

Objects		
classification of	79	
extended	53	
relative positions of	125	
spatial density of	54	
Organization, this book	4	

Index termsLinks**P**

Parametric information	375	
Path length		
comparison	47	
fluctuations	46	
Pentagamma function	242	
Phase delay	26	
Phase difference distribution	336	
C-band	425	
characteristics	336	
examples	339	
HH-W	370	373
multilook	344	
shape	339	
<i>See also</i> Amplitude ratio distribution		
Phase difference (PD) method	48	
defined	49	
multiple scatterers and	54	
Phase gradient (PG) method	48	49
Phase modulation		
effects of	44	
unwanted	43	
Pixel-based change detection	385	
false alarm probability	387	
probability	387	
threshold values	387	389
<i>See also</i> Change detection; Target detection		
Point spread function (PSF)	4	85
azimuth	32	69
direct measurements	34	
ERS-1	35	
ideal form of	23	

Index terms**Links**

Point spread function (PSF) (<i>Continued</i>)		
slant range	21	
Poisson distribution	325	
Polarimetric channels	333	
combining pairs of	334	
estimation of	341	
Polarimetric data	7	30
AirSAR	421	435
calibrated	324	369
at C-, L-, and P-bands	435	436
classification and	421	
distributions	322	
fourth-order field moments for	333	
Gaussian	341	
segmentation of	393	
stationary speckle model into	327	
texture observations in	352	
theoretical formulation	324	
uncalibrated	324	
Polarimetric filtering		
full	381	
matched	434	
optimal	378	
output	379	
whitening	379	434
Polarimetric measurements	320	
Polarimetric parameters		
C-band	329	
empirical behavior of	422	
L-band	330	
P-band	331	

<u>Index terms</u>	<u>Links</u>
Polarimetric reconstruction	367
gamma MAP estimation	373
MMSE	368
multilook	368
Power spectral density (PSD)	66
Pre-averaging	108
Precision image (PRI)	18
ERS-1	29 397 398 402
	439
illustrated	19
near/far range	20
Principle components transformation (PCX)	383
analysis	384
defined	383
function of	385
Probability density function (PDF)	124
amplitude	134
background	280
candidate	128
data type representation	274
edge detector	274
empirical	125 127
estimating	235
gamma	131 134
Gaussian	202 236 332
intensity	126 133
joint	88 111 169 268 343
of likelihood difference estimate	268
log normal	127 234 266
MLE derivation for	236
single-pixel intensity	288

Index terms**Links**

Probability density function (PDF) (<i>Continued</i>)					
speckle	133				
of spectral coefficients	167				
theoretical	128	135			
two-parameter	127				
Weibull	136				
Processor gain	37				
Product model	123	130	369	457	
number fluctuations and	360				
processes	130				
speckle in	130				
validity for natural SAR clutter	141				
Prominent point processing (PPP) autofocus	48				
defined	49				
restriction	51				
Pulse compression	25				
Pulse length	12	26			
Pulse repetition frequency (PRF)	12	15			

Q

Quadratic distance correlation classification	307				
Quadrature (Q) channel	36	93			

R

Radar cross section (RCS)	6	125			
background	282	283			
classification	195				
deterministic	6				
distribution sampling	112	304			
estimating	93	99	178		
fluctuations	102	114	128	138	
	197	234	426		

<u>Index terms</u>	<u>Links</u>
Radar cross section (RCS) (<i>Continued</i>)	
gamma-distributed	6 133 134 140
259 428	
mean	131
measurements of	83
ML estimates of	203
reconstruction filters	157 197
spatial stability of	401
swell	131
temporal stability of	401
variations	112 130
<i>See also</i> RCS model	
Radarsat	417 425
fine-mode image	440
flexibility	417
Radiometric distortion	55
minimizing	60
residual	60
Range	12 14
far	15 20
fluctuations	46
ground	15 17
intensity correlation coefficients	20
near	15 20
processing	25
PSF	30
pulse compression	25
raw data	32
slant	15 16 17 21
swathwidth	15
variation	30 31
<i>See also</i> Azimuth	
Ratioing	404

Index terms**Links**

Rayleigh distribution	89	129		
Rayleigh resolution criterion	308			
RCS exploitation	218			
algorithm properties	218			
application example	221			
flowchart	219			
<i>See also</i> Radar cross section (RCS)				
RCS model	131			
constant	179	182		
correlated gamma-distributed	142			
gamma-distributed	134			
reconstruction with	165			
sloping	180	189		
<i>See also</i> Radar cross section (RCS)				
Reconstruction	157			
algorithm comparison	184			
algorithm execution times	187			
algorithm selection	188			
Bayesian	161	189		
comparison	223			
correlated neighborhood model	167			
gamma MAP	166	187	188	373
global MAP	176	178		
by iterating structured neighborhood model	175			
MMSE	164	172	368	
multilook	368			
with nonlinear iterated processing	171			
polarimetric	367			
properties	158			
quality of	220	222		
with RCS model	165			
single-stage	160			
with speckle model	162			

Index termsLinks

Reconstruction (<i>Continued</i>)				
structural adaptive	170			
visual inspection and	159			
Region of interest (ROI)	281	284	301	302
averaging background over	283			
rectangular	306			
Regions	253			
boundaries between	124			
fitting	208			
merging	202			
RCS difference between	291			
target	302			
texture	253			
Relief effects	404			
Repeat-pass interferometry	114	430		
Resolution	83			
azimuth	27			
ground range	17			
slant range	16			
spatial	4	27		
RGW	199	222	254	
comparison	201			
defined	199			
edge-detection criterion	199	395		
edge maps	224			
flow diagram	200			
multidimensional	393	403		
operation of	200			
selecting	217			
<i>See also</i> Segmentation				
Root mean square (rms)	60			
Rule-based methods	9			

Index termsLinks**S**

Sample circular variance	340
SAR	
2-look	198
6-look	198
airborne	13 17 68 418
calibration	5
correlation	37
data display	17
effective use of	4
focusing	27 38
interferometry	114
as linear measurement system	29
orbital	27
polarimetric	7 114
processor	37
role of	459
sensitivity of	442 443
sideways-looking	48
simulators	145
single-look	198 259 282 286
spaceborne	14 418
system parameters	12
SAR data	
analysis of	458
application of	34
multidimensional	98 319
single-channel	98 319
variance	384
SAREX program	229
image	230
texture analysis	244

Index terms**Links**

SAR images	
area-based difference measures	388
availability of	1
classification	8 413
defects and correction	43
DRA C-band	124
DRA X-band	3 144 158 190
formation principles	11
formulation of	4 98 126
geometry illustrations	13 14
global structure	4
high-resolution	158 296
histograms and	405
homogeneous region in	341
information extraction from	9
intensity ratio	187
local structure	4
multidimensional	114 365
nature of information in	77
pixel-based change detection	385
properties of	5 75
quality of	184 212
SAREX	230
simulated	296 297 298
thresholding	407
SAR processing	11
essence of	26
flexibility of	117
Scanned window, center edge (SWCE)	
configuration	205 249 250 273
edge-detection probability	272 275
FWSE vs.	273
test	206

Index terms**Links**

Scatterers	87
Scattering	
matrix	29
mechanism	435
Sea-ice classification	432
Segmentation	197
algorithm comparison	212
algorithm selection	217
annealed	209 219
classes of	198
conflicting requirements in	198
dual role	220
edge detection	199
execution times	217
failure	216
image quality and	212
ML split/merge theory and	203
multichannel	391
multidimensional annealed	395
multidimensional RGW	393 403
prerequisites	197
ratio measures for	216
region fitting	208
region merging	202
usefulness of	222
SCAN	212 222 251 253
	254
comparative execution times	254
consistency	224
edge maps	224
excess fluctuations and	215
“flecks” and	214
global	214

Index terms**Links**

SCAN (<i>Continued</i>)						
illustrated	213					
selecting	217					
<i>See also</i> Segmentation						
Shift-invariant two-dimensional pattern matching	307					
Sidelobe levels						
excess	62					
peak	63					
Sideways-looking SAR	48					
Siegert relationship	102	381				
Signal-based MOCO	58	71				
antenna stabilization and	59					
application of	58	59	71			
combined with conventional MOCO	66					
refinements to	63					
<i>See also</i> Motion-compensation (MOCO)						
Signal-to-clutter ratio (SCR)	52	104	286			
infinite	113					
large values of	113					
leading	55					
variation	289	290	291	293		
Signal-to-noise ratio (SNR)	104					
Simulated annealing	176					
comparison	211					
Metropolis algorithm	176					
Simulated SAR images	296					
illustrated	297					
variations of	298					
<i>See also</i> SAR images						
Simulation	145					
comparison	152					
correlated K-distributed image	150					

Index terms**Links**

Simulation (<i>Continued</i>)				
stages	146			
texture	145	148		
Sine function	23			
Single-channel image types	84			
Single-channel segmentation	394			
Single-frequency polarimetric classification	430			
Single-look distributions	333			
Singular value decomposition (SVD)	308			
SIR-C				
SIR-C/X-SAR	417			
texture	442			
Slant range	15			
data	17			
PSF	21			
resolution	16			
<i>See also</i> Range				
Slant range complex (SLC)	18			
illustrated	19			
near/far range	20			
Sloping RCS model	180	192		
Smoothing	198			
Spaceborne SAR	30	418		
geometry	14			
multitemporal data	418			
<i>See also</i> SAR; SAR images				
Spatial bandwidth	27			
Spatial correlation	99	105	119	164
data	341			
effects on multilooking	105			
estimating	110			
problems with	107			

Index terms**Links**

Spatial correlation (<i>Continued</i>)			
system-induced	107		
Spatial density	54		
Spatial filtering	438		
Spatial resolution	4	27	
Speckle	6	31	124
contribution	160		
defined	85		
distributions	404		
fluctuations	125		
Gaussian	131	308	
model	91		
as multiplicative noise	76	96	
noise and	85		
PDF	133		
in product model	130		
pure, SD for	216		
reduction	170	366	375
removing	229		
unit mean term	367		
vector	326		
<i>See also</i> Despeckling			
Speckle model	157	159	
for distributed targets	119		
limitations on	113		
reconstruction with	162		
Speckle-reducing filter	380		
Spotlight mode	27		
Spotlight SAR systems	44		
Standard deviation (SD)	160	161	
of intensity ratio	187	216	
for pure speckle	216		

Index terms**Links**

Standard deviation (SD) (<i>Continued</i>)	
relative, comparison of	243
in uniform regions	187
Stationary multiplicative noise model	327
Stirling's formula	346
Stokes scattering operators	369 378
contents	349
defined	347
formulation	347
multilook	349
pre-average	349
Stokes vectors	322 347
Strip map mode	27
Structural adaptive filtering	170
Structural information	365 375
defined	366
extraction of	366
Structured neighborhood model	175
Subsampling	107
Synthetic aperture	
length	26
splitting	29
<i>See also</i> SAR, SAR images	

T

TABOO algorithm	179
Target classification	305 434
confusion matrix for	307
description of	314
eigenimage	307
quadratic distance correlation	307
shift-invariant two-dimensional pattern matching	307

Index terms**Links**

Target classification (*Continued*)

See also Targets

Target detection	83	279
applied to airborne X-band SAR image	303	
Bayesian	278	279
CFAR	279	282
change	305	306
configuration diagram	281	
configuration drawback	295	
false alarms and	300	304
introduction to	279	
MAP criterion	280	
ML criterion	280	
optimized	284	
optimized for textured target model	289	
probability	281	285
refinements to	294	
target type and	295	
<i>See also</i> Targets		
Target discrimination	299	314
defined	300	
features	301	
Target recognition	279	296
ATR	296	305
introduction to	296	
with SAR images	296	
target discrimination and	299	
theoretical framework for	306	
Targets	277	
calibration	322	
characterizing	278	
defined	277	
discriminating from false alarms	304	

Index terms**Links**

Targets (*Continued*)

distributed	38	91	99	102
homogeneous	112			
localized	311			
point	38	54		
superimposed on uniform clutter background	311			
Swerling 1	286	290		
types of	295			
uniform	32			

See also Target detection; Target recognition

Target super-resolution	308			
conclusions	313			
example	311			
reconstruction stages	312			
theory	308			
Taylor expansion	47	164	311	
Tetragamma function	241			
Texture classification	245	425		
annealed	247			
average probabilities for	247			
by fitting	245	266		
correct, average probability comparison	247			
correlated	266			
direct	246			
direct spectrum	266			
likelihood	247			
performance	271			
<i>See also</i> Textures				
Textured target model	289	455		
defined	289			
optimized detection for	289			
Texture exploitation	229			
flow diagram	254			

Index terms**Links**

Texture exploitation (<i>Continued</i>)	
model-free	231
Textures	83
ACF	274
boundaries	124
comparison of	146 148
correlated	259
defined	124
K-distributed	240
likelihood	247
measurements	91
model-based parameter estimation	231 235
natural clutter	125
in polarimetric data	350
regions	253
simulated	145 148
woodland	140 148
Texture segmentation	249
algorithm comparison	253
annealed	251
edge detection	249
joint mean and order parameter	252
model-based	251
<i>See also</i> Segmentation; Textures	
Theoretical distributions	90
Time-bandwidth product	23
Touzi ratio	205
U	
Uncorrelated channels	431
Urban areas	454

Index termsLinks**V**

Voltage, converting 36

W

Weibull distribution 127 128 129 136
Wiener filter 310
World models 5 157

Z

Zero-padding 109